SCHOOL OF EARTH SCIENCES AND ENGINEERING

Department of Sustainable Natural Resources

MULTI-PROXY CONSTRAINTS ON THE ORIGIN, DYNAMICS, AND GEOCHEMICAL EVOLUTION OF SOIL INORGANIC CARBON IN SEMI-ARID LANDSCAPES OF BOTSWANA

by

FERDINAND JUNIOR DINA EBOUEL

Student ID number: 22017760

BSc (Geology) University of Yaoundé 1, MSc (Geology) University of Yaoundé 1

A Thesis Submitted to the School of Earth Sciences and Engineering in Partial Fulfilment of the Requirements for the Award of the Degree of Doctor of Philosophy in Environmental Science of BIUST

Supervised by

Professor Peter N. Eze

Department of Sustainable Natural Resources

School of Earth Sciences and Engineering

Botswana International University of Science and Technology

Professor Thierry Bineli Betsi

Department of Geology and Geological Engineering

School of Earth Sciences and Engineering

Botswana International University of Science and Technology

August, 2026

BOTSWANA INTERNATIONAL UNIVERSITY OF SCIENCE & TECHNOLOGY

POSTGRADUATE SCHOOL

Declaration Regarding the Work and Copyright

DECLARATION REGARDING THE WORK AND COPYRIGHT

Candidate (please write in caps or type) FERDINAND JUNIOR DINA EBOUEL

Student ID: 22017760

Thesis Titled: MULTI-PROXY CONSTRAINTS ON THE ORIGIN, DYNAMICS, AND GEOCHEMICAL EVOLUTION OF SOIL INORGANIC CARBON IN SEMI-ARID LANDSCAPES OF BOTSWANA

I, the **Candidate**, certify that the Thesis is all my own original work and that I have not obtained a degree in this University or elsewhere on the basis of any of this work.

(If the thesis is based on a group project, then the student must indicate the extent of her / his contribution, with reference to any other theses submitted or published by each collaborator in the project, and a declaration to this effect must be included in the thesis)

This dissertation/thesis is copyright material protected under the Berne Convention, the Copyright and Neighbouring Rights Act, Act. No. 8 of 2000 and other international and national enactments, in that behalf, on intellectual property. It must not be reproduced by any means, in full or in part, except for short extracts in fair dealing; for researcher private study, critical scholarly review or discourse with an acknowledgement, without the written permission of the office of the Postgraduate School, on behalf of both the author and the BIUST.

Signed: ---------- Date: 18/08/2026

Primary Supervisor (please write in caps or type) Prof. Peter N. Eze

I, the Candidate's **Primary Supervisor**, hereby confirm that I have inspected the above titled thesis and, to the best of my knowledge, it is based on the original work of the candidate.

Signed: ---------- Date: 17.08.2026

Abstract

Soil inorganic carbon (SIC) constitutes a major component of the terrestrial carbon pool, particularly in dryland environments where pedogenic carbonates dominate long-term carbon sequestration. Despite its diverse environmental and ecological importance, SIC remains largely underrepresented in global carbon budgets, a deficit compounded by a lack of research into its formation dynamics and role as a proxy for paleoenvironmental and climatic evolution. This thesis addresses the prominent theoretical and methodological gaps through a progressive, multi-scale investigation of SIC in the semi-arid landscapes of Botswana. Using pedological and sedimentological approaches, the study characterised SIC formation pathways across major landscape units by integrating morphological examinations, mineralogical analyses, major and trace element geochemistry, and stable isotopes ($\delta^{13}C$, $\delta^{18}O$). The findings highlight a regional dominance of pedogenic carbonate accumulation, driven by the mobilisation of calcium ions within distinct hydrological and geological settings. In the Kalahari Basin, this process is driven by felsic rock weathering and local fluviolacustrine reworking of lithogenic materials. Two mechanisms operate simultaneously. Mobilised calcium may originate from the *in-situ* dissolution of pre-existing carbonates or from the upward movement of calcium-enriched soil solutions through evapotranspiration. While on the Eastern Hardveld, calcium is primarily supplied by the weathering of silicate-rich basaltic rocks. The results highlight an *in-situ* mobilisation mechanism linked to the weathering of basaltic rock fragments reworked into the soils, in addition to upward movement. Stable isotope of carbon ($\delta^{13}C$) and oxygen ($\delta^{18}O$) signatures in carbonates indicate persistent semi-arid conditions and C3-C4 mixed vegetation. Furthermore, REE fractionation patterns and negative cerium anomalies provide robust, independent constraints for distinguishing pedogenic from lithogenic signatures, overcoming limitations of major-element-based interpretations. Collectively, these results advance the geochemical understanding of SIC formation in underrepresented regions and provide a

transferable methodological framework for investigating soil carbon dynamics. This work reduces critical uncertainties in the global carbon budget and establishes a transferable framework for tracing SIC formation across semi-arid environments.

Dedication

Dedicated to my mother, Bitoumou Nteme Josephine. Your twenty-five years of resilient strength and your belief in the transformative power of education provided the foundation for this work. Thank you for the love and sacrifice that made this PhD possible.

And to my children, Grace Divine Bidjogo Ebouel, Samuel Nathanael Ngotty Ebouel and Adriel Claude Bissene Ebouel. You are so young, yet you have already shared in the sacrifice of this journey. I hope that one day you will look at this work and understand that every moment apart was driven by my love for you and my desire to build a better future for us all.

Acknowledgments

As this academic endeavour comes to an end, my first words of gratitude go to my two supervisors, Professor Peter N. Eze and Professor Bineli Betsi. It has been an extraordinary journey working with you, and I am deeply grateful for your constant support, both scientific and personal. Your guidance, encouragement, and open-mindedness have profoundly shaped my scientific thinking. Thank you for the trust you placed in me and for providing a stimulating environment that allowed me to grow throughout this work.

I am also indebted to the Botswana International University of Science and Technology (BIUST) for providing the institutional environment that supported this research, and for the Postgraduate Research Grant (REF: DVC/RDI/2/1/7 V (281)), which funded my fieldwork and a significant portion of the laboratory analyses.

My sincere thanks go to Professor Stefan Norra from University of Potsdam, Germany, and Professor Elisabeth Eiche from Karlsruhe Institute of Technology, Germany, whose support made possible the elemental and isotopic geochemical analyses central to this study. I also thank them for their valuable scientific contributions as co-authors of several research articles included in this thesis.

I am deeply grateful to the amazing academic and non-academic staff of Sustainable Natural Resources Department, for their numerous supports. Your warmth, friendliness and readiness to render assistance at a short notice is highly appreciated. I am lucky to have crossed path with you all.

I extend my warmest gratitude to Professors Timoleon Kofane and Conrad Tabi from Physics and Astronomy Department and Dr Jerome Yendaw from Geology and Geological Engineering Department for their constant support, precious advice, and guidance.

I would like to thank Dr Trust Manyiwa and Dr Tebogo Kelepile for their respective contributions and guidance, and laboratory technicians Mr. Madiba Mothusi and Mr. Tshepho Gaogane for their assistance during the analytical phases.

To my postgraduate colleagues in the Departments of Sustainable Natural Resources and Geology and Geological Engineering: sharing this journey with you has been an exceptional experience. I would like to extend special thanks to Kono Charles, Tsholofelo Molale, Trhas Kahsay, Hengari Mosimanegape, and Katlarelo Lenny Sefatlhi, who contributed to various stages of this project.

Thank you to Patience Ponyane for the assistance and constant moral support, and to Edwin Francis Memirieki and his family. Being their neighbour has been a privilege, and I truly value the warm social environment and friendship they provided during my studies.

To Nguetse Tiobou Richard, my brother who has never stopped supporting me and who has given his all to help me move forward. I cannot find the words to thank you as I should; from the bottom of my heart, thank you.

To my friends Donfack Temgoua Zephirin, Komolo Koumda Armand and Zackarie Armel Ekoa Bessa, I am grateful for both your moral and financial support.

Finally, I would like to thank my relatives, especially my older sister Bela Ngotty Rosine, my younger sister Ekosso Ebouel, and my younger brother Andang Philippe. I also wish to thank Sandrine Eyenga Nomo, the mother of my children Grace and Samuel, for her support. And Victorine Ambassa Bela for the moral support. Your contributions have been essential to the success of this journey.

To all those, friends, family, instructors, and others, who contributed to this journey and whose names may have been inadvertently omitted, I offer my sincere apologies. Such omissions are unintentional, and I remain deeply grateful for every form of support I received. Thank you all.

Table of Contents

Abstract ii

Dedication iv

Acknowledgments v

Table of Contents vii

List of Figures xv

List of Tables xx

List of Appendices xxii

CHAPTER ONE 1

1.1. Global Context: Climate Change and Carbon Neutrality 1

1.2. The Terrestrial Carbon Cycle and the "Missing" Sink 2

1.3. Regional Focus: The African Drylands 2

1.4. Problem Statement and Research Gaps 3

1.5. Research Objectives 4

1.6. Methodology 4

1.7. Structure of the Thesis 6

References 8

CHAPTER TWO 15

Abstract 15

2.1. Introduction 17

2.2. Trends in global SIC research in the last two decades (2003-2022) 19

2.3. SIC formation pathways 26

2.3.1. Abiotic soil carbonate precipitation 28

2.3.2. Biotic soil carbonate precipitation 30

2.4. Characterisation of soil inorganic carbon 31

2.4.1. Macromorphological description 32

2.4.2. Micromorphological description 32

2.4.3. Stable isotope geochemistry 35

2.4.4. Strontium isotope ratio ($^{87}Sr/^{86}Sr$) to trace calcium origin. 39

2.4.5. Elemental geochemistry and mineralogy 41

2.5. Quantitative techniques in soil inorganic carbon measurements 44

2.5.1. Calcimetric method 44

2.5.2. Dry combustion method 45

2.5.3. Titration 46

2.5.4. Spectroscopic methods 46

2.5.5. Ramped combustion and Loss of ignition 48

2.6. Soil inorganic carbon dynamics 50

2.6.1. Soil inorganic carbon storage 52

2.6.2. Pedogenic carbonate storage 53

2.7. Modelling soil inorganic carbon 54

2.8. Multidisciplinary applications of SIC 58

2.8.1. Ecosystem services 58

2.8.2. Pedogenic carbonate and palaeoreconstruction 59

2.8.3. Geochronology 61

2.8.4. Geoarchaeology 63

2.9. Critical knowledge gaps and future directions for SIC research 64

2.10. Synthesis and Conclusion 67

References 69

CHAPTER THREE 97

Abstract 97

3.1. Introduction 99

3.2. Environmental setting 101

3.3. Materials and methods 104

3.3.1. Materials 104

3.3.2. Laboratory analysis 109

3.3.3. Data processing 111

3.4. Results 112

3.4.1. Soil pH and carbonate content 112

3.4.2. Major elements 113

3.4.3. Rare earth elements 116

3.4.4. Relationships between REEs, calcium carbonate content, and pH 119

3.4.5. Correlation between REEs and major elements 122

3.5. Discussion 126

3.5.1. Distribution of REEs 126

3.5.2. Calcium carbonate, pH and REE as tracers of carbonate origin in the soils 129

3.5.3. Influences of major elements on REE distributions in the studied soil profiles 133

3.6. Conclusions 135

References 136

Appendices 147

CHAPTER FOUR 154

Abstract 154
4.1. Introduction 156
4.2. Geographical and environmental setting 159
4.3. Materials and methods 161
4.3.1. Field investigation and sampling 161
4.3.2. Laboratory analyses 162
4.4. Results 166
4.4.1. Morphological characterisation and physicochemical properties 166
4.4.2. Bulk and clay mineralogy 173
4.4.3. Geochemistry 175
4.5. Discussion 181
4.5.1. Implications for pedogenic processes and depositional environment 181
4.5.2. Sediments Provenance and Weathering 183
4.5.3. Calcium Origin and Pedogenic Carbonate Accumulation 186
4.6. Conclusions 189
References 191
CHAPTER FIVE 201
Abstract 201
5.1. Introduction 203
5.2. Environmental setting 205
5.3. Material and methods 207
5.3.1. Field investigations and sampling 207
5.3.2. Laboratory analysis 208
5.3.3. Data processing 210

5.4. Results 213
5.4.1. Morphological characterisation and physicochemical properties 213
5.4.2. Particle size analysis and micromorphology of the selected sandy layers 223
5.4.3. Geochemistry 226
5.5. Discussion 231
5.5.1. Sedimentary controls and depositional environments 231
5.5.2. Pedogenic controls and processes 233
5.6. Conclusions 238
References 240
CHAPTER SIX 247
Abstract 247
6.1. Introduction 249
6.2. Environmental setting 252
6.3. Material and methods 254
6.3.1. Field sampling and sections description 254
6.3.2. Mineralogical analyses 260
6.3.3. Elemental geochemistry 262
6.3.4. Data treatment 263
6.4. Results 265
6.4.1. Characterisation of soil parent materials and carbonate features 265
6.4.2. Geochemistry 272
6.5. Discussion 276

6.5.1. Indices of the mafic lithology contribution to Ca furniture in carbonate features 276
6.5.2. Calcium transfer and mobilisation pathways 279
6.6. Conclusions 283
References 285
Appendices 293
CHAPTER SEVEN 295
Abstract 295
7.1. Introduction 297
7.2. Materials and methods 299
7.2.1. Study site and sampling strategy 299
7.2.2. Sample preparation 305
7.2.3. Iron and manganese elemental analysis 306
7.2.4. Stable isotope analyses 307
7.3. Results 308
7.3.1. Manganese and iron concentration in the sections 308
7.3.2. Manganese and iron concentration in carbonate features 310
7.3.3. Stable isotope of carbon and oxygen in carbonate features 313
7.4. Discussion 316
7.4.1. Vegetation dynamics and stable carbon isotopes in pedogenic carbonates 316
7.4.2. Climate dynamics and stable oxygen isotopes in pedogenic carbonates 318
7.4.3. Hydrological conditions and carbonate precipitation 321
7.5. Conclusions 326
References 328

Appendices....337

CHAPTER EIGHT....339

Abstract....339

8.1. Introduction....340

8.2. Material and methods....342

8.2.1. Study area....342

8.2.2. Sampling strategy....344

8.2.3. Analytical methods....345

8.2.4. Data treatment....347

8.3. Results....349

8.3.1. Physico-chemical properties of the soils....349

8.3.2. Ca and Mg in Carbonates....350

8.3.3. REEs in the soil profiles....351

8.3.4. REEs in the pedogenic carbonates....355

8.3.5. Principal component analysis....357

8.4. Discussion....362

8.4.1. REE signatures of pedogenic carbonates and their controls....362

8.4.2. REEs in pedogenic carbonate as indicator of redox and environmental conditions....364

8.4.3. Pedogenic vs. lithogenic origin: A high-resolution approach....367

8.5. Conclusions....368

References....370

Appendices....376

CHAPTER NINE....379

9.1. Recapitulation of the problem statement and objectives 379
9.2. Synthesis of key findings 379
9.3. Significance and contributions 380
9.4. Limitations of the study 381
9.5. Perspectives and recommendations 382
References 383

List of Figures

Fig. 2.1. Description of the process used for the bibliometric analysis 21

Fig. 2.2. **a**. Trend in the number of scientific publications relating to the SIC between 2003 and 2022; **b**. Trend in the number of scientific publications relating to the SOC compared to the number of scientific publications relating to SIC between 2003 and 2022. 23

Fig. 2.3. Box plots of the number of SIC-related publications over the period 2003-2012 compared with the period 2013-2022. 23

Fig. 2.4. Major SIC research topics identified by bibliometric analysis between 2003 and 2022 24

Fig. 2.5. Spearman correlation matrix (p-value=0.01) for the main SIC research topics identified by the bibliometric analysis. The cells marked with a cross indicate that there is no correlation between the two variables at the significance level. **AQT**: Advances in quantification techniques; **CAFP**: Characterisation and identification of formation processes; **ADS**: Assessment of sic dynamics and storage; **MM**: Modelling and Mapping; **SQES**: Carbon cycle, Soil quality and ecosystem services; **PGA**: Palaeoenvironmental reconstruction and geoarchaeology; **Total**: Total number of research publication.....26

Fig. 2.6. Progression rate (%) in SIC research from 2003-2012 decade to 2013-2022, classified by topic.....28

Fig. 2.7. Geographical output of SIC research based on the identified themes. 30

Fig. 2.8. Factors affecting SIC dynamics.....49

Fig. 2.9. Ecosystem services of SIC based on the work of Groshans et al. (2018). 59

Fig. 3.1. Geological background of the sampling area. 104

Fig. 3.2. Calcium carbonate features in the study profiles A. Diffuse powder coating sand grains in K1P1; B. Indurate layer in M1P1; C. soft nodules and diffuse powder coating peds in

Vertisols in profile SP3; D. Soft carbonate nodules in TK2; E. Diffuse powder coating peds in TK2. 109
Fig. 3.3. Boxplot showing the variation in A. calcium carbonate content (wt.%) and B. pH in the study soil profiles. The box (orange for calcium carbonate content and grey for pH) represents the interquartile range. The lower and upper limits of the box represent the 25th percentile and the 75th percentile respectively. The horizontal line inside the box represents the median. The whiskers extend to the minimum and maximum values within 1.5 × IQR. The cross represents the mean..... 113
Fig. 3.4. Distribution of major elements (%) in the soil profiles. The box represents the interquartile range; the lower and upper limits of the box represent the 25th percentile and the 75th percentile respectively. The horizontal line inside the box represents the median. The whiskers extend to the minimum and maximum values within 1.5 × IQR. The cross represents the mean. 115
Fig. 3.5. REE contents normalised to the UCC in the twelve soil profiles..... 117
Fig. 3.6. Correlation matrix of REEs indices, pH and calcium carbonate content (wt.%) in A. All the study profiles; B. The northern profiles; C. The central profiles; D. The southern profiles 121
Fig. 3.7. Correlation matrix of REEs indices, pH and calcium carbonate content (wt.%) in A. All the study profiles; B. The northern profiles; C. The central profiles; D. The southern profiles. 123
Fig. 3.8. Correlation circle of REE indices and major elements A. All the study profiles; B. The northern profiles; C. The central profiles; D. The southern profiles. 125
Fig. 4.1. A simplified model for pedogenic carbonate formation in arid environments..... 157
Fig. 4.2. Regional context of the study area showing the Parakarungu open quarry location 161

Fig. 4.3. A. Schematic representation and photograph of the section of the Parakarungu open quarry; B. shell fragments observed in the Ck layer; C. accumulation of carbonate in the tunnels left by termites in C_{kk} layers; D. gravel in the fine sand matrix of C_{VFS} layers; E. gravel showing signs of weathering (oxidation) in C_{VFS} layers. 169

Fig. 4.4. Particle size distribution based on inclusive statistics parameter (Folk and Ward, 1957). 173

Fig. 4.5. A. Correlation circle of major oxides; B. Biplot samples-major oxides; C. results of linear regression between carbonate and calcium; D. results of linear regression between Calcium and strontium.....178

Fig. 4.6. A. Trends of Ca/Sr along the section; B. Trends of Al/Si along the section. 179

Fig. 4.7. Projection of Parakarungu samples in the ternary diagram: Mafic-Felsic-RW.....180

Fig. 4.8. Pedogenic model of carbonate accumulation in Parakarungu open quarry section.189

Fig. 5.1. A. Location map of the study area; B. A zoomed-out map of the study area; C. 3D topographic model of the study area. 208

Fig. 5.2. Field Photographs and Correlative Stratigraphic Representations of A. Section 01 (SC01); B. Section 02 (SC02); C. Section 03 (SC03); and D. Section 04 (SC04). 213

Fig. 5.3. Particle size distribution with depth in the four sections. 216

Fig. 5.4. A. Soft carbonate concretions isolated from the layer Bkkb of SC01; B. Pseudomycelia observed in layers CB4b of SC01; C. Gravels isolated from the layer C1 of SC01; D. Gravels isolated from SC02; E. Hard carbonate concretions isolated from the layer BCkkb of SC03; F. Hard carbonate concretions isolated from the layer BCkkb of SC04. 220

Fig. 5.5. (A–E). Images of the sand fraction, observed under a petrographic microscope using Plane Polarised Light (PPL), detailing the morphological characteristics of the grains. Images B, C, and D show the sand fraction from Layer C1 across Sections SC01, SC02, and SC03,

respectively. Image E illustrates the sand fraction from Layer C2 within the same section SC03. Image F provides the observation for the Layer AC in section SC04. 225
Fig. 5.6. Vertical distribution profiles of five geochemical indices: calcification index, Mg/Ca ratio, salinisation, clayeyness index, and robust index of chemical weathering (RW), across the depth of the respective studied sections. 229
Fig. 6.1. A. Location map of the study area; B. A zoomed-out map of the study area; SC01 to SC04. field photographs of the study sections. 254
Fig. 6.2. Representation of the studied sections. The naming of horizons follows the recommendations of the IUSS Working Group WRB (2022). 256
Fig. 6.3. Representative rock fragments isolated from the pedosedimentary sections. (A) Sandstone fragment from SC02; (B) sandstone and dolerite fragments from SC03; (C–D) micrographs of a preserved dolerite fragment from SC01; (E–F) micrographs of partially weathered sandstone from SC02; (G–H) micrographs of partially weathered amygdaloidal basalt from SC01, in which primary minerals remain clearly identifiable. 258
Fig. 6.4. A. Amygdaloidal basalt sample; B. Dolerite sample; C. Sandstone sample; D. Mudstone sample; E. Pseudomycelia carbonate accumulation observed in AB3b (SC01); F. Calcium carbonate nodules observed in BCkb (SC03).....261
Fig. 6.5. Photomicrographs of the main lithology: dolerite (A: XPL; B: PPL); amygdaloidal basalt (C: XPL; D: PPL); sandstone (E: XPL; F: PPL); and mudstone (G: XPL; H: PPL)...269
Fig. 6.6. Carbonate features XPL microphotographs. A. Nodule Nd01 collected from Bk2 in SC01 (Nd01); B. Pseudomycelium Ps collected from AB3b in SC01; C. Nodule Nd03 collected from Bkb in SC01; D. Nodule Nd06 collected from BCk2b in SC02; E. Nodule Nd10 collected from BCk1b in SC03; F. Nodule Nd14 collected from BCk1b in SC04. 271
Fig. 6.7. Projection of samples in the ternary diagram: Mafic-Felsic-RW (Cho and Ohta, 2022) 275

Fig. 7.1. A. localisation of the study area in the map of Botswana; B. 3D topographic model of the study area, showing the river setting and the four selected sections.....303
Fig. 7.2. a, d, e, f. Stratigraphy of the four study sections; b. photograph of calcium carbonate nodules isolated from SC04; and c. photograph of pseudomycelia calcium carbonate accumulation in SC01. 305
Fig. 7.3. Trend of Mn and Fe in the four study sections (SC01, SC02, SC03 and SC04).....309
Fig. 7.4. Patterns of Mn/Fe ratio of the selected carbonate features.....312
Fig. 7.5. Stable carbon and oxygen isotopes of carbonate features. 315
Fig. 7.6. Cross-plot of $\delta^{13}C$ and $\delta^{18}O$ for pedogenic carbonate features. 321
Fig. 7.7. Cross-plot of $\delta^{18}O$ and Mn/Fe of pedogenic carbonate features. 325
Fig. 8.1. a. isolated pedogenic carbonates nodules; b. pseudomycelia carbonate (Ps) in P01 (the coin and the geologist's hammer are used as a scale). 344
Fig. 8.2. Patterns of REEs in each of the studies soil profiles 354
Fig. 8.3. Patterns of REEs in the pedogenic carbonates. 357
Fig. 8.4. **a.** and **c.** correlation circle and biplot showing relationship between physico-chemical properties, REEs abundance and REEs indices in the soil; **b.** and **d.** correlation circle and biplot showing relationships between Ca, Mg, REEs concentrations and REEs indices in pedogenic carbonates. 361

List of Tables

Table 2.1. Technique used for micromorphological description of SIC.....34

Table 2.2. Comparison of methods for measuring SIC content.....51

Table 2.3. Summary of modelling approaches used for SIC studies.....56

Table 3.1. Geographical coordinates and background knowledge of the studied soil profiles 102

Table 3.2. Physico-chemical properties of northern soil profiles.....106

Table 3.3. Physico-chemical properties of central soil profiles.....107

Table 3.4. Physico-chemical properties of southern soil profiles.....108

Table 3.5. Cerium anomalies (Ce/Ce*), europium anomalies (Eu/Eu*) and LREE/HREE ratios normalised to the UCC in the study profile 119

Table 4.1. Morphological properties of the section.....170

Table 4.2. Physicochemical properties of the section.....171

Table 4.3. Semiquantitative composition of the bulk and clay mineralogy of the Parakarungu open quarry section.....175

Table 4.4. Composition of major oxides, robust index of chemical weathering (RW), chemical index alteration (CIA), weathering index of Parker (WIP), index of compositional variability (ICV) and strontium content in the Parakarungu open quarry.....177

Table 5.1. Morphological characteristics and physicochemical properties of section SC01.215

Table 5.2. Morphological characteristics and physicochemical properties of section SC02.218

Table 5.3. Morphological characteristics and physicochemical properties of section SC03.221

Table 5.4. Morphological characteristics and physicochemical properties of section 04 222

Table 5.5. Statistical grain size parameters (Mz: mean size; σI: inclusive standard deviation/sorting; SkI: inclusive skewness; KG: graphic kurtosis) for the selected sandy layers (C1, C2, and AC) across the studied sections (SC01–SC04). 223

Table 5.6. Elements concentration of the four sections 228

Table 6.1. Samples repartition and coding.....259

Table 6.2. Semi-quantitative mineralogical composition of the samples 267

Table 6.3. Element content of samples 273

Table 7.1. Manganese and iron contents (mol%) in the selected carbonate features 311

Table 8.1. Location of the studied sections.....343

Table 8.2. Ca, Mg, REEs concentration and fractionation indices of REEs in the carbonates 351

Table 8.3. Concentration of REEs and fractionation indices of REEs in the studied soil profiles 353

Table 8.4. Contribution of each variable to the first three dimensions of PCA of soil profiles. 358

Table 8.5. Contribution of each variable to the first three dimensions of PCA of carbonates. 360

List of Appendices

Appendix 3.1. Ba/Eu ratio of the study samples.....147

Appendix 3.2. Major elements contents (wt.%) in the profiles of the study 149

Appendix 3.3. REE contents (mg kg^{-1}) in the study area.....151

Appendix 6.1. Quality control. 293

Appendix 6.2. Major oxides in weight percent.....294

Appendix 7.1 Stable isotope ratios of carbon ($^{13}C/^{12}C$) and oxygen ($^{18}O/^{16}O$) in carbonate features and laboratory quality control. 337

Appendix 7.2. Fe, Mn concentration in molar percent and Mn/Fe ratio in the study sections. 338

Appendix 8.1. Physico-chemical properties of the studied soil profiles.....376

Appendix 8.2. REEs concentration in the studied soil profiles. 377

Appendix 8.3. Correlation matrix between REE indices, Mg and Ca within carbonate features. 378

CHAPTER ONE

General Introduction

1.1. Global Context: Climate Change and Carbon Neutrality

Anthropogenic climate change, driven by rising greenhouse gas (GHG) concentrations, is a central challenge for both Earth system stability and socioeconomic resilience (Dumortier et al., 2021; Lathouwers et al., 2025; Martinez and Iglesias, 2021; Martins et al., 2024). Furthermore, the impacts highlight the inequalities between developed and developing countries, with the latter being more severely affected (Adom, 2024; Malik et al., 2026; Wu et al., 2026). Reducing atmospheric CO_2 emissions has therefore become a critical global priority (Calvin et al., 2023).

A central international objective is to limit global warming to 1.5 °C. Achieving this target requires a reduction in total GHGs of around 45% by 2030, compared with 2010 levels. This is an essential step towards achieving the target of "carbon neutrality" by 2050, which involves ensuring that all remaining human-caused emissions are fully offset by carbon sequestration (Masson-Delmotte et al., 2019). The commitments of the Paris Agreement have led to significant progress in the development of renewable energy technologies (UNFCCC, 2025). They have also encouraged the emergence of carbon dioxide removal (CDR) technologies such as enhanced rock weathering (ERW) (Beerling et al., 2020).

It is, however, necessary to make an exhaustive inventory of natural carbon sinks and storage pathways, without which it is difficult to develop conservation or management policies (Fan and Wei, 2022; van der Ploeg and Haigh, 2024). The terrestrial subsurface is an essential, albeit not yet fully quantified, component of the global carbon cycle. According to the 2024 Global Carbon Budget (Friedlingstein et al., 2025), while soils store significantly more carbon than the atmosphere and biomass combined, uncertainties associated with biospheric fluxes

significantly contribute to the imbalance in the global carbon budget. Nevertheless, the importance of this carbon reservoir is confirmed by its absorption capacity: the terrestrial sink sequestered around 30% of CO_2 emissions between 2014 and 2023 (Friedlingstein et al., 2025).

1.2. The Terrestrial Carbon Cycle and the "Missing" Sink

Soil carbon exists in two forms: organic, which results from the decomposition of organic matter, and inorganic, which is associated with carbonate minerals. The former is known as soil organic carbon (SOC), while the latter is known as soil inorganic carbon (SIC). However, their sequestration potentials are not equally considered. While tremendous efforts are being made to raise awareness, preserve and enhance SOC across various land-use systems (Koutika et al., 2025), SIC is largely overlooked (Sharififar et al., 2023). Though, SIC accounts for a significant proportion of soil carbon in dry environments, which cover over 40% of the Earth's land surface (Naorem et al., 2022). SIC is even considered a long-term carbon sink, surviving through geological timescales and constituting palaeoenvironmental and palaeoclimatic archives capable of surviving potential diagenetic reworking (Breecker et al., 2025; Ning et al., 2025).

1.3. Regional Focus: The African Drylands

Despite its relevance, SIC remains critically understudied in Africa, where there are very few research initiatives (Raza et al., 2024). It remains largely absent from continental climate and land management frameworks (African Union, 2015). Yet nearly 35% of the continent is made up of arid and semi-arid environments (Naorem et al., 2022). Including dry sub-humid areas, drylands account for nearly 70% of the African continent (Cherlet et al., 2018). This suggests that soil carbon potential is significantly underestimated in continental budgets. At the same time, SIC resources may be vulnerable to degradation (decarbonisation) under current land-use systems due to the absence of targeted conservation measures (Ferdush and Paul, 2021).

Conversely, a thorough investigation of resources, potential, and formation processes would pave the way for SIC consideration in various land uses, particularly in agroecosystems and in the conservation and restoration of natural areas. Furthermore, the study of pedogenic carbonates (SIC resulting from pedogenesis) provides a reliable indicator for reconstructing palaeoenvironmental and palaeoclimatic changes in this region (Zamanian et al., 2016). This is of particular importance given the paucity of terrestrial archives capable of recording long-term environmental changes in African soils on a geological timescale (Levin et al., 2011).

Botswana serves as a quintessential example of a dryland region in Africa. The entire country experiences a semi-arid climate, with mean annual precipitation varying from 312 mm in the southwestern part to 574 mm in the northeastern region (Batisani and Yarnal, 2010). Numerous studies emphasize the prevalence of carbonates in the landscape (Diaz et al., 2019; Mccarthy et al., 1991; White and Eckardt, 2006). However, their capacity to sequester atmospheric carbon or to indicate past environmental and climatic changes in the area is seldom discussed. Yet, the geological landscape, marked by the existence of Stormberg basaltic lavas (Bordy, 2020; Smith, 1984), positions it as a natural laboratory, suggesting a significant potential for atmospheric CO_2 sequestration through weathering processes. Additionally, there is evidence that carbonates have developed within palaeosols (Eze, 2022; Franchi et al., 2021).

1.4. Problem Statement and Research Gaps

Despite its importance, several key limitations hinder the integration of SIC into global carbon strategies. First, there is a lack of comprehensive synthesis, with research trends and analytical limitations remaining poorly constrained. Second, mechanistic understanding of calcium sources and the distinction between lithogenic and pedogenic carbonates remains limited, particularly in complex geological settings. Third, the scarcity of spatiotemporal datasets in Africa restricts robust palaeoenvironmental reconstructions. It is essential to address these gaps not only for accurate carbon accounting, but also to develop informed conservation policies in

arid regions. Addressing these challenges requires an integrated geochemical and isotopic framework capable of constraining SIC sources, formation mechanisms, and environmental significance.

1.5. Research Objectives

The main objectives of this thesis are to:

- Characterise and quantify the spatial distribution and geochemical properties of SIC in the semi-arid landscapes of Botswana.
- Identify the main sources of calcium and reconstruct its mobilisation pathways through the combined use of geochemical tracers.
- Distinguish between pedogenic and sedimentary controls on carbonate accumulation to differentiate between in situ formation processes and lithogenic legacy.
- Reconstruct high-resolution palaeoenvironmental and palaeoclimatic conditions by interpreting the stable isotope signatures ($\delta^{13}C$ and $\delta^{18}O$) preserved in the carbonate record.

1.6. Methodology

This study adopts an integrated multi-proxy methodological framework combining field-based pedological investigations, mineralogical and geochemical analyses, and stable isotope geochemistry to investigate SIC dynamics. The framework is structured around four complementary methodological components aligned with the research objectives.

To characterise and quantify the spatial distribution of SIC, twelve representative soil profiles were collected across contrasting geomorphological and lithological environments, following a sampling design aligned with the Botswana Kalahari Transect, known to reflect the country's rainfall and vegetation gradients (Mphale et al., 2014; Ringrose et al., 2003). Given the size and environmental heterogeneity of Botswana, this sampling does not capture the full national

variability of SIC accumulation processes but provides a first insight into these processes at a large scale. Following analysis of the twelve profiles, two prominent landscapes were selected for detailed investigation, as they presented the first evidence of contrasting carbonate formation processes: a quarry in Parakarungu, in the northern part of the country, developed on fluvio-lacustrine sediments of the Kalahari Group; and a pedosedimentary landscape in Serowe, in the central part, developed on sandstone and basaltic lava of the Karoo Supergroup. Field investigations involved soil profile description and horizon differentiation following the FAO Guidelines for Soil Description (2006). Carbonate features including diffuse powder, nodules, and pseudomycelia were identified to determine stages of carbonate development according to Gile (1993). SIC contents were quantified as $CaCO_3$ equivalents using an Eijkelkamp calcimeter, while mineralogical composition was determined through X-ray diffraction (XRD).

To identify the principal sources of calcium and reconstruct its mobilisation pathways, the study adopted an integrated approach combining mineralogical and morphological characterisation with elemental geochemistry. Emphasis was placed on the robust chemical weathering index (Cho and Ohta, 2022), which enables the identification of mafic versus felsic source materials in environment characterised by secondary accumulations. Other geochemical indices such Mg/Ca, Sr/Ca were also used to refines the interpretations. Mineralogical analyses and micromorphological observations were further used to evaluate carbonate redistribution and mobilisation processes within the soil system.

The distinction between pedogenic and sedimentary carbonate accumulation was established using a progressive and integrated approach combining field observations, geochemical indicators, and REE fingerprint analysis. Initial differentiation relied on REE signatures to identify regions dominated by pedogenic carbonate accumulation from those dominated by lithogenic carbonates. This approach was subsequently supported by weathering indices and

elemental mobility proxies to assess the intensity of pedogenic weathering. The REE-based method was further refined by focusing on the signature of carbonate features rather than bulk soil horizons, where calcification-related REE signals may be obscured by other pedogenic processes.

Palaeoenvironmental reconstruction was conducted using stable isotope analyses of pedogenic carbonates. Carbon ($\delta^{13}C$) and oxygen ($\delta^{18}O$) isotope compositions were used to infer vegetation dynamics, hydrological conditions, and palaeoclimatic variability. These isotopic proxies were coupled with Mn/Fe ratios to assess redox fluctuations and palaeohydrological conditions during carbonate formation. In addition, rare earth element (REE) signatures provided complementary information on environmental conditions and weathering dynamics associated with carbonate formation.

1.7. Structure of the Thesis

The work is structured around nine chapters, including this general introduction.

Chapter 2 presents a comprehensive review of global research on inorganic soil carbon. It analyses analytical techniques and ecosystem functions and identifies critical knowledge gaps that form the basis of this thesis.

Chapter 3 investigates the use of rare earth elements (REEs) as tracers to identify carbonate sources in soils of the Kalahari Basin, examining the influence of parent materials on pedogenic processes.

Chapter 4 investigates the use of a multi-proxy approach, including mineralogy, weathering indices and Ca/Sr ratios, to reconstruct depositional environments and sediment provenance in northern Botswana.

Chapter 5 examines the interaction between fluvial sedimentation and pedogenesis. It demonstrates how geochemical indices can be used to distinguish sedimentary controls from secondary calcification processes.

Chapter 6 examines basalt weathering as a primary source of calcium and its role in driving pedogenic carbonate formation within the riverine landscapes of central Botswana.

Chapter 7 discusses the use of stable carbon ($\delta^{13}C$) and oxygen ($\delta^{18}O$) isotopes to decouple climatic signals from local hydrology, thereby offering new insights into past climate stability in Botswana.

Chapter 8 explores the use of REE signatures as high-resolution indicators to distinguish the formation mechanisms of pedogenic carbonates from lithogenic carbonates in the landscapes of the Eastern Hardveld.

Finally, Chapter 9 summarises the thesis's main findings, discusses their implications for the African carbon budget, and proposes recommendations for integrating SIC into land management and climate mitigation policies.

References

Adom, P.K., 2024. The socioeconomic impact of climate change in developing countries over the next decades: A literature survey. Heliyon 10, e35134. https://doi.org/https://doi.org/10.1016/j.heliyon.2024.e35134

African Union, 2015. Agenda 2063 : the Africa we want. African Union Commission.

Batisani, N., Yarnal, B., 2010. Rainfall variability and trends in semi-arid Botswana: Implications for climate change adaptation policy. Applied Geography 30, 483–489. https://doi.org/10.1016/j.apgeog.2009.10.007

Beerling, D.J., Kantzas, E.P., Lomas, M.R., Wade, P., Eufrasio, R.M., Renforth, P., Sarkar, B., Andrews, M.G., James, R.H., Pearce, C.R., Mercure, J.-F., Pollitt, H., Holden, P.B., Edwards, N.R., Khanna, M., Koh, L., Quegan, S., Pidgeon, N.F., Janssens, I.A., Hansen, J., Banwart, S.A., 2020. Potential for large-scale CO2 removal via enhanced rock weathering with croplands. Nature 583, 242–248. https://doi.org/10.1038/s41586-020-2448-9

Bordy, E.M., 2020. Depositional style changes during the Permo-Carboniferous–Early Jurassic evolution of the Central Kalahari Karoo Sub-basin, Botswana. Geological Journal 55, 5514–5539. https://doi.org/https://doi.org/10.1002/gj.3751

Breecker, D.O., Michel, L.A., Rasmussen, C., Tabor, N.J., 2025. A biogeochemical perspective on pedogenesis from soils to paleosols, in: Anbar, A., Weis, D. (Eds.), Treatise on Geochemistry (Third Edition). Elsevier, Oxford, pp. 353–409. https://doi.org/https://doi.org/10.1016/B978-0-323-99762-1.00094-2

Calvin, K., Dasgupta, D., Krinner, G., Mukherji, A., Thorne, P.W., Trisos, C., Romero, J., Aldunce, P., Barrett, K., Blanco, G., Cheung, W.W.L., Connors, S., Denton, F., Diongue-Niang, A., Dodman, D., Garschagen, M., Geden, O., Hayward, B., Jones, C., Jotzo, F., Krug, T., Lasco, R., Lee, Y.-Y., Masson-Delmotte, V., Meinshausen, M., Mintenbeck, K., Mokssit, A., Otto, F.E.L., Pathak, M., Pirani, A., Poloczanska, E., Pörtner, H.-O., Revi, A., Roberts, D.C., Roy,

J., Ruane, A.C., Skea, J., Shukla, P.R., Slade, R., Slangen, A., Sokona, Y., Sörensson, A.A., Tignor, M., van Vuuren, D., Wei, Y.-M., Winkler, H., Zhai, P., Zommers, Z., Hourcade, J.-C., Johnson, F.X., Pachauri, S., Simpson, N.P., Singh, C., Thomas, A., Totin, E., Alegría, A., Armour, K., Bednar-Friedl, B., Blok, K., Cissé, G., Dentener, F., Eriksen, S., Fischer, E., Garner, G., Guivarch, C., Haasnoot, M., Hansen, G., Hauser, M., Hawkins, E., Hermans, T., Kopp, R., Leprince-Ringuet, N., Lewis, J., Ley, D., Ludden, C., Niamir, L., Nicholls, Z., Some, S., Szopa, S., Trewin, B., van der Wijst, K.-I., Winter, G., Witting, M., Birt, A., Ha, M., 2023. IPCC, 2023: Climate Change 2023: Synthesis Report. Contribution of Working Groups I, II and III to the Sixth Assessment Report of the Intergovernmental Panel on Climate Change [Core Writing Team, H. Lee and J. Romero (eds.)]. IPCC, Geneva, Switzerland. https://doi.org/10.59327/IPCC/AR6-9789291691647

Cherlet, M., Hill, J., Hutchinson, C., Reynolds, J., Sommer, S., Von Maltitz, G., 2018. World atlas of desertification – Rethinking land degradation and sustainable land management. Publications Office. https://doi.org/doi/10.2760/06292

Cho, T., Ohta, T., 2022. A robust chemical weathering index for sediments containing authigenic and biogenic materials. Palaeogeogr. Palaeoclimatol. Palaeoecol. 608, 111288. https://doi.org/10.1016/J.PALAEO.2022.111288

Diaz, N., Armitage, S.J., Verrecchia, E.P., Herman, F., 2019. OSL dating of a carbonate island in the Chobe Enclave, NW Botswana. Quat. Geochronol. 49, 172–176. https://doi.org/https://doi.org/10.1016/j.quageo.2018.03.001

Dumortier, J., Carriquiry, M., Elobeid, A., 2021. Impact of climate change on global agricultural markets under different shared socioeconomic pathways. Agricultural Economics 52, 963–984. https://doi.org/https://doi.org/10.1111/agec.12660

Eze, P.N., 2022. Soil Development in the Eastern Hardveld, in: Eckardt, F.D. (Ed.), Landscapes and Landforms of Botswana. Springer International Publishing, Cham, pp. 327–344. https://doi.org/10.1007/978-3-030-86102-5_19

Fan, Y., Wei, F., 2022. Contributions of Natural Carbon Sink Capacity and Carbon Neutrality in the Context of Net-Zero Carbon Cities: A Case Study of Hangzhou. Sustainability 14. https://doi.org/10.3390/su14052680

Ferdush, J., Paul, V., 2021. A review on the possible factors influencing soil inorganic carbon under elevated CO2. Catena (Amst). https://doi.org/10.1016/j.catena.2021.105434

Food and Agriculture Organization of the United Nations, 2006. Guidelines for soil description. Food and Agriculture Organization of the United Nations.

Franchi, F., Kelepile, T., Di Capua, A., De Wit, M.C.J., Kemiso, O., Lasarwe, R., Catuneanu, O., 2021. Lithostratigraphy, sedimentary petrography and geochemistry of the Upper Karoo Supergroup in the Central Kalahari Karoo Sub-Basin, Botswana. Journal of African Earth Sciences 173. https://doi.org/10.1016/j.jafrearsci.2020.104025

Friedlingstein, P., O'Sullivan, M., Jones, M.W., Andrew, R.M., Hauck, J., Landschützer, P., Le Quéré, C., Li, H., Luijkx, I.T., Olsen, A., Peters, G.P., Peters, W., Pongratz, J., Schwingshackl, C., Sitch, S., Canadell, J.G., Ciais, P., Jackson, R.B., Alin, S.R., Arneth, A., Arora, V., Bates, N.R., Becker, M., Bellouin, N., Berghoff, C.F., Bittig, H.C., Bopp, L., Cadule, P., Campbell, K., Chamberlain, M.A., Chandra, N., Chevallier, F., Chini, L.P., Colligan, T., Decayeux, J., Djeutchouang, L.M., Dou, X., Duran Rojas, C., Enyo, K., Evans, W., Fay, A.R., Feely, R.A., Ford, D.J., Foster, A., Gasser, T., Gehlen, M., Gkritzalis, T., Grassi, G., Gregor, L., Gruber, N., Gürses, Ö., Harris, I., Hefner, M., Heinke, J., Hurtt, G.C., Iida, Y., Ilyina, T., Jacobson, A.R., Jain, A.K., Jarníková, T., Jersild, A., Jiang, F., Jin, Z., Kato, E., Keeling, R.F., Klein Goldewijk, K., Knauer, J., Korsbakken, J.I., Lan, X., Lauvset, S.K., Lefèvre, N., Liu, Z., Liu, J., Ma, L., Maksyutov, S., Marland, G., Mayot, N., McGuire, P.C., Metzl, N., Monacci, N.M.,

Morgan, E.J., Nakaoka, S.-I., Neill, C., Niwa, Y., Nützel, T., Olivier, L., Ono, T., Palmer, P.I., Pierrot, D., Qin, Z., Resplandy, L., Roobaert, A., Rosan, T.M., Rödenbeck, C., Schwinger, J., Smallman, T.L., Smith, S.M., Sospedra-Alfonso, R., Steinhoff, T., Sun, Q., Sutton, A.J., Séférian, R., Takao, S., Tatebe, H., Tian, H., Tilbrook, B., Torres, O., Tourigny, E., Tsujino, H., Tubiello, F., van der Werf, G., Wanninkhof, R., Wang, X., Yang, D., Yang, X., Yu, Z., Yuan, W., Yue, X., Zaehle, S., Zeng, N., Zeng, J., 2025. Global Carbon Budget 2024. Earth Syst. Sci. Data 17, 965–1039. https://doi.org/10.5194/essd-17-965-2025

Gile, L.H., 1993. Carbonate Stages in Sandy soils of Leasburg surface, Souther New Mexico. Soil Sci. 156.

Koutika, L.-S., Henry, B., Schepp, C., Olaleye, A., Amiraslani, F., Minasny, B., Ma, Y., Ladha, J., Cardinael, R., Bossio, D., Chenu, C., Espinoza, A.F., Madari, B., Soussana, J.-F., Varela-Ortega, C., Skowronska, M., 2025. Enhancing “4 per 1000” initiative implementation through region-specific agricultural and forestry practices. Soil Advances 4, 100057. https://doi.org/https://doi.org/10.1016/j.soilad.2025.100057

Lathouwers, M., Beenaerts, N., Evens, R., Artois, T., Conway, G., Henderson, I., Shewring, M., Cross, T., Ulenaers, E., Dendoncker, N., 2025. Impact of future climate change and land-use change on habitat suitability for a long-distance avian migrant under diverse socioeconomic-emission scenarios. Glob. Ecol. Conserv. 62, e03777. https://doi.org/https://doi.org/10.1016/j.gecco.2025.e03777

Levin, N.E., Brown, F.H., Behrensmeyer, A.K., Bobe, R., Cerling, T.E., 2011. Paleosol carbonates from the Omo Group: Isotopic records of local and regional environmental change in East Africa. Palaeogeogr. Palaeoclimatol. Palaeoecol. 307, 75–89. https://doi.org/https://doi.org/10.1016/j.palaeo.2011.04.026

Malik, M.M., Asim, H.W., Kazmi, S.A.A., Mujahid, K., Ansari, M.W., 2026. ANN and regression based quantification framework for climate change impact assessment on a weak transmission

grid of a developing country across Horizon 2050 plus. Environ. Dev. Sustain. 28, 261–280. https://doi.org/10.1007/s10668-024-04977-9

Martinez, A., Iglesias, G., 2021. Wind resource evolution in Europe under different scenarios of climate change characterised by the novel Shared Socioeconomic Pathways. Energy Convers. Manag. 234, 113961. https://doi.org/https://doi.org/10.1016/j.enconman.2021.113961

Martins, Flavio Pinheiro, Paschoalotto, Marco Antonio Catussi, Closs, Jose, Bukowski, Meike, Veras, Mariana M, 2024. The Double Burden: Climate Change Challenges for Health Systems. Environ. Health Insights 18, 11786302241298788. https://doi.org/10.1177/11786302241298789

Masson-Delmotte, V., Zhai, P., Pörtner, H.-O., Roberts, D., Skea, J., Shukla, P.R., Pirani, A., Moufouma-Okia, W., Péan, C., Pidcock, R., Connors, S., Matthews, J.B.R., Chen, Y., Zhou, X., Gomis, M.I., Lonnoy, E., Maycock, T., Tignor, M., Waterfield, T., 2019. Global warming of 1.5°C An IPCC Special Report on the impacts of global warming of 1.5°C above pre-industrial levels and related global greenhouse gas emission pathways, in the context of strengthening the global response to the threat of climate change, sustainable development, and efforts to eradicate poverty Edited by Science Officer Science Assistant Graphics Officer Working Group I Technical Support Unit.

Mccarthy, T.S., Mciver, J.R., Verhagen, B.T., 1991. Groundwater evolution, chemical sedimentation and carbonate brine formation on an island in the Okavango Delta swamp, Botswana, Applied Geochcmish-y.

Naorem, A., Jayaraman, S., Dalal, R.C., Patra, A., Rao, C.S., Lal, R., 2022. Soil Inorganic Carbon as a Potential Sink in Carbon Storage in Dryland Soils—A Review. Agriculture (Switzerland) 12. https://doi.org/10.3390/agriculture12081256

Ning, M., Luo, J., Liang, Z., Huang, P., Xing, C., Shen, B., 2025. Pedogenic carbonates in deep time: Characteristics, geological significance, and co-evolution with plant terrestrialization. Earth. Sci. Rev. 271, 105314. https://doi.org/https://doi.org/10.1016/j.earscirev.2025.105314

Raza, S., Irshad, A., Margenot, A., Zamanian, K., Li, N., Ullah, S., Mehmood, K., Ajmal Khan, M., Siddique, N., Zhou, J., Mooney, S.J., Kurganova, I., Zhao, X., Kuzyakov, Y., 2024. Inorganic carbon is overlooked in global soil carbon research: A bibliometric analysis. Geoderma 443, 116831. https://doi.org/https://doi.org/10.1016/j.geoderma.2024.116831

Sharififar, A., Minasny, B., Arrouays, D., Boulonne, L., Chevallier, T., van Deventer, P., Field, D.J., Gomez, C., Jang, H.J., Jeon, S.H., Koch, J., McBratney, A.B., Malone, B.P., Marchant, B.P., Martin, M.P., Monger, C., Munera-Echeverri, J.L., Padarian, J., Pfeiffer, M., Richer-de-Forges, A.C., Saby, N.P.A., Singh, K., Song, X.D., Zamanian, K., Zhang, G.L., van Zijl, G., 2023. Soil inorganic carbon, the other and equally important soil carbon pool: Distribution, controlling factors, and the impact of climate change, in: Advances in Agronomy. Academic Press Inc., pp. 165–231. https://doi.org/10.1016/bs.agron.2022.11.005

Smith, A., R., 1984. The Lithostratigraphy of the Karoo Supergroup in Botswana. Geol. Mag. 123, 710–711. https://doi.org/DOI: 10.1017/S0016756800024328

UNFCCC, 2025. Second annual global stocktake dialogue.

van der Ploeg, R., Haigh, M., 2024. The importance of natural land carbon sinks in modelling future emissions pathways and assessing individual country progress towards net-zero emissions targets. Front. Environ. Sci. Volume 12-2024.

White, K.H., Eckardt, F., 2006. Geochemical mapping of carbonate sediments in the Makgadikgadi basin, Botswana using moderate resolution remote sensing data. Earth Surf. Process. Landf. 31, 665–681. https://doi.org/10.1002/esp.1289

Wu, X., Zhao, J., Tian, J., 2026. Educational impacts of climate change: the role of climate finance in sustaining education in developing countries. Clim. Change 179, 25. https://doi.org/10.1007/s10584-026-04115-6

Zamanian, K., Pustovoytov, K., Kuzyakov, Y., 2016. Pedogenic carbonates: Forms and formation processes. Earth. Sci. Rev. https://doi.org/10.1016/j.earscirev.2016.03.003

CHAPTER TWO

Soil Inorganic Carbon: A Review of Global Research Trends, Analytical Techniques, Ecosystem Functions and Critical Knowledge Gaps[1]

Abstract

Soil inorganic carbon (SIC) is a crucial component of the global carbon cycle, especially in drylands, and it plays critical roles in ecosystem functioning. The last two decades have witnessed a global surge in SIC research. As a result, the analytical methods have become many and research themes, broader. This can create confusion for researchers in identifying contemporary SIC research hotspots and the choice of suitable analytical techniques. In this review, a bibliometric analysis spanning the last twenty years (2003-2022) was used to provide insight into global research trends, analytical techniques, ecosystem functions, and research gaps in SIC research. Five research hotspots were identified: formation processes and morphological characterization of SIC, quantitative measurement of SIC, storage and SIC dynamics, modelling and mapping of SIC stock, and the environmental and ecosystem implications of SIC including ecosystem management, past environment and climate reconstruction, geochronology, and archaeology. The characterisation of SICs requires the use of a range of complementary methods, but the choice must be made according to the objectives pursued, financial resources, and technical and environmental advantages. For quantitative measurements, dry combustion seems to give good results in terms of accuracy; however, it is less environmentally friendly, more expensive, and slower than spectroscopic methods, which are suitable for large-scale studies. This study has highlighted the need for further research

[1] *This chapter is based on a paper co-authored with Thierry Bineli Betsi and Peter N. Eze; published in Catena, 242 (2024), 108112*. https://doi.org/10.1016/j.catena.2024.108112

into the role of SIC as a key soil property influencing ecosystem services. It also calls for more in-depth analysis of the long-term effects of land management regimes on SIC dynamics. This review provides reference topics for an in-depth study of SICs to improve understanding of their role in the global carbon cycle and ecosystem services.

Keywords: Drylands; Soil organic carbon; Geochronology; Palaeosol carbonates; Land use change.

2.1. Introduction

After geological and oceanic pools, soil is the third largest pool of carbon on Earth (Shi et al., 2017). Soil carbon can be in the form of either soil organic carbon (SOC) or soil inorganic carbon (SIC) (Lal et al., 2015). For many years, SIC was overlooked as a potential factor influencing atmospheric carbon dioxide levels. Its role in sequestering atmospheric carbon dioxide was long thought to be negligible (Lal, 2009). This is because SIC is considered to be the result of a slow and gradual accumulation over geological time largely controlled by abiotic processes (Gile et al., 1966; Machette, 1985) and is therefore difficult to promote carbon sequestration in soils.

More recently, however, SIC has gained considerable interest, notably as an important potential solution for soil carbon storage (Verrecchia et al., 2006; Sanderman, 2012; Bughio et al., 2016; Gao et al., 2017; Assadi Langroudi et al., 2021). In dry regions (hyper-arid, arid, semi-arid and semi-humid), a great deal of research has been carried out on the subject (Raheb et al., 2016; An et al., 2019; Carmi et al., 2019). In these environments, SIC is considered to be the most important form of soil carbon (Díaz-Hernández et al., 2003a; Wang et al., 2015). But its potential to sequester carbon dioxide is also being investigated in temperate and glacial climates (Becze-Deàk et al., 1997; Kovda et al., 2014a; Szendrei et al., 2012), and even tropical regions with the oxalate carbonate pathway (Mujinya et al., 2011; Cailleau et al., 2011; Bravo et al., 2015; Hervé et al., 2018; Rowley et al., 2017).

The burgeoning global interest in SIC stems from its contribution to atmospheric carbon dioxide (Raza et al., 2021; Song et al., 2022), due to poor land management (An et al., 2019; Ayala-Niño et al., 2020; Wilsey et al., 2020) and agricultural practices (Shaoxuan et al., 2016; Bulysheva et al., 2020; Lu et al., 2020). Additionally, the use of soil carbonate for radiocarbon dating (Diaz et al., 2016; Dal Sasso et al., 2018), palaeoclimate and palaeoenvironmental reconstruction (Violette et al., 2010; Achyuthan et al., 2012; Eze and Meadows, 2014a; Xiong

et al., 2022), and archaeology (Macharia et al., 2012; Paul and Mauldin, 2013), as well as its role in ecosystem functioning (Groshans et al., 2018; Pal, 2019; Parsons et al., 2022), have contributed to its receiving considerable attention.

Thus, one of the most fascinating observations about soil carbonate research themes is that they cover a wide range of often concomitant research questions. For instance, the utilisation of soil carbonates to reconstruct palaeoclimate and palaeoenvironment is inherently dependent on preliminary dating. Without it, palaeoenvironmental and palaeoclimate reconstruction would be meaningless. Furthermore, this analysis provides insight into the formation conditions and processes of carbonate features and serves as a basis for an improved understanding of the carbon cycle and the factors involved in the dissolution-recrystallisation of carbonates. Another intriguing observation about the various research themes is the wide range of analytical techniques, some of which are often involved in the analysis of different research questions. For example, to estimate variations in the rate of pedogenic carbonate formation in Saskatchewan soils (Canada), Landi et al. (2003) used stable carbon isotope values in soil carbonates and parent material. The same approach was used but combined with X-ray diffraction analyses to differentiate between pedogenic and lithogenic carbonate features later in their work. Therefore, it is necessary to discuss recent trends in SIC research, as well as methodological approaches used in both field and laboratory analysis. There are a lot of brilliant reviews on the SIC, discussing either the forms and processes of formation of some specific type of soil carbonate (e.g. Alonso-Zarza and Wright, 2010; Zamanian et al., 2016), or the dynamics of SIC (Sanderman, 2012; Khalidy et al., 2022; Naorem et al., 2022), or SIC as a potential source of atmospheric CO_2 (Ferdush and Paul, 2021; Raza et al., 2021). More recently, Sharififar et al. (2023) emphasized the importance of the SIC pool by reviewing its global distribution, digital mapping applied to this theme, SOC relationships, human influences, and the effects of climate change. But none of these reviews discussed either the

methods, which are numerous and confusing or the global research trends, which are necessary to highlight achievements and identify future research directions. Therefore, the objectives of this review are to: (i) conduct a bibliometric analysis of peer-reviewed scientific articles on SIC over the last 20 years (2003-2022) to identify the contemporary research hotspots and key research questions, (ii) review the current state of knowledge on SIC pathways, (iii) discuss the leading methods and approaches used to characterise, quantify, and analyse SIC, (iv) explore the environmental and ecological implications of SIC, and (v) identify critical knowledge gaps and future directions for SIC research.

2.2. Trends in global SIC research in the last two decades (2003-2022)

This section is based on a bibliometric analysis to highlight the major progress made in SIC research over the last twenty years. The bibliometric information used here is provided by two scientific databases: Google Scholar and Scopus, to incorporate the maximum amount of available data and reduce bias, as recommended by Ferreira et al. (2023). A step-by-step explanation of the process used is described in Fig. 2.1. A filter was applied to each database to limit the target period from 2003 to 2022, and to select peer-reviewed articles published in the English language only.

A systematic search of scientific publications conducted on Google Scholar using the terms "Soil inorganic carbon" returned 2,930 results; "Pedogenic carbonate" showed 5,910 results, while "Carbonate in soil" turned out 761 results. A total of 9,601 results were found, which is approximately 95% of the available results when a language filter is not applied. A total of 448 articles were selected, following a rigorous process (page after page) of both research and review articles. Articles were either downloaded or bibliographic information was obtained in BibTeX format. After removing duplicates in Mendeley Reference Manager, 395 articles from Google Scholar were retained. Compared to the number of returned results, the articles

retrieved from Google Scholar represent only 4%. This can be explained by the fact that many results did not match the key terms, which is the reason why page by page selection process was chosen. Data from books and conferences were further excluded from bibliometric analysis. Moreover, some documents with English titles were written in languages other than English, such as Chinese, which cannot be included here due to our limited comprehension of the language.

On the Scopus database, the search was conducted on all publications with either the title, or containing in their abstract, or having as keywords: “Soil inorganic carbon”, “Pedogenic carbonate”, or “Carbonate in soil”. The search was further restricted to research and review articles only. At the end of the process, 806 documents were selected out of a total of 849 articles. This fraction represents approximately 95% of the documents available in the database during the period of interest. All the bibliographic information from these documents were exported in BibTeX file format and later imported into the Mendeley Reference Manager for analysis.

The data from the two databases were combined in Mendeley Reference Manager and after eliminating duplicates, 1,040 articles were selected. These publications were classified according to the research questions addressed, and it was at the end of this phase that the main research themes were identified. To observe the general trend of SIC research over our target period, the number of articles published was grouped into two-year classes. The R software (version 4.3.3) was used to perform the Mann-Whitney U test (between the first 5 classes of observation and the last 5 classes, corresponding to the comparison of the distribution of the decade 2003-2012 with the 2013-2022 decade) and the Spearman correlation test (to analyse possible relationships in the evolution of the main research questions), as recommended for non-parametric statistical data (Deb et al., 2020). Finally, the geographical distribution of research on SIC was analysed on a global scale.

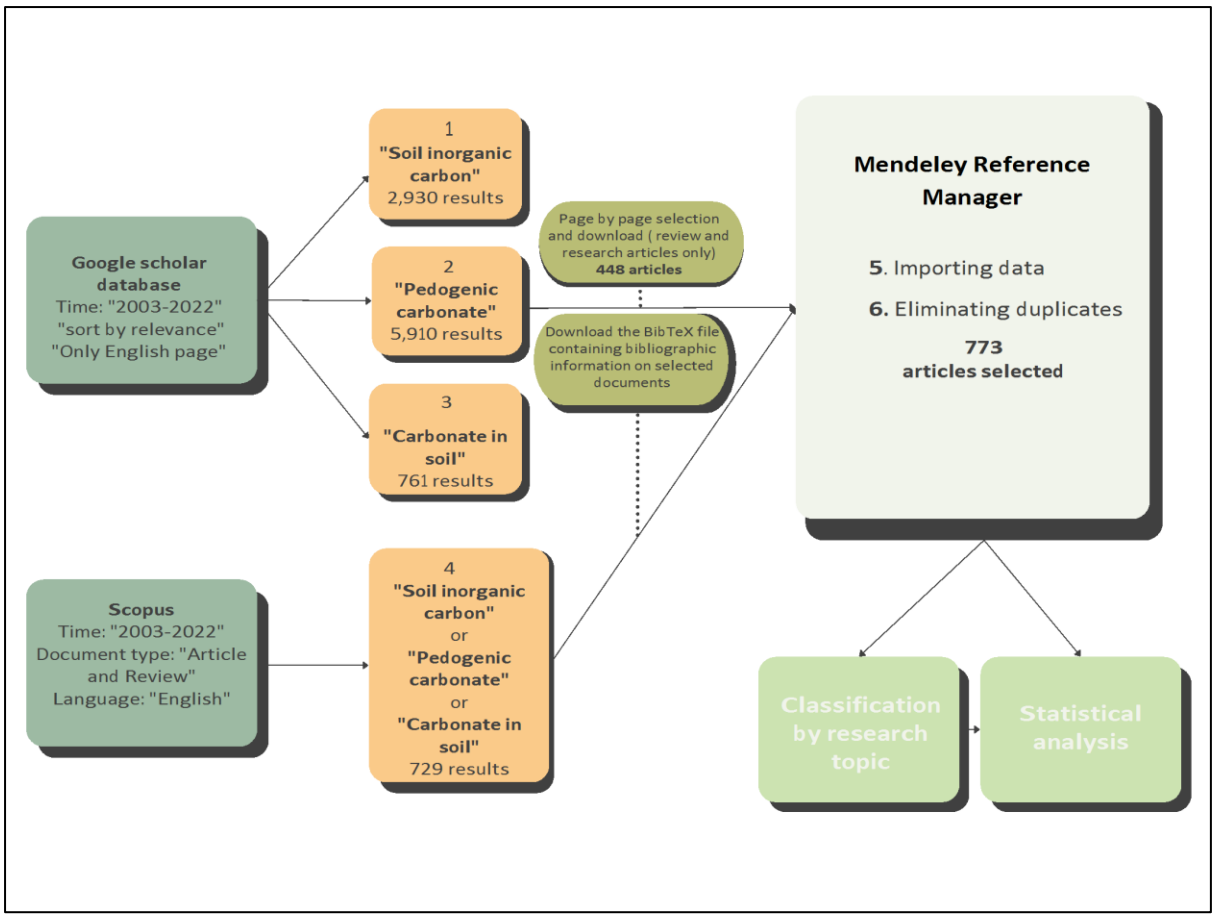


Fig. 2.1. Description of the process used for the bibliometric analysis

If we consider our approach in the Scopus database, we obtain a total production of 1172 scientific documents (of all types) covering the SIC from 1905 (the year of the oldest publication) to 2022. Over our target period (2003-2022), there are 932, representing 82%. This shows that the choice of this period seems reasonable enough to assess recent progress on the subject and represents an overwhelming proportion of the total publications on SIC in the era of modern science. However, if we compare the production of articles on the SIC with that on the SOC over the same period, the former appears derisory compared with the 21,934 articles on the SOC. As shown in Fig. 2.2a, interest in SIC-related topics has increased over the last 20 years. Although this progression is marked by two negative peaks in 2007-2008 and 2017-2018 time slices, which is characterised by a decline. Furthermore, compared with the SOC (Fig. 2.2b), where the increase is more marked, the gap has evolved over the reported time. In 2003,

it was 87%, rising to 96% in 2022. This indicates that research output on the SOC is 23 times greater than that on the SIC. These results underline the need to make a major effort to advance SIC research given its role in optimal ecosystem functioning.

Examining the increase in the number of peer-reviewed articles published (Fig. 2.2a), it is challenging to determine any difference in distribution between the first decade (2003-2012) and the subsequent one (2022-2022). However, the result of the Bartlett test of the homogeneity of variance, with a p-value = 0.4378, which is above the significance threshold of 0.05, shows that it cannot be concluded that there is homogeneity in the distribution of the samples from these two subgroups. Additionally, the Wilcoxon rank sum test resulted in a p-value of 0.007937, which is below the significance level of 0.05, indicating a significant difference between the two decades. The box plot in Fig. 2.3 highlights the distribution difference between the first and second decades. The average number of articles published from 2003-2012 was 67, while during 2013-2022, it was more than double at 140 (Fig. 2.3). These observations indicate a significant increase in SIC research output over the last decade.

Several research themes were also identified linked to a variety of concerns, the most recurrent of which are summarized in Fig. 2.4.

- SIC dynamics as a function of various natural and anthropogenic factors are most frequently investigated (32%).
- SIC characterization (27%). This is often linked to the analysis of formation processes.
- The use of pedogenic carbonates in the reconstruction of palaeoclimatic and palaeoenvironmental conditions and geoarchaeology (15%).
- Advances in quantitative methods (12%) to adopt methods that are more accurate, less time-consuming, and more environmental friendly.
- The role of SIC in the evolution of other soil properties, carbon cycles, and ecosystem services (11%); and

- the development of models for predicting the spatiotemporal evolution of SIC (3%).

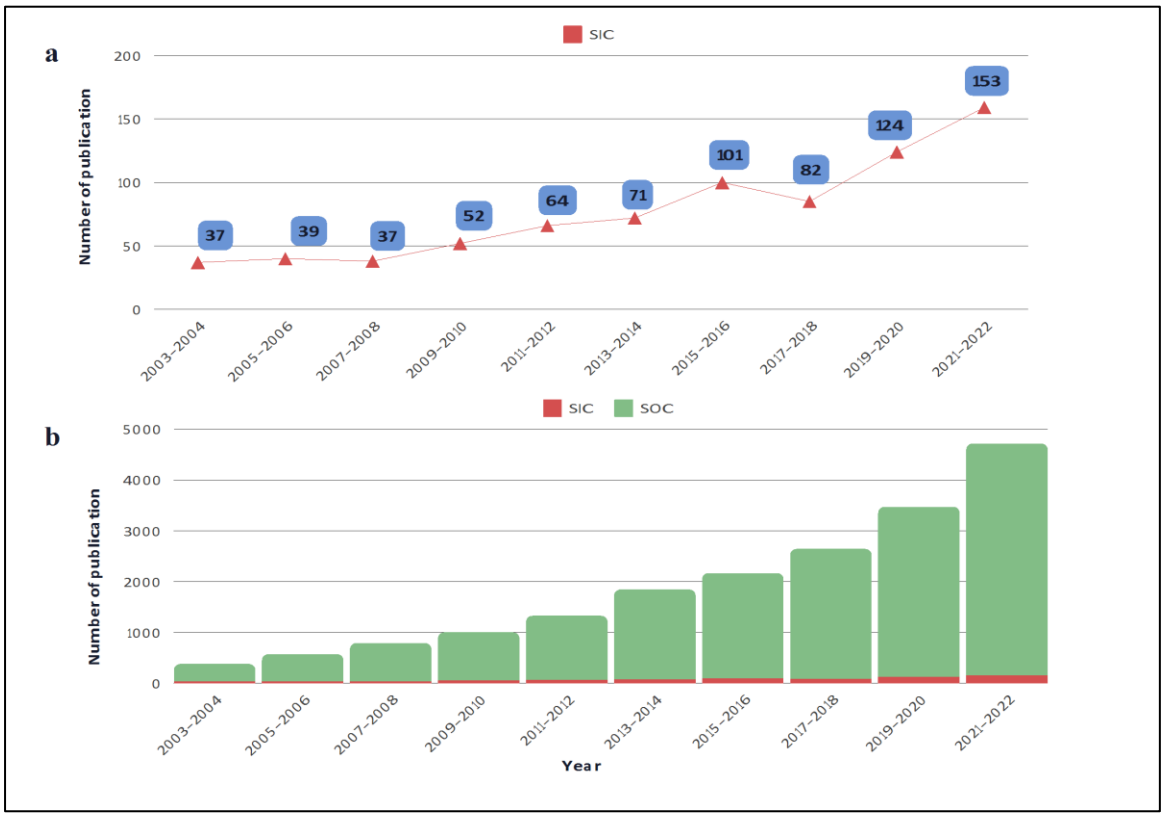


Fig. 2.2. **a**. Trend in the number of scientific publications relating to the SIC between 2003 and 2022; **b**. Trend in the number of scientific publications relating to the SOC compared to the number of scientific publications relating to SIC between 2003 and 2022.

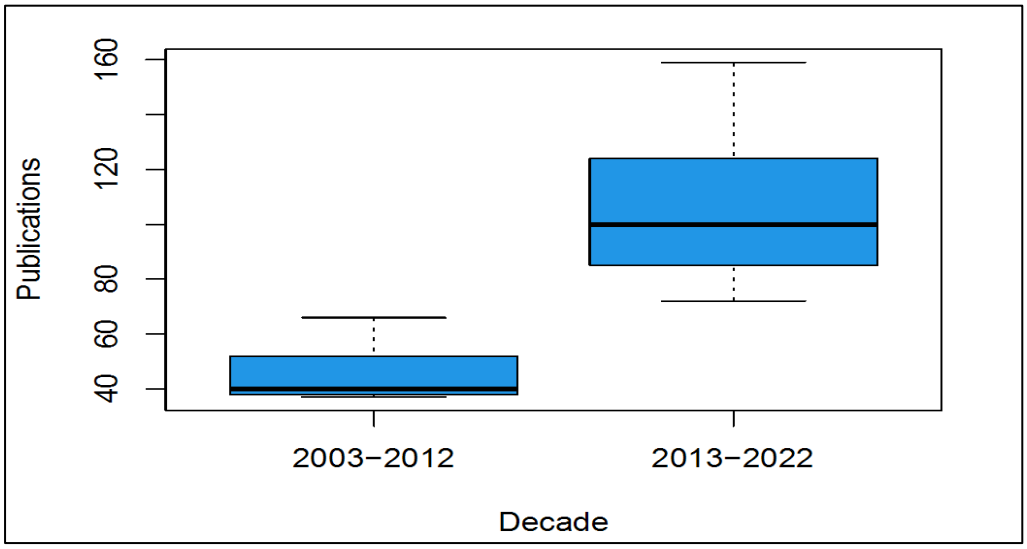


Fig. 2.3. Box plots of the number of SIC-related publications over the period 2003-2012 compared with the period 2013-2022.

Spearman's correlation test (p-value = 0.01) and the resulting correlation matrix (Fig. 2.5) show that the general trend in SIC research (all subjects combined) presents a strong and significant positive correlation with subjects related to the use of SIC for palaeoenvironmental and palaeoclimate reconstruction, radiochronology and archaeology (R=0.96), those related to the development of quantification techniques (R=0.91), those related to the dynamics of SIC (R=0.89), and finally those related to the role of SIC in the ecosystem and soil quality (R=0.71). Fig. 2.6 illustrates a rise in the number of publications for all research questions between the two decades. However, this progression is more significant for the development of techniques for SIC quantification, for the analysis of SIC dynamics and storage, and for palaeoenvironmental reconstruction, radiochronology and archaeology, with an increment of 900%, 544% and 309% respectively.

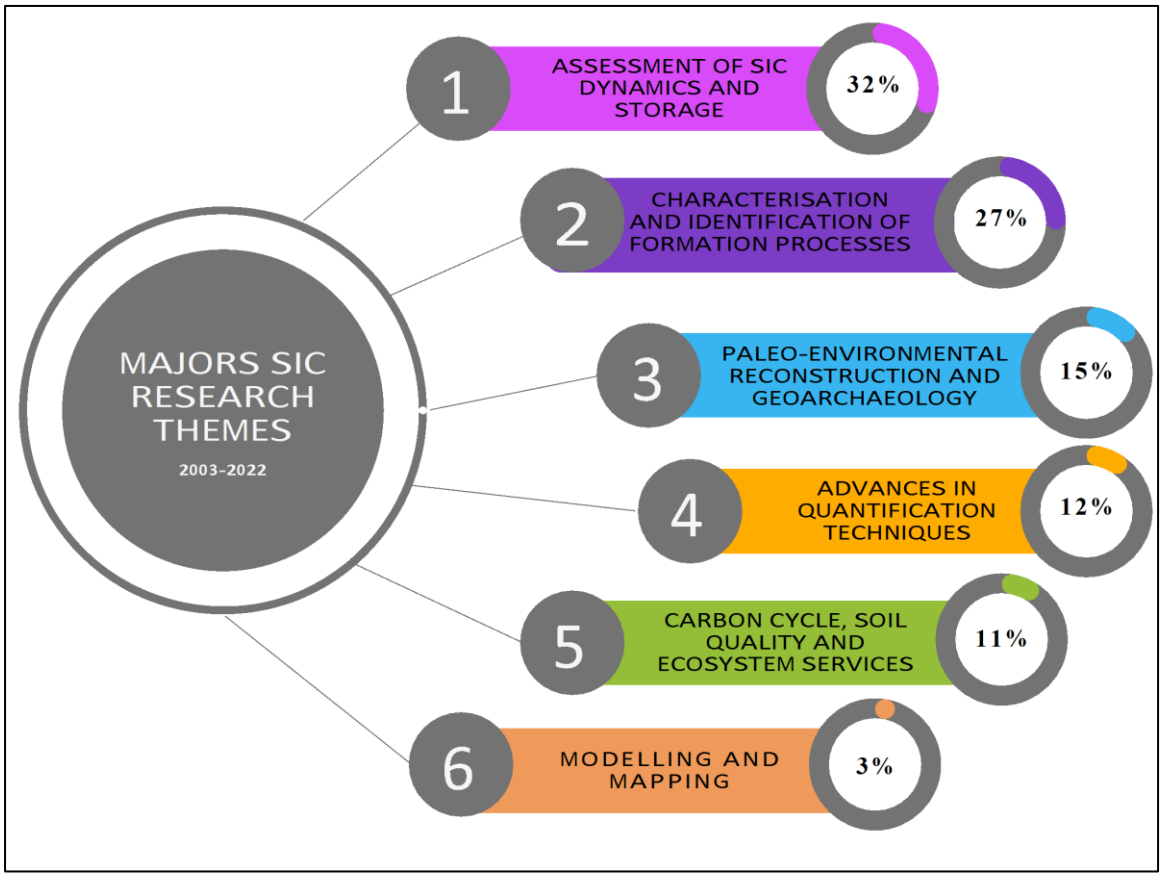


Fig. 2.4. Major SIC research topics identified by bibliometric analysis between 2003 and 2022

In terms of geographic distribution, the attractiveness of the subject varies across continents depending on the research questions addressed (Fig. 2.7). China has produced the most scientific articles on SIC. However, most studies have focused on SIC dynamics as functions of natural and anthropogenic factors (more than 60%). This can be explained by the dominance of arid and semi-arid climates in a large part of China (Yin et al., 2019). Soils with pedogenic carbonate cover about 30% of China (Mi et al., 2008). On the other hand, research into measurement techniques is dominated by Europe and North America, which are also one step ahead on questions relating to the role of SIC in the ecosystem. The reason for this leadership could be explained by the motivation of researchers in these regions to improve soil monitoring networks on a national and continental scale by using increasingly less tedious techniques (Marchant et al., 2015). Or to better estimate the financial impact of properties such as the SIC on the management of ecosystem services (Groshan et al., 2018). The rest of Asia has produced a significant amount of SIC-related research. However, the themes are diverse. They focused as much on improving quantification techniques by analysing the conditions favouring the formation of SIC, the role of SIC in the global carbon cycle and ecosystem services, and its use in palaeoenvironmental and palaeoclimatic reconstruction. In Africa, Central and South America, and Australia, the level of research remains relatively low. We did not report many scientific articles for research carried out in Australia during our reference period. However, it is possible that a significant amount of work was done before this target period. Many articles cited in Sanderman's (2012) review of SIC in Australia appear to be outside the period of concern. Africa, Central America, and South America have vast arid and semiarid zones. The Kalahari and Sahara in Africa, the Atacama, Patagonia, and Sonora in Central and South America, but SIC research in these areas is largely underexplored. Relatively, few studies have been carried out over the last two decades on palaeoclimatic and palaeoenvironmental reconstruction and archaeology using pedogenic carbonates (Dietrich et al., 2021a, 2017a;

Potts et al., 2009). Stepping up research into SIC in these regions could help to better quantify SIC stock and its role in soil carbon sequestration in these rich and diverse ecosystems. We opine that the large expanse of drylands in Africa, Central and South America would invariably act as natural laboratories for the advancement of our understanding of SIC dynamics.

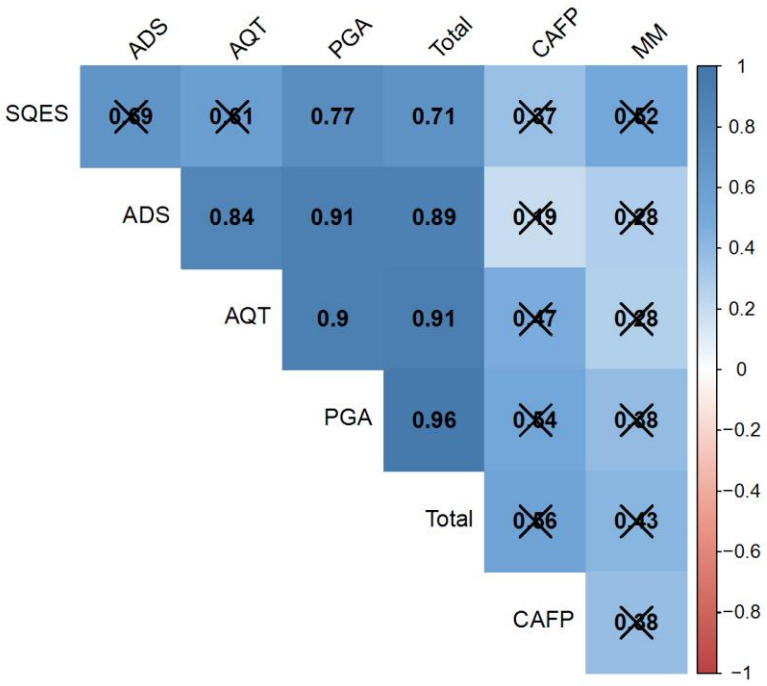


Fig. 2.5. Spearman correlation matrix (p-value=0.01) for the main SIC research topics identified by the bibliometric analysis. The cells marked with a cross indicate that there is no correlation between the two variables at the significance level. **AQT**: Advances in quantification techniques; **CAFP**: Characterisation and identification of formation processes; **ADS**: Assessment of sic dynamics and storage; **MM**: Modelling and Mapping; **SQES**: Carbon cycle, Soil quality and ecosystem services; **PGA**: Palaeoenvironmental reconstruction and geoarchaeology; **Total**: Total number of research publication.

2.3. SIC formation pathways

As a recapitulation, SIC formation pathways are described here, but for a more thorough review, see Alonso-Zarza and Wright, (2010) and Zamanian et al., (2016). It is important to

point out that the inorganic carbon in the soil does not originate from pedogenic processes alone. Depending on the origin, SIC can be classified into three groups (Sharififar et al., 2023):

- **Geogenic carbonates**, which result from the alteration of primary carbonate formations (limestone, dolomite and marble). In some cases, fragments of carbonate rock formed in a pre-existing environment (continental or marine) are transported by water, wind, or ice over a distance and reworked into the soil (ex-situ formation). In other cases, particularly in soils formed on carbonate parent material, the fragments present in the soil are relics that have resisted weathering (in situ formation).
- **Biogenic carbonates**, which result from the accumulation of animal and plant remains, including animal skeletons and mollusc shells. They are generally found in soils formed beneath sedimentary deposits.
- **Pedogenic carbonates**, which are generally formed on site (in-situ formation) by various pedogenic processes involving either direct or indirect biotic processes, or the intervention of abiotic processes. SICs derived from pedogenic processes are also called secondary carbonates because they generally result from the recrystallisation of pre-existing carbonates, which are considered primary.

The first two (geogenic and biogenic) are often referred to as lithogenic (Monger et al., 2015) as they are derived from lithogenic processes. However, inorganic carbon in soil is also present in the form of dissolved ions (Ferdush and Paul, 2021). This is known as dissolved inorganic carbon (DIC) including carbonate ions (CO_3^{2-}), bicarbonate ions (HCO_3^-), dissolved carbon dioxide (CO_2solute) and carbonic acid (H_2CO_3).

The precipitation of carbonate in the soil requires some conditions:

a. The availability of Ca^{2+} or Mg^{2+} ions in the environment. These generally come either from the weathering of local silicate or carbonate parent materials (Durand et al., 2006; Sun et al.,

2022; Watanabe et al., 2004) or aeolian deposits (Bockheim and Douglass, 2006; Mikhailova et al., 2013). They are mobilised either by capillary uptake, dissolution, or evaporation.

b. The availability of carbon dioxide. CO_2 generally comes from the respiration of roots and soil micro-organisms (Gocke et al., 2010, 2011; Zhao et al., 2016).

In addition, the water content of the soil also plays an important role, as precipitation generally occurs when the water content decreases, either through evaporation (Khokhlova et al., 2021) or evapotranspiration (Li et al., 2018). In some cases, the partial pressure of carbon dioxide (pCO_2) in the soil also plays a role in precipitation (Karberg et al., 2005).

In general, two main pathways are suggested for pedogenic carbonate precipitation in soils: the abiotic pathway (dissolution-recrystallisation) and the biotic pathway, which emphasises the participation of organisms and/or micro-organisms in carbonate formation.

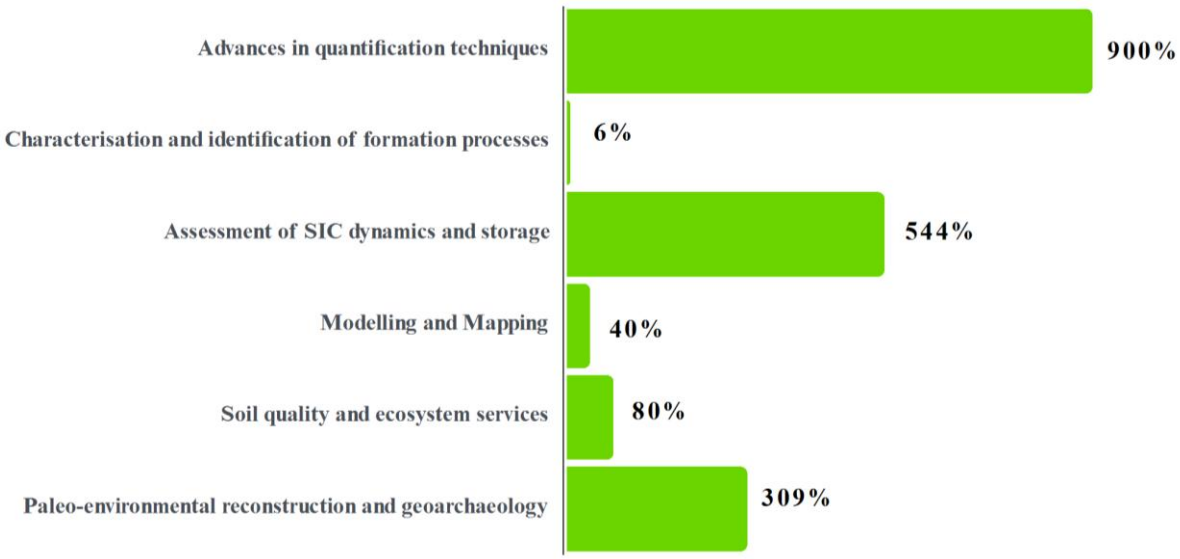


Fig. 2.6. Progression rate (%) in SIC research from 2003-2012 decade to 2013-2022, classified by topic.

2.3.1. Abiotic soil carbonate precipitation

In this approach, the weathering of silicate minerals (Eq. 2.1) or carbonate minerals (Eq. 2.2) under the action of carbonic acid would result in the availability of Ca^{2+}ions, which in dry

environments (arid and semi-arid) are fixed by bicarbonate ions to allow the precipitation of pedogenic carbonates (Eq. 2.3) within the soil profile. The same model explains that in a more leaching humid environment, bicarbonate ions are transported to rivers and then to the oceans where they are precipitated as lithogenic carbonate (Monger et al., 2015). This process is also known as physicochemical formation (Tlili et al., 2021). It is exclusively influenced by the physicochemical properties of the soil and some physicochemical environmental factors of the medium (e.g., climate, topography, parent material).

$$2CO_2 + 3H_2O + CaSiO_3 \rightarrow Ca^{2+} + 2HCO_3^- + H_4SiO_4 \quad \text{Eq. 2.1}$$

$$CaCO_3 + H_2CO_3 \leftrightarrow Ca^{2+} + 2HCO_3^- \quad \text{Eq. 2.2}$$

$$Ca^{2+} + 2HCO_3^- \rightarrow CaCO_3 + CO_2 + H_2O \quad \text{Eq. 2.3}$$

The dissolution-recrystallisation pathway has been widely used to explain the formation of certain types of pedogenic carbonate features such as nodules and laminar crusts in dry regions (Monger, 2014; Dietrich et al., 2017). Khokhlova et al. (2021) have also suggested that nodule precipitation in the Central Russian Uplands is associated with a decrease in water content due to evaporation. However, the formation of other types of pedogenic carbonates, such as rhizolites, can be linked to the activity of a particular type of plant. Sun et al. (2020, 2022) show, for example, that rhizolites formed in the deserts of China (Tengeri and Badain Jaran) are associated with Artemesia. In this type of soil carbonate, although the conditions described above are still valid, root activity remains the determining factor in carbonate precipitation.

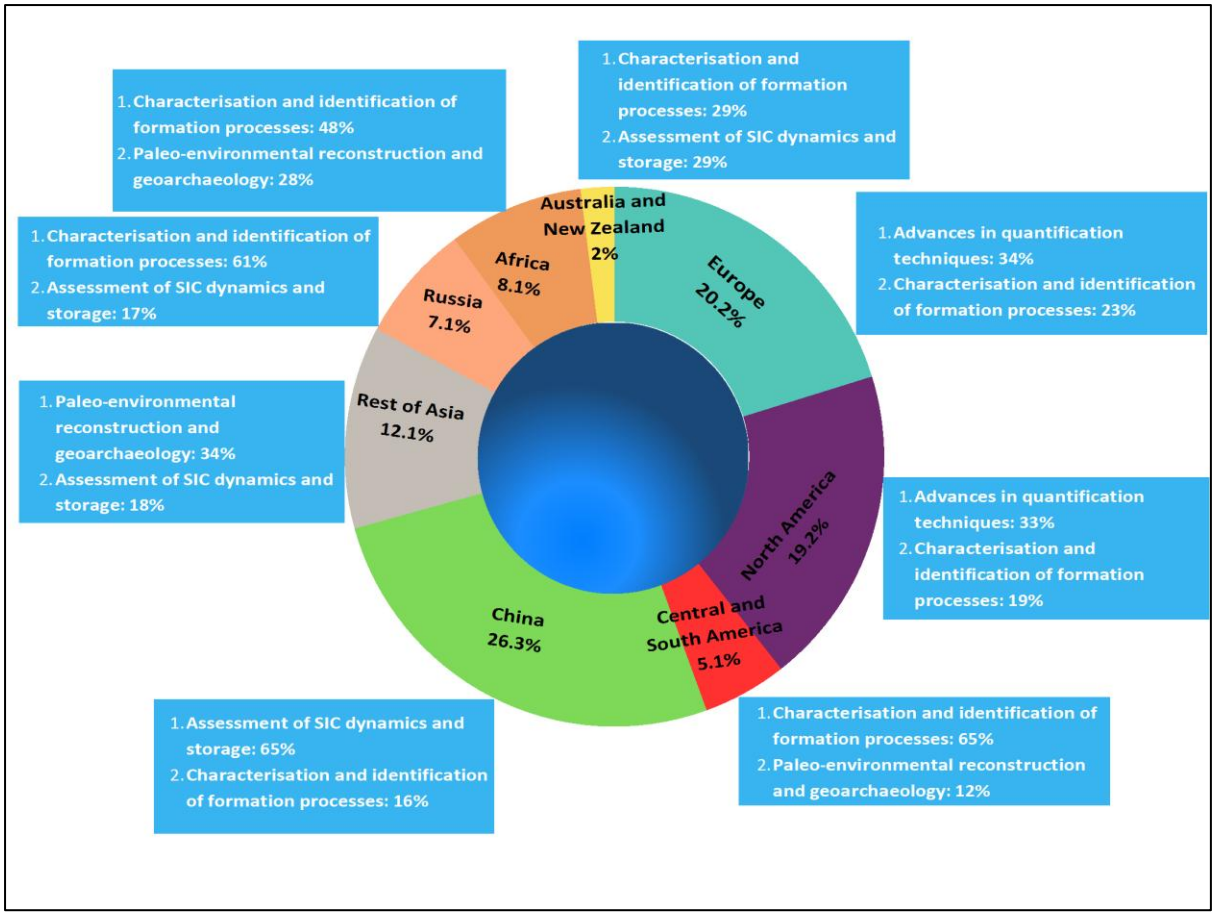


Fig. 2.7. Geographical output of SIC research based on the identified themes.

2.3.2. Biotic soil carbonate precipitation

The dissolution-recrystallisation model under physicochemical action failed to explain the formation of some microfeatures of soil carbonates. Needle-fibre calcite for example, are often described as the result of a combined action of physicochemical processes and microbial transformations (Becze-Deàk et al., 1997; Cailleau et al., 2009; Millière et al., 2019; Tlili et al., 2021). Moreover, the precipitation of soil carbonate has in some cases been linked to the action of microbial activity, promising biomineralization rather than a physicochemical process (Párraga et al., 2004; Lian et al., 2006; Zhang et al., 2010; Laudicina et al., 2013; Liu et al., 2018). In addition, recent works have highlighted biomineralization via the oxalate-carbonate pathway (Aragno and Verrecchia, 2012; Cailleau et al., 2011, 2014; Gadd et al., 2014; Uren, 2018; Sun et al., 2019; Syed et al., 2020; Hervé et al., 2021; Álvarez-Rivera et al., 2021; Gatz-

Miller et al., 2022). According to Verrecchia et al. (2006), oxalate crystals are produced by fungi during the fixing of atmospheric CO_2 by photosynthesis in certain plants. This carbon is used by oxalotrophic bacteria to release Ca^{2+} ions and CO_2 into the soil solution (Eq. 2.4) and later to precipitate $CaCO_3$ (Eq. 2.5).

$$CaC_2O_3.nH_2 + \frac{1}{2}O_2 \rightarrow Ca^{2+} + 2CO_2 + (n-1)H_2O + 2OH^- \quad \text{Eq. 2.4}$$

$$Ca^{2+} + 2OH^- + CO_2 \rightarrow CaCO_3 + H_2O \quad \text{Eq. 2.5}$$

This approach is particularly interesting because it has demonstrated the sequestration of carbon dioxide, even in tropical environments (Aragno and Verrecchia, 2012; Gatz-Miller et al., 2022). However, the capacity of this system is still unknown, as are all the tree species and microorganisms involved in the process. Moreover, some tree species reportedly struggle to return the fixed calcium carbonate to the soil (Hervé et al., 2018).

2.4. Characterisation of soil inorganic carbon

Characterizing SIC is crucial for understanding its exact role in sequestering carbon dioxide in the soil and the processes responsible for its accumulation in soil profiles. This approach is based on the differentiation between inorganic carbon derived from pedogenic processes and inorganic carbon derived from other (non-pedogenic) processes, which implies an analysis of carbonate formation processes in soils. Characterizing SIC generally entails, but is not limited to, morphological identification and description of different scales (macro, micro, meso). The use of geochemical methods, which are done separately or combined with morphological characterization, makes it possible to analyse the processes and environments of carbonate formation in the soil, and the use of analytical techniques to identify the mineralogical species that make up soil carbonates. This approach involves combining different types of analytical procedures from field to laboratory observations and from macromorphological to micromorphological observations.

2.4.1. Macromorphological description

Macromorphological descriptions are generally the first step in characterizing SIC. It is based on certain criteria, such as carbonate form, presence or absence of fossils, and SIC distribution patterns (West et al., 1988). This process provides the first indication of the type of carbonate present in the soil and allows for differentiation based on the observed shape (Zamanian et al., 2016) and the degree of evolution of carbonates in the horizon (Machette, 1985). However, the differentiation of carbonates in the soil cannot be limited to macroscopic observations alone, as discrimination between pedogenic and non-pedogenic carbonates based only on macroscopic observations can lead to erroneous conclusions (cf. West et al., 1988). It is complemented by micromorphology, which is more accurate and widely used as a reference method (Wolff et al., 2017; Kowalska et al., 2020; Menezes et al., 2021). Therefore, given the cost and difficulty of access to the equipment needed for microscopic observations, it would be necessary to develop more accurate methods for macromorphological discrimination between pedogenic and non-pedogenic carbonates.

2.4.2. Micromorphological description

Soil micromorphology has been effectively used in SIC research. Depending on the objectives of the study and the soil characteristics, different sample collection techniques are used to determine soil micromorphology. The sampling technique based on the Kubiëna box is the most used (Verrecchia and Trombino, 2021). However, if the circumstances do not permit it, or in the case of studies that concentrate on specific features such as nodules, hardpans, and pebbles, the sample can be carefully hand-picked (Kovda et al., 2006; Achyuthan et al., 2012) or with the help of a small chisel and hammer (Landi et al., 2003).

The steps in the preparation of thin sections of soil samples are explained by Verrecchia and Trombino, in "A Visual Atlas for Soil micromorphologists" (2021). Briefly, the procedure involves air-drying the samples for a few weeks, then impregnating them with a resin (usually

an epoxy resin, combined with acetone to increase viscosity and a catalyst) to stabilise their structure. After impregnation, a vacuum system is used to remove any residual air from the samples. Once solidified, the samples are cut using a diamond saw to obtain tiles approximately 1 to 2 cm thick, mounted on a glass slide and then polished to a thickness of 20 to 30 µm.

Various microscopic observation techniques have been used in SIC research (see Table 2.1). Some of these are presented in the following paragraphs: In general, a polarised microscope (PL) is used to identify carbonate microstructures and analyse the relationships between them and the other features present (Kovda et al., 2003;Durand et al., 2007; Menezes et al., 2021). In some cases, it can also be used to differentiate between pedogenic and non-pedogenic carbonates using criteria such as the presence or absence of fossils, the distribution of carbonate structures, the shape of these structures, Fe-Mn staining, and other criteria presented by West et al. (1988). Cathodoluminescence microscopy (CL) observations are also used to describe carbonate microstructures. They help, for example, in analysing alteration or accumulation processes (Violette et al., 2010; Millière et al., 2019), but also in discriminating between carbonate types (Dal Sasso et al., 2018; Ruidas et al., 2020). However, fluorescence microscopy (FL) observations are not widespread. In contrast, Khormali et al. (2006) showed that they can also be used to discriminate between pedogenic and non-pedogenic carbonate microstructures. Scanning electron microscope (SEM) observations generally help describe carbonate microstructures and their internal and external arrangements (Landi et al., 2003;Bajnóczi and Kovács-Kis, 2006; Sun et al., 2023). In other words, all these micromorphological description techniques are very useful for characterizing SIC. However, the choice of one or more of them is guided not only by the objectives of the study but by the financial resources available, as some of them may lead to the same conclusions.

Table 2.1. Technique used for micromorphological description of SIC

Technique	Objective(s)	Reference
Polarised microscope	Analysis of the processes involved in the formation of the Bk horizon; Morphological identification of carbonate microstructures; Analyse their relationship with other elements; Differentiates pedogenic from non-pedogenic carbonates	West et al., 1988; Kovda et al., 2003; Bockheim and Douglass, 2006; Khormali et al., 2006; Durand et al., 2007; Violette et al., 2010; al Sasso et al., 2018; Kowalska et al., 2020; Dietrich et al., 2021; Menezes et al., 2021
Scanning electron microscope	Describe carbonate microstrutures; Analysis of the processes involved in the accumulation of these microstructures. Mapping chemical composition of microstructures	Landi et al., 2003; Bajnóczi and Kovács-Kis, 2006; Khormali et al., 2006; Violette et al., 2010; Eze & Meadows, 2014a, 2014b; Eze & Meadows, 2015 Eze et al., 2016; Dal Sasso et al., 2018; Prokof'eva et al., 2021; Valera Fernández et al., 2022; Sun e al., 2023)
Cathodoluminescence microscope	Identify carbonate microstructures; Analyse alteration or accumulation processes; Differentiates pedogenic from non-pedogenic carbonates	Khormali et al., 2006; Violette et al., 2010; Dal Sasso et al., 2018; Millière et al., 2019; Ruidas et al., 2020; Menezes et al., 2021
Fluorescence microscope	Differentiates pedogenic from non-pedogenic carbonates	Khormali et al., 2006
Microprobe microscopy	Quantitative chemistry Mapping the distribution of elements mineralogical and geochemical composition of microscopic particles such as microscopic nodules, soft masses	Kovda et al., 2003; Kuznetsova & Khokhlova, 2010; Diaz-Hernandez et al., 2018 ; Prokof'eva et al., 2021; Schweizer et al., 2023

2.4.3. Stable isotope geochemistry

Stable isotope geochemistry is based on isotope fractionation, in other words on the distribution of isotopes between two substances or two phases of the same substance with different isotope ratios, either through isotope exchange or kinetic effects (Hoefs, 2009a). These variations in isotopic composition are extremely small and are generally expressed in a specific unit δ as follows (Allègre, 2008):

$$\delta = \left(\frac{sample\ isotope\ ratio - standard\ isotope\ ratio}{standard\ isotope\ ratio}\right) \times 10^3 \qquad \text{Eq. 2.6}$$

δ is the relative deviation from the standard and is expressed as the number of parts per mil (‰). The isotope ratios are obtained using mass spectrometry. The operating principles of the mass spectrometry methods and laboratory techniques have been explained by Hoefs (2009). In SIC studies, the isotopes of interest are carbon and oxygen. They are used to differentiate pedogenic carbonates from lithogenic carbonates (West et al., 1988; Landi et al., 2003). They are also used in studies on the formation processes of pedogenic carbonates (Salehi et al., 2004; Kovda et al., 2014).

2.4.3.1. Carbon stable isotopes

On Earth, carbon has two stable isotopes, ^{12}C=98.93% and ^{13}C=1.07%. According to Hoefs (2009a), the fractionation process in the case of inorganic carbon occurs through isotope exchange reactions within the "atmospheric CO_2 - dissolved bicarbonate - solid carbonate" system and leads to an enrichment of ^{13}C in carbonates. In most cases, the $\delta^{13}C$ value is calculated using the standard Pee Dee belemnite value (V-PDB). The differentiation between pedogenic and non-pedogenic carbonates is based on the assumption that the carbon incorporated in pedogenic carbonates originates from soil CO_2 resulting from root and microbial respiration (Cerling, 1984; Hasinger et al., 2015). Thus, $\delta^{13}C$ values of pedogenic carbonates are strongly linked to vegetation. Other forms of carbonates of non-pedogenic origin retain the isotopic signature of the environment in which they were formed (Zamanian et al.,

2021). West et al. (1988) estimate, for example, that carbonates formed in soil have more negative $\delta^{13}C$ values (-1.3 to -6.4‰) than marine limestones (-0.7 to + 1.6‰). Diaz-Hernandez et al. (2018) also demonstrated that the negative $\delta^{13}C$ values of pedogenic carbonates (from −9 to −6‰) in a soil profile developed as a result of volcanic tephra weathering on the island of Gran Canaria and are related to CO_2 respiration by plants with CAM photosynthesis or a mixture of C3 and C4 plants. There are three pathways to photosynthesis, the first of which involves the plant fixing atmospheric carbon to form 3-phosphoglycerate, known as a C3 plant. In the C4 and CAM pathways, photosynthesis first leads to the production of sugar with four carbon atoms, which is then reduced to C3 (Lawson et al., 2022). The abundance of these plants may be characteristic of the climatic conditions of the environment. C4 and CAM plants are generally typical of arid and semi-arid environments. In contrast, carbonate spring deposits from this area showed positive $\delta^{13}C$ values (+2.63 to +4.29‰) related to carbon depth. $\delta^{13}C$ values can also differ from one form of pedogenic carbonate to another, depending on the morphological characteristics (Kovda et al., 2006; Achyuthan et al., 2012; Kovda et al., 2014; Menezes et al., 2021). This is generally linked to changes in the formation conditions, particularly in terms of vegetation and climate, or to morphological evolution over time. Although the use of $\delta^{13}C$ values can help solve research questions for differentiating lithogenic carbonate from pedogenic carbonate and discussing the conditions of formation of pedogenic carbonates, it can also be confusing. How can we distinguish variations between pedogenic carbonate types from those between pedogenic and non-pedogenic carbonates? It would be interesting to further investigate this aspect of pedogenic carbonate research.

2.4.3.2. Oxygen stable isotopes

Oxygen has three stable isotopes with the following abundances: ^{16}O (99.757%), ^{17}O (0.038%), ^{18}O (0.205%). The $\delta^{18}O$ values in this case is obtained from the ^{16}O and ^{18}O values. $\delta^{18}O$ values are obtained using the Pee Dee Belemnite value (V-PDB) as a standard or Vienna Standard

Mean Ocean Water (V-SMOW) (Hoefs, 2009b). The $\delta^{18}O$ of pedogenic carbonate is controlled by the oxygen isotopic composition of the meteoric water from which the carbonates originate (Cerling, 1984). It can be used to differentiate carbonate types in soils. Diaz-Hernandez (2018) assigned the most negative $\delta^{18}O$ values to calcite and the least to dolomite. However, it is also linked to the climatic conditions of the region at the time of carbonate deposition (Dar et al., 2015; Raigemborn et al., 2018). This makes it possible to better analyse the climatic conditions that favour the precipitation of carbonates. Like $\delta^{13}C$ values, the use of $\delta^{18}O$ values also raises questions. Which values are linked to the mineralogical type of carbonate and which to climatic conditions? It would thus be interesting to investigate this aspect of the research further.

2.4.3.3. Clumped isotopes geochemistry

Clumped isotope geochemistry is based on the measurement of the abundance of molecules containing two or more rare (isotopologues) isotopes in natural materials. This abundance can provide unique information on the geological, geochemical, and chemical processes (Hoefs, 2009a). Clumped isotope analyses use values of Δ_i to denote the excess or deficit of isotopologue i relative to the amount expected if a material conforms to the stochastic distribution. For pedogenic carbonates, this technique is very effective for analysing the temperature conditions that prevailed during the accumulation of carbonates in soils (Quade et al., 2013; Gallagher and Sheldon, 2016). The Δ_{47} value for CO_2 is estimated based on the abundance of ^{13}C-^{18}O bonds in the carbonate network. Δ_{47} is measured as the amount of CO_2 extracted from a carbonate mineral by digestion with dry phosphoric acid (Affek, 2012). Although this method has provided important information on the temperatures of formation of pedogenic carbonates, it does not allow us to understand the seasonal timing. Quade et al. (2013) investigating clumped isotope geothermometer in carbonates from modern soils with differing rainfall seasonality (Arizona, Nevada, Tibet, Pakistan, and India) and from a deeply buried palaeosol carbonate in the Himalaya, observed that T˚C (Δ_{47}) exceeded the mean annual

temperature (MAAT) by 10-15˚C due to a summer bias in soil carbonate formation and summer heating by incident radiation. They also found a control of depth and shading on T˚C (Δ_{47}). However, they demonstrated a strong correlation (r^2=0.92) between MAAT and soil T˚C (Δ_{47}) in the site across a broad temperature range (0-30˚C) and characterised by the following equation:

$$MAAT(^{\circ}C) = (T^{\circ}C\ (\Delta 47)_0) - 21.72 \qquad \text{Eq. 2.7}$$

Where $T^{\circ}C\ (\Delta 47)_0$ is the effective air temperature at the site estimated from T˚C (Δ_{47}). Based on this result, they concluded that the mean annual temperature of the past, which governed the formation of carbonate in a palaeosol, could be reconstructed from the T˚C (Δ_{47}) values of the carbonates of this palaeosol. However, this assumes that the studied palaeosol was formed under the same environmental conditions as those of their study. Peter et al. (2013), studying the relationship between soil temperatures and carbonate formation temperatures estimated using clumped isotope thermometry (T˚C (Δ_{47})), on a Holocene carbonate soil along the eastern flank of the Andes, show that at a depth of 1 m, the average T˚C (Δ_{47}) values for soil carbonates sampled above 2 km altitude reflect summer soil temperatures. However, T˚C (Δ_{47}) values below ~2 km follows the mean annual soil temperature. This discrepancy was credited to the difference in moisture regime. But Ringham et al. (2016) in a study on the eastern Andean piedmont of Argentina showed that T˚C (Δ_{47}) was invariant with depth. To explain the difference between their T˚C (Δ_{47}) values and those of Peter et al. (2013) close to their study site, they suggested a potential site-to-site variability due to soil hydrology this assumption is also supported by Gallagher and Sheldon (2016) results obtained on ten different sites across the western United States. The results of Ringham et al. (2016) study also suggest that the deeper T˚C (Δ_{47}) values (≥40 cm) are consistent with carbonate formation during the early part of soil drying immediately after large midsummer rainstorms. Carbonate formation ≤ 40 cm depth may be biased by soil drying after small, frequent rainfall events. This result was

supported by Burgener et al. (2016) in a Holocene carbonate soil in Chile. According to their study, only the highest precipitation events affect soil moisture at depths >40 cm. They further highlight the role of the soil moisture regime in modulating the timing of soil carbonate formation, which affects the resulting carbonate values. All these studies highlight a gap in the understanding of the global and local factors affecting the deposition and preservation of pedogenic carbonates (Fischer-Femal and Bowen, 2021).

2.4.4. Strontium isotope ratio ($^{87}Sr/^{86}Sr$) to trace calcium origin.

The strontium (Sr) isotope method is a powerful tool for studying chemical weathering and soil genesis, cation provenance, and mobility. It is a sensitive geochemical tracer applicable to large-scale ecosystem studies and centimetre-scale examinations of cation mobility within a soil profile (Capo et al., 1998). It has been established that the calcium present in pedogenic carbonate comes, in some cases, from the previous alteration of a carbonate mineral, a rock, or a silicate mineral rich in calcium ions and/or in other cases from deposits of dust rich in calcium ions (Capo and Chadwick, 1999; Dietrich et al., 2017)

The principle behind using the Sr isotopic ratio ($^{87}Sr/^{86}Sr$) to trace the origin of Ca in pedogenic carbonates is that the ratio of Sr isotopes in the soil reflects the geology of the parent material from which the soil was formed (Capo et al., 1998). Calcium, a major component of pedogenic carbonate, is derived from the breakdown of rocks and minerals in the soil. As calcium is taken up by plants and incorporated into pedogenic carbonate, it carries the isotopic signature of the parent material. Strontium, which has a similar ionic radius and chemistry to calcium, is also present in the parent material of the soil. However, unlike calcium, which is relatively immobile in the soil, strontium is more mobile and can be exchanged between the soil and groundwater (Dubchak, 2018). As a result, the ratio of Sr isotopes in pedogenic carbonate can provide a unique signature of the geology of the parent material from which the soil was formed. This

signature can then be compared to the Sr isotopic composition of rocks and minerals in the surrounding area to determine the origin of calcium in pedogenic carbonate.

This method requires prior identification of the potential parent material. It is also important to define the Sr/Ca ratio, which gives an indication of the fractionation of calcium and strontium ions. According to Capo et al (1998), the amount of calcium that does not fractionate from the Sr contributed by an end member in a two-component system can be calculated from Sr isotopic data, provided that the Sr/Ca concentration ratio is known for each component. The fraction of Ca contributed to this mixture by the component 1 is given the following equation:

$$\frac{M_1^{Ca}}{M_1^{Ca}+M_2^{Ca}} = \frac{(\delta_{mix}-\delta_2)K_2}{(\delta_{mix}-\delta_2)K_2+(\delta_1-\delta_{mix})K_1} \quad \text{Eq. 2.8}$$

where K_1 and K_2 are the Sr/Ca concentration ratios for components 1 and 2.

This method has been widely used to trace calcium sources in pedogenic carbonates (Capo and Chadwick, 1999; Bockheim and Douglass, 2006; Millière et al., 2019; Monhonval et al., 2023). Van der Hoven and Quade (2002) demonstrated that strontium isotopic ratio ($^{87}Sr/^{86}Sr$) can be used to trace the spatial and temporal variation of Ca sources in pedogenic soil carbonates developed in Quaternary basalt flows and an ash deposit in the Zuni-Bandera volcanic field, New Mexico (USA). Their results identified the chemical weathering of carbonate minerals contained in the dust as the main source of Ca and the chemical weathering of silicate minerals originating either in the dust or in the underlying basalt as a secondary source. In contrast, Dietrich et al. (2017) prioritised weathering of parent material (granite and greenstone) as the source of Ca in pedogenic nodules formed in clay-rich parent material in the Far North region of Cameroon. Saharan dust was identified as an additional source These two examples are set in different contexts. In the far north of Cameroon, plagioclase weathering of the parent material took place during humid climatic phases, which favoured the availability of calcium, fixed later in the soil during more arid phases. In contrast, in the Zuni-Bandera volcanic field, the composition of the dust appears to have remained relatively constant over the last 0.7 Ma,

and its calcium contribution outweighs that derived from weathering of the overlying parent material. However, this demonstrates the robustness of this method for tracing the origin of calcium in contests where various sources are involved. The use of strontium isotopes as tracers for Ca in soil carbonate research is interesting because it provides insight into the potential for atmospheric carbon sequestration (Monger et al., 2014).

More recently, some studies have also used calcium isotope ratio ($\delta^{44/40}Ca$) to trace the origin of calcium in soil carbonate features such as needle fibre calcite, (Millière et al., 2019) and soil profiles (Laudicina et al., 2021; Haldar et al., 2023). In contrast to the strontium method, it offers a direct approach and therefore more realistic results. However, more information is still needed to understand the mechanisms of Ca fractionation during calcite precipitation (Millière et al., 2019).

2.4.5. Elemental geochemistry and mineralogy

The processes that drive carbonate accumulation in soils can also be studied based on elemental geochemical balance using a variety of analytical methods that are as diverse as they are confusing. These methods very often vary from one author to another, although the objectives pursued are often concomitant. For example, to analyse the weathering and pedogenic processes that led to the accumulation of carbonates in southern India, Achyuthan et al. (2012) combined different tools, including the flame photometer to determine Na_2O and K_2O contents, the spectrophotometer for SiO_2 and Al_2O_3 contents, titrimetry for Mg and Ca contents, the atomic absorption spectrometer (AAS) for Fe, Mn and trace element contents, and inductively coupled plasma atomic emission spectroscopy (ICP-AES) for rare element contents. While for the same objective Diaz-Hernandez et al (2018) on the island of Gran Canaria, recommended X-ray fluorescence spectroscopy for major elements and Zr, and inductively coupled plasma mass spectrometry (ICP-MS) for trace elements. Other examples can be added to these (Durand

et al., 2007; Wolff et al., 2017). This set of facts highlights the need for a harmonised standard operating procedure for the analysis of total elemental composition of pedogenic carbonates.

The behaviour of geochemical elements, individually or in combination, is widely used in SIC research, mainly to differentiate lithogenic carbonates from pedogenic carbonates, or to identify pedogenic processes. For example, Valera-Fernández et al. (2020) showed that there are differences between rare Earth elements (REE) concentration of the compact carbonate crust (calcretes) and the indurated coastal limestone sediments (calcarenites) that cover it, in the Yucatan Peninsula (Mexico). The REE concentration was higher in the calcarenites (lithogenic) than in the calcretes (pedogenic). The authors explained this difference by the influence of pedogenic processes, particularly the dissolution of large volumes of carbonates during pedogenesis, which would have resulted in a considerable loss of REE. They also explained the enrichment in heavy rare Earth elements (HREE) and the negative anomaly in Ce in calcretes by the alkaline environment, where Ce^{4+} easily forms soluble complexes with $CO_3^{2-}$and HCO_3^- and can be extracted from the soil mass by runoff. Dietrich et al (2021) also observed a high concentration of REE in pedogenic carbonate nodules in the Far North region of Cameroon. They explained these high REE concentrations by carbonate complexation favoured by the proximity of the ionic radii of Ca^{2+} and REE. They also observed a strong negative anomaly of Ce in the carbonate nodules, which they linked to the oxic conditions in the environment during the precipitation of the carbonate nodules. In addition, we explained in section 2.4.4 that the Sr^{2+}/Ca^{2+} ratio is used to trace the source of the calcium contained in pedogenic carbonates. However, one of the most remarkable applications was carried out by Dietrich et al. (2021) for the quantitative assessment of calcium accumulation in a palaeo-vertisol from the Far North region of Cameroon. Calcium depletion in the parent material and the accumulation in the palaeo-Vertisol residue was calculated by normalising it with an

immobile element (titanium, considered to be generally preserved and unchanged in Vertisols) according to following equation.

$$\%Ca = \left(\frac{[Ca]_{Res}/[Ti]_{Res}}{[Ca]_{PM}/[Ti]_{PM}}\right) \quad \text{Eq. 2.9}$$

Where $[\mathrm{Ca}]_{\mathrm{Res}}$ and $[\mathrm{Ti}]_{\mathrm{Res}}$ represent the respective residual Ca and Ti concentrations in the residual elements of the palaeo-vertisol. $[\mathrm{Ca}]_{\mathrm{PM}}$ and $[\mathrm{Ti}]_{\mathrm{PM}}$ are the respective Ca and Ti concentrations in the parent material. To estimate calcium accumulation in the carbonate phase of palaeo-vertisols, the authors used volumetric ratios between parent material and palaeo-vertisol, considering variations in density and volume. The volumetric deformation (ε) was calculated using the equation of Egli and Fitze (2000).

$$\varepsilon = \frac{\rho_{PM} \times [Ti]_{Res}}{\rho_{Res} \times [Ti]_{PM}} \quad \text{Eq. 2.10}$$

Where ρ_{PM} and ρ_{Res} are the densities of parent material and palaeo-Vertisol respectively. The accumulation of calcium in the carbonate phases was then calculated using the following equation.

$$\%Ca_{accu} = \frac{\alpha_{Accu} \times [Ca]_{Accu} \times \rho_{sAccu}}{\alpha_{Res} \times [Ca]_{PM} \times \rho_{PM}} \times \varepsilon \quad \text{Eq. 2.11}$$

Where α is the volumetric fraction of the different kinds of palaeo-Vertisols (% of skeleton for carbonate nodules, % of carbonate in soil fine earth for micritic soil carbonate, and the missing fraction necessary to reach 100% is attributed to the residue). According to the authors, the errors can be as high as 46% and are mainly due to the variability of the skeletal content. This approach remains questionable, since accumulation processes take place in an open environment, and calcium could come from a variety of sources, as shown by Dietrich et al. (2017).

X-ray diffraction is used to mineralogically identify the types of carbonates present in the soil (Hamidi et al., 2001; Sun et al., 2023). This method can be combined with other methods to differentiate between pedogenic carbonates and lithogenic carbonates (Landi et al., 2003; Diaz-

Hernandez et al., 2018). Landi et al. (2003), for example, used XRD results of pedogenic carbonates combined with micromorphological observations (SEM) to show that, although calcite is the dominant pedogenic carbonate in Saskatchewan soils, a small amount of dolomite was trapped in their structure during their formation. Furthermore, the use of energy-dispersive X-rays (EDX) has become increasingly popular. EDX is commonly associated with scanning electron microscopes (SEM) or transmission electron microscopes (TEM) and allows for the mapping of carbonate in relation to other minerals (Diaz-Hernandez et al., 2018), analysis of spatial arrangement (Shweizer et al., 2023), and identification of areas of accumulation (Prokof'eva et al., 2021).

2.5. Quantitative techniques in soil inorganic carbon measurements

Several laboratory methods can be used to determine SIC content. These methods vary in their accuracy, precision, and complexity (Table 2.2). The choice of method depends on the specific research question and the available resources.

2.5.1. Calcimetric method

Described by Sherrod et al (2002) and Fonnesbeck et al. (2013), SIC determination using the pressure calcimeter method is now widely used particularly for calcareous soils (Wang et al., 2010; Zhang et al., 2015; Raheb et al., 2017; Zhang et al., 2018). The principle of the method is to estimate the pressure associated with the release of carbon dioxide produced by the dissolution of calcium carbonate in an acid-treated soil sample. The SIC concentration is determined by assuming that all carbonates are derived from calcium and multiplying the calcium carbonate concentration by the mass proportion of C in the calcium carbonate (0.12 g C g^{-1} $CaCO_3$) (Apesteguia et al., 2018).

This method has been developed for Calcisols and other soils rich in calcium carbonate. It is not recommended for soils rich in dolomite (Apesteguia et al., 2018). It also has the limitation

that it only allows the estimation of SIC, to the detriment of other methods that also allow the estimation of SOC (Leogrande et al., 2021). In addition, it is an indirect method, since the SIC content is estimated as a function of the carbon dioxide pressure released. It would therefore be interesting to analyse the extent to which either the operation of the system or the conversion could affect the results obtained. Better still, being a destructive method, which also requires the use of chemical reagents and the release of carbon dioxide, it is nonetheless linked to a non-negligible environmental footprint.

2.5.2. Dry combustion method

Dry combustion is also a widely used method for determining the SIC content (Wang et al., 2012; Wang et al., 2014; Zhang et al., 2021). This method is based on the combustion of a soil sample at high temperatures. It is assumed that all carbon present in the sample is oxidized to carbon dioxide. This includes both organic and inorganic carbon. However, if the sample is first treated to remove organic carbon, the remaining carbon measured after combustion is derived solely from inorganic carbon. Similarly, if a sample is first treated to remove inorganic carbon, the carbon remaining after combustion is measured only as organic carbon. In some cases, one subsample is pre-treated with HCl to remove inorganic carbon, and then subjected to dry combustion to determine the organic carbon content. Another subsample is subjected to dry combustion without pre-treatment to obtain the total carbon content (Shi et al., 2017; Xu et al., 2021). Alternatively, the organic carbon content is determined by another method and then subtracted from the total carbon content, which was determined by dry combustion (Lu et al., 2020; Wang et al., 2022).

In both cases, the inorganic carbon content is determined by subtracting the organic carbon content from the total carbon content according to the following equation:

$$SIC = STC - SOC$$ Eq. 2.12

where STC, SIC, and SOC represent the soil total carbon, soil inorganic carbon, and soil organic carbon respectively.

According to Leogrande et al. (2021), dry combustion provides reliable and accurate results in soils with different calcium carbonate contents by comparing the results of the calcimetric method and offers the advantage of estimating both SIC and SOC contents. Similar to the calcimetric method, dry combustion is also a destructive method. This also results in a certain environmental footprint. In addition, it would be interesting to analyse the extent to which the pre-treatment applied for the destruction of either the SIC or the SOC can affect the results at the end of the process.

2.5.3. Titration

The method for determining SIC content by rapid titration has been described by Bundy and Bremner (1972). The soil sample is treated with 2M HCl at room temperature for 16-24 hours in a sealed bottle containing 2M KOH and The CO_2 released from the carbonates by this treatment is determined by titrating the KOH solution with standard HCl. In some cases, a coulometric indicator (bromothymol blue) is used and KOH is replaced with NaOH (Moharana et al., 2021). This is one of the oldest methods used to estimate inorganic carbon content in soil. However, these are less commonly used. The results depend significantly on the operator. It is also less rapid and accurate than other methods such as calcimetric method, which uses fewer chemicals (Elfaki et al., 2016). Moreover, it is a destructive method that requires a large quantity of chemical reagents. It is therefore the method with the greatest footprint on the environment.

2.5.4. Spectroscopic methods

These are the most recent methods for quantifying SIC content and are already widely used (Grinand et al., 2012; Comstock et al., 2019; Barthès et al., 2020; Gomez et al., 2022). The

general principle of these methods is to calibrate the spectroscope with a wide range of samples whose contents have been determined by other pre-established methods. Once the calibration is complete, the contents of the other samples can be measured.

Mid-Infrared reflectance spectroscopy (MIRS) is a powerful tool for determining the SIC content. The principle of MIRS is based on the interaction of light with matter, specifically the reflection of infrared radiation by soil particles. The MIRS method involves measuring the reflectance spectra of soil samples in the mid-infrared region (4000-400 cm^{-1}). Spectra are generated by shining a beam of infrared light onto the soil surface and measuring the intensity of the reflected light. Reflectance spectra provide information on the chemical composition of the soil, including the presence and amount of the SIC. Overall, MIRS is a non-destructive, rapid, and cost-effective method for determining the SIC content of soil samples. This is particularly useful for large-scale soil surveys, where traditional laboratory methods are time consuming and expensive (Barthès et al., 2020; Gomez et al., 2022). However, it is less accurate than both calcimetry and dry combustion (Grinand et al., 2012).

Fourier transform mid infrared photoacoustic spectroscopy (FTIR-PAS) has also been used to determine the carbonate content of the soil (Du et al., 2013). The FTIR-PAS technique is based on the absorption of electromagnetic radiation by analyte molecules. Subsequently, non-radiative relaxation processes lead to the local warming of the sample matrix. The pressure fluctuations generated by the thermal expansion are then detected using a highly sensitive microphone. The resulting spectrum differs from the transmittance or reflectance mid-infrared spectra because it detects non-radiative transitions within the sample. In photoacoustic spectroscopy, the detected signal is proportional to the sample concentration, and FTIR-PAS analysis can be used to analyse samples that strongly absorb mid-infrared radiation without pre-treatment. This reduces the processing time and makes the technique very useful and applicable for soil-testing purposes.

Although there are few applications to date, it would be a suitable alternative for the analysis of solid soil samples with high infrared absorption, and the technique allows for the accurate and rapid determination of the carbonate content of the soil.

2.5.5. Ramped combustion and Loss of ignition

Ramped combustion (Apesteguia et al., 2018) or the thermal gradient method (Vuong et al., 2013) is a method used for simultaneous analysis of total carbon, SOC, and SIC content. It consists of placing soil samples in a simultaneous thermal flow and measuring the amount of CO_2 released by infrared detection, which is converted to carbon content. Samples are first heated from room temperature to 105 at 10 °C.min^{-1} and held at this temperature for 15 min. to remove moisture, then heated to 850 °C at 10 °C.min^{-1}. The total carbon concentration of the sample is determined using the cumulative amount of CO_2 evolved between 120 and 850 °C. Organic carbon concentrations are determined from the CO_2 released between 120 and 550°C, while inorganic carbon concentrations are determined from the CO_2 released between 550 and 850°C. The selection of 550 °C as the cut-off temperature between organic and inorganic carbon was based on the conventional temperature used for organic carbon determination using loss on ignition (LOI) methods and observation of the temperatures of the minima in CO_2 thermograms. The limit between SOC and SIC is not clearly marked in this method. In a similar manner, Vuong et al. (2013) used 900 °C as the limit for inorganic carbon, Apesteguia et al. (2018) set the limit to 850 °C. These discrepancies may have consequences on the measured values.

According to Apesteguia et al. (2018), ramped combustion appears to be a preferable single-sample method for the simultaneous quantification of SOC and SIC in limestone-enriched soils, providing a relatively fast, economical, and efficient method that excludes the use of hazardous reagents such as those used in the acid fumigation used in dry combustion.

The loss of the ignition method is quite close to that of ramped combustion. The SOC is estimated by the loss of ignition at 450°C and the SIC by the loss of ignition at 950°C (Hussain et al., 2019). The samples are dried in the oven by pre-treatment at 105 °C. The difference between the weights at 450 °C and 105 °C gives the loss of organic matter, converted to organic carbon by multiplying by van Bemmelen factor of 1.724. The SIC content is obtained by observing the weight loss between 450 °C and 950 °C and multiplying it by a conversion factor of 0.273 to convert the mass of CO_2 into mass of carbon.

This method is interesting for applications involving many samples. Furthermore, it allows for the determination of organic, inorganic, and total carbon. It has demonstrated its ability to estimate the SOC and SIC in arid regions (Wang et al., 2012).

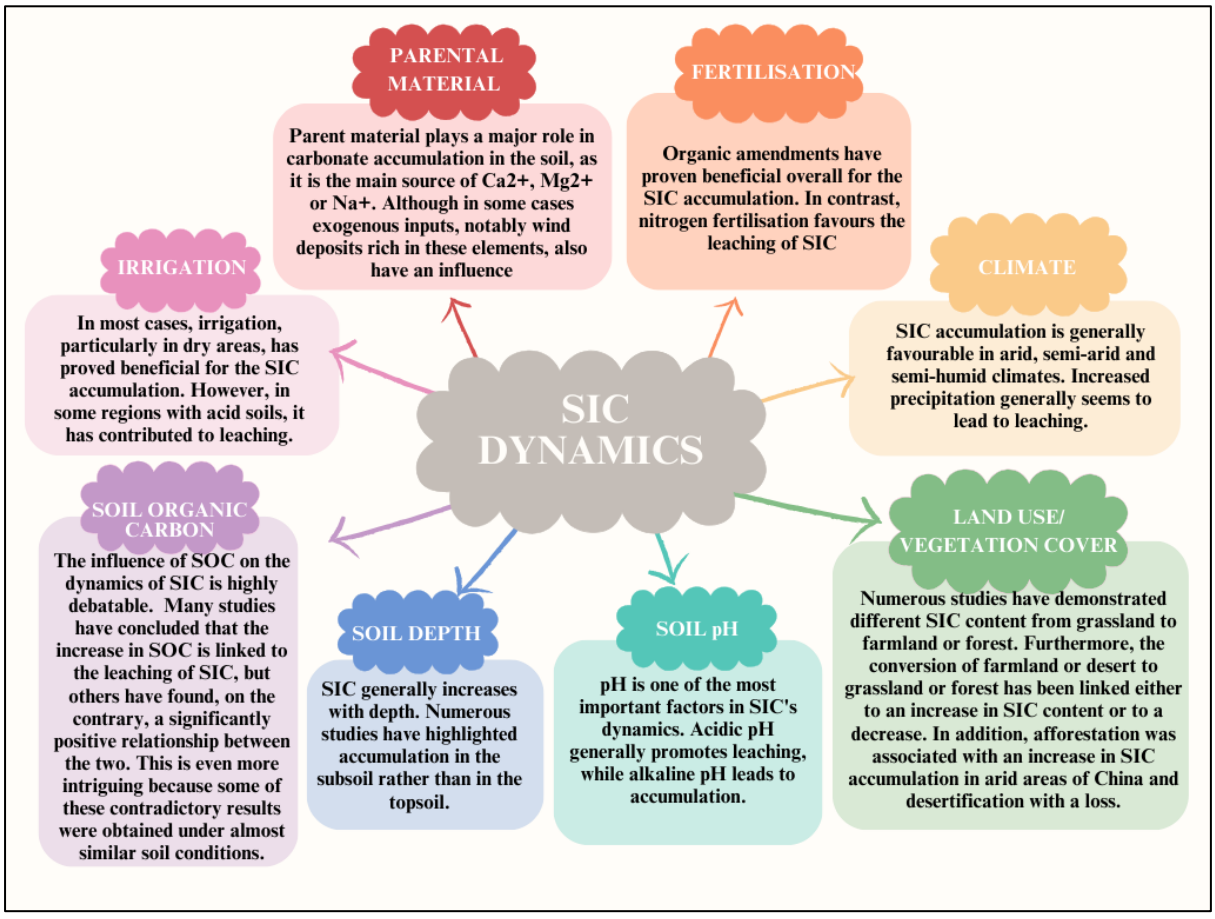


Fig. 2.8. Factors affecting SIC dynamics.

2.6. Soil inorganic carbon dynamics

This involves measuring the amount of inorganic carbon in the soil and assessing its spatio-temporal variations. The aim is to quantify the capacity of soil to store carbon and identify factors that may enhance or reduce soil carbon sequestration. In most cases, the calculation of SIC stock is a powerful tool for assessing the evolution of the inorganic carbon pool related to land use (Wu et al., 2009), especially in agriculture with fertilization (Bughio et al., 2016) and irrigation (Zhang et al., 2015), or to changes in vegetation cover, especially in drylands with afforestation (Chang et al., 2012) or desertification (An et al., 2019). The results highlight the factors that lead to the accumulation or loss of SIC, as shown in Fig. 2.8.

Estimation of carbon storage is generally based on two analytical approaches that use distinct processes. The first is the estimation of SIC storage, which is limited to estimating the capacity of the soil to sequester inorganic carbon, regardless of SIC type (Ellert et al., 2007; Mi et al., 2008; Ayala-Niño et al., 2020). The second category focuses solely on the storage of SIC in the form of pedogenic carbonates (Rabenhorst et al., 1984; Liu et al., 2023).

Table 2.2. Comparison of methods for measuring SIC content.

Methods	Usage	Accuracy	Rapidity of the measurement process	Cost	Use of chemical reagents	Possibility of operator error	Environmental friendliness	Improvement
Calcimetry	SIC	+	-	+	+	+	+	+
Dry combustion	SIC, SOC, STC	++	+	+	+	+	-	+
Titration	SIC	-	-	++	++	++	-	-
MIRS	SIC	+	++	-	-	-	++	++
Ramped combustion	SIC, SOC, STC	+	+	+	-	+	-	+
LOI	SIC, SOC, STC	+	+	-	-	+	-	+

- low or reduce; + good or important; ++ very good or very important

2.6.1. Soil inorganic carbon storage

Estimating SIC storage or stock requires knowledge of soil inorganic carbon content and bulk density. It is generally based on three parameters: SIC content, layer thickness, and bulk density.

The commonly used equation is as follows:

$$SICs_i = D_i \times H_i \times SIC_i \times \frac{1}{100} \quad \text{Eq. 2.13}$$

When the thickness of the soil under study is several layers, the equation becomes.

$$SIC_s = \sum_{i=1}^{n} D_i \times H_i \times SIC_i \times \frac{1}{100} \quad \text{Eq. 2.14}$$

where $SICs_i$, D_i, H_i and SIC_i are the soil inorganic storage (kg m^{-2}), bulk density (g cm^{-3}), thickness (cm), and soil inorganic carbon content (g kg^{-1}) of layer i. n is the number of layers.

The inorganic carbon stock of the soil can also be calculated using the Batjes (1996) equation to calculate the organic carbon stock for an individual profile with k layers, which was rewritten and adapted for inorganic carbon (Wang et al., 2010).

$$SIC_i = \rho_i \times P_i \times D_i \times (1 - S_i) \quad \text{Eq. 2.15}$$

This equation was used for the case of one layer. When the profile consists of several layers, the equation becomes.

$$SIC_d = \sum_{i=1}^{k} SIC_i = \sum_{i=1}^{k} \rho_i \times P_i \times D_i \times (1 - S_i) \quad \text{Eq. 2.16}$$

where k is the number of horizons, SIC_i is the soil inorganic carbon content (Mg m^{-2}), ρ_i is the bulk density (Mg m^{-3}), P_i is the proportion of inorganic carbon (gC g^{-1}) in layer i, D_i is the thickness of this layer (m), and S_i is the volume fraction of fragments >2 mm.

The first estimation method is the most widely used for computing SIC storage. For example, Tan et al. (2014) used it to assess SIC stocks under different soil types and land uses in the Loess Plateau region of China. Liu et al. (2022) also used this method to analyse SIC storage

in steppe riparian wetlands under pressure from human activity. Many other studies have used it to estimate the evolution of carbon stock (organic and inorganic) under different land use regimes (Wu et al., 2009; Zhang et al., 2015; Shi et al., 2017; Zhang et al., 2021). The difference between the two approaches lies in the fact that the second (Eq. 2.13) considers the proportion of the volume of soil considered occupied by the granulometric fraction greater than 2 mm (rock fragments). This contrasts with the second approach, which only considers the fine fraction (less than 2 mm). For soils with a large coarse fraction, the Batjes (1996) approach seems more realistic, as the first approach could result in an overestimation of the carbon stock.

2.6.2. Pedogenic carbonate storage

The approach for estimating pedogenic carbonate stocks was that of Salomons and Mook (1976). The calculation is based on stable carbon isotope values according to the following equation:

$$\%PC = \frac{\delta^{13}C_{(soil)} - \delta^{13}C_{(PM)}}{\delta^{13}C_{(PC)} - \delta^{13}C_{(PM)}} \times 100 \qquad \text{Eq. 2.17}$$

where $\%\ PC$ is the proportion of total pedogenic carbonate, $\delta^{13}C_{(soil)}$ is the measured bulk carbonate value for a particular soil depth, $\delta^{13}C_{(PM)}$ is the measured bulk carbonate value of the parent material, and $\delta^{13}C_{(PC)}$ is the measured pedogenic carbonate value.

The method was originally developed by Rabenhorst et al. (1984) to estimate the amount of pedogenic carbonate in the soil profile. It has proven useful for analysing the formation of pedogenic carbonates related to fertilization and irrigation (Wang et al., 2014; Bughio et al., 2016), variation in vegetation cover (Landi et al., 2003) and conversion of natural vegetation to agricultural land (Mikhailova et al., 2018).

In comparison with the approach involving the calculation of SIC storage without discriminating the type of inorganic carbon, it seems more realistic in estimating the evolution of the carbonate stock resulting from pedogenetic processes. However, the approach based on

estimating the evolution of SIC still allows for an idea of the evolution of the inorganic carbon pool, and studying changes over the chronosequence provides a fairly realistic picture of the dynamics in relation to any factor.

2.7. Modelling soil inorganic carbon

There has recently been growing interest in the use of models that predict the spatial and temporal variation of soil properties (Heuvelink et al., 2021; Liu et al., 2022; Yan et al., 2022). Recent advances in statistical, geostatistical and machine learning techniques has considerably increased the ability to collect, analyse and predict spatial information relating to soils (Brevik et al., 2016). As highlighted by Sun et al (2021), understanding spatio-temporal changes in soil conditions is important to support food production, environmental sustainability and adaptation to climate change. Few studies have been conducted to analyse the spatial and temporal distributions of inorganic carbon in the soil (Table 2.3). Compared to SOC modelling, scientific work on SIC modelling is not as well-developed. The objectives pursued in the development of models vary enormously, as do the modelling methods and environmental parameters. For example, Hirmas et al. (2010) aim to develop a process-based model predicting the evolution of pedogenic calcite that takes account of hydrology and landscape position and to apply the model to understand the response of SIC to elevated atmospheric CO_2 concentrations. The environmental parameters in this case are the precipitation threshold and the topographic index threshold. A one-dimensional compartmental thermodynamic model is used to simulate calcite precipitation and dissolution. Such a model is difficult to reproduce in other contexts because it is limited to a particular type of landscape, in this case mountainous terrain (South Fry Mountains, USA). More recent models (Sreenivas et al., 2016; Yang et al., 2017; Filippi et al., 2020) focus more on the distribution of SIC at larger scales (regions, countries). They are all based on numerical approaches. However, the choice of the predictive model and variables differs. While Sreenivas et al. (2016) and Yang et al. (2017) opt for random forest (RM) as a

predictive model, Wilford et al. (2015) preferred a cubist model while Filippi et al. (2020) choose a two-step approach. Random forest model to predict the presence or absence of SIC and separate model to predict SIC content. If the random forest model that appears here in most of these studies would have proven its ability to predict reliable values for other soil properties such as SOC (Khaledian and Miller, 2020), the high heterogeneity of SIC in soil must be considered, which justifies the use of the two-step approach (Filippi et al., 2020). Furthermore, except for de Soto (2017) these models do not consider other soil properties among the environmental parameters, however it has been shown the influence of pH on distribution of SIC (Shi et al., 2012; Yang et al., 2012). Succinctly put, all this highlights the need for continued development and testing of more predictive models for studying the spatial and temporal evolution of SIC with minimal uncertainty.

Table 2.3. Summary of modelling approaches used for SIC studies

Approach	Goal	Region and extent	Number of samples or pits	Parameters	Inputs or environmental co-variable	Depth (m)	Regression	Reference
One-dimensional compartmentalized thermodynamic model	Develop a process-based pedogenic calcite model that accounts for landscape hydrology and geomorphic position	USA, southern Fry Mountains -	16 pits	- Precipitation threshold (Ω) - Topographic index threshold (Λ)	Geomorphic delineation; sediment collected from dust traps; Detailed soil descriptions (percent sand and clay, and bulk density); Precipitation; Temperature; Time step (optically stimulated luminescence dates)	1.5	-	(Hirmas et al., 2010a)
Machine learning using Cubist model	Understand the environmental controls on soil carbonate formation and preservation in the landscape	Australia	1311 samples	Soil Carbonate distribution	Soil and geological maps; Climate; Vegetation; Terrain; Remotely sensed mineralogy and geochemistry	0.0-0.1 0.6-0.8	0.5	(Wilford et al., 2015a)
Machine learning using Random Forests model	Predicting the spatial distribution of SIC content	India	1198 samples	SIC content	Climate; Land cover; Rock type Soil type; Multi-year NDVI; Irrigation status	1	-	(Sreenivas et al., 2016a)

Table2.3 (continued)

Approach	Goal	Region and extent	Number of samples or pits	Parameters	Inputs or environmental co-variable	Depth (m)	Regression	Reference
Machine learning using Random Forests model	Analyse the vertical distribution of SIC based on pedogenic knowledge in different landscapes	China, northeastern Tibetan Plateau	99 pits	SIC stock	Digital elevation model; Climate data; Landsat 5 Thematic Mapper; Latitude and longitude	1	0.84–0.86	(Yang et al., 2017a)
PHREEQC numerical model	Analysing the effect of irrigation on carbonate dynamics in the ploughed layer of agricultural soils	Spain, Ebro Basin	-	Carbonate content	Land uses systems; monthly soil water balances; soil characteristics	0.2	-	(de Soto et al., 2017a)
Two step modelling approach, random forest model to predict the presence or absence and separate model to predict SIC content	predict the presence or absence of SIC in the study area, then using a separate model to predict SIC content	Australia, South Wale	154 samples	SIC presence and SIC content	Satellite imagery; Land use; Topographic data; Geological units; Gamma radiometrics	0.3-0.5		(Filippi et al., 2020a)

2.8. Multidisciplinary applications of SIC

2.8.1. Ecosystem services

The term "ecosystem service" refers to the functioning of the Earth's life support system and the direct and indirect benefits humans derive from nature. Therefore, it represents part of the planet's total economic value (Costanza et al., 1997). To this end, soil properties including pH, bulk density, cation exchange capacity and SOC are considered from the angle of their influence on so-called "ecosystem services", classified into four categories (Adhikari and Hartemink, 2016): (i) provisioning services (direct or indirect food for humans, fresh water, wood, fiber, and fuel); (ii) regulating services (regulation of gas and water, climate, floods, erosion, biological processes such as pollination, and diseases); (iii) cultural services (aesthetic, spiritual, educational, and recreational); and (iv) supporting services (nutrient cycling, production, habitat, and biodiversity).

Although these key properties do not include SIC at the onset, Groshan et al. (2018) demonstrated that SIC is important for all four categories of ecosystem services (Fig. 2.9). According to his study, the entire projected value of SIC storage in the top two meters of soil is evaluated at $5.17 trillion for the United States of America. This is not insignificant and leads the authors to suggest that SIC should be included in the ecosystem services framework for the United Nations (UN) Sustainable Development Goals. A study by Mikhailova et al. (2021) demonstrates that the total estimated monetary midpoint value for SIC on ecosystem services is estimated at $17.22 billion in the state of South Carolina (USA). While it is much lower compared to that of SOC, which is $107.14 billion, it is still significant and shows that sustainable management policies can help avoid additional carbon dioxide emissions. It enables the quantification of the impact of SIC on services and commodities. This should be further developed to establish clear sustainable development goals, as in the case of organic carbon.

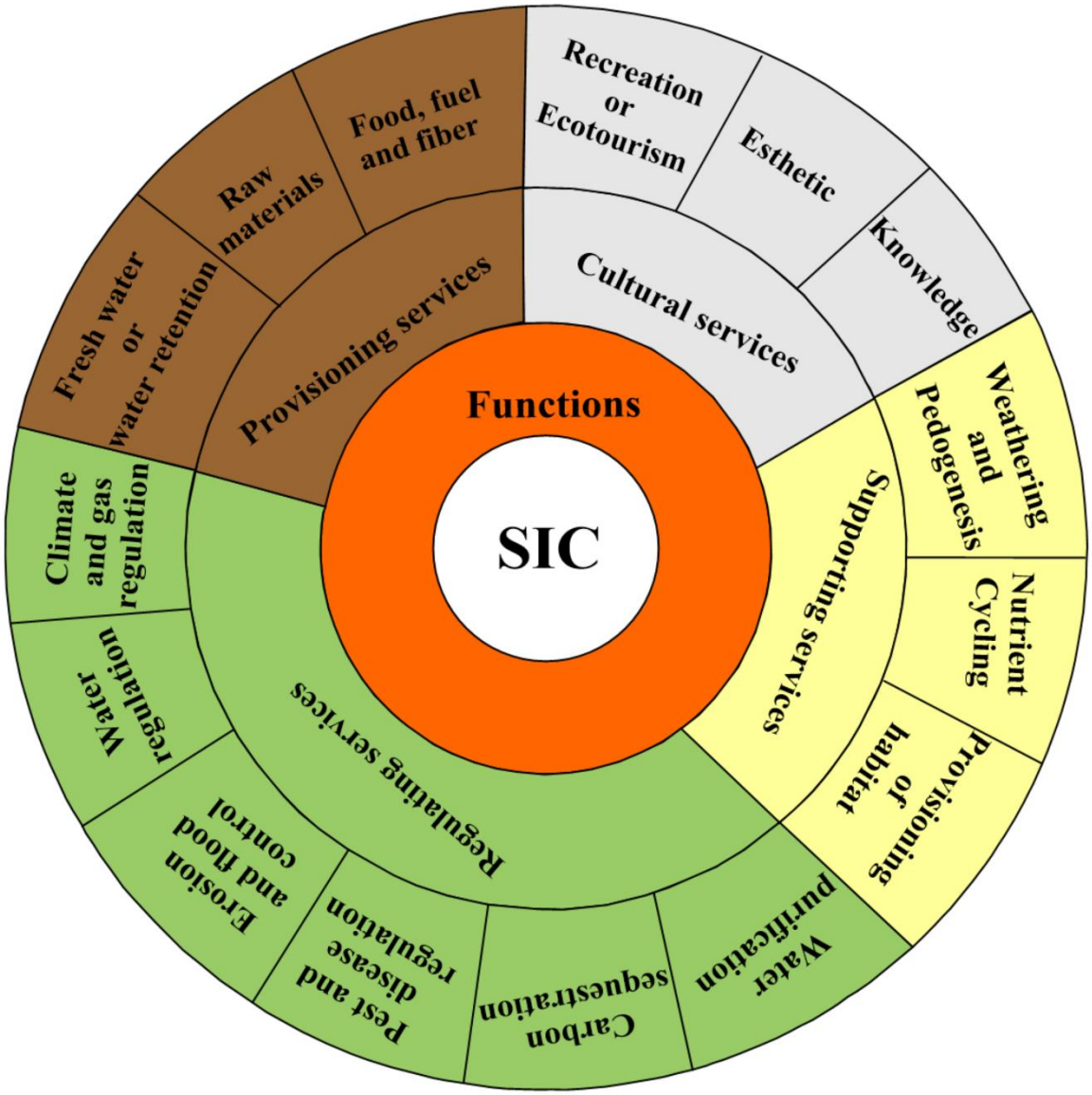


Fig. 2.9. Ecosystem services of SIC based on the work of Groshans et al. (2018).

2.8.2. Pedogenic carbonate and palaeoreconstruction

Pedogenic carbonates-based proxies are widely used for analysing past environmental conditions that prevail during their formation (Dar et al., 2015; Khormali et al., 2020). This information on past carbonate pedofeatures is related to their stable carbon and oxygen isotope compositions. In principle, as shown by Cerling (1984), the isotopic signatures of $\delta^{13}C$ and $\delta^{18}O$ in pedogenic carbonate are controlled by the isotopic compositions of soil CO_2 and water, respectively (cf. Section 2.4.3).

The $\delta^{13}C$ values of pedogenic carbonates can be used to infer the types of plants that grow in the area, which can help researchers to understand past ecological and environmental conditions. The relative abundance of C3 and C4 plants in local vegetation controls the $\delta^{13}C$ value of pedogenic carbonate. Owing to isotopic discrimination by photosynthetic pathways, the $\delta^{13}C$ of CO_2 under C3 plant species (-27 ‰ on average) differs from that under C4 species (-13 ‰ on average) (Cerling et al., 1997). Furthermore, the development of a particular vegetation type might be associated with climatic conditions. For example, Dar et al. (2015), in a Late Quaternary loess palaeosol sequence, associated C4 plant biomass development towards the top of sections with water stress and/or reduced atmospheric pCO_2 and increased aridity.

The $\delta^{18}O$ values of pedogenic carbonate are controlled by the oxygen isotopic composition of the meteoric water from which the carbonates originated (Cerling, 1984). In most cases, this can be linked to the climatic conditions of the region, particularly the rainfall (Liu et al., 1996) and temperature (Orr et al., 2022). One of the most effective methods is the clumped isotope method. This provides a better picture of the temperatures that prevailed during the formation of pedogenic carbonates (Eiler, 2011).

The isotopic composition of pedogenic carbonates can also be useful for palaeolandscape analysis (Heilbronn et al., 2015). Palaeoenvironmental reconstruction through pedogenic carbonates is an interesting tool not only for understanding past environments, but also for analysing the natural processes favouring the precipitation of carbonates in the soil. However, its use is delicate and meticulous because Monger et al. (2009) show that the analysis of $\delta^{13}C$ as an indicator of the biome varies according to the scale of observation. Furthermore, the precipitation–recrystallization processes of carbonates within the same profile could affect the carbon and oxygen isotope values.

2.8.3. Geochronology

Pedogenic carbonates can also provide chronology of past events. By dating the formation of carbonates, researchers can determine the timing of environmental changes such as changes in vegetation cover or climate conditions. Radiocarbon dating is the most used method to date pedogenic carbonates (Dal Sasso et al., 2018; Ernst et al., 2019; Golubtsov et al., 2021). However, other dating methods have also been used, such as the uranium–thorium method (Bockheim & Douglass, 2006; Durand et al., 2007; Valera-Fernández et al., 2020) and optically stimulated luminescence (OSL) dating (Diaz et al., 2016; Dietrich et al., 2021).

The principle of radiometric dating is based on the disintegration of a parent isotope into a daughter isotope. As explained by Ambers (2005), Uranium series dating utilises the two natural uranium decay chains (from parent ^{238}U and ^{235}U) and their progeny. The zeroing process here is usually the formation of calcite from carbonates (with uranium present as an impurity) carried in solution. Since the primary long-lived daughter, ^{230}Th, is largely water insoluble, in any process involving dissolution and redeposition of uranium there will be effectively no thorium present in the newly formed crystal matrix, and provided the system remains closed, the proportions of generated thorium and other daughters can be used as a clock. Age ranges and precision vary with uranium content of each sample, but in general the method can cover a period between 1000 and 100000 years before present (BP) to error limits of ~±1% of age.

For radiocarbon dating, it is assumed that the parent carbon is derived from soil carbon dioxide and is fixed by calcium or magnesium ions to precipitate pedogenic carbonate (Amundson et al., 1994). The ^{14}C activity measured and the age of the pedogenic carbonate are linked by the following decay equation (Pigati, 2013).

$$A = A_0 e^{-\lambda t} \qquad \text{Eq. 2.18}$$

Where A and A_0 are the measured and initial ^{14}C activities of the material, respectively; λ is the decay constant of ^{14}C; and t is the time elapsed since precipitation.

According to Amundson et al (1994), carbon dioxide in soils is a mixture of CO_2 from two biological sources: the respiration of living plant roots and the respiration of micro-organisms decomposing soil humus. The relative proportion of these two sources of CO_2 can significantly affect the initial ^{14}C content of the pedogenic carbonate: the greater the contribution of humus-derived CO_2, the higher the initial ^{14}C age of the carbonate mineral. As the soil ages, the ^{14}C age of soil humus increases, as does the ^{14}C age of steady-state soil CO_2 and the initial ^{14}C age of any pedogenic carbonate which forms. The average ^{14}C age of a nodule or a complete layer of pedogenic carbonate underestimates the true age of the soil carbonate. This discrepancy increases with the age of the soil. According to Callen et al (1983), radiocarbon dating of pedogenic carbonates in the southern Strzelecki Desert, South Australia, showed inversions and inconsistencies along single horizons. The authors attribute these observations to a certain recrystallisation of the carbonate, characterised by several generations of micrites. However, Kovda et al. (2014) showed that ^{14}C dating of carbonate pedofeatures performed for selected specimens was a reliable technique in the southern part of European Russia. This demonstrates that the use of the radiocarbon dating technique is only necessary if certain preconditions are met. Firstly, the initial ^{14}C activity of a material must be in isotopic equilibrium with atmospheric ^{14}C at the time it precipitated. Secondly, it must behave like a closed system in terms of carbon after precipitation, i.e. secondary carbon (contaminant) is not added to or exchanged with atmospheric carbon (Pigati, 2013). This is why Amundson et al. (1994) recommended partial removal of the outer (and younger) carbonate layers, which considerably improves the relationship between the measured ^{14}C age and the true age. In general, it is better to opt for a multidisciplinary approach that combines dating and micromorphological observations to overcome this difficulty (Dal Sasso et al., 2018).

Some recent work has introduced OSL dating to determine the age of pedogenic carbonates. OSL dating is based on the fact that if a mineral is exposed to sufficient light (e.g., sunlight), some or all of the stored energy will be lost. It allows researchers to obtain dates from mineral

grains (Elias, 2023). The approach to dating pedogenic carbonates is to target fractions of residual minerals trapped in the carbonate features concerned. As with other dating methods, the results of Diaz et al. (2016) obtained for the dating of pedogenic carbonate nodules in the Far north of Cameroon show that minerals from the inner part of the nodule are suitable for OSL dating. This technique, which is currently being developed, would undoubtedly merit more attention for the dating of pedogenic carbonates, particularly in systems where aeolian inputs are predominant.

2.8.4. Geoarchaeology

Soil carbonates can be used as indicators of past human life patterns, and to study the distribution and environment of past animal life. This approach is based on the relationship between stable carbon and oxygen isotopes in soil carbonates, vegetation, and the climate. Hopley et al. (2023) established that carbon isotope data from fossil carnivores are in close agreement with palaeo-vegetation reconstructions from $\delta^{13}C$ of palaeosol carbonates from the same geological members, as well as a similar long-term trend in $\delta^{13}C$ values, reflecting a progressive increase in the proportion of C4 grasses in the Turkana Basin. In the Turkana Basin, Quinn and Lepre (2020) revisited the study of Wynn (2000), which focused on the reconstruction of Australopithecus anamensis habitats from stable isotopes of carbon and oxygen analyses of pedogenic nodules collected from palaeosols spanning the Kanapoi stratigraphic interval showed that Kanapoi provided Australopithecus anamensis with a variety of habitats and a wide range of C3-C4 resources as the C4 biome expanded in East Africa. Pedogenic carbonates collected from palaeosols are therefore an interesting tool for studying archaeological sites. Given the active role of irrigation and fertilization in the concentration of pedogenic carbonates in modern agricultural soils, this tool could also be of interest for analysing palaeo-land use at certain archaeological sites.

2.9. Critical knowledge gaps and future directions for SIC research

Much has been done to advance research into SIC, however, compared with SOC, there is still a lot to be done to improve our understanding of SIC dynamics. Notable among the areas that need further studies are:

The preferential precipitation of certain forms of carbonate like rhizolith around the roots of specific plant species in drylands as highlighted by some studies, remains to be explained, suggesting some kind of biological mediation. Some forms of carbonate involve the concomitant action of both abiotic and biotic pathways, but the respective contribution of each pathway and the interactions between them remain unclear.

The biomineralization of carbon dioxide by oxalotrophic bacteria is an emerging research field that is tending to demonstrate a pathway for the accumulation of SIC in tropical forest regions. However, no quantification of the potential of this approach at landscape scale has been provided. Furthermore, the transfer of fixed carbon from plants to the soil is also an interesting issue in terms of the potential of this pathway.

The stable isotopes of carbon and oxygen, and the clumped isotopes now make it possible to understand the climatic and ecological environmental conditions that favoured the formation of pedogenic carbonates. They are therefore used to reconstruct palaeoclimate and palaeoenvironment. However, the accuracy of reconstructing atmospheric temperature using clumped isotopes and stable isotope values is debated for two main reasons: seasonal variation in the accumulation of pedogenic carbonates and post-formation changes are still not well understood.

By using the $^{87}Sr/^{86}Sr$ isotope ratio, combined with the volume or mass ratio between the quantity of calcium contained in the parent material and the quantity contained in the soil or in pedogenic carbonate components, it is now possible to quantify the carbon dioxide sequestered through the formation of pedogenic carbonates. However, this type of analysis is still recent and raises a number of reservations. The first concerns the tracing of the origin of calcium,

based on an indirect approach that assumes similar geochemical behaviour between strontium and calcium ions, which have the same ionic radius. More direct analyses using calcium isotope ratios are currently being developed and could help to give a more realistic picture. The second caveat is that current quantifications have been carried out based on a single parent material responsible for supplying calcium ions to the system, whereas many studies demonstrate the contribution of several sources. It would therefore be necessary to develop approaches that consider the contributions of each of the sources in the sequestration balance.

Much work has been done on the dynamics of SIC stocks as a function of land management, particularly the effects of afforestation (Gao et al., 2017; Hong and Chen, 2022; Liu et al., 2022), desertification (Moharana et al., 2023; An et al., 2019), agriculture (Bughio et al., 2017a; Deane McKenna et al., 2022), and land cover (Kuznetsova et al., 2010; Shi et al., 2012; Liu et al., 2020), in the arid regions of China, Australia, North America, Russia and the rest of Asia. However, very few studies have been carried out in that regards in Africa and Latin America, even though they have huge dryland. It is therefore necessary to extend this type of approach to these two important regions of the world. A World-scale strategy for analysing the dynamics of SIC is needed. This will provide a more realistic picture of current SIC stocks. In addition, it is necessary to highlight all the factors that influence the SIC dynamics.

The most used SIC quantification techniques today are either slow, limited to SIC analysis only, imprecise, or too polluting (Elfaki et al., 2016; Apesteguia et al., 2018; Leogrande et al., 2021). The spectroscopic techniques already used in some studies (McCarty et al., 2002; Grinand et al., 2012; Du et al., 2013), should be further explored as they are less time-consuming, do not destroy samples, are environmentally friendly and have already produced good results. They are also well suited for large-scale studies (Bricklemyer et al., 2011; Grinand et al., 2012; Martin et al., 2013; Comstock et al., 2019; Barthès et al., 2020). Efforts are needed to calibrate them on the largest possible number of soils and to continue developing non-destructive, environmentally friendly techniques.

Few studies have been carried out to develop models for predicting changes in the SIC (Sharififar et al., 2023). The random forest model is the most widely used and has produced very good results (Sreenivas et al., 2016; Yang et al., 2017; Filippi et al., 2020). However, more realistic models that consider the high concentration heterogeneity in the SIC distribution should be developed (Filippi et al., 2020b). The choice of appropriate environmental parameters also remains a problem, as the parameters used vary considerably from one study to another (Hirmas et al., 2010; Wilford et al., 2015; de Soto et al., 2017). This would likely affect the accuracy of the models obtained.

As Groshans et al. (2018) show, quantifying the impact of SIC management on ecosystem services provides a clear financial picture of the damage caused by poor policy choices in terms of ecosystem management. However, this type of analysis is not yet widespread enough around the world. It would be interesting to analyse it on a larger scale.

As the scope of this paper is inherently broad, mapping global research trends, hotspots and methodological developments in SIC research over the past two decades rather than providing an in-depth, mechanistic treatment of every process discussed in the underlying literature. We therefore recognise that a number of process-related issues have not been fully addressed in this analysis, including, amongst others: (i) the influence of temperature on carbonate precipitation in soils, and its interaction with other pedogenic factors; (ii) whether a threshold or boundary condition in climate can be defined that favours the development of carbonate features on felsic versus mafic parent rocks; (iii) the extent to which the degree of soil carbonation can be predicted from parent material and/or climate; (iv) the information that can be extracted from the macromorphology of carbonate nodules and concretions, and how this complements the micromorphological and geochemical proxies discussed in Section 4; (v) the differentiation of C3, C4 and CAM plant carbon sources within carbonate nodules, which remains difficult to resolve, particularly where several vegetation types have coexisted or shifted over time; (vi) the influence of carbonate morphology on the isotopic signature of

carbonate features; and (vii) the dissolution-precipitation-reprecipitation behaviour of calcium and magnesium carbonates in soils, since the present review has focused predominantly on calcium carbonate and has given comparatively little attention to dolomite and other Mg-bearing carbonates.

We further recognise that, as with any bibliometric analysis, our results may be subject to a geographic and language bias inherent in the databases used. Scopus and Google Scholar, while broad in coverage, tend to index a larger proportion of English-language journals and research originating from North America, Europe, and parts of Asia than from other regions. This may partly explain the apparent underrepresentation of SIC research from Africa and Latin America among the hotspots identified in Section 2.3, despite the extensive drylands present in these regions. Future bibliometric assessments of SIC research would benefit from incorporating regional and non-English-language databases to provide a more complete picture of global research effort.

2.10. Synthesis and Conclusion

The future of soil inorganic carbon research is promising. It has gained global traction among soil and carbon scientists in the last two decades. Geography and technological know-how tend to have influence on the SIC research themes. Drylands provide suitable environments and act as natural laboratories to unravel SIC dynamics. More studies should therefore be better carried out in dryland ecosystems. This review has identified a need to develop a global research strategy for the creation of awareness on the potentials of SIC given its prevalence in dry environments, which account for 30 % of the world's continental land. In the wake of the United Nations Sustainable Development Goals, the role of SIC in providing life-sustaining ecosystem services deserves more attention. The USA has been able to tag a monetary value to SIC-associated ecosystem services. It is important to extend similar valuation exercises to other environments as this would promote the conservation and sustainable use and management of SIC resources.

Scientific strides to improve our understanding of SIC formation pathways should further explore the biomineralization of carbon dioxide by oxalotrophic bacteria. This emerging research field holds great prospects to provide insight into pathways of SIC accumulation in both tropical forest regions and drylands. Such an approach could enable scientists to better assess the effective contribution of this pathway to soil carbon sequestration.

Analytical methods in SIC research should be further developed to improve the accuracy of the results while being environmentally friendly. There is a need to further develop predictive models and the resulting digital mapping, which would not only give us an idea of the current SIC sink, but also help us to analyse future stock trends. This will allow to construct a global scale strategy in SIC management. Beaming more research light on the poorly understood aspects of SIC will invariably bridge the knowledge gaps needed for management of SIC for robust ecosystem functioning and achieving soil-relevant sustainable development goals.

References

Achyuthan, H., Shankar, N., Braida, M., Ahmad, S.M., 2012. Geochemistry of calcretes (calcic palaeosols and hardpan), Coimbatore, Southern India: Formation and Paleoenvironment. Quaternary International 265, 155–169. https://doi.org/10.1016/j.quaint.2012.01.037

Adhikari, K., Hartemink, A.E., 2016. Linking soils to ecosystem services — A global review. Geoderma 262, 101–111. https://doi.org/https://doi.org/10.1016/j.geoderma.2015.08.009

Affek, H.P., 2012. Clumped Isotope Paleothermometry: Principles, Applications, and Challenges. The Paleontological Society Papers 18, 101–114. https://doi.org/10.1017/s1089332600002576

Allègre, C.J., 2008. Stable isotope geochemistry, in: Isotope Geology. Cambridge University Press, pp. 358–435. https://doi.org/10.1017/CBO9780511809323.008

Alonso-Zarza, A.M., Wright, V.P., 2010. Chapter 5 Calcretes, in: Alonso-Zarza, A.M., Tanner, L.H. (Eds.), Developments in Sedimentology. Elsevier, pp. 225–267. https://doi.org/https://doi.org/10.1016/S0070-4571(09)06105-6

Álvarez-Rivera, O.O., Estrada-Medina, H., Jiménez-Osornio, J.J., O'Connor-Sánchez, I.A., Navarro-Alberto, J.A., Ferrer, M.M., Canto-Canché, B., Tzec-Gamboa, M. del C., 2021. Differences in oxalate–carbonate pathway of Brosimum alicastrum in karst homegarden and forest soils. Soil Science Society of America Journal 85, 691–702. https://doi.org/10.1002/saj2.20228

Ambers, J., 2005. ARCHAEOMETRY AND ANTIQUE ANALYSIS | Dating of Artifacts, in: Worsfold, P., Townshend, A., Poole, C. (Eds.), Encyclopedia of Analytical Science (Second Edition). Elsevier, Oxford, pp. 109–117. https://doi.org/https://doi.org/10.1016/B0-12-369397-7/00019-4

Amundson, R., Wang, Y., Chadwick, O., Trumbore, S., McFadden, L., McDonald, E., Wells, S., DeNiro, M., 1994. Factors and processes governing the 14C content of carbonate in desert soils. Earth Planet Sci Lett 125, 385–405. https://doi.org/https://doi.org/10.1016/0012-821X(94)90228-3

An, H., Li, Q.L., Yan, X., Wu, X.Z., Liu, R. Tao, Fang, Y., 2019. Desertification control on soil inorganic and organic carbon accumulation in the topsoil of desert grassland in Ningxia, northwest China. Ecol Eng 127, 348–355. https://doi.org/10.1016/j.ecoleng.2018.12.014

Apesteguia, M., Plante, A.F., Virto, I., 2018. Methods assessment for organic and inorganic carbon quantification in calcareous soils of the Mediterranean region. Geoderma Regional 12, 39–48. https://doi.org/10.1016/j.geodrs.2017.12.001

Aragno, M., Verrecchia, E., 2012. The oxalate-carbonate pathway: A reliable sink for atmospheric CO2 through calcium carbonate biomineralization in ferralitic tropical soils, in: Microorganisms in Environmental Management: Microbes and Environment. Springer Netherlands, pp. 191–199. https://doi.org/10.1007/978-94-007-2229-3_9

Assadi Langroudi, A., Theron, E., Ghadr, S., 2021. Sequestration of carbon in pedogenic carbonates and silicates from construction and demolition wastes. Constr Build Mater 286. https://doi.org/10.1016/j.conbuildmat.2021.122658

Ayala-Niño, F., Maya-Delgado, Y., García-Calderón, N.E., Olmedo, G., Guevara, M., Troyo-Diéguez, E., 2020. Spatial distribution of soil carbon storage in desert shrubland ecosystems of northwest Mexico. J Arid Environ 183. https://doi.org/10.1016/j.jaridenv.2020.104251

Bajnóczi, B., Kovács-Kis, V., 2006. Origin of pedogenic needle-fiber calcite revealed by micromorphology and stable isotope composition—a case study of a Quaternary paleosol from Hungary. Geochemistry 66, 203–212. https://doi.org/https://doi.org/10.1016/j.chemer.2005.11.002

Barthès, B.G., Kouakoua, E., Coll, P., Clairotte, M., Moulin, P., Saby, N.P.A., Le Cadre, E., Etayo, A., Chevallier, T., 2020. Improvement in spectral library-based quantification of soil properties using representative spiking and local calibration – The case of soil inorganic carbon prediction by mid-infrared spectroscopy. Geoderma 369. https://doi.org/10.1016/j.geoderma.2020.114272

Batjes, N.H., 1996. Total carbon and nitrogen in the soils of the world, European Journal of Soil Science.

Becze-Deàk, J., Langohr, R., Verrecchia, E.P., 1997. Small scale secondary CaCO3 accumulations in selected sections of the European loess belt. Morphological forms and potential for paleoenvironmental reconstruction. Geoderma 76, 221–252. https://doi.org/https://doi.org/10.1016/S0016-7061(96)00106-1

Bockheim, J.G., Douglass, D.C., 2006. Origin and significance of calcium carbonate in soils of southwestern Patagonia. Geoderma 136, 751–762. https://doi.org/10.1016/j.geoderma.2006.05.013

Bravo, D., Braissant, O., Cailleau, G., Verrecchia, E., Junier, P., 2015. Isolation and characterization of oxalotrophic bacteria from tropical soils. Arch Microbiol 197, 65–77. https://doi.org/10.1007/s00203-014-1055-2

Brenden J. Fischer-Femal, Gabriel J. Bowen, 2021.Coupled carbon and oxygen isotope model for pedogenic carbonates. Geochimica et Cosmochimica Acta 294, 126-144. https://doi.org/10.1016/j.gca.2020.10.022.

Brevik, E.C., Calzolari, C., Miller, B.A., Pereira, P., Kabala, C., Baumgarten, A., Jordán, A., 2016. Soil mapping, classification, and pedologic modeling: History and future directions. Geoderma 264, 256–274. https://doi.org/https://doi.org/10.1016/j.geoderma.2015.05.017

Bricklemyer, R.S., Brown, D.J., Barefield, J.E., Clegg, S.M., 2011. Intact Soil Core Total, Inorganic, and Organic Carbon Measurement Using Laser-Induced Breakdown Spectroscopy. Soil Science Society of America Journal 75, 1006–1018. https://doi.org/10.2136/sssaj2009.0244

Bughio, M.A., Wang, P., Meng, F., Chen, Q., Li, J., Shaikh, T.A., 2017. Neoformation of pedogenic carbonate and conservation of lithogenic carbonate by farming practices and their contribution to carbon sequestration in soil. Zeitschrift fur Pflanzenernahrung und Bodenkunde 180, 454–463. https://doi.org/10.1002/jpln.201500650

Bughio, M.A., Wang, P., Meng, F., Qing, C., Kuzyakov, Y., Wang, X., Junejo, S.A., 2016. Neoformation of pedogenic carbonates by irrigation and fertilization and their contribution to carbon sequestration in soil. Geoderma 262, 12–19. https://doi.org/10.1016/j.geoderma.2015.08.003

Bulysheva, A.M., Khokhlova, O.S., Bakunovich, N.O., Rusakov, V.A., Myakshina, T.N., Ryumin, A.G., 2020. Changes in the Carbonate Status of Chernozems of Azov Region upon Their Conversion from Cropland to Long-Term Fallow. Eurasian Soil Science 53, 1182–1194. https://doi.org/10.1134/S1064229320080025

Bundy, L.G., Bremner, J.M., 1972. A Simple Titrimetric Method for Determination of Inorganic Carbon in Soils. Soil Science Society of America Journal 36, 273–275. https://doi.org/https://doi.org/10.2136/sssaj1972.03615995003600020021x

Cailleau, G., Braissant, O., Verrecchia, E.P., 2011. Turning sunlight into stone: The oxalate-carbonate pathway in a tropical tree ecosystem. Biogeosciences 8, 1755–1767. https://doi.org/10.5194/bg-8-1755-2011

Cailleau, G., Mota, M., Bindschedler, S., Junier, P., Verrecchia, E.P., 2014. Detection of active oxalate-carbonate pathway ecosystems in the Amazon Basin: Global implications of a natural potential C sink. Catena (Amst) 116, 132–141. https://doi.org/10.1016/j.catena.2013.12.017

Cailleau, G., Verrecchia, E.P., Braissant, O., Emmanuel, L., 2009. The biogenic origin of needle fibre calcite. Sedimentology 56, 1858–1875. https://doi.org/10.1111/j.1365-3091.2009.01060.x

Callen, R.A., Wasson, R.J., Gillespie, R., 1983. Reliability of radiocarbon dating of pedogenic carbonate in the Australian arid zone. Sediment Geol 35, 1–14. https://doi.org/https://doi.org/10.1016/0037-0738(83)90067-2

Capo, R.C., Chadwick, O.A., 1999. Sources of strontium and calcium in desert soil and calcrete, Earth and Planetary Science Letters.

Capo, R.C., Stewart, B.W., Chadwick, O.A., 1998. Strontium isotopes as tracers of ecosystem processes: theory and methods, Geoderma.

Carmi, I., Kronfeld, J., Moinester, M., 2019. Sequestration of atmospheric carbon dioxide as inorganic carbon in the unsaturated zone under semi-arid forests. Catena (Amst) 173, 93–98. https://doi.org/10.1016/j.catena.2018.09.042

Cerling, T.E., 1984. The stable isotopic composition of modern soil carbonate and its relationship to climate, Earth and Planetary Science Letters.

Cerling, T.E., Harris, J.M., MacFadden, B.J., Leakey, M.G., Quadek, J., Eisenmann, V., Ehleringer, J.R., 1997. Global vegetation change through the Miocene/Pliocene boundary, Nature © Macmillan Publishers Ltd.

Chang, R., Fu, B., Liu, G., Wang, S., Yao, X., 2012. The effects of afforestation on soil organic and inorganic carbon: A case study of the Loess Plateau of China. Catena (Amst) 95, 145–152. https://doi.org/10.1016/j.catena.2012.02.012

Comstock, J.P., Sherpa, S.R., Ferguson, R., Bailey, S., Beem-Miller, J.P., Lin, F., Lehmann, J., Wolfe, D.W., 2019. Carbonate determination in soils by mid-IR spectroscopy with regional and continental scale models. PLoS One 14. https://doi.org/10.1371/journal.pone.0210235

Costanza, R., d'Arge, R., de Groot, R., Farber, S., Grasso, M., Hannon, B., Limburg, K., Naeem, S., O'Neill, R. V, Paruelo, J., Raskin, R.G., Sutton, P., van den Belt, M., 1997. The value of the world's ecosystem services and natural capital. Nature 387, 253–260. https://doi.org/10.1038/387253a0

Curtis Monger, H., Kraimer, R.A., Khresat, S., Cole, D.R., Wang, X., Wang, J., 2015. Sequestration of inorganic carbon in soil and groundwater. Geology 43, 375–378. https://doi.org/10.1130/G36449.1

Dal Sasso, G., Zerboni, A., Maritan, L., Angelini, I., Compostella, C., Usai, D., Artioli, G., 2018. Radiocarbon dating reveals the timing of formation and development of pedogenic calcium

carbonate concretions in Central Sudan during the Holocene. Geochim Cosmochim Acta 238, 16–35. https://doi.org/10.1016/j.gca.2018.06.037

Dar, R.A., Chandra, R., Romshoo, S.A., Lone, M.A., Ahmad, S.M., 2015. Isotopic and micromorphological studies of Late Quaternary loess-paleosol sequences of the Karewa Group: Inferences for palaeoclimate of Kashmir Valley. Quaternary International 371, 122–134. https://doi.org/10.1016/j.quaint.2014.10.060

de Soto, I.S., Virto, I., Barré, P., Fernández-Ugalde, O., Antón, R., Martínez, I., Chaduteau, C., Enrique, A., Bescansa, P., 2017. A model for field-based evidences of the impact of irrigation on carbonates in the tilled layer of semi-arid Mediterranean soils. Geoderma 297, 48–60. https://doi.org/10.1016/j.geoderma.2017.03.005

Deane McKenna, M., Grams, S.E., Barasha, M., Antoninka, A.J., Johnson, N.C., 2022. Organic and inorganic soil carbon in a semi-arid rangeland is primarily related to abiotic factors and not livestock grazing. Geoderma 419. https://doi.org/10.1016/j.geoderma.2022.115844

Deb, D., Deb, S., Choudhury, A., 2020. Application of Statistical Techniques in Soil Research. pp. 19–32. https://doi.org/10.1007/978-981-15-2039-6_2

Diaz, N., King, G.E., Valla, P.G., Herman, F., Verrecchia, E.P., 2016. Pedogenic carbonate nodules as soil time archives: Challenges and investigations related to OSL dating. Quat Geochronol 36, 120–133. https://doi.org/10.1016/j.quageo.2016.08.008

Díaz-Hernández, J.L., Barahona Fernández, E., Linares González, J., 2003. Organic and inorganic carbon in soils of semiarid regions: A case study from the Guadix-Baza basin (Southeast Spain). Geoderma 114, 65–80. https://doi.org/10.1016/S0016-7061(02)00342-7

Diaz-Hernandez, J.L., Sánchez-Navas, A., Delgado, A., Yepes, J., Garcia-Casco, A., 2018. Textural and isotopic evidence for Ca-Mg carbonate pedogenesis. Geochim Cosmochim Acta 222, 485–507. https://doi.org/https://doi.org/10.1016/j.gca.2017.11.006

Dietrich, F., Diaz, N., Deschamps, P., Ngounou Ngatcha, B., Sebag, D., Verrecchia, E.P., 2017. Origin of calcium in pedogenic carbonate nodules from silicate watersheds in the Far North

Region of Cameroon: Respective contribution of in situ weathering source and dust input. Chem Geol 460, 54–69. https://doi.org/10.1016/j.chemgeo.2017.04.015

Dietrich, F., Diaz, N., Deschamps, P., Sebag, D., Verrecchia, E., 2021. Calcium transfer and mass balance associated with soil carbonate in a semi-arid silicate watershed (North Cameroon): An overlooked geochemical cascade? Depositional Record 2021. https://doi.org/10.1002/dep2.134ï

Du, C., Ma, Z., Zhou, J., Goyne, K.W., 2013. Application of mid-infrared photoacoustic spectroscopy in monitoring carbonate content in soils. Sens Actuators B Chem 188, 1167–1175. https://doi.org/10.1016/j.snb.2013.08.023

Dubchak, S., 2018. Distribution of Strontium in Soil: Interception, Weathering, Speciation, and Translocation to Plants, in: Gupta, D.K., Walther, C. (Eds.), Behaviour of Strontium in Plants and the Environment. Springer International Publishing, Cham, pp. 33–43. https://doi.org/10.1007/978-3-319-66574-0_3

Durand, N., Ahmad, S.M., Hamelin, B., Gunnell, Y., Curmi, P., 2006. Origin of Ca in South Indian calcretes developed on metamorphic rocks. J Geochem Explor 88, 275–278. https://doi.org/10.1016/j.gexplo.2005.08.055

Durand, N., Gunnell, Y., Curmi, P., Ahmad, S.M., 2007. Pedogenic carbonates on Precambrian silicate rocks in South India: Origin and paleoclimatic significance. Quaternary International 162–163, 35–49. https://doi.org/10.1016/j.quaint.2006.10.026

Egli, M., Fitze, P., 2000. FORMULATION OF PEDOLOGIC MASS BALANCE BASED ON IMMOBILE ELEMENTS: A REVISION. Soil Sci 165.

Eiler, J.M., 2011. Paleoclimate reconstruction using carbonate clumped isotope thermometry. Quat Sci Rev. https://doi.org/10.1016/j.quascirev.2011.09.001

Elfaki, J.T., Gafei, M.O., Sulieman, M.M., Ali, M.E., 2016. Assessment of Calcimetric and Titrimetric Methods for Calcium Carbonate Estimation of Five Soil Types in Central Sudan.

Journal of Geoscience and Environment Protection 04, 120–127. https://doi.org/10.4236/gep.2016.41014

Elias, S.A., 2023. History of Quaternary science☆, in: Reference Module in Earth Systems and Environmental Sciences. Elsevier. https://doi.org/10.1016/B978-0-323-99931-1.00058-1

Ellert, B.H., Janzen, H.H., VandenBygaart, A.J., Bremer, E., 2007. Measuring change in soil organic carbon storage, in: Soil Sampling and Methods of Analysis: Second Edition. CRC Press, pp. 25–38. https://doi.org/10.1201/9781420005271.ch3

Entry, J.A., Sojka, R.E., Shewmaker, G.E., 2004. Irrigation increases inorganic carbon in agricultural soils. Environ Manage 33. https://doi.org/10.1007/s00267-003-9140-3

Ernst, M., Thiemeyer, H., Lüdecke, T., 2019. Stable isotope signatures of radiocarbon dated pedogenic carbonate from tell chuera (Ne syria) reveal fluctuating paleoenvironmental patterns in the pleistocene levant. Zeitschrift fur Geomorphologie 62, 59–84. https://doi.org/10.1127/zfg_suppl/2019/0553

Eze, P.N., Knight, J., Evans, M., 2016. Tracing recent environmental changes and pedogenesis using geochemistry and micromorphology of alluvial soils, Sabie-Sand River Basin, South Africa. Geomorphology 268, 312–321. https://doi.org/10.1016/j.geomorph.2016.06.023

Eze, P.N., Meadows, M.E., 2015. Geochemistry and palaeoclimatic reconstruction of a palaeosol sequence at Langebaanweg, South Africa. Quaternary International 376, 75–83. https://doi.org/https://doi.org/10.1016/j.quaint.2013.09.048

Eze, P. N., Meadows, M. E., 2014a. Multi-proxy palaeosol evidence for late Quaternary (MIS 4) environmental and climate shifts on the coasts of South Africa. Quaternary International, 343, 159-168.

Eze, P. N., Meadows, M.E., 2014b. Mineralogy and micromorphology of a late Neogene paleosol sequence at Langebaanweg, South Africa: Inference of paleoclimates. Palaeogeogr Palaeoclimatol Palaeoecol 409, 205–216. https://doi.org/10.1016/j.palaeo.2014.05.008

Eze, P. N., Meadows, M.E., 2014c. Texture contrast profile with stonelayer in the Cape Peninsula, South Africa: Autochthony and polygenesis. Catena (Amst) 118, 103–114. https://doi.org/https://doi.org/10.1016/j.catena.2014.01.014

Ferdush, J., Paul, V., 2021. A review on the possible factors influencing soil inorganic carbon under elevated CO2. Catena (Amst). https://doi.org/10.1016/j.catena.2021.105434

Ferreira, V.G., Rosa, J., Almeida, N.M. et al., 2023. A comparison of three main scientific literature databases using a search in aquatic ecology. Hydrobiologia 850, 1477–1486. https://doi.org/10.1007/s10750-022-05067-5

Filippi, P., Cattle, S.R., Pringle, M.J., Bishop, T.F.A., 2020. A two-step modelling approach to map the occurrence and quantity of soil inorganic carbon. Geoderma 371. https://doi.org/10.1016/j.geoderma.2020.114382

Fonnesbeck, B.B., Boettinger, J.L., Lawley, J.R., 2013. Improving a Simple Pressure-Calcimeter Method for Inorganic Carbon Analysis. Soil Science Society of America Journal 77, 1553–1562. https://doi.org/10.2136/sssaj2012.0381

Gadd, G.M., Bahri-Esfahani, J., Li, Q., Rhee, Y.J., Wei, Z., Fomina, M., Liang, X., 2014. Oxalate production by fungi: Significance in geomycology, biodeterioration and bioremediation. Fungal Biol Rev. https://doi.org/10.1016/j.fbr.2014.05.001

Gallagher, T.M., Sheldon, N.D., 2016. Combining soil water balance and clumped isotopes to understand the nature and timing of pedogenic carbonate formation. Chem Geol 435, 79–91. https://doi.org/10.1016/j.chemgeo.2016.04.023

Gao, Y., Tian, J., Pang, Y., Liu, J., 2017. Soil inorganic carbon sequestration following afforestation is probably induced by pedogenic carbonate formation in Northwest China. Front Plant Sci 8. https://doi.org/10.3389/fpls.2017.01282

Gatz-Miller, H.S., Gérard, F., Verrecchia, E.P., Su, D., Mayer, K.U., 2022. Reactive transport modelling the oxalate-carbonate pathway of the Iroko tree; Investigation of calcium and carbon

sinks and sources. Geoderma 410, 115665. https://doi.org/https://doi.org/10.1016/j.geoderma.2021.115665

GILE, L.H., PETERSON, F.F., GROSSMAN, R.B., 1966. MORPHOLOGICAL AND GENETIC SEQUENCES OF CARBONATE ACCUMULATION IN DESERT SOILS. Soil Sci 101.

Gocke, M., Pustovoytov, K., Kuzyakov, Y., 2011. Carbonate recrystallization in root-free soil and rhizosphere of Triticum aestivum and Lolium perenne estimated by 14C labeling. Biogeochemistry 103, 209–222. https://doi.org/10.1007/s10533-010-9456-z

Gocke, M., Pustovoytov, K., Kuzyakov, Y., 2010. Effect of CO2 concentration on the initial recrystallization rate of pedogenic carbonate - Revealed by 14C and 13C labeling. Geoderma 155, 351–358. https://doi.org/10.1016/j.geoderma.2009.12.018

Golubtsov, V., Bronnikova, M., Khokhlova, O., Cherkashina, A., Turchinskaia, S., 2021. Morphological and isotopic study of pedogenic carbonate coatings from steppe and forest-steppe areas of Baikal region, South-Eastern Siberia. Catena (Amst) 196. https://doi.org/10.1016/j.catena.2020.104817

Gomez, C., Chevallier, T., Moulin, P., Arrouays, D., Barthès, B.G., 2022. Using carbonate absorbance peak to select the most suitable regression model before predicting soil inorganic carbon concentration by mid-infrared reflectance spectroscopy. Geoderma 405. https://doi.org/10.1016/j.geoderma.2021.115403

Grinand, C., Barthès, B.G., Brunet, D., Kouakoua, E., Arrouays, D., Jolivet, C., Caria, G., Bernoux, M., 2012. Prediction of soil organic and inorganic carbon contents at a national scale (France) using mid-infrared reflectance spectroscopy (MIRS). Eur J Soil Sci 63, 141–151. https://doi.org/10.1111/j.1365-2389.2012.01429.x

Groshans, G.R., Mikhailova, E.A., Post, C.J., Schlautman, M.A., 2018. Accounting for soil inorganic carbon in the ecosystem services framework for United Nations sustainable development goals. Geoderma 324, 37–46. https://doi.org/10.1016/j.geoderma.2018.02.009

Haldar, U., Chakrabarti, R., Rudnick, R.L., 2023. Enrichment of heavy calcium isotopes in saprolite due to secondary mineral formation. Chem Geol 637. https://doi.org/10.1016/j.chemgeo.2023.121666

Hamidi, E.M., Colin, F., Michard, A., Boulangé, B., Nahon, D., 2001. Isotopic tracers of the origin of Ca in a carbonate crust from the Middle Atlas, Morocco. Chem Geol 176, 93–104. https://doi.org/https://doi.org/10.1016/S0009-2541(00)00373-9

Heilbronn, G., Boulvais, P., Marchand, E., Robin, C., Bourquin, S., Barrier, L., Jia, Y., Fu, B., Jolivet, M., 2015. Stable isotope characterization of pedogenic and lacustrine carbonates from the Chinese Tian Shan: Constraints on the Mesozoic-Lower Cenozoic palaeoenvironmental evolution. Chemie der Erde 75, 133–141. https://doi.org/10.1016/j.chemer.2014.11.004

Hervé, V., Clerc, M., Cailleau, G., Bueche, M., Junier, T., Verrecchia, E., Junier, P., 2018. Carbonate Accumulation in the Bark of Terminalia bellirica: A New Habitat for the Oxalate-Carbonate Pathway. Geomicrobiol J 35, 31–39. https://doi.org/10.1080/01490451.2017.1309087

Hervé, V., Simon, A., Randevoson, F., Cailleau, G., Rajoelison, G., Razakamanarivo, H., Bindschedler, S., Verrecchia, E., Junier, P., 2021. Functional diversity of the litter-associated fungi from an oxalate–carbonate pathway ecosystem in madagascar. Microorganisms 9. https://doi.org/10.3390/microorganisms9050985

Heuvelink, G.B.M., Angelini, M.E., Poggio, L., Bai, Z., Batjes, N.H., van den Bosch, R., Bossio, D., Estella, S., Lehmann, J., Olmedo, G.F., Sanderman, J., 2021. Machine learning in space and time for modelling soil organic carbon change. Eur J Soil Sci 72, 1607–1623. https://doi.org/10.1111/ejss.12998

Hirmas, D.R., Amrhein, C., Graham, R.C., 2010. Spatial and process-based modeling of soil inorganic carbon storage in an arid piedmont. Geoderma 154, 486–494. https://doi.org/10.1016/j.geoderma.2009.05.005

Hoefs, J. (Ed.), 2009a. Theoretical and Experimental Principles, in: Stable Isotope Geochemistry. Springer Berlin Heidelberg, Berlin, Heidelberg, pp. 1–33. https://doi.org/10.1007/978-3-540-70708-0_1

Hoefs, J. (Ed.), 2009b. Isotope Fractionation Processes of Selected Elements, in: Stable Isotope Geochemistry. Springer Berlin Heidelberg, Berlin, Heidelberg, pp. 35–92. https://doi.org/10.1007/978-3-540-70708-0_2

Hong, S., Chen, A., 2022. Contrasting Responses of Soil Inorganic Carbon to Afforestation in Acidic Versus Alkaline Soils. Global Biogeochem Cycles 36. https://doi.org/10.1029/2021GB007038

Hopley, P.J., Cerling, T.E., Crété, L., Werdelin, L., Mwebi, O., Manthi, F.K., Leakey, L.N., 2023. Stable isotope analysis of carnivores from the Turkana Basin, Kenya: Evidence for temporally-mixed fossil assemblages. Quaternary International 650, 12–27. https://doi.org/https://doi.org/10.1016/j.quaint.2022.04.004

Hussain, S., Sharma, V., Arya, V.M., Sharma, K.R., Rao, S., 2019. Total organic and inorganic carbon in soils under different land use/land cover systems in the foothill Himalayas. Catena (Amst) 182. https://doi.org/10.1016/j.catena.2019.104104

Huth, T. E., Cerling, T. E., Marchetti, D. W., Bowling, D. R., Ellwein, A. L., & Passey, B. H., 2019. Seasonal bias in soil carbonate formation and its implications for interpreting high-resolution paleoarchives: Evidence from southern Utah. Journal of Geophysical Research: Biogeosciences, 124, 616–632. https://doi.org/10.1029/2018JG004496

Jin, Z., Dong, Y., Wang, Yunqiang, Wei, X., Wang, Yafeng, Cui, B., Zhou, W., 2014. Natural vegetation restoration is more beneficial to soil surface organic and inorganic carbon sequestration than tree plantation on the Loess Plateau of China. Science of the Total Environment 485–486, 615–623. https://doi.org/10.1016/j.scitotenv.2014.03.105

Karberg, N.J., Pregitzer, K.S., King, J.S., Friend, A.L., Wood, J.R., 2005. Soil carbon dioxide partial pressure and dissolved inorganic carbonate chemistry under elevated carbon dioxide and ozone. Oecologia 142, 296–306. https://doi.org/10.1007/s00442-004-1665-5

Khaledian, Y., Miller, B.A., 2020. Selecting appropriate machine learning methods for digital soil mapping. Appl Math Model 81, 401–418. https://doi.org/https://doi.org/10.1016/j.apm.2019.12.016

Khalidy, R., Arnaud, E., Santos, R.M., 2022. Natural and Human-Induced Factors on the Accumulation and Migration of Pedogenic Carbonate in Soil: A Review. Land (Basel). https://doi.org/10.3390/land11091448

Khokhlova, O., Myakshina, T., Kuznetsova, A., 2021. Origins of hard carbonate nodules in arable Chernozems in the Central Russian Upland. Eur J Soil Sci 72, 326–342. https://doi.org/10.1111/ejss.12948

Khormali, F., Abtahi, A., Stoops, G., 2006. Micromorphology of calcitic features in highly calcareous soils of Fars Province, Southern Iran. Geoderma 132, 31–46. https://doi.org/10.1016/j.geoderma.2005.04.024

Khormali, F., Shahriari, A., Ghafarpour, A., Kehl, M., Lehndorff, E., Frechen, M., 2020. Pedogenic carbonates archive modern and past precipitation change – A transect study from soils and loess-paleosol sequences from northern Iran. Quaternary International 552, 79–90. https://doi.org/10.1016/j.quaint.2019.12.011

Kovda, I. V., Wilding, L.P., Drees, L.R., 2003. Micromorphology, submicroscopy and microprobe study of carbonate pedofeatures in a Vertisol gilgai soil complex, South Russia, in: Catena. Elsevier, pp. 457–476. https://doi.org/10.1016/S0341-8162(03)00121-8

Kovda, I., Mora, C.I., Wilding, L.P., 2006. Stable isotope compositions of pedogenic carbonates and soil organic matter in a temperate climate Vertisol with gilgai, southern Russia. Geoderma 136, 423–435. https://doi.org/10.1016/j.geoderma.2006.04.016

Kovda, I., Morgun, E., Gongalsky, K., 2014. Stable isotopic composition of carbonate pedofeatures in soils along a transect in the southern part of european Russia. Catena (Amst) 112, 56–64. https://doi.org/10.1016/j.catena.2013.01.005

Kowalska, J.B., Zaleski, T., Mazurek, R., 2020. Micromorphological features of soils formed on calcium carbonate–rich slope deposits in the Polish Carpathians. J Mt Sci 17, 1310–1332. https://doi.org/10.1007/s11629-019-5829-5

Kuznetsova, A.M., Khokhlova, O.S., Chendev, Y.G., Aleksandrovskii, A.L., 2010. Evolution of the Carbonate State of Agrogenically Transformed Dark Gray Forest Soils in the Central Forest-Steppe. Eurasian Soil Science 43, 1527–1534. https://doi.org/10.1134/S1064229310130119

Lal, R., 2009. Sequestering carbon in soils of arid ecosystems. Land Degrad Dev 20, 441–454. https://doi.org/10.1002/ldr.934

Lal, R., Negassa, W., Lorenz, K., 2015. Carbon sequestration in soil. Curr Opin Environ Sustain. https://doi.org/10.1016/j.cosust.2015.09.002

Landi, A., Mermut, A.R., Anderson, D.W., 2003. Origin and rate of pedogenic carbonate accumulation in Saskatchewan soils, Canada. Geoderma 117, 143–156. https://doi.org/10.1016/S0016-7061(03)00161-7

Landon Burgener, Katharine W. Huntington, Gregory D. Hoke, Andrew Schauer, Mallory C. Ringham, Claudio Latorre, Francisca P. Díaz, 2016. Variations in soil carbonate formation and seasonal bias over >4 km of relief in the western Andes (30°S) revealed by clumped isotope thermometry. Earth and Planetary Science Letters 441, 188-199. https://doi.org/10.1016/j.epsl.2016.02.033.

Laudicina, V.A., Scalenghe, R., Pisciotta, A., Parello, F., Dazzi, C., 2013. Pedogenic carbonates and carbon pools in gypsiferous soils of a semiarid mediterranean environment in south Italy. Geoderma 192, 31–38. https://doi.org/10.1016/j.geoderma.2012.07.015

Lawson, T., Emmerson, R., Battle, M., Pullin, J., Wall, S., Hofmann, T.A., 2022. Chapter 3 - Carbon fixation, in: Ruban, A., Foyer, C.H., Murchie, E.H. (Eds.), Photosynthesis in Action. Academic Press, pp. 31–58. https://doi.org/https://doi.org/10.1016/B978-0-12-823781-6.00008-3

Leogrande, R., Vitti, C., Castellini, M., Mastrangelo, M., Pedrero, F., Vivaldi, G.A., Stellacci, A.M., 2021. Comparison of two methods for total inorganic carbon estimation in three soil types in mediterranean area. Land (Basel) 10. https://doi.org/10.3390/land10040409

Li, Y., Zhang, W., Aydin, A., Deng, X., 2018. Formation of calcareous nodules in loess–paleosol sequences: Reviews of existing models with a proposed new "per evapotranspiration model." J Asian Earth Sci 154, 8–16. https://doi.org/10.1016/j.jseaes.2017.12.002

Lian, B., Hu, Q., Chen, J., Ji, J., Teng, H.H., 2006. Carbonate biomineralization induced by soil bacterium Bacillus megaterium. Geochim Cosmochim Acta 70, 5522–5535. https://doi.org/10.1016/j.gca.2006.08.044

Liu, E., Zhou, J., Yang, X., Jin, T., Zhao, B., Li, L., Wen, Y., Soldatova, E., Zamanian, K., Gopalakrishnan, S., Mei, X., Kuzyakov, Y., 2023. Long-term organic fertilizer-induced carbonate neoformation increases carbon sequestration in soil. Environ Chem Lett. https://doi.org/10.1007/s10311-023-01568-4

Liu, J., Wu, P., Zhao, Z., Gao, Y., 2022. Afforestation on cropland promotes pedogenic inorganic carbon accumulation in deep soil layers on the Chinese loess plateau. Plant Soil 478, 597–612. https://doi.org/10.1007/s11104-022-05494-2

Liu, S., Zhou, L., Li, H., Zhao, X., Yang, Y., Zhu, Y., Hu, H., Chen, L., Zhang, P., Shen, H., Fang, J., 2020. Shrub encroachment decreases soil inorganic carbon stocks in Mongolian grasslands. Journal of Ecology 108, 678–686. https://doi.org/10.1111/1365-2745.13298

Liu, X., Lu, X., Yu, R., Sun, H., Li, Xiangwei, Li, Xiang, Qi, Z., Liu, T., Lu, C., 2022. Distribution and storage of soil organic and inorganic carbon in steppe riparian wetlands under human activity pressure. Ecol Indic 139. https://doi.org/10.1016/j.ecolind.2022.108945

Liu, Z., Lei, H., Lei, L., Sheng, H., 2022. Spatial Prediction of Total Nitrogen in Soil Surface Layer Based on Machine Learning. Sustainability (Switzerland) 14. https://doi.org/10.3390/su141911998

Liu, Z., Zhang, Y., Fa, K., Zhao, H., Qin, S., Yan, R., Wu, B., 2018. Desert soil bacteria deposit atmospheric carbon dioxide in carbonate precipitates. Catena (Amst) 170, 64–72. https://doi.org/10.1016/j.catena.2018.06.001

Lu, T., Wang, X., Xu, M., Yu, Z., Luo, Y., Smith, P., 2020. Dynamics of pedogenic carbonate in the cropland of the North China Plain: Influences of intensive cropping and salinization. Agric Ecosyst Environ 292. https://doi.org/10.1016/j.agee.2020.106820

Macharia, A.N., Uno, K.T., Cerling, T.E., Brown, F.H., 2012. Isotopically distinct modern carbonates in abandoned livestock corrals in northern Kenya. J Archaeol Sci 39, 2198–2205. https://doi.org/10.1016/j.jas.2012.02.005

Machette, M.N., 1985. Calcic soils of the southwestern United States.

Mallory C. Ringham, Gregory D. Hoke, Katharine W. Huntington, Julieta N. Aranibar, 2016. Influence of vegetation type and site-to-site variability on soil carbonate clumped isotope records, Andean piedmont of Central Argentina (32–34°S). Earth and Planetary Science Letters 440, 1-11. https://doi.org/10.1016/j.epsl.2016.02.003.

Marchant, B.P., Villanneau, E.J., Arrouays, D., Saby, N.P.A., Rawlins, B.G., 2015. Quantifying and mapping topsoil inorganic carbon concentrations and stocks: approaches tested in France. Soil Use Manag 31, 29–38. https://doi.org/https://doi.org/10.1111/sum.12158

Martin, M.Z., Mayes, M.A., Heal, K.R., Brice, D.J., Wullschleger, S.D., 2013. Investigation of laser-induced breakdown spectroscopy and multivariate analysis for differentiating inorganic and organic C in a variety of soils. Spectrochim Acta Part B At Spectrosc 87, 100–107. https://doi.org/10.1016/j.sab.2013.05.026

McCarty, G.W., Reeves, J.B., Reeves, V.B., Follett, R.F., Kimble, J.M., 2002. Mid-Infrared and Near-Infrared Diffuse Reflectance Spectroscopy for Soil Carbon Measurement. Soil Science Society of America Journal 66, 640–646. https://doi.org/10.2136/sssaj2002.6400a

Menezes, M.N., Dal' Bó, P.F., Smith, J.J., Rodrigues, A.G., 2021. The influence of ancient soil biota on the precipitation and distribution of pedogenic carbonate in paleosols of the Marília Formation (Upper Cretaceous, Brazil). Palaeogeogr Palaeoclimatol Palaeoecol 571. https://doi.org/10.1016/j.palaeo.2021.110375

Mi, N., Wang, S., Liu, J., Yu, G., Zhang, W., Jobbágy, E., 2008. Soil inorganic carbon storage pattern in China. Glob Chang Biol 14, 2380–2387. https://doi.org/10.1111/j.1365-2486.2008.01642.x

Mikhailova, Elena A., Hamdi A. Zurqani, Christopher J. Post, Mark A. Schlautman, Gregory C. Post, Lili Lin, and Zhenbang Hao, 2021. Soil Carbon Regulating Ecosystem Services in the State of South Carolina, USA. Land 10, no. 3: 309. https://doi.org/10.3390/land10030309

Mikhailova, E.A., Bryant, R.B., Galbraith, J.M., Wang, Y., Post, C.J., Khokhlova, O.S., Schlautman, M.A., Cope, M.P., Shen, Z., 2018. Pedogenic carbonates and radiocarbon isotopes of organic carbon at depth in the Russian chernozem. Geosciences (Switzerland) 8. https://doi.org/10.3390/geosciences8120458

Mikhailova, E.A., Goddard, M.A., Post, C.J., Schlautman, M.A., Galbraith, J.M., 2013. Potential Contribution of Combined Atmospheric Ca2+ and Mg2+ Wet Deposition Within the Continental U.S. to Soil Inorganic Carbon Sequestration. Pedosphere 23, 808–814. https://doi.org/10.1016/S1002-0160(13)60072-7

Millière, L., Gussone, N., Moritz, T., Bindschedler, S., Verrecchia, E.P., 2019. Origin of strontium and calcium in pedogenic needle fibre calcite (NFC). Chem Geol 524, 329–344. https://doi.org/10.1016/j.chemgeo.2019.06.022

Moharana, P.C., Jena, R.K., Kumar, N., Singh, R.S., Rao, S.S., 2021. Assessment of soil organic and inorganic carbon stock at different soil depths after conversion of desert into arable land in

the hot arid regions of India. Carbon Manag 12, 153–165. https://doi.org/10.1080/17583004.2021.1893128

Monger, H.C., 2014. Soils as Generators and Sinks of Inorganic Carbon in Geologic Time, in: Soil Carbon. Springer International Publishing, pp. 27–36. https://doi.org/10.1007/978-3-319-04084-4_3

Monger, H.C., Cole, D.R., Buck, B.J., Gallegos, R.A., 2009. Scale and the isotopic record of C 4 plants in pedogenic carbonate: from the biome to the rhizosphere, CONCEPTS & SYNTHESIS EMPHASIZING NEW IDEAS TO STIMULATE RESEARCH IN ECOLOGY Ecology.

Mujinya, B.B., Mees, F., Boeckx, P., Bodé, S., Baert, G., Erens, H., Delefortrie, S., Verdoodt, A., Ngongo, M., Van Ranst, E., 2011. The origin of carbonates in termite mounds of the Lubumbashi area, D.R. Congo. Geoderma 165, 95–105. https://doi.org/10.1016/j.geoderma.2011.07.009

Naorem, A., Jayaraman, S., Dalal, R.C., Patra, A., Rao, C.S., Lal, R., 2022. Soil Inorganic Carbon as a Potential Sink in Carbon Storage in Dryland Soils—A Review. Agriculture (Switzerland). https://doi.org/10.3390/agriculture12081256

Nathan A. Peters, Katharine W. Huntington, Gregory D. Hoke, 2013. Hot or not? Impact of seasonally variable soil carbonate formation on paleotemperature and O-isotope records from clumped isotope thermometry. Earth and Planetary Science Letters. 361, 208-218. https://doi.org/10.1016/j.epsl.2012.10.024.

Olivier Hasinger, Jorge E. Spangenberg, Laure Millière, Saskia Bindschedler, Guillaume Cailleau, Eric P. Verrecchia, 2015. Carbon dioxide in scree slope deposits: A pathway from atmosphere to pedogenic carbonate. Geoderma, 247–248, 129-139. https://doi.org/10.1016/j.geoderma.2015.02.012.Orr, T.J., Wurster, C.M., Roberts, E.M., Singleton, R.E., Stevens, N.J., O'Connor, P.M., 2022. Paleoatmospheric CO2 oscillations through a cool middle/Late Cretaceous recorded from pedogenic carbonates in Africa. Cretac Res 135. https://doi.org/10.1016/j.cretres.2022.105191

Ortiz, A.C., Jin, L., Ogrinc, N., Kaye, J., Krajnc, B., Ma, L., 2022. Dryland irrigation increases accumulation rates of pedogenic carbonate and releases soil abiotic CO2. Sci Rep 12. https://doi.org/10.1038/s41598-021-04226-3

Pal, D.K., 2019. Is Soil Inorganic Carbon (CaCO3, SIC) Sequestration a Bane or a Hidden Treasure in Soil Ecosystem Services?, in: Pal, D.K. (Ed.), Ecosystem Services and Tropical Soils of India. Springer International Publishing, Cham, pp. 53–64. https://doi.org/10.1007/978-3-030-22711-1_4

Párraga, J., Rivadeneyra, M.A., Martín-García, J.M., Delgado, R., Delgado, G., 2004. Precipitation of carbonates by bacteria from a saline soil, in natural and artificial soil extracts. Geomicrobiol J 21, 55–66. https://doi.org/10.1080/01490450490253464

Parsons, R.F., Attiwill, P.M., Uren, N.C., Kopittke, P.M., 2022. Calcium oxalate and calcium cycling in forest ecosystems. Trees - Structure and Function 36, 531–536. https://doi.org/10.1007/s00468-021-02226-4

Paul, D., Mauldin, R., 2013. Implications for Late Holocene climate from stable carbon and oxygen isotopic variability in soil and land snail shells from archaeological site 41KM69 in Texas, USA. Quaternary International 308–309, 242–252. https://doi.org/10.1016/j.quaint.2012.08.006

Pigati, J.S., 2013. Radiocarbon Dating of Terrestrial Carbonates, in: Rink, W.J., Thompson, J. (Eds.), Encyclopedia of Scientific Dating Methods. Springer Netherlands, Dordrecht, pp. 1–9. https://doi.org/10.1007/978-94-007-6326-5_152-1

Pravash Chandra Moharana, S. Dharumarajan, Brijesh Yadav, Roomesh Kumar Jena, Upendra Kumar Pradhan, Sonalika Sahoo, Ram Swaroop Meena, Mahaveer Nogiya, Roshan Lal Meena, Ram Sakal Singh, Surendra Kumar Singh & Brahma Swarup Dwivedi, 2023. Prediction of Soil Inorganic Carbon at Multiple Depths Using Quantile Regression Forest and Digital Soil Mapping Technique in the Thar Desert Regions of India, Communications in Soil Science and Plant Analysis, 54:21, 2977-2994, DOI: 10.1080/00103624.2023.2253840

Prokof'eva, T., Shishkov, V., Kiriushin, A., 2021. Calcium carbonate accumulations in Technosols of Moscow city. J Soils Sediments 21, 2049–2058. https://doi.org/10.1007/s11368-020-02696-y

Quade, J., Eiler, J., Daëron, M., Achyuthan, H., 2013. The clumped isotope geothermometer in soil and paleosol carbonate. Geochim Cosmochim Acta 105, 92–107. https://doi.org/10.1016/j.gca.2012.11.031

Quinn, R.L., Lepre, C.J., 2020. Revisiting the pedogenic carbonate isotopes and paleoenvironmental interpretation of Kanapoi. J Hum Evol 140. https://doi.org/10.1016/j.jhevol.2018.11.005

Rabenhorst, M.C., Wilding, L.P., West, L.T., 1984. Identification of Pedogenic Carbonates Using Stable Carbon Isotope and Microfabric Analyses 1.

Raheb, A., Heidari, A., Mahmoodi, S., 2017. Organic and inorganic carbon storage in soils along an arid to dry sub-humid climosequence in northwest of Iran. Catena (Amst) 153, 66–74. https://doi.org/10.1016/j.catena.2017.01.035

Raheb, A., Heidari, A., Mahmoodi, S., 2016. Storage of organic and inorganic carbon in arid-semihumid soils: A case study of the rangelands of northwestern Iran. Soil Sci 181, 473–486. https://doi.org/10.1097/SS.0000000000000183

Raigemborn, M.S., Krapovickas, V., Beilinson, E., Gómez Peral, L.E., Zucol, A.F., Zapata, L., Kay, M.R.F., Bargo, M.S., Vizcaíno, S.F., Sial, A.N., 2018. Multiproxy studies of Early Miocene pedogenic calcretes in the Santa Cruz Formation of southern Patagonia, Argentina indicate the existence of a temperate warm vegetation adapted to a fluctuating water table. Palaeogeogr Palaeoclimatol Palaeoecol 500, 1–23. https://doi.org/10.1016/j.palaeo.2018.03.037

Raza, S., Zamanian, K., Ullah, S., Kuzyakov, Y., Virto, I., Zhou, J., 2021. Inorganic carbon losses by soil acidification jeopardize global efforts on carbon sequestration and climate change mitigation. J Clean Prod. https://doi.org/10.1016/j.jclepro.2021.128036

Rowley, M.C., Estrada-Medina, H., Tzec-Gamboa, M., Rozin, A., Cailleau, G., Verrecchia, E.P., Green, I., 2017. Moving carbon between spheres, the potential oxalate-carbonate pathway of

Brosimum alicastrum Sw.; Moraceae. Plant Soil 412, 465–479. https://doi.org/10.1007/s11104-016-3135-3

Ruidas, D.K., Pomoni-Papaioannou, F.A., Banerjee, S., Gangopadhyay, T.K., 2020. Petrographical and geochemical constraints on carbonate diagenesis in an epeiric platform deposit: Late Cretaceous Bagh Group in central India. Carbonates Evaporites 35. https://doi.org/10.1007/s13146-020-00624-2

Salehi, M.H., Khademi, H., Eghbal, M.K., Mermut, A.R., 2004. Stable isotope geochemistry of carbonates and organic carbon in selected soils from Chaharmahal Bakhtiari Province, Iran. Commun Soil Sci Plant Anal 35, 1681–1697. https://doi.org/10.1081/CSS-120038562

Salomons, W., Mook, W.G., 1976. ISOTOPE GEOCHEMISTRY OF CARBONATE DISSOLUTION AND REPRECIPITATION IN SOILS. Soil Sci 122.

Sanderman, J., 2012. Can management induced changes in the carbonate system drive soil carbon sequestration? A review with particular focus on Australia. Agric Ecosyst Environ. https://doi.org/10.1016/j.agee.2012.04.015

Shaoxuan, H., Zongsuo, L., Ruilian, H., Yong, W., Guobin, L., 2016. Soil carbon dynamics during grass restoration on abandoned sloping cropland in the hilly area of the Loess Plateau, China. Catena (Amst) 137, 679–685. https://doi.org/10.1016/j.catena.2015.01.027

Sharififar, A., Minasny, B., Arrouays, D., Boulonne, L., Chevallier, T., van Deventer, P., Field, D.J., Gomez, C., Jang, H.J., Jeon, S.H., Koch, J., McBratney, A.B., Malone, B.P., Marchant, B.P., Martin, M.P., Monger, C., Munera-Echeverri, J.L., Padarian, J., Pfeiffer, M., Richer-de-Forges, A.C., Saby, N.P.A., Singh, K., Song, X.D., Zamanian, K., Zhang, G.L., van Zijl, G., 2023. Soil inorganic carbon, the other and equally important soil carbon pool: Distribution, controlling factors, and the impact of climate change, in: Advances in Agronomy. Academic Press Inc., pp. 165–231. https://doi.org/10.1016/bs.agron.2022.11.005

Sherrod, L.A., Dunn, G., Peterson, G.A., Kolberg, R.L., 2002. Inorganic Carbon Analysis by Modified Pressure-Calcimeter Method. Soil Science Society of America Journal 66, 299–305. https://doi.org/10.2136/sssaj2002.2990

Shi, H.J., Wang, X.J., Zhao, Y.J., Xu, M.G., Li, D.W., Guo, Y., 2017. Relationship between soil inorganic carbon and organic carbon in the wheat-maize cropland of the North China Plain. Plant Soil 418, 423–436. https://doi.org/10.1007/s11104-017-3310-1

Shi, Y., Baumann, F., Ma, Y., Song, C., Kühn, P., Scholten, T., He, J.S., 2012. Organic and inorganic carbon in the topsoil of the Mongolian and Tibetan grasslands: Pattern, control and implications. Biogeosciences 9, 2287–2299. https://doi.org/10.5194/bg-9-2287-2012

Song, X.D., Yang, F., Wu, H.Y., Zhang, J., Li, D.C., Liu, F., Zhao, Y.G., Yang, J.L., Ju, B., Cai, C.F., Huang, B., Long, H.Y., Lu, Y., Sui, Y.Y., Wang, Q.B., Wu, K.N., Zhang, F.R., Zhang, M.K., Shi, Z., Ma, W.Z., Xin, G., Qi, Z.P., Chang, Q.R., Ci, E., Yuan, D.G., Zhang, Y.Z., Bai, J.P., Chen, J.Y., Chen, J., Chen, Y.J., Dong, Y.Z., Han, C.L., Li, L., Liu, L.M., Pan, J.J., Song, F.P., Sun, F.J., Wang, D.F., Wang, T.W., Wei, X.H., Wu, H.Q., Zhao, X., Zhou, Q., Zhang, G.L., 2022. Significant loss of soil inorganic carbon at the continental scale. Natl Sci Rev 9. https://doi.org/10.1093/nsr/nwab120

Sreenivas, K., Dadhwal, V.K., Kumar, S., Harsha, G.S., Mitran, T., Sujatha, G., Suresh, G.J.R., Fyzee, M.A., Ravisankar, T., 2016. Digital mapping of soil organic and inorganic carbon status in India. Geoderma 269, 160–173. https://doi.org/10.1016/j.geoderma.2016.02.002

Sun, Q., Li, J., Finlay, R.D., Lian, B., 2019. Oxalotrophic bacterial assemblages in the ectomycorrhizosphere of forest trees and their effects on oxalate degradation and carbon fixation potential. Chem Geol 514, 54–64. https://doi.org/10.1016/j.chemgeo.2019.03.023

Sun, Q., Zamanian, K., Huguet, A., Bayat, O., Wang, H., Badawy, H.S., 2022. Genesis and soil environmental implications of intact in-situ rhizoliths in dunes of the Badain Jaran Desert, northwestern China. Acta Geochimica 41, 811–822. https://doi.org/10.1007/s11631-022-00543-0

Sun, Q., Zamanian, K., Huguet, A., Fa, K., Wang, H., 2020. Characterization and formation of the pristine rhizoliths around Artemisia roots in dune soils of Tengeri Desert, NW China. Catena (Amst) 193. https://doi.org/10.1016/j.catena.2020.104633

Sun, Q., Zamanian, K., Huguet, A., Wiesenberg, G.L.B., Zhao, T., Lei, Z., 2023. Carbonate cementing minerals in rhizoliths from Badain Jaran Desert: Implication for pedo-diagenesis and environment of dune soil. Rhizosphere 25. https://doi.org/10.1016/j.rhisph.2022.100647

Sun, X.-L., Minasny, B., Wang, H.-L., Zhao, Y.-G., Zhang, G.-L., Wu, Y.-J., 2021. Spatiotemporal modelling of soil organic matter changes in Jiangsu, China between 1980 and 2006 using INLA-SPDE. Geoderma 384, 114808. https://doi.org/https://doi.org/10.1016/j.geoderma.2020.114808

Syed, S., Buddolla, V., Lian, B., 2020. Oxalate Carbonate Pathway—Conversion and Fixation of Soil Carbon—A Potential Scenario for Sustainability. Front Plant Sci. https://doi.org/10.3389/fpls.2020.591297

Szendrei, G., Kovács-Pálffy, P., Földvári, M., Gál-Sólymos, K., 2012. The mineralogical composition of calcium and calcium-magnesium carbonate pedofeatures of calcareous soils in the European prairie ecodivision in Hungary. Central European Geology 55, 397–416. https://doi.org/10.1556/CEuGeol.55.2012.4.3

Tan, W.F., Zhang, R., Cao, H., Huang, C.Q., Yang, Q.K., Wang, M. kuang, Koopal, L.K., 2014. Soil inorganic carbon stock under different soil types and land uses on the Loess Plateau region of China. Catena (Amst) 121, 22–30. https://doi.org/10.1016/j.catena.2014.04.014

Tlili, F., Ayari, A., Regaya, K., 2021. Bio-mineral needle fiber calcite (NFC) in Tunisian Pleistocene calcretes (topology and crystallization). Journal of Earth System Science 130. https://doi.org/10.1007/s12040-020-01528-4

Uren, N.C., 2018. Calcium oxalate in soils, its origins and fate-a review. Soil Research. https://doi.org/10.1071/SR17244

Valera Fernández, D., Solleiro Rebolledo, E., Sedov, S., Pustovoitov, K., 2022. Provenance, and environment context of pedogenic carbonates formation from MIS 3 to MIS 1 in the Teotihuacan Valley, Mexico. Quaternary International 618, 52–69. https://doi.org/10.1016/j.quaint.2021.03.019

Valera-Fernández, D., Cabadas-Báez, H., Solleiro-Rebolledo, E., Landa-Arreguín, F.J., Sedov, S., 2020. Pedogenic carbonate crusts (calcretes) in karstic landscapes as archives for paleoenvironmental reconstructions – A case study from Yucatan Peninsula, Mexico. Catena (Amst) 194, 104635. https://doi.org/https://doi.org/10.1016/j.catena.2020.104635

Van der Hoven, S.J., Quade, J., 2002. Tracing spatial and temporal variations in the sources of calcium in pedogenic carbonates in a semiarid environment. Geoderma 108, 259–276. https://doi.org/https://doi.org/10.1016/S0016-7061(02)00134-9

Verrecchia, E.P., Braissant, O., Cailleau, G., 2006. The oxalate-carbonate pathway in soil carbon storage: The role of fungi and oxalotrophic bacteria, in: Fungi in Biogeochemical Cycles. Cambridge University Press, pp. 289–310. https://doi.org/10.1017/CBO9780511550522.013

Verrecchia, E.P., Trombino, L., 2021. Observation of Soils: From the Field to the Microscope, in: A Visual Atlas for Soil Micromorphologists. Springer International Publishing, pp. 1–17. https://doi.org/10.1007/978-3-030-67806-7_1

Violette, A., Riotte, J., Braun, J.J., Oliva, P., Marechal, J.C., Sekhar, M., Jeandel, C., Subramanian, S., Prunier, J., Barbiero, L., Dupre, B., 2010. Formation and preservation of pedogenic carbonates in South India, links with paleo-monsoon and pedological conditions: Clues from Sr isotopes, U-Th series and REEs. Geochim Cosmochim Acta 74, 7059–7085. https://doi.org/10.1016/j.gca.2010.09.006

Virto, I., Antón, R., Apesteguía, M., Plante, A., 2017. Role of Carbonates in the Physical Stabilization of Soil Organic Matter in Agricultural Mediterranean Soils, in: Soil Management and Climate Change: Effects on Organic Carbon, Nitrogen Dynamics, and Greenhouse Gas Emissions. Elsevier, pp. 121–136. https://doi.org/10.1016/B978-0-12-812128-3.00009-4

Vuong, T.X., Heitkamp, F., Jungkunst, H.F., Reimer, A., Gerold, G., 2013. Simultaneous measurement of soil organic and inorganic carbon: Evaluation of a thermal gradient analysis. J Soils Sediments 13, 1133–1140. https://doi.org/10.1007/s11368-013-0715-1

Wang, K.-B., Ren, Z.-P., Deng, L., Zhou, Z.-C., Shangguan, Z.-P., Shi, W.-Y., Chen, Y.-P., 2016. Profile Distributions and Controls of Soil Inorganic Carbon along a 150-Year Natural Vegetation Restoration Chronosequence. Soil Science Society of America Journal 80, 193–202. https://doi.org/10.2136/sssaj2015.08.0296

Wang, S., Lu, W., Zhang, F., 2022. Vertical Distribution and Controlling Factors of Soil Inorganic Carbon in Poplar Plantations of Coastal Eastern China. Forests 13. https://doi.org/10.3390/f13010083

Wang, X., Wang, J., Xu, M., Zhang, W., Fan, T., Zhang, J., 2015. Carbon accumulation in arid croplands of northwest China: Pedogenic carbonate exceeding organic carbon. Sci Rep 5. https://doi.org/10.1038/srep11439

Wang, X., Wang, J., Zhang, J., 2012. Comparisons of Three Methods for Organic and Inorganic Carbon in Calcareous Soils of Northwestern China. PLoS One 7. https://doi.org/10.1371/journal.pone.0044334

Wang, X.J., Xu, M.G., Wang, J.P., Zhang, W.J., Yang, X.Y., Huang, S.M., Liu, H., 2014. Fertilization enhancing carbon sequestration as carbonate in arid cropland: assessments of long-term experiments in northern China. Plant Soil 380, 89–100. https://doi.org/10.1007/s11104-014-2077-x

Wang, Y., Li, Y., Ye, X., Chu, Y., Wang, X., 2010. Profile storage of organic/inorganic carbon in soil: From forest to desert. Science of the Total Environment 408, 1925–1931. https://doi.org/10.1016/j.scitotenv.2010.01.015

Watanabe, Y., Stewart, B.W., Ohmoto, H., 2004. Organic- and carbonate-rich soil formation ~2.6 billion years ago at Schagen, East Transvaal district, South Africa. Geochim Cosmochim Acta 68, 2129–2151. https://doi.org/10.1016/j.gca.2003.10.036

West, L.T., Drees, L.R., Wilding, L.P., Rabenhorst, M.C., 1988. Differentiation of Pedogenic and Lithogenic Carbonate Forms in Texas*, Geoderma.

Wilford, J., de Caritat, P., Bui, E., 2015. Modelling the abundance of soil calcium carbonate across Australia using geochemical survey data and environmental predictors. Geoderma 259–260, 81–92. https://doi.org/10.1016/j.geoderma.2015.05.003

Wilsey, B., Xu, X., Polley, H.W., Hofmockel, K., Hall, S.J., 2020. Lower soil carbon stocks in exotic vs. native grasslands are driven by carbonate losses. Ecology 101. https://doi.org/10.1002/ecy.3039

Wolff, K., Tiddy, C., Giles, D., Hill, S.M., Gordon, G., 2017. Distinguishing pedogenic carbonates from weathered marine carbonates on the Yorke Peninsula, South Australia: Implications for mineral exploration. J Geochem Explor 181, 81–98. https://doi.org/10.1016/j.gexplo.2017.06.019

Wu, H., Guo, Z., Gao, Q., Peng, C., 2009. Distribution of soil inorganic carbon storage and its changes due to agricultural land use activity in China. Agric Ecosyst Environ 129, 413–421. https://doi.org/10.1016/j.agee.2008.10.020

Wynn, J.G., 2000. Paleosols, stable carbon isotopes, and paleoenvironmental interpretation of Kanapoi, Northern Kenya. J Hum Evol 39, 411–432. https://doi.org/https://doi.org/10.1006/jhev.2000.0431

Xiong, Z., Liu, X., Ding, L., Farnsworth, A., Spicer, R.A., Xu, Q., Valdes, P., He, S., Zeng, D., Wang, C., Li, Z., Guo, X., Su, T., Zhao, C., Wang, H., Yue, Y., 2022. The rise and demise of the Paleogene Central Tibetan Valley Reconstructing the Paleogene topography and climate of central Tibet informs understanding of collisional tec-tonic mechanisms and their links to climate and biodiversity. Radiometric dates of volcanic/sedimentary rocks and paleotemperatures based on clumped isotopes within ancient soil carbonate nodules from the Lunpola, Sci. Adv.

Xu, T., Zhang, M., Ding, S., Liu, B., Chang, Q., Zhao, X., Wang, Y., Wang, J., Wang, L., 2021. Grassland degradation with saline-alkaline reduces more soil inorganic carbon than soil organic carbon storage. Ecol Indic 131. https://doi.org/10.1016/j.ecolind.2021.108194

Yan, X., Li, G., Zhang, W., Muneer, M.A., Yu, W., Ma, C., Wu, L., 2022. Spatio-Temporal Variation of Soil Phosphorus and Its Implications for Future Pomelo Orcharding System Management: A Model Prediction From Southeast China From 1985–2100. Front Environ Sci 10. https://doi.org/10.3389/fenvs.2022.858816

Yang, R.M., Yang, Fan, Yang, Fei, Huang, L.M., Liu, F., Yang, J.L., Zhao, Y.G., Li, D.C., Zhang, G.L., 2017. Pedogenic knowledge-aided modelling of soil inorganic carbon stocks in an alpine environment. Science of the Total Environment 599–600, 1445–1453. https://doi.org/10.1016/j.scitotenv.2017.05.055

Yin, Y., Ma, D., Wu, S., 2019. Enlargement of the semi-arid region in China from 1961 to 2010. Clim Dyn 52, 509–521. https://doi.org/10.1007/s00382-018-4139-x

Zamanian, K., Lechler, A.R., Schauer, A.J., Kuzyakov, Y., Huntington, K.W., 2021. The δ13C, δ18O and Δ47 records in biogenic, pedogenic and geogenic carbonate types from paleosol-loess sequence and their paleoenvironmental meaning. Quat Res 101, 256–272. https://doi.org/DOI: 10.1017/qua.2020.109

Zamanian, K., Pustovoytov, K., Kuzyakov, Y., 2016. Pedogenic carbonates: Forms and formation processes. Earth Sci Rev. https://doi.org/10.1016/j.earscirev.2016.03.003

Zhang, F., Wang, X., Guo, T., Zhang, P., Wang, J., 2015. Soil organic and inorganic carbon in the loess profiles of Lanzhou area: Implications of deep soils. Catena (Amst) 126, 68–74. https://doi.org/10.1016/j.catena.2014.10.031

Zhang, G., Bai, J., Zhao, Q., Jia, J., Wang, Xin, Wang, W., Wang, Xinyan, 2021. Soil carbon storage and carbon sources under different Spartina alterniflora invasion periods in a salt marsh ecosystem. Catena (Amst) 196. https://doi.org/10.1016/j.catena.2020.104831

Zhang, L., Zhao, W., Zhang, R., Cao, H., Tan, W., 2018. Profile distribution of soil organic and inorganic carbon following revegetation on the Loess Plateau, China. Environmental Science and Pollution Research 25, 30301–30314. https://doi.org/10.1007/s11356-018-3020-0

ZHANG, N., HE, X.D., GAO, Y.B., LI, Y.H., WANG, H.T., MA, D., ZHANG, R., YANG, S., 2010. Pedogenic Carbonate and Soil Dehydrogenase Activity in Response to Soil Organic Matter in Artemisia ordosica Community. Pedosphere 20, 229–235. https://doi.org/10.1016/S1002-0160(10)60010-0

Zhao, X., Zhao, C., Wang, J., Stahr, K., Kuzyakov, Y., 2016. CaCO3 recrystallization in saline and alkaline soils. Geoderma 282, 1–8. https://doi.org/10.1016/j.geoderma.2016.07.004

CHAPTER THREE

Distribution and Potential of Rare Earth Elements Fingerprinting as Tracers for Carbonate Sources in Soils Developed on Contrasting Parent Materials[2]

Abstract

While the use of rare earth elements (REE) to examine soil processes is an increasingly popular approach, very few studies have investigated its application to the study of dominant soil genetic processes at the landscape scale in semi-arid environments. This study analyses the distribution and fractionation of REEs in 12 soil profiles from different lithologies in the Kalahari Basin of Botswana (BKB) and examines their relationships with pedogenetic processes, calcium carbonate origin and pH. The results show significant variability in total REE contents (12.8 - 193.2 mg kg^{-1}) in the soil profiles, depending on the soil parent material. Total REE abundance within soil profiles show a strong correlation with clay-associated elements, such as Al ($r = 0.8$) and K ($r = 0.7$), as well as with iron Fe ($r = 0.6$). These correlations suggest that clay formation plays a primary role in REE enrichment in the soil profiles. On the other hand, the moderate positive correlation with Ca ($r = 0.4$) indicates a minor contribution from calcium carbonate accumulation to REE enrichment. pH shows weak positive correlations with REE content across the full soil profile ($r < 0.2$), reflecting negligeable influence on REE distribution in the study soil profiles. The fractionation ratios between light REEs and heavy REEs (LREEs/HREEs) range from 0.6–1.5 in soil profiles on alluvial and fluvio-lacustrine sediments, 0.4–0.9 from those on basaltic and sandstones rock, and 0.7–1.1 from those on sands, clays, calcretes and silcrete. Given the previously demonstrated preferential complexation of HREEs in pedogenic carbonates, these results suggest a mixed pedogenic and

[2] *This chapter is based on a paper co-authored with Charles Kono Ebede, Thierry Bineli Betsi, and Peter N. Eze; published in Geoderma Regional, 43 (2025), e01009*. https://doi.org/10.1016/j.geodrs.2025.e01009

lithogenic origin for calcium carbonates in soil on alluvial and fluvio-lacustrine sediments, and in soils on sands, clays, calcretes and silcretes. Soils on basaltic and sandstone rocks, on the other hand, have a purely pedogenic origin. The results of this study provide a solid baseline for understanding REE distributions in the BKB and tracing the origin of calcium carbonate in semi-arid environments.

Keywords: Arenosols; Calcisols; Geochemical proxies; Pedogenesis; Vertisols.

3.1. Introduction

Rare earth elements (REEs) are attracting increasing interest because of their use in various fields, including manufacturing, electronics and medicine, but above all, in the development of renewable energies, particularly batteries used in electric vehicles, which are set to become the world's main transport solution (Balaram, 2019). Also, their distribution and fractionation in the Earth's crust, soil, water and plants, has gained global scientific attraction. This is because they can be used not only to guide REEs exploration (Cao et al., 2024; Gadea and Khan, 2024; Sababa et al., 2021) or the exploration of other mineral resources (Batch et al., 2024; Carrasco-Godoy et al., 2024) and identifying potential environmental issues (Li et al., 2020; Sharma et al., 2024), but also to trace geochemical and geodynamic processes (Bozkaya et al., 2024; Li et al., 2024; Zhang and Shields, 2023).

Due to their unique pattern in geological materials, REEs in soils present a vast and complex field, with numerous studies demonstrating their significant contributions to various soil processes. For example, numerous works have shown that REEs can influence soil organic carbon and nitrogen cycles (Chu et al., 2007; Song et al., 2025). Additionally, these elements are frequently utilised as indicators of specific soil processes, such as soil aggregate dynamics (Peng et al., 2017; Pucetaite et al., 2025; Wang et al., 2020) or erodibility. Numerous studies have demonstrated that REE fractionation in soils is associated with pedogenic processes, such as the accumulation of secondary minerals, including clays, iron, aluminium and manganese oxides, and carbonates (Andrade et al., 2022; Cantrell and Byrne, 1987; Haldar et al., 2025; Laveuf et al., 2008). Moreover, REE fractionation in soil is associated with soil properties such as organic matter content and pH (Lin et al., 2022a; Nouazi Momo et al., 2019). Gradually, studies are establishing large-scale analyses not only of the distribution of REEs in soils but also of their fractionation as a function of soil type, thus establishing the links between REEs and pedogenic processes, as well as the respective contributions of pedogenetic factors to REE distribution and fractionation (Alfaro et al., 2018; Mihajlovic et al., 2019; Temga et al., 2021).

Nevertheless, the use of REEs fingerprinting to trace pedogenetic processes is largely under-studied using soils from southern Africa's arid and semi-arid regions, where it could provide a better understanding of pedogenic processes, especially in the differentiation of the origin of calcium carbonate in soil. Soil calcium carbonate, also known as soil inorganic carbon (SIC), constitutes both an important carbon reservoir in the soils of this region and a pathway for trapping atmospheric carbon dioxide (Dina Ebouel et al., 2024). It should be noted that carbon sequestration through this pathway is largely dependent on its origin. Pedogenic carbonates are formed through the fixation of calcium ions (Ca^{2+}) from parent material weathering in the soil by bicarbonate ions (HCO_3^-), which themselves may come from root and microbial respiration (Zamanian et al., 2016). Lithogenic carbonate, on the other hand, originates from accumulation through sedimentary processes of calcium carbonate over geological timescales (Monger, 2014b). To ascertain the origin of soil carbonates, Laveuf and Cornu (2009) explained that differentiation between pedogenic and lithogenic carbonates could be performed via the LREE/HREE ratio, as pedogenic carbonate accumulation favours enrichment in HREE rather than LREE and is therefore linked to LREE/HREE < 1. In contrast, lithogenic carbonates favour enrichment in LREE rather than HREE and are characterised by LREE/HREE > 1.

The Botswana Kalahari Basin (BKB) presents a natural laboratory where the interplay of a strong semi-arid climate, vast and relatively uniform aeolian parent materials, diverse underlying geology, and a long, dynamic environmental history creates a rich environment for dissecting the intricate processes of pedogenetic processes including, clay formation and calcium carbonate accumulation. Therefore, this study uses twelve prominent soil profiles in three contrasting geological settings in the Botswana Kalahari Basin to investigate the distribution of REEs in the semi-arid soils and, explore relationship between REE and pedogenic processes, including the origin of calcium carbonate. The results demonstrate that total REEs distribution in the study was controlled by the lithology, whereas clay and calcium carbonate were the main controller of variation within soil profile. Moreover, REEs elements

allow to differentiate areas dominated by lithogenic carbonates from those dominated by pedogenic carbonates.

3.2. Environmental setting

As shown in Table 3.1, the study area covers seven distinct localities, stretching from southern to northern Botswana. It is characterised by two major geological units in Botswana, covering almost 80 % of Botswana's surface area including the Carboniferous to Jurassic Karoo Supergroup and the overlying Post-Cretaceous Kalahari Group (Key and Ayres, 2000).

The Karoo Supergroup Formations lithostratigraphic descriptions highlight two units (Lower and Upper Karoo) separated by an unconformity (Bordy, 2020; Smith, 1984). The Lower Karoo consists of Permo-Carboniferous glacial deposits of the Dwyka Group (diamictite, varvite and sandstone) overlain by Permian coal-bearing fluvio-deltaic deposits of the Ecca Group (coal-bearing, carbonaceous mudstone, white poorly cemented arkosic sandstone) and Permo-Triassic fluvio-lacustrine Formations of the Beaufort Group (non-carbonaceous mudstone, thin limestone, claystones). The Upper Karoo on the other hand consists of fluvial and aeolian deposits from the Upper Triassic to Lower Jurassic of the Lebung Group (red mudstone and sandstone), underlain by Lower Jurassic basaltic lavas of the Stromberg Group. The Kalahari Group defines the sedimentary deposits that make up the Kalahari Basin. According to Haddon and McCarthy (2005), the Kalahari Basin formed in response to progressive uplift of the interior of southern Africa, probably starting from the late Cretaceous. This process modified the regional drainage and initiated the filling of the basin with sediments. The first deposits, dated to the Cretaceous, consisted of coarse gravels, poorly sorted gravels, interbedded sands and clays, and thick layers of clay. The second phase of deposition, dating from the mid-Miocene, took place in a context of tectonic stability and is associated with the formation of silcretes and calcretes. This phase was followed by tectonic uplift (late Miocene to Pliocene), which led to erosion, reworking and redeposition of the sand by aeolian processes during drier periods and characterised by the sand deposits (Kalahari dunes). The last phase

was characterised by the extension of the East African rift system into southern Africa, which led to the formation of local depressions such as the Okavango Rift Zone, accompanied by the formation of alluvial fans (McCarthy et al., 1997).

Table 3.1. Geographical coordinates and background knowledge of the studied soil profiles

Place	Longitude E	Latitude S	Profile		WRB Soil classification	Parent Material	Full profile description in
Parakarungu	24.311566	18.040334	Northern	POQ	Arenic Kastanozems	Fluvio-lacustrine sediment of the Kalahari Group	Dina Ebouel et al., 2025; Eze and Molwalefhe, 2024; Eze et al., 2021
Shorobe	23.750539	19.68151		SHP3	Arenosols		
Maun	23.552429	19.894046		M1P1	Calcisols		
Orapa	25.361653	21.370347		K1P1	Arenosols		
Serowe	26.724539	22.397943	Central	SP1	Vertisols	Sandstone of Lebung Group and basaltic lava of the Stormberg Group	Eze et al., 2025
Serowe	26.73758	22.409965		SP2	Vertisols		
Serowe	26.699978	22.372358		SP3	Vertisols		
Serowe	26.730806	22.444278		SP4	Luvic Vertisols		
Takatokwane	24.327817	24.007793	Southern	TK1	Arenosols	Alluvial sands and clays, calcretes and silcretes duricrusts of the Kalahari Group	Matshameko et al., 2022 ; Matshameko et al., 2023
Takatokwane	24.319076	23.319076		TK2	Arenosols		
Letlhakeng	25.036667	24.107063		LT1	Calcisols		
Letlhakeng	25.020381	24.110472		LT2	Calcisols		

As illustrate in Fig. 3.1, the soil profiles in the northern part (POQ, SHP3, M1P1 and K1P1) are underlain by a series of alluvial and fluvio-lacustrine deposits of the Kalahari Group. These sediments would have been deposited during several fluctuation cycles of a Quaternary mega-palaeolake including the depression fan formed by the Okavango Rift Zone and the Makgadikgadi Basin (Burrough et al., 2009). The landscape at Okavango consists of dunes, marshes, sand ridges and carbonate islands; which is the result of palaeoenvironmental and palaeodrainage changes during the Quaternary; and is associated with (neo)tectonic processes (Mokatse et al., 2022a). The landforms of the Makgadikgadi Basin include salt pans, dunes, shorelines and deltas (Burrough, 2022). The vegetation comprises a mixture of forest and grassland areas. The main types of forest vegetation are mopane forests, dominated by *Colophospermum mopane*, and Baikiaea forests, while the grasslands are dominated by

communities of grasses covered by a few *Acacia* spp. *Terminalia sericea* or *Philenoptera nelsi* (Vittoz et al., 2020).

The soil profiles in the central part of Botswana, located around Serowe (SP1, SP2, SP3 and SP4) are characterised by soils formed on outcrops of Formations from the Karoo Supergroup. In particular, the basaltic lavas of the Stormberg Group and the sandstone Formations of the Lebung Group (Franchi et al., 2021). The geomorphological unit of the sector is the eastern Hardveld, which covers the southeastern to east-central areas of Botswana. It is distinguished by gently sloping plains that protect Precambrian mountains and hills as well as lone ravines connected to severe erosion (Atlhopheng et al., 2022). The typical vegetation is a bush savannah (Ringrose et al., 2003), characterised by woody species such as *Acacia erioloba*, *A. mellifera*, *A. hebeclada, A. fleckii, Terminalia sericea*, *Lonchocarpus nelsii, Boscia albitruna, Grewia flava, G. retinervis, Dichrostachys cinerea, Ziziphus mucronate* and herbaceous species such as *Aristidia uniplumis, Eragrostis latimanniana, Schmidtia bulbosa, Antephora pubescens, and Aristida meridionalis* (Ringrose et al., 1998). This natural land cover is deeply marked by agricultural activities and infrastructure development (Atlhopheng et al., 2022).

The southern soil profiles (TK1, TK2, LT1 and LT2) are formed on sand, clay, calcretes and silcretes of the Kalahari Group (Kampunzu et al., 2007). These superficial deposits are rarely thicker than 30 m, but they change to other unconsolidated sands with intermediate layers of calcrete and silcrete (Carney, 1994). They overlie a thick layer of basaltic lava (Stormberg Group) and fluvio-glacial, deltaic, and lacustrine sedimentary rocks (Smith, 1984). This zone is characterised by savannah vegetation, consisting mainly of *Ziziplus Mucronata, Terminalia Sericea, Acacia Tortius*, *Boscia Albitrunca* and grass species. The soils are mainly used for agriculture, in particular for grazing and the production of food crops, but also for the extraction of clay for pottery (Matshameko et al., 2022). The study area is covered by a semi-arid climate, with average annual rainfall decreasing from north to south from 600 mm to approximately 300 mm (Andringa, 1984).

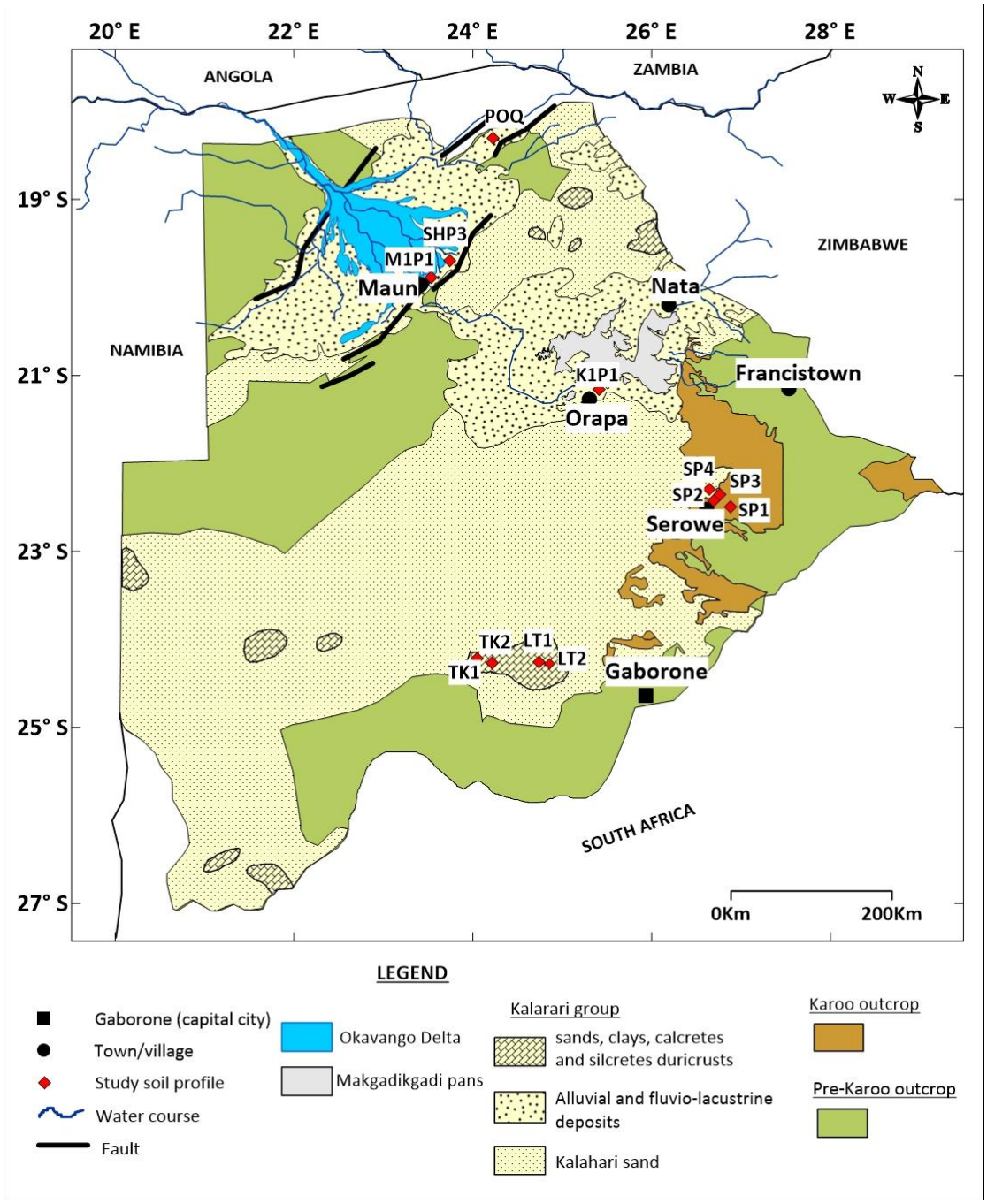


Fig. 3.1. Geological background of the sampling area.

3.3. Materials and methods

3.3.1. Materials

Reconnaissance field trips were organised from 2020–2022, spanning from the north to the south of Botswana. Following this reconnaissance phase, 12 representative soil profiles were selected (Fig. 3.1). The profiles were described in accordance with the FAO (2006) soil description guidelines.

Four soil profiles were selected from the fluvio-lacustrine deposits of northern Botswana, including a 6 m profile along an open quarry at Parakarungu (POQ) and three 2 m soil pits at Shorobe, Maun and Orapa (SHP3, M1P1 and K1P1). Description resulted in the classification of the POQ profile as arenic Kastonozems, characterised by a sand fraction greater than 70 wt.%, a dark black colour, an organic matter content greater than 0.6 wt.% in the topsoil horizon and calcium carbonate accumulation in powder form or as soft nodules. SHP3 and K1P1 were classified as Arenosols, characterised by sand fraction greater than 70 wt.% and calcium carbonate accumulation as powder coating sand particles (Fig. 3.2A). M1P1 was classified as Calcisols, characterised by and indurated calcic horizon (Fig. 3.2B) with a calcium carbonate content 31 wt.%. Details descriptions are given in Dina Ebouel et al. (2025); Eze et al. (2021) and Eze and Molwalefhe (2024). The physico-chemical properties are summarised in Table 2. Based on macromorphological descriptions, calcium carbonates features observed along those soil sections have been described from pedogenic origin (Eze et al., 2021; Eze and Molwalefhe, 2024), while Nash (2022) highlighted a lithogenic origin.

Table 3.2. Physico-chemical properties of northern soil profiles

Profile	Horizon	Silt (wt.%)	Clay (wt.%)	Sand (wt.%)	EC (µS/cm)	SOM (wt.%)
M1P1	A	0.8	14.8	84.4	200	0.6
	Bkk1	1.9	15.7	82.2	800	0.4
	Bkk2	1.8	23.3	74.9	900	0.3
	Bkk3	2.4	34.7	62.9	5500	0.2
	Ck	1.6	19.0	79.4	1500	0.2
K1P1	A	6.4	30.4	63.2	230	0.4
	AC	1.3	18.3	80.4	4650	0.3
	C1	0.6	12.9	86.5	2050	0.3
	C2	0.1	13.5	86.4	800	0.2
POQ	AP	4.3	45.4	50.3	220	0.5
	AC	1.1	14.4	84.5	190	0.4
	Ck1	1.3	18.3	80.4	190	0.3
	Ck2	0.6	12.9	86.5	550	0.3
	Ck3	0.1	13.5	86.4	580	0.2
	Ck4	1.4	15.0	83.7	780	0.2
	CFS	0.6	5.8	93.6	200	0.2
	CVFS	2.7	38.0	59.3	1081	0.2
SHP3	A1	2.5	28.2	69.4	300	0.5
	AC	2.6	40.9	56.5	750	0.2
	C1	3.5	40.2	56.4	2570	0.2
	C2	3.4	51.6	45.0	1700	0.2
	C3	3.0	37.0	60.0	1330	0.4

Particle size distribution of the samples was determined by laser diffraction using a Malvern 2000 Mastersizer analyser; EC was determined in a solution with a soil/deionised water ratio of 1/2.5, in accordance with the recommendations of the FAO guidelines for soil description (WRB, 2006); SOM was determined by wet oxidation (Walkley and Black, 1934).

Four soil profiles formed on the Stormberg basalt and Lebung sandstone Formations were also selected in central Botswana, around Serowe. Four soil pits of 2 m (SP1, SP2, SP3 and SP4) were used for descriptions. SP1, SP2 and SP3 have been classified as Vertisols, characterised by deep, wide cracks, Gilgai microrelief and slickensides. The clay fraction was greater than 30 wt.% and consisted mainly of montmorillonite. SP4 was classified as Luvic Vertisols, characterised by deep, wide cracks, Gilgai microrelief and slickensides. But the clay fraction was 20 wt.% and consisted mainly of montmorillonite. Soft nodules of calcium carbonates and diffuse powder were observed in the four described profiles (Fig. 3.2C). Morphological characterisation of Eze et al. (2025), point out a pedogenic origin. Details descriptions of the soil profiles are given by Eze et al. (2025). Nevertheless, Table 3.3 presents the physico-chemical properties of the soil profiles.

Table 3.3. Physico-chemical properties of central soil profiles

Profile	Horizon	Silt (wt.%)	Clay (wt.%)	Sand (wt.%)	EC (µS/cm)	SOM (wt.%)
SP1	A	21.3	10.0	68.7	70	0.9
	Bk1	33.3	10.0	56.7	100	0.9
	Bk2	35.3	8.0	56.7	140	1.0
	Bk3	37.3	14.0	48.7	220	1.2
	Bss1	33.3	12.0	54.7	250	1.4
	Bss2	5.3	10.0	84.7	230	1.4
SP2	Ap	25.3	14.0	60.7	120	0.5
	Bss1	47.3	8.0	44.7	590	0.6
	Bss2	45.3	10.0	44.7	1090	0.6
	Bss3	51.3	8.0	40.7	1110	0.6
	Bkss	39.3	12.0	48.7	920	0.4
	Bt	33.3	6.0	60.7	670	0.3
SP4	A	21.3	30.0	48.7	120	1.4
	Bkss1	35.3	30.0	34.7	140	1.2
	Bkss2	37.3	34.0	28.7	400	1.2
	Bk	35.3	28.0	36.7	290	1.1
	Bkkm1	45.3	18.0	36.7	300	0.9
	Bkkm2	43.3	16.0	40.7	250	0.6
SP5	Ap	35.3	18.0	46.7	130	3.5
	Bt1	45.3	14.0	40.7	100	2.6
	Bt2	49.3	16.0	34.7	180	2.7
	Bk	1.3	24.0	74.7	100	3.5
	Bkkm1	1.3	10.0	88.7	90	0.9
	Bkkm2	1.3	6.0	92.7	100	1.0

Particle size distribution of the samples was determined by laser diffraction using a Malvern 2000 Mastersizer analyser; EC was determined in a solution with a soil/deionised water ratio of 1/2.5, in accordance with the recommendations of the FAO guidelines for soil description (WRB, 2006); SOM was determined by wet oxidation (Walkley and Black, 1934).

Four soil profiles formed on sands, clays, calcretes and silcretes of the Kalahari Group were selected in the southern Botswana. Soil pits of 2 m, two at Takatokwane (TK1 and TK2) and two at Letlhakeng (LT1 and LT2) were used for descriptions. TK1 and TK2 were classified as Arenosols, characterised by more than 70 wt.% of sand fraction and single grain structure. A diffuse powder of calcium carbonate was observed throughout the profile, coating the sand grains. LT1 and LT2 were classified as Calcisols, characterised by soft calcium carbonate nodules features in the Bk horizon (Fig. 3.2D) and diffuse powder coating soil peds (Fig. 3.2E). Calcium carbonate features in this environment originated from both lithogenic and pedogenic processes (Kampunzu et al., 2007). Details descriptions of these soil profiles are given in Matshameko et al. (2023, 2022). However, key physico-chemical properties are presented in Table 3.4.

Table 3.4. Physico-chemical properties of southern soil profiles

Profile	Horizon	Silt (wt.%)	Clay (wt.%)	Sand (wt.%)	EC (µS/cm)	SOM (wt.%)
	A	6.0	25.9	68.1	110	4.7
	AB	4.0	27.7	68.3	120	4.4
	Bk1	12.0	31.9	56.1	130	3.9
	Bk2	15.6	25.4	59.0	130	3.6
LT1	Bt1	15.9	30.9	53.2	180	2.7
	A	7.8	25.3	66.9	100	4.6
	AB	12.0	31.8	56.2	800	4.0
	Bk1	3.9	25.8	60.3	100	4.8
	Bk2	11.9	27.8	60.3	200	4.0
LT2	Bt1	16.8	29.4	63.8	750	2.8
	TK1 01	14.8	19.2	66.0	6450	1.3
	TK1 02	3.9	28.1	68.0	4600	1.8
	TK1 03	12.8	49.2	38.0	4290	1.7
	TK1 04	8.8	35.2	56.0	3640	1.1
	TK1 05	4.8	17.2	78.0	1920	0.9
TK1	TK1 06	3.9	15.0	81.1	3850	0.9
	TK2 01	2.0	8.9	89.1	2520	1.2
	TK2 02	3.2	20.0	76.1	3120	0.8
	TK2 03	8.8	53.2	38.0	4650	1.1
	TK2 04	2.0	21.2	76.8	4310	1.1
	TK2 05	4.4	13.2	82.4	4210	1.7
TK2	TK2 06	1.5	23.2	75.3	4420	1.1

Particle size distribution of the samples was determined by laser diffraction using a Malvern 2000 Mastersizer analyser; EC was determined in a solution with a soil/deionised water ratio of 1/2.5, in accordance with the recommendations of the FAO guidelines for soil description (WRB, 2006); SOM was determined by wet oxidation (Walkley and Black, 1934).

A total of 68 soil samples were taken according to genetic horizons for further analysis in the laboratory.

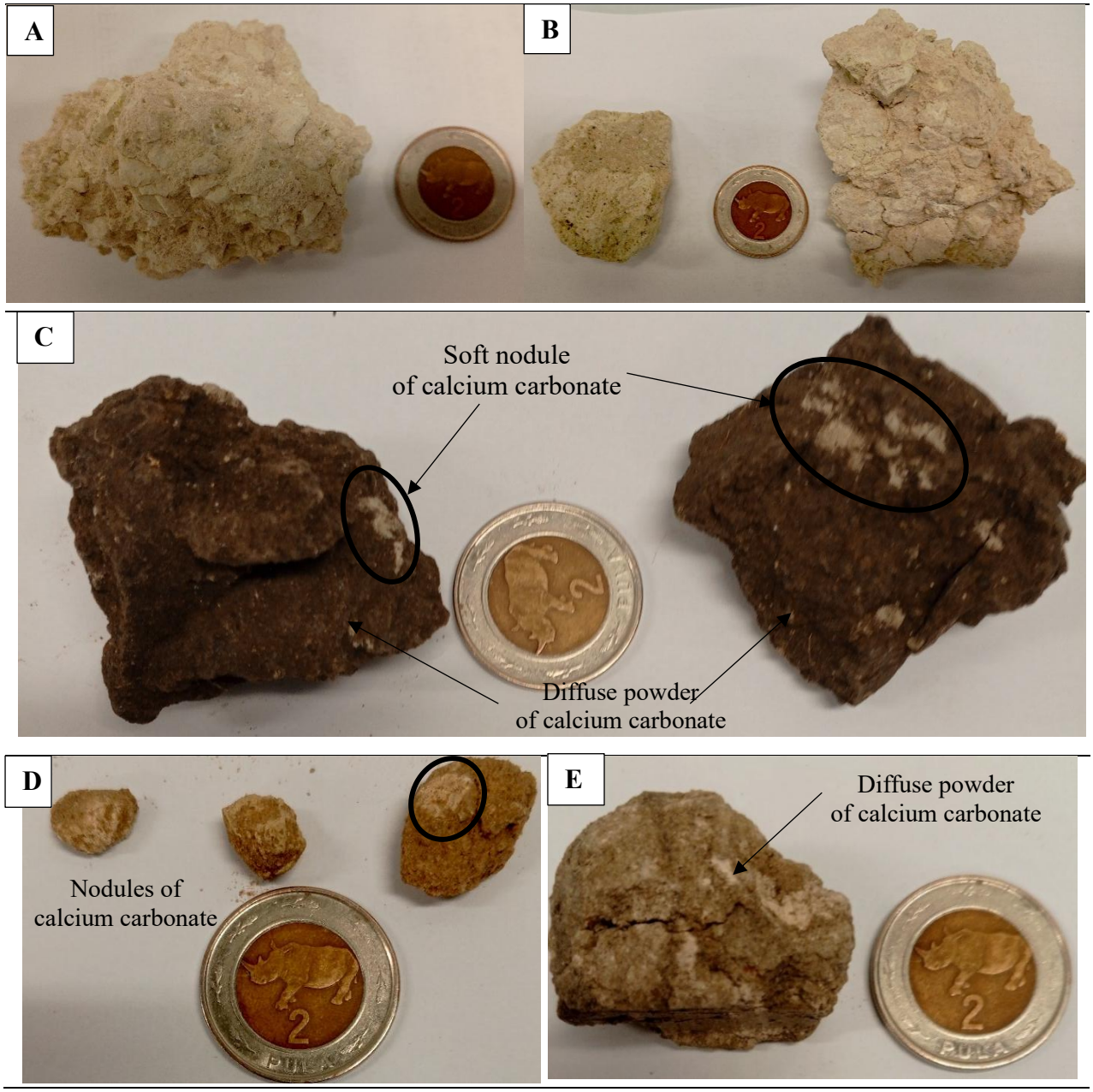


Fig. 3.2. Calcium carbonate features in the study profiles A. Diffuse powder coating sand grains in K1P1; B. Indurate layer in M1P1; C. soft nodules and diffuse powder coating peds in Vertisols in profile SP3; D. Soft carbonate nodules in TK2; E. Diffuse powder coating peds in TK2.

3.3.2. Laboratory analysis

The soil pH was determined in a 1/2.5 soil: deionised water ratio solution as recommended in FAO Guidelines for soil description (WRB, 2006). The carbonate content of the soil was determined with an Eijkelkamp calcimeter using the Scheibler method, in accordance with NEN-ISO 10693. In this method, the carbonates present in the sample react with hydrochloric

acid (4 M HCl), generating CO_2 gas. The volume of CO_2 produced is measured volumetrically using a burette system and the carbonate content is expressed as calcium carbonate equivalent ($CaCO_3$). Calibration was carried out using calcium carbonate standards (0.2 g and 0.4 g $CaCO_3$), and blank determinations were performed to account for potential contamination. Results were calculated using the standard formula, incorporating corrections for blank values and moisture content (ISO 11465). Results obtained in g kg^{-1} were converted to weight percent. The total elemental composition of the samples was determined at the Minerals-Geochem Laboratory of SGS, Randfontein, South Africa. The suite of major rock-forming oxides (reported in wt.%) was determined via the XRF (X-ray fluorescence) borate fusion method. A sample weighing 0.7 g was mixed with lithium tetraborate flux and fused to form a homogenous glass bead. The borate fusion was followed by analysis of the glass beads via a wavelength dispersive X-ray fluorescence spectrometer. The loss on ignition (LOI) at 1000 °C was determined separately by gravimetry. The REE contents were determined by inductively coupled plasma–mass spectrometry (ICP-MS), using the sodium peroxide fusion method. A sample (0.2–2.0 g) was weighed into a crucible containing Na_2O_2 and NaOH. The mixture was then fused. The sample was leached, acidified and brought to volume. The sample was then analysed via ICP–MS, and the results are reported in mg kg^{-1}. Analytical quality control was maintained throughout the analysis by including certified reference materials, analytical blanks and duplicate samples in each batch of analysis. OREAS 906, AMIS0355 and AMIS0534 certified reference materials were systematically analysed at the beginning and end of each analytical run. The concentrations measured for these certified reference materials were systematically within ± 5% of their certified values, confirming the accuracy of the analytical methods. Analytical blanks were also included to control for potential contamination, and all values measured in the blanks were below the respective detection limits. Precision was assessed by analysing duplicate samples, with relative percentages of difference generally

below 5% for most elements whose concentrations were above their detection limits. The exception was P, for which the difference was 10%.

Potential spectral interference between barium (Ba) and europium (Eu) isotopes, particularly from BaO polyatomic ions on Eu, is a well-documented concern in samples analysed by ICP-MS (Pourret et al., 2022). This interference typically becomes significant when the Ba/Eu ratio exceeds 10000 (Zepeda et al., 2024). Crucially, for the samples in this study, all measured Ba/Eu ratios were found to be below 2500 (Appendix 3.1), indicating that this specific interference did not significantly impact the accuracy of the Eu measurements.

3.3.3. Data processing

Given the large number of soil profiles involved in this study, boxplots were used to represent the vertical variation in pH and $CaCO_3$ content for each profile. The vertical variation of each major element was also represented in the same way.

The REE contents in the soil profiles of the study were normalised to the concentrations of the upper continental crust (UCC) (Taylor and McLennan, 1985) to illustrate vertical variation of REEs. The cerium (Ce/Ce*) and europium (Eu/Eu*) anomalies, along with the LREE/HREE fractionation ratio, were calculated using UCC values as a reference (Taylor and McLennan, 1985).

To analyse potential relationships between pH or $CaCO_3$ and REEs distribution and fractionation in the study area, a correlation matrix was calculated using Spearman's rank correlation coefficient, a non-parametric method that evaluates monotonic relationships between variables. The results were visualised in a heat map, where a colour gradient was used to indicate the strength and direction of the correlations. The same approach was also used to analyse the relationship between major elements and REEs, but a complementary principal component analysis (PCA) was used to identify the major identified groups. All these statistical analyses and representations were carried out using R version 4.3.3. A rigorous pre-processing procedure was undertaken to ensure the robustness and meaningful interpretation of the results.

Values below the detection limit were initially replaced by half their respective lower detection limits. Subsequently, a natural logarithm transformation (log(x)) was applied to all variables to mitigate the undue influence of highly concentrated elements and to normalise their distributions. Finally, standardisation was performed by subtracting the mean of each variable from its individual values and then dividing by its standard deviation. This ensured that all variables contributed equally to the PCA, possessing a mean of zero and a standard deviation of one.

3.4. Results

3.4.1. Soil pH and carbonate content

Soil pH and the calcium carbonate content in each of the studied soil profiles are presented via boxplots in Fig. 3.3. The general pattern shows great variability in calcium carbonate content and pH between the profiles. The $CaCO_3$ content varies greatly among the different profiles, from an average of 2.6 wt.% in SP3 to 18.5 wt.% in M1P1. Two main groups can be distinguished. The first group highlights the profiles with relatively high $CaCO_3$ contents (M1P1, POQ, SP4, LT1, LT2, TK1, and TK2), average of content varies from 9.1 wt.% to 18.5 wt.%. The second group highlights those with relatively low $CaCO_3$ contents (K1P1, SHP3, SP1, SP2, and SP3). The average content ranges from 2.6 wt.% to 6.9 wt.%. The northern (M1P1, POQ, SHP3, K1P1) and southern (LT1, LT2, TK1, TK2) profiles with average content generally above 10 wt.%, except K1P1 and SHP3, have relatively high calcium carbonate contents, whereas the central profiles (SP1, SP2, SP3, SP4), with average content below 7 wt.%, except for SP4, have relatively low contents. The pH also varies considerably between the profiles, ranging from approximately 7–10. Two main groups can be observed, one with a neutral to slightly alkaline pH (SP1, SP2, SP3, and SP4) and the other with alkaline to strongly alkaline pH (M1P1, K1P1, POQ, SHP3, LT1, LT2, TK1, and TK2). The northern and southern soil profiles have relatively high pH values, with average pH mostly above 8, whereas the

central soil profiles have relatively low pH values, with average pH commonly below 8, except for SP2.

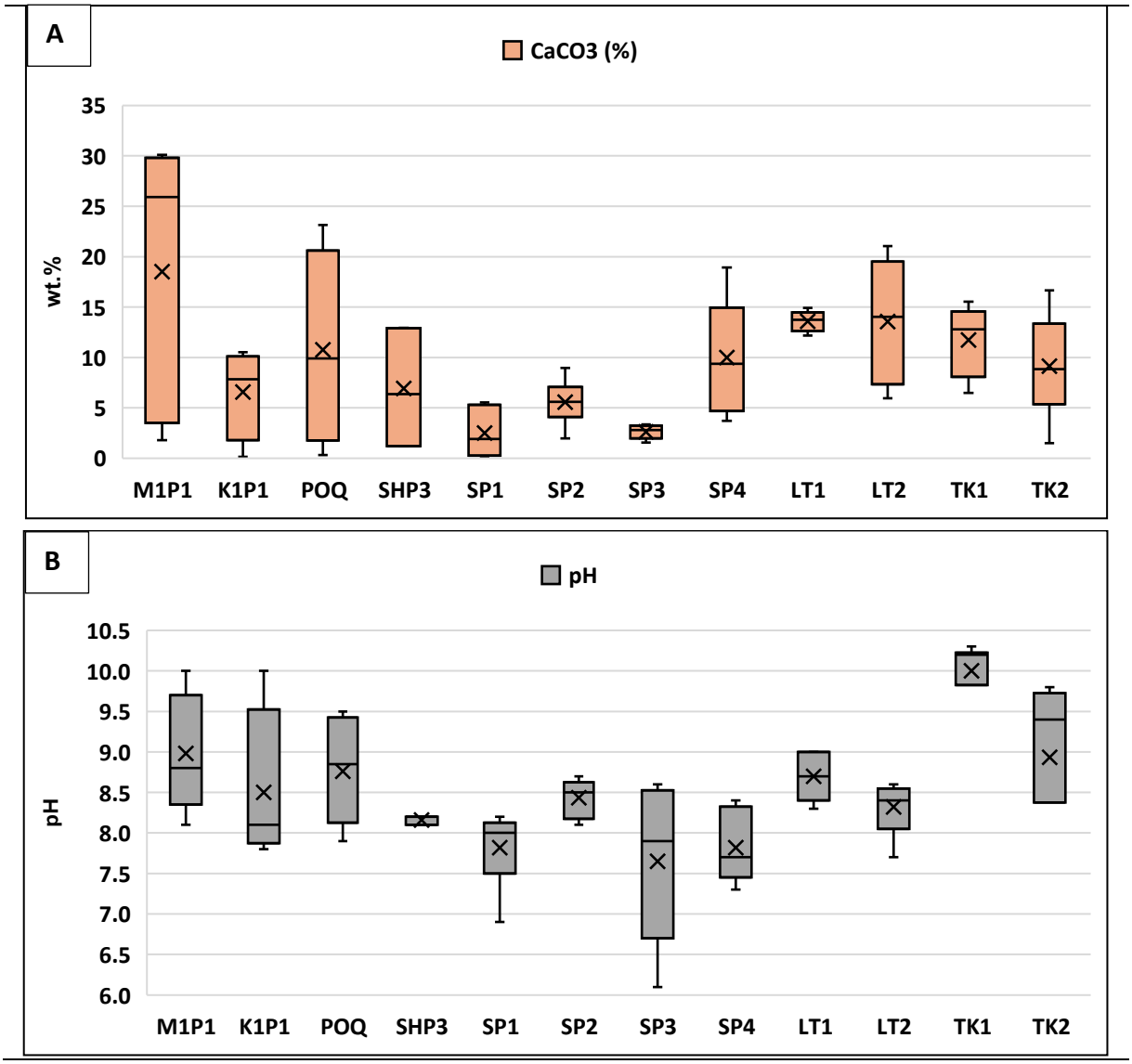


Fig. 3.3. Boxplot showing the variation in A. calcium carbonate content (wt.%) and B. pH in the study soil profiles. The box (orange for calcium carbonate content and grey for pH) represents the interquartile range. The lower and upper limits of the box represent the 25th percentile and the 75th percentile respectively. The horizontal line inside the box represents the median. The whiskers extend to the minimum and maximum values within 1.5 × IQR. The cross represents the mean.

3.4.2. Major elements

The major element contents for all the profiles are presented in a table on the Appendix 3.2. The general pattern shows that Si is the dominant element across all profiles, with

concentrations ranging from 25.1 to 45.9 wt.%. Other significant elements include Ca (0.1–13.8 wt.%), Al (0.1–7.5 wt.%), Fe (0.5–7.2 wt.%), and Mg (0.1–4.6 wt.%). Potassium is generally less than 2 wt.%, Na remains under 1.8 wt. There are a few peculiarities in this general pattern. As Fig. 3.4 shows, in the central profiles (SP1 to SP4), Al is the second most abundant element after Si, with average values ranging from 4.5 wt.% to 7.1 wt.%. In contrast, in the northern (M1P1, K1P1, POQ, and SHP1) and southern (LT1, LT2, TK1 and TK2) profiles, Ca is the second most abundant element, with averages ranging from 1.9 wt.% to 6.6 wt.% in the north and 3.8 wt.% to 9.9 wt.% in the south.

The boxplots (Fig. 3.4) also show different trends in major elements distribution along the profiles. While Si values are relatively clustered around the mean in almost all the profiles, the other elements show very contrasting distributions along the profile, generally in relation to location. The alkali and alkaline-earth element (Ca, Mg, Na, and K) exhibit distinct distribution patterns. However, when the three observation groups (northern, central, and southern profiles) are considered, a general trend emerges. These elements are most abundant in the south, followed by centre, while the lowest concentrations are observed in the north. In the northern profiles, the average concentrations range from 1.9 to 6.6 wt.% for Ca, 0.9 to 1.4 wt.% for Mg, 0.1 to 0.8 wt.% for K, and 0.2 to 0.3 wt.% for Na. In the central profiles, Ca ranges from 2.2 to 8.5 wt.%, Mg from 1.0 to 3.4 wt.%, K from 0.4 to 0.7 wt.%, and Na from 0.4 to 1.2 wt.%. Finally, in the southern profile, Ca varies from 3.8 to 8.7 wt.%, Mg from 0.9 to 2.2 wt.%, K from 0.8 to 1.5 wt.%, and Na from 0.4 to 1.0 wt.%. Iron follows broadly similar distribution patterns across the study area. The highest concentrations are found in the central profiles, where Fe ranges from 3.0 to 6.8 wt.%. The southern profile has intermediate values, with Fe ranging from 0.9 to 2.5 wt.% The lowest concentrations occur in the northern profiles, where Fe varies between 1.0 and 1.5 wt. %.

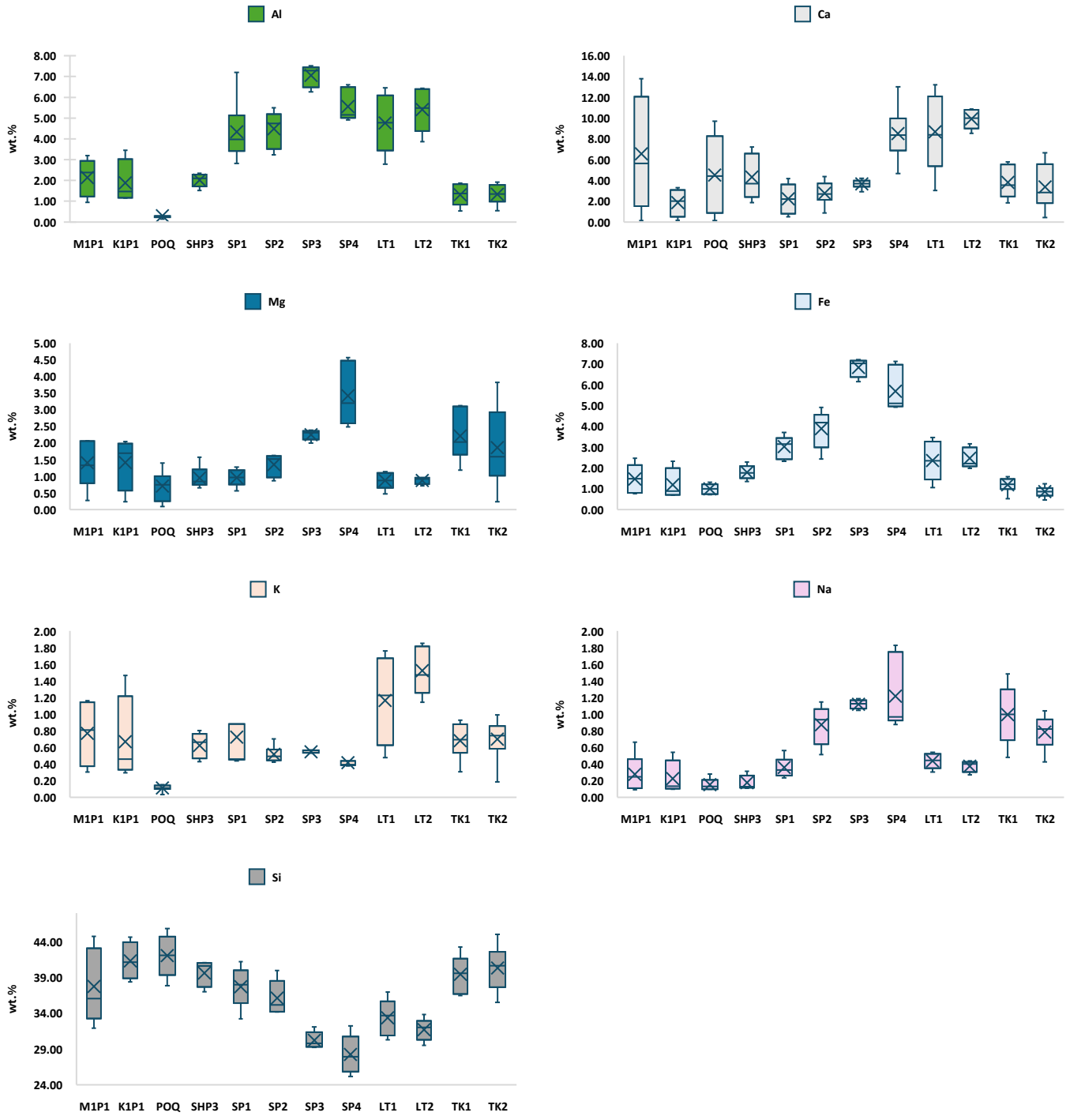


Fig. 3.4. Distribution of major elements (%) in the soil profiles. The box represents the interquartile range; the lower and upper limits of the box represent the 25th percentile and the 75th percentile respectively. The horizontal line inside the box represents the median. The whiskers extend to the minimum and maximum values within 1.5 × IQR. The cross represents the mean.

3.4.3. Rare earth elements

The concentrations of each REE across all profiles are presented in the table Appendix 3.3. The UCC-normalised curves of each of the studied profiles are presented in Fig. 3.5. The europium (Eu/Eu*) and cerium (Ce/Ce*) anomalies and LREE/HREE ratios are shown in Table 3.5.

Vertical variation, characterised by the graduation range on the y axis, reveals two main behaviours. M1P1, K1P1, SHP3, SP1, LT1 and LT2 are represented by larger ranges (maximums vary from 2 to 4), whereas POQ, SP2, SP3, SP4, TK1 and TK2 are represented by smaller ranges (maximums vary from 0.8 to 1.5). The curves at the top in all the northern profiles, except POQ, represent horizons rich in calcium carbonate (Bk, Bkk or Ck). On the other hand, the top curves in the central profiles represent clay horizons (Bt or Bss). The southern profiles present contrasting situations. The curves at the top of LT1 are those of horizons rich in calcium carbonates (Bk1 and Bk2), whereas for LT2 they are both clay horizons (Bt) and horizons rich in calcium carbonates (Bk1 and Bk2). The curves at the top of the TK profiles represent horizons rich in calcium carbonate (Ck).

Furthermore, the shapes of the normalisation curves reveal three distinct patterns, all typified by positive Eu anomalies. In the northern profiles, the curves are relatively flat on both the left and right sides of Eu. The majority have a convex inflection at Eu. In the central profiles, the curves mostly have positive slopes from La to Eu before flattening out from Eu to Lu. In the southern profiles, the normalisation curves have predominantly gentle positive slopes from La to Eu, followed by gentle negative slopes from Eu to Lu. A convex inflection is also observed.

In the northern profiles, the Ce/Ce* vary as follows: 0.8–1.1 in M1P1, 0.7–1.1 in K1P1, 0.7–1.1 in POQ, and 0.4–1.2 in SHP3. The Eu/Eu* range from 1.0–3.8 in M1P1, 1.2–3.2 in K1P1, 1.8–5.6 in POQ, and 1.1–5.6 in SHP3. The LREE/HREE ratios vary between 0.6 and 1.1 in M1P1, 0.8 and 1.1 in K1P1, 0.7 and 1.5 in POQ, and 0.9 and 2.0 in SHP3. In the central profiles, the Ce/Ce* varies from 0.8 to 1.0 in SP1, 0.7 to 0.8 in SP2, approximately 0.9 in SP3, and approximately 1.0 in SP4. The Eu/Eu* are between 1.1 and 1.5 in SP1, 1.3 and 1.5 in SP2, 1.3

and 1.5 in SP3, and 1.4 and 1.6 in SP4. The LREE/HREE ratio ranges from 0.6 to 0.9 in SP1, approximately 0.6 in SP2, 0.5 in SP3, and approximately 0.5 in SP4. In the southern profile, the Ce/Ce* is approximately 1.0 in LT1 and LT2 and approximately 0.9 in TK1 and TK2. The Eu/Eu* ranges from 1.4–3 in LT1, 1.0–1.7 in LT2, 1.3–1.5 in TK1, and 1.1–1.5 in TK2. The LREE/HREE ratio is between 0.7 and 1.1 in LT1, 0.7 and 0.9, approximately 0.8 in TK1, and between 0.7 and 0.9.

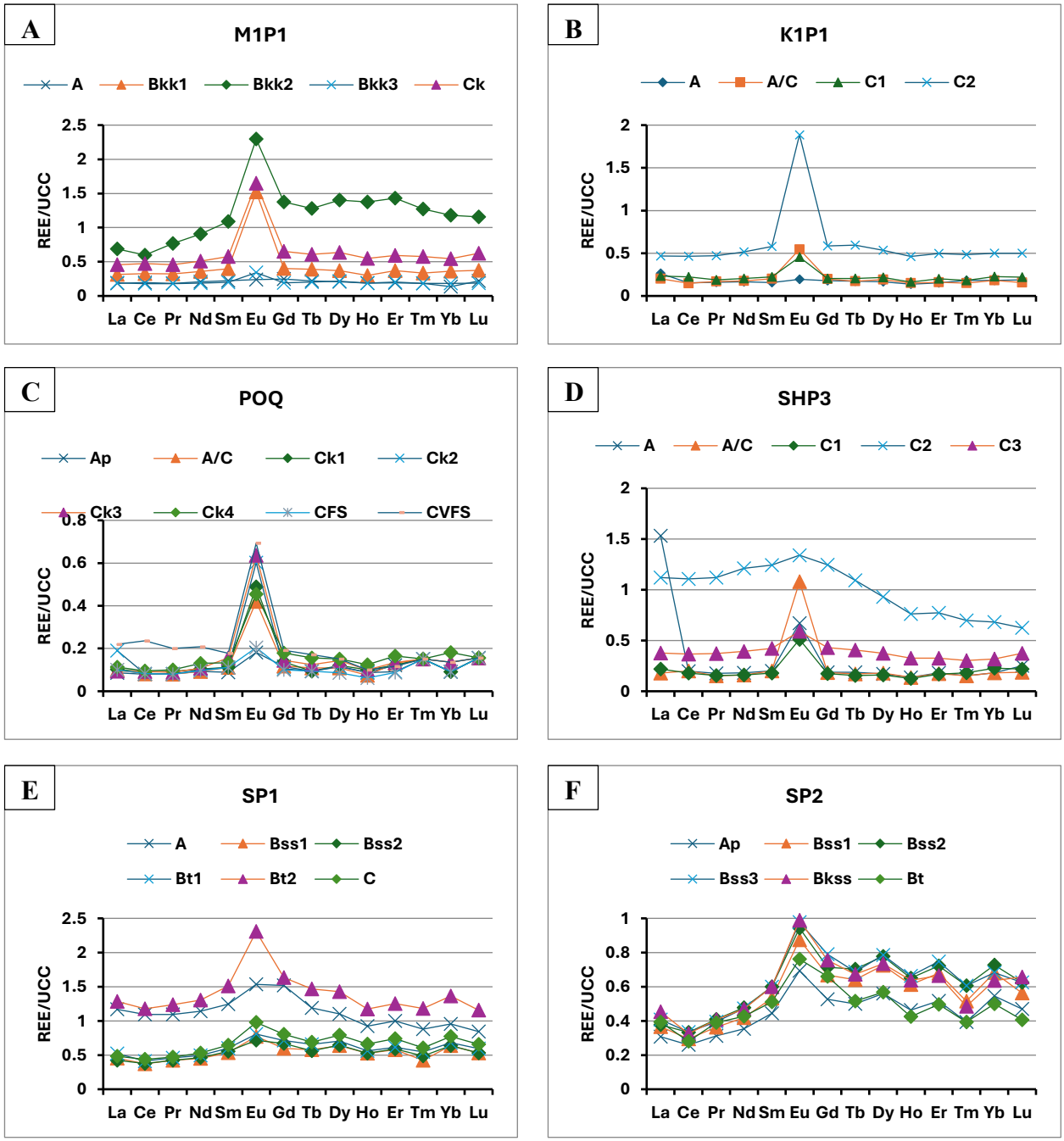


Fig. 3.5. REE contents normalised to the UCC in the twelve soil profiles

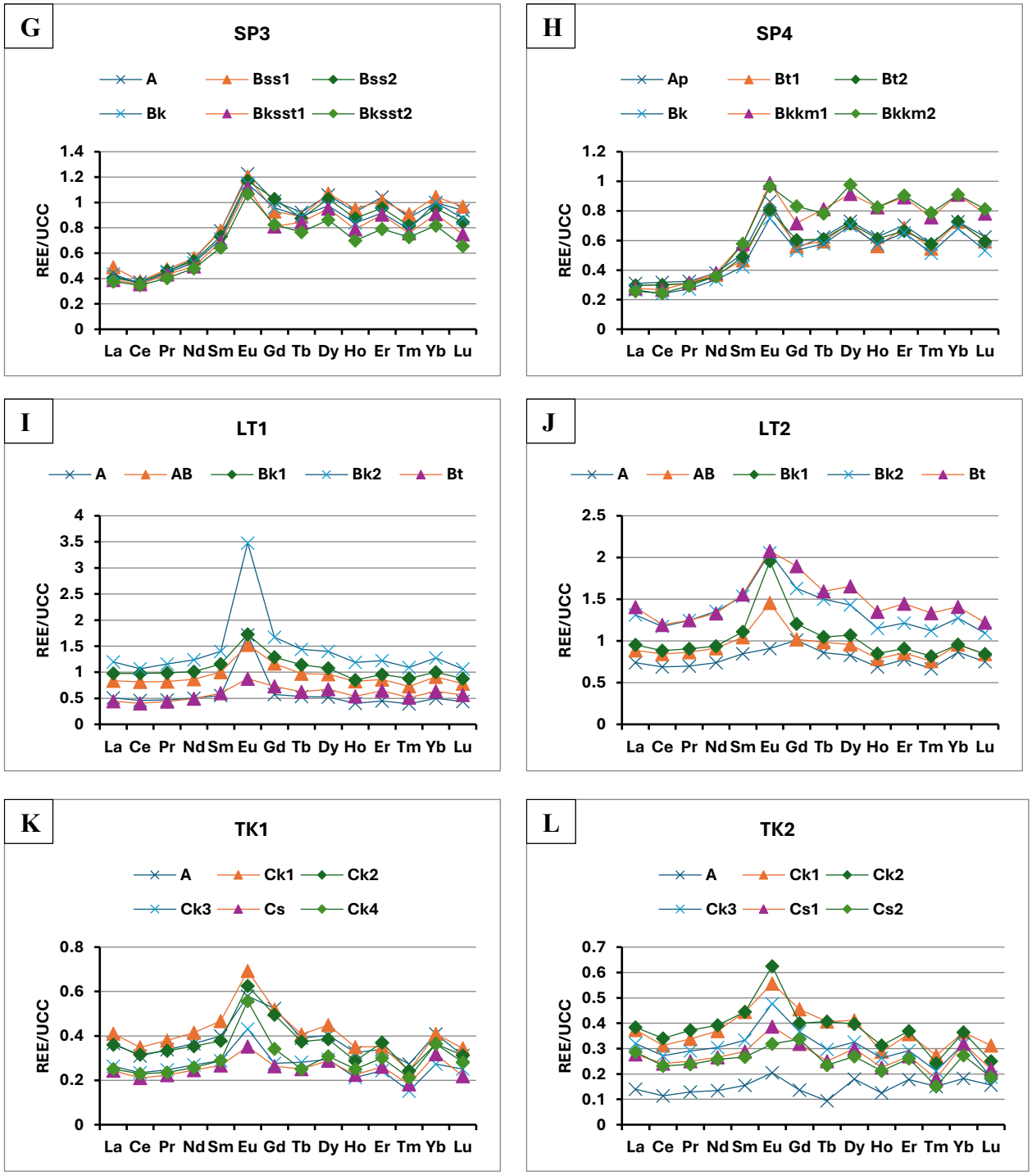


Fig. 3.5. REE contents normalised to the UCC in the twelve soil profiles (continued)

Table 3.5. Cerium anomalies (Ce/Ce*), europium anomalies (Eu/Eu*) and LREE/HREE ratios normalised to the UCC in the study profile

Profile	Layer	Ce/Ce*	Eu/Eu*	LREE/HREE	Profile	Layer	Ce/Ce*	Eu/Eu*	LREE/HREE	Profile	Layer	Ce/Ce*	Eu/Eu*	LREE/HREE
M1P1	A	1.1	1.0	0.8	SP1	A	1.0	1.1	0.9	LT1	A	0.9	3.0	1.1
	Bkk1	1.0	3.8	1.1		Bss1	0.8	1.4	0.7		AB	1.0	1.4	0.8
	Bkk2	0.8	1.9	0.6		Bss2	0.9	1.2	0.6		Bk1	1.0	1.4	0.8
	Bkk3	1.0	1.7	0.8		Bt1	0.8	1.2	0.7		Bk2	0.9	2.3	0.9
	Ck	1.0	2.7	0.9		Bt2	0.9	1.5	0.8		Bt	0.9	1.3	0.7
K1P1	A	0.7	1.2	0.8		C	0.9	1.4	0.6	LT2	A	1.0	1.0	0.7
	AC	0.8	2.7	1.1	SP2	Ap	0.8	1.4	0.6		AB	1.0	1.4	0.8
	C1	1.1	2.1	0.9		Bss1	0.8	1.5	0.6		Bk1	1.0	1.7	0.9
	C2	1.0	3.2	1.1		Bss2	0.8	1.4	0.6		Bk2	0.9	1.3	0.8
POQ	Ap	0.9	1.8	0.7		Bss3	0.8	1.4	0.6		Bt	0.9	1.2	0.7
	AC	0.9	3.7	0.9		Bkss	0.8	1.5	0.6	TK1	A	0.9	1.3	0.8
	Ck1	0.9	4.0	1		Bt	0.7	1.3	0.7		Ck1	0.9	1.4	0.9
	Ck2	0.7	5.6	1.3	SP3	A	0.9	1.4	0.5		Ck2	0.9	1.4	0.8
	Ck3	1.0	4.2	1.1		Bss1	0.8	1.4	0.5		Ck3	0.9	1.5	0.9
	Ck4	0.9	2.9	0.8		Bss2	0.8	1.3	0.5		Cs	0.9	1.3	0.8
	CFS	0.9	1.9	0.8		Bt1	0.8	1.4	0.5		Ck4	0.9	1.8	0.8
	CVFS	1.1	3.8	1.5		Bt2	0.9	1.5	0.5	TK2	A	0.8	1.4	0.7
SHP3	A	0.4	3.5	2		Bt3	0.9	1.5	0.5		Ck1	0.9	1.2	0.8
	AC	1.2	5.6	1.4	SP4	A	1.0	1.6	0.5		Ck2	0.9	1.5	0.9
	C1	1.0	2.9	1		Bss	1.0	1.6	0.5		Ck3	0.9	1.4	0.9
	C2	1.0	1.1	1		Btk1	1.0	1.5	0.5		Cs1	0.9	1.3	0.8
	C3	1.0	1.4	0.9		Btk2	0.9	1.6	0.5		Cs2	0.9	1.1	0.8
						Ck1	0.9	1.5	0.4					
						Ck2	0.9	1.4	0.4					

3.4.4. Relationships between REEs, calcium carbonate content, and pH

Rare earth element indices, including Ce/Ce*, Eu/Eu*, LREE/HREE, LREE, HREE, and ∑REE, were correlated with pH and calcium carbonate content using a Spearman correlation matrix at significance level $\alpha = 0.05$ (Fig. 3.6).

The general dataset is presented in the matrix of Fig. 3.6A reveals several interesting relationships between the studied parameters. $CaCO_3$ content has a weak positive correlation with the LREE/HREE ratio (r = 0.3), Eu/Eu* (r = 0.2), and Ce/Ce* ratio (r = 0.3). The pH of the samples has a moderate negative correlation with HREEs (r = -0.3), and a moderate positive correlation with LREE/HREE (r = 0.3).

The second matrix (Fig. 3.6B) presents the results for the northern profiles (M1P1, K1P1, POQ and SHP3). No correlation is observed, neither between $CaCO_3$ content and REE indices, nor between pH and REE indices.

The third matrix (Fig. 3.6C) shows the results in the central profiles (SP1 to SP4). The $CaCO_3$ content has a strong negative correlation with ∑REE (r = -0.6) and LREE (r = -0.6). In contrast, a strong positive correlation is observed with Eu/Eu* (r = 0.7). No correlation is observed between the pH and REE indices.

The fourth matrix (Fig. 3.6D) shows the results for the southern profiles (LT1, LT2, TK1 and TK2). The $CaCO_3$ content has a moderate positive correlation with LREE/HREE (r = 0.5) and Ce/Ce* (r = 0.5). In contrast, the pH is strongly negatively correlated with ∑REE (r = -0.7) and HREE (r = -0.7).

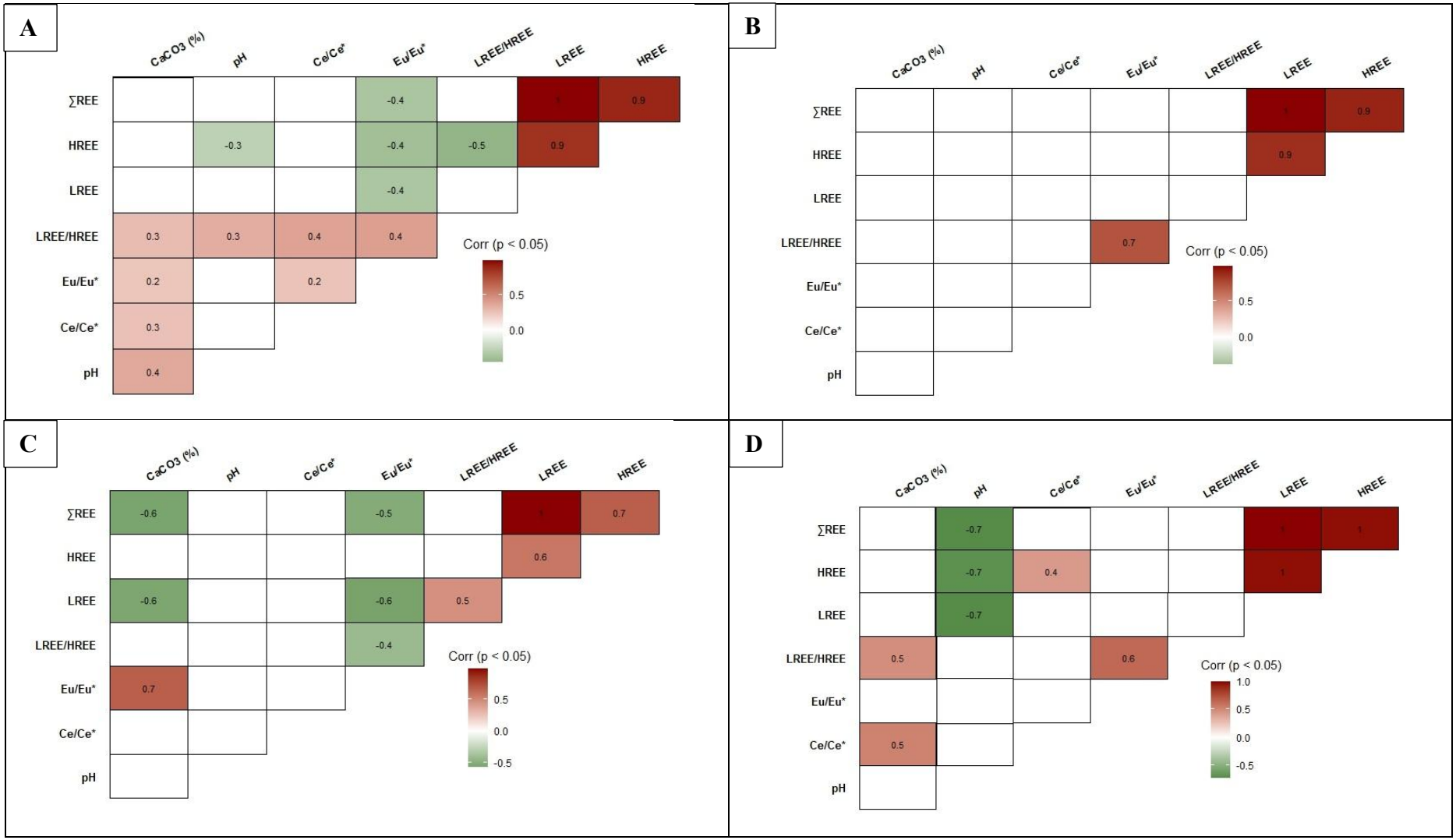


Fig. 3.6. Correlation matrix of REEs indices, pH and calcium carbonate content (wt.%) in A. All the study profiles; B. The northern profiles; C. The central profiles; D. The southern profiles

3.4.5. Correlation between REEs and major elements

The correlation results between REE indices and major elements for all the studied profiles, assessed at significance level $\alpha = 0.05$, are shown in the matrix in Fig. 3.7A. The major observations are presented below.

∑REE is strongly positively correlated with Al (r = 0.8), Fe (r = 0.6) and K (r = 0.7). ∑REE shows moderate positive correlations with Ca (r = 0.4) and weak correlations with Na (r = 0.3. No correlation is observed between ∑REE and Mg, while a strong negative correlation is observed with Si (r = -0.6). HREEs exhibit very strong positive correlations with Al and Fe (r ≥ 0.8), strong positive correlations with K (r = 0.6), and moderate positive correlations with Ca and Na (r = 0.4–0.5). It shows a weak positive correlation with Mg (r = 0.2), while a strong negative correlation with Si (r = -0.8) is observed. LREE is strongly positively correlates with Al and K (r = 0.6–0.7), moderately with Fe (r = 0.5), weakly with Ca and Na (r = 0.3), and not at all with Mg. A strong negative correlation is observed with Si (r = -0.6). LREE/HREE shows a moderate positive correlation with Si (r = 0.5) , and strong negative correlations with Al, Fe and Na (r = -0.6 to -0.7). Eu/Eu* shows a weak negative correlation with Al and Na (r = -0.2 to -0.3). Ce/Ce* weakly correlates with Ca (r = 0.3) and has weak negative correlations with Na, (r = -0.3).

This general pattern contrasts with the situation observed in each of the groups studied, categorised by parent material. In the northern part (Fig. 3.7B), REE abundance (LREE, HREE and ∑REE) shows a very strong positive correlation with Al, K, and Ti, a strong positive correlation with Fe, while a very strongly negative is observed with Si. REE indices (LREE/HREE, Eu/Eu* and Ce/Ce*) are generally characterised by low correlation coefficients with the major elements. In the central region, the correlation matrix (Fig. 3.7C) shows a generally weak correlation between the abundance of REE, REE indices, and the major elements. In the southern part (Fig. 3.7D), the abundance of REEs shows a strong positive correlation with Al, Ca, Fe, Mn, P and Ti, and a strong negative correlation with Si. The REEs indices are characterised mainly by a weak correlation.

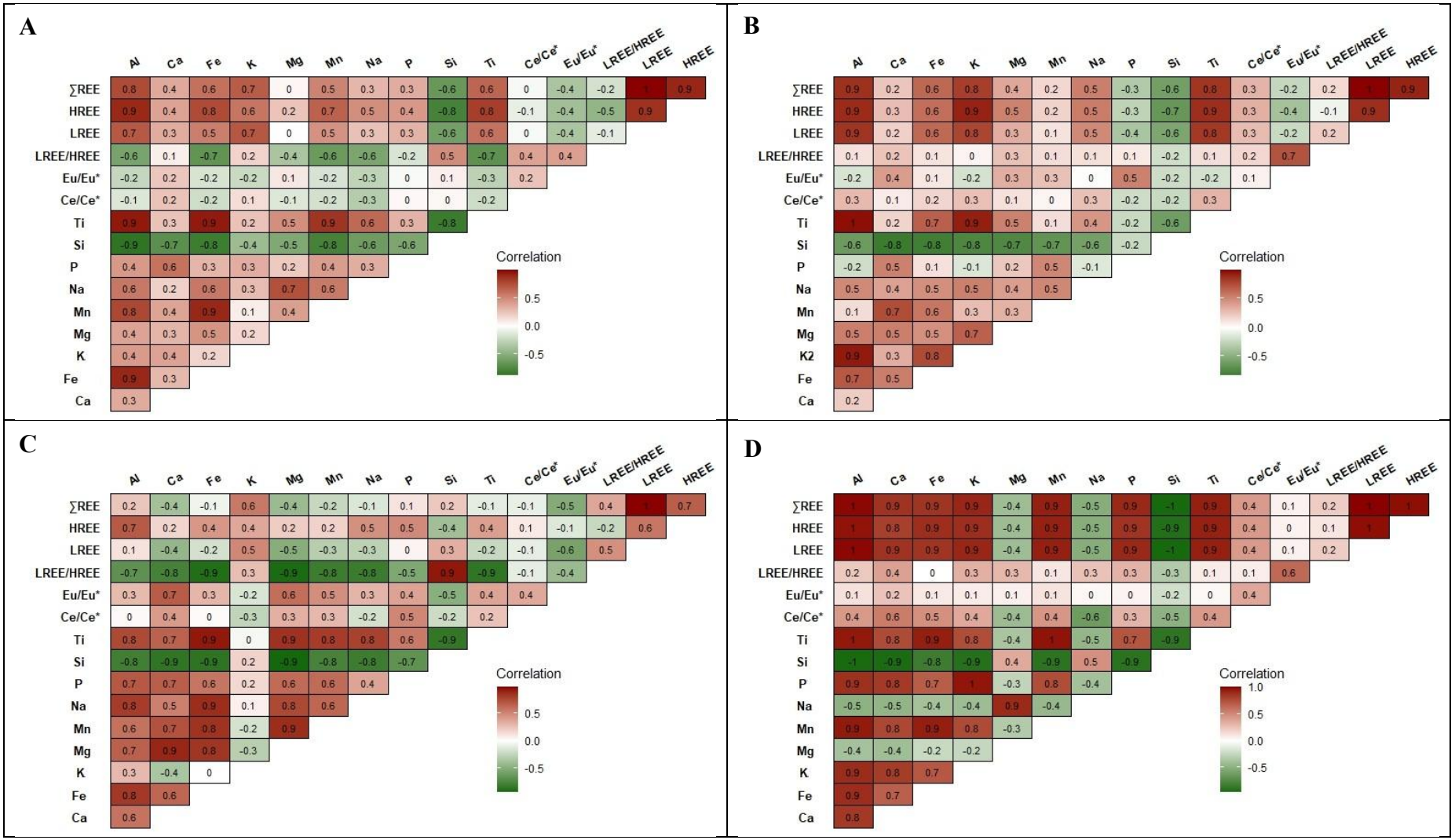


Fig. 3.7. Correlation matrix of REEs indices, pH and calcium carbonate content (wt.%) in A. All the study profiles; B. The northern profiles; C. The central profiles; D. The southern profiles.

Principal component analyses (PCA) were conducted to visualise the relationships between variables. The results for the general pattern are illustrated in the correlation circle (Fig. 3.8A). The first two principal components (Dim1 = 52.3 % and Dim2 = 14.5 %) capture 66.8 % of the total variance. Most major elements (Al, Fe, Mg, K, Ca, Na) and the ΣREE, LREE and HREE are clustered together, pointing towards the positive direction of Dim1. Nevertheless, K, Al, LREE, HREE and ΣREE are projected in the positive direction of Dim2, while Ca, Mg, Na and Fe are in the negative direction. Silica, LREE/HREE, and Eu/Eu* are located on the left side of the plot, pointing towards the negative direction of Dim1. Silica and LREE/HREE are positively correlated with each other and align somewhat with the positive Dim2 axis. Aluminium, Fe, Mg, Na, HREE, ΣREE, LREE, K, Si, LREE/HREE are represented by long vectors, close to the circle, while Eu/Eu* and Ca are represented by short vectors. Ce/Ce* is represented by very short and centred vector.

The PCA for the northern part (Fig. 3.8B) confirmed the results observed in the correlation matrix, with a cluster comprising REE abundance, Al, Ti, K and Fe, all of which were positively correlated with Dim1 (47.3% of the total variance). Nevertheless, Dim2 (15.4% of the total variance) is positively correlated with Eu/Eu* and Ca. These first two dimensions of the PCA account for 62.7% of the total variance.

The PCA of the central part (Fig. 3.8C) also confirmed the weak correlation observed between the concentration of major elements and abundance of REE. However, the cluster composed of Mn, Fe, Ti and Mg, which is strongly positively correlated with Dim1 (51.7% of the total variance), is negatively correlated with the LREE/HREE ratio. Dim1 (25.3% of the total variance) is strongly positively correlated with the HREEs, Eu/Eu* and K. The first two dimensions account for 77% of the total variance.

The PCA of the southern part (Fig. 3.8D) reveals a cluster comprising all the major elements except Mg and Na, all of which are strongly positively correlated with REE abundance and Dim1 (61.5%

of the total variance). Silicon, in contrast, appears in the opposite direction, reflecting a strong negative correlation. Dimension Dim2 accounts for 13.8% of the total variance and is strongly correlated with the LREE/HREE ratio and Eu/Eu*. The first two dimensions of the PCA explain 75.3% of the total variance.

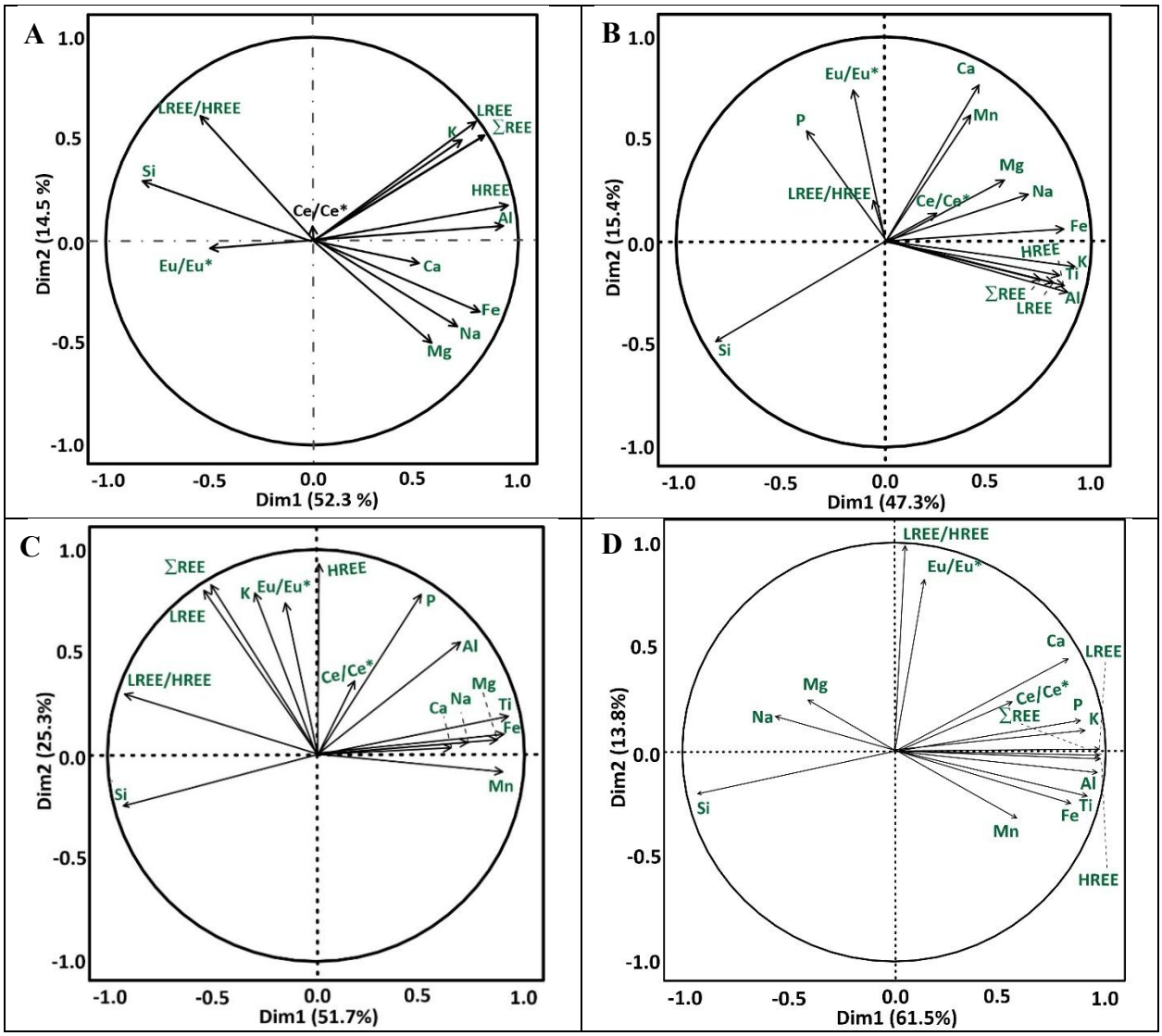


Fig. 3.8. Correlation circle of REE indices and major elements A. All the study profiles; B. The northern profiles; C. The central profiles; D. The southern profiles.

3.5. Discussion

3.5.1. Distribution of REEs

The distribution of REEs across the study area suggests considerable variability between the soil profiles, ranging from a minimum average of 12.8 mg kg^{-1} in POQ profile to a maximum average of 193.2 mg kg^{-1} in LT2 profile. The overall pattern suggests differences in REE contents among the three contrasting parent materials. The northern profiles, on alluvial and fluvio-lacustrine deposits of the Kalahari Group are characterised by wide variations between (12.8 mg kg^{-1} for POQ and 68.5 mg kg^{-1} for SHP3. The central profiles, on sandstone and basaltic parent material of the Karoo Supergroup are characterised by relatively intermediate values and a less pronounced variation in the average values between profiles (average value ranges from 57.4 to 69.9 mg kg^{-1}), except for SP1 (103.8 mg kg^{-1}). The southern profiles, the domain of sands, clays, calcretes and silcretes of the Kalahari Group, show a contrast between the two observation sites. Profiles LT1 and LT2 are characterised by relatively high values (average value are 117 mg kg^{-1} and 150.6 mg kg^{-1} respectively for LT1 and LT2), while TK1 and TK2 are characterised by relatively low values (average value are 40 mg kg^{-1} and 44.3 mg kg^{-1} respectively for LT1 and LT2). The distribution of REEs in the absence of any human intervention (anthropogenic activities) is explained by two main factors: parent material and soil development (Ambrosino et al., 2022; Laveuf and Cornu, 2009). Thus, following this approach, the variations along the profile, which generally show enrichment or depletion of certain REEs compared with others, are attributed to soil factors (soil development and soil properties), while the differences in content between soil profiles largely reflect the changes in parent materials, from which the soil inherits its REE concentration (de Sá Paye et al., 2016).

In the northern region, the parent material is made of alluvial and fluvio-lacustrine sediments, which are themselves derived from the weathering of diverse parent rocks drained by watercourses such as those that make up the Okavango delta today or the mega palaeolake

(Burrough et al., 2009; McCarthy et al., 1997). Moreover, the sediments in the area also result from the weathering of nearby geological Formations (Mokatse et al., 2023; Vainer et al., 2018), relatively to the Okavango rift formation. Furthermore, aeolian deposits from the Kalahari sand also contribute to the composition of sediments in this area (Garzanti et al., 2022). This diverse composition of the parent material could therefore explain the high variability in REE contents observed between these profiles. Low REE values could result from highly reworked alluvial deposits, whereas high REE values may be associated with sandstone, clay and calcretes (Haddon and McCarthy, 2005).

According to Eze et al. (2025), the Vertisols and Luvic Vertisols in the central profiles mostly originated from the weathering of Stormberg basaltic parent materials. This may explain the relatively low variation in the average REEs between these profiles, as these soil profiles are derived from the same parent material. Moreover, mafic rocks such as basalt tend to have lower total REE concentrations than felsic rocks such as granite (Alfaro et al., 2018) do. This explains the relatively intermediate values (compared with other profiles in the north and the south), which are probably greater than those in the reworked sand sediment in the north and are less important than those in some sandstones. However, the exception of SP1 probably highlights the intervention of a different parent material, as sandstones are intermingled with basaltic rocks in the region (Franchi et al., 2021).

In the southern soil profiles developed on clay, sand, calcrete and silcrete, the contrasting values observed between the LT profiles and TK soil profiles could also be attributed to deep variation in the parent materials. Kampunzu et al. (2007) have shown that soils around Letlhakeng are predominantly formed over duricrusts, including calcrete and silcrete, and intergrade with cal-silcrete, which develop on diverse geological materials, such as the Mmamabula Formation (Ecca Group, Karoo Supergroup), as well as underlying igneous rocks

and red beds. The Takatokwane soil profiles, on the other hand, were formed on a saline pan (Matshameko et al., 2023).

The variations in REEs along the profiles demonstrate contrasting behaviours. In the northern part on alluvial and fluvio-lacustrine deposits most of the profiles, are characterised by relatively high vertical variation (from 27–163 mg kg^{-1} for M1P1, for example). Moreover, top curves in the UCC-normalised diagrams (Fig. 3.5), rich calcium carbonate horizons are the main influencers of the vertical variability. The central profiles, except for SP1, mostly displayed relatively low variability (from 47–67 mg kg^{-1} for SP2, for example). But all these profiles have shown that clayey horizons are the dominant actor of vertical differentiation. The southern profiles presented high variability for LT (from 67–173 mg kg^{-1} for LT1, for example) and rich calcium carbonates and clayey horizons contribute the most to vertical variability. Low variability is observed for TK profiles (from 34–56 mg kg^{-1} for TK1, for example), and rich calcium carbonate horizon are the most important driver of vertical variability. As demonstrate by several works before, soil formation processes or soil properties, are the main factors influencing vertical variations in soil profiles (Cao et al., 2022; de Sá Paye et al., 2016; Mihajlovic et al., 2019). In this case, calcium carbonate and clay tend to have a major influence on the vertical variation in the investigated profiles. calcium carbonate influence alongside of pH will be specifically discuss in section 3.5.2, while element behaviour discuss in section 3.5.3 could provide more information about clay influence. Nevertheless, significant environmental changes from a humid to semi-arid environment have been demonstrated during the development of soil in the northern profiles (Dina Ebouel et al., 2025; Eze et al., 2021; Eze and Molwalefhe, 2024). These soil profiles reflect alternating wet and dry periods. This could also explain the relatively high vertical variability in these profiles (Lin et al., 2022b; Wu et al., 2024). Moreover, local parameter such as topographic position also has an influence on the vertical variability of REE (Liu et al., 2022; Yuan et al., 2021).

In summary, the distribution of REEs among the studied profiles is related to lithology. The vertical variation within the profiles is primarily influenced by clay abundance in some profiles, such as SP and TK, and by calcium carbonate accumulation in others.

3.5.2. Calcium carbonate, pH and REE as tracers of carbonate origin in the soils

As it is often the case in semi-arid environments, the soil profiles show the accumulation of calcium carbonate in various forms, although diffuse powders coating peds or infillings and nodules are the most common forms observed across the studied soil profiles (Fig. 3.2). The influence of pH and $CaCO_3$ on the distribution, mobility and fractionation of REEs in the soil environment is well documented. Numerous studies have shown, for example, that acidic conditions favour the dissolution and mobilisation of REEs, whereas alkaline conditions favour their complexation and immobilisation by calcium carbonate (Cao et al., 2001; Nagasawa et al., 2024; Wang et al., 2023). Furthermore, Laveuf and Cornu (2009) reported that pedogenic carbonate formation in arid and semi-arid environments is accompanied by REE complexation, driven by pH enhancement associated with bicarbonate production. Pourret et al. (2007) also show that competition for the complexation of REE in the soil by humic compounds and carbonates is highly dependent on soil pH. Carbonate complexation is maximal at a pH of 10 and increases with alkalinity and the atomic number of the REE ($LuCO_3 \gg LaCO_3$). In other words, alkaline pHs facilitate carbonate complexation of HREEs at the expense of LREEs. According to Laveuf and Cornu (2009), pedogenic carbonates can be differentiated from other forms of carbonate (lithogenic) using the LREE/HREE fractionation ratio. Pedogenic carbonates generally result from the transport of REEs by bicarbonate ions $(REEHCO_3)^{2+}$. Their characteristic signatures include a low LREE/HREE fractionation ratio, which is linked to the preferential complexation of HREEs by bicarbonate ions. In addition, these carbonates exhibit a negative cerium anomaly, as cerium is less readily transported in solution than other LREEs, often due to its oxidation and preferential retention in the solid phase of the soil

(Kraemer et al., 2017). In the studied context, the general pattern shows no correlation between the calcium carbonate and REE contents. Nevertheless, a weak positive correlation is observed with the LREE/HREE fractionation ratio (r = 0.3), with europium (Eu/Eu*, r = 0.2) and cerium (Ce/Ce*, r = 0.3) anomalies. pH was weakly negatively correlated with HREE content and weakly positively correlated with the LREE/HREE fractionation ratio. These results demonstrate that pH and calcium carbonate may not be the primary factors controlling the abundance and distribution of REEs in the soil profiles. However, the weak correlations observed with the LREE/HREE fractionation ratio and europium, and cerium anomalies reflect their roles alongside other factors in the mobility and distribution of specific REEs within the soil. Furthermore, correlation matrices using the three groups (northern, central and southern profiles) resulted in very contrasting relationships between pH, calcium carbonate content and REEs.

In the northern profiles on alluvial and fluviolacustrine deposits, correlation matrix results failed to establish calcium carbonate and pH contribution to REE abundance. Given the importance of calcium carbonate in these soils, a strong correlation was expected as normalisation diagram highlighted the major contribution of rich carbonate horizons on the vertical distribution of REEs in this environment. These unexpected results could be explained by the formation processes of calcium carbonate (lithogenic or pedogenic) in these profiles. As explained by Laveuf and Cornu (2009), pedogenic carbonates are characterised by LREE/HREE < 1 and negative cerium anomalies. Thus, the high variation in the europium anomaly (Eu/Eu* = 1–5), cerium anomaly (Ce/Ce* = 0.4–1.2) and the LREE/HREE fractionation ratio (0.6–1.5) contradict this hypothesis. This discrepancy could highlight the coexistence of both lithogenic and pedogenic carbonates in these soils. This is consistent with previous studies carried out in the area. While some authors emphasise the formation of

pedogenic carbonates as a major pedogenic process (Eze et al., 2021; Romanens et al., 2019), others show a predominance of carbonates of lithogenic origin (Nash and McLaren, 2003).

For the soils that developed on sandstone and basalt parent materials in central Botswana, calcium carbonate has a more pronounced influence on the ∑REE abundance, especially on LREEs. Nevertheless, the calcium carbonate content seems to be related to a decrease in the REE content, as illustrated by the strong negative correlation of $CaCO_3$ with ∑REEs (r = -0.6) and LREEs (r = -0.6). These intriguing results highlight the complex geochemical behaviour of Vertisols. These soils are characterised by the abundance of smectite clays, particularly montmorillonite (Eze et al., 2025), which have been highlighted by normalisation curves to play a major role in the vertical variability of REEs in these profiles. Moreover, montmorillonite is known for its enormous capacity to adsorb REEs (Fang et al., 2021). Furthermore, Vertisols are also associated with the accumulation of pedogenic carbonate in semi-arid zones (Dietrich et al., 2021a; Miller et al., 2007), characterised in the present study by soft nodules and diffuse powders coating soil peds (Fig. 3.2C). Although calcium carbonates are also known for their high REE complexation capacity, their negative influence on REE enrichment and fractionation in this context could be explained by exchanges between the calcium ions trapped in the inter-layer space of montmorillonite and the REEs in the carbonates, as demonstrated by He et al. (2023). Moreover, the negative cerium anomalies (Ce/Ce* = 0.7-0.8) in the calcium carbonate-rich horizons and low LREE/HREE fractionation ratio (0.4–0.9) are consistent with an exclusive pedogenic origin of carbonate features (Laveuf and Cornu, 2009).

In the southern soils which developed on clay, sand, calcrete and silcrete, the correlation matrix revealed no significant relationship between calcium carbonate content, ∑REE, HREE and LREE abundances. Conversely, pH demonstrated a strong negative influence on ∑REE, HREE and LREE abundance (r = -0.7). Nevertheless, moderate positive correlations are observed

between the calcium carbonate content, the fractionation ratio LREE/HREE (r = 0.5), and the cerium anomaly Ce/Ce* (r = 0.5). Thus, calcium carbonate accumulation in these soil profiles is associated with REE redistribution. As for the northern profiles, it is difficult to highlight a specific process to explain the formation of calcium carbonate in this environment based on the conclusions of Laveuf and Cornu (2009). The LREE/HREE are between 0.7–1.1, while very weak cerium negative anomalies (Ce/Ce* ≈ 1) and positive europium anomalies (Eu/Eu* = 1–3) are observed. Furthermore, normalisation curves demonstrated the importance of calcium carbonate in the vertical variability of REEs in these profiles. Nevertheless, the early stage of calcium carbonate features observed in the area (Fig. 3.2D and E) may indicate dissolution-reprecipitation related to seasonal variations in climate (Domínguez-Villar et al., 2022). Consequently, lithogenic and pedogenic carbonates coexist in this environment. pH has a negative influence, as illustrated by a strong negative correlation with the REE content (r = -0.7 for ∑REEs, HREEs and LREEs). This negative influence of pH in this context highlights the need to improve our understanding of the interaction between strongly alkaline pH and REEs enrichment. Although the influence of acidic pH on the dissolution of REEs has been demonstrated (Nagasawa et al., 2024), not much have been done to deepen understanding of the phenomenon observed at pH values above 10.

In summary, the use of correlations on the entire dataset does not allow us to unambiguously conclude on the role of pH and calcium carbonate content in the enrichment and fractionation of REEs in the studied soils. However, analysis based on parent materials provides more nuanced results. The approach proposed by Laveuf and Cornu (2009) allowed us to deduce a dominance of pedogenic carbonates in Vertisols on sandstone and basaltic parent material. In contrast, the calcium carbonate accumulations in the other two cases result from the coexistence of pedogenic and lithogenic carbonates (northern and southern soil profiles). These conclusions should be considered with great caution. At this scale, other processes such as the

complexation of organic matter or the adsorption of clay are in competition with the complexation of REEs by carbonates. The approach of Laveuf and Cornu (2009) would therefore be more suitable for comparison based on specific carbonate features (e.g. nodules, rhizoliths, etc.), rather than a comparison of soil profiles as suggested in this work.

3.5.3. Influences of major elements on REE distributions in the studied soil profiles

Even though PCA did not provide a clear picture of the structure of the total variance in the first two components, which account for less than 70 % of the total variance (Jolliff, 2002), the groups identified are consistent with the major trends observed in the correlation matrix. The correlations between major elements and REEs in the studied soil profiles revealed very strong correlations among ∑REEs, LREEs and HREEs. These findings indicate almost equivalent contributions of LREE and HREEs to the total distribution of REEs in all the profiles studied. Aluminium, Fe and K exhibit strong positive correlations with REE abundance (∑REE, LREE, and HREE), whereas Ca and Na show moderate positive correlations. In contrast, Si has a strong negative correlation with REE abundance. These results indicate that the primary elements influencing REE abundance in the study soil profile are Al, Fe, K and Si, whereas Ca and Na have a minor influence, and the Mg contribution is meaningless. Silica seems to reduce the abundance of REEs. Since the study soils are mostly constituted of sand fraction, which is generally above 50 wt.% (Eze et al., 2025, 2021; Matshameko et al., 2023, 2022). Therefore, Si negative influence could reflect the contribution of Kalahari aeolian deposits to soil formation. Furthermore, as these deposits are made up of highly reworked and weathered sand, they have very low REE contents (Thomas and Shaw, 1990). The association of these deposits with developing soils dilutes the overall REE content, thus justifying the negative influence observed. In contrast, the significant positive contribution of Al and K can be explained by the predominance of clay-rich soils; in particular, the montmorillonite in Vertisols (Eze et al., 2025), as clay, is known for its high potential for REE fixation (Andrade et al., 2022; Wang et

al., 2023). In addition, the formation of clays is accompanied by the precipitation of metallic elements (Nguetnkam et al., 2007; Paterson et al., 1991; Zhao et al., 2023). Moreover, Fe has also been associated with REE enrichment in soils (Ambrosino et al., 2022; Lin et al., 2022a). The contribution of Ca in REEs enrichment in the study profiles are less important, despite being in semi-arid environments where calcification through accumulation of pedogenic carbonate contributes to REEs enrichment (Dietrich et al., 2021). This could be related to the dominance of clay accumulation as the major adsorbent of REEs in most of the studied soils. The Na minor influence on REEs distribution may be related to the low concentration of this element in the studied soils.

In sum, Al, Fe and K are the primary major elements contributing to REEs enrichment in the studied soil. This reflects the dominance of type 2/1 clays in these soils, which mainly influence REE concentration in these soils. Silica tends to have a strong negative influence due to the abundance of highly reworked sand from the Kalahari Basin. The minor role of Ca and Na highlights a low relative contribution.

One of the limitations of this study is that the calcium carbonate content and rare earth element (REE) concentrations were determined from bulk soil samples rather than from the carbonate formations themselves (e.g. nodules, rhizoliths, powdery coatings or hardpan horizons). Consequently, the REE signal attributed to carbonates in this study reflects the combined influence of several concurrent pedogenic processes, as highlighted in the discussion (clay formation, complexation of organic matter and adsorption of Fe/Al oxides), rather than that of the carbonate fraction taken in isolation. This probably explains why the correlations between CaCO3 content and REE indices were often weak or inconsistent from one study profile to another, and why the LREE/HREE approach developed by Laveuf and Cornu (2009), whilst highly informative, could only be applied approximately at the scale of complete soil profiles. Direct sampling and analysis of distinct carbonate features would allow the REE fractionation

signal to be attributed more directly to carbonate formation processes and would likely lead to a clearer and more robust distinction between the pedogenic and lithogenic origins of carbonates. Future work should therefore prioritise targeted sampling of individual carbonate morphologies rather than comprehensive sampling of soil horizons when using REEs to trace the origin of carbonates.

3.6. Conclusions

This research investigated the distribution of REEs in twelve prominent soil profiles developed on three contrasting parent materials (alluvial and fluvio-lacustrine sediments of the Kalahari Group, sandstone and basaltic rocks of the Karoo Supergroup, and sands, clay, calcrete and silcrete of the Kalahari Group) across Botswana. It also explores the relationship of REE geochemical indices and pedogenetic processes. It is established that REE variability in the landscape of the region is mainly controlled by the parent material, while the distribution and fractionation of REE in the soil profiles is controlled by dominant pedogenetic processes. Clay formation is the primary factor in REE redistribution within soil profile. Calcium carbonates, although abundant in the profiles, only play a secondary role. However, the use of the LREE/HREE fractionation ratio helped to highlight areas dominated by pedogenic carbonates. Although the LREE/HREE approach remains approximate, it demonstrates the significant potential of secondary (pedogenic) calcium carbonate formation for CO_2 sequestration on local and regional scales. Improving the LREE/HREE approach could enable large-scale analyses to be carried out and a more realistic carbon balance to be obtained by incorporating soil inorganic carbon, which is often overlooked.

References

Alfaro, M.R., Nascimento, C.W.A. do, Biondi, C.M., Silva, Ygor Jacques Agra Bezerra da, Silva, Yuri Jacques Agra Bezerra da, Accioly, A.M. de A., Montero, A., Ugarte, O.M., Estevez, J., 2018. Rare-earth-element geochemistry in soils developed in different geological settings of Cuba. Catena (Amst) 162, 317–324. https://doi.org/10.1016/J.CATENA.2017.10.031

Ambrosino, M., Albanese, S., De Vivo, B., Guagliardi, I., Guarino, A., Lima, A., Cicchella, D., 2022. Identification of Rare Earth Elements (REEs) distribution patterns in the soils of Campania region (Italy) using compositional and multivariate data analysis. J Geochem Explor 243, 107112. https://doi.org/10.1016/J.GEXPLO.2022.107112

Andrade, G.R.P., Cuadros, J., Barbosa, J.M.P., Vidal-Torrado, P., 2022. Clay minerals control rare earth elements (REE) fractionation in Brazilian mangrove soils. Catena (Amst) 209, 105855. https://doi.org/10.1016/J.CATENA.2021.105855

Andringa, J., 1984. The climate of Botswana in histograms.

Atlhopheng, J., Brown Mthanganyika Mapeo, R., Eckardt, F.D., 2022. Introduction to the Landscapes and Landforms of Botswana, in: Eckardt, F.D. (Ed.), Landscapes and Landforms of Botswana. Springer International Publishing, Cham, pp. 1–13. https://doi.org/10.1007/978-3-030-86102-5_1

Balaram, V., 2019. Rare earth elements: A review of applications, occurrence, exploration, analysis, recycling, and environmental impact. Geoscience Frontiers 10, 1285–1303. https://doi.org/10.1016/J.GSF.2018.12.005

Batch, T., Tiddy, C., Brotodewo, A., Giles, D., Little, G., Belperio, A., Taylor, M., Metelka, V., 2024. REE-bearing phosphate mineral chemistry for iron sulfide-copper-gold exploration: A study at Jericho, NW Queensland, Australia. J Geochem Explor 267, 107608. https://doi.org/10.1016/J.GEXPLO.2024.107608

Bordy, E.M., 2020. Depositional style changes during the Permo-Carboniferous–Early Jurassic evolution of the Central Kalahari Karoo Sub-basin, Botswana. Geological Journal 55, 5514–5539. https://doi.org/https://doi.org/10.1002/gj.3751

Bozkaya, Ö., Başıbüyük, Z., Yalçın, H., Bozkaya, G., Hozatlıoğlu, D., Szczerba, M., 2024. Geochemistry of hydrothermal illitizations in Eocene Kösedağ magmatic rocks, Zara-Suşehri area, NE Sivas, East-Central Anatolia: Origin and age of alteration. Geochemistry 84, 126121. https://doi.org/10.1016/J.CHEMER.2024.126121

Burrough, S.L., 2022. The Makgadikgadi Basin, in: Eckardt, F.D. (Ed.), Landscapes and Landforms of Botswana. Springer International Publishing, Cham, pp. 77–90. https://doi.org/10.1007/978-3-030-86102-5_5

Burrough, S.L., Thomas, D.S.G., Bailey, R.M., 2009. Mega-Lake in the Kalahari: A Late Pleistocene record of the Palaeolake Makgadikgadi system. Quat Sci Rev 28, 1392–1411. https://doi.org/https://doi.org/10.1016/j.quascirev.2009.02.007

Cantrell, K.J., Byrne, R.H., 1987. Rare earth element complexation by carbonate and oxalate ions. Geochim Cosmochim Acta 51, 597–605. https://doi.org/10.1016/0016-7037(87)90072-X

Cao, L., Chen, X., Jiang, J., Garba, A.A., Li, H., Chao, N., Hu, P., Lv, X., 2024. Geochronology of cassiterite in the Nassarawa-Keffi rare metal pegmatite belt, Nigeria: Tectonic linkages to the Gondwana-forming orogeny. Ore Geol Rev 175, 106339. https://doi.org/10.1016/J.OREGEOREV.2024.106339

Cao, X., Chen, Y., Wang, X., Deng, X., 2001. Effects of redox potential and pH value on the release of rare earth elements from soil. Chemosphere 44, 655–661. https://doi.org/10.1016/S0045-6535(00)00492-6

Cao, Y.-W., Liu, X.-M., Wang, C., Bai, E., Wu, N., 2022. Rare earth element geochemistry in soils along arid and semiarid grasslands in northern China. Ecol Process 11, 29. https://doi.org/10.1186/s13717-022-00375-z

Carney, J.N., 1994. The geology of Botswana. Geological Survey of Botswana 37:17.

Carrasco-Godoy, C., Campbell, I.H., Cajal, Y., 2024. Quantifying the Criteria Used to Identify Zircons from Ore-Bearing and Barren Systems in Porphyry Copper Exploration. Economic Geology 119, 1035–1058. https://doi.org/10.5382/econgeo.5086

Chu, H., Zhu, J., Lin, X., Yin, R., Xie, Z., Cao, Z., Fujii, T., 2007. Short-term decomposition of 14C-labelled glucose in a fluvo-aquic soil as affected by lanthanum amendment. Biol Fertil Soils 43, 811–814. https://doi.org/10.1007/s00374-007-0173-2

de Sá Paye, H., de Mello, J.W.V., de Magalhães Mascarenhas, G.R.L., Gasparon, M., 2016. Distribution and fractionation of the rare earth elements in Brazilian soils. J Geochem Explor 161, 27–41. https://doi.org/10.1016/J.GEXPLO.2015.09.003

Dietrich, F., Diaz, N., Deschamps, P., Sebag, D., Verrecchia, E., 2021. Calcium transfer and mass balance associated with soil carbonate in a semi-arid silicate watershed (North Cameroon): An overlooked geochemical cascade? Depositional Record 2021. https://doi.org/10.1002/dep2.134ï

Dina Ebouel, F.J., Betsi, T.B., Eze, P.N., 2024. Soil inorganic carbon: A review of global research trends, analytical techniques, ecosystem functions and critical knowledge gaps. Catena (Amst) 242, 108112. https://doi.org/https://doi.org/10.1016/j.catena.2024.108112

Domínguez-Villar, D., Bensa, A., Švob, M., Krklec, K., 2022. Causes and implications of the seasonal dissolution and precipitation of pedogenic carbonates in soils of karst regions – A thermodynamic model approach. Geoderma 423, 115962. https://doi.org/10.1016/J.GEODERMA.2022.115962

Eze, P.N., Ebouel, F.J.D., Nkonga, I., Musiol, A., Schleicher, A.M., Günter, C., Norra, S., 2025. Weathering intensity and trace elements (Ni, Sr, Zn, and Cr) distribution in Vertisols developed on basalt in a semiarid environment: agronomic implications. Frontiers in Soil Science 5. https://doi.org/10.3389/fsoil.2025.1530962

Eze, P.N., Molwalefhe, L.N., 2024. Late Quaternary palaeoenvironmental reconstruction of a Chobe Enclave landform (NW Botswana) based on pedological and geochemical indices. Journal of Sedimentary Environments 9, 35–45. https://doi.org/10.1007/s43217-023-00155-5

Eze, P.N., Molwalefhe, L.N., Kebonye, N.M., 2021. Geochemistry of soils of a deep pedon in the Okavango Delta, NW Botswana: Implications for pedogenesis in semi-arid regions. Geoderma Regional 24. https://doi.org/10.1016/j.geodrs.2020.e00352

Fang, Z., Suhua, H., Xu, L., Jian, F., Qi, L., Zhiwei, W., Chuanchang, L., Yuanlai, X., 2021. Adsorption kinetics and thermodynamics of rare earth on Montmorillonite modified by sulfuric acid. Colloids Surf A Physicochem Eng Asp 627, 127063. https://doi.org/10.1016/J.COLSURFA.2021.127063

Fendorf, S., Fendorf, M., 1996. Sorption Mechanisms of Lanthanum on Oxide Minerals. Clays Clay Miner 44, 220–227. https://doi.org/DOI: 10.1346/CCMN.1996.0440207

Food and Agriculture Organization of the United Nations, 2006. Guidelines for soil description. Food and Agriculture Organization of the United Nations.

Franchi, F., Kelepile, T., Di Capua, A., De Wit, M.C.J., Kemiso, O., Lasarwe, R., Catuneanu, O., 2021. Lithostratigraphy, sedimentary petrography and geochemistry of the Upper Karoo Supergroup in the Central Kalahari Karoo Sub-Basin, Botswana. Journal of African Earth Sciences 173. https://doi.org/10.1016/j.jafrearsci.2020.104025

Gadea, O.C.A., Khan, S.D., 2024. Identification of a Potential Rare Earth Element Deposit at Ivanpah Dry Lake, California Through the Bastnäsite Indices. Remote Sens (Basel) 16, 4540. https://doi.org/10.3390/rs16234540

Garzanti, E., Pastore, G., Stone, A., Vainer, S., Vermeesch, P., Resentini, A., 2022. Provenance of Kalahari Sand: Paleoweathering and recycling in a linked fluvial-aeolian system. Earth Sci Rev. https://doi.org/10.1016/j.earscirev.2021.103867

Haddon, I.G., McCarthy, T.S., 2005. The Mesozoic–Cenozoic interior sag basins of Central Africa: The Late-Cretaceous–Cenozoic Kalahari and Okavango basins. Journal of African Earth Sciences 43, 316–333. https://doi.org/https://doi.org/10.1016/j.jafrearsci.2005.07.008

Haldar, U., Chakrabarti, R., Rudnick, R.L., 2025. Extreme rare earth element (REE) enrichment during weathering recorded in saprolites from South Carolina. Chem Geol 673, 122553. https://doi.org/10.1016/J.CHEMGEO.2024.122553

He, Z., Nie, W., Yang, H., Tang, Y., Sha, A., Qu, J., Xu, Z., Chi, R., 2023. Effects of cations on rare earth adsorption and desorption in binding sites of montmorillonite. Physicochemical Problems of Mineral Processing 59, 168280. https://doi.org/10.37190/ppmp/168280

Jolliff, I.T., 2002. Choosing a Subset of Principal Components or Variables, in: Jolliffe, I.T. (Ed.), Principal Component Analysis. Springer New York, New York, NY, pp. 111–149. https://doi.org/10.1007/0-387-22440-8_6

Kampunzu, A.B., Ringrose, S., Huntsman-Mapila, P., Harris, C., Vink, B.W., Matheson, W., 2007. Origins and palaeo-environments of Kalahari duricrusts in the Moshaweng dry valleys (Botswana) as detected by major and trace element composition. Journal of African Earth Sciences 48, 199–221. https://doi.org/10.1016/J.JAFREARSCI.2006.10.007

Key, R.M., Ayres, N., 2000. The 1998 edition of the National Geological Map of Botswana. Journal of African Earth Sciences 30, 427–451. https://doi.org/10.1016/S0899-5362(00)00030-0

Kraemer, D., Tepe, N., Pourret, O., Bau, M., 2017. Negative cerium anomalies in manganese (hydr)oxide precipitates due to cerium oxidation in the presence of dissolved siderophores. Geochim Cosmochim Acta 196, 197–208. https://doi.org/https://doi.org/10.1016/j.gca.2016.09.018

Laveuf, C., Cornu, S., 2009. A review on the potentiality of Rare Earth Elements to trace pedogenetic processes. Geoderma 154, 1–12. https://doi.org/10.1016/J.GEODERMA.2009.10.002

Laveuf, C., Cornu, S., Juillot, F., 2008. Rare earth elements as tracers of pedogenetic processes. Comptes Rendus Geoscience 340, 523–532. https://doi.org/10.1016/J.CRTE.2008.07.001

Li, Y., Sun, C.Y., Xu, W.L., Zhang, X.M., 2024. In situ geochemistry of apatite: Petrogenetic and tectonic interpretations of Jurassic felsic magmatism in the Yanbian area, NE China. Lithos 486–487, 107764. https://doi.org/10.1016/J.LITHOS.2024.107764

Li, Z., Liang, T., Li, K., Wang, P., 2020. Exposure of children to light rare earth elements through ingestion of various size fractions of road dust in REEs mining areas. Science of The Total Environment 743, 140432. https://doi.org/10.1016/J.SCITOTENV.2020.140432

Lin, Z., Wei, G., Zhang, J., Liang, X., Huang, G., 2022a. Origin and distribution of rare earth elements (REEs) in the soils of Meizhou City, southern China with high abundance of regolith-hosted REEs. Applied Geochemistry 147, 105514. https://doi.org/10.1016/J.APGEOCHEM.2022.105514

Lin, Z., Wei, G., Zhang, J., Liang, X., Huang, G., 2022b. Origin and distribution of rare earth elements (REEs) in the soils of Meizhou City, southern China with high abundance of regolith-hosted REEs. Applied Geochemistry 147, 105514. https://doi.org/10.1016/J.APGEOCHEM.2022.105514

Liu, W., Li, Y., Wang, X., Cui, L., Zhao, Z., Liu, C., Xu, Z., 2022. Weathering stage and topographic control on rare earth element (REE) behavior: New constraints from a deeply weathered granite hill. Chem Geol 610, 121066. https://doi.org/10.1016/J.CHEMGEO.2022.121066

Matshameko, Y., Kebonye, N.M., Eze, P.N., 2022. Ethnopedological knowledge and scientific assessment of earthenware pottery-making soils of southern Botswana for natural resource management. Geoderma Regional 31, e00580. https://doi.org/10.1016/J.GEODRS.2022.E00580

Matshameko, Y., Okolo, C.C., Eze, P.N., 2023. Near-surface pedosediments of Takatokwane saline pan, southern Botswana: Properties, pedogenic processes, and inferences of environmental change. Geoderma Regional 34, e00696. https://doi.org/10.1016/J.GEODRS.2023.E00696

McCarthy, T.S., Barry, M., Bloem, A., Ellery, W.N., Heister, H., Merry, C.L., Rüther, H., Sternberg, H., 1997. The gradient of the Okavango fan, Botswana, and its sedimentological and tectonic implications. Journal of African Earth Sciences 24, 65–78. https://doi.org/10.1016/S0899-5362(97)00027-4

Mihajlovic, J., Bauriegel, A., Stärk, H.J., Roßkopf, N., Zeitz, J., Milbert, G., Rinklebe, J., 2019. Rare earth elements in soil profiles of various ecosystems across Germany. Applied Geochemistry 102, 197–217. https://doi.org/10.1016/J.APGEOCHEM.2019.02.002

Miller, D.L., Mora, C.I., Driese, S.G., 2007. Isotopic variability in large carbonate nodules in Vertisols: Implications for climate and ecosystem assessments. Geoderma 142, 104–111. https://doi.org/10.1016/j.geoderma.2007.08.007

Mokatse, T., Diaz, N., Shemang, E., Van Thuyne, J., Vittoz, P., Vennemann, T., Verrecchia, E.P., 2022. Landscapes and Landforms of the Chobe Enclave, Northern Botswana, in: Eckardt, F.D. (Ed.), Landscapes and Landforms of Botswana. Springer International Publishing, Cham, pp. 91–116. https://doi.org/10.1007/978-3-030-86102-5_6

Mokatse, T., Prud'Homme, C., Vainer, S., Adatte, T., Shemang, E., Verrecchia, E.P., 2023. Sepiolite as a multifactorial indicator of paleoenvironments in the Chobe Enclave (northern Botswana). Sediment Geol 454, 106459. https://doi.org/https://doi.org/10.1016/j.sedgeo.2023.106459

Monger, H.C., 2014. Soils as Generators and Sinks of Inorganic Carbon in Geologic Time, in: Soil Carbon. Springer International Publishing, pp. 27–36. https://doi.org/10.1007/978-3-319-04084-4_3

Nagasawa, M., Shimizu, Y., Yamaguchi, A., Tokunaga, K., Mukai, H., Aoyagi, N., Mei, H., Takahashi, Y., 2024. Interpretation of vertical migration and enrichment processes of rare earth

elements (REEs) in ion-adsorption-type mineralization in Japan based on REE speciation analyses. Chem Geol 670, 122431. https://doi.org/10.1016/J.CHEMGEO.2024.122431

Nash, D.J., 2022. Calcretes, Silcretes and Intergrade Duricrusts, in: Eckardt, F.D. (Ed.), Landscapes and Landforms of Botswana. Springer International Publishing, Cham, pp. 223–246. https://doi.org/10.1007/978-3-030-86102-5_13

Nash, D.J., McLaren, S.J., 2003. Kalahari valley calcretes: their nature, origins, and environmental significance. Quaternary International 111, 3–22. https://doi.org/10.1016/S1040-6182(03)00011-9

Nguetnkam, J.P., Kamga, R., Villieras, F., Ekodeck, G.E., Yvon, J., 2007. Pedogenic formation of smectites in a vertisol developed from granitic rock from Kaélé (Cameroon, Central Africa). Clay Miner 42, 487–501. https://doi.org/10.1180/claymin.2007.042.4.07

Nouazi Momo, M., Beauvais, A., Tematio, P., Ambrosi, J.P., Yemefack, M., Yerima, B.P.K., Yongue-Fouateu, R., 2019. Lateritic weathering of trachyte, and bauxite formation in West Cameroon: Morphological and geochemical evolution. J Geochem Explor 205, 106324. https://doi.org/10.1016/J.GEXPLO.2019.06.006

Paterson, E., Goodman, B.A., Farmer, V.C., 1991. The Chemistry of Aluminium, Iron and Manganese Oxides in Acid Soils, in: Ulrich, B., Sumner, M.E. (Eds.), Soil Acidity. Springer Berlin Heidelberg, Berlin, Heidelberg, pp. 97–124. https://doi.org/10.1007/978-3-642-74442-6_5

Peng, X., Zhu, Q., Zhang, Z., Hallett, P.D., 2017. Combined turnover of carbon and soil aggregates using rare earth oxides and isotopically labelled carbon as tracers. Soil Biol Biochem 109, 81–94. https://doi.org/10.1016/J.SOILBIO.2017.02.002

Pourret, O., Davranche, M., Gruau, G., Dia, A., 2007. Competition between humic acid and carbonates for rare earth elements complexation. J Colloid Interface Sci 305, 25–31. https://doi.org/https://doi.org/10.1016/j.jcis.2006.09.020

Pourret, O., van der Ent, A., Hursthouse, A., Irawan, D.E., Liu, H., Wiche, O., 2022. The ‘europium anomaly’ in plants: facts and fiction. Plant Soil 476, 721–728. https://doi.org/10.1007/s11104-021-05210-6

Pucetaite, M., Persson, P., Parker, J., Johansson, U., Hammer, E.C., 2025. Visualization of soil aggregate structures provides insights into their formation mechanisms induced by litter inputs. Soil Biol Biochem 202, 109686. https://doi.org/10.1016/J.SOILBIO.2024.109686

Ringrose, S., Matheson, W., Vanderpost, C., 1998. Analysis of soil organic carbon and vegetation cover trends along the B otswana Kalahari Transect, Journal of A rid Environments.

Ringrose, S., Matheson, W., Wolski, P., Huntsman-Mapila, P., 2003. Vegetation cover trends along the Botswana Kalahari transect, in: Journal of Arid Environments. Academic Press, pp. 297–317. https://doi.org/10.1006/jare.2002.1092

Romanens, R., Pellacani, F., Mainga, A., Fynn, R., Vittoz, P., Verrecchia, E.P., 2019. Soil diversity and major soil processes in the Kalahari basin, Botswana. Geoderma Regional 19. https://doi.org/10.1016/j.geodrs.2019.e00236

Sababa, E., Essomba Owona, L.G., Temga, J.P., Ndjigui, P.-D., 2021. Petrology of weathering materials developed on granites in Biou area, North-Cameroon: implication for rare-earth elements (REE) exploration in semi-arid regions. Heliyon 7. https://doi.org/10.1016/j.heliyon.2021.e08581

Sharma, P., Jha, A.B., Dubey, R.S., 2024. Addressing lanthanum toxicity in plants: Sources, uptake, accumulation, and mitigation strategies. Science of The Total Environment 929, 172560. https://doi.org/10.1016/J.SCITOTENV.2024.172560

Smith, A., R., 1984. The Lithostratigraphy of the Karoo Supergroup in Botswana. Geol Mag 123, 710–711. https://doi.org/DOI: 10.1017/S0016756800024328

Song, A., Si, Z., Xu, D., Wei, B., Wang, E., Chong, F., Fan, F., 2025. Lanthanum and cerium added to soil influence microbial carbon and nitrogen cycling genes. J Environ Manage 373, 123509. https://doi.org/10.1016/J.JENVMAN.2024.123509

Taylor, S.R., McLennan, S.M., 1985. The Continental Crust: Its Composition and Evolution. Geol Mag 122, 673–674. https://doi.org/DOI: 10.1017/S0016756800032167

Temga, J.P., Sababa, E., Mamdem, L.E., Bijeck, M.L.N., Azinwi, P.T., Tehna, N., Zo'o Zame, P., Onana, V.L., Nguetnkam, J.P., Bitom, L.D., Ndjigui, P.D., 2021. Rare earth elements in tropical soils, Cameroon soils (Central Africa). Geoderma Regional 25, e00369. https://doi.org/10.1016/J.GEODRS.2021.E00369

Thomas, D.S.G., Shaw, P.A., 1990. The deposition and development of the Kalahari Group sediments, Central Southern Africa, Journal of African Earth Sciences.

Vainer, S., Erel, Y., Matmon, A., 2018. Provenance and depositional environments of Quaternary sediments in the southern Kalahari Basin. Chem Geol 476, 352–369. https://doi.org/10.1016/j.chemgeo.2017.11.031

Vittoz, P., Pellacani, F., Romanens, R., Mainga, A., Verrecchia, E.P., Fynn, R.W.S., 2020. Plant community diversity in the chobe enclave, botswana: Insights for functional habitat heterogeneity for herbivores. Koedoe 62, 1–17. https://doi.org/10.4102/koedoe.v62i1.1604

Wang, X., Yin, L., Dijkstra, F.A., Lu, J., Wang, P., Cheng, W., 2020. Rhizosphere priming is tightly associated with root-driven aggregate turnover. Soil Biol Biochem 149, 107964. https://doi.org/10.1016/J.SOILBIO.2020.107964

Wang, Y., Liu, L., Sun, M., Huang, J., Huang, Y., Liang, X., Tan, W., He, H., Zhu, J., 2023. Distribution and Fractionation of Rare Earth Elements (REE) in the Ion Adsorption-type REE Deposit (IAD) at Maofeng Mountain, Guangzhou, China. Clays Clay Miner 71, 340–361. https://doi.org/DOI: 10.1007/s42860-023-00251-7

Wu, C.Y., Zehetner, F., Chen, Z.S., Jien, S.H., Hseu, Z.Y., 2024. Fractionation of rare earth elements in soil profiles along an elevation gradient in central Taiwan. Catena (Amst) 235, 107659. https://doi.org/10.1016/J.CATENA.2023.107659

Yuan, Y., Liu, S., Wu, M., Zhong, M., Shahid, M.Z., Liu, Y., 2021. Effects of topography and soil properties on the distribution and fractionation of REEs in topsoil: A case study in Sichuan Basin, China. Science of The Total Environment 791, 148404. https://doi.org/10.1016/J.SCITOTENV.2021.148404

Zamanian, K., Pustovoytov, K., Kuzyakov, Y., 2016. Pedogenic carbonates: Forms and formation processes. Earth Sci Rev. https://doi.org/10.1016/j.earscirev.2016.03.003

Zepeda, V.K., Kamber, B.S., Ghidan, O.Y.A., 2024. Direct accurate Eu anomaly analysis in very high Ba/Eu silicate samples by triple-quadrupole ICP-MS in MS/MS mass shift mode. Chem Geol 647, 121827. https://doi.org/https://doi.org/10.1016/j.chemgeo.2023.121827

Zhang, K., Shields, G.A., 2023. Early diagenetic mobilization of rare earth elements and implications for the Ce anomaly as a redox proxy. Chem Geol 635, 121619. https://doi.org/10.1016/J.CHEMGEO.2023.121619

Zhao, F., Zhang, G., Jiang, Y., Wang, H., Cao, C., Qi, Y., Wang, Q., Zhao, H., 2023. The Formation and Transformation of Manganese Oxide Minerals on the Surface of Kaolinite. Clays Clay Miner 71, 106–118. https://doi.org/DOI: 10.1007/s42860-023-00236-6

Appendices

Appendix 3.1. Ba/Eu ratio of the study samples

Profile	Horizon	Ba (mg kg^{-1})	Eu (mg kg^{-1})	Ba/Eu
	A	150	0.21	714
	Bkk1	1.50E+03	1.3	1.12E+03
	Bkk2	1.76E+03	2	871
	Bkk3	385	0.3	1.28E+03
M1P1	Ck	1.60E+03	1.4	1.10E+03
	A	149	0.17	876
	AC	459	0.48	956
	C1	391	0.4	978
K1P1	C2	1.90E+03	1.7	1.14E+03
	A	348	0.16	2.18E+03
	AC	384	0.37	1.04E+03
	Ck1	661	0.43	1.54E+03
	Ck2	595	0.53	1.12E+03
	Ck3	656	0.56	1.17E+03
	Ck4	398	0.4	995
	CFS	173	0.18	961
POQ	CVFS	747	0.61	1.22E+03
	A	819	0.59	1.39E+03
	AC	1.43E+03	0.95	1.50E+03
	C1	654	0.45	1.45E+03
	C2	306	1.2	259
SHP3	C3	294	0.52	565
	A	182	1.4	135
	Bss1	207	0.68	304
	Bss2	262	0.63	416
	Bt1	241	0.71	339
	Bt2	1.90E+03	2	936
SP1	C	315	0.86	366
	A	267	0.61	438
	Bss1	325	0.77	422
	Bss2	396	0.83	477
	Bss3	331	0.86	385
	Bkss	316	0.87	363
SP2	Bt	323	0.67	482
	A	289	1.1	268
	Bss1	297	1.1	280
	Bss2	289	1	281
	Bk	285	1	282
	Bksst1	295	0.98	301
SP3	Bksst2	298	0.94	317
	Ap	257	0.76	338
	Bt1	235	0.72	326
	Bt2	264	0.71	372
	Bk	240	0.66	364
	Bkkm1	261	0.87	300
SP4	Bkkm2	245	0.85	288

Appendix 3.1 (continued)

Profile	Horizon	Ba (mg kg^{-1})	Eu (mg kg^{-1})	Ba/Eu
	2.10E+03	1.5	1.39E+03	2.10E+03
	1.15E+03	1.3	858	1.15E+03
	1.13E+03	1.5	743	1.13E+03
	3.46E+03	3.1	1.13E+03	3.46E+03
LT1	268	0.77	348	268
	A	351	0.8	439
	AB	1.00E+03	1.3	781
	Bk1	1.75E+03	1.7	1.02E+03
	Bk2	1.26E+03	1.8	696
LT2	Bt	1.03E+03	1.8	563
	A	316	0.51	620
	C1	436	0.61	715
	C2	382	0.55	695
	C3	295	0.38	776
	C4	229	0.31	739
TK1	C5	508	0.49	1.04E+03
	A	142	0.18	789
	C1	321	0.49	655
	C2	407	0.55	740
	C3	356	0.42	848
	C4	278	0.34	818
TK2	C5	243	0.28	868

Appendix 3.2. Major elements contents (wt.%) in the profiles of the study

Profile	Sample	Al	Ca	Fe	K	Mg	Na	Si
M1P1	A	0.95	0.14	0.83	0.30	0.27	0.09	44.74
	Bkk1	2.38	10.33	1.48	0.81	2.07	0.12	34.63
	Bkk2	3.19	5.63	2.46	1.16	2.05	0.24	36.04
	Bkk3	1.50	2.93	0.76	0.44	1.33	0.25	41.45
	Ck	2.68	13.79	1.81	1.12	1.31	0.66	31.90
K1P1	A	1.15	0.16	0.75	0.29	0.23	0.10	44.63
	AC	1.24	2.49	0.69	0.44	1.58	0.14	41.89
	C1	1.71	3.29	1.01	0.47	2.04	0.12	40.38
	C2	3.46	1.53	2.32	1.46	1.80	0.54	38.39
POQ	AP	0.27	2.58	0.78	0.11	0.60	0.10	43.58
	AC	0.28	3.60	1.05	0.11	0.65	0.09	42.67
	Ck1	0.29	5.22	0.93	0.12	0.84	0.18	41.49
	Ck2	0.29	5.49	1.17	0.13	1.04	0.10	41.06
	Ck3	0.23	9.71	1.32	0.15	1.39	0.28	37.86
	Ck4	0.22	9.21	1.22	0.15	0.89	0.16	38.76
	CFS	0.14	0.13	0.71	0.03	0.09	0.10	45.85
	CVFS	0.69	0.28	0.73	0.10	0.13	0.22	45.10
SHP3	A1	1.52	3.70	1.35	0.43	0.84	0.12	41.00
	AC	1.89	5.93	1.65	0.51	1.57	0.11	38.38
	C1	2.23	1.85	1.89	0.66	0.85	0.13	41.07
	C2	2.34	7.22	2.28	0.80	0.83	0.31	36.98
	C3	2.10	2.93	1.76	0.72	0.65	0.21	40.62
SP1	A	2.82	0.51	2.31	0.46	0.56	0.23	41.22
	Bk1	3.61	0.89	2.97	0.46	0.81	0.27	39.58
	Bk2	3.87	1.74	3.35	0.44	0.91	0.30	38.45
	Bk3	4.08	2.66	3.33	0.46	1.02	0.35	37.52
	Bss1	7.20	4.19	2.45	2.02	1.16	0.56	33.23
	Bss2	4.44	3.43	3.71	0.50	1.28	0.42	36.15
SP2	Ap	3.60	2.56	3.18	0.50	1.00	0.51	38.05
	Bss1	4.89	4.38	4.39	0.42	1.57	0.89	34.22
	Bss2	5.09	3.49	4.43	0.45	1.61	1.03	34.45
	Bss3	5.50	2.67	4.91	0.48	1.63	1.15	34.15
	Bkss	4.59	2.70	3.97	0.53	1.46	0.97	35.86
	Bt	3.23	0.86	2.43	0.70	0.87	0.68	39.97
SP3	A	7.42	4.21	7.15	0.53	2.39	1.12	29.20
	Bkss1	7.51	3.92	7.21	0.53	2.33	1.16	29.30
	Bkss2	7.41	3.62	7.08	0.54	2.35	1.19	29.64
	Bk	7.17	3.79	6.98	0.53	2.28	1.13	29.90
	Bkkm1	6.56	3.55	6.45	0.56	2.14	1.07	31.08
	Bkkm2	6.27	2.91	6.16	0.57	2.00	1.05	32.08
SP4	Ap	5.21	4.67	5.16	0.55	2.48	0.94	32.21
	Bt1	4.91	8.35	4.97	0.39	2.63	0.87	30.24
	Bt2	5.09	8.97	5.05	0.38	2.77	0.94	29.49
	Bk	5.04	13.00	4.93	0.39	3.63	0.99	26.33
	Bkkm1	6.46	7.63	6.91	0.40	4.45	1.72	26.05
	Bkkm2	6.60	8.38	7.12	0.39	4.57	1.83	25.14

.

Appendix 3.2 (continued)

Profile	Sample	Al	Ca	Fe	K	Mg	Na	Si
LT1	A	2.78	13.22	1.05	0.77	0.47	0.44	33.67
	AB	4.78	7.73	1.83	1.23	0.83	0.30	34.40
	Bk1	5.71	10.99	3.08	1.58	0.87	0.39	30.29
	Bk2	6.46	8.40	2.35	1.76	1.06	0.50	31.48
	Bt1	4.11	3.03	3.46	0.48	1.13	0.54	36.95
LT2	A	3.87	10.00	1.97	1.14	0.71	0.27	33.81
	AB	4.89	10.71	2.19	1.37	0.82	0.34	32.01
	Bk1	5.49	9.46	2.21	1.47	0.95	0.40	32.08
	Bk2	6.37	8.53	3.16	1.78	0.96	0.41	31.03
	Bt1	6.43	10.88	2.83	1.85	0.92	0.44	29.51
TK1	A	1.55	3.66	1.26	0.75	1.93	1.48	39.12
	C1	1.87	5.78	1.43	0.93	3.12	1.24	36.46
	C2	1.81	5.46	1.57	0.86	3.10	1.18	36.73
	C3	1.19	3.42	1.18	0.61	2.12	0.82	40.04
	C4	0.53	1.85	0.52	0.31	1.19	0.48	43.24
	C5	0.93	2.65	1.14	0.64	1.80	0.76	41.09
TK2	A	0.54	0.43	0.46	0.18	0.24	0.42	45.04
	C1	1.75	2.73	0.97	0.81	1.47	0.70	40.57
	C2	1.91	6.65	1.24	0.99	3.82	1.04	35.52
	C3	1.41	5.20	0.89	0.76	2.63	0.90	38.33
	C4	1.28	2.96	0.84	0.73	1.70	0.85	40.74
	C5	1.13	2.28	0.73	0.72	1.28	0.79	41.77

Appendix 3.3. REE contents (mg kg^{-1}) in the study area

Profile	Layer	La	Ce	Pr	Nd	Sm	Eu	Gd	Tb	Dy	Ho	Er	Tm	Yb	Lu	LREE	HREE	∑REE
M1P1	A	5.5	12.6	1.3	5.4	1	0.21	0.94	0.14	0.73	0.15	0.44	0.06	0.3	0.07	26	2.8	28.8
	Bkk1	9.4	20.9	2.28	9.3	1.8	1.34	1.53	0.25	1.29	0.24	0.85	0.11	0.8	0.12	45	5.2	50.2
	Bkk2	20.6	38.3	5.44	23.6	4.9	2.02	5.22	0.82	4.91	1.1	3.29	0.42	2.6	0.37	94.9	18.7	113.6
	Bkk3	5.7	11.5	1.28	4.9	0.9	0.3	0.73	0.13	0.75	0.15	0.47	0.06	0.4	0.06	24.6	2.8	27.3
	Ck	13.7	30.2	3.26	13.2	2.6	1.45	2.48	0.39	2.23	0.44	1.36	0.19	1.2	0.2	64.4	8.5	72.9
K1P1	A	7.9	9.8	1.13	4.3	0.7	0.17	0.68	0.11	0.58	0.11	0.35	0.06	0.4	0.06	24	2.4	26.4
	AC	6	9.5	1.21	4.6	0.9	0.48	0.75	0.11	0.67	0.12	0.37	0.05	0.4	0.05	22.7	2.5	25.2
	C1	7	14.2	1.34	5.3	1	0.4	0.77	0.13	0.76	0.13	0.46	0.06	0.5	0.07	29.2	2.9	32.1
	C2	14	29.7	3.34	13.4	2.6	1.66	2.23	0.38	1.87	0.37	1.14	0.16	1.1	0.16	64.7	7.4	72.1
POQ	A	2.6	5.1	0.58	2.4	0.4	0.16	0.44	0.06	0.4	0.07	0.28	0.05	0.2	0.05	11.2	1.6	12.8
	AC	3	5.2	0.57	2.4	0.5	0.37	0.45	0.07	0.38	0.06	0.3	0.05	0.3	0.05	12	1.7	13.7
	Ck1	3.1	5.8	0.66	2.7	0.5	0.43	0.52	0.06	0.42	0.08	0.28	0.05	0.2	0.05	13.2	1.7	14.9
	Ck2	5.7	5.2	0.58	2.6	0.5	0.53	0.4	0.06	0.41	0.07	0.21	0.05	0.2	0.05	15.1	1.5	16.6
	Ck3	2.8	5.9	0.63	2.8	0.7	0.56	0.55	0.08	0.5	0.08	0.31	0.05	0.3	0.05	13.4	1.9	15.3
	Ck4	3.4	6.1	0.71	3.4	0.6	0.4	0.68	0.1	0.53	0.1	0.38	0.05	0.4	0.05	14.6	2.3	16.9
	CFS	3	5.3	0.57	2.5	0.5	0.18	0.38	0.06	0.3	0.05	0.2	0.05	0.2	0.05	12.1	1.3	13.3
	CVFS	6.6	15.1	1.42	5.4	0.8	0.61	0.73	0.11	0.53	0.08	0.27	0.05	0.3	0.05	29.9	2.1	32.1
SHP3	A	46	12.6	1.26	4.7	0.9	0.59	0.71	0.12	0.6	0.11	0.42	0.05	0.4	0.08	66.1	2.5	68.5
	A/C	5.4	12.8	1.08	4.2	0.9	0.95	0.7	0.11	0.63	0.11	0.4	0.05	0.4	0.06	25.3	2.5	27.8
	C1	6.6	11.5	1.1	4.2	0.8	0.45	0.66	0.1	0.56	0.1	0.39	0.06	0.5	0.07	24.7	2.4	27.1
	C2	33.6	70.9	7.96	31.5	5.6	1.18	4.74	0.7	3.26	0.61	1.78	0.23	1.5	0.2	150.7	13	163.8
	C3	11.3	23.4	2.63	10.2	1.9	0.52	1.64	0.26	1.31	0.26	0.75	0.1	0.7	0.12	50	5.1	55.1

Appendix 3.3. (continued)

Profile	Layer	La	Ce	Pr	Nd	Sm	Eu	Gd	Tb	Dy	Ho	Er	Tm	Yb	Lu	LREE	HREE	∑REE
SP1	A	35.1	70.1	7.76	29.7	5.6	1.35	5.77	0.76	3.86	0.74	2.3	0.29	2.1	0.27	149.6	16.1	165.7
	Bss1	13.7	23.8	3	11.7	2.4	0.68	2.27	0.37	2.23	0.42	1.33	0.14	1.4	0.17	55.3	8.3	63.6
	Bss2	12.7	24.1	3.01	12	2.5	0.63	2.55	0.36	2.26	0.42	1.36	0.16	1.4	0.17	54.9	8.7	63.6
	Bt1	15.7	26.4	3.26	12.9	2.7	0.71	2.71	0.42	2.47	0.45	1.41	0.18	1.5	0.19	61.7	9.3	71
	Bt2	38.5	75.3	8.78	33.9	6.8	2.03	6.21	0.94	5	0.94	2.88	0.39	3	0.37	165.3	19.7	185
	C	14.5	28	3.35	13.8	2.9	0.86	3.05	0.44	2.77	0.53	1.7	0.2	1.7	0.21	63.4	10.6	74
SP2	A	9.2	16.6	2.22	9.2	2	0.61	2	0.32	1.96	0.37	1.19	0.13	1.2	0.15	39.8	7.3	47.2
	Bss1	11	18.9	2.58	10.9	2.4	0.77	2.54	0.41	2.54	0.49	1.56	0.17	1.5	0.18	46.6	9.4	55.9
	Bss2	11.3	21.3	2.9	12.4	2.7	0.83	2.71	0.45	2.72	0.52	1.66	0.2	1.6	0.2	51.4	10.1	61.5
	Bss3	12.2	21.4	2.8	12.3	2.7	0.86	3	0.44	2.75	0.53	1.72	0.2	1.5	0.2	52.3	10.3	62.6
	Bkss	13.6	20.8	2.89	12.2	2.7	0.87	2.87	0.43	2.57	0.51	1.53	0.16	1.4	0.21	53.1	9.7	62.7
	Bt	11.8	17.9	2.77	11.1	2.3	0.67	2.51	0.33	1.99	0.34	1.14	0.13	1.1	0.13	46.5	7.7	54.2
SP3	A	12.4	23.8	3.23	14.4	3.5	1.08	3.84	0.59	3.71	0.74	2.4	0.29	2.2	0.3	58.4	14.1	72.5
	Bss1	14.7	24.3	3.36	14.6	3.5	1.06	3.53	0.57	3.75	0.76	2.33	0.3	2.3	0.31	61.5	13.9	75.4
	Bss2	12.2	23.5	3.28	14	3.3	1.03	3.91	0.56	3.6	0.7	2.2	0.27	2.1	0.27	57.3	13.6	70.9
	Bk	13.1	22.7	3.18	13.6	3.2	1.01	3.64	0.57	3.41	0.67	2.11	0.26	2.2	0.28	56.8	13.1	69.9
	Bksst1	11.7	22.8	3.07	12.9	3.1	0.98	3.08	0.54	3.33	0.63	2.08	0.25	2	0.24	54.6	12.2	66.7
	Bksst2	11.3	22.2	2.87	12.5	2.9	0.94	3.14	0.49	3.02	0.56	1.82	0.24	1.8	0.21	52.7	11.3	64
SP4	Ap	9.3	20.3	2.31	9.9	2.3	0.76	2.09	0.4	2.56	0.5	1.62	0.19	1.6	0.2	44.9	9.2	54
	Bt1	8.9	19.3	2.2	9.6	2.1	0.72	2.14	0.38	2.52	0.45	1.58	0.18	1.6	0.19	42.8	9	51.9
	Bt2	8.9	19.2	2.19	9.3	2.2	0.71	2.29	0.39	2.5	0.49	1.53	0.19	1.6	0.19	42.5	9.2	51.7
	Bk	8	15.4	1.94	8.7	1.9	0.66	2.03	0.37	2.45	0.46	1.5	0.17	1.5	0.17	36.6	8.7	45.3
	Bkkm1	8.3	17.1	2.24	9.9	2.6	0.87	2.72	0.52	3.2	0.66	2.05	0.25	2	0.25	41	11.7	52.7
	Bkkm2	7.7	15.6	2.09	9.3	2.6	0.85	3.16	0.5	3.42	0.66	2.08	0.26	2	0.26	38.1	12.3	50.5

Appendix 3.3.(Continued)

Profile	Layer	La	Ce	Pr	Nd	Sm	Eu	Gd	Tb	Dy	Ho	Er	Tm	Yb	Lu	LREE	HREE	∑REE
LT1	A	15.2	29.4	3.33	13.1	2.5	1.51	2.18	0.34	1.83	0.32	1.03	0.13	1.1	0.14	65	7.1	72.1
	AB	25.1	52.2	5.83	22.5	4.5	1.34	4.44	0.62	3.36	0.66	1.98	0.24	2	0.25	111.5	13.6	125
	Bk1	29.3	62.6	6.99	26.3	5.2	1.52	4.89	0.73	3.77	0.68	2.2	0.29	2.2	0.28	131.9	15	147
	Bk2	35.9	68.3	8.2	32.2	6.3	3.06	6.34	0.92	4.9	0.95	2.81	0.36	2.8	0.34	154	19.4	173.4
	Bt	13.3	25.8	3.12	12.8	2.7	0.77	2.77	0.4	2.36	0.43	1.48	0.17	1.4	0.18	58.5	9.2	67.7
LT2	A	22.2	44	4.96	19.2	3.8	0.8	3.83	0.55	2.9	0.55	1.79	0.22	1.9	0.24	95	12	106.9
	AB	26.6	53.9	6.14	23.7	4.7	1.28	3.87	0.63	3.35	0.63	1.97	0.25	2.1	0.27	116.3	13.1	129.4
	Bk1	28.6	56.6	6.42	24.4	5	1.72	4.58	0.67	3.74	0.68	2.09	0.27	2.1	0.27	122.7	14.4	137.1
	Bk2	39.3	75.1	8.84	35.2	6.9	1.81	6.19	0.96	5.01	0.92	2.79	0.37	2.8	0.35	167.2	19.4	186.5
	Bt	42.2	76.3	8.86	34.6	7	1.83	7.21	1.02	5.79	1.08	3.33	0.44	3.1	0.39	170.8	22.4	193.2
TK1	A	11	19.8	2.4	9.5	1.8	0.51	1.99	0.25	1.41	0.26	0.78	0.09	0.9	0.1	45	5.8	50.8
	C1	12.3	22.3	2.69	10.8	2.1	0.61	1.97	0.26	1.57	0.28	0.81	0.08	0.9	0.11	50.8	6	56.8
	C2	10.8	20.2	2.37	9.2	1.7	0.55	1.88	0.24	1.35	0.23	0.85	0.08	0.8	0.1	44.8	5.5	50.4
	C3	7.9	15	1.75	7	1.3	0.38	1.05	0.18	1.03	0.17	0.56	0.05	0.6	0.08	33.3	3.7	37.1
	C4	7.3	13.5	1.59	6.4	1.2	0.31	1	0.16	1.01	0.18	0.6	0.06	0.7	0.07	30.3	3.8	34.1
	C5	7.5	14.7	1.67	6.7	1.3	0.49	1.3	0.16	1.08	0.2	0.69	0.07	0.8	0.09	32.4	4.4	36.8
TK2	A	4.2	7.3	0.92	3.5	0.7	0.18	0.52	0.06	0.63	0.1	0.41	0.05	0.4	0.05	16.8	2.2	19
	C1	11.2	20	2.4	9.6	2	0.49	1.73	0.26	1.44	0.23	0.82	0.09	0.8	0.1	45.7	5.5	51.2
	C2	11.5	21.8	2.64	10.2	2	0.55	1.52	0.26	1.39	0.25	0.85	0.08	0.8	0.08	48.7	5.2	53.9
	C3	9.6	17.4	2.06	7.9	1.5	0.42	1.39	0.19	1.14	0.21	0.67	0.07	0.7	0.06	38.9	4.4	43.3
	C4	8.3	15.4	1.78	6.9	1.3	0.34	1.21	0.16	1.05	0.18	0.62	0.06	0.7	0.07	34	4.1	38.1
	C5	8.6	14.8	1.69	6.7	1.2	0.28	1.28	0.15	0.94	0.17	0.6	0.05	0.6	0.06	33.3	3.9	37.1

CHAPTER FOUR

A Multi-Proxy Pedosedimentary Insight into Calcium Origin, Sediment Provenance, And Depositional Environments in A NW Botswana Landform[3]

Abstract

Calcium carbonates are key components of the global terrestrial geochemical carbon cycle and can influence carbon sequestration, climate interactions, and agricultural productivity. In the soils of the Chobe Enclave (northern Botswana), calcium carbonates are widespread, yet their origin and accumulation processes remain poorly understood. This study investigates a pedosedimentary section using multiple proxies, including morphological descriptions, physicochemical properties, particle size inclusive statistic, bulk and clay mineralogy, and geochemical indices such as the Chemical Index of Alteration (CIA), the Weathering Index of Parker (WIP), the Robust Index of Chemical Weathering (RW), the Index of Compositional Variability (ICV), and the calcium-strontium ratio (Ca/Sr). In the upper part of the section, CIA (1.7–6.9) and RW (10.5–23.2) are of low values, while the lower part records higher values (CIA: 40.0–72.2, RW: 26.0–33.3). Conversely, WIP (13.4–40.5) and ICV (9.9–37.7) are higher in the upper part but decrease in the lower part (WIP: 2.4–10.5, ICV: 0.3–0.9). The Mafic-Felsic-RW projection suggests a felsic origin for the entire sediment sequence. The Ca/Sr ratio ranges from 384 to 803 in the carbonate-rich (5–23 wt. %) upper section and from 190 to 1011 in the carbonate-poor (< 1 wt. %) lower section. These results indicate a shift in depositional environment from shallow lacustrine to alluvial floodplain with temporary flow. The results point to the weathering of alluvial felsic sediments as a plausible major contributor of calcium

[3] *This chapter is based on a paper co-authored with Loago N. Molwalefhe, Thierry Bineli Betsi, and Peter N. Eze; published in Earth Systems and Environment, 9, 1937–1957 (2025).* https://doi.org/10.1007/s41748-025-00724-w

to the pedogenic carbonates, although a diversity of sources, including aeolian and geogenic inputs, cannot be excluded. While strontium or stable isotope analyses would provide more conclusive constraints, the multiproxy approach used in this study offers a useful, indirect means of constraining calcium origin in the absence of such data. Unravelling calcium carbonate origin is essential for improved understanding of soil formation, function and management, especially in drylands.

Keywords: Alluvial Plains; Chemical weathering indices; Kalahari Basin; Kastanozems; Semi-arid environments

4.1. Introduction

Soil inorganic carbon (SIC) is the dominant form of soil carbon in dryland ecosystems including hyper-arid, arid, and semi-arid regions (Sharififar et al., 2023). It therefore serves as major carbon sink in arid zones effectively mitigating global climate change. However, the equilibrium of SIC is fragile. Numerous factors mainly associated with human activities such as agriculture (Liu et al., 2023; Ortiz et al., 2022) and deforestation (Golubtsov et al., 2021; Khokhlova and Myakshina, 2018; Khokhlova et al., 2013) and natural changes in climate and vegetation (Hui An et al., 2019; Pfeiffer et al., 2023), have been shown to affect the net balance of SIC stock. These factors are influence the accumulation and dissolution of carbonates within soil profiles. SIC results from a range of processes, including pedogenic, lithogenic, and biogenic processes (Zamanian et al., 2016). Recently, the fraction resulting from pedogenic processes (pedogenic carbonates) has received increasing attention given that they have been recognised as an important pathway for sequestering atmospheric carbon dioxide in arid environments (Bughio et al., 2017; Bughio et al.,2016; Dina Ebouel et al., 2024; Liu et al., 2023).

Despite the increasing interest, one important aspect of pedogenic carbonate that is still largely poorly understood is the origin of calcium in pedogenic carbonate minerals. Earlier studies reported that calcium ions can originate from either the weathering of previous carbonate rocks or minerals (calcite, dolomite, aragonite) or from the weathering of calcium-rich silicate minerals such as calcic plagioclase like Anorthite, Bytownite, Labradorite (Curtis Monger et al., 2015). Also, the efficiency of atmospheric carbon sequestration by pedogenic carbonates has been demonstrated when calcium comes from silicate minerals (Fig. 4.1). While the weathering of Ca-minerals such as anorthite (Eq. 4.1) consume CO_2 and precipitation of calcium carbonate emits CO_2 (Eq. 4.2). So far, the approaches used to trace the origin of the calcium contained in pedogenic carbonates are based mainly on radiogenic isotope analysis

(Dina Ebouel et al., 2024), including mostly the use of the strontium isotope ratio ($^{87}Sr/^{86}Sr$) of pedogenic carbonate and the possible parent material (Capo and Chadwick, 1999; Dietrich et al., 2017; Millière et al., 2019). Strontium is known for its geochemical behaviour similar to that of calcium, since the two elements have a similar atomic radius. Therefore, Sr is used to trace calcium (Capo et al., 1998). However, these methods are expensive and not readily available everywhere. It is therefore necessary to explore other approaches to trace the origin of calcium in pedogenic carbonates.

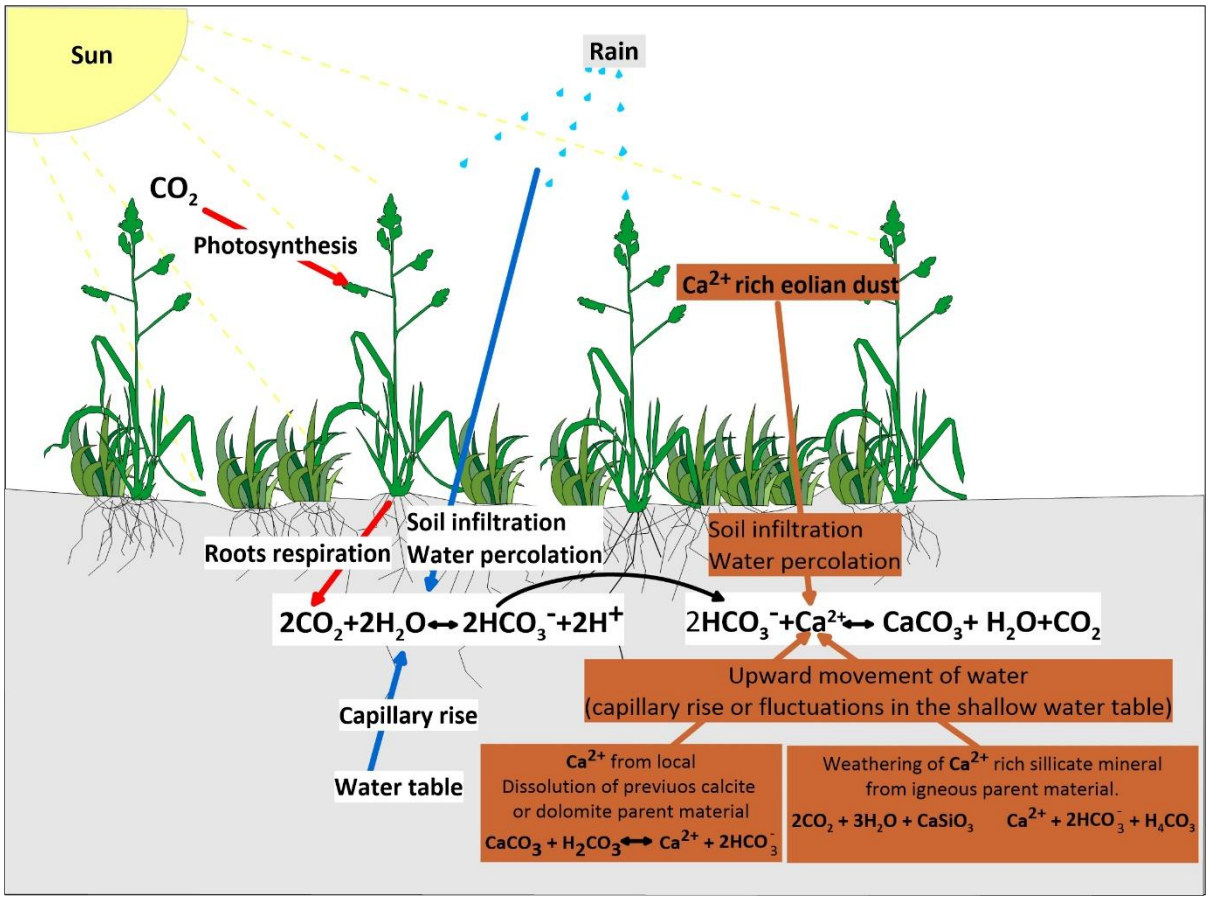


Fig. 4.1. A simplified model for pedogenic carbonate formation in arid environments

$$CaAl_2Si_2O_8 + 2CO_2 + 2H_2O \rightarrow Al_2Si_2O_5(OH_4) + Ca^{2+} + 2HCO_3^- \quad \text{Eq. 4.1}$$

$$Ca^{2+} + 2HCO_3^- \rightarrow CaCO_3 + CO_2 + H_2O \quad \text{Eq. 4.2}$$

The weathering index of Parker (Parker, 1970) and the chemical index of alteration (Nesbitt and Young, 1982), both developed to reflect the degree of chemical weathering of silicate

minerals, provide information about the origin of the parent material and the prevalent climate conditions. While the CIA gives priority to the subsequent accumulation of aluminium through the formation of phyllosilicate minerals, which is very interesting for analysing environmental changes, the WIP gives priority to highly mobile alkaline and alkaline-earth elements, which is very interesting in the context of chemical weathering without the accumulation of secondary clay minerals. Thus, their combination provides a scientifically reliable analysis of environmental changes and the mobility of alkaline and alkaline-earth elements such as calcium. In fact, by combining these chemical weathering indices with mineralogical analysis, it is possible to trace the origin, movement and accumulation of calcium within a soil profile. However, for soils formed above alluvial sediments, which are transitional materials in this circumstance, tracing the origin of these sediments can provide a better picture of all the processes involved and the nature of the source rocks. In an environment with potential presence of non-silicate minerals such as pedogenic carbonates or any authigenic and biogenic contribution, the addition of the robust chemical weathering index (RW) developed by Cho and Ohta (2022), could strengthen this approach and give a better picture of the processes involved, by identifying the type of parent material, the degree of chemical weathering, and hence the palaeoenvironmental conditions.

In northern Botswana, particularly in the Chobe Enclave, previous studies have highlighted the widespread presence of calcium carbonate in the soils (Diaz et al., 2019; Eze et al., 2021; Eze and Molwalefhe, 2024; Romanens et al., 2019). Although they have been considered by some authors to be the result of pedogenic processes (Eze and Molwalefhe, 2024; Romanens et al., 2019), lithogenic carbonate layers have also been reported (Diaz et al., 2019). It is therefore essential not only to differentiate the processes by which carbonates accumulate, but also to trace the origin of the calcium fixed in their structural composition. As mentioned above, the origin of calcium ions plays a key role in the discussion of the capacity of pedogenic carbonates

to trap carbon dioxide. A prominent open quarry in the Parakarungu plains, NW Botswana presents a rare exposure of approximately 6 m pedosedimentary sequence suitable for exploring calcium carbonate accumulation in soil environments.

This study aims to constrain the possible origin(s) of calcium in pedogenic carbonates, processes of alluvial sediment deposition and soil formation, and traces sediment provenance. The approach is based on the use of multiply proxies (morphological, physicochemical and geochemical soil/sediment characteristics). Geochemical weathering indices (CIA, WIP, and RW), mineralogy, and particle size distribution can help assess sediment origin and depositional conditions. The Ca/Sr ratios, combined with $CaCO_3$, Ca, and Mg contents, provides insights into calcium mobility, accumulation, and provenance. The results show that, in the absence of radiogenic or stable isotope data, the combined use of multiple geochemical proxies can help narrow down the plausible sources of calcium, even where a single, unambiguous origin cannot be established.

4.2. Geographical and environmental setting

The study area is located in the administrative district of Chobe in the northern part of Botswana, and the studied pedosedimentary section is located at 18.038333° S and 24.31163° E (Fig. 4.2). It is underlain by a graben resulting from an active fault system known as the Okavango Rift Zone. The origin and kinematics of this fault system is still under debate. It has long been considered the end member of the southwestern extension of the East African rift system (Bufford et al., 2012; Kinabo et al., 2007). Recent analysis suggests instead that it is a deformation zone hosting differential movements between the Nubian and Somali, Victoria and Rovuma plates, on the one hand, and between the rigid Congo and Kalahari cratons within the slightly less stable Nubian plate, on the other hand (Pastier et al., 2017). However, the sedimentary deposits that filled the graben have been related to the Kalahari Basin and characterised by fluvio-lacustrine sediments (Burrough and Thomas, 2008; Grey and Cooke,

1977; Ringrose et al., 2008). These sediments were deposited over several cycles beneath a Quaternary mega-peleolake, which, at its peak, covered an area of approximately 66,000 km^2 (Burrough et al., 2009). As highlighted in Mokatse et al. (2022), the actual landscape, which consists of sand dunes, pans, sand ridges, and carbonate islands, is the result of palaeoenvironmental and palaeodrainage changes through the Quaternary and is associated with (neo)tectonic processes. Carbonate islands are considered relics of palustrine environments dated between Marine Isotope Stage (MIS) 6 to MIS 1, which corresponds to a period from approximately 70,000 years ago to the present day (Diaz et al., 2019).

Throughout the year, temperatures generally vary between 9°C and 35°C. They rarely fall below 6°C and rarely exceed 38°C. The mean annual precipitation is 650 mm. According to Moses et al. (2023), one-day and three-day rainfall contribute significantly to seasonal totals (10% and 17%, respectively, on average but up to 30% in some years). Weather systems favouring rainfall include a deeper Angolan low and a weaker Botswana high. The rainy season begins in January and peaks in March, dominated by convective systems such as tropical cloud bands and moisture flows from the Indian Ocean and South Atlantic (Moses et al., 2023). While Arenosols are the dominant soil unit, there is a wide diversity of soils in the region, including Chernozems, Phaeozems, Kastanozems, Solonchaks, Solonetzs, and Calcisols (Romanens et al., 2019a). As reported by Eze and Molwalefhe (2024), pedogenic processes in the area involve a gradual obliteration of sediment layers and a consecutive carbonate concentration in the soil. The vegetation includes a mix of forested and grassland areas. The main forest vegetation types are Mopane forests, which are dominated by *Colophospermum mopane*, and Baikiaea forests, which are dominated by *Baikiaea plurijua, Baphia massaiensis, Croton gratissimus*. The grassland area is dominated by grass communities covered by a few *Acacia* spp., *Terminalia sericea* or *Philenoptera nelsii* (Vittoz et al., 2020).

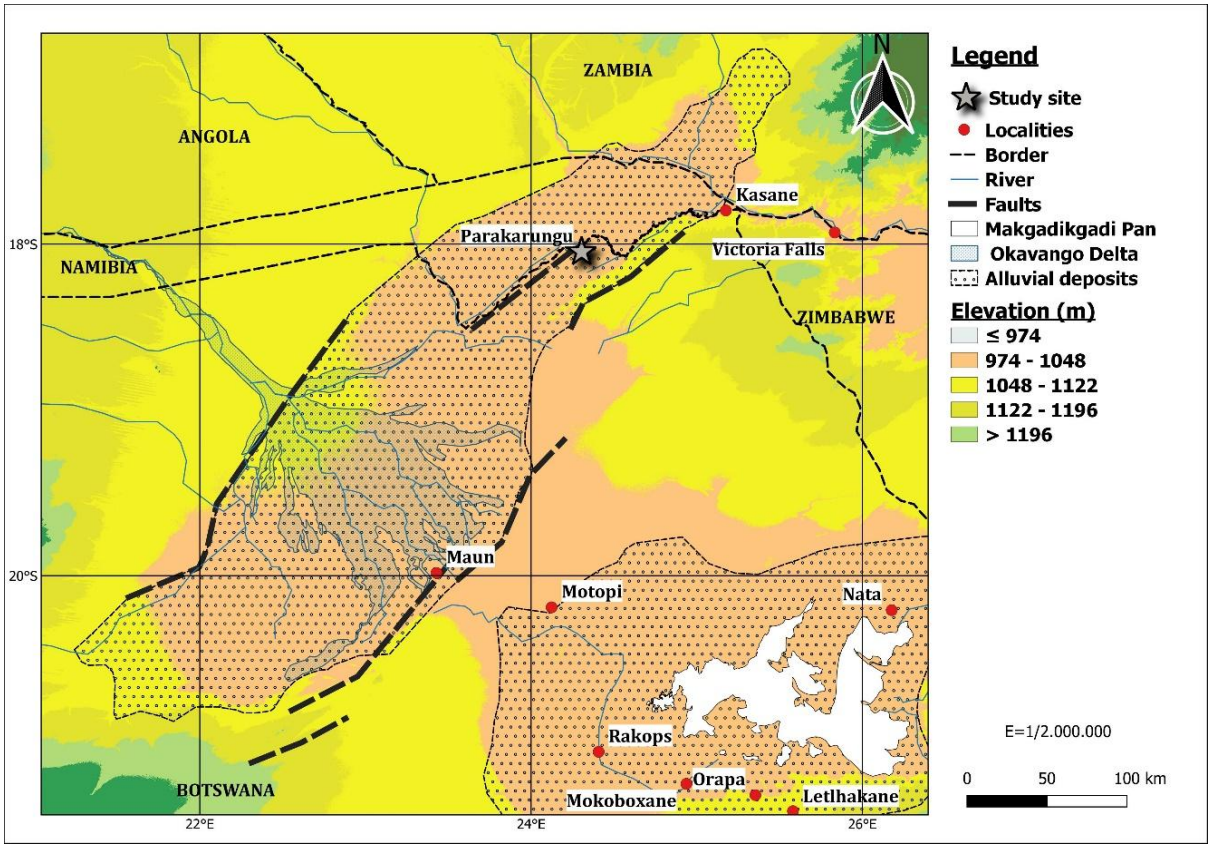


Fig. 4.2. Regional context of the study area showing the Parakarungu open quarry location

4.3. Materials and methods

4.3.1. Field investigation and sampling

A field trip was organised in September 2022 around the Chobe Enclave to identify and describe interesting soil sections developed on the alluvial sediments and presenting some evidence of pedogenic carbonate accumulation. For this purpose, a 10% HCl solution was used to test the presence of calcium carbonates. During this trip, a prominent pedosedimentary section of approximately 6 m was identified at the Parakarungu open quarry (Fig. 4.3). A description of the section was carried out according to FAO Guidelines for soil description (2006). After this, 13 soil and sediment samples were collected from each genetic soil horizons/layers. These samples were later shipped to the laboratory for analysis.

4.3.2. Laboratory analyses

4.3.3.1. Physicochemical soil characterisation

A subsample from each of the 13 collected samples was pre-treated prior to physicochemical analysis in the Soil Science laboratory of Botswana International University of Science and Technology. The pretreatments included air drying at room temperature, removal of large roots and sieving with a 2 mm sieve. The soil pH and electrical conductivity (EC) were determined in a 1/2.5 soil: deionised water ratio solution as recommended by FAO guideline for soil description (2006). The measurements were performed using a pH meter and EC glass electrodes. The particle size distribution of the samples was determined via laser diffraction granulometry, using a Malvern 2000 Mastersizer after pretreatment with a 30% hydrogen peroxide solution (H_2O_2) for 24 hours to remove organic matter, followed by further pretreatment with 10% hydrochloric solution (HCl) to remove carbonates and dispersion with sodium hexametaphosphate as a dispersant. The soil organic matter (SOM) content was determined via wet oxidation (Walkley and Black, 1934), and the carbonate content was determined via an Eijkelkamp calcimeter following the procedure described by Sherrod et al. (2002).

4.3.2.2. Bulk and clay mineralogy

Bulk mineralogy and clay mineralogy were carried out using different pretreatments. Two 10 g subsamples for each of the identified layers were taken. The first subsample, used for bulk mineralogy, was ground using an agate mortar. The second subsample, used for clay mineralogy, was treated with 30% H_2O_2 for 24 hours and then with a 10% HCl. After rinsing and decanting, the clay fraction was isolated and mounted on a glass slide. X-ray diffraction was carried out at the Materials Characterisation Laboratory of Botswana International University of Science and Technology using a Bruker D8 Advance powder diffractometer equipped with a Cu-tube X-ray source and a Lynx Eye XE energy-dispersive strip detector.

The radiation used was Cu-Kα radiation with a wavelength of 1.5418 A at 2θ values between 5 and 90 degrees for the bulk mineralogy and 5 to 30 degrees for the clay mineralogy, using a step of 0.02 degrees with a time of 0.200 sec/step. The machine was operated at 40 mA and 40 kV.

4.3.2.3. Bulk geochemistry

The analysis of the total elemental composition of the samples was carried out at the Minerals-Geochem Laboratory of SGS, Randfontein, South Africa. The suite of major oxides (reported in wt.%) was determined via the borate fusion method. A sample weighing 0.7 g was mixed with lithium tetraborate flux and fused to form a homogenous glass bead. The borate fusion was followed by analysis of the glass beads via a wavelength dispersive X-ray fluorescence spectrometer. The loss on ignition (LOI) at 1000 °C was determined separately by gravimetry. The minor and trace element contents were determined via the sodium peroxide fusion method. A sample (0.2–2.0 g) was weighed into a crucible containing Na_2O and NaOH. The mixture was then fused. The sample was leached, acidified and brought to volume. The sample was then analysed via inductively coupled plasma optical emission spectroscopy (ICP-OES) and the results reported in mg kg^{-1}.

4.3.2.4. Data processing

Various statistical analysis techniques were used to process the data. For the particle size distribution, the results obtained with the Malvern Mastersizer suggest seven distinct particle size classes based on the United States Department of Agriculture standard (Skaggs et al., 2001), including: very coarse sand (1000-2000 μm), coarse sand (500-1000 μm), medium sand (250-500 μm), fine sand (100-250 μm), very fine sand (50-100 μm), silt (2-50 μm) and clay (< 2 μm). Inclusive statistical variables, including kurtosis, skewness, standard deviation and mean, were calculated in MS Excel software to infer the palaeoenvironmental conditions of the deposit (Folk and Ward, 1957).

The XRD data were processed using Origin Lab software (version 2024) to identify the peaks of mineral phases, and a semiquantitative analysis was carried out based on a comparison of the relative intensities of the characteristic peaks of each phase calculated using MS Excel software.

The geochemical data were analysed via various indices and ratios as follows.

The CIA (Nesbitt and Young, 1982), calculated using the equation (Eq. 4.3) was combined with the clayeyness, calculated using Al/Si ratio (Sheldon and Tabor, 2009) to infer the degree of weathering and the palaeoenvironmental conditions.

$$\mathrm{CIA} = \left(\frac{\mathrm{Al_2O_3}}{\mathrm{Al_2O_3 + CaO^* + Na_2O + K_2O}}\right) \times 100 \qquad \text{Eq. 4.3}$$

Since CIA is based on the formation of clay as result of the chemical weathering, the WIP (Parker, 1970) calculated using the equation (Eq. 4.4) was also used to quantify the intensity of chemical weathering based on the depletion of base cations (Ca, Mg, Na, K), which could be useful for quantifying the mobility of elements in environments where the degree of weathering of silicate minerals is not consecutive with the formation of clays.

$$\mathrm{WIP} = \left(\frac{2\mathrm{Na_2O}}{0.35} + \frac{\mathrm{MgO}}{0.9} + \frac{2\mathrm{K_2O}}{0.25} + \frac{\mathrm{CaO^*}}{0.7}\right) \times 100 \qquad \text{Eq. 4.4}$$

The above indices and ratios were calculated using the molar content of the various oxides. The CaO* used to calculate CIA and WIP was estimated from the calcium oxide content of the fraction derived from silicate rocks only (Eq. 4.5). The CaO∗ correction aims to minimise CaO contributions from carbonate minerals, ensuring that the CIA only reflects weathering of aluminosilicate. The resulting value is adopted if the molar ratio of CaO* is less than that of Na_2O, otherwise CaO* is equivalent to Na_2O (McLennan, 1993).

$$\mathrm{CaO^*} = \mathrm{CaO} - 10/3 \times \mathrm{P_2O_5} \qquad \text{Eq. 4.5}$$

The index of Compositional Variability (ICV) expressed in equation (Eq. 4.6) was used to assess maturity of sedimentary material (Cox et al., 1995).

$$ICV = \frac{(Fe_2O_3 + K_2O + Na_2O + CaO^* + MgO + MnO + TiO_2)}{Al_2O_3} \quad \text{Eq. 4.6}$$

To calculate the ICV, the oxides are expressed as a mass percentage (wt. %), CaO* is the quantity of CaO contained in the silicate component of the rock, estimated in equation (Eq. 4.7). Correction of CaO∗ in the ICV removes carbonate-derived calcium, ensuring that the index accurately shows the proportion of alterable silicate minerals in the source(s).

$$CaO^* = 0.35 \times 2Na_2O/62 \quad \text{Eq. 4.7}$$

The RW index (Eq. 4.8) has been used to ascertain if there is an intervention of pedogenic accumulation (pedogenic carbonate, given the semi-arid actual environment) and to trace the origin of parent materials through the ternary diagram mafic–felsic–RW as explain by Cho and Ohta (2022).

$$RW = 0.152\ln(TiO_2) + 0.198\ln(Al_2O_3) + 0.148\ln(Fe_2O_3) - 0152\ln(MgO) - 0.503\ln(Na_2O) + 0.156\ln(K_2O) - 0.506 \quad \text{Eq. 4.8}$$

The Ca/Sr ratio calculated with mass percent value was used as an indicator of the geochemical fractionation between calcium and strontium during weathering and precipitation processes (Dietrich et al., 2017).

R software (version 4.2) was used to perform the statistical analyses, including principal component analysis for the major oxides, to identify the main trends along the section. A correlation between carbonate content and Ca concentrations was performed using linear regression to investigate the contribution of calcium to carbonate accumulation. Another correlation was performed between Ca and Sr contents via linear regression to verify their interdependence.

4.4. Results

4.4.1. Morphological characterisation and physicochemical properties

The section, which appears in an open quarry, reveals several layers of sediment capped by a relatively thin topsoil horizon (Fig. 4.3A). From the top to the bottom, is constituted by the following arrangement: A_1—AC—C_k—C_{kk}—C_{FS}—C_{VFS}. The morphological characteristics are described in Table 4.1, and the physicochemical properties are summarised in Table 4.2. The description layer by layer is presented from top to bottom as follows:

The topsoil horizon A_1, from 0 to 24 cm depth, is characterised by a gray colour (10YR 5/1) when dry and a black colour (10YR 2/1) when wet. The texture is sandy loam, root activity is abundant, and there are a few termite galleries. The 10% HCl acid test reveals that it is moderately calcareous, which is also consistent with carbonate content of 5.7 wt.%. The organic matter (OM) content is 0.5 wt.%, which represents a very low OM content. The pH is 7.9, corresponding to a moderate alkaline pH, and the electrical conductivity (EC) is 220 $\mu S.cm^{-1}$, referring to a non-saline environment.

The AC horizon under the topsoil, from 24 to 63 cm depth and gray in dry conditions (10YR 6/1), evolves to dark gray (10YR 4/1) with moisture. It represents a gradual transition from the topsoil to the sedimentary layers below. It is also moderately calcareous, with a carbonate content of 8.1 wt.%, with a strong- to moderate granular structure, but the texture is loamy sand, similar to that of the sedimentary layer immediately below. The OM content is approximately 0.4 wt.%, corresponding to very low OM. The pH is 8.1, reflecting a moderately alkaline environment and the EC is 190 $\mu S.cm^{-1}$, corresponding to non-saline medium.

The C_k layer (subdivided into C_{k1} and C_{k2}), from 63 to 210 cm depth, appears light gray when dry (10YR 7/1) and dark gray when wet (10YR 4/1). It exhibits a weak-to moderate granular structure, a sandy loam texture, and shell fragments (see Fig. 4.3B) and dead roots are present. The 10% HCl test reveals that this layer is strongly calcareous, the carbonate content is ranged

from 11.7 wt.% to 13.9 wt.%. However, the carbonate is in a powdery form, coating sand grains and shell fragments or filling cavities left by termites and dead roots (see Fig. 4.3C). The OM content is very low, ranged from 0.2 wt.% to 0.3 wt.%. From the top to the bottom of the layer, the pH slightly increases from 8.2 to 8.6, reflecting an evolution from moderate to strong alkaline medium and the EC increased sharply from 190 to 550 $\mu S.cm^{-1}$, but remains non-saline.

The C_{kk} layer (subdivided into C_{kk1} and C_{kk2}) extends from depths of 210 to 283 cm. It is distinctly separated from the previous boundary by a sharp boundary and has a very pale brown colour (10YR 8/2) when dry, which becomes light yellowish brown (2.5YR 6/4) when wet. The structure is weak-to moderately blocky and subangular, and the texture is loamy sand. The 10% HCl test reveal strong calcareous layer, which is supported by a carbonate content of 23 wt.%. Carbonate is more abundant but still in powdery form, preferentially accumulating in cavities left by termites and dead roots. From C_{kk1} to C_{kk2}, the OM content remained at approximately 0.2 wt.%, thus reflecting a very low OM content. The pH is ranging between 9.1 and 9.5, referring a strong alkaline level, and the EC slightly increased from and from 580 to 780 $\mu S.cm^{-1}$, remains non-saline.

The depth of the fine sand layer C_{FS} ranged from 283 to 343 cm. The transition from the previous layer is sharp, and the layer is characterised by a white colour (2.5YR8/1) under dry conditions and a pale brown colour (2.5YR8/2) under wet conditions. The structure is massive, and the texture is sandy. It is non-calcareous with a carbonate content of 0.3 wt.%, indicating a relatively sharp decrease compared with that of the previous layer (C_{kk}). The OM content is approximately 0.2 wt.%, consistent with a very low OM content. The EC is 200 $\mu S.cm^{-1}$, which is also a considerable reduction compared with that of C_{kk} and correspond to a non-saline environment. In contrast, the soil pH remained unchanged at 9.5, corresponding to strong alkaline medium.

At the bottom of the section, there is a succession very fine sandy layers (C_{VFS}), extending from 343 to +500 cm. The boundaries between layers are distinct, but the colour is similar. They are generally light gray (2.5YR7/1) when dry and turn gray (2.5YR5/1) when wet. The structure is massive, and the texture is sandy loam, except for a single sublayer of silty loam (C_{VFS5}). Although they all contain common gravels (10 to 20 vol.%) embedded in the very fine sand matrix, some sublayers contain black gravels (5Y2.5/1) that are clearly distinguishable from the sandy matrix (see Fig. 4.3D). Other sublayers contain brownish-yellow gravels (10YR6/6) whose progression towards the matrix reveals a reddish crown (see Fig. 4.3E). The OM content values in these layers are around 0.2 wt.%, except for the bottom sublayer (C_{VFS6}), whose OM content is approximately 0.4 wt.%. The carbonate content is less than 1 wt.%, while the pH decreases overall from 9.2 to 7.1 between the top and the base, ranging from very strong to moderate alkaline level. The EC has the highest values in the section. However, it fluctuates from one sublayer to another, although the overall trend increases towards the base. The maximum is observed at the second sublayer (4650 $\mu S.cm^{-1}$), which correspond to moderately saline environment.

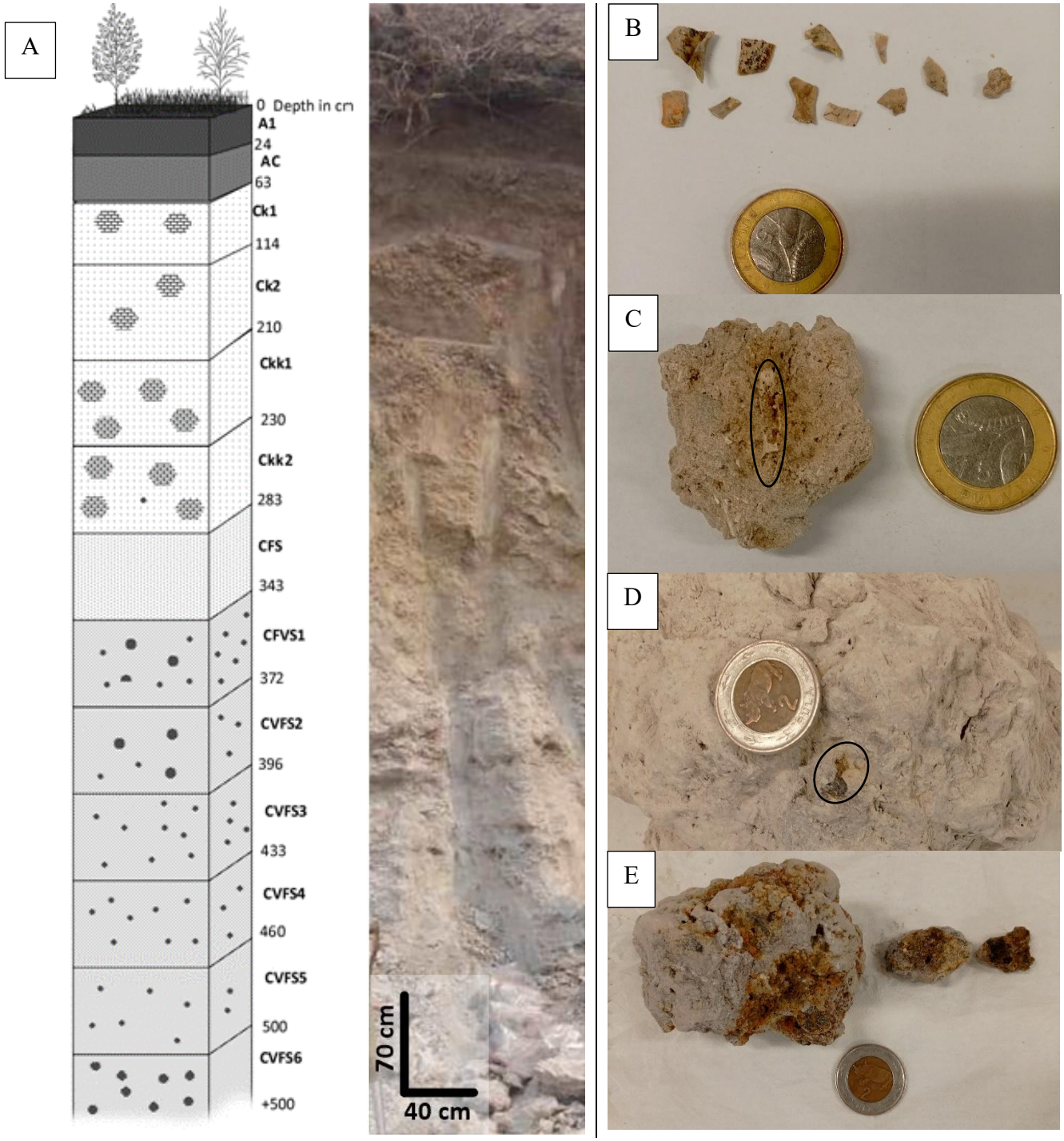


Fig. 4.3. A. Schematic representation and photograph of the section of the Parakarungu open quarry; B. shell fragments observed in the Ck layer; C. accumulation of carbonate in the tunnels left by termites in C_{kk} layers; D. gravel in the fine sand matrix of C_{VFS} layers; E. gravel showing signs of weathering (oxidation) in C_{VFS} layers.

Table 4.1. Morphological properties of the section

Horizon/Layer	Depth (cm)	Colour moist	Colour dry	Secondary features	Secondary features colour	Structure	Carbonate test (10% HCl)	Carbonate features	Biological activity
A_1	0-24	10YR5/1 Gray	10YR2/1 Black	No visible	-	strong to moderate granular	Moderate calcareous	No visible	Abondant roots, few termites galleries
AC	24-63	10YR6/1 Gray	10YR4/1 Dark gray	No visible	-	strong to moderate granular	Moderate calcareous	No visible	Common roots, termites galleries, few mollusc shells
C_{k1}	63-114	10YR7/1 Light gray	10YR4/1 Dark gray	interstitial carbonate powder, filling cavities left by dead roots and termite galleries	10YR7/1Light gray	Weak to moderate granular	Strongly Calcareous	Interstitial carbonate powder, filling cavities left by dead roots and termite galleries	few dead roots, common termites galleries, few mollusc shells
C_{k2}	114-210	10YR7/1 Light gray	10YR4/1 Dark gray	Diffuse carbonate powder and fine soft carbonate concretion		Weak to moderate granular	Strongly Calcareous	Diffuse carbonate powder and fine soft carbonate concretion	Few mollusc shells
C_{kk1}	210-230	10YR8/2 very pale brown	2.5YR6/4 Light yellowish brown	Common black soft inclusion	10YR7/1Light gray	Weak to moderate blocky subangular	Strongly Calcareous	Diffuse carbonate powder	Termites galleries
C_{kk2}	230-283	2.5YR7/3 Pale brown	2.5YR6/4 Light yellowish brown	Common black soft inclusion	10YR7/1Light gray	Weak to moderate blocky subangular	Strongly Calcareous	Diffuse carbonate powder	Termites galleries
C_{FS}	283-343	2.5YR8/1 White	2.5YR8/2 Pale brown			Massive	Non Calcareous		
C_{VFS1}	343-372	2.5YR8/1 White	2.5YR8/2 Pale brown	Common medium gravel	5Y2.5/1 Black	Massive	Slightly Calcareous		
C_{VFS2}	372-396	2.5YR7/1 Light gray	2.5YR5/2 Grayish brown	Common medium gravel with oxydation marks	10YR6/6 Brownish yellow	Massive	Slightly Calcareous		
C_{VFS3}	396-433	2.5YR8/2 Pale brown	2.5YR7/1 Light gray	Few medium gravel with oxydation marks	10YR6/6 Brownish yellow	Massive	Non Calcareous		
C_{VFS4}	433-460	2.5YR7/2 Light gray	2.5YR5/1 Gray	Common medium gravel with oxydation marks	10YR6/6 Brownish yellow	Massive	Non Calcareous		
C_{VFS5}	460-500	2.5YR7/2 Light gray	2.5YR5/1 Gray	Common medium gravel	5Y2,5/1 Black	Massive	Non Calcareous		
C_{VFS6}	500+	2.5YR7/2 Light gray	2.5YR4/1 Dark gray	Common medium gravel with oxydation marks	10YR6/6 Brownish yellow	Massive	Slightly Calcareous		

Table 4.2. Physicochemical properties of the section

Horizon or layer	EC	pH (H_2O)	OM	$EqCaCO_3$	Clay (<2 µm)	Silt (2 - 50 µm)	Sand (50-2000 µm)	Texture
Unit	µS/cm	-	wt.%		vol.%			
A_1	220	7.9	0.52	5.71	4.27	45.41	50.32	sandy loam
AC	190	8.1	0.38	8.12	1.06	14.41	84.53	loamy sand
Ck_1	190	8.2	0.32	11.70	1.33	18.31	80.36	loamy sand
Ck_2	550	8.6	0.25	13.96	0.58	12.9	86.53	loamy sand
C_{k1}	580	9.1	0.22	22.81	0.11	13.52	86.37	loamy sand
C_{k2}	780	9.5	0.18	23.13	1.36	14.98	83.66	loamy sand
C_{FS}	200	9.5	0.19	0.33	0.63	5.8	93.57	sand
C_{VFS1}	1081	9.2	0.19	0.44	2.73	38.00	59.27	sandy loam
C_{VFS2}	4650	7.7	0.21	0.88	2.45	28.16	69.39	sandy loam
C_{VFS3}	2050	7.9	0.20	0.18	2.61	40.92	56.47	sandy loam
C_{VFS4}	2570	7.4	0.22	0.22	3.47	40.18	56.35	sandy loam
C_{VFS5}	1700	7.5	0.22	0.16	3.44	51.58	44.98	silty loam
C_{VFS6}	1330	7.1	0.38	0.28	2.96	37.04	60.00	sandy loam

The particle size distribution is shown in Table 4.2. Over the whole section, sand is the dominant fraction, most often greater than 50 vol.%, whereas clay is the lowest fraction, generally around 1 vol.%. A_1 has a different composition from the other upper layers of the section (from AC to C_{kk2}). It has relatively high clay (5 vol.%) and silt (45 vol.%) contents and a relatively lower sand fraction (50 vol.%), whereas the other layers in the upper part of the section (from AC to C_{kk2}) are characterised mainly by a very low clay fraction (approximately 1 vol.%), lower values of the silt fraction (approximately 15 vol.%) and a very high sand fraction (over 80 vol.%). The C_{FS} layer is characterised by the highest value of the sand fraction (93 vol.%), while the clay fraction is less than 1 vol.%, and the silt fraction is 5 vol.%. From C_{VFS1} to C_{VFS6}, the sand fraction decreases. It is approximately 60 vol.% overall, whereas the

silt and clay fractions increase. These values are approximately 35 vol.% and 3 vol.%, respectively.

The inclusive statistical results of the particle size distributions ranged according to Folk and Ward (1957) classification are presented in Fig. 4.4. Kurtosis, which measures the peak of the grain size distribution, reveals five main sequencies. The A_1 horizon with a kurtosis equal to 1.1 is mesokurtic, showing a normal distribution of the grain size. The kurtosis of the layer AC is 1.6, corresponding to very leptokurtic, reflecting a high peak in the distribution. From layers C_{k1} to C_{kk2}, the kurtosis is between 1.3 and 1.5, corresponding to a leptokurtic kurtosis, indicating a moderate peak in the distribution. The layer C_{FS} has a kurtosis of 1.8, indicating a very leptokurtic distribution and represented by a high peak in the distribution. The lower layers (from C_{VFS1} to C_{VFS6}) show a kurtosis ranged from 0.6 to 0.9, corresponding to a platykurtic kurtosis, indicating a flat distribution. The skewness which represents the asymmetry of the grain size distribution presents four groups of values. In the layer A_1, the skewness is 0.28 (fine skewed), indicating an asymmetric distribution influenced by finer grains. From AC to C_{kk2}, the skewness is ranged from 0.35 to 0.52 (strongly fine skewed), reflecting an asymmetric distribution dominated by fine particles. The bottom of the section (from C_{FS} to C_{VFS6}) with exception of the layer C_{VFS2} is characterised by skewness values ranged from 0.16 to 0.28 (fine skewed), demonstrating an asymmetric distribution dominated by finer grains. The layer C_{VFS2} is strongly fine skewed (Ski = 0.37). The standard deviation describes the degree of sorting. It shows three typical trends. The upper part of the section (A_1 to C_{kk2}) is characterised by values between 1.13 and 1.96, corresponding to poorly sorted layers and indicating significant variation in grain size. The standard deviation in the C_{FS} layer is 0.86 indicating a moderately sorted layer, showing a relatively uniform distribution. The lower layers (C_{VFS1} to C_{VFS6}) are characterised by values between 2.54 and 2.88, all very poorly sorted, showing extreme variation in grain size. The mean indicates the average of particle. The upper part of the section

(A_1 to C_{FS}) is dominate by change in the mean of particle. The layer A_1 is characterised by an average of silt particles in (Mz = 4.59). while the layers AC and C_{k1} and C_{kk2} are dominated by very fine sand particle (Mz is egal to 3.01, 3.35, and 3.04 respectively). The layers C_{k2}, C_{kk1} and C_{FS} are represented by an average of fine sand particles (Mz is egal to 2.95, 2.95 and 2.65 respectively). The bottom of the section (C_{VFS1} to C_{VFS6}) with exception of C_{VFS5} are characterised by an average of very fine sand particles. The layer C_{VFS5} is characterised by an average of silt particles in (Mz = 4.36).

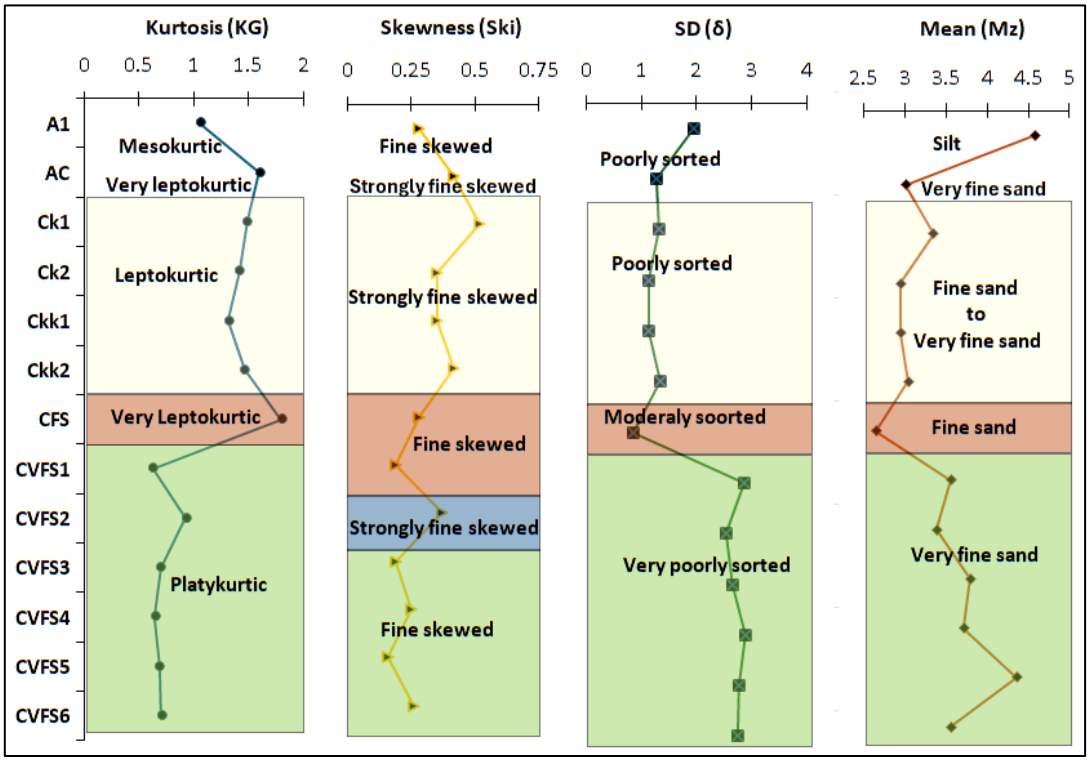


Fig. 4.4. Particle size distribution based on inclusive statistics parameter (Folk and Ward, 1957).

4.4.2. Bulk and clay mineralogy

The semiquantitative results of the bulk and clay mineralogy are presented in Table 4.3. It is important to emphasise that the clay fraction is very low (less than 5 wt.%). Consequently, the proportions of mineralogical clay expressed in Table 4.3 are estimated in accordance with the relative abundance of the clay minerals identified. The overall pattern shows that quartz is the

dominant mineral (> 50 wt.%) in the section in the bulk fraction, while montmorillonite is the dominant clay mineral (> 50 wt.%) in the upper part of the section (A_1— C_{kk}), and kaolinite is most represented (> 50 wt.%) in the lower part (C_{VFS} layers). The second most represented mineral in the bulk fraction is antigorite (10-25 wt.%), which appears throughout the section but shows a relative decrease in the lower part of the section. The bulk mineralogy also shows that calcite only appears in the upper layers (A_1—C_{kk}). The maximum concentration of calcite is observed in the layer C_{kk} (25-50 wt.%). Some minerals, such as aragonite (C_k layer), muscovite (C_k and C_{VFS} layers), enstatite (C_{kk} layer), ilmenite (C_{FS} layer), and goethite (C_{VFS} layers), were also observed in minor proportions in the bulk fraction (<10 wt.%). Illite is also well represented in the clay fraction throughout the section (10-25 wt.%).

Table 4.3. Semiquantitative composition of the bulk and clay mineralogy of the Parakarungu open quarry section

	Bulk mineralogy		***Clay mineralogy**	
Layer	Mineral	Abundance	Mineral	Abundance
	Quartz	++++	Montmorillonite	+++
	Antigorite	++	Kaolinite	++
	Calcite	+	Illite	++
A			Chlorite	+
	Quartz	++++	Montmorillonite	++++
	Antigorite	++	Illite	++
	Calcite	++	Kaolinite	++
	Muscovite	+	Chlorite	+
Ck	Aragonite	+		
	Quartz	++++	Montmorillonite	++++
	Calcite	+++	Illite	++
	Antigorite	++		
Ckk	Enstatite	+		
	Quartz	++++		
	Antigorite	++		
CFS	Ilmenite	+		
	Quartz	++++	Kaolinite	++++
	Kaolinite	++	Illite	++
	Antigorite	+	Montmorillonite	+
	Goethite	+		
CVFS	Muscovite	+		

++++: > 50%; +++: 25-50%; ++: 10-25%; +: <10%

** All the samples in this study are very low in clay: the clay fraction is less than 5%. The representation symbols used for clay mineralogy are therefore based on the relative proportions of clay minerals.*

4.4.3. Geochemistry

The composition of the major oxides in mass percentage (wt.%), as well as the CIA, the WIP, the RW all in percent, the strontium concentration in mg kg^{-1} and the ICV are shown in Table 4.4. For the major oxides, four different trends were identified, as shown in the correlation

circle (Fig. 4.5A). Specific high concentrations can be observed in certain layers or relatively invariant concentrations along the section (Fig. 4.5B). SiO_2 is the dominant oxide, with relatively high values throughout the section. They are generally higher than 70 wt.%. In contrast, K_2O, although not the oxide with the lowest concentrations, shows very low and relatively stable values throughout the section, all below 0.2 wt.%. On the other hand, two subgroups of oxides are observed with radically opposite trends. The first consists of CaO, MgO and MnO, characterised by relatively high values in the upper part of the section (A_1 to C_{FS}). The values are above 3 wt.%, 0.9 wt.% and 0.4 wt.% for CaO, MgO and MnO, respectively. However, they are all low in the bottom part of the section (C_{FVS} layers), below 2 wt.%, 0.6 wt.% and 0.03 wt.%, respectively. The other subgroup is made up of Al_2O_3, Fe_2O_3, Na_2O and TiO_2, which are characterised by generally low concentrations in the upper part of the section (less than 0.6 wt.%, 2 wt.%, 0.2 wt.% and 0.2 wt.%, respectively), whereas the lower part (C_{VFS} layers) is characterised by generally high values. They can even reach 10, 5, 3 and 2 times the concentrations observed in the upper part for Al_2O_3, Fe_2O_3, Na_2O and TiO_2, respectively.

For the RW index, the upper part of the section (A_1—C_{FS}) is characterised by a range of values between 10% and 22%. In the lower part (C_{VFS} layers), the values are between 25% and 33%. However, the C_{kk1}, C_{k1} and C_{kk2} layers have the lowest values, with 10.52, 15.06 and 16.28% respectively. The CIA generally exhibits weak values in the upper part of the profile (A_1—C_{kk2}), whereas those observed in the lower part are generally high. They range from 2 to 7% in the upper part, compared with 31 to 72% in the lower part. The WIP presented globally high values in the top part, ranging from 13—36%, whereas they were low in the bottom part, ranging from 2—10%. The ICV typically shows two contrasting trends. The upper part of the section (A_1 to C_{kk2}) is characterised by high values ranged from 9.94 to 37.7. The layer C_{FS} is

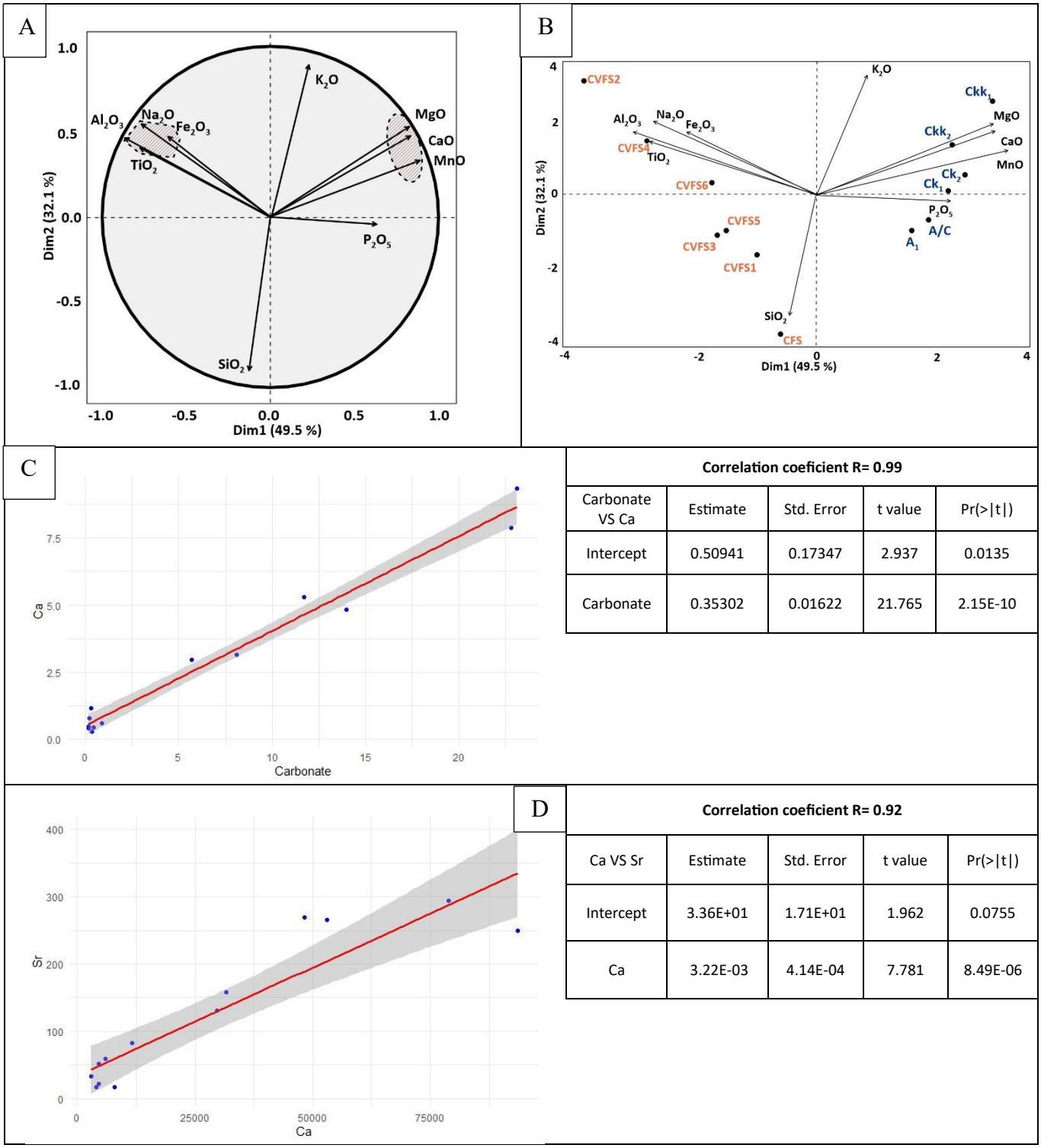
characterised by an ICV of 2.3 whereas the bottom part of the section (C_{VFS1} to C_{VFS6}) is presenting values below 1, ranged from 0.37 to 0.91.

Table 4.4. Composition of major oxides, robust index of chemical weathering (RW), chemical index alteration (CIA), weathering index of Parker (WIP), index of compositional variability (ICV) and strontium content in the Parakarungu open quarry

Horizon /Layer	Depth (cm)	Al_2O_3	CaO	Fe_2O_3	K_2O	MgO	MnO	Na_2O	P_2O_5	SiO_2	TiO_2	RW	CIA	WIP	ICV	Sr
		wt.%										%			-	mg kg^{-1}
A_1	0-24	0.48	3.42	1.06	0.12	0.94	0.04	0.13	0.12	88.40	0.12	21.66	6.88	13.43	9.94	131
AC	24-63	0.49	4.74	1.41	0.12	1.01	0.04	0.12	0.14	85.80	0.12	23.16	5.24	16.87	12.55	158
C_{k1}	63-114	0.51	6.73	1.22	0.13	1.28	0.04	0.22	0.14	81.80	0.10	15.06	3.87	23.69	16.67	265
C_{k2}	114-210	0.50	7.06	1.54	0.14	1.58	0.05	0.12	0.08	80.80	0.12	21.69	3.66	24.57	18.14	269
C_{kk1}	210-230	0.39	12.00	1.66	0.16	2.04	0.06	0.33	0.03	71.50	0.11	10.52	1.70	40.57	37.70	294
C_{kk2}	230-283	0.37	11.50	1.56	0.16	1.32	0.04	0.19	0.02	74.00	0.09	16.28	1.70	36.03	35.95	250
C_{FS}	283-343	0.27	0.19	1.02	0.04	0.15	0.02	0.13	<0.01	98.70	0.11	21.70	30.96	2.43	2.38	33
C_{VFS1}	343-372	1.24	0.38	0.99	0.11	0.20	0.02	0.28	0.01	92.00	0.14	26.04	49.51	5.03	0.91	22
C_{VFS2}	372-396	6.45	0.70	7.57	0.17	0.54	0.02	0.63	0.01	76.90	0.30	32.93	72.18	10.51	0.37	59
C_{VFS3}	396-433	2.38	0.31	0.98	0.10	0.28	0.02	0.39	0.01	89.60	0.17	23.73	64.55	6.00	0.53	52
C_{VFS4}	433-460	4.16	0.95	10.10	0.12	0.46	0.02	0.45	0.02	75.80	0.21	33.32	61.65	8.84	0.532	17
C_{VFS5}	460-500	2.43	0.43	1.02	0.11	0.27	0.02	0.37	0.01	89.00	0.16	25.21	61.80	6.18	0.56	17
C_{VFS6}	500+	2.41	1.27	10.60	0.11	0.41	0.01	0.31	0.02	75.00	0.11	33.08	45.17	8.14	0.92	83

The strontium (Sr) concentration is globally high in the upper part of the section (A_1—C_{kk2}), ranging from 131—294 mg kg^{-1}. In contrast, relatively low values are shown at the bottom (C_{FS} to C_{VFS6}). Linear regression between carbonate and Ca shows a very strong positive correlation between the carbonate content and the Ca concentration with a correlation coefficient R = 0.99 (see Fig. 4.5C). The obtained prediction model also reveals a highly significant relationship, characterised by a p-value of 2.15×10^{-10}, which is well below the significance level of 0.05. The regression analysis of strontium and calcium (Fig. 4.5D) reveals a strong significant dependence on the distribution of these two elements across the section. The p-value is extremely low (8.49×10^{-6}), demonstrating that their relationship can be represented via a linear

regression model and supporting the use of the Ca/Sr ratio to analyse the movement of calcium along the section.



Correlation coeficient R= 0.99				
Carbonate VS Ca	Estimate	Std. Error	t value	Pr(>|t|)
Intercept	0.50941	0.17347	2.937	0.0135
Carbonate	0.35302	0.01622	21.765	2.15E-10

Correlation coeficient R= 0.92				
Ca VS Sr	Estimate	Std. Error	t value	Pr(>|t|)
Intercept	3.36E+01	1.71E+01	1.962	0.0755
Ca	3.22E-03	4.14E-04	7.781	8.49E-06

Fig. 4.5. A. Correlation circle of major oxides; B. Biplot samples-major oxides; C. results of linear regression between carbonate and calcium; D. results of linear regression between Calcium and strontium

The Ca/Sr ratio shown in the Fig. 4.6A falls within a wide range of values from 189 to 1011 and shows no typical trend along the section. However, the upper part of the section generally has a relatively high ratio. The maximum (Ca/Sr = 1011), on the other hand, is observed in the C_{VFS4} layer at the bottom of the section. The C_{VFS5} layer also has a relatively high ratio.

The Al/Si ratio presented in the Fig. 4.6B shows weak values all along the section, ranged from 0.003 to 0.098. This is consistent to the high proportion of SiO_2 and the domination of the sand fraction in the section as shown by the result of particle size distribution. Nevertheless, relative low values are observed in the upper part of the section (A_1 to C_{FS}) ranged from 0.003 to 0.007, while relatively high values are observed at the bottom (C_{VFS}), ranged between 0.016 and 0.098. The maximum (0.098) is observed in layer C_{VFS2}.

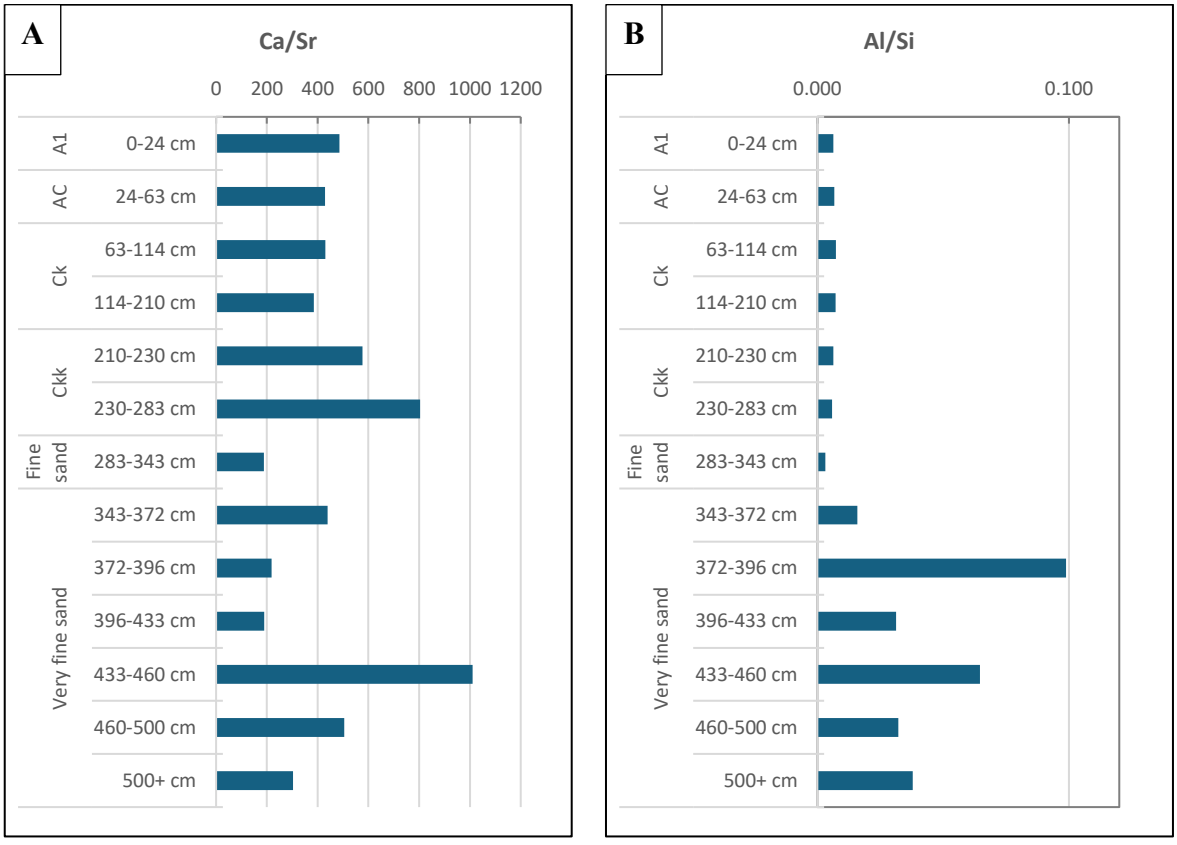


Fig. 4.6. A. Trends of Ca/Sr along the section; B. Trends of Al/Si along the section.

The projection of the Parakarungu samples in the Mafic-felsic-RW diagram (Cho and Ohta, 2022) is shown in the Fig. 4.7. While all the samples show a proximity to the felsic pole and a

low degree of chemical weathering, there is also a clustering around two blocks. The first group made up of the layers in the upper part of the section (A_1—C_{kk2}) is much closer to the felsic pole and some samples have undergone a very low degree of chemical weathering to the point of being projected into the fresh igneous rock zone (C_{kk1}, C_{kk2}, C_{k2}). The C_{FS} layer appears slightly above this group (from the felsic pole to the mafic pole) and seems to represent a transition to the second group. The second group, made up of the layers in the lower part of the section (the C_{VFS} layers), although still located in the felsic half of the diagram, slightly evolved to the mafic pole. Samples from this group would have undergone a greater degree of weathering than those from the first group. It should be noted, however, that two sub-groups stand out within this second group. Sub-group A (C_{VFS2}, C_{VFS4} and C_{VFS6}) has a relatively higher degree of chemical weathering and is derived from a relatively more felsic parent material, whereas sub-group B (C_{VFS1}, C_{VFS3} and C_{VFS5}) is relatively less altered and is derived from a relatively more mafic parent material (but still felsic).

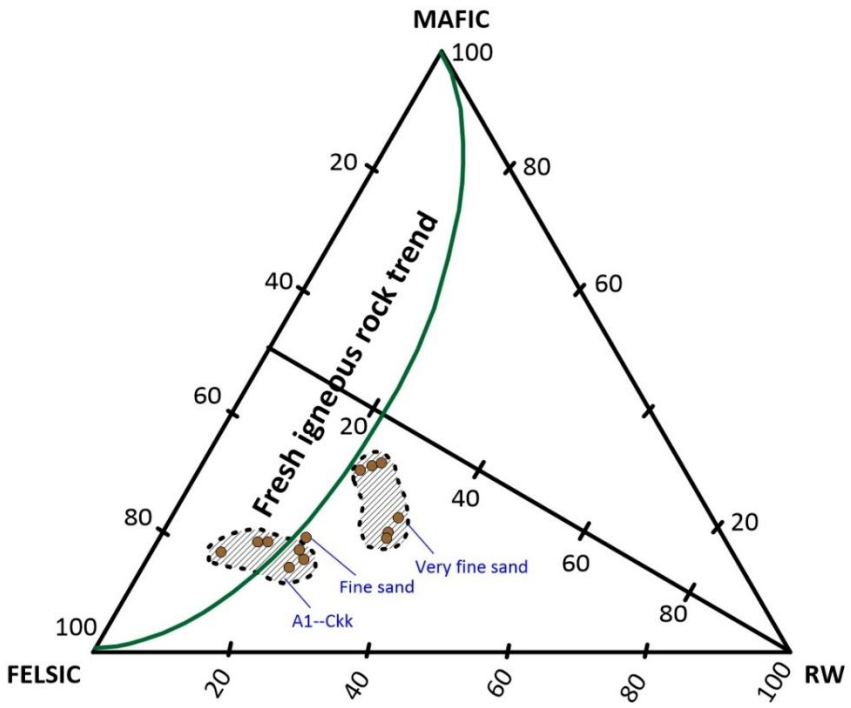


Fig. 4.7. Projection of Parakarungu samples in the ternary diagram: Mafic-Felsic-RW

4.5. Discussion

4.5.1. Implications for pedogenic processes and depositional environment

The Parakarungu section consists of relatively poorly developed soil overlying three cycles of sedimentary deposition (see Fig. 4.3A). Pedogenic processes are generally observed in the first two layers (horizons) A_1 and AC. These horizons are characterised by a gradual transition down to the subjacent horizon or layer, typical of pedogenesis (FAO guideline for soil description 2006). The dark colour of the A_1 horizon highlights the melanisation due to the high contribution of OM under conditions of low decomposition (Prescott and Vesterdal, 2021). This dark colour and the presence of carbonate in the horizon reflect the characteristics of the mollic horizons observed in the Kastanozems (Spaargaren, 2008). These moderately calcareous horizons (5.71—8.12 wt.%) could suggest that calcification, i.e. the accumulation of carbonates, is a key pedogenetic process in the developing soil. This is a common occurrence in dry environments where there are limited rainfall and high evaporation, resulting in the accumulation of calcium carbonate in the soil (Naorem et al., 2022). Moreover, numerous studies have highlighted the prevalence of this process in the region (Eze et al., 2021; Eze and Molwalefhe, 2024; Matshameko et al., 2023). The two pedogenic features described (dark colour of the A_1 and accumulation of pedogenic carbonate) are characteristic of the Kastanozems (IUSS Working Group WRB, 2022). Nevertheless, the high proportion of the sand fraction observed (>50 vol.%) is characteristic of Arenosols (IUSS Working Group WRB, 2022). Consequently, this soil can be classified as arenic Kastanozem, with characteristics of both Kastanozem (major) and Arenosol. Moreover, arenic Kastanozems with similar characteristics have already been identified in the region (Romanens et al., 2019).

The layers below AC correspond to sedimentary deposits, characterised by a regular and sharp transition between the layers, a weak level of pedogenic activity, and sporadic shell fragments

(FAO guideline for soil description 2006). The statistics on particle size distribution and mineralogy reveal three distinct phases in the evolution of the deposition environment.

The carbonate-rich sand layers (C_k and C_{kk}) exhibit fine- to very fine-grained sand, with poor sorting, leptokurtic kurtosis, and a strongly fine-skewed distribution. These characteristics reflect deposition in a low-energy environment with fluctuating flow conditions (Folk and Ward, 1957). The poor sorting and strong fine skewness indicate an abundant fine suspended load and less effective winnowing, typical of overbank deposition (Awasthi, 1970). The high calcite content in these layers (10—50 wt.%) could indicate detrital carbonate accumulation, suggesting a change in the river's provenance to include carbonate bedrock (Müller et al., 2022). Moreover, this type of carbonate accumulation has been documented in the area (Diaz et al., 2019). It can also be the result of authigenic precipitation (possibly pedogenic), suggesting a shift towards the actual semi-arid conditions (Ferdush and Paul, 2021). Besides, the carbonate features are mainly concentrated around dead roots or in channels left by termites. Therefore, the pedogenic process should be considered a significant contributor to the accumulation of carbonates in these layers. Furthermore, the prevalence of semi-arid conditions is also supported by the dominance of montmorillonite within the clay fraction (Reinoso Carbonell et al., 2022).

The fine-grained sand layer (C_{FS}) is characterised by very leptokurtic, fine-skewed, and moderately sorted sediments. These characteristics indicate a more energetic and coherent flow regime (Folk and Ward, 1957). The moderate sorting and highly leptokurtic distribution imply efficient transport and sorting by a dominant process (Das et al., 2025), while the fine skewness suggests that fine-grained particles were still present, perhaps because of a decreasing flow (Javanbakht et al., 2022). Such features reflect deposition in an active fluvial channel (Ghsoub et al., 2020), suggesting that the fluvial channel was much closer to or actively crossing the study site. This phase is represented by a thinner layer, at 60 cm thick compared to 220 cm for

the upper phase (C_k and C_{kk}) and more than 250 cm for the lower phase (C_{VFS}). This can suggest a relatively short period of deposition. This implies a shift in the depositional environment, most likely associated with tectonic uplift and erosion, revealing a less weathered bedrock (Mokatse et al., 2022a).

The very fine-grained sand layers (C_{VFS}) are characterised by platykurtic, fine skewed, and very poorly sorted sediment layers. These picture a very low-energy, calm environment with highly variable deposition and/or a mixture of several sediment populations, where fine skewness highlights the significant settling of fine-grained particles (Folk and Ward, 1957). This could indicate a variety of environments, such as a low-energy lake, a quiet lagoon, or a deep-water area far from shore, where fine sediments can accumulate without being disturbed by strong currents or waves action (Awasthi, 1970). However, the current case could correspond to a shallow lacustrine environment, justified by variations in deposits and the mixing of several sediment populations (Vessia and Di Curzio, 2018). Moreover, the shift from a shallow lacustrine environment to the current alluvial floodplain has also been demonstrated by numerous studies in the region (Mokatse et al., 2023; Vainer et al., 2024). Furthermore, the dominance of kaolinite in the clay fraction may indicate an area with high rainfall, good drainage and a warm, humid climate (Lyu and Lu, 2024).

4.5.2. Sediments Provenance and Weathering

According to the Mafic-Felsic-RW diagram (Fig. 4.7), the sediments in the section were derived from a weak degree of chemical weathering of felsic parent materials. This is consistent with the dominance of quartz in the bulk mineralogy and the content of SiO_2 observed all along the section. Nevertheless, antigorite is generally formed by hydrothermal alteration, specifically serpentinization of olivine and pyroxene minerals in ultramafic rocks (Hoinkes et al., 2005). This complexity in the origin of the sediments is also highlighted by the ICV trend along the section. In the basal part (C_{FS} and C_{VFS} layers), sediments showed high maturity (ICV

<1). This reflects intense chemical weathering of the parent rock, long transport, or multiple reworking processes, resulting in a dominance of stable minerals (such as quartz) in the sediments (Cox et al., 1995). In the upper part (A_l—C_{kk}), the sediments exhibited extreme immaturity (ICV >>1). This suggests a weak degree of chemical weathering of the parent material and short transport distances (Cox et al., 1995). Consequently, the ICV in the upper part aligns with the Mafic-Felsic-RW diagram results. However, a discrepancy in the degree of weathering is evident in the basal part, as the Mafic-Felsic-RW diagram indicates a weak degree of weathering.

Furthermore, the WIP, the RW and the CIA exhibited contrasting patterns across the section. The highest WIP values and the lowest CIA and RW values were observed in the upper part of the section. Conversely, in the basal part, the opposite trend was observed. The CIA and the WIP are two widely used indices for estimating the degree of chemical weathering. However, the underlying principles of their application differ slightly. In the case of the CIA, the formula (Eq. 3.3) highlights the relative enrichment of Al_2O_3 due to the loss of mobile cations such as Ca^{2+}, Na^{+}, and K^{+} during the chemical weathering of primary silicate minerals. This loss leads to an accumulation of Al^{3+} within clay minerals (Nesbitt and Young, 1982). Thus, the CIA does not depend on the absolute concentration of these elements in the parent rock, but rather on the ratio between the loss of mobile elements (Ca^{2+}, Na^{+}, and K^{+}) from the parental material and the formation of clay minerals (Cho and Ohta, 2022). This implies that rocks with a low initial concentration of these elements, which undergo intense weathering, leading to the formation of clay minerals, will exhibit a high CIA (Goldberg and Humayun, 2010; Odoma et al., 2015). This is likely the case for the C_{VFS} layers, which result from highly recycled materials (ICV<1). While such material would already be depleted in mobile cations due to previous weathering cycles, the high intensity of the weathering process drives a maximal transformation of

remaining primary mineral relics into clay minerals (high Al/Si), explaining the high CIA despite the initial low concentration of these elements.

In the case of WIP, its application is only based on the loss of four alkali and alkaline earth cations (Ca^{2+}, Mg^{2+}, Na^{+} and K^{+}) during the chemical weathering of primary silicate minerals (Eq. 3.4). From this point of view, the initial richness of the parent material in respect of these elements may influence the WIP and explain the low values observed in the C_{VFS} layers. However, under certain conditions, particularly a low degree of chemical weathering, the loss of these alkali and alkaline-earth cations is not always followed by the formation of clay minerals. For example, arid or semi-arid conditions can lead to the precipitation of carbonate minerals (Díaz-Hernández et al., 2013; Eze et al., 2021). Thus, the transition from low WIP values in the C_{VFS} layers to high values in the upper part (C_k and C_{kk}) may be related to a change in the parent materials and in the weathering conditions.

Discrepancies between CIA and WIP trends have been reported by Shao et al. (2012) in Chinese river floodplain sediments. They described an environment characterised by the influence of various source rocks, high relief, active tectonic uplift overall poor vegetation and soil development. These conditions are quite similar to those in the study area. The soils are very poorly developed (Eze et al., 2021; Eze and Molwalefhe, 2024). The alluvial fan is underlain by a system of active faults, which cause tectonic uplift (Kinabo et al., 2007; Pastier et al., 2017). Furthermore, certain phases of the filling of the alluvial fan may have taken place at the expense of the weathering of neighbouring geological formations whose composition is also highly diverse (Bordy et al., 2010; Elias and Bineli Betsi, 2023). This amalgamation probably led to the chemical rejuvenation of the deposits and the incorporation of ultramafic rocks, from which minerals such as antigorite are derived. The evidence for this can be observed in the gravel fragments that are still undergoing chemical weathering (Fig. 4.3E). It may explain the low degree of chemical weathering attributed to the C_{VFS} layers in the Mafic-

Felsic-RW diagram. All these aspects illustrate a diverse origin, as suggested by other studies carried out on the Kalahari sedimentary basin (Mokatse et al., 2023; Vainer et al., 2018), Nevertheless, felsic rocks should predominate, given the results of the Mafic-Felsic-RW diagram. The presence of sediments in this basin is controlled not only by the tectonic deformation that accompanies the establishment of the alluvial fan but also by the resulting changes in hydrological flow (Kinabo et al., 2008; Mokatse et al., 2022b; Vainer et al., 2021). In addition, studies have shown that tributary contributions cover a large portion of the Congo and Zimbabwe cratons, which explains the high diversity of sediments within the basin (Haddon and McCarthy, 2005).

4.5.3. Calcium Origin and Pedogenic Carbonate Accumulation

As shown in Fig. 4.5C, carbonate accumulation in this section is significantly correlated with the presence of calcium, for which the prediction model is consistent with the observed values (p-value = 2.15×10^{-10}). This suggests a substantial dependence of carbonate precipitation on calcium availability and dominance of calcite at the expense of other types of carbonates, such as dolomite. While this model should be treated with great caution given the small amount of data considered, these findings are supported by the mineralogy, which highlights calcite as the important carbonate type in the section. However, a tiny fraction of aragonite was also found. In the absence of detailed analyses, such as micromorphological analyses or sophisticated isotopic analyses (including the use of stable isotopes of carbon and oxygen, and strontium isotope ratio), the prioritisation of one formation process over another may be misleading (Dina Ebouel et al., 2024). However, carbonate accumulation is in the initial stage, designated as stage I by Gile (1993). This is corroborated by the predominant accumulations, either in powder form in soil pores (coating soil clods or filling termite tunnels), or along the roots of dead plants. Both cases reflect the dominance of pedogenic processes. In the case of accumulation around plant roots (rhizoliths), Zamanian et al. (2016), highlighted the fixation

of upward-moving Ca^{2+} (evaporation or capillarity) by CO_2 from root respiration. They also pointed out that pore accumulation (hypocoatings or pseudomycelia) is linked to the penetration of percolating water through the soil matrix. During this penetration, the CO_2 is affected by a strong decrease in pressure when moving from the large or medium pore sizes to the micropores. This leads to the crystallisation of $CaCO_3$ in the pore space.

In carbonate-rich sand layers, there is a high rate of WIP, which reflects losses of bases, including Ca, Mg, Na and K from a silicates minerals source (Parker, 1970). Moreover, as shown by Cho and Ohta (2022), the low RW observed in these layers could be associated with the formation of pedogenic carbonates. This is further corroborated by the low CIA values, which indicate that losses are not followed by clay formation, as also confirmed by the low Al/Si ratio. As explained in the section 4.5.2, the combination of high WIP and low CIA in this context can be explained by significant leaching of cations released by weak weathering of silicates minerals, probably during wet periods (rainy season). The alkaline pH and semi-arid climate lead to precipitation in soil voids (pores, termite tunnels, dead roots channels) of carbonates (pedogenic) in the same layer or in the soil horizons above (Naorem et al., 2022). This is encouraged by the availability of carbon and oxygen through biological activities such as root respiration (Zamanian et al., 2016) and termite activity (Mujinya et al., 2011). This prioritises *in situ* accumulation processes, either by dissolution-recrystallisation of pre-existing carbonates, or by the weathering of Ca^{2+}-rich primary silicates as the formation process for carbonates in these layers.

The linear regression model between strontium and calcium resulted in a strong positive correlation ($R = 0.92$) between the two variables in this section. This demonstrates a close relationship between their fractionation processes and the usefulness of the Ca/Sr ratio for tracing calcium movements. A high Ca/Sr ratio indicates preferential incorporation of Ca over Sr and vice versa (Sinclair, 2011; Zhang et al., 2020). Thus, the high Ca/Sr in the upper section

is consistent with the accumulation of $CaCO_3$. Nevertheless, the elevated Ca/Sr ratio in C_{VFS4}, which exhibits a low $CaCO_3$ content, may instead be indicative of the presence of substantial quantities of Ca-rich silicate minerals. This is consistent with the presence of weakly weathered gravel and fresh rock in the context described in section 4.5.2. This suggests that CVFS layers are also suppliers of Ca^{2+}. Thus, the Ca^{2+} from the weathering of the basal layers of the section is mobilised by upward movement (capillary rise, evaporation) towards the upper layers where the carbonate accumulates (Zamanian et al., 2016). Nevertheless, as previous studies have shown, the origin of calcium in pedogenic carbonate generally involves a diversity of sources (Dietrich et al., 2021; Durand et al., 2006). Therefore, a conclusion on the overall origins of calcium in this system cannot be drawn without a precise and rigorous identification of the potential parent materials (Capo and Chadwick, 1999). The contribution of aeolian deposits very prominent in the area (Dougill and Thomas, 2004) or geogenic carbonates cannot be excluded as mentioned by several studies in the region (Diaz et al., 2019; Nash, 2022).

In summary, and as shown in Fig. 4.8, the movement and accumulation of calcium within the section highlights two types of mechanism. Firstly, an upward movement, from the C_{VFS} base layers towards the accumulation layers (C_{kk}, C_k and AC), then a local transfer expressed by an *in-situ* movement of the minerals undergoing weathering towards the pedogenic carbonates.

It is worth highlighting a methodological limitation concerning the use, in this study, of weathering indices corrected for CaO* (CIA, WIP). Correction relative to CaO* is based on an a priori assumption regarding the distribution of CaO between silicate and carbonate sources, which caps the fraction of silicate origin relative to Na_2O (McLennan 1993). Given that one of the central objectives of this study is precisely to determine the origin of calcium in pedogenic carbonates, this introduces an element of circularity (these indices are themselves partly conditioned by an assumption regarding this origin). This limitation is common to CaO*-based indices in general and is difficult to overcome without independent geochemical constraints,

such as data on radiogenic or stable isotopes, which were beyond the scope of this study. To address this, the interpretations of the origin of calcium presented in Section 4.5.3 do not rely solely on the CIA and WIP, but are cross-checked with independent data (Ca/Sr ratios and their correlation with $CaCO_3$ and Ca contents, mineralogical identification of carbonate phases (XRD) and field observations of carbonate morphology). Future work incorporating strontium or stable isotope analyses would enable this limitation to be addressed more directly.

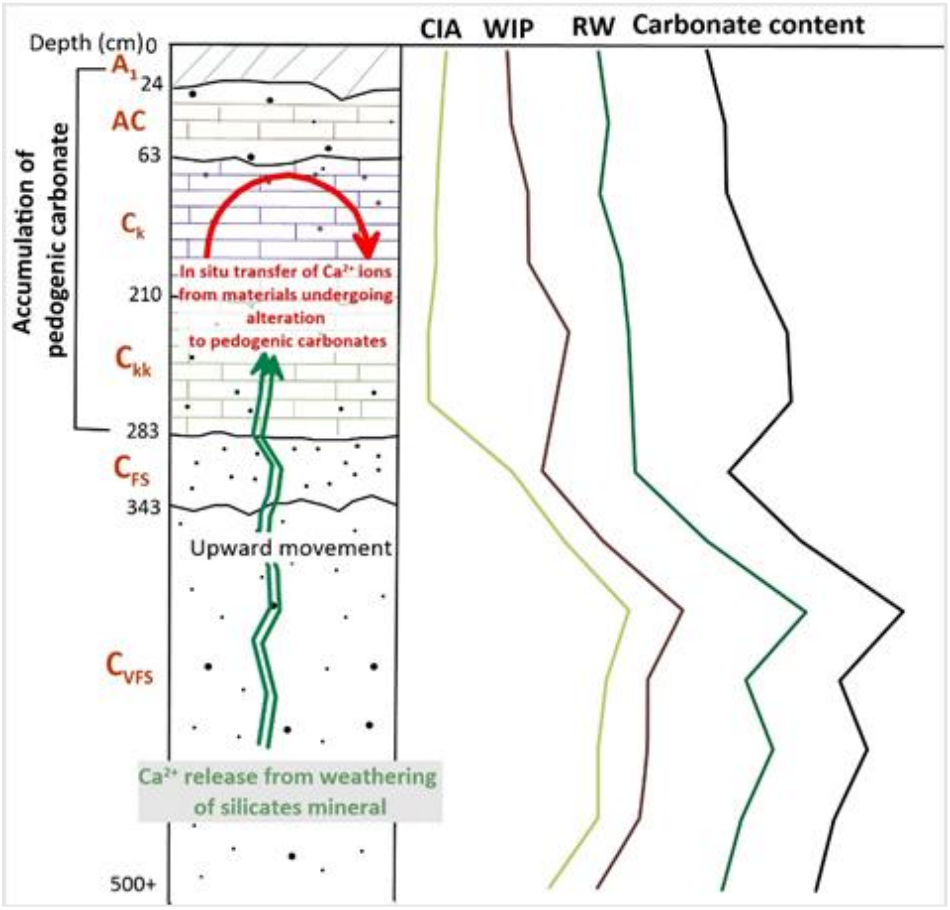


Fig. 4.8. Pedogenic model of carbonate accumulation in Parakarungu open quarry section.

4.6. Conclusions

Important research questions concerning the origin of calcium, formation and depositional processes of calcium carbonates in a prominent landform in the Chobe Enclave (northern Botswana) has been addressed in this study using a multiple proxy approach. The key findings show that environmental and climate change in the area would have influenced its landscape

evolution and carbonate formation. The accumulation of pedogenic carbonates is guided by two calcium movement mechanisms. The first is an upward movement from the base of the section following the chemical weathering of silicate minerals (Cf. Eq. 4.1) to the pedogenic carbonate accumulation layer (Cf. Eq. 4.2). The second is characterised by an *in-situ* translocation of pre-existing carbonate minerals or silicate minerals subject to chemical weathering towards the pedogenic carbonates accumulating in the same layer. These results demonstrate the interesting but often underestimated potential of pedogenic carbonates to trap atmospheric carbon dioxide since the formation of calcium carbonate as a result of the weathering of silicates enables one mole of carbon dioxide to be trapped in the system (Cf. Eq. 4.1 and Eq. 4.2). They therefore highlight the contribution of the region's geological substratum to carbon sequestration in the local soils. Though no evidence has been found to support the exclusivity of this pathway in the present case. However, these methods are based on the analysis of a single section, although fairly representative of the study area, are still very limited and require analysis on a larger scale. Furthermore, the methods used are indirect and could be supplemented by more direct approaches (micromorphological and isotopic analyses). Therefore, future research should compare these results to improve approaches and increase the scale of observation.

References

An H, Li QL, Yan X, et al (2019) Desertification control on soil inorganic and organic carbon accumulation in the topsoil of desert grassland in Ningxia, northwest China. Ecol Eng 127:348–355. https://doi.org/10.1016/j.ecoleng.2018.12.014

Awasthi AK (1970) Skewness as an environmental indicator in the solani river system, Roorkee (India). Sediment Geol 4:177–183. https://doi.org/https://doi.org/10.1016/0037-0738(70)90010-2

Bordy EM, Segwabe T, Makuke B (2010) Sedimentology of the Upper Triassic-Lower Jurassic (?) Mosolotsane Formation (Karoo Supergroup), Kalahari Karoo Basin, Botswana. Journal of African Earth Sciences 58:127–140. https://doi.org/10.1016/j.jafrearsci.2010.02.006

Bufford KM, Atekwana EA, Abdelsalam MG, et al (2012) Geometry and faults tectonic activity of the Okavango Rift Zone, Botswana: Evidence from magnetotelluric and electrical resistivity tomography imaging. Journal of African Earth Sciences 65:61–71. https://doi.org/https://doi.org/10.1016/j.jafrearsci.2012.01.004

Bughio MA, Wang P, Meng F, et al (2016) Neoformation of pedogenic carbonates by irrigation and fertilization and their contribution to carbon sequestration in soil. Geoderma 262:12–19. https://doi.org/10.1016/j.geoderma.2015.08.003

Bughio MA, Wang P, Meng F, et al (2017) Neoformation of pedogenic carbonate and conservation of lithogenic carbonate by farming practices and their contribution to carbon sequestration in soil. Zeitschrift fur Pflanzenernahrung und Bodenkunde 180:454–463. https://doi.org/10.1002/jpln.201500650

Burrough SL, Thomas DSG (2008) Late Quaternary lake-level fluctuations in the Mababe Depression: Middle Kalahari palaeolakes and the role of Zambezi inflows. Quat Res 69:388–403. https://doi.org/DOI: 10.1016/j.yqres.2008.02.003

Burrough SL, Thomas DSG, Bailey RM (2009) Mega-Lake in the Kalahari: A Late Pleistocene record of the Palaeolake Makgadikgadi system. Quat Sci Rev 28:1392–1411. https://doi.org/https://doi.org/10.1016/j.quascirev.2009.02.007

Capo RC, Chadwick OA (1999) Sources of strontium and calcium in desert soil and calcrete

Capo RC, Stewart BW, Chadwick OA (1998) Strontium isotopes as tracers of ecosystem processes: theory and methods

Cho T, Ohta T (2022) A robust chemical weathering index for sediments containing authigenic and biogenic materials. Palaeogeogr Palaeoclimatol Palaeoecol 608:111288. https://doi.org/10.1016/J.PALAEO.2022.111288

Cox R, Lowe DR, Cullers RL (1995) The influence of sediment recycling and basement composition on evolution of mudrock chemistry in the southwestern United States. Geochim Cosmochim Acta 59:2919–2940. https://doi.org/https://doi.org/10.1016/0016-7037(95)00185-9

Curtis Monger H, Kraimer RA, Khresat S, et al (2015) Sequestration of inorganic carbon in soil and groundwater. Geology 43:375–378. https://doi.org/10.1130/G36449.1

Das M, Chakraborty K, Rahaman S, et al (2025) Deciphering bed-load characteristics of the fluvially dynamic Balason River in Darjeeling of the Sub-Himalayan foreland, India. Journal of Sedimentary Environments. https://doi.org/10.1007/s43217-025-00239-4

Diaz N, Armitage SJ, Verrecchia EP, Herman F (2019) OSL dating of a carbonate island in the Chobe Enclave, NW Botswana. Quat Geochronol 49:172–176. https://doi.org/https://doi.org/10.1016/j.quageo.2018.03.001

Díaz-Hernández JL, Sánchez-Navas A, Reyes E (2013) Isotopic evidence for dolomite formation in soils. Chem Geol 347:20–33. https://doi.org/https://doi.org/10.1016/j.chemgeo.2013.03.018

Dietrich F, Diaz N, Deschamps P, et al (2017) Origin of calcium in pedogenic carbonate nodules from silicate watersheds in the Far North Region of Cameroon: Respective contribution of in

situ weathering source and dust input. Chem Geol 460:54–69. https://doi.org/10.1016/j.chemgeo.2017.04.015

Dietrich F, Diaz N, Deschamps P, et al (2021) Calcium transfer and mass balance associated with soil carbonate in a semi-arid silicate watershed (North Cameroon): An overlooked geochemical cascade? Depositional Record 2021:. https://doi.org/10.1002/dep2.134ï

Dina Ebouel FJ, Betsi TB, Eze PN (2024) Soil inorganic carbon: A review of global research trends, analytical techniques, ecosystem functions and critical knowledge gaps. Catena (Amst) 242:108112. https://doi.org/https://doi.org/10.1016/j.catena.2024.108112

Dougill AJ, Thomas AD (2004) Kalahari sand soils: Spatial heterogeneity, biological soil crusts and land degradation. Land Degrad Dev 15:233–242. https://doi.org/10.1002/ldr.611

Durand N, Ahmad SM, Hamelin B, et al (2006) Origin of Ca in South Indian calcretes developed on metamorphic rocks. J Geochem Explor 88:275–278. https://doi.org/10.1016/j.gexplo.2005.08.055

Elias E, Bineli Betsi T (2023) Petrological and geochemical characterisation of the Kgwebe volcanic formation in the Ghanzi-Chobe belt portion of the Kalahari copper belt, Western Botswana. Journal of African Earth Sciences 206:105038. https://doi.org/https://doi.org/10.1016/j.jafrearsci.2023.105038

Eze PN, Molwalefhe LN (2024) Late Quaternary palaeoenvironmental reconstruction of a Chobe Enclave landform (NW Botswana) based on pedological and geochemical indices. Journal of Sedimentary Environments 9:35–45. https://doi.org/10.1007/s43217-023-00155-5

Eze PN, Molwalefhe LN, Kebonye NM (2021) Geochemistry of soils of a deep pedon in the Okavango Delta, NW Botswana: Implications for pedogenesis in semi-arid regions. Geoderma Regional 24:. https://doi.org/10.1016/j.geodrs.2020.e00352

Ferdush J, Paul V (2021) A review on the possible factors influencing soil inorganic carbon under elevated CO2. Catena (Amst) 204

Folk RL, Ward WC (1957) Brazos River bar [Texas]; a study in the significance of grain size parameters. Journal of Sedimentary Research 27:3–26. https://doi.org/10.1306/74D70646-2B21-11D7-8648000102C1865D

Food and Agriculture Organization of the United Nations (2006) Guidelines for soil description. Food and Agriculture Organization of the United Nations

Ghsoub M, Fakhri M, Courp T, et al (2020) River signature over coastal area (Eastern Mediterranean): Grain size and geochemical analyses of sediments. Reg Stud Mar Sci 35:101169. https://doi.org/https://doi.org/10.1016/j.rsma.2020.101169

Gile LH (1993) Carbonate Stages in Sandy soils of Leasburg surface, Souther New Mexico. Soil Sci 156:

Goldberg K, Humayun M (2010) The applicability of the Chemical Index of Alteration as a paleoclimatic indicator: An example from the Permian of the Paraná Basin, Brazil. Palaeogeogr Palaeoclimatol Palaeoecol 293:175–183. https://doi.org/https://doi.org/10.1016/j.palaeo.2010.05.015

Golubtsov V, Bronnikova M, Khokhlova O, et al (2021) Morphological and isotopic study of pedogenic carbonate coatings from steppe and forest-steppe areas of Baikal region, South-Eastern Siberia. Catena (Amst) 196:. https://doi.org/10.1016/j.catena.2020.104817

Grey DRC, Cooke HJ (1977) Some problems in the quaternary evolution of the landforms of northern Botswana. Catena (Amst) 4:123–133. https://doi.org/https://doi.org/10.1016/0341-8162(77)90014-5

Haddon IG, McCarthy TS (2005) The Mesozoic–Cenozoic interior sag basins of Central Africa: The Late-Cretaceous–Cenozoic Kalahari and Okavango basins. Journal of African Earth Sciences 43:316–333. https://doi.org/https://doi.org/10.1016/j.jafrearsci.2005.07.008

Hoinkes G, Hauzenberger CA, Schmid R (2005) METAMORPHIC ROCKS | Classification, Nomenclature and Formation. In: Selley RC, Cocks LRM, Plimer IR (eds) Encyclopedia of Geology. Elsevier, Oxford, pp 386–402

IUSS Working Group WRB (2022) World Reference Base for Soil Resources. International soil classification system for naming soils and creating legends for soil maps, 4th edition. International Union of Soil Sciences, Vienna

Javanbakht M, Beheshtipur MR, Raftari Farimani S (2022) Factors affecting average grain size changes in rivers of a catchment area (Ardak catchment area, northeast Iran). Arabian Journal of Geosciences 15:448. https://doi.org/10.1007/s12517-021-08512-2

Khokhlova O, Myakshina T (2018) Dynamics of carbonates in soils under different land use in forest-steppe area of russia using stable and radiogenic carbon isotope data. Geosciences (Switzerland) 8:. https://doi.org/10.3390/geosciences8040144

Khokhlova OS, Chendev YG, Myakshina TN, Shishkov VA (2013) The pool of pedogenic carbon in the soils of different types and durations of use as croplands in the forest-steppe of the Central Russian Upland. Eurasian Soil Science 46:530–540. https://doi.org/10.1134/S1064229313050062

Kinabo BD, Atekwana EA, Hogan JP, et al (2007) Early structural development of the Okavango rift zone, NW Botswana. Journal of African Earth Sciences 48:125–136. https://doi.org/https://doi.org/10.1016/j.jafrearsci.2007.02.005

Kinabo BD, Hogan JP, Atekwana EA, et al (2008) Fault growth and propagation during incipient continental rifting: Insights from a combined aeromagnetic and Shuttle Radar Topography Mission digital elevation model investigation of the Okavango Rift Zone, northwest Botswana. Tectonics 27:. https://doi.org/https://doi.org/10.1029/2007TC002154

Liu E, Zhou J, Yang X, et al (2023) Long-term organic fertilizer-induced carbonate neoformation increases carbon sequestration in soil. Environ Chem Lett. https://doi.org/10.1007/s10311-023-01568-4

Lyu H, Lu H (2024) Precipitation is the main control on the global distribution of soil clay minerals. Earth Sci Rev 257:104891. https://doi.org/https://doi.org/10.1016/j.earscirev.2024.104891

Matshameko Y, Okolo CC, Eze PN (2023) Near-surface pedosediments of Takatokwane saline pan, southern Botswana: Properties, pedogenic processes, and inferences of environmental change. Geoderma Regional 34:e00696. https://doi.org/10.1016/J.GEODRS.2023.E00696

McLennan SM (1993) Weathering and Global Denudation. J Geol 101:295–303. https://doi.org/10.1086/648222

Millière L, Gussone N, Moritz T, et al (2019) Origin of strontium and calcium in pedogenic needle fibre calcite (NFC). Chem Geol 524:329–344. https://doi.org/10.1016/j.chemgeo.2019.06.022

Mokatse T, Diaz N, Shemang E, et al (2022a) Landscapes and Landforms of the Chobe Enclave, Northern Botswana. In: Eckardt FD (ed) Landscapes and Landforms of Botswana. Springer International Publishing, Cham, pp 91–116

Mokatse T, Prud'Homme C, Vainer S, et al (2023) Sepiolite as a multifactorial indicator of paleoenvironments in the Chobe Enclave (northern Botswana). Sediment Geol 454:106459. https://doi.org/https://doi.org/10.1016/j.sedgeo.2023.106459

Mokatse T, Vainer S, Irving J, et al (2022b) Geometry of sedimentary deposits and evolution of the landforms in the Chobe Enclave, Northern Botswana. Geomorphology 415:108406. https://doi.org/https://doi.org/10.1016/j.geomorph.2022.108406

Moses O, Blamey RC, Reason CJC (2023) Extreme rainfall events over the Okavango river basin, southern Africa. Weather Clim Extrem 41:100589. https://doi.org/https://doi.org/10.1016/j.wace.2023.100589

Mujinya BB, Mees F, Boeckx P, et al (2011) The origin of carbonates in termite mounds of the Lubumbashi area, D.R. Congo. Geoderma 165:95–105. https://doi.org/10.1016/j.geoderma.2011.07.009

Müller G, Börker J, Sluijs A, Middelburg JJ (2022) Detrital Carbonate Minerals in Earth's Element Cycles. Global Biogeochem Cycles 36:e2021GB007231. https://doi.org/https://doi.org/10.1029/2021GB007231

Naorem A, Jayaraman S, Dalal RC, et al (2022) Soil Inorganic Carbon as a Potential Sink in Carbon Storage in Dryland Soils—A Review. Agriculture (Switzerland) 12:. https://doi.org/10.3390/agriculture12081256

Nash DJ (2022) Calcretes, Silcretes and Intergrade Duricrusts. In: Eckardt FD (ed) Landscapes and Landforms of Botswana. Springer International Publishing, Cham, pp 223–246

Nesbitt HW, Young GM (1982) Early Proterozoic climates and plate motions inferred from major element chemistry of lutites. Nature 299:715–717. https://doi.org/10.1038/299715a0

Odoma AN, Obaje NG, Omada JI, et al (2015) Mineralogical, chemical composition and distribution of rare earth elements in clay-rich sediments from Southeastern Nigeria. Journal of African Earth Sciences 102:50–60. https://doi.org/https://doi.org/10.1016/j.jafrearsci.2014.10.013

Ortiz AC, Jin L, Ogrinc N, et al (2022) Dryland irrigation increases accumulation rates of pedogenic carbonate and releases soil abiotic CO2. Sci Rep 12:. https://doi.org/10.1038/s41598-021-04226-3

Parker A (1970) An Index of Weathering for Silicate Rocks. Geol Mag 107:501–504. https://doi.org/DOI: 10.1017/S0016756800058581

Pastier A-M, Dauteuil O, Murray-Hudson M, et al (2017) Is the Okavango Delta the terminus of the East African Rift System? Towards a new geodynamic model: Geodetic study and geophysical review. Tectonophysics 712–713:469–481. https://doi.org/https://doi.org/10.1016/j.tecto.2017.05.035

Pfeiffer M, Padarian J, Vega MP (2023) Soil inorganic carbon distribution, stocks and environmental thresholds along a major climatic gradient. Geoderma 433:116449. https://doi.org/https://doi.org/10.1016/j.geoderma.2023.116449

Prescott CE, Vesterdal L (2021) Decomposition and transformations along the continuum from litter to soil organic matter in forest soils. For Ecol Manage 498:119522. https://doi.org/https://doi.org/10.1016/j.foreco.2021.119522

Reinoso Carbonell V V, Collo G, Wunderlin CA, et al (2022) Clay mineral assemblages as indicators of paleoenvironmental and diagenetic dynamics in the Neogene Fiambalá Basin, NW Argentina. J South Am Earth Sci 118:103949. https://doi.org/https://doi.org/10.1016/j.jsames.2022.103949

Ringrose S, Huntsman-Mapila P, Downey W, et al (2008) Diagenesis in Okavango fan and adjacent dune deposits with implications for the record of palaeo-environmental change in Makgadikgadi–Okavango–Zambezi basin, northern Botswana. Geomorphology 101:544–557. https://doi.org/https://doi.org/10.1016/j.geomorph.2008.02.008

Romanens R, Pellacani F, Mainga A, et al (2019) Soil diversity and major soil processes in the Kalahari basin, Botswana. Geoderma Regional 19:e00236. https://doi.org/https://doi.org/10.1016/j.geodrs.2019.e00236

Shao J, Yang S, Li C (2012) Chemical indices (CIA and WIP) as proxies for integrated chemical weathering in China: Inferences from analysis of fluvial sediments. Sediment Geol 265–266:110–120. https://doi.org/https://doi.org/10.1016/j.sedgeo.2012.03.020

Sharififar A, Minasny B, Arrouays D, et al (2023) Soil inorganic carbon, the other and equally important soil carbon pool: Distribution, controlling factors, and the impact of climate change. In: Advances in Agronomy. Academic Press Inc., pp 165–231

Sheldon ND, Tabor NJ (2009) Quantitative paleoenvironmental and paleoclimatic reconstruction using paleosols. Earth Sci Rev 95:1–52. https://doi.org/https://doi.org/10.1016/j.earscirev.2009.03.004

Sherrod LA, Dunn G, Peterson GA, Kolberg RL (2002) Inorganic Carbon Analysis by Modified Pressure-Calcimeter Method. Soil Science Society of America Journal 66:299–305. https://doi.org/10.2136/sssaj2002.2990

Sinclair DJ (2011) Two mathematical models of Mg and Sr partitioning into solution during incongruent calcite dissolution: Implications for dripwater and speleothem studies. Chem Geol 283:119–133. https://doi.org/https://doi.org/10.1016/j.chemgeo.2010.05.022

Spaargaren O (2008) Kastanozems. In: Chesworth W (ed) Encyclopedia of Soil Science. Springer Netherlands, Dordrecht, pp 421–423

Vainer S, Erel Y, Matmon A (2018) Provenance and depositional environments of Quaternary sediments in the southern Kalahari Basin. Chem Geol 476:352–369. https://doi.org/10.1016/j.chemgeo.2017.11.031

Vainer S, Matmon A, Erel Y, et al (2021) Landscape responses to intraplate deformation in the Kalahari constrained by sediment provenance and chronology in the Okavango Basin. Basin Research 33:1170–1193. https://doi.org/https://doi.org/10.1111/bre.12509

Vainer S, Schmidt C, Garzanti E, et al (2024) Chronology of Sedimentation and Landscape Evolution in the Okavango Rift Zone, a Developing Young Rift in Southern Africa. J Geophys Res Earth Surf 129:e2023JF007554. https://doi.org/https://doi.org/10.1029/2023JF007554

Vessia G, Di Curzio D (2018) Lacustrine Deposits. In: Bobrowsky P, Marker B (eds) Encyclopedia of Engineering Geology. Springer International Publishing, Cham, pp 1–6

Vittoz P, Pellacani F, Romanens R, et al (2020) Plant community diversity in the chobe enclave, botswana: Insights for functional habitat heterogeneity for herbivores. Koedoe 62:1–17. https://doi.org/10.4102/koedoe.v62i1.1604

Walkley A, Black IA (1934) An examination of the degtjareff method for determining soil organic matter, and a proposed modification of the chromic acid titration method. Soil Sci 37:

Zamanian K, Pustovoytov K, Kuzyakov Y (2016) Pedogenic carbonates: Forms and formation processes. Earth Sci Rev 157:1–17

Zhang S, Zhou R, DePaolo DJ (2020) The seawater Sr/Ca ratio in the past 50 Myr from bulk carbonate sediments corrected for diagenesis. Earth Planet Sci Lett 530:115949. https://doi.org/https://doi.org/10.1016/j.epsl.2019.115949

CHAPTER FIVE

Pedogenic and Sedimentary Controls on Carbonate Accumulation in Semi-arid Fluvial Landscape, Central Botswana[4]

Abstract

The formation and accumulation of pedogenic carbonates represent an important pathway for long-term carbon sequestration in global dryland regions. However, accurately assessing their contribution to the regional carbon budget requires distinguishing between pedogenic (in-situ soil formation) and sedimentary processes, which often occur concurrently in dynamic environments. This study investigated the formation and accumulation of carbonate features within four pedosedimentary sections located along ephemeral stream banks in semi-arid Central Botswana. The method used involved combining morphological and physicochemical characterisation with geochemical indices in the observed horizons/layers. Geochemical indices include the robust chemical weathering index (RW), the calcification index ((Mg + Ca)/Al), the clayeyness index (Al/Si) and Mg/Ca ratios. Analysis of the sections reveals a cyclical palaeoenvironmental history marked by buried palaeosols whose development was repeatedly interrupted by successive episodes of fluvial sedimentary deposition, followed by the resumption of modern pedogenesis. Particle size analysis of the deposit layers confirms a pulsed fluvial regime, with sediments ranging from poorly sorted fine sand upstream to extremely poorly sorted coarse silt downstream, indicating hydraulic sorting according controlled by flood energy. Geochemically, the low RW values, ranging overall between 30% and 60%, and the clay index generally below 0.3 indicate a limited degree of chemical weathering and low clay neoformation, reflecting the predominance influence of the arid

[4] *This chapter is based on a research article co-authored with Thierry Bineli Betsi, Elisabeth Eiche, Stefan Norra, and Peter N. Eze; currently under review in Geoderma Regional*

environment. Calcification was identified as the dominant pedogenic process in all sections (both ancient and modern), characterised by a high $CaCO_3$ content (14 to 22%), confirmed by the calcification index in the calcic horizons. The low Mg/Ca ratio strongly suggests the predominance of calcite as the main pedogenic carbonate phase. These findings highlight that the total carbonate accumulation in the study area is a direct result of the complex interplay between repetitive fluvial deposition (pedosedimentary history) and subsequent in-situ pedogenic calcification. The results underscore the critical importance of pedogenic carbonate accumulation in the soils of Botswana, a major process that plays a significant role in the regional carbon balance and should be accounted for in carbon budget models for semi-arid fluvial systems.

Keywords: Buried palaeosol; Depositional environments; Pedogenesis; Sedimentation; Soil inorganic carbon.

5.1. Introduction

One of the most pressing environmental challenges of the twenty-first century is the global rise in the amount of carbon dioxide (CO_2) in the atmosphere (Nunes, 2023). As CO_2 builds up, it has a bigger effect on radiative forcing, which speeds up global warming and makes ecosystems around the planet less stable. Reducing atmospheric carbon dioxide emission therefore is a global priority. To solve this problem, there is a need to do more than just cut emissions at their source. It is important to make natural carbon sinks better at removing CO_2 from the air. Soil is one of the Earth's most important carbon reservoirs, with about 2157-2293 Pg ($1Pg=10^{15}$ g) of carbon in the upper 100 cm (Batjes, 2014). The significance of this pool highlights the critical function of belowground activities in the global terrestrial carbon cycle. Soil can serve as either a net sink or a source of atmospheric CO_2, contingent upon its management and biogeochemical dynamics (Bhattacharyya et al., 2017). From a research perspective, it is important not only to evaluate the capacity of major carbon sinks to reduce atmospheric carbon dioxide levels, but also to examine in detail their potential contributions to changes in atmospheric CO_2 dynamics into the atmosphere (Kuzyakov et al., 2019).

For a long time, studies on soil carbon have mostly looked at soil organic carbon (SOC). But growing evidence reveals that soil inorganic carbon (SIC) is just as essential (Dina Ebouel et al., 2024; Raza et al., 2024), but not always recognised, as an important part of how carbon moves through the soil, especially in drylands. For example, numerous studies have highlighted that SIC is typically the dominant carbon pool in arid and semi-arid regions, often exceeding SOC content and playing a crucial role in the global carbon cycle (Díaz-Hernández et al., 2003; Raheb et al., 2016; Turgut et al., 2025). Moreover, arid, semi-arid and dry sub-humid areas, collectively known as drylands, cover approximately 45% of the Earth's total land area (Prăvălie, 2016). Within these landscapes, the formation, accumulation, redistribution, and stabilization of secondary (pedogenic) carbonates represent a major pathway for carbon storage

(Naorem et al., 2022). These carbonates occur mainly in two categories (Ferdush and Paul, 2021): dissolved inorganic carbon (DIC), consisting of hydrated species of CO_2 in solution, such as dissolved CO_2 (CO_2(aq)), carbonic acid (H_2CO_3), bicarbonate ion (HCO_3^-) and carbonate ion (CO_3^{2-}); and solid carbonates, which are crystalline minerals, mainly include calcite ($CaCO_3$), but also dolomite ($CaMg(CO_3)_2$) and siderite ($FeCO_3$). In contrast to organic carbon, which is prone to microbial degradation, pedogenic carbonates develop highly stable mineral phases that can persist over geological timescales (Monger, 2014). Their accumulation therefore constitutes a substantial geochemical process for carbon sequestration.

Soil inorganic carbon occurs in two distinct forms: lithogenic carbonates, which are inherited from geological processes, specifically the sedimentary accumulation of calcium carbonates subsequently reworked into the soil; or pedogenic carbonates, which result from secondary accumulation associated with soil-forming processes (Monger, 2014). In the latter case, the weathering of lithogenic silicate or carbonate parent material leads to the release of calcium ions (Ca^{2+}), which then bind with bicarbonate ions (HCO_3^-), facilitating the crystallisation or recrystallisation of the pedogenic carbonates. Quantifying the contributions of pedogenic and lithogenic carbonates to atmospheric CO_2 reduction is difficult, mostly due to the challenge of differentiating them within the soils. In several arid environments such as fluvial systems, colluvial pediments, and aeolian-affected landscapes sedimentary inputs may simultaneously occur with pedogenic processes. Consequently, carbonate nodules, coatings, or accumulations present in soils may not invariably indicate local soil development. However, it is necessary to differentiate between these sources, as pedogenic carbonates facilitate active carbon sequestration, while lithogenic carbonates do not. This divergence has significant consequences for carbon accounting, climate change mitigation methods, and the understanding of soil formation processes.

The role of pedogenic carbonates in soil functioning, carbon sequestration, and palaoenvironmental reconstruction in areas like Botswana and the wider southern African drylands is inadequately researched. Here, carbonate accumulations either in the form of calcretes or other features like diffuse powder, pseudomycelia (rhizoliths) and nodules are widespread (Dina Ebouel et al., 2025a; Nash, 2022). In the Central District of Botswana, numerous studies have highlighted the abundance of these accumulations in the soil (Dina Ebouel et al., 2025b; Eze, 2022; Eze et al., 2025). However, none of these previous studies examined in depth how landscapes containing these carbonate features have evolved over time to arrive at their current configuration. These landscapes show complex geomorphic histories, episodic sedimentation, and dynamic soil formation processes influenced by climate gradients. The coexistence of pedogenic and sedimentary carbonates poses an analytical problem that limits the precision of carbon budgets and the interpretation of palaeoclimatic signals. Therefore, a comprehensive understanding of carbonate accumulation processes in this fluvial system is essential for guiding sustainable land management, improving carbon sequestration potential, and refining models of ecosystem responses to ongoing climate change. This study seeks to advance our understanding of the evolution of a prominent fluvial landscape in Serowe, Central Botswana and how this may have influenced the formation of carbonate features in the pedosedimentary sections. Ultimately, this study fills gaps in dryland soil research and emphasises the importance of inorganic carbon processes in global carbon cycling, landscape evolution and palaeoenvironmental reconstruction by understanding pedogenic carbonate formation and accumulation mechanisms.

5.2. Environmental setting

The study site is in Serowe, which is situated in the Central District of Botswana, at geographical coordinates of 22.34°–22.42° south latitude and 26.67°–26.76° east longitude (Fig. 5.1). The geological substrate is mainly composed of formations from the Karoo

Supergroup, dating from the Late Carboniferous to the Early Jurassic (Smith, 1984). Although not extensive within the study area, unconsolidated aeolian deposits of the Kalahari Group, whose accumulation began in the Cenozoic era and continues today (Haddon and McCarthy, 2005), overlie the Karoo Supergroup at certain locations. According to the lithostratigraphic description of Franchi et al. (2021), the Lower Karoo Supergroup (comprising the Ecca and Beaufort groups) is characterised by a basal sequence of conglomerates and breccias that fines upward into coal-rich mudrocks with organic shales, followed by poorly lithified, grey-to-purple claystones (Beaufort Group). The Upper Karoo Supergroup (Lebung Group), however, begins with coarse-grained, cross-bedded sandstones often containing carbonate cements and fossil fragments, which dominate the sequence. This part of the Basin is capped by basaltic deposits (Stormberg Lava Group). Unconformably overlying this entire sequence are the unconsolidated aeolian deposits of the Kalahari Group, consisting of fine- to medium-grained sands with carbonates. The geomorphological unit of the area is the eastern Hardveld, which expands from the south-eastern to east-central Botswana. It is characterised by gently sloping plains that protect the Precambrian mountains and hills as well as lone ravines connected to severe erosion (Atlhopheng et al., 2022).

According to the Köppen-Geiger climate classification, Central Botswana belongs to the BSh type (hot, dry semi-arid climate), which is characterised by hot, dry conditions for most of the year, with a rainy summer season occurring from November to March. The mean annual precipitation ranges from a minimum of 222.9 mm to a maximum of 970.2 mm, with an overall mean of 442.4 mm recorded over 22 days of rain per year (Batisani and Yarnal, 2010). This region experiences a wide range of temperatures, with a minimum of 0°C (33°F) in June during the winter and a maximum of 45°C (112°F) in October. The average temperature is 22°C (72°F), reflecting the region's fluctuating thermal dynamics. Many studies have reported a strong variability in climate over time, characterised by numerous drought episodes (e.g.,

Akinyemi, 2021; Frank and Sarthi, 2025). Moreover, flooding is frequently observed, as in various regions of Botswana (Moses et al., 2023; Motsholapheko et al., 2011). Surface waters are mainly ephemeral and limited to the rainy season, as there are no permanent watercourses (Setimela, 2009). These waters have low mineralisation and a chemical composition dominated by Ca–HCO_3 to Ca–Mg–HCO_3 facies, characteristic of recent meteoric waters with limited water–soil interaction (Stadler et al., 2010). Despite their ephemeral nature, surface waters thus play an important hydrological role as an indirect source of recharge for aquifers in the region (Setimela, 2009; Stadler et al., 2010).

The typical vegetation is a bush savannah (Ringrose et al., 2003), characterised by woody species as *Acacia erioloba*, *A. mellifera*, *A. hebeclada*, *A. fleckii*, *Terminalia sericea*, *Lonchocarpus nelsii*, *Boscia albitruna*, *Grewia flava*, *G. retinervis*, *Dichrostachys cinerea*, *Ziziphus mucronate* and herbaceous species as *Aristidia uniplumis*, *Eragrostis latimanniana*, *Schmidtia bulbosa*, *Antephora pubescens*, *Aristida meridionalis* (Ringrose et al., 1998). But this natural land cover is deeply marked by agricultural activities and infrastructures development (Atlhopheng et al., 2022). According to Eze (2022), the dominant soil groups are Arenosols, Cambisols, Calcisols and Vertisols, while the main pedogenic processes include salinisation, calcification and decalcification, illuviation, eluviation and erosion.

5.3. Material and methods

5.3.1. Field investigations and sampling

Following reconnaissance investigation of environmental conditions, including auger surveys designed to assess the representativeness of carbonate accumulations in the soils on the fluvial landscape, four pedosedimentary sections (SC01, SC02, SC03 and SC04) along the banks of an ephemeral river, named Metsimasweu were selected. These sections were chosen for their overall representativeness and for the presence of carbonate features within one or more of their horizons or layers (Fig. 5.2). The selected soil sections were described in the field in

accordance with FAO soil guideline for soil profile description (FAO ood and Agriculture Organization of the United Nations, 2006). Bulk soil samples were collected from each of the pedogenetic horizons identified during the field sampling. The carbonate features were carefully hand-picked and preserved for further laboratory analysis.

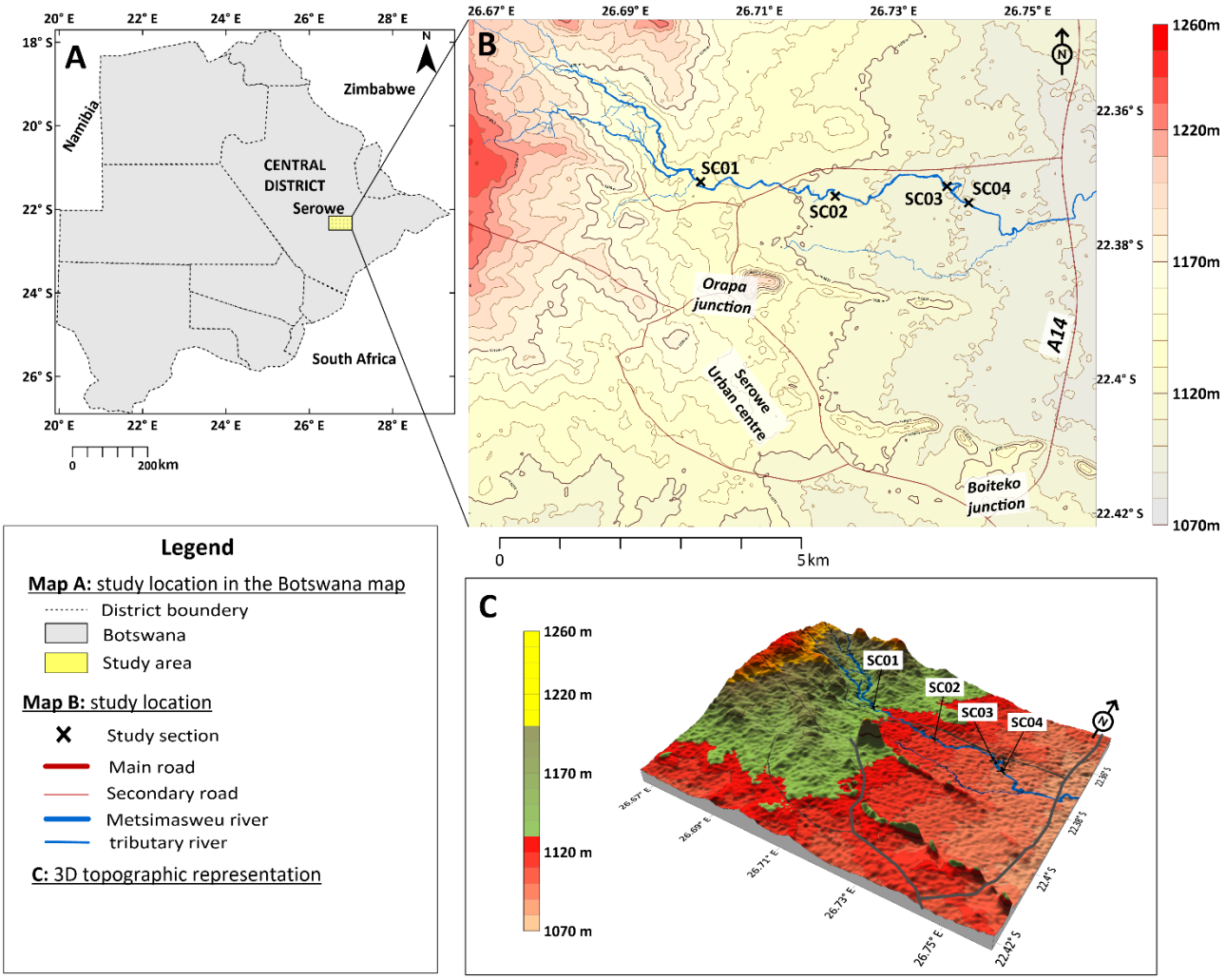


Fig. 5.1. A. Location map of the study area; B. A zoomed-out map of the study area; C. 3D topographic model of the study area.

5.3.2. Laboratory analysis

Air-dried samples were passed through a 2 mm sieve to remove coarse particles and root fragments. The <2 mm fraction was subsequently subjected to routine physicochemical analyses, including pH, electrical conductivity (EC), SOM content, calcium carbonate ($CaCO_3$)

content, and soil particle size analysis, to provide essential information complementing the field descriptions.

In brief, the soil pH and EC were determined in a 1/2.5 soil:deionised water ratio solution as recommended in FAO Guidelines for soil description (Food and Agriculture Organization of the United Nations, 2006). The carbonate content ($CaCO_3$) of the soil was determined with an Eijkelkamp calcimeter using the Scheibler method, in accordance with NEN-ISO 10693. In this method, the carbonates present in the sample react with hydrochloric acid (4 M HCl), generating CO_2 gas. The volume of CO_2 produced is measured volumetrically using a burette system and the carbonate content is expressed as calcium carbonate equivalent ($CaCO_3$). Calibration was carried out using calcium carbonate standards (0.2 g and 0.4 g $CaCO_3$), and blank determinations were carried out to ensure accuracy. Results were calculated using the standard formula, incorporating corrections for blank values and moisture content (ISO 11465). Results obtained in g kg^{-1} were converted to weight percentages. The soil organic matter (SOM) content was determined via wet oxidation (Walkley and Black, 1934). To determine the soil texture, the sample underwent a two-step pretreatment process. This involved treating the sample with a 30% hydrogen peroxide solution for 24 hours to remove organic matter, followed by treatment with a 10% hydrochloric acid solution for 24 hours to remove carbonates. The sample was then dispersed using sodium hexametaphosphate before the Bouyoucos hydrometer method was applied to determine the particle size distribution.

From field description, conspicuous sandy layers exhibiting minimal pedogenesis were identified across the four pedosedimentary sections. Given the minimal pedogenesis, they are suitable for studying the depositional environment. A total of five sandy layers, one in SC01 (C1), one in SC02 (C2), two in SC03 (C1 and C2) and one in SC04 (AC) were sampled. For each of these sandy layers, a laser diffraction grain size analysis was performed using Malvern Panalytical Mastersizer 3000 equipment, following the protocol described by Bittelli et al.

(2022). These samples were also submitted to micromorphological observation in thin section under a petrographic microscope (Stoops et al., 2018).

The major element composition analysis, including Si, Al, Fe, Mn, Mg, Ca, Na, K, Ti and P (all reported as the mass percentage of oxides), was performed on fused beads using an S4 Explorer (Bruker AXS) wavelength dispersive X-ray fluorescence spectroscope (WDX) at the Geochemistry lab of Karlsruhe Institute of Technology, Germany. Prior to element quantification, the loss on ignition (LOI) of the pulverised samples was determined by heating them to 950 °C for 3 hours and recording the weight difference before and after heating. Fused beads were prepared by mixing the ignited sample powder with a 66.5:33.5 ratio of Li-tetraborate and Li-metaborate (Spectroflux 110, Alfa Aesar) before melting it at 1000–1100 °C using a fusion instrument. An Rh X-ray tube (50 keV, 1 kW) was used as the radiation source. Signals were detected using a proportional flow counter (Ar-CH_4 gas) and a scintillation counter. XS-55, LIF2000 and PET were used as analyser crystals. Four certified reference materials, including AGV-1, GXR-2, GXR-5 and Soil 7, were used to verify the accuracy of the produced data.

5.3.3. Data processing

Morphological and physicochemical properties were used to classify modern soils and buried palaeosols according to the criteria of the international union of soil sciences working group on the world reference base for soil resources (IUSS-WRB, 2022). These criteria were augmented by soil taxonomy adapted to buried palaeosols (Nordt et al., 2025).

The results obtained with the Malvern Mastersizer suggest seven distinct particle size classes based on the United States Department of Agriculture standard (Skaggs et al., 2001), including: very coarse sand (1000-2000 μm), coarse sand (500-1000 μm), medium sand (250-500 μm), fine sand (100-250 μm), very fine sand (50-100 μm), silt (2-50 μm) and clay (< 2 μm). The

different mass proportions of these grain size classes enabled the software integrated into the analysis instrument to obtain the inclusive statistical parameters of Folk and Ward (1957).

Geochemical data were analysed using five geochemical indices including calcification index, Mg/Ca ratio, Salinisation index, clayeyness index and the robust index of chemical weathering (RW). The following four indices (calcification index, Mg/Ca ratio, salinisation index, clay index) were calculated based on the molar ratio as recommended by Sheldon (2003), while RW was estimated based on the mass percentage of the elements (Cho and Ohta, 2022).

The calcification index (Eq. 5.1) was used to measure the accumulation of carbonates across the soil profiles. This index is based on the principle that the formation of pedogenic carbonates increases the concentration of magnesium (Mg) and calcium (Ca) relative to aluminium (Al), with the latter being characteristic of stable clay minerals (Eze et al., 2021; Retallack, 2001).

$$Calcification\ index = \frac{Ca + Mg}{Al} \quad \text{Eq. 5.1}$$

The Mg/Ca ratio was used to investigate the dominant mineralogical type of pedogenic carbonate accumulation. Since carbonates that accumulate in semi-arid environments are primarily either calcite ($CaCO_3$) or dolomite ($CaMg(CO_3)_2$) (Diaz-Hernandez et al., 2018), the dominance of one mineralogical form over the other significantly affects the elemental ratio and provides crucial information about the nature of the accumulation (Achyuthan et al., 2012; Pinheiro Junior et al., 2021).

The salinisation index (Eq. 5.2) is based on the fact that the molar ratio between K and Na relative to Al is a function of the salinisation of soils and palaeosols (Eze et al., 2021; Sheldon, 2006).

$$Salinisation\ index = \frac{Na+K}{Al}$$ Eq. 5.2

The clayeyness index, which is based on the Al/Si ratio, is a recognised geochemical proxy in soil science and palaeoclimatology (Sheldon and Tabor, 2009). Clay accumulation leads to an increase in aluminium (Al) concentration relative to silicon (Si).

As the accumulation of pedogenic carbonates in semi-arid environments can compromise standard indices, a robust measure was needed to accurately assess the intensity of chemical weathering. For this reason, the robust chemical weathering index (Eq. 5.3) developed by Cho and Ohta (2022) was selected for investigating the intensity of chemical weathering along the studied sections, since it is specifically designed to remain unaffected by these secondary accumulations.

$$\mathrm{RW} = 0.152\ln(\mathrm{TiO_2}) + 0.198\ln(\mathrm{Al_2O_3}) + 0.148\ln(\mathrm{Fe_2O_3}) - 0152\ln(\mathrm{MgO}) - 0.503\ln(\mathrm{Na_2O}) + 0.156\ln(\mathrm{K_2O}) - 0.506$$ Eq. 5. 3

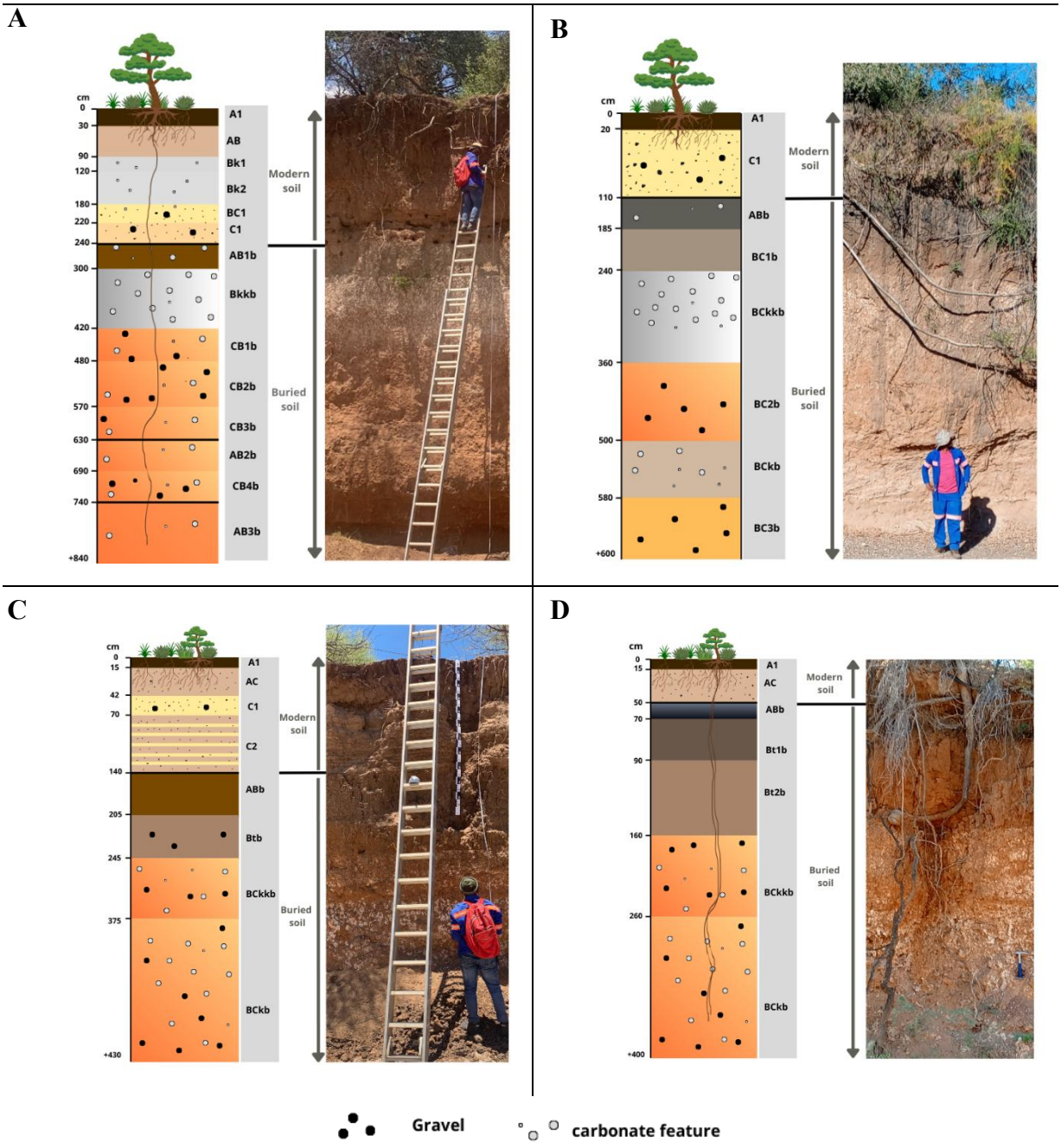


Fig. 5.2. Field Photographs and Correlative Stratigraphic Representations of A. Section 01 (SC01); B. Section 02 (SC02); C. Section 03 (SC03); and D. Section 04 (SC04).

5.4. Results

5.4.1. Morphological characterisation and physicochemical properties

The four pedosedimentary sections occur along the slope of an ephemeral river, from upstream (SC01) to downstream (SC04), as shown in Fig. 5.1. Layering and horizonation of the

respective sections are presented in Fig. 5.2. The detailed morphological characteristics and physicochemical properties of SC01, SC02, SC03, and SC04 are presented in Tables 5.1, 5.2, 5.3, and 5.4, respectively. The description of each section is as follows. SC01 presents 14 soil horizons (Fig. 5.2A). The boundaries between horizons are mostly gradual and wavy. However, the boundaries between the horizons C1 and AB1b, CB3b and AB2b, CB4b and AB3b are abrupt, while the boundary between AB1b and Bkkb is clear and smooth. SOM is typically low, ranging from 0.19 to 0.41 wt.%. The maximum is observed in the topsoil (A1). The texture is mostly sandy loam or loamy sandy. The sand is the dominant fraction generally above 60 wt.% with a maximum observed in layer C1 (84 wt.%) (Fig. 5.3). The clay fraction, on the other hand, is generally very low, below 10 wt.%, except for the top two layers, which are around 19 wt.%. The pH of the soil ranges from 6.8 (near neutral soil pH) to 8.3 (moderately alkaline soil pH) (Table 5.1). The maximum pH was observed in layer C1, while the minimum was found in the topsoil (A1). The EC is mostly low, ranging from 0.21 to 1.67 $dS.m^{-1}$ (Table 1). The maximum EC value is observed in the bottom layer AB3b. There is a strong variation in $CaCO_3$ content, ranging from 0.07 wt.% in topsoil (A1) to 24.61 wt.% in Bkkb. Many of the horizons showed the presence of carbonate features that accumulated mainly as soft nodules (Fig. 5.4.A) or diffuse powder. Nevertheless, the two basal layers (CB4b and AB3b) exhibited more accumulations in the form of pseudomycelia, i.e. carbonate infilling in pores, resembling mycelia (Fig. 5.4.B). Some layers, including BC1 and C1 in the upper part of the section and all layers below CB1b, contain some gravel. These are mainly fragments of basaltic and sandstone rocks of the Karoo Supergroup (Fig. 5.4.C).

Table 5.1. Morphological characteristics and physicochemical properties of section SC01

Horizon /Layer	Depth cm	Munsell colour (moist)	10% HCl reaction	Visible carbonate features	Other secondary features	pH (H_2O)	EC $dS.m^{-1}$	SOM wt.%	$CaCO_3$ wt.%
A1	0-30	10YR2/2 Very dark brown	SL	No	No	6.8	0.21	0.41	0.07
AB	30-90	10YR3/2 Very dark grayish brown	SL	No	No	7.6	0.22	0.31	0.10
Bk1	90-120	10YR3/2 Very dark grayish brown	ST	Soft concretions, nodule 2-10 mm	No	7.8	0.56	0.34	2.62
Bk2	120-180	10YR4/4 Dark yellowish brown	ST	Soft concretions, nodule 2-10 mm	No	8.0	0.56	0.24	6.35
BC1	180-220	10YR5/4 Yellowish brown	ST	Disperse powder	Few gravel (2-10 cm)	8.1	0.40	0.28	3.56
C1	220-240	10YR5/4 Yellowish brown	ST	rare soft concretions (nodule 2-10 mm) + Disperse powder	Few gravel (2-10 cm)	8.3	0.28	0.21	1.62
AB1b	240-300	10YR4/2 Dark grayish brown	EX	Abundant soft concretions (nodule 2-5 cm) + Disperse powder	No	7.9	1.44	0.24	9.39
Bkkb	300-420	10YR6/2 Light brownish gray	EX	Abundant soft concretions (nodule 2-5 cm) + Disperse powder	No	8.1	0.94	0.21	24.61
CB1b	420-480	10YR4/6 Dark yellowish brown	ST	rare soft concretions (nodule 2-5 cm) + Disperse powder	Few gravel (2-10 cm)	8.0	0.87	0.28	0.92
CB2b	480-570	7.5YR3/4 Dark brown	MO	rare soft concretions 2-5 cm	Few gravel (2-10 cm)	7.7	1.17	0.25	0.98
CB3b	570-630	7.5YR4/3 Brown	MO	rare soft concretions 2-5 cm	Few gravel (2-10 cm)	7.8	0.81	0.24	0.57
AB2b	630-690	7.5YR3/3 Dark brown	MO	rare soft concretions 2-5 cm	Few gravel (2-10 cm)	7.7	1.41	0.19	0.73
CB4b	690-740	7.5YR3/4 Dark brown	ST	Pseudomycelia	Few gravel (2-10 cm)	7.7	1.00	0.19	1.05
AB3b	740-840+	7.5YR3/4 Dark brown	ST	Pseudomycelia	Few gravel (2-10 cm)	7.7	1.67	0.24	2.18

*SL = 0-2% Slightly calcareous; MO = 2-10% Moderately calcareous; ST = 10-25% Strongly calcareous; EX ≥ 25% Extremely calcareous

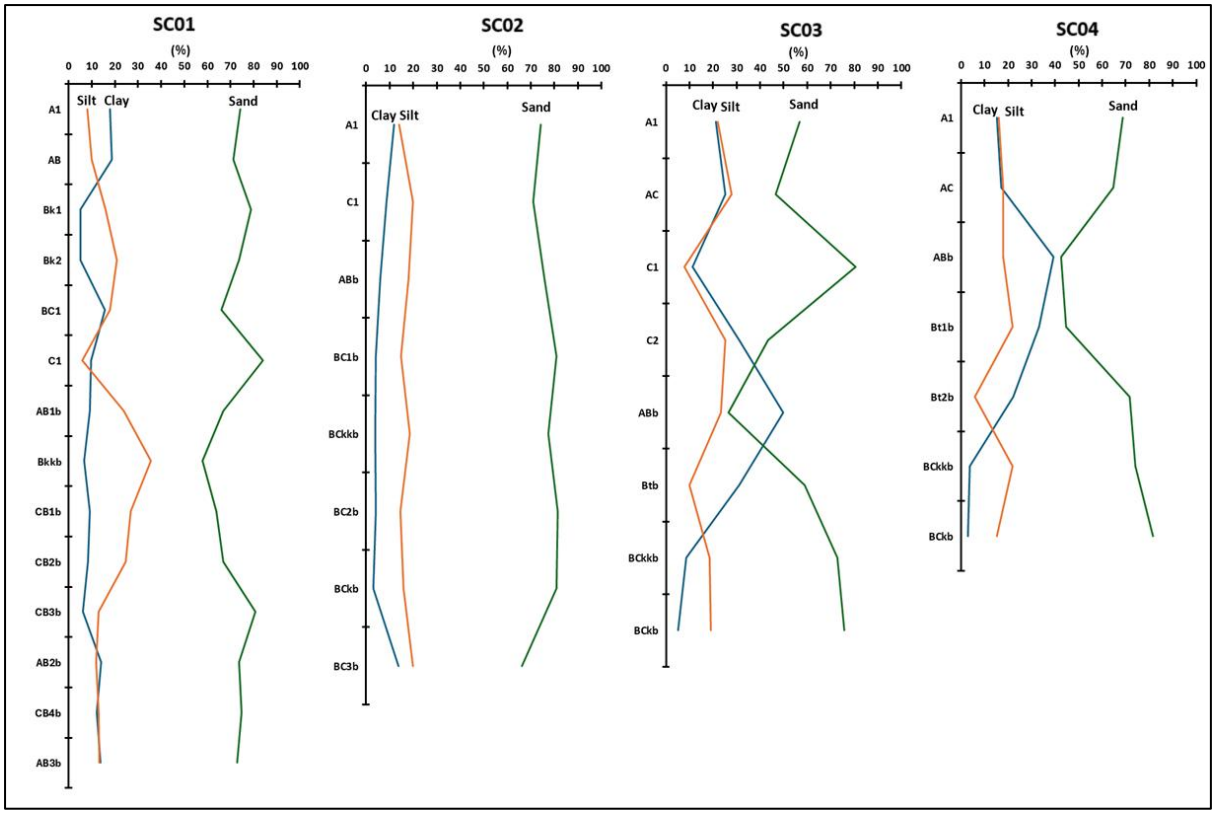


Fig. 5.3. Particle size distribution with depth in the four sections.

The section SC02 presented eight different horizons (Fig. 5.2B). Boundaries between horizons are mostly gradual and wavy. Nevertheless, the boundary between the layer C1 and ABb is sharp and smooth, while the one between BC1b and BCkkb is clear and smooth. SOM is typically low, ranging from 0.19 to 0.52 wt.%, with the maximum observed in the topsoil (A1). The horizon, ABb, also show a relatively high value as compared to the C1 above and BC1b immediately below. The texture along the section is mainly variating between loamy sand and sand loamy texture. Sand fraction is dominant across the section, ranging from 66 to 81wt.%, with the maximum observed in the bottom part of the section (BC1b to BCkb), except for layer BC3b, where the sand fraction is the lowest observed in the whole section. The clay fraction is mostly below 10 wt.%, except for the topsoil (A1), where the proportion of is around 12%, and the bottom layer BC3b, with a 14 wt.% of clay (Fig. 5.3). The soil pH ranges from a 6.9 (near neutral) in the topsoil A1 to 8.4 (moderately alkaline) in the layer BC3b. The EC on the other hand, ranges from 0.21 to 2.81 $dS.m^{-1}$, with the maximum value observed in the layer BCkkb.

Horizons below C1, show relatively high values of EC as compared to the upper part of the section (A1 and C1) (Table 2). The $CaCO_3$ content varies from a minimum of 0.22 wt.% in the topsoil to a maximum of 14.24 wt.% in the layer BCkkb. The layer BCkb is also characterised by a relatively high $CaCO_3$ content (5.94 wt.%) as compared to the other layers within the section. Carbonates feature along the section mostly accumulate in form of diffuse powder in all the layers except for A1 and BC3b. Nevertheless, some pseudomycelia carbonate are also observed in the layer BC2b. Gravel fragments are rare to common in certain layers, particularly C1, BCkkb, BC2b, and BCkb. These gravels consist mainly of basalt and sandstone fragments of the Kalahari Supergroup undergoing weathering (Fig. 5.4.D).

Table 5.2. Morphological characteristics and physicochemical properties of section SC02

Horizon /Layer	Depth cm	Munsell colour (moist)	10% HCl reaction	Visible carbonate features	Other secondary features	pH (H_2O)	EC $dS.m^{-1}$	SOM wt.%	$CaCO_3$ wt.%
A1	0-20	10YR3/2 Very dark grayish brown	SL	No	No	6.9	0.35	0.52	0.22
C1	20-110	10YR5/2 Brown	ST	Hard concretions (10YR8/1 White)	Black gravels (10YR3/1 Very dark gray); Light gray gravels (10YR7/2)	7.4	0.21	0.27	1.52
ABb	110-185	10YR2/1 Black	ST	Soft concretions (10YR7/1 Light gray), filling the porosity	_	7.6	1.55	0.38	1.18
BC1b	185-240	7.5YR4/4 Brown	ST	Disperse powder	_	7.6	1.95	0.21	1.56
BCkkb	240-360	7.5YR5/4 Brown	EX	Coating gravel + disperse powder + soft concretions	light gray gravel (10YR7/1)	7.8	2.81	0.26	14.24
BC2b	360-500	7.5YR5/6 Strong brown	ST	rare soft concretions + pseudomycelia	Rare black gravels (7.5YR2.5/1 Black)	7.9	2.50	0.19	1.96
BCkb	500-580	7.5YR5/6 Strong brown	EX	Common soft concretions	Common black gravels (7.5YR2.5/1 Black)	8.0	2.40	0.21	5.94
BC3b	580-600+	7.5YR5/4 Brown	SL	_	_	8.4	0.34	0.28	0.29

*SL = 0-2% Slightly calcareous; MO = 2-10% Moderately calcareous; ST = 10-25% Strongly calcareous; EX ≥ 25% Extremely calcareous

The section, SC03, is characterised by eight horizons as shown in Fig. 5.2C. The boundaries between horizons are generally gradual and wavy, except for the boundary between C1 and C2, and that between C2 and ABb, which are sharp and smooth. SOM is generally low, ranging from 0.21 to 0.43 wt.% (Table 5.3). Unlike SC01 and SC02, the maximum content is not

observed in the topsoil, but in layer ABb, while SOM content in A1 is 0.41 wt.%. The soil texture differs considerably from one layer to another. The clay fraction is dominant with 50% in the ABb layer, which has a clayey texture. In the other layers of the section, the sandy fraction is dominant. However, layers such as Btb, C2, A1 and AC are characterised by a relatively high proportion of clay, ranging from 21 to 31 wt.% (Fig. 5.3). The textures are sandy clay loam, clay loam, sandy clay loam and loam for Btb, C2, A1 and AC respectively. It is essential to note the organisation of layer C2, which is characterised by alternating sub-layers of varying thickness, ranging from 5 to 10 cm. Dark loamy (10YR3/4) sub-layers alternate with yellowish brown sandy (10YR5/4) sub-layers. Furthermore, this arrangement closely looks like the deposits currently observed in the riverbed. Layer C1 and the two layers at the bottom of the section (BCkkb and BCkb) are characterised by a predominance of sandy fraction, ranging from 71 to 81 wt.%, with a maximum observed in layer C1, and a low clay fraction, generally below 10 wt.%. The textures are sandy loam to loamy sand. The pH values along the section vary between 7.3 and 7.8. The lowest value is observed in the topsoil (A1), corresponding to a slightly alkaline pH. In fact, the pH is slightly alkaline within the section. The EC is typically low, ranging from 0.22 to 0.38 $dS.m^{-1}$. The maximum is observed in the layer C2, while the minimum is observed in the layer BCkb at the bottom of the section. The $CaCO_3$ content is characterised by a huge variation along the section ranging from 0.28 in the layer Btb to 16.25 wt.% in the layer BCkkb. Carbonate features are mostly in the form of disperse powder, while hard concretions are observed in the two bottom layers BCkkb and BCkb (Fig. 5.4.E). As in the case of the sections described above (SC01 and SC02), fragments of basaltic and sandstone rocks of the Kalahari Supergroup are very common in certain layers, particularly C1, BCkkb and BCkb.

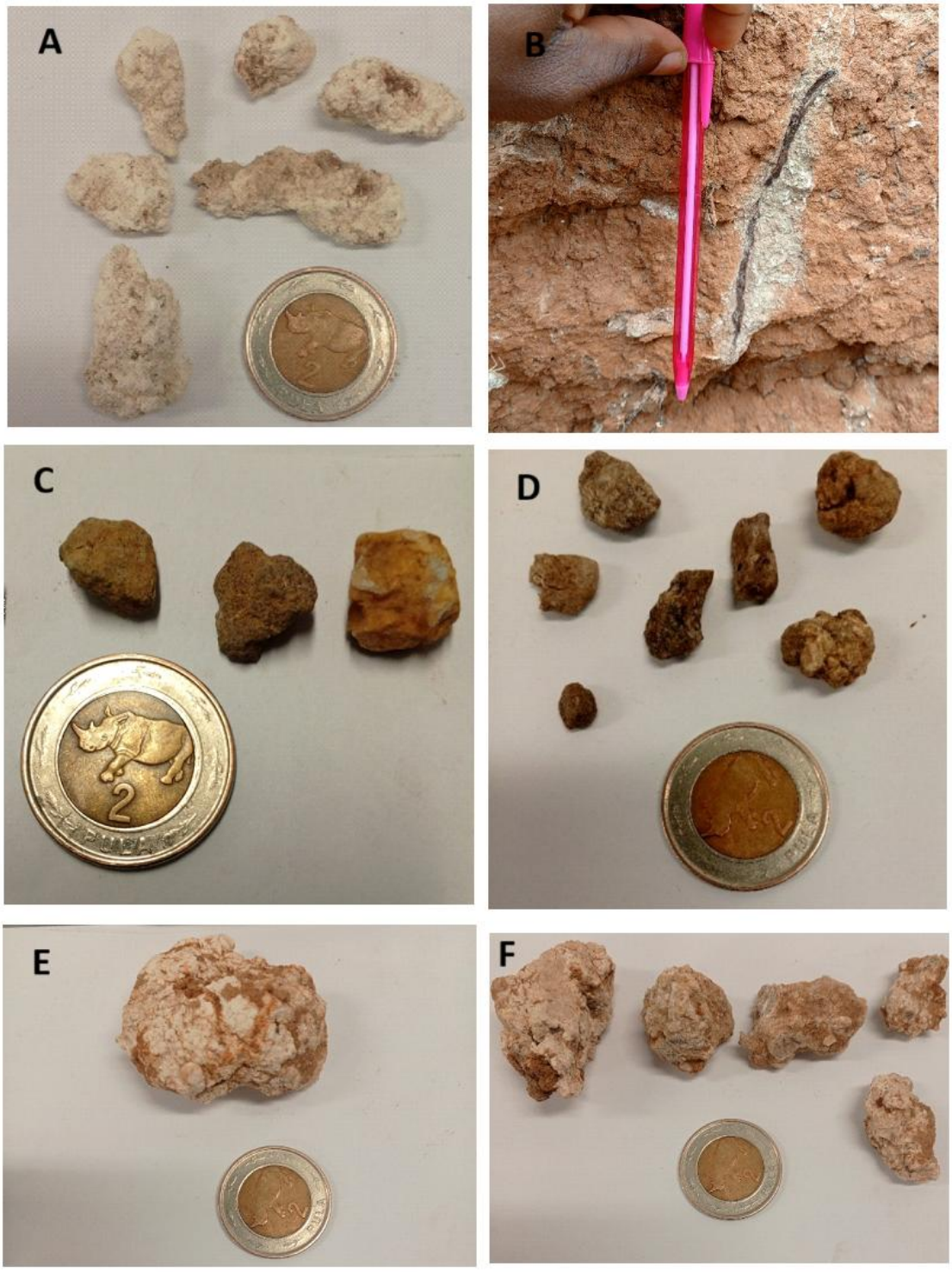


Fig. 5.4. A. Soft carbonate concretions isolated from the layer Bkkb of SC01; B. Pseudomycelia observed in layers CB4b of SC01; C. Gravels isolated from the layer C1 of SC01; D. Gravels isolated from SC02; E. Hard carbonate concretions isolated from the layer BCkkb of SC03; F. Hard carbonate concretions isolated from the layer BCkkb of SC04.

Table 5.3. Morphological characteristics and physicochemical properties of section SC03

Horizon /Layer	Depth cm	Munsell colour (moist)	10% HCl reaction	Visible carbonate features	Other secondary features	pH (H_2O)	EC $dS.m^{-1}$	SOM wt.%	$CaCO_3$ wt.%
A1	0-15	10YR3/2 Very dark grayish brown	SL	No	No	7.3	0.31	0.41	0.58
AC	15-42	7.5YR3/3 Dark brown	ST	Disperse powder	No	7.6	0.26	0.34	2.44
C1	42-70	7.5YR4/2 Brown	ST	Disperse powder	Black gravel (7.5YR2.5/1)	7.6	0.24	0.25	1.11
C2	70-140	10YR4/1 Dark gray	ST	Disperse powder	No	7.8	0.38	0.34	1.70
ABb	140-205	10YR3/4 Dark yellowish brown	EX	Disperse powder	Light red marks cavity (2.5YR6/6)	7.8	0.35	0.43	2.91
Btb	205-245	7.5YR5/6 Strong brown	SL	No	No	7.7	0.28	0.33	0.28
BCkkb	245-375	7.5YR5/4 Brown	EX	Hard concretions (10YR8/1 White)	Black gravel (7.5YR2.5/1)	7.8	0.25	0.24	16.25
BCkb	375-430+	7.5YR6/6 Reddish yellow	EX	Hard concretions (10YR8/1 White)	Black gravel (7.5YR2.5/1)	7.8	0.22	0.21	4.00

*SL = 0-2% Slightly calcareous; MO = 2-10% Moderately calcareous; ST = 10-25% Strongly calcareous; EX ≥ 25% Extremely calcareous

The section SC04 is characterised by seven horizons (Fig. 5.2D). The boundaries between horizons are generally gradual and smooth, except for the boundary between AC and ABb, and that between Bt1b and BCkkb, which are sharp and smooth. The SOM content varies between 0.23 and 0.62 wt.% with a maximum value observed in A1. ABb and Btb are characterised by relatively high SOM content, 0.43 and 0.48 wt.% respectively. As in SC03, soil texture varies considerably from one horizon to another. The sandy fraction remains dominant in all layers, varying from 43 to 82 wt.% (Fig. 5.3). The highest values are observed in the basal layers, Bt2, Ckkb and Ckb, which have loamy sand textures. A1 and AC are characterised by sandy loam textures, while ABb and Bt1b have a relatively high clay content, 39 and 33 wt.% respectively.

The texture of these two layers is clay loam. The pH ranges from 6.4 (slightly acidic) in the layer A1 to 7.7 (slightly alkaline) in the layer BCkb. The EC is mostly low all along the section, ranging from 0.14 to 0.78 $dS.m^{-1}$. The $CaCO_3$ content varies from 0.02 wt.% in the layer A1 to 21.09 wt.% in the layer BCkkb. Carbonate features are observed in the BCkkb and BCkb layers, mainly in the form of diffuse powder, sometimes coating gravel, or in the form of soft concretions (Fig. 5.4F). Gravel-sized rock fragments of the Kalahari Supergroup are also abundant within these horizons.

Table 5.4. Morphological characteristics and physicochemical properties of section 04

Horizon /Layer	Depth cm	Munsell colour (moist)	10% HCl reaction	Visible carbonate features	Other secondary features	pH (H2O)	EC $dS.m^{-1}$	SOM wt.%	$CaCO_3$ wt.%
A1	0-15	10YR3/1 Very dark brown	SL	No	No	6.4	0.14	0.62	0.02
AC	15-50	10YR3/2Very dark grayish brown	SL	No	No	6.8	0.25	0.34	0.07
ABb	50-70	10YR3/1 Very dark brown	ST	No	No	7.4	0.37	0.43	1.73
Bt1b	70-90	10YR2/1 Black	SL	No	No	7.3	0.78	0.48	0.50
Bt2b	90-160	5YR3/3 Dark reddish brown	SL	No	No	7.4	0.41	0.36	0.29
BCkkb	160-260	5YR5/3 Reddish brown	EX	Coating gravel + disperse powder + soft concretions	Black gravel (7.5YR2.5/1)	7.5	0.42	0.24	21.09
BCkb	260-400+	5YR5/6 Yellowish red	EX	Coating gravel + disperse powder + soft concretions	Black gravel (7.5YR2.5/1)	7.7	0.34	0.23	6.19

*SL = 0-2% Slightly calcareous; MO = 2-10% Moderately calcareous; ST = 10-25% Strongly calcareous; EX ≥ 25% Extremely calcareous

5.4.2. Particle size analysis and micromorphology of the selected sandy layers

The inclusive statistical parameters obtained from the particle size analysis of sandy layers C1, sections SC01, SC02 and SC03, as well as layer C2 of SC03 and layer AC of SC04, are presented in Table 5.5. In general, the sandy layers in SC01, SC02 and SC03 (layer C1) all have an average fine sand size (Mz between 2.30 Φ and 2.68 Φ), are poorly sorted (σI: 1.66 to 1.99), have positive or slightly positive skewness (SkI: 0.15 to 0.25) and are classified as highly leptokurtic (KG: 2.11 to 2.40). In contrast, layers C2 in section SC03 and AC in section SC04 show a spike towards a coarse silt average size (Mz is 4.61 Φ and 4.78 Φ for C2 and AC, respectively), are extremely poorly sorted (σI: 3.03 and 3.28), show very positive skewness (SkI: 0.45 and 0.58) and are classified as leptokurtic to very leptokurtic (KG: 1.27 and 1.57 for C2 and AC, respectively).

Table 5.5. Statistical grain size parameters (Mz: mean size; σI: inclusive standard deviation/sorting; SkI: inclusive skewness; KG: graphic kurtosis) for the selected sandy layers (C1, C2, and AC) across the studied sections (SC01–SC04).

Sample	Mz (Mean Size)		σI (Sorting)		SkI (Skewness)		KG (Kurtosis)	
SC01C1	2.68 Φ	Fine Sand	1.82	Poorly Sorted	0.22	Positive	2.4	Very Leptokurtic
SC02C1	2.57 Φ	Fine Sand	1.66	Poorly Sorted	0.15	Slightly Positive	2.12	Very Leptokurtic
SC03C1	2.3 Φ	Fine Sand	1.99	Poorly Sorted	0.25	Positive	2.11	Very Leptokurtic
SC03C2	4.61 Φ	Coarse Silt	3.28	Extremely Poorly Sorted	0.45	Very Positively Skewed	1.27	Leptokurtic
SC04AC	4.78 Φ	Coarse Silt	3.03	Extremely Poorly Sorted	0.58	Very Positively Skewed	1.57	Very Leptokurtic

Micromorphology of the sandy layers (C1 in SC01, SC02, SC03, C2 in section SC03 and AC in section SC04) are presented in Fig. 5.5. A to E. Observations across all five images (A-E) reveal that the sand fraction is predominantly composed of transparent, colourless quartz grains. Accessory dark, opaque minerals and coloured minerals (appearing brown or reddish)

are present in all views. Clear quartz grains represent the dominant population in the C1 layers of the three upstream sections (Fig. 5.5. A, B and C), characterised by a shape that is predominantly angular to sub-angular. Their edges are typically sharp and show little wear, and their outlines are irregular, indicative of limited mechanical abrasion. The minor part, which is dark (ranging from opaque to brownish red), exhibits a wide heterogeneity of shapes. These dark minerals parts include both highly angular and irregular fragments, typical of very fine splinters or small residual particles, as well as elongated, ovoid, or sub-rounded grains whose angularity is visibly less pronounced than that of the main quartz fraction. This latter, smoother morphology is particularly noticeable on the larger dark fragments. This dark material also incorporates very fine, diffuse particles which appear as a patina or coating associated with the quartz grains. Image B (SC02, C1) appears to contain some of the largest individual quartz grains among the C1 samples, while the grains in image C (SC03, C1) display a particularly high degree of angularity.

In contrast, the two downstream layers, C2 of SC03 (panel D) and AC of SC04 (panel E), show a significantly lower concentration of grains per unit area and a reduced mean grain size compared to the C1 layers, confirming an overall shift to the silt-dominated matrix indicated by the mean particle size. In panel D, the grains appear more dispersed within the matrix, although the primary quartz grains remain angular. Similarly, panel E (SC04AC) presents a dispersed population of mostly sub-angular quartz, with the overall view reflecting a much finer-grained environment than seen in the C1 layers.

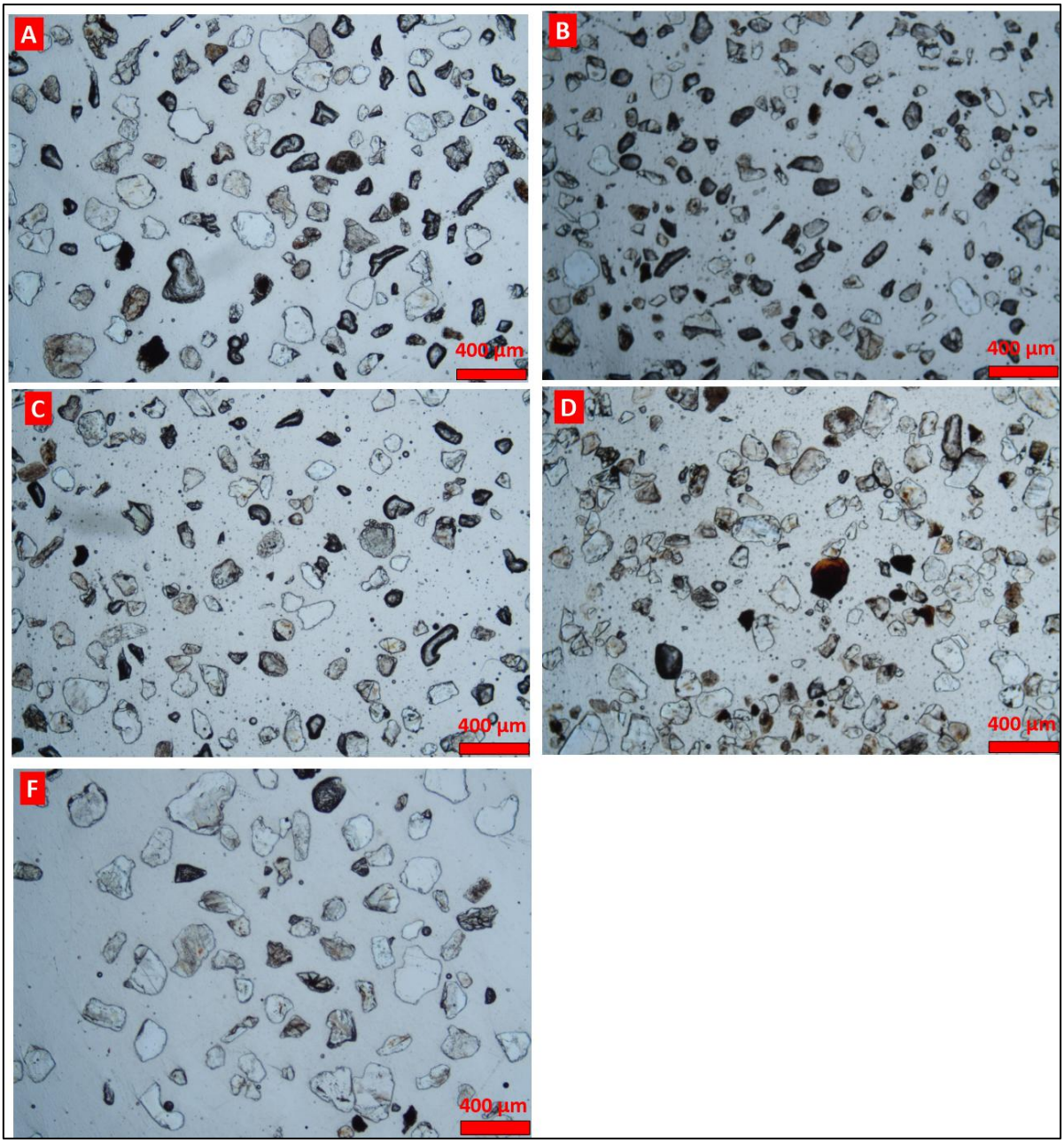


Fig. 5.5. (A–E). Images of the sand fraction, observed under a petrographic microscope using Plane Polarised Light (PPL), detailing the morphological characteristics of the grains. Images B, C, and D show the sand fraction from Layer C1 across Sections SC01, SC02, and SC03, respectively. Image E illustrates the sand fraction from Layer C2 within the same section SC03. Image F provides the observation for the Layer AC in section SC04.

5.4.3. Geochemistry

As presented in Table 5.6, silicon is the dominant element along within the studied sections with concentrations ranging from 61 and 88 wt.%. Aluminium and Fe also showed relatively high concentrations ranging from 4.7 and 14.0 wt.%, and from 3.6 to 10.0 wt.%, respectively. The concentration of Ca, on the other hand, shows a very contrasting pattern, with relatively high concentrations (5.2 to 17.3 wt.%) observed in horizons with a high $CaCO_3$ content, while the other horizons generally have concentrations below 5 wt.%. Magnesium also shows a contrasting pattern, with concentrations ranging from 0.5 to 3.6 wt.%. Sodium, K and Ti are generally present in minor proportions, while Mn and P are generally found in trace concentrations.

The overall trends observed for the five geochemical indices applied in this study are presented in Fig. 5.6.

In SC01, the calcification index varies from 0.38 to 2.32, with a peak in the Bkkb horizon and a minimum in the A1 topsoil layer. The AB1b (1.07–1.17) and Bk2 (0.89–0.91) horizons also have relatively high values. The Mg/Ca ratio, which varies between 0.22 and 1.23, shows a general decrease in the carbonate-rich horizons (Bk2, AB1b, Bkkb and AB3b) and reaches its minimum in Bkkb, where the highest calcification index and $CaCO_3$ content are observed. In SC02, the calcification index varies between 0.39 and 1.21, with maximum values in BCkkb and relatively high indices in BCkb. The Mg/Ca ratio varies between 0.50 and 2.81. As in SC01, horizons with a high calcification index and high $CaCO_3$ content are characterised by a low Mg/Ca ratio. SC03 is characterised by a calcification index between 0.2 and 1.97, with a peak in BCkkb parallel to the lowest Mg/Ca ratio in the section. However, unlike SC01 and SC02, an increase in $CaCO_3$ does not systematically correspond to a higher calcification index or a lower Mg/Ca ratio, as seen in BCkb, which maintains a high $CaCO_3$ but a low calcification index and the second highest Mg/Ca ratio (1.22). Finally, SC04 has a calcification index

ranging from 0.17 to 2.64, where the maximum in BCkkb and the high values in BCkb (0.55-0.73) follow the upstream pattern (SC01 and SC02) of high calcification indices contrasting with low Mg/Ca ratios in carbonate-rich layers.

The salinisation index remains low overall in all sections, generally below 0.30. It fluctuates between 0.19 and 0.30 in section SC01, while stabilising in similar ranges for SC02 (0.12 to 0.32) and SC03 (0.12 to 0.30). Finally, section SC04 stands out with the lowest values, ranging from 0.08 to 0.20.

The clayeyness index is generally low across all study sections. In SC01 and SC02, values range from 0.03 to 0.24 and 0.07 to 0.13, respectively, while SC04 exhibits a similarly restricted range of 0.06 to 0.18. By contrast, SC03 shows more pronounced fluctuations, with indices spanning from 0.06 to 0.28. Notably, horizons identified via grain-size analysis as having high clay content such as C2, ABb, and A, consistently align with the highest clayeyness indices recorded.

The RW index shows contrasting trends depending on the sections studied. In section SC01, it varies between 25 and 48%, with higher values in the upper horizons (A1 and AB) and localised peaks in C1, CB4b and AB3b. For SC02, the indices range from 29 to 60%, with the highest values in the ABb and BC1b horizons. Section SC03 shows higher values than the previous two, ranging from 32 to 82%; the maximum is observed in Btb, while the lowest indices are found in the upper part (A1 to C2). Finally, SC04 has the highest values in the transect, ranging from 36 to 83%, with a maximum identified in Bt2b and minimum values recorded between horizons A1 and Bt1b.

Table 5.6. Elements concentration of the four sections

Section	Horizon /Layer	Depth (cm)	Si	Al	Fe	Mn	Mg	Ca	Na	K	Ti	P	Total
			wt. %										
	A1	0-30	86	6.0	4.2	0.073	0.8	1.0	0.41	0.83	0.55	0.038	100
	AB	30-90	86	6.1	4.2	0.079	1.0	1.2	0.44	0.76	0.54	0.030	100
	Bk1	90-120	79	8.1	5.5	0.128	1.8	3.4	0.62	0.77	0.62	0.036	100
	Bk2	120-180	75	8.7	5.8	0.127	2.2	5.6	0.76	0.80	0.63	0.038	100
	BC	180-220	79	7.8	5.1	0.096	2.0	3.9	0.80	0.79	0.61	0.032	100
	C1	220-240	86	5.0	3.7	0.069	1.5	2.4	0.46	0.63	0.55	0.026	100
	AB1b	240-300	72	9.0	6.3	0.110	3.1	6.8	0.75	0.73	0.65	0.022	100
	Bkkb	300-420	61	9.0	6.8	0.119	3.5	17.3	0.82	0.53	0.66	0.030	100
	CB1b	420-480	66	12.9	10.2	0.075	3.4	4.1	1.60	0.75	1.02	0.054	100
	CB2b	480-570	66	13.0	10.1	0.068	3.1	4.1	1.50	0.77	0.98	0.057	100
	CB3b	570-630	66	11.9	10.2	0.086	3.6	5.1	1.58	0.74	1.06	0.073	100
	AB2b	630-690	68	12.9	10.0	0.070	2.8	3.6	1.30	0.76	0.97	0.055	100
	CB4b	690-740	76	9.0	7.9	0.059	1.6	2.7	0.79	0.76	0.97	0.033	100
SC01	**AB3b**	740-840+	72	10.3	8.4	0.064	2.0	4.2	0.98	0.77	0.92	0.039	100
	A1	0-20	85	5.8	4.4	0.065	1.3	1.8	0.46	0.86	0.58	0.051	100
	C1	20-110	84	5.2	4.3	0.069	1.6	2.9	0.54	0.72	0.61	0.041	100
	ABb	110-185	83	7.4	5.0	0.075	1.3	1.8	0.27	0.59	0.55	0.027	100
	BC1b	185-240	86	6.4	4.2	0.047	1.1	1.5	0.16	0.49	0.47	0.018	100
	BCkkb	240-360	79	7.4	4.8	0.047	2.1	5.2	0.36	0.51	0.54	0.018	100
	BC2b	360-500	81	7.8	5.3	0.059	2.1	1.8	0.55	0.55	0.60	0.019	100
	BCkb	500-580	74	8.6	6.4	0.120	2.4	6.2	0.88	0.58	0.69	0.041	100
SC02	**BC3b**	580-600+	86	6.3	4.0	0.050	1.5	0.7	0.40	0.65	0.54	0.015	100
	A1	0-15	79	8.5	5.4	0.080	1.7	2.5	0.85	0.99	0.62	0.051	100
	AC	15-42	71	11.6	7.2	0.107	2.4	4.4	1.25	1.09	0.73	0.061	100
	C1	42-70	86	4.7	3.6	0.055	1.4	2.4	0.46	0.60	0.48	0.037	100
	C2	70-140	72	12.0	7.4	0.111	2.3	3.6	1.04	1.06	0.73	0.055	100
	ABb	140-205	67	14.4	9.1	0.127	2.6	4.1	0.82	1.07	0.82	0.062	100
	Btb	205-245	85	7.5	4.5	0.062	0.8	0.6	0.05	0.77	0.53	0.018	100
	BCkkb	245-375	75	8.4	5.9	0.078	1.8	7.4	0.26	0.68	0.61	0.022	100
SC03	**BCkb**	375-430+	81	8.0	4.9	0.076	1.6	2.7	0.15	0.76	0.56	0.017	100
	A1	0-15	83	7.0	4.7	0.054	1.4	1.9	0.66	0.93	0.57	0.045	100
	AC	15-50	80	7.9	5.4	0.076	1.7	2.2	0.80	0.97	0.60	0.044	100
	ABb	50-70	71	12.3	8.0	0.112	2.3	3.6	0.96	1.06	0.79	0.056	100
	Bt1b	70-90	75	10.7	7.1	0.114	1.7	2.5	0.84	1.11	0.75	0.040	100
	Bt2b	90-160	88	5.4	4.3	0.052	0.6	0.6	0.04	0.57	0.48	0.023	100
	BCkkb	160-260	70	6.3	5.1	0.058	1.6	15.5	0.18	0.50	0.53	0.027	100
SC04	**BCkb**	260-400+	75	9.1	6.5	0.069	2.2	5.4	0.46	0.62	0.68	0.023	100

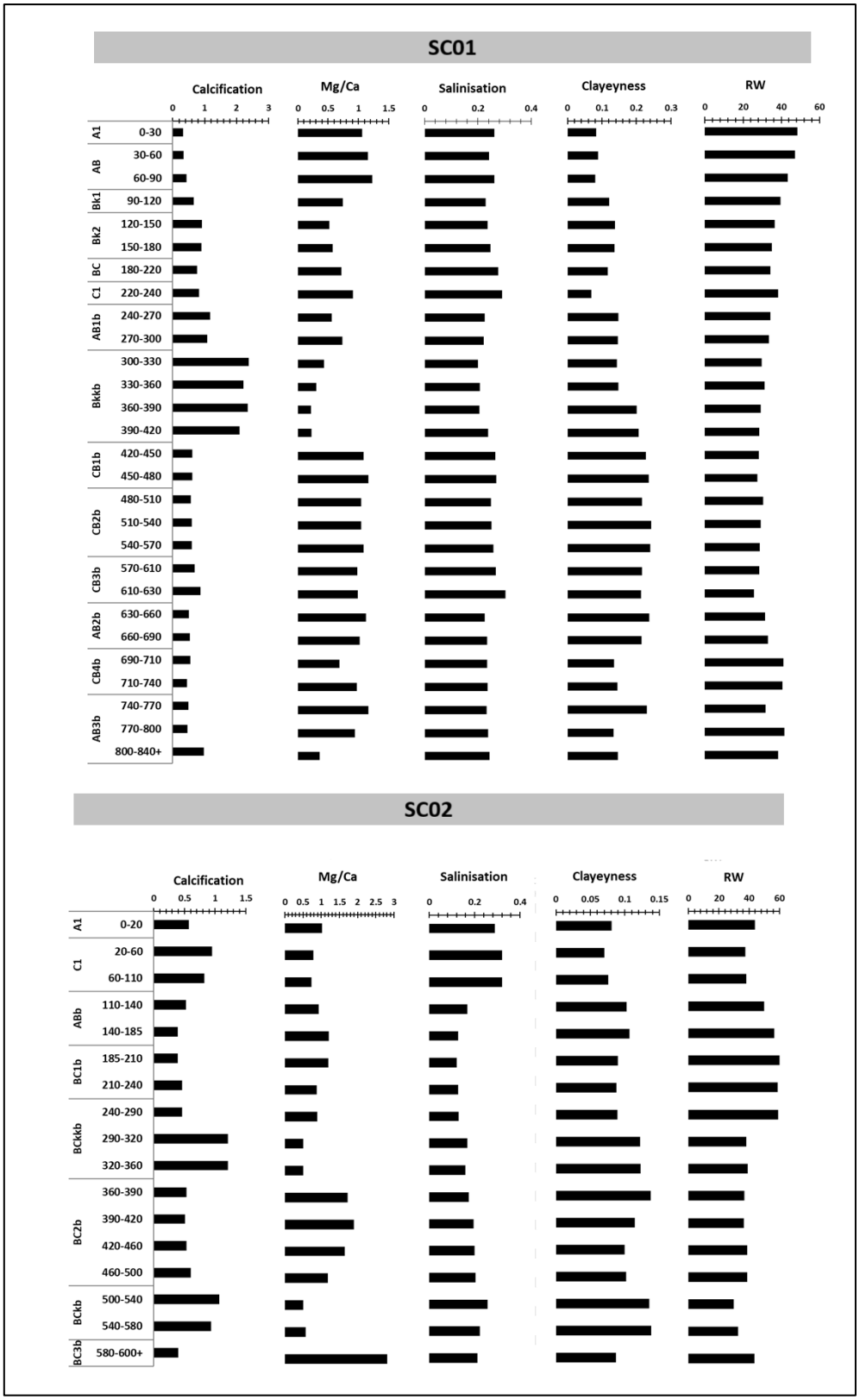


Fig. 5.6. Vertical distribution profiles of five geochemical indices: calcification index, Mg/Ca ratio, salinisation, clayeyness index, and robust index of chemical weathering (RW), across the depth of the respective studied sections.

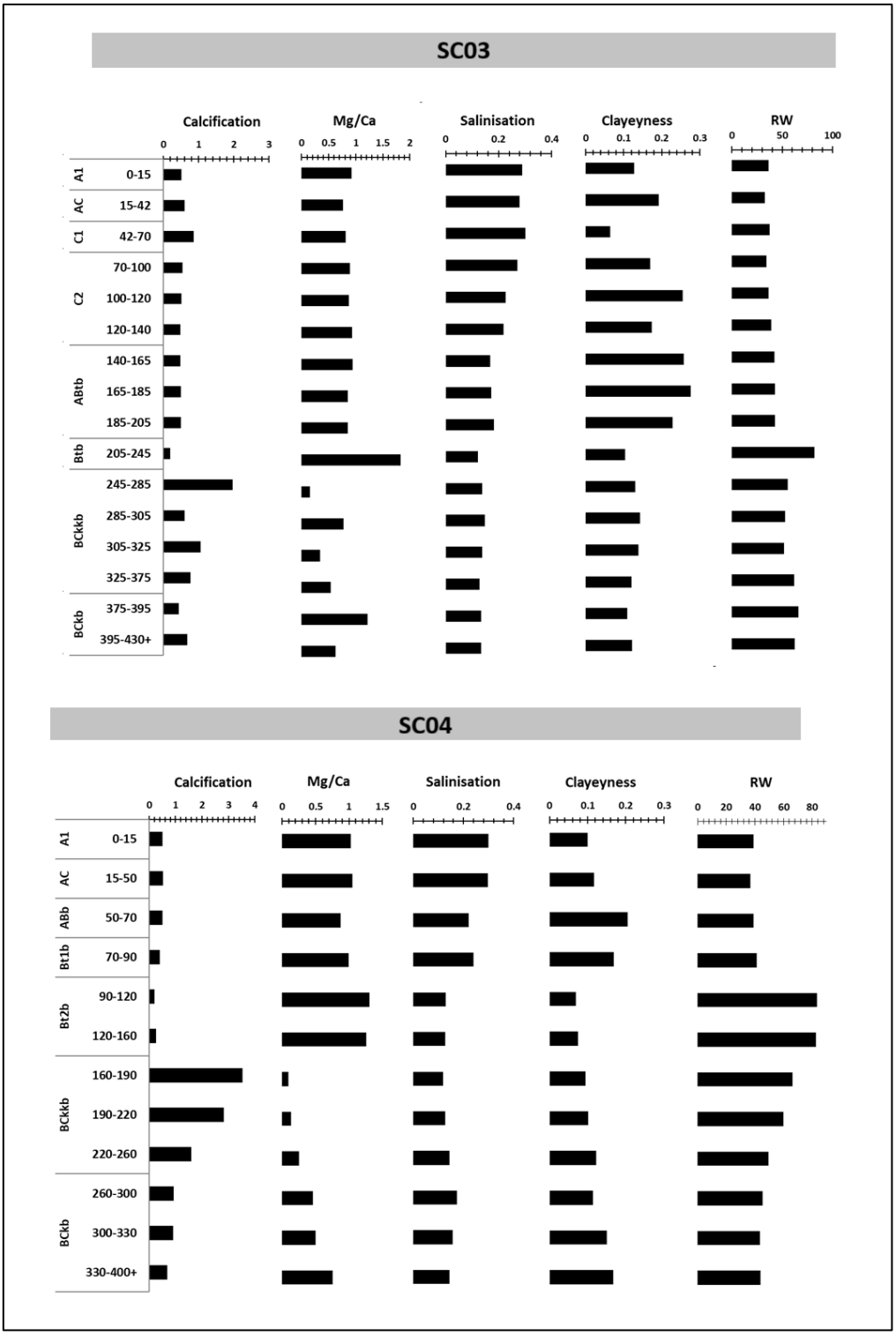


Fig. 5. 6. (continued)

5.5. Discussion

5.5.1. Sedimentary controls and depositional environments

The general pattern of the results, derived from morphological characteristics, sand grain micromorphology and geochemistry, consistently highlights that the current landscape is the product of combined pedogenic and depositional phases. The most significant evidence for this comes from section SC01, which is over 8 metres thick and demonstrates an alternation between multiple cycles of stability and deposition. This is evident in the form of sharp boundaries that signify the periodic interruption of pedogenesis and the subsequent burial of existing soil by newly arrived sediments (Nordt et al., 2025). Three distinct buried soil profiles are identified within this section, with the upper boundaries characterised by horizons AB1b, AB2b and AB3b. In contrast, the other downstream sections (SC02, SC03 and SC04), which are less thicker (6 m, 4.3 m and 4 m respectively), primarily highlight the most recent cycle. This cycle is characterised by the arrival of sediment layers C1 in sections SC01 and SC02, C1 and C2 in section SC03, and AC in section SC04.

The morphological characteristics observed in the buried soil (spanning from the AB1b to CB3b horizons) beneath the C1 layer in section SC01 (Fig. 5.2A) reflect the description by Franchi et al. (2021) of a well-developed calcic palaeosol, rich in carbonate nodules, and buried under 10 metres of Kalahari sand sediment. In fact, the study area, located at the transition between the Eastern Hardveld and the Sandveld, is characterised by a balance between erosion and deposition within a context of geodynamic stability, spanning the Palaeogene and continuing into the Quaternary, which has resulted in the prominence of relict hill masses (Eze, 2022). Moreover, this is consistent with the 3D topographic model (Fig. 5.1.C), which depicts these relict hill masses rising from

relatively flat terrain. Consequently, the buried palaeo-landscapes beneath the Kalahari sand deposits are exposed there.

Sand grain micromorphology and the inclusive statistical parameters of the particle size analysis for the layers constituting the final depositional phase (i.e., layer C1 in sections SC01 and SC02, layers C1 and C2 in section SC03, and layer AC in section SC04) are characterised by a variation in the depositional regime from upstream to downstream. The C1 layers consist of fine sand (Mz: 2.30–2.68 Φ), poorly sorted and composed mainly of angular to subangular quartz grains (Fig. 5.5.C–E). In contrast, the C2 layers beneath C1 in SC03 and AC in SC04 are characterised by coarse silt (Mz: 4.61–4.78 Φ), extremely poorly sorted, but also composed mainly of angular to subangular quartz grains (Fig. 5.4.E–F). The shape of the grains indicates transport over a short distance in a high-energy fluvial environment (Baek and Jo, 2025; Madhavaraju et al., 2021). These are also consistent by the presence of fragments of neighbouring parent material (basalt and sandstone fragments) in these layers. Furthermore, the fact that layer C2, covered by C1 in section SC03, is morphologically similar to the current riverbed deposits indicates similar deposition conditions. In other words, the deposits were formed under intermittent river flow, reflecting the current semi-arid climate. The clear sandy beds indicate times of strong current and high dynamics, which were able to move fine particles and leave behind coarser sand. In contrast, the dark loamy beds formed during the dry periods when the flow slowed or stopped, allowing finer particles and organic matter to settle and accumulate, resulting in an increase in SOM compared to C1. This is also evidenced by the very poor sorting observed in the layer, which results from this association between fine and coarse particles (Sumner et al., 2008). Thus, this layer would have been part of the riverbed for an extended period, given its thickness (layer C2). However, layers C1 are typical of high-energy deposition, probably linked to massive colluvial inputs given the high degree of

heterogeneity, reflected not only in the presence of debris from parent material, but also in the poor sorting observed (Mücher et al., 2018). Furthermore, while the thickness of the deposits is considerable in SC01, it gradually decreases downstream. The characteristics of the AC layer deposits (SC04) support a rapid decrease in energy. However, it is important to treat the particle size characteristics of AC with caution. This horizon is marked by a low degree of pedoturbation, evidenced by considerable root activity and a very dark greyish brown colour (10YR3/2), consistent with a gradual accumulation of SOM. On the other hand, the C1 deposits are probably linked to floods, given the stable geodynamic context and the fact that flood events have often been recorded in the area (Moses et al., 2023; Motsholapheko et al., 2011).

5.5.2. Pedogenic controls and processes

5.5.2.1. Modern soils

The modern soil varies in thickness from upstream to downstream. The modern soil profile in SC01 is as follows: A1–AB–Bk1–Bk2–BC–C1 (Fig. 5.2A). Based on IUSS Working Group WRB (2022) , this reflects a Calcaric Cambisol. Although the sand fraction is significant, the upper horizons have a clay content of more than 15%, which does not qualify as Arenosols. Similarly, it is excluded from the Calcisols reference group (soils with significant carbonate accumulation) because its B horizon, which although contains nodules, has a $CaCO_3$ content of only 6%, which is well below the 15% threshold required for the formation of a diagnostic calcic horizon. Consequently, the soil is classified as Cambisols, representing a moderately developed soil that shows minimal alteration (B horizon) but does not meet the diagnostic criteria of the other reference groups. The presence of a secondary accumulation of carbonates, although below the diagnostic threshold of 15%, justifies the application of the primary qualifier, resulting in its classification as Calcaric Cambisols. This is also supported by a RW ranging from 38 to 48%

characteristic of the low degree of chemical weathering observed (Cho and Ohta, 2022). Moreover, the low observed clayeyness index also highlights the poor degree of chemical weathering. Nevertheless, as mentioned above, the clay content is not negligible in the two upper horizons. In addition, the RW index also increases significantly upwards. This shows that although the degree of chemical weathering, and in particular hydrolysis, is low, it makes a considerable contribution to the ongoing soil formation process. The climatic conditions of arid and semi-arid environments are generally conducive for the accumulation of soluble salts within the soil in the form of secondary gypsum or carbonates (FAO, 2006). In the present case, the low salinisation index, combined with low EC values, indicates a very low degree of salinisation. However, the calcification index shows a significant increase in layers Bk1 and Bk2 (Fig. 5.6. SC01), also supported by the presence of diffuse powder and nodules (Table 5.1). Furthermore, the increase in the calcification index is coupled with a decrease in the Mg/Ca ratio, which would suggest an accumulation of carbonates, mineralogically related to calcite (Pinheiro Junior et al., 2021).

The modern soil in SC02 is represented by the profile A1–C1 (Fig. 5.2B). The total depth of the profile is greater than 100 cm, with a dominant proportion of sand, generally greater than 70%, while the clay content is less than 15%. This corresponds to the classification criteria for Arenosols (IUSS Working Group WRB, 2022b). The RW index is generally low (Fig. 5.6. SC02), although there is an increase towards the surface soil (A1) in line with the increase in clay content and the clayeyness index which, as in the case of the previous profile, suggests a minimal but not negligible contribution of hydrolysis in the soil formation processes. Although the $CaCO_3$ content of horizon C1 is relatively low (1.52%), the increase in the calcification index and the presence of some nodules within this horizon indicate the accumulation of pedogenic carbonates, though to a lesser

extent than SC01. Furthermore, the concomitant decrease in the Mg/Ca ratio indicates calcite precipitation. The salinisation index and EC are low, reflecting a very low degree of salinisation.

The modern soil in SC03 is represented the profile A1–AC–C1–C2 (Fig. 5.2C). As with SC01, this profile shows an accumulation of pedogenic carbonate in the AC horizon, but this is not sufficiently developed to allow it to be classified as Calcisols ($CaCO_3$ is well below the 15% threshold). Furthermore, although sand is dominant throughout the profile, the clay content in the upper horizons (A1 and AC) is greater than 15%. Therefore, given the poor development of the profile, it should be classified as Calcaric Cambisols. The RW index is relatively low compared to SC02. Nevertheless, the clayeyness index and clay content highlight the importance of clay. While this could be interpreted as evidence of a significant contribution of clay formation to the ongoing pedogenesis, the contrast between the two indices shows that great caution is advised, as the deposition processes discussed in the previous section could have promoted the accumulation of clays. This implies a translocation of clay particles from upstream (SC01, SC02) to downstream (SC03, SC04) due to the decrease in depositional energy. This is consistent with the high clayeyness index and clay content of C2. The calcification index highlights a calcification process within horizons AC and C1. However, as in the case of clay accumulation, the contribution of parent materials cannot be ruled out given the nature of layer C1. Furthermore, the increase in the calcification index in this layer is not accompanied by a concomitant decrease in the Mg/Ca ratio, which could indicate the presence of dolomite (Pinheiro Junior et al., 2021). The hard nodules observed, which are inconsistent with the degree of pedogenic evolution of the layer, would mainly result from sedimentary processes. As in the case of the profiles described above, salinisation remains a minor process.

The modern soil profile in section SC04 is as follows: A1–AC (Fig. 5.2D). It is a Cambisols due to its shallow depth and low $CaCO_3$ content. Pedogenic processes are very poorly developed. However, as in the case of SC03, translocation has probably contributed to the relatively high clay content observed.

In summary, the modern soil profiles predominantly reveal poorly developed soils, mainly classified as Cambisols and Arenosols, which aligns with certain soil groups described in the region by Eze (2022). The dominant pedogenetic process observed is calcification, which is supplemented by the neoformation of clays resulting from the geochemical alteration of sediments. This entire pattern of minimal pedogenic development, calcification, and neoformation is confirmed by previous results in the region (Dina Ebouel et al., 2025b; Eze et al., 2025).

5.5.2.2. Buried palaeosols

The thickness of the buried palaeosol profiles also varies between upstream and downstream. SC01 revealed three successive cycles. The most superficial palaeosol profile is as follows: AB1b–Bkkb–CB1b–CB2b–CB3b (Fig. 5.2A). Given the high $CaCO_3$ content observed in the Bkk horizon (24.61%) and the abundance of carbonate features, including nodules and diffuse powder, it corresponds to palaeo-Calcisols (Nordt et al., 2025). Calcification is therefore the most important pedogenic process, characterised by an accumulation of calcite, as shown by the decrease in the Mg/Ca ratio coinciding with the increase in the calcification index in AB1b and Bkkb. Chemical weathering and salinisation, on the other hand, are very low, as shown by the RW and clayeyness indices in the first case and the salinisation index in the second. The second buried palaeosol of SC01, immediately below, consists of layers AB2b and CB4b. It has a very sandy profile (>70%), low SOM content (0.19%) and peds. It therefore corresponds to palaeo-Entisol (Nordt et al., 2025). The above description shows little to moderate pedogenesis, but there are accumulations of $CaCO_3$

in the form of pseudomycelia and a few soft nodules. The last buried palaeosol of SC01 is capped by AB3b. It is difficult to discuss this cycle, which comprises only a single exposed layer. However, a few rare pseudomycelia are also observed.

The palaeosol profile buried in SC02 is as follows: ABb–BC1b–BCkkb–BC2b–BCkb–BC3b. The presence of BCkkb, consisting of soft nodules and diffuse powder and of coating gravels, demonstrates calcic characteristics. However, the $CaCO_3$ content is slightly less than 15%. Furthermore, the high sand content (above 60%) and low clay content (below 15%) throughout the profile is characteristic of Arenosols (IUSS Working Group WRB, 2022), equivalent to palaeo-Aridisols (Nordt et al., 2025). The high calcification indices in the BCkkb and BCkb layers show that calcification is the dominant pedogenic process, leading to the accumulation of calcite, as evidenced by the decrease in the Mg/Ca ratio in these layers. However, the significant presence of sandstone parent rock remnants in a context where some are often characterised by carbonate cement (Franchi et al., 2021) could also indicate a partially lithogenic origin for the observed accumulations. The low clayeyness indices are consistent with the low clay content. However, the ABb and BC1b layers have relatively high RW indices, indicating greater chemical weathering. This contrast can be explained by the loss of fine particles (clay and SOM) in the upstream, as explained earlier. The relatively high EC measured in the profile contradicts the low salinisation index values. This discrepancy indicates that ion accumulation is not primarily due to salts. This situation can be explained by the abundant presence of basalt rock fragments undergoing chemical weathering within the profile. The hydrolysis of these rocks releases a significant amount of highly conductive cations (Na^+, K^+, Ca^{2+} and Mg^{2+}), which are responsible for the increase in EC (Anda et al., 2015).

The palaeosol profile buried in SC03 is as follows: ABb–Btb–BCkkb–BCkb. The diagnostic BCkkb, characterised by hard carbonate nodules, refers to palaeo-Calcisols. Calcification is the dominant pedogenic process, as shown by the high calcification indices in BCkkb and BCkb. The decrease in the Mg/Ca ratio in these layers, as in the previous cases, is indicative of calcite. Despite high clayeyness index and content in the ABb and Btb layers, the RW index is low, indicating a low degree of chemical weathering and supporting the deposition of translocated clay particles from upstream.

The buried palaeosol profile of SC04 is as follows: ABb–Bt1b–Bt2b–BCkkb–BCkb. As in the case of SC03, this also corresponds to palaeo-Calcisols. Calcification is the predominant pedogenic process, characterised by the accumulation of calcite. However, the RW index is very high in the Bt horizons (over 80%). The values observed are similar to those found in tropical soils (Cho and Ohta, 2022). This is inconsistent with the clay index and is probably characteristic of a change in the parent material. The multiple fragments of sandstone undergoing weathering may be responsible for these high RW values.

In sum, across all sections, Calcification is the most important pedogenic process. Chemical weathering is generally low, supporting the classification of these profiles as typical of semi-arid or arid palaeoenvironments.

5.6. Conclusions

This comprehensive study of the pedosedimentary sequences in central Botswana reveals that the landscape evolved as a result of cyclical palaeoenvironmental changes occurring within a context of long-term geodynamic stability. The findings confirm the existence of a consistent alternation between periods of pedogenic stability, during which multi-layered palaeosols formed (e.g. SC01), and periods of abrupt sedimentary deposition driven by a pulsed fluvial regime. Sedimentological

evidence, including abrupt horizon boundaries and downstream fining, corroborates these interruptions and subsequent burial events. The morphology of the deposits (alternating sandy and loamy beds) reflects intermittent river flow, analogous to the current semi-arid climate. Calcification is the dominant and persistent process across all profiles (both ancient and modern). This is evidenced by high $CaCO_3$ contents and diagnostic features that classify palaeosols primarily as Calcisols (SC01, SC03, SC04) or Arenosols (SC02), and modern soils as Calcaric Cambisols or Arenosols. Geochemical analysis indicates an overall low degree of chemical weathering (low RW), reflecting the region's arid conditions. However, localised anomalies, such as high EC with low salinisation attributed to the release of conductive cations (Ca^{2+}, Mg^{2+}) from basalt weathering and unexpectedly high RW values in SC04, underscore the influence of lithogenic factors (parent material change and basalt weathering) on soil chemistry. The study validates pedogenic carbonate accumulation as the dominant pedogenic process in the soils of the region, linking the present-day chemical landscape directly to Quaternary environmental cyclicity and highlighting its significance for the regional carbon balance. Nevertheless, these results have limited value without tracing the origin of the calcium, which is critical in carbon balances and understanding the processes of calcium ion mobilisation within carbonates in these environments.

References

Achyuthan, H., Shankar, N., Braida, M., Ahmad, S.M., 2012. Geochemistry of calcretes (calcic palaeosols and hardpan), Coimbatore, Southern India: Formation and Paleoenvironment. Quaternary International 265, 155–169. https://doi.org/10.1016/j.quaint.2012.01.037

Akinyemi, F.O., 2021. Vegetation Trends, Drought Severity and Land Use-Land Cover Change during the Growing Season in Semi-Arid Contexts. Remote Sens (Basel) 13. https://doi.org/10.3390/rs13050836

Anda, M., Shamshuddin, J., Fauziah, C.I., 2015. Improving chemical properties of a highly weathered soil using finely ground basalt rocks. Catena (Amst) 124, 147–161. https://doi.org/https://doi.org/10.1016/j.catena.2014.09.012

Atlhopheng, J., Brown Mthanganyika Mapeo, R., Eckardt, F.D., 2022. Introduction to the Landscapes and Landforms of Botswana, in: Eckardt, F.D. (Ed.), Landscapes and Landforms of Botswana. Springer International Publishing, Cham, pp. 1–13. https://doi.org/10.1007/978-3-030-86102-5_1

Baek, S., Jo, K., 2025. Surface microtextures of quartz grains under intermittent sediment transport in a gravel bed in the Hantan River, South Korea. Sediment Geol 481, 106874. https://doi.org/https://doi.org/10.1016/j.sedgeo.2025.106874

Batisani, N., Yarnal, B., 2010. Rainfall variability and trends in semi-arid Botswana: Implications for climate change adaptation policy. Applied Geography 30, 483–489. https://doi.org/10.1016/j.apgeog.2009.10.007

Batjes, N.H., 2014. Total carbon and nitrogen in the soils of the world. Eur J Soil Sci 65, 10–21. https://doi.org/10.1111/ejss.12114_2

Bhattacharyya, T., Wani, S.P., Pal, D.K., Sahrawat, K.L., 2017. Soil as Source and Sink for Atmospheric CO2, in: Goel, M., Sudhakar, M. (Eds.), Carbon Utilization: Applications for the

Energy Industry. Springer Singapore, Singapore, pp. 61–68. https://doi.org/10.1007/978-981-10-3352-0_4

Bittelli, M., Pellegrini, S., Olmi, R., Andrenelli, M.C., Simonetti, G., Borrelli, E., Morari, F., 2022. Experimental evidence of laser diffraction accuracy for particle size analysis. Geoderma 409, 115627. https://doi.org/https://doi.org/10.1016/j.geoderma.2021.115627

Cho, T., Ohta, T., 2022. A robust chemical weathering index for sediments containing authigenic and biogenic materials. Palaeogeogr Palaeoclimatol Palaeoecol 608, 111288. https://doi.org/10.1016/J.PALAEO.2022.111288

Díaz-Hernández, J.L., Barahona Fernández, E., Linares González, J., 2003. Organic and inorganic carbon in soils of semiarid regions: A case study from the Guadix-Baza basin (Southeast Spain). Geoderma 114, 65–80. https://doi.org/10.1016/S0016-7061(02)00342-7

Diaz-Hernandez, J.L., Sánchez-Navas, A., Delgado, A., Yepes, J., Garcia-Casco, A., 2018. Textural and isotopic evidence for Ca-Mg carbonate pedogenesis. Geochim Cosmochim Acta 222, 485–507. https://doi.org/10.1016/j.gca.2017.11.006

Dina Ebouel, F.J., Betsi, T.B., Eze, P.N., 2024. Soil inorganic carbon: A review of global research trends, analytical techniques, ecosystem functions and critical knowledge gaps. Catena (Amst) 242, 108112. https://doi.org/https://doi.org/10.1016/j.catena.2024.108112

Dina Ebouel, F.J., Kono Ebede, C.G., Bineli Betsi, T., Eze, P.N., 2025. Distribution and potential of rare earth elements fingerprinting as tracers for carbonate sources in soils developed on contrasting parent materials. Geoderma Regional 43, e01009. https://doi.org/https://doi.org/10.1016/j.geodrs.2025.e01009

Dina Ebouel, F.J., Molwalefhe, L.N., Betsi, T.B., Eze, P.N., 2025. A Multi-Proxy Pedosedimentary Insight into Calcium Origin, Sediment Provenance, and Depositional Environments in a NW

Botswana Landform. Earth Systems and Environment. https://doi.org/10.1007/s41748-025-00724-w

Eze, P.N., 2022. Soil Development in the Eastern Hardveld, in: Eckardt, F.D. (Ed.), Landscapes and Landforms of Botswana. Springer International Publishing, Cham, pp. 327–344. https://doi.org/10.1007/978-3-030-86102-5_19

Eze, P.N., Ebouel, F.J.D., Nkonga, I., Musiol, A., Schleicher, A.M., Günter, C., Norra, S., 2025. Weathering intensity and trace elements (Ni, Sr, Zn, and Cr) distribution in Vertisols developed on basalt in a semiarid environment: agronomic implications. Frontiers in Soil Science 5. https://doi.org/10.3389/fsoil.2025.1530962

Eze, P.N., Molwalefhe, L.N., Kebonye, N.M., 2021. Geochemistry of soils of a deep pedon in the Okavango Delta, NW Botswana: Implications for pedogenesis in semi-arid regions. Geoderma Regional 24. https://doi.org/10.1016/j.geodrs.2020.e00352

Ferdush, J., Paul, V., 2021. A review on the possible factors influencing soil inorganic carbon under elevated CO2. Catena (Amst). https://doi.org/10.1016/j.catena.2021.105434

Food and Agriculture Organization of the United Nations, 2006. Guidelines for soil description. Food and Agriculture Organization of the United Nations.

Franchi, F., Kelepile, T., Di Capua, A., De Wit, M.C.J., Kemiso, O., Lasarwe, R., Catuneanu, O., 2021. Lithostratigraphy, sedimentary petrography and geochemistry of the Upper Karoo Supergroup in the Central Kalahari Karoo Sub-Basin, Botswana. Journal of African Earth Sciences 173. https://doi.org/10.1016/j.jafrearsci.2020.104025

Frank, Lydia.O., Sarthi, P.P., 2025. The impact of seasonal variability of rainfall and drought on vegetation and livestock population in Central District, eastern Botswana. Grassland Research 4, 93–104. https://doi.org/https://doi.org/10.1002/glr2.70008

Haddon, I.G., McCarthy, T.S., 2005. The Mesozoic–Cenozoic interior sag basins of Central Africa: The Late-Cretaceous–Cenozoic Kalahari and Okavango basins. Journal of African Earth Sciences 43, 316–333. https://doi.org/https://doi.org/10.1016/j.jafrearsci.2005.07.008

IUSS Working Group WRB, 2022. World Reference Base for Soil Resources. International soil classification system for naming soils and creating legends for soil maps., 4th ed. Vienna, Austria.

Kuzyakov, Y., Horwath, W.R., Dorodnikov, M., Blagodatskaya, E., 2019. Review and synthesis of the effects of elevated atmospheric CO2 on soil processes: No changes in pools, but increased fluxes and accelerated cycles. Soil Biol Biochem 128, 66–78. https://doi.org/https://doi.org/10.1016/j.soilbio.2018.10.005

Madhavaraju, J., Armstrong-Altrin, J.S., James, R.A., Hussain, S.M., 2021. Palaeoenvironment and provenance signatures inferred from quartz grain surface features: A case study from Huatabampo and Altata beaches, Gulf of California, Mexico. J South Am Earth Sci 111, 103441. https://doi.org/https://doi.org/10.1016/j.jsames.2021.103441

Monger, H.C., 2014. Soils as Generators and Sinks of Inorganic Carbon in Geologic Time, in: Soil Carbon. Springer International Publishing, pp. 27–36. https://doi.org/10.1007/978-3-319-04084-4_3

Moses, O., Blamey, R.C., Reason, C.J.C., 2023. Extreme rainfall events over the Okavango river basin, southern Africa. Weather Clim Extrem 41, 100589. https://doi.org/https://doi.org/10.1016/j.wace.2023.100589

Motsholapheko, M.R., Kgathi, D.L., Vanderpost, C., 2011. Rural livelihoods and household adaptation to extreme flooding in the Okavango Delta, Botswana. Physics and Chemistry of the Earth, Parts A/B/C 36, 984–995. https://doi.org/https://doi.org/10.1016/j.pce.2011.08.004

Mücher, H., van Steijn, H., Kwaad, F., 2018. Chapter 2 - Colluvial and Mass Wasting Deposits, in: Stoops, G., Marcelino, V., Mees, F. (Eds.), Interpretation of Micromorphological Features of Soils and Regoliths (Second Edition). Elsevier, pp. 21–36. https://doi.org/https://doi.org/10.1016/B978-0-444-63522-8.00002-4

Naorem, A., Jayaraman, S., Dalal, R.C., Patra, A., Rao, C.S., Lal, R., 2022. Soil Inorganic Carbon as a Potential Sink in Carbon Storage in Dryland Soils—A Review. Agriculture (Switzerland) 12. https://doi.org/10.3390/agriculture12081256

Nash, D.J., 2022. Calcretes, Silcretes and Intergrade Duricrusts, in: Eckardt, F.D. (Ed.), Landscapes and Landforms of Botswana. Springer International Publishing, Cham, pp. 223–246. https://doi.org/10.1007/978-3-030-86102-5_13

Nordt, L., Stinchcomb, G., McCarthy, P., Driese, S., 2025. Soil Taxonomy adapted to buried paleosols: First approximation. Earth Sci Rev 266, 105141. https://doi.org/https://doi.org/10.1016/j.earscirev.2025.105141

Nunes, L.J.R., 2023. The Rising Threat of Atmospheric CO2: A Review on the Causes, Impacts, and Mitigation Strategies. Environments 10. https://doi.org/10.3390/environments10040066

Pinheiro Junior, C.R., Pereira, M.G., Azevedo, A.C. de, Van Huyssteen, C., Anjos, L.H.C. dos, Fontana, A., Silva Neto, E.C. da, Vieira, J.N., Santos, T.G., 2021. Genesis and classification of carbonate soils in the State of Rio de Janeiro, Brazil. J South Am Earth Sci 108. https://doi.org/10.1016/j.jsames.2021.103183

Prăvălie, R., 2016. Drylands extent and environmental issues. A global approach. Earth Sci Rev 161, 259–278. https://doi.org/https://doi.org/10.1016/j.earscirev.2016.08.003

Raheb, A., Heidari, A., Mahmoodi, S., 2016. Storage of organic and inorganic carbon in arid-semihumid soils: A case study of the rangelands of northwestern Iran. Soil Sci 181, 473–486. https://doi.org/10.1097/SS.0000000000000183

Raza, S., Irshad, A., Margenot, A., Zamanian, K., Li, N., Ullah, S., Mehmood, K., Ajmal Khan, M., Siddique, N., Zhou, J., Mooney, S.J., Kurganova, I., Zhao, X., Kuzyakov, Y., 2024. Inorganic carbon is overlooked in global soil carbon research: A bibliometric analysis. Geoderma 443, 116831. https://doi.org/https://doi.org/10.1016/j.geoderma.2024.116831

Retallack, G.J., 2001. Soils of the past: an introduction to paleopedology. John Wiley & Sons.

Ringrose, S., Matheson, W., Vanderpost, C., 1998. Analysis of soil organic carbon and vegetation cover trends along the B otswana Kalahari Transect, Journal of A rid Environments.

Ringrose, S., Matheson, W., Wolski, P., Huntsman-Mapila, P., 2003. Vegetation cover trends along the Botswana Kalahari transect, in: Journal of Arid Environments. Academic Press, pp. 297–317. https://doi.org/10.1006/jare.2002.1092

Sheldon, N.D., 2006. Abrupt chemical weathering increase across the Permian–Triassic boundary. Palaeogeogr Palaeoclimatol Palaeoecol 231, 315–321. https://doi.org/https://doi.org/10.1016/j.palaeo.2005.09.001

Sheldon, N.D., 2003. Pedogenesis and geochemical alteration of the Picture Gorge subgroup, Columbia River basalt, Oregon. GSA Bulletin 115, 1377–1387. https://doi.org/10.1130/B25223.1

Sheldon, N.D., Tabor, N.J., 2009. Quantitative paleoenvironmental and paleoclimatic reconstruction using paleosols. Earth Sci Rev 95, 1–52. https://doi.org/https://doi.org/10.1016/j.earscirev.2009.03.004

Smith, A., R., 1984. The Lithostratigraphy of the Karoo Supergroup in Botswana. Geol Mag 123, 710–711. https://doi.org/DOI: 10.1017/S0016756800024328

Stoops, G., Marcelino, V., Mees, F., 2018. Chapter 30 - Micromorphological Features and Their Relation to Processes and Classification: General Guidelines and Overview, in: Stoops, G., Marcelino, V., Mees, F. (Eds.), Interpretation of Micromorphological Features of Soils and Regoliths (Second Edition). Elsevier, pp. 895–917. https://doi.org/https://doi.org/10.1016/B978-0-444-63522-8.00030-9

Sumner, E.J., Amy, L.A., Talling, P.J., 2008. Deposit Structure and Processes of Sand Deposition from Decelerating Sediment Suspensions. Journal of Sedimentary Research 78, 529–547. https://doi.org/10.2110/jsr.2008.062

Turgut, Y.S., Hartemink, A.E., Koca, Y.K., 2025. Controlling factors of soil organic and inorganic carbon in North Adana, Türkiye. Geoderma Regional 40, e00933. https://doi.org/https://doi.org/10.1016/j.geodrs.2025.e00933

Walkley, A., Black, I.A., 1934. An examination of the degtjareff method for determining soil organic matter, and a proposed modification of the chromic acid titration method. Soil Sci 37.

CHAPTER SIX

Basaltic Weathering: The Source and Driver of Calcium Enrichment in Pedogenic Carbonates of the Central Botswana Fluvial Landscape[5]

Abstract

This study investigates the contribution of local mafic lithologies to the calcium supply of pedogenic carbonates within pedosedimentary sequences in semi-arid Central Botswana. Four pedosedimentary sections were examined alongside local basaltic, sandstone, and mudstone formations using an integrated approach of mineralogy (XRD), petrography, and elemental geochemistry. Mineralogical results identify basaltic rocks as the primary calcium reservoir, containing significant labradorite [$(Na,Ca)(Al,Si)_4O_8$] (up 43%) and augite [$(Ca, Na)(Mg, Fe, Al)(Si, Al)_2O_6$] (up to 34%). Carbonate features are dominated by calcite (40–75%), spatially associated with basaltic alteromorphs, smectite, and secondary iron-manganese oxides. Petrographic analysis reveals a significant structural evolution from open, porous fabrics to dense calcitic-crystallitic b-fabrics. The preservation of basaltic lithorelicts exhibiting pellicular weathering patterns, alongside the development of single-spaced porphyric distributions in mature nodules, confirms substantial material gain and expansive crystallisation pressure within the soil matrix. Geochemically, the Mafic–Felsic–RW diagram demonstrate a strong proximity between carbonate features and basaltic precursors and a negligible contribution from felsic detrital sources, although a minor contribution from other sources, such as aeolian inputs, cannot be entirely ruled out without isotopic constraints. Calcium mobilisation is driven by two distinct pathways: an

[5] *This chapter is based on a research article co-authored with Thierry Bineli Betsi, Elisabeth Eiche, Stefan Norra, and Peter N. Eze; currently under review in CATENA*.

autochthonous route involving the in-situ chemical weathering of reworked basaltic fragments, and an allochthonous route involving the translocation of ions via soil solutions and groundwater. These processes are regulated by the interplay between regional semi-arid climate cycles and local fluvial dynamics. These findings underscore the potential of semi-arid basaltic environments as significant long-term carbon sinks. Furthermore, the natural role of basalt in carbonate formation provides a robust scientific basis for Carbon Dioxide Removal (CDR) strategies through Enhanced Rock Weathering (ERW).

Keywords: Basalt weathering; Calcification; Carbon sequestration; Elemental geochemistry; Mineralogical proxies; Soil inorganic carbon.

6.1. Introduction

The biogeochemical cycle of calcium (Ca) is intrinsically linked to carbon sequestration, acting as a primary regulator of the Earth's long-term climate (Ridgwell and Zeebe, 2005). The cycle is initiated by the chemical weathering of continental rocks: atmospheric CO_2 dissolves in rainwater to form weak carbonic acid, which reacts with silicate and carbonate minerals to release calcium ions (Ca^{2+}) and bicarbonate (HCO_3^-). These solutes are transported by river systems to the oceans. More than 90% of the carbon in the oceans is in the form of bicarbonate ions, while the remaining fraction precipitates to form carbonate rocks (limestone, dolostone)(Ussiri and Lal, 2017). Recognition of this relatively stable carbon sequestration pathway has stimulated growing interest in its application within agrosystems, particularly through ERW, which involves the deliberate addition of Ca-rich rock powders to soils to accelerate the uptake of atmospheric CO_2 (Haque et al., 2021; Vienne et al., 2022).

In pedosphere environments, Ca carbonate represents the inorganic component of the carbon cycle, commonly referred to as soil inorganic carbon (SIC). In these systems, Ca ions released by the weathering of silicate minerals or the dissolution of pre-existing carbonates react with CO_2 dissolved in soil pore water, leading to the precipitation of secondary minerals known as pedogenic carbonates. This pathway of soil carbon sequestration is naturally promoted in arid and semi-arid regions, where it has been shown to function as an important long-term carbon sink (Monger, 2014).

It is essential to note that, while carbonate weathering is a closed cycle, silicate mineral weathering represents a net removal of atmospheric CO_2, as half of the sequestered carbon is buried in marine sediments as limestone, effectively removing it from the atmosphere-ocean system for millions of years (Lal et al., 2021). Crucially, the net carbon balance of this cycle is governed by the source

of Ca. While the recycling of pre-existing carbonates (e.g., calcite or dolomite) is effectively carbon neutral, the chemical weathering of silicate minerals, such as calcium plagioclase, generates a net carbon sink by sequestering two moles of CO_2 for every mole of Ca released (Monger et al., 2015). Consequently, determining the origin of calcium in pedogenic carbonates is essential to accurately assess the magnitude and effectiveness of carbon sequestration through this pathway.

Numerous studies have investigated the origin of Ca in pedogenic carbonates as highlighted in Dina Ebouel et al. (2024). In most cases, the methodologies employed rely on isotopic proxies, such as the $^{87}Sr/^{86}Sr$ ratio, to fingerprint potential endmembers. More specifically, the isotopic signatures preserved in carbonates are measured against those of presumed parent materials to determine their origin (Chen et al., 2022; Dietrich et al., 2017; Millière et al., 2019; Van Der Hoven and Quade, 2002). While these isotopic approaches have proven effective in discriminating among contributing Ca reservoirs, they remain inaccessible (costly) in many contexts, particularly in countries of the Global South where this issue is highly relevant. For instance, arid and semi-arid environments cover for nearly 35% of the African continent (Naorem et al., 2022), yet only a limited number of laboratories are equipped to perform such specialised isotopic analyses. As highlighted by Dina Ebouel et al. (2024), this methodological constraint slows down the progress of research on the SIC in this region, at a time when research into solutions that promote the sequestration of atmospheric CO_2 is more important than ever. Thus, the development of alternative methodology is needed to improve the investigation of SIC sequestration pathway in these environments.

Dina Ebouel et al. (2025a) have demonstrated that a multi-proxy approach, specifically combining elemental geochemistry and macromorphological observations, can robustly constrain the origin of Ca and the processes governing its mobilisation and incorporation into carbonate features. Such

an approach offers a valuable and more accessible alternative for assessing pedogenic carbonate formation and associated carbon sequestration pathways by integrating geochemical indices, elemental ratios, and field-scale morphological evidence, particularly in environments with limited data and infrastructure. Nevertheless, although this type of approach can provide general indications about the source material, the specific minerals responsible for the calcium supply are only deduced based on assumed mineralogical compositions of the source rock. As a result, the weathering processes involved, and the mineralogical sequence leading to the release of Ca, remain poorly understood. This represents a significant gap in current knowledge, as the precise identification of Ca-bearing minerals and their weathering pathways is essential for process-based interpretations and for the effective replication or optimisation of these mechanisms in agrosystems. However, this limitation can be overcome by mineralogical and petrographic (micromorphological) analysis (Bajnóczi and Kovács-Kis, 2006; Bockheim and Douglass, 2006). Thus, the use of elemental geochemical proxies, combined with mineralogical and petrographic analysis, would be an excellent tool for tracing the source minerals of Ca and its mobilisation mechanisms within pedogenic carbonates.

In the Central District of Botswana, pedogenic carbonates have been identified within carbonate accumulation horizons along pedosedimentary sequences developed on basalt and sandstone (Eze, 2022). The main features observed are nodules, pseudomycelia and diffuse powders. The mechanisms involved in the formation of these pedosedimentary sections have been previously described, and the pedogenic nature of the carbonate features has been clearly established (Dina Ebouel et al., n.d.). However, although these studies highlight the reworking of local rock fragments within the fluvial–colluvial deposits that constitute the pedosedimentary sequences, no investigation has specifically addressed their contribution to the supply of calcium. This is

particularly relevant given that the Stormberg basaltic lavas may represent a significant potential source of calcium. The specific objectives are to identify and constrain the most plausible sources of Ca, acknowledging that a fully quantitative partitioning of sources requires isotopic data beyond the scope of this study, and to discuss the processes and mechanisms governing its transfer. The specific objectives are to identify potential sources of Ca and to discuss the processes and mechanisms governing its transfer from the source material to the pedosedimentary sections, as well as its subsequent mobilisation within carbonate features.

6.2. Environmental setting

The study area is located near Serowe in the Central District of Botswana ranged from 22.34° to 22.42° S and from 26.67°–26.76° E (Fig. 6.1). The area marks the transition between Botswana's two main geomorphological units: the Sandveld (Kalahari Desert), characterised by sand deposits and dune, and the Eastern Hardveld, where the Precambrian basement and the Karoo Supergroup (dating from the Upper Carboniferous to the Lower Jurassic) are exposed (Atlhopheng et al., 2022). The landscape is characterised by gently sloping plains interspersed with isolated ravines affected by active erosion (Eze, 2022). The geological context is characterised by formations of the Karoo Supergroup dated Late Carboniferous–Early Jurassic (Smith, 1984). They are locally overlain by unconsolidated aeolian deposits of the Kalahari Group (Franchi et al., 2021). Two types of geological formations belonging to the Karoo Supergroup are prominent in the landscape, namely the Stormberg Group, also referred to as the Stormberg lavas and characterised by amygdaloidal basalts and dolerites, and the Lebung Group, represented by sandstones and mudstones (Dina Ebouel et al., n.d.).

The region experiences a hot semi-arid climate (BSh in Köppen–Geiger classification), marked by long dry periods and a short rainy season from November to March. Mean annual rainfall averages

about 442 mm, with high interannual variability and frequent droughts, but episodic flooding also occurs. Temperatures range from winter minima near 0°C to summer maxima exceeding 45°C (Batisani and Yarnal, 2010). Surface waters are ephemeral, occurring only during the rainy season, and are characterised by low mineralisation with Ca–HCO_3 to Ca–Mg–HCO_3 chemical facies, typical of recent meteoric waters (Stadler et al., 2010).

Vegetation corresponds to a bush savannah ecosystem, dominated by woody species such as *Acacia, Terminalia, and Boscia*, with a diverse herbaceous layer of perennial grasses (Ringrose et al., 1998). However, this natural vegetation is strongly modified by agricultural activities and infrastructure development (Atlhopheng et al., 2022). The pedosedimentary sections of the region show alternating phases of sedimentary deposition and soil formation, with calcification as the major pedogenic process (Eze, 2022). As is often the case in arid environments, local pedogenic processes are dominated by the accumulation of secondary calcium carbonates (diffuse powders, nodules and pseudomycelia) as well as by the influence of aeolian deposits (Dina Ebouel et al., 2025a). Regarding the latter, Garzanti et al. (2022) demonstrate that aeolian inputs, originating primarily from the Kalahari, are predominantly composed of highly reworked quartz, which frequently exceeds 90% of their composition. Furthermore, their study indicates that localised enrichments in alkali and alkaline earth elements are generally linked to the local geological framework, particularly the weathering of Karoo basaltic rocks (Garzanti et al., 2022). Eze et al. (2025) also demonstrated that the mobilisation of alkali and alkaline earth elements, as well as trace elements, active in the formation of Vertisols in this environment, mostly originates from the weathering of local basaltic source rocks, though the resulting pedosedimentary sections are polygenic.

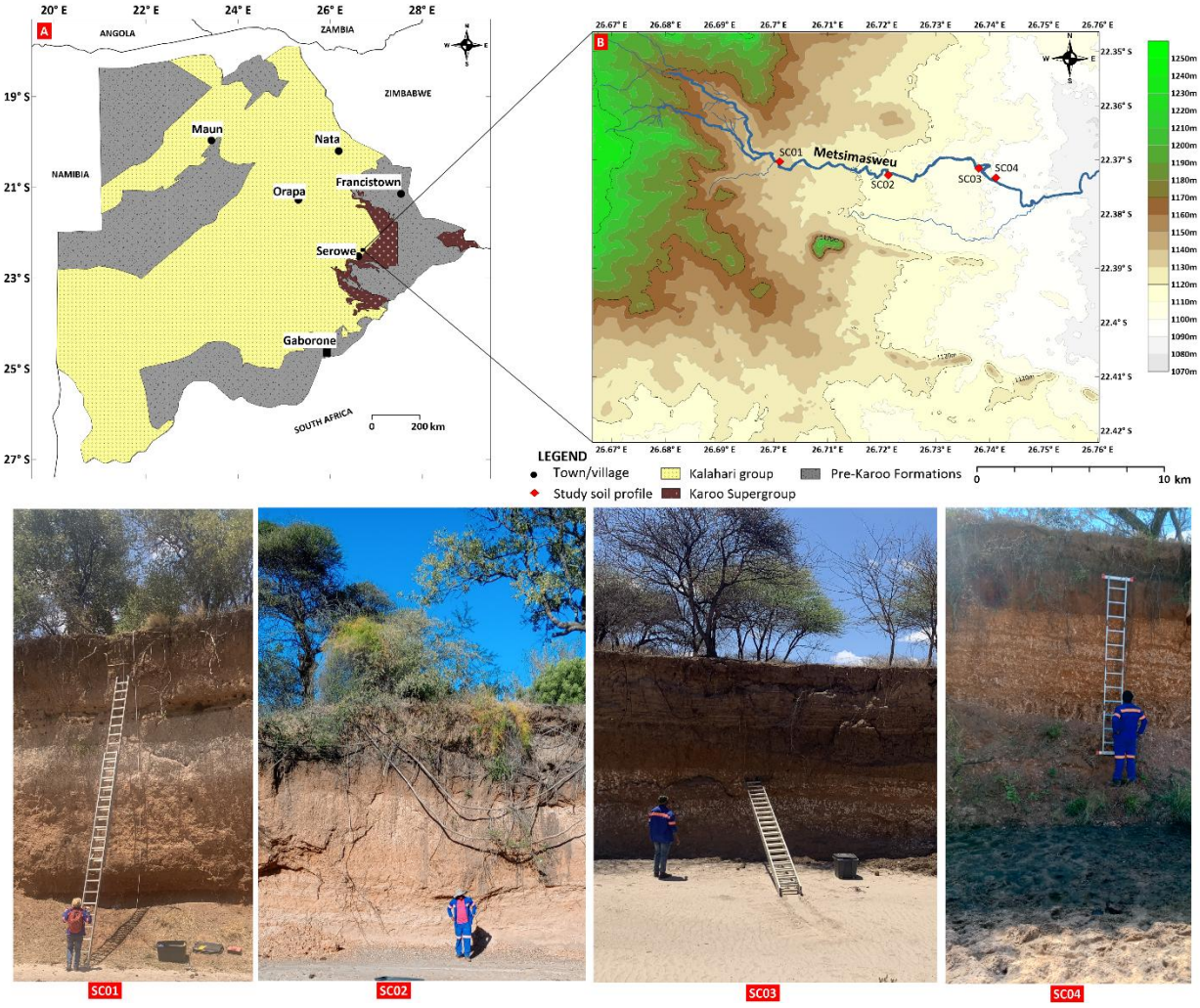


Fig. 6.1. A. Location map of the study area; B. A zoomed-out map of the study area; SC01 to SC04. field photographs of the study sections.

6.3. Material and methods

6.3.1. Field sampling and sections description

Four pedosedimentary sections were selected along an ephemeral watercourse known locally as Metsimasweu (Fig. 6.1). A full description of the selected sections is provided in Dina Ebouel et al. (n.d.). Briefly, the studied sections record a landscape defined by repeated alternations between sediments deposition and pedogenetic processes. The result is a complex architecture of modern

soils and palaeosols buried under sediment, justifying their qualification as pedosedimentary landscapes.

SC01 (Fig. 6.2A) is the most complex soil section, comprising 14 horizons. It is dominated by a sandy loam to loamy sand texture (sand > 60%) and maintains a moderately alkaline pH (6.8–8.3). Calcification is highly pronounced here, with $CaCO_3$ content reaching a study-wide maximum of 24.61 wt.% in the Bkb horizon. Carbonate features primarily manifest as soft nodules and diffuse powder, though the two basal layers (CB4b and AB3b) are distinct for their pseudomycelia (fine carbonate infillings within soil pores).

SC02 (Fig. 6.2B) consists of eight horizons. The pH is moderately alkaline, with a peak of 8.4 in the lower parts. The carbonate content is lower than that of SC01, reaching 14.24% by weight in the BCk1b layer. The carbonate features are mainly in the form of diffuse powder and nodules, with occasional pseudomycelia observed specifically in the BC2b layer.

SC03 (Fig. 6.2C) also contains eight horizons, but exhibits significant textural complexity, including a unique C2 layer with alternating silty and sandy sublayers resembling modern fluvial deposits. It has the highest clay concentration, with the ABb layer reaching 50% clay. The $CaCO_3$ content varies considerably, with a peak of 16.25 wt.%. While most layers contain diffuse powder, the basal horizons BCk1b and BCk2b are distinguished by the presence of hard concretions and a few pseudomycelia.

SC04 (Fig. 6.2D) is the most downstream. It consists of seven horizons and has the greatest textural diversity, with intermediate layers rich in clay (up to 39% clay). It is the only profile with a slightly acidic topsoil layer (pH 6.4). Carbonate accumulation remains high at depth, with a peak of 21.09 wt.% by weight in the BCk1b layer. Here, the carbonates occur as diffuse powder (sometimes covering the gravel) and soft concretions.

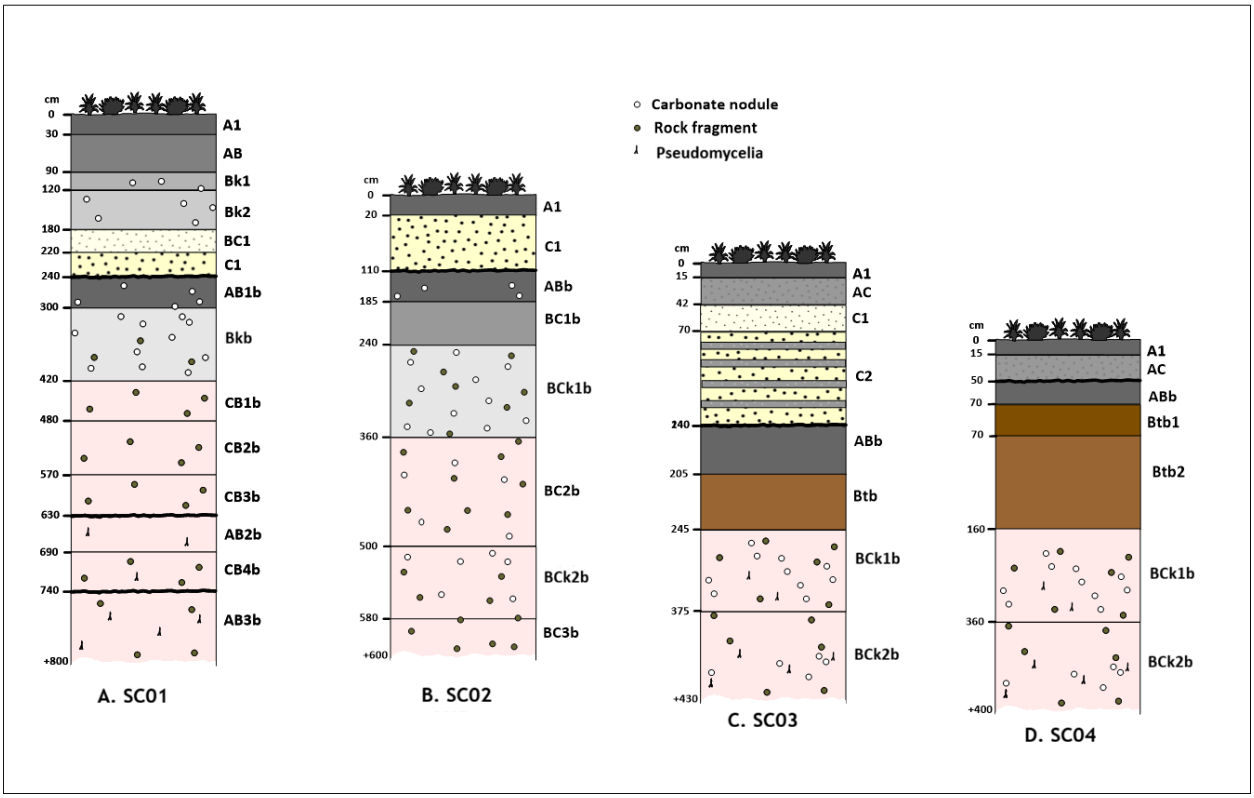


Fig. 6.2. Representation of the studied sections. The naming of horizons follows the recommendations of the IUSS Working Group WRB (2022).

Dina Ebouel et al. (n.d.) also document extensive reworking of surrounding rock fragments within the pedosedimentary sections, as evidenced by the presence of gravels at various stages of weathering (Fig. 6.3). These features are interpreted as the result of active fluvial dynamics. Consistently, granulometric analyses indicate high-energy depositional conditions, characteristic of episodic flood events.

Modern soils are generally weakly developed, reflecting limited chemical weathering under semi-arid climatic conditions. They are mainly classified as Cambisols and Arenosols, depending on texture and profile development. Cambisols (SC01, SC03, SC04) show incipient horizon differentiation with moderate clay contents and local accumulation of pedogenic carbonates, but $CaCO_3$ contents remain below the threshold required for Calcisols. Arenosols (SC02) are

dominated by sand throughout the profile, with minimal structural development. Across all modern soils, calcification is the dominant pedogenic process, evidenced by diffuse carbonate accumulations and nodules, while chemical weathering and salinisation remain weak. Clay formation and enrichment are locally observed but are partly attributed to sedimentary inputs and downstream translocation rather than in situ weathering alone.

The buried palaeosols show clearer and more advanced pedogenic signatures, particularly in the form of calcic horizons. Several profiles are classified as palaeo-Calcisols, characterised by high $CaCO_3$ contents, abundant carbonate nodules, and calcite-dominated mineralogy, indicating prolonged periods of landscape stability under semi-arid to arid conditions. Calcification is consistently the dominant process, while chemical weathering and salinisation remain limited. In contrast, some buried profiles with very sandy textures and weak horizon development correspond to palaeo-Entisols or palaeo-Aridisols, reflecting shorter-lived or less stable pedogenic phases. Elevated clay contents in certain buried horizons are interpreted as the result of sedimentary translocation from upstream areas, rather than intense in situ weathering.

Overall, both modern soils and palaeosols indicate that calcification overwhelmingly controls soil evolution, with only moderate contributions from hydrolysis and clay neoformation. The persistence of weak chemical weathering signatures, even in buried profiles, supports the interpretation of long-term semi-arid environmental conditions, punctuated by episodic sedimentation that governs soil preservation, burial, and lateral redistribution of fine materials (Dina Ebouel et al., 2026).

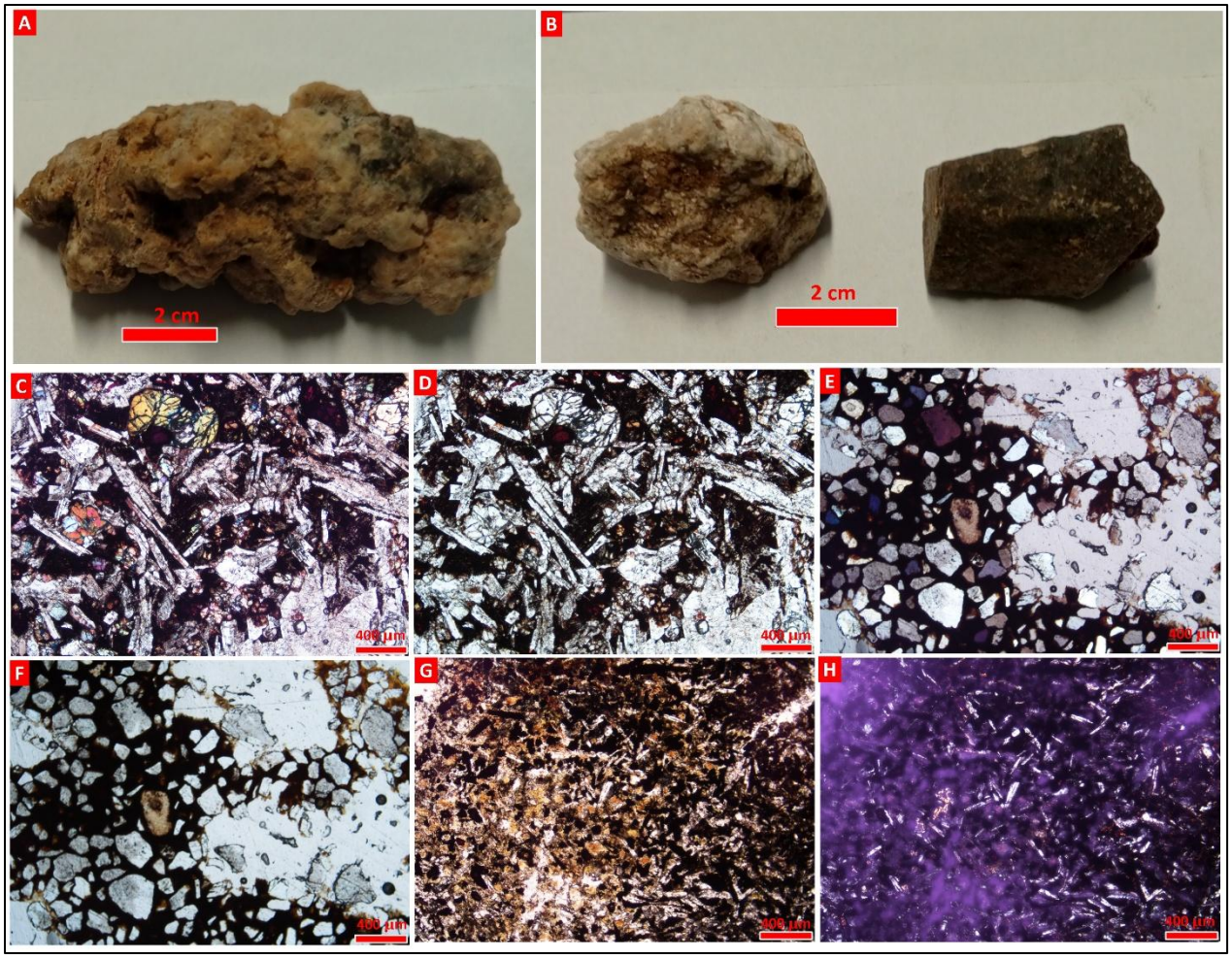


Fig. 6.3. Representative rock fragments isolated from the pedosedimentary sections. (A) Sandstone fragment from SC02; (B) sandstone and dolerite fragments from SC03; (C–D) micrographs of a preserved dolerite fragment from SC01; (E–F) micrographs of partially weathered sandstone from SC02; (G–H) micrographs of partially weathered amygdaloidal basalt from SC01, in which primary minerals remain clearly identifiable.

This work is based on the analysis of four rock samples from the main rock outcrops identified in the study area. These include an amygdaloidal basalt (Fig. 6.4A), a dolerite (Fig. 6.4B), a sandstone (Fig. 6.4C) and a mudstone (Fig. 6.4D). Carbonate features, including nodules and pseudomycelia (Fig. 6.4E and F), were carefully hand-picked from the calcareous horizons.

A total of 19 carbonate samples were considered, including one pseudomycelia (Ps) from horizon AB3b of SC01 and 18 nodules (Nd01—Nd18), as shown in Table 6.1.

Bulk soil samples were collected from each of the pedogenetic horizons identified during the field sampling.

Table 6.1. Samples repartition and coding

Section	Layer	Depth (cm)	Sample	Type of samples
-	-	-	Dolerite	**Rocks**
-	-	-	Amygdaloidal Basalt	
-	-	-	Sandstone	
-	-	-	Mudstone	
SC01	Bk2	120-150	Nd01	**Carbonate nodules**
	AB1b	240-300	Nd02	
	Bkb	300-330	Nd03	
		330-360	Nd04	
	AB3b	740-840+	Ps	**Pseudomycelia**
SC02	BCk1b	240-360	Nd05	**Carbonate nodules**
	BCk2b	500-540	Nd06	
		540-580	Nd07	
SC03	BCk1b	245-285	Nd08	**Carbonate nodules**
		285-305	Nd09	
		305-345	Nd10	
		345-375	Nd11	
	BCk2b	375-400	Nd12	
SC04	BCk1b	160-190	Nd13	**Carbonate nodules**
		190-220	Nd14	
		220-260	Nd15	
	BCk2b	260-300	Nd16	
		300-330	Nd17	
		330-400+	Nd18	

6.3.2. Mineralogical analyses

X-ray diffraction (XRD) analysis and petrographic observations were conducted on representative specimens of the primary lithologies identified in the study area (dolerite, amygdaloidal basalt, sandstone, and mudstone). Regarding pedogenic carbonates, a selective sampling strategy was implemented to capture the diversity of pedogenic cycles while maintaining the consistency of the original approach of the study. In the complex SC01 section, three distinct features were analysed to represent the stratigraphic evolution: Nd01 (modern soil Bk2 horizon), Nd03 (buried Bkb palaeosol), and Ps (basal pseudomycelia). For sections SC02, SC03, and SC04, a single representative nodule was selected per section. This representative sub-sampling strategy is justified by appearance of nodules only in the buried palaeosol in these sections. Moreover, stable isotope data ($\delta^{13}C$ and $\delta^{18}O$), reveal tightly clustered values with minimal internal dispersion within each section. Such isotopic homogeneity indicates that the carbonate features within these sections precipitated under similar environmental and hydrological conditions, thereby ensuring that the selected mineralogical samples are representative of the entire buried palaeosol calcification process (Dina Ebouel et al., 2026). Calcification is not yet in an advanced stage in the modern soil of theses sections to produce nodules. Only diffuse powder accumulations are observed (Dina Ebouel et al., n.d.).

Pulverisation was conducted in all the samples using an agate planetary ball mill to ensure a high degree of fineness while preventing trace metal contamination. The pulverised samples were submitted to X-ray diffraction (XRD) that was carried out at the Materials Characterisation Laboratory of Botswana International University of Science and Technology (BIUST), using a Bruker D8 Advance powder diffractometer equipped with a Cu-tube X-ray source and a Lynx Eye XE energy-dispersive strip detector. The radiation used was Cu-Kα radiation with a wavelength

of 1.5418 A at 2θ values between 5 and 90 degrees for the bulk mineralogy and 5 to 30 degrees for the clay mineralogy, using a step of 0.02 degrees with a time of 0.200 sec/step. The machine was operated at 40 mA and 40 kV.



Fig. 6.4. A. Amygdaloidal basalt sample; B. Dolerite sample; C. Sandstone sample; D. Mudstone sample; E. Pseudomycelia carbonate accumulation observed in AB3b (SC01); F. Calcium carbonate nodules observed in BCkb (SC03).

Thin sections of the different lithology (dolerite, amygdaloidal basalt, sandstone and mudstone) were prepared following standard petrographic procedures. To preserve their internal structure and porosity, the pedogenic carbonate features (nodules and pseudomycelia) were vacuum impregnated with epoxy resin prior to sectioning. All sections were then grinded and polished to a standard thickness of 30 μm for analysis under a polarised light microscope at the Mineral Dressing Laboratory of BIUST.

6.3.3. Elemental geochemistry

The element compositions of pulverised samples, including Si, Al, Fe, Mn, Mg, Ca, Na, K, Ti and P (all reported as the mass percentage of oxides), and Sr reported in mg/kg was performed on fused beads using an S4 Explorer (Bruker AXS) wavelength dispersive X-ray fluorescence spectroscope (WDX) at the Laboratory for the Environmental and Raw Materials Analysis (LERA), Institute of Applied Geosciences, Karlsruhe Institute of Technology (KIT),Germany. Prior to element quantification, the loss on ignition (LOI) of the pulverised samples was determined by heating them to 950 °C for 3 hours and recording the weight difference before and after heating. Fused beads were prepared by mixing the ignited sample powder with a 66.5:33.5 ratio of Li-tetraborate and Li-metaborate (Spectroflux 110, Alfa Aesar) before melting it at 1000–1100 °C using a fusion instrument. An Rh X-ray tube (50 keV, 1 kW) was used as the radiation source. Signals were detected using a proportional flow counter (Ar-CH_4 gas) and a scintillation counter. XS-55, LIF2000 and PET were used as analyser crystals. Four certified reference materials, including AGV-1, GXR-2, GXR-5 and Soil 7, were used to verify the accuracy of the produced data (Appendix 6.1).

6.3.4. Data treatment

The XRD data were processed using the Rietveld Profex refinement software (version 5.2) from BGMN (Doebelin and Kleeberg, 2015). Qualitative phase identification was based on structural data from the Crystallography Open Database (COD), whilst quantitative mineralogical analysis was carried out using the Rietveld method, involving least-squares refinement of the entire diffraction profile. This approach considers the crystal structure, peak broadening and background noise, thereby ensuring greater accuracy than methods relying solely on the relative intensities of characteristic peaks. To maintain stoichiometric consistency with the measured concentrations of the main oxides, the refinement of the identified phases was strictly constrained by the elemental data obtained by XRF.

Micrographs of pedogenic carbonate features were described in accordance with the general guidelines set out by Stoops et al. (2018).

To facilitate stoichiometric comparison, bulk geochemical data from samples, originally reported as oxide weight percentages (wt.%) were recalculated into elemental molar percentage (mol%). For each oxide, the weight percentage was divided by its molecular weight to determine the corresponding oxide molar proportion. This value was subsequently multiplied by the cation stoichiometric coefficient of the oxide (e.g. 2 for Al_2O_3; 1 for CaO) to derive the unnormalised cation molar proportion. Elemental molar percentages (mol%) were obtained by normalising these values to the total molar sum of all analysed elements (Rollinson and Pease, 2021). The raw elemental data, expressed as weight percentages of oxides, including LOI and the conversion procedure are presented in Appendix 6.2.

To trace the source of materials contributing to pedogenic carbonate formation, the RW approach based on the Mafic–Felsic–RW diagram (Cho and Ohta, 2022) was used. This methodology is

specifically designed to overcome the limitations of conventional weathering indices (e.g., CIA, W index), which are often unreliable in systems enriched in non-silicate phases such as authigenic carbonates. Its robustness lies first in its mathematical immunity to calcification. The RW index is calculated within a sub-compositional space that excludes CaO, SiO_2, and P_2O_5, ensuring that carbonate accumulation does not bias the geochemical signal or artificially shift samples towards the mafic pole. The approach also relies on Independent Component Analysis (ICA), which separates statistically independent variables related to source composition (IC1) and weathering intensity (IC2). This allows the extraction of the dominant geochemical lineage of the silicate fraction (e.g., mafic versus felsic affinity), even in complex and heterogeneous systems. This aspect is particularly critical in the present study, where the pedosedimentary context reflects a mixed and reworked assemblage rather than a single, well-defined parent material. In such settings, the RW index does not attempt to define a unique parent material sensu stricto, but rather identifies the prevailing geochemical signature inherited from contributing lithologies. Finally, the validity of this approach has been demonstrated empirically in carbonate-rich and compositionally mixed systems, such as palaeosols developed from combined granitic saprolite and aeolian inputs, where the RW index successfully constrained source affinity and weathering trends while conventional indices failed. Consequently, despite the dominance of authigenic carbonate in pedogenic features, the RW approach remains a reliable tool for preserving and interpreting the silicate-derived geochemical signal and for assessing the contribution of mafic materials within mixed pedosedimentary environments.

6.4. Results

6.4.1. Characterisation of soil parent materials and carbonate features

The proportions of mineral phases in mass percentage (wt.%) of rock samples and carbonate features identified by XRD are presented in Table 6.2. The dolerite (Fig. 6.4B) is made up of 43% labradorite, 34% augite, 14% forsterite, and 9% opaque minerals. The amygdaloidal basalt (Fig. 6.4A) is composed of 48% of labradorite, 22% of augite, 12% of zeolites (heulandite), 10% of chlorite and 8% opaque minerals. The sandstone (Fig. 6.4C) is constituted of 90% of quartz, 5% of microcline, 2% of illite, 1% of kaolinite and 2% of secondary oxides. The mudstone (Fig. 6.4D) is composed of 39% of albite, 21% of quartz, 20% of illite, 15% of kaolinite and 5% of secondary oxides.

In carbonates features, calcite is the dominant mineralogical phase. Primary phases including quartz, augite, and labradorite are also observed alongside other secondary minerals including dolomite, clays and oxides. Nevertheless, augite and labradorite only appears in Nd01 and Ps. The relative proportions of these mineral phases vary significantly between individual features. In sample Nd01 of section SC01, collected from Bk2, quartz (23%) is second dominant mineral after calcite (54%). Dolomite represents 10%, while the remaining fraction is made up of 4% of augite, 4% of smectite, 3% labradorite and 2% secondary oxides. In Nd03 from Bkb, dolomite (15%) is the second abundant phase after calcite (60%), while quartz is 14%, smectite 7% and secondary oxides 4%. Pseudomycelia (Ps) in the horizon AB3b is constituted of 40% calcite, 30% quartz, 10% smectite, 8% dolomite, 5% labradorite and 2% augite. In SC02, Nd06 is characterised by 66% calcite, 10% quartz, 10% dolomite, 10% smectite and 4% of secondary oxides. Sample Nd10 in section SC03 is composed of 74% calcite, 12% quartz, 5% illite, 5% secondary oxydes and 4%

dolomite. In sample Nd14 from SC04, calcite represents 75% of the mineral composition. Quartz accounts for 10%, whilst illite, secondary oxides and dolomite each account for 5%.

Table 6.2. Semi-quantitative mineralogical composition of the samples

Mineralogical composition (wt.%)	Rock sample				Carbonate features sample					
	Dolerite	Amygdaloidal basalt	Sandstone	Mudstone	SC01			SC02	SC03	SC04
					Nd01	Nd03	Ps	Nd06	Nd10	Nd14
Labradorite	43	48	-	-	3	-	5	-	-	-
Augite	34	22	-	-	4	-	2	-	-	-
Forsterite	14	-	-	-	-	-	-	-	-	-
Zeolite	-	12	-	-	-	-	-	-	-	-
Opaque minerals	9	8	-	-	-	-	-	-	-	-
Chlorite	-	10	-	-	-	-	-	-	-	-
Quartz	-	-	90	21	23	14	30	10	12	10
Microcline	-	-	5	-	-	-	-	-	-	-
Illite	-	-	2	20	-	-	-	-	5	5
Albite	-	-	-	39	-	-	-		-	
Kaolinite	-	-	1	15	-	-	-	-	-	-
Secondary oxides	-	-	2	5	2	4	5	4	5	5
Calcite	-	-		-	54	60	40	66	74	75
Dolomite	-	-	-	-	10	15	8	10	4	5
Smectite	-	-		-	4	7	10	10	-	-

Petrographic observations of the rocks are generally consistent with the XRD results. The abbreviations for mineral names shown in the images are in accordance with those proposed by Whitney and Evans (2010). Plagioclase is the most abundant mineral in dolerite (Fig. 6.5A and B), appearing as elongated, slat-shaped crystals and amygdaloidal basalt where they appear much smaller (microlites) (Fig. 6.5C and D). Clinopyroxenes (probably augite) are also well represented. These are irregular subsequent crystals located between the plagioclase lamellae. Prominent cleavage is visible in some grains of dolerite. In the amygdaloidal basalt Clinopyroxene are represented in PPL by beige to brown-grey grains with a marked relief, while they show vivid second-order interference colours (blue, pink, green) in XPL. Olivine in dolerite is represented by several larger, somewhat rounded crystals (phenocrystals), often displaying characteristic

fractures. Zeolites (heulandite) fill the vesicles of the amygdaloidal basalt. In PPL, they appear as large circular or ovoid white/light areas. In XPL, they have very low relief and very dark grey to black interference colours. Opaque minerals are represented by completely black and irregular areas in PPL and XPL. They are scattered throughout the matrix.

The quartz-dominant mineralogy (90%) identified through XRD is strongly corroborated by petrographic observations of the sandstone. Micrographs (Fig. 6.5D and F) reveal an abundance of angular to sub-angular quartz framework grains embedded in a dense, reddish-brown matrix.

The micrographs of the mudstone (Fig. 6.5G and H) reveal a dense, fine-grained fabric where individual grains are difficult to distinguish. Albite is the major component, likely forming the silt-sized crystalline framework that appears as brighter, speckled points in the XPL. Quartz acts as a secondary framework mineral, smaller and less abundant than in the sandstone samples analysed previously. Clay minerals account for 35% of the sample. They form the primary micromass, creating the cohesive, dense background observed in both images. Although (only 5%), secondary oxides exert a dominant influence on the sample's appearance. The reddish-purple to tan staining of the matrix and the prominent dark, opaque clusters (orthic nodules or aggregates) distributed throughout the images are direct evidence of these iron and manganese oxides. Their presence as fine-grained coatings on the clay minerals provides the rock its characteristic colour.

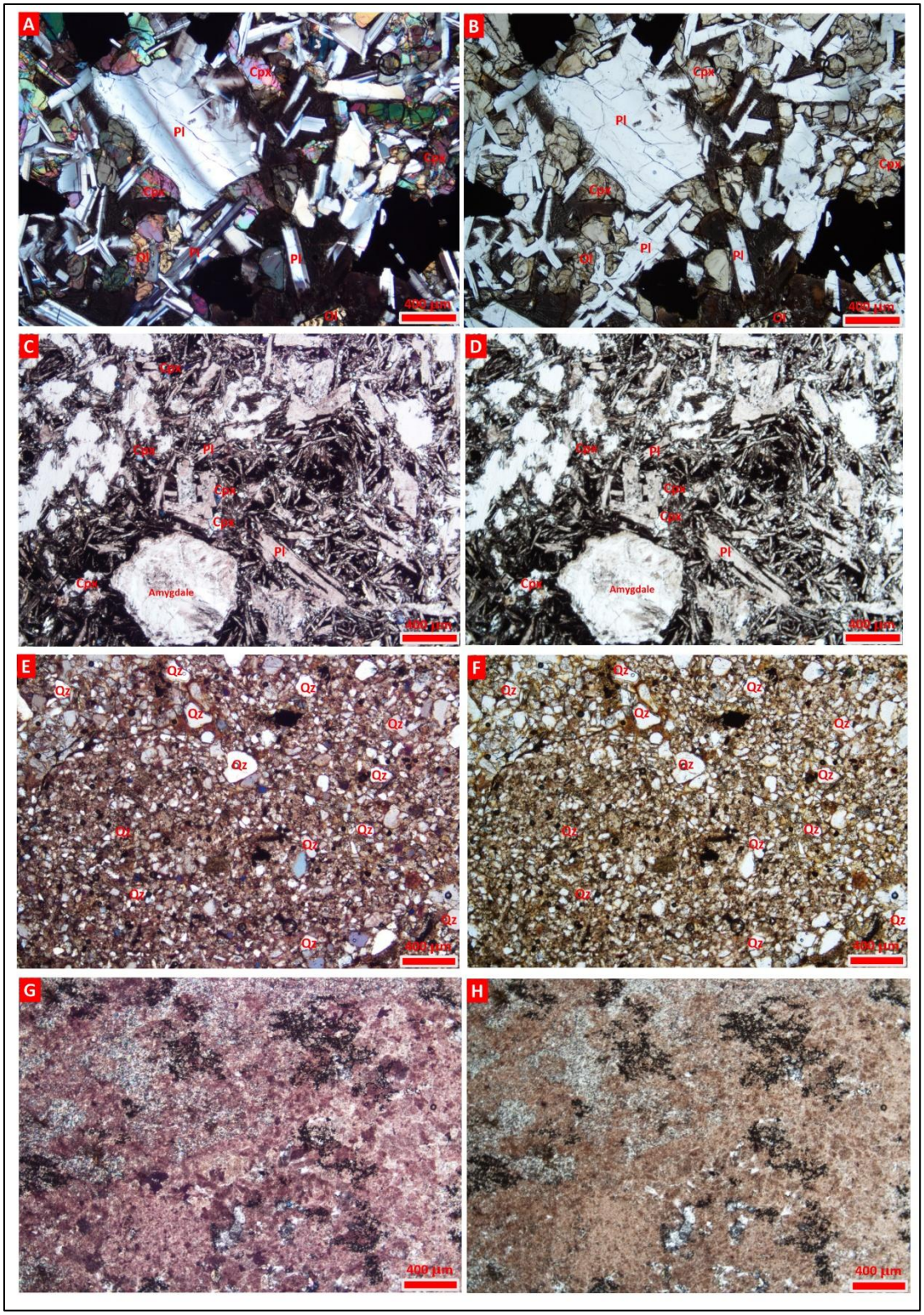


Fig. 6.5. Photomicrographs of the main lithology: dolerite (A: XPL; B: PPL); amygdaloidal basalt (C: XPL; D: PPL); sandstone (E: XPL; F: PPL); and mudstone (G: XPL; H: PPL).

Microscopic observations of pedogenic features (Fig. 6.6) align with XRD data. In both the nodules Nd01 (Fig. 6.6A) and pseudomycelia Ps (Fig. 6.6B), inherited coarse material consisting of easily alterable minerals, such as augite and plagioclase, is preserved. The groundmass is dominated by a crystallitic b-fabric, characterised by a secondary micritic carbonate matrix. Within this micromass, augite remains recognisable by its high relief and distinct oblique cleavage planes, with some grains displaying high-order interference colours under crossed-polarised light. Plagioclase occurs as elongated, lamellar grains, occasionally retaining relict polysynthetic twinning. Most of these primary grains are encompassed by coronary pedofeatures, consisting of either a sparitic circum-granular pro-anisotropic rim or a thin ferruginous hypo-coating. Secondary iron and manganese oxides are prominent, occurring as orthic nodules with distinct internal fabric, and as reddish-brown impregnative typic coatings concentrated along grain boundaries and vughy porosity. Furthermore, allochthonous quartz grains are present, characterised by undulating extinction and a sharp, plane contact with the surrounding calcitic matrix.

Nodules Nd03, Nd06, Nd10, and Nd14 (Panels C, D, E, and F, Fig. 6.6) demonstrate remarkably consistent micromorphological characteristics. They are defined by a pervasive calcitic-crystallitic b-fabric, where the fine micromass is heavily impregnated with micritic calcite crystals. This groundmass also hosts distinct drusy sparitic accumulations within central vughs, visible as brighter, coarser crystalline patches. The coarse fraction consists primarily of angular to sub-rounded quartz grains acting as inherited resistant relicts. Interstitial clay minerals (smectite/illite) form a dense component of the micromass, though their optical expression is frequently masked by the dominant carbonate fabric. These components are arranged in a single-spaced porphyric c/f-related distribution pattern. Secondary oxides are present as small, opaque orthic nodules or clusters acting as impregnative pedofeatures throughout the matrix. Finally, the nodules exhibit a

vesicular to vughy microstructure, with porosity comprising irregular vughs and rounded vesicles, clearly visible as resin-filled areas.

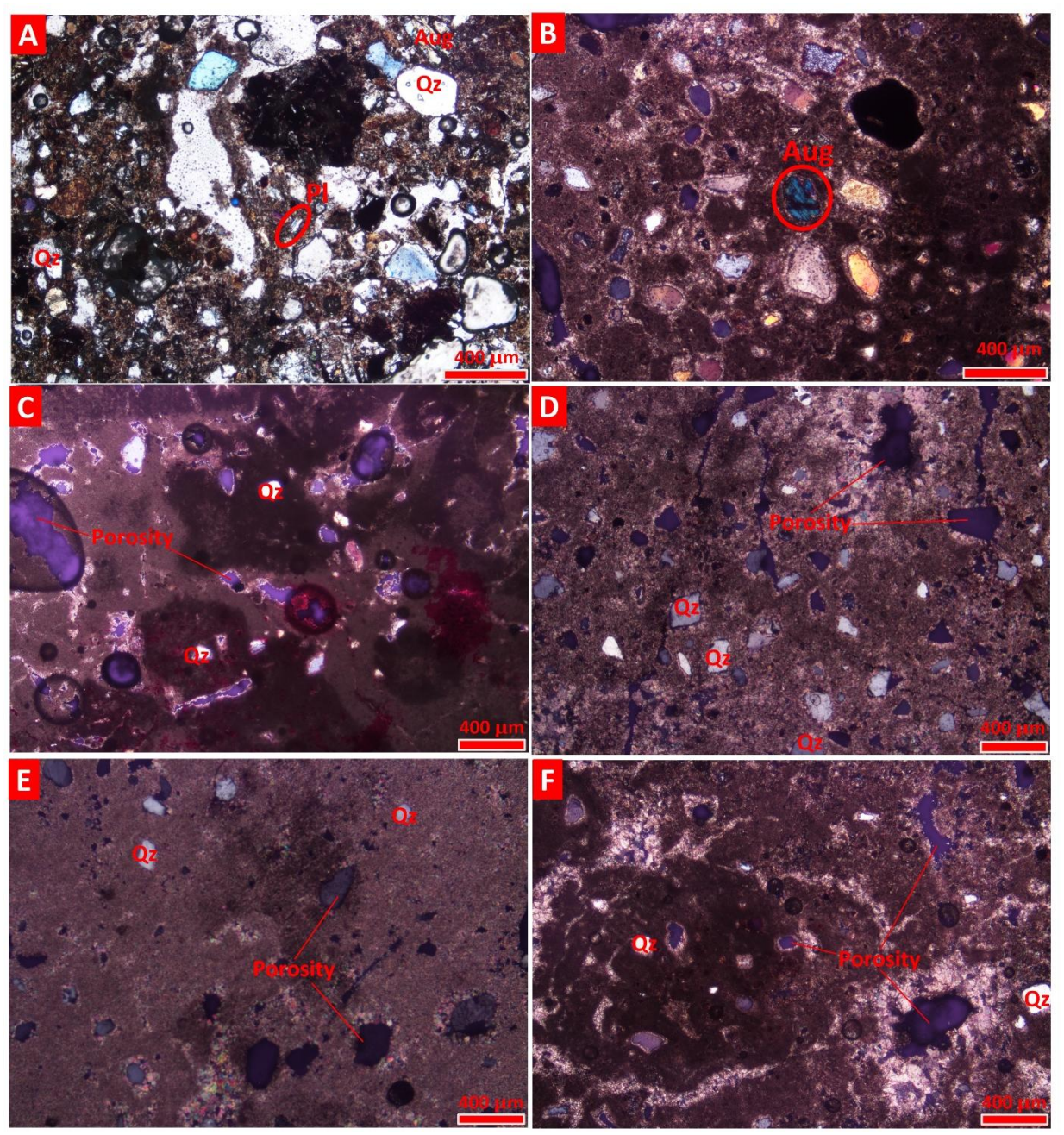


Fig. 6.6. Carbonate features XPL microphotographs. A. Nodule Nd01 collected from Bk2 in SC01 (Nd01); B. Pseudomycelium Ps collected from AB3b in SC01; C. Nodule Nd03 collected from

Bkb in SC01; D. Nodule Nd06 collected from BCk2b in SC02; E. Nodule Nd10 collected from BCk1b in SC03; F. Nodule Nd14 collected from BCk1b in SC04.

6.4.2. Geochemistry

As mentioned in section 6.3.4, molar percentage (mol%) are used to represent the abundance of elements (Table 6.3). Silicon is the dominant element among all the potential source materials (dolerite, amygdaloidal basalt, sandstone and mudstone). It is respectively 48.65% and 46.9% in dolerite and amygdaloidal basalt, while it is 95.23% in the sandstone and 57.25% in the mudstone. Aluminium is the second most important component, it is 14.23% in dolerite, 18.26% in amygdaloidal basalt, 2.69% in the sandstone and 23.78% in the mudstone. Basaltic rocks have relatively high Fe, Ca, Mg and Na contents, with values of 11.64%, 9.68%, 7.15% and 4.19% in dolerite, and 8.17%, 9.28%, 8.78% and 8.76% in amygdaloidal basalt. Titanium is relatively high in dolerite (3.02%), while is on minor proportion in amygdaloidal basalt. Potassium and Mn are in a minor proportion, while Sr is 0.033% and 0.008% respectively in dolerite and amygdaloidal basalt. Significant K proportion is observed in sandstone (1.35%), while other elements including Fe, Ca, Mg, Na, Ti and P are in minor or trace contents. Mudstone is characterised by significant Fe, Na, Mg and K (2.78%, 8.66%, 1.66% and 4.53% respectively), while Ca and Ti are minor (0.37% and 0.85%). Manganese and P are in trace proportion, less than 0.1%. Strontium in the sandstone and the mudstone has the same concentration (0.001%).

Table 6.3. Element content of samples

Section	Layer	Depth (cm)	Sample	Si	Al	Fe	Mn	Mg	Ca	Na	K	Ti	P	Sr	RW
				Molar percent (mol%)											
-	-	-	Dolerite	48.65	14.28	11.64	0.16	7.15	9.68	4.19	0.90	3.02	0.33	0.033	16.76
-	-	-	A. Basalt	46.94	18.26	8.17	0.13	8.76	9.28	7.44	0.22	0.69	0.13	0.008	5.22
-	-	-	Sandstone	95.23	2.69	0.26	0.01	0.22	0.12	0.05	1.35	0.06	0.01	0.001	57.60
-	-	-	Mudstone	57.25	23.78	2.78	0.06	1.66	0.37	8.66	4.53	0.85	0.07	0.001	13.00
SC01	Bk2	120-150	Nd01	38.89	5.75	2.49	0.06	9.00	42.15	0.84	0.54	0.26	0.02	0.024	15.38
	AB1b	240-300	Nd02	23.35	3.59	1.16	0.11	10.70	60.19	0.45	0.28	0.17	0.01	0.023	12.25
	Bkkb	300-330	Nd03	27.33	3.93	1.22	0.09	16.91	49.73	0.37	0.24	0.18	0.01	0.023	11.63
		330-360	Nd04	28.08	4.62	1.53	0.08	6.04	58.63	0.54	0.26	0.21	0.01	0.012	15.10
	AB3b	740-840+	Ps	49.32	6.73	3.14	0.03	3.58	35.06	1.09	0.64	0.40	0.02	0.009	20.46
SC02	BCkkb	240-360	Nd05	17.12	2.45	0.62	0.01	6.95	72.47	0.15	0.10	0.11	0.01	0.017	14.08
	BCkb	500-540	Nd06	21.14	3.40	1.01	0.16	3.64	70.09	0.32	0.08	0.15	0.02	0.011	13.15
		540-580	Nd07	21.26	3.03	0.91	0.22	3.16	70.84	0.27	0.14	0.14	0.02	0.006	17.39
SC03	BCkkb	245-285	Nd08	13.35	1.84	0.59	0.10	1.93	81.84	0.17	0.07	0.11	0.01	0.004	16.52
		285-305	Nd09	16.72	2.26	0.61	0.05	2.24	77.69	0.24	0.08	0.10	0.02	0.004	14.00
		305-345	Nd10	15.64	2.52	0.69	0.04	2.29	78.33	0.24	0.11	0.11	0.02	0.004	17.33
		345-375	Nd11	14.55	1.77	0.42	0.05	1.97	80.88	0.20	0.05	0.08	0.02	0.004	12.08
	BCkb	375-400	Nd12	21.17	2.78	0.69	0.15	2.15	72.51	0.37	0.06	0.12	0.01	0.005	11.06
SC04	BCkkb	160-190	Nd13	21.59	2.52	0.86	0.06	2.34	72.24	0.09	0.15	0.13	0.02	0.033	32.93
		190-220	Nd14	17.54	1.84	0.62	0.03	2.14	77.53	0.08	0.10	0.10	0.02	0.008	28.17
		220-260	Nd15	21.66	3.22	1.04	0.07	2.54	70.96	0.18	0.16	0.15	0.02	0.001	25.57
	BCkb	260-300	Nd16	19.83	2.53	0.78	0.03	2.25	74.13	0.17	0.14	0.13	0.01	0.001	23.24
		300-330	Nd17	16.38	2.24	0.61	0.05	2.31	78.02	0.15	0.13	0.11	0.01	0.024	22.50
		330-400+	Nd18	18.29	3.05	0.90	0.02	2.62	74.58	0.23	0.15	0.16	0.02	0.023	21.45

A comprehensive description of the distribution of major elements within the four sections is provided by Dina Ebouel et al. (n.d). In brief, Si is the dominant element along the studied sections with concentrations ranging from 61.00 to 88.00%. Aluminium and Fe also showed relatively high concentrations ranging from 4.70 to14.00%, and from 3.60 to 10.00%, respectively. The concentration of Ca, on the other hand, shows a very contrasting pattern, with relatively high concentrations (5.20 to 17.30%) observed in horizons with a high $CaCO_3$ content, while the other horizons generally have concentrations below 5%. Magnesium also shows a contrasting pattern,

with concentrations ranging from 0.50 to 3.60%. Sodium, K and Ti are generally present in minor proportions, while Mn and P are generally found in trace concentrations.

Calcium is the dominant elements in almost all the carbonate features, mostly above 50%. The maximum is observed in Nd11 (88.08%). The minimum observed in sample Ps (35.00%) represents an exception, where Si is the dominant element (49.32%). Aside this exception, Si is the second most abundant elements, with a content ranging from 13.34 and 49.32%. Magnesium in carbonate features exhibits contrasting behaviour, with concentrations above 10% observed in Nd02 and Nd03 (SC01), while concentrations between 5% and less than 10% are observed in Nd01 (SC01), Nd04 and Nd05 (SC02). The other carbonate features show relatively low values, although they remain s between 1.93 and 3.64%. Aluminium and Fe also show a contrasted pattern, most important values are observed in the features of SC01, respectively 5.75% in Nd01 for Al, and 3.14% in Ps for Fe. The lowest value of Al (1.77%) is observed in Nd11 (SC03), while the lowest value of Fe (0.62%) is observed in Nd05 (SC02). Sodium, K and Ti are mostly in minor proportion, while Mn and P are globally in trace proportion in all the carbonate features.

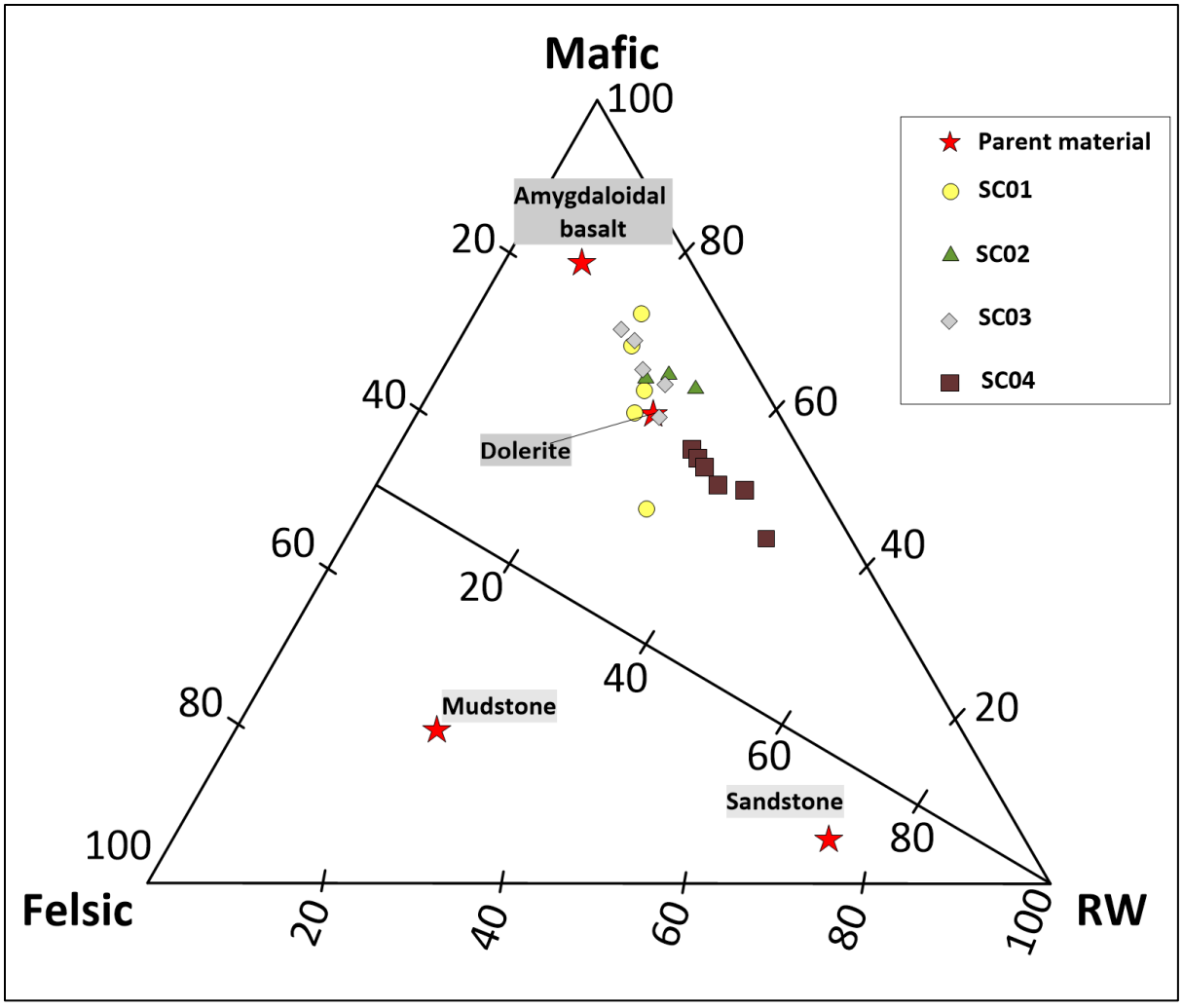


Fig. 6.7. Projection of samples in the ternary diagram: Mafic-Felsic-RW (Cho and Ohta, 2022)

As expected, the two basaltic materials appear near the mafic pole in the tertiary diagram Mafic-Felsic-RW (Fig. 6.7). Amygdaloidal basalt is tightly related to the fresh mafic rock pole, while dolerite sample reflect a low weathered mafic rock. Mudstone sample is plotted as a low weathered felsic material, while sandstone sample is plotted as a seriously weathered felsic material. All carbonate features are plotted as low weathered mafic samples. They are all represented very close to dolerite in the diagram, with some samples even above the point representing dolerite.

6.5. Discussion

6.5.1. Indices of the mafic lithology contribution to Ca furniture in carbonate features

Mineralogical analysis of the main lithology observed in the area identified the two basaltic rocks as potential sources of calcium, whereas the mudstone and sandstone were found to lack significant calcium-bearing minerals. Minerals such as labradorite [$(Na,Ca)(Al,Si)_4O_8$], representing 43% of the dolerite and 48% of the amygdaloidal basalt; augite [$(Ca, Na)(Mg, Fe, Al)(Si, Al)_2O_6$], with respective contributions of 34% and 22% in dolerite and amygdaloidal basalt; and heulandite [$CaAl_2Si_7O_{18}.6H_2O$], 12% constituting of the amygdaloidal basalt are all potentials providers of calcium through weathering. If the soil and the palaeosol of the sections mostly derived from the weathering of fluvio-colluvial sediments, as evidenced by the dominance of the sand fraction (Dina Ebouel et al., n.d.). The reworked fragments of these mafic materials might have a significant contribution in calcium furniture necessary to pedogenic carbonates formations in these pedosedimentary section.

The direct contribution of the local mafic lithology is petrographically confirmed by the presence of lithorelicts and alteromorphs of basaltic origin within the carbonate groundmass of the pseudomycelia (Ps) and transitional nodules (Nd01). Petrographic analysis (Fig. 6.6A and B) reveals that labradorite and augite grains frequently exhibit pellicular and irregular linear weathering patterns (Stoops et al., 2018), indicating that the dissolution of the silicate framework was coupled with the localised precipitation of circum-granular sparitic rims. This porphyric c/f-related distribution demonstrates that the carbonate features developed by encompassing the pre-existing mafic skeleton, trapping minerals in various stages of chemical degradation.

The mineralogical suite identified via XRD further reinforces this lithogenic link. The presence of smectite and secondary iron/manganese oxides within the carbonate features provides a diagnostic

chemical fingerprint of basaltic weathering. Within the micromorphological fabric, these oxides manifest as orthic nodules and impregnative pedofeatures, such as ferruginous hypo-coatings, which represent the immobile residual fraction of the primary ferromagnesian minerals (e.g., augite). Similarly, the identification of smectite (a typical byproduct of the hydrolysis of Ca-plagioclase and pyroxenes in semi-arid environments) marks the aluminosilicate residue of the same weathering process that liberated the calcium for carbonatisation.

A stark contrast is observed in the more mature nodules (Nd03–Nd14). In these features, the easily alterable basaltic minerals have been largely consumed by weathering, leaving a groundmass dominated by a calcitic-crystallitic b-fabric (up to 74% calcite). The only remaining coarse fraction consists of allochthonous quartz grains, which act as inherited resistant relicts. Unlike the mafic minerals, these quartz grains display plane contacts with the micritic matrix and frequently exhibit wavy extinction, typical of transport-derived material from distal felsic or sedimentary sources.

Furthermore, the presence of orthic iron and manganese nodules and impregnative pedofeatures (such as ferruginous hypo-coatings) within the mature carbonate matrix provides a "chemical fingerprint" of the vanished mafic minerals. These oxides represent the immobile residual fraction of the basalt weathering process. This mineralogical divergence (where the unstable mafic phases are progressively replaced by a carbonate-oxide-clay assemblage while the stable quartz remains physically unchanged) verifies that the chemical supply for carbonatisation is mineralogically tied to the local dissolution of the basaltic precursor.

This interpreted lineage is further validated by the projection of the carbonate features on the Mafic-Felsic-RW ternary diagram (Fig. 6.8). The samples cluster significantly towards the Mafic apex, aligning with the chemical signature of the local dolerites and amygdaloidal basalts. Their position on the diagram indicates that these pedogenic features are the direct result of the chemical

weathering of mafic source materials, with only a minor felsic contribution. Furthermore, when considering the trajectories of basalt weathering in the MFW (Mafic-Felsic-Weathering) diagram as described by Ohta and Arai (2007), the position occupied by the carbonate features aligns directly with the established basalt weathering pathway. The low degree of chemical weathering observed is consistent with the findings of Dina Ebouel et al. (2026), who demonstrated the predominance of semi-arid conditions throughout the landscape's evolution. Under such arid to semi-arid regimes, water–rock interaction is typically limited, a fact further supported by the preservation of highly susceptible minerals like labradorite and augite within the carbonate features. However, while the regional climate remained predominantly dry, local river dynamics appear to have played a critical role in facilitating ongoing weathering and the mobilisation of elements. Moreover, labradorite is highly susceptible to chemical weathering due to its calcium-rich composition and its thermodynamic instability under near-surface conditions (Goldich, 1938), reflecting its tendency to weather rapidly through hydrolysis and calcium leaching (White, 1995). Consequently, its preservation within carbonate features indicates limited water–rock interaction and short weathering durations, thereby supporting the inference of a low degree of chemical weathering. Furthermore, previous work in the sector all highlights the low degree of chemical weathering and the significant contribution of basaltic source materials to the development of soil (Dina Ebouel et al., 2025a; Eze et al., 2025).

Nevertheless, this conclusion must be considered with great caution, as all processes take place in an open system where contributions from multiple sources often take precedence over those from a single source (Dietrich et al., 2021). In semi-arid and arid environments, where aeolian transport of particles is considerable, it has been demonstrated that aeolian deposits can constitute a primary source for calcium ions trapped in pedogenic carbonates (Capo and Chadwick, 1999; Van Der

Hoven and Quade, 2002). In addition, Ca appears to be the third most important element after silica and nitrogen in the composition of the ambient air in Serowe, with an average concentration of 1158 ng/m^3 (Moloi et al., 2002).

Thus, aeolian deposits may have also provided the calcium ions to the pedogenic carbonates. However, such a contribution would be minimal, as the aeolian sediments in the Kalahari Basin, resulting from transport over very long distances and highly reworked material, are characterised by low alkali and alkaline earth element content (Garzanti et al., 2022). Besides, instead of a single contribution from amygdaloidal basalt, both types of basalt and even the carbonate identified in sandstones and mudstones (Carney, 1994; Franchi et al., 2021) could all have contributed to supplying calcium ions. This is consistent with a cascade model of calcium ions furniture as suggested by Dietrich et al. (2021) in the northern Cameroon.

Thus, while amygdaloidal basalt might be an important source of calcium ions of the carbonate features observed in the four describe sections, the contribution of other sources should not be overlooked in the overall assessment of inputs.

6.5.2. Calcium transfer and mobilisation pathways

Understanding pathways of Ca transfer from the bedrock to the soil profile and its subsequent mobilisation in carbonate features is critical to have an overview of the processes involved. In this case, given the location of the sections on the riverbanks, the dynamics of the river flow could have contributed significantly to the transfer of Ca ions from the basalt to the soil profile. The stratigraphic descriptions by Dina Ebouel et al. (n.d.) revealed a significant presence of basaltic rock fragments undergoing active weathering within the pedosedimentary sections (Fig. 6.3). While these sections did not develop directly *in-situ* on the basaltic basement, the mechanical disintegration of local basaltic units provides a continuous supply of fragments. Transported by

runoff and seasonal streamflow, these fragments are incorporated into the fluvial sediments as lithorelicts, serving as the primary source material for subsequent soil development. This pattern is common in soils formed in fluvial environments, where the mobilisation of surrounding rock fragments contributes significantly to soil development (Zádorová et al., 2025). This transfer model is also supported by the presence of labradorite relics, as highlighted by the mineralogy of all carbonate features considered in this study. However, as shown by Stadler et al. (2010), the superficial water chemistry, characterised with Ca–HCO_3 to Ca–Mg–HCO_3 chemical facies, highlights transport through solution. The chemical weathering of the lithological substrate, caused by the hydrolysis of Ca plagioclase (labradorite), zeolites and ferromagnesian minerals such as pyroxene and olivine, under the effect of meteoric water infiltration, mobilises dissolved cations (Ca^{2+} and Mg^{2+}). These are then transported to the drainage network via interstitial flows and groundwater discharges. This mechanism represents a significant source of Ca ions for soils in arid and semi-arid environments. Under these conditions, the hypersaturation of soil solutions caused by intense evapotranspiration triggers the precipitation of pedogenic carbonates in the soil profile during prolonged periods of drought (Monger et al., 2015).

Consequently, two distinct pathways contribute to the mobilisation of Ca^{2+} within the soil profile: (i) the autochthonous pathway, resulting from the *in-situ* chemical weathering of lithorelicts (reworked basaltic fragments), and (ii) the allochthonous or translocated pathway, where ions are supplied by the soil solution flux via vertical infiltration or lateral groundwater discharge.

Three main morphologies of carbonate accumulations predominate in studied profiles: diffuse powders, pseudomycelia and nodules. According to the morphogenetic classification of Gile (1993), the predominance of one of these types over the others is a direct indicator of the stage of evolution of the carbonate accumulation. Horizons characterised by the predominance of

pseudomycelia and diffuse powders (e.g., AB3b of SC03) indicate that carbonate is deposited in the porosity without altering the structure of the horizon. This is the initial stage of carbonate accumulation (Stage I). According to (Zamanian et al., 2016), pseudomycelia crystallisation is triggered by physical degassing occurring when percolating water passes from macropores to micropores. This transition causes a sudden drop in CO_2 pressure, which reduces the solubility of bicarbonates and leads to the immediate precipitation of carbonate in macro and medium pores. They are very often associated with fluctuations in the water table (Durand et al., 2010). This explains why they are observed in the basal layers of the sections. Calcium ions are probably mobilised by upward capillary flow and evapotranspiration, processes that intensify with aridification, moving Ca to the upper horizons (Bkb and AB1b). However, the presence of pseudomycelia represents localised enrichment relative to the host matrix. This indicates *in-situ* accumulation, albeit on an incipient or minor scale that has not yet compensated for the overall geochemical deficit of the horizon.

Petrographic evidence for this incipient stage is provided by the micritic coatings and infillings found within the vughy and channel porosity of the basal layers. Unlike the massive nodules, these pseudomycelia exhibit an enaulic to hemi-porphyric c/f-related distribution, where the carbonate crystals are concentrated along the walls of conducting pores rather than throughout the entire micromass (Durand et al., 2018). This specific arrangement suggests that the Ca^{2+}-rich solutions, driven by capillary rise, precipitated rapidly as they encountered the drier, more aerated environment of the upper matrix (Zamanian et al., 2016). The preservation of primary mineral relics with only thin circum-granular ferruginous hypo-coatings within these features further confirms that the accumulation is in its initial phase; the carbonate has yet to exert enough expansive crystallisation pressure to displace the original soil fabric or fully mask the optical

expression of the interstitial clay minerals. Consequently, the pseudomycelia serve as a visual record of the transition point where dissolved ions begin to fix into the solid phase, marking the onset of the carbonatisation process within a still-depleted matrix.

Many horizons with high $CaCO_3$ content (Bkb in SC01, BCk1b and BCk2b in SC02, SC03 and SC04) are characterised by predominance of nodules, corresponding to stage II of the morphogenetic classification of Gile (1993). According to Durand et al. (2018), the formation of carbonate nodules results from a gradual, polyphasic pedogenic process dominated by repeated cycles of $CaCO_3$ dissolution and precipitation. During relatively humid phases, $CaCO_3$ is partially dissolved and mobilised in soil solutions. During dry periods, or when the partial pressure of carbon dioxide decreases, the solutions become supersaturated with Ca ions and carbonate precipitates locally, initiating or feeding the growth of nodules. This description is consistent with the fact that horizons containing nodules appear in buried soils. They therefore, correspond to a gradual, polyphasic accumulation (Zamanian et al., 2016). Based on the position of AB1b and Bkb in SC01, it is suggested that upward movement during dry period are also contributing to accumulation of carbonate in the concerned horizons.

Thus, Ca is supplied to the soil profile through the mechanical incorporation of basaltic fragments and the chemical hydrolysis of basalt fragments Ca-bearing minerals, which are transported and concentrated by the dynamics of the river and its fluctuating water table. These ions are then mobilised via an autochthonous pathway from *in-situ* weathering and an allochthonous pathway driven by seasonal streamflow, vertical infiltration, or upward capillary rise during aridification. Initial stage I features, such as pseudomycelia, form through CO_2 degassing in the basal layers influenced by the river's proximity, indicating minor accumulation within a net-depleted matrix.

In contrast, stage II nodules represent advanced, polyphasic accumulation resulting from repeated cycles of wetting by the river and subsequent drying.

The natural contribution of local basaltic formations to the calcium supply for carbonate features provides a robust scientific basis for implementing CDR solutions within local agricultural development, specifically through ERW (Taksavasu, 2025). Furthermore, as highlighted by Eze et al. (2025), the weathering of these basalts (which play a fundamental role in the formation of regional Vertisols) does not pose a pollution risk via the release or accumulation of toxic trace elements.

6.6. Conclusions

This study demonstrates a significant contribution of the weathering basaltic rock in the furniture of Ca ions necessary for the pedogenic carbonates developed in the pedosedimentary sequences of Central Botswana. Particularly amygdaloidal basalt rich in labradorite, augite and zeolites. The integration of mineralogical, petrographic, and geochemical data consistently shows that felsic detrital rocks (sandstones and mudstones) play a negligible role in calcium supply, despite their regional abundance. The Mafic–Felsic–RW diagram, provide arguments in favour of a predominantly mafic origin of Ca, even in an open pedological system subject to sedimentary and aeolian inputs. The results also highlight complex mechanisms of Ca transfer and redistribution within the profiles. The coexistence of different carbonate morphologies (diffuse powders, pseudomycelia and nodules) reflects distinct evolutionary stages of pedogenic calcification, from early accumulations linked to CO_2 degassing to polyphasic nodules resulting from repeated dissolution–precipitation cycles. These processes are closely controlled by groundwater fluctuations, river dynamics and wet-dry climate cycles characteristic of semi-arid environments. However, certain limitations must be highlighted. The absence of isotopic data (Sr, Ca) makes it

impossible to accurately quantify the relative contribution of different potential sources of calcium, particularly wind-borne inputs or possible regional carbonate sources. Furthermore, the absence of apparent density data limits the estimation of absolute flows of Ca and sequestered carbon. Finally, the spatial variability of sedimentary and hydrological inputs along the studied watercourse introduces a heterogeneity that cannot be fully captured by four sections. Despite these limitations, this study represents a major methodological advance for regions where access to isotopic analyses is limited. It demonstrates that a multi-proxy approach based on mineralogy, petrography and elemental geochemistry can effectively constrain the origin of calcium and the processes of pedogenic carbonate formation. At the regional scale, these results reinforce the idea that basaltic substrates play a key role in the formation of inorganic soil carbon in semi-arid southern Africa. On a global scale, our results highlight the potential of semi-arid basaltic environments as Ca source and by inference, a long-term carbon sinks through the formation of pedogenic carbonates, with important implications for understanding the carbon cycle and developing CO_2 sequestration strategies based on silicate weathering. It also highlights possible implementation of ERW with local lithology.

References

Atlhopheng, J., Brown Mthanganyika Mapeo, R., Eckardt, F.D., 2022. Introduction to the Landscapes and Landforms of Botswana, in: Eckardt, F.D. (Ed.), Landscapes and Landforms of Botswana. Springer International Publishing, Cham, pp. 1–13. https://doi.org/10.1007/978-3-030-86102-5_1

Bajnóczi, B., Kovács-Kis, V., 2006. Origin of pedogenic needle-fiber calcite revealed by micromorphology and stable isotope composition—a case study of a Quaternary paleosol from Hungary. Geochemistry 66, 203–212. https://doi.org/https://doi.org/10.1016/j.chemer.2005.11.002

Batisani, N., Yarnal, B., 2010. Rainfall variability and trends in semi-arid Botswana: Implications for climate change adaptation policy. Applied Geography 30, 483–489. https://doi.org/10.1016/j.apgeog.2009.10.007

Bockheim, J.G., Douglass, D.C., 2006. Origin and significance of calcium carbonate in soils of southwestern Patagonia. Geoderma 136, 751–762. https://doi.org/10.1016/j.geoderma.2006.05.013

Brimhall, G.H., Dietrich, W.E., 1987. Constitutive mass balance relations between chemical composition, volume, density, porosity, and strain in metasomatic hydrochemical systems: Results on weathering and pedogenesis. Geochim. Cosmochim. Acta 51, 567–587. https://doi.org/https://doi.org/10.1016/0016-7037(87)90070-6

Capo, R.C., Chadwick, O.A., 1999. Sources of strontium and calcium in desert soil and calcrete, Earth and Planetary Science Letters.

Carney, J.N., 1994. The geology of Botswana. Geological Survey of Botswana 37:17.

Chadwick, O.A., Brimhall, G.H., Hendricks, D.M., 1990. From a black to a gray box — a mass balance interpretation of pedogenesis. Geomorphology 3, 369–390. https://doi.org/https://doi.org/10.1016/0169-555X(90)90012-F

Chen, B.B., Li, S.L., Pogge von Strandmann, P.A.E., Wilson, D.J., Zhong, J., Sun, J., Liu, C.Q., 2022. Calcium isotopes tracing secondary mineral formation in the high-relief Yalong River Basin, Southeast Tibetan Plateau. Science of the Total Environment 827. https://doi.org/10.1016/j.scitotenv.2022.154315

Cho, T., Ohta, T., 2022. A robust chemical weathering index for sediments containing authigenic and biogenic materials. Palaeogeogr. Palaeoclimatol. Palaeoecol. 608, 111288. https://doi.org/10.1016/J.PALAEO.2022.111288

Curtis Monger, H., Kraimer, R.A., Khresat, S., Cole, D.R., Wang, X., Wang, J., 2015. Sequestration of inorganic carbon in soil and groundwater. Geology 43, 375–378. https://doi.org/10.1130/G36449.1

Dietrich, F., Diaz, N., Deschamps, P., Ngounou Ngatcha, B., Sebag, D., Verrecchia, E.P., 2017. Origin of calcium in pedogenic carbonate nodules from silicate watersheds in the Far North Region of Cameroon: Respective contribution of in situ weathering source and dust input. Chem. Geol. 460, 54–69. https://doi.org/10.1016/j.chemgeo.2017.04.015

Dietrich, F., Diaz, N., Deschamps, P., Sebag, D., Verrecchia, E., 2021. Calcium transfer and mass balance associated with soil carbonate in a semi-arid silicate watershed (North Cameroon): An overlooked geochemical cascade? Depositional Record 2021. https://doi.org/10.1002/dep2.134ï

Dina Ebouel, F.J., Betsi, T.B., Eze, P.N., 2024. Soil inorganic carbon: A review of global research trends, analytical techniques, ecosystem functions and critical knowledge gaps. Catena (Amst). 242, 108112. https://doi.org/https://doi.org/10.1016/j.catena.2024.108112

Dina Ebouel, F.J., Bineli Betsi, T., Eiche, E., Norra, S., n.d. Pedogenic and Sedimentary Controls on Secondary Carbonate Accumulation in Semi-Arid Fluvial Landscape, Central Botswana. https://doi.org/http://dx.doi.org/10.2139/ssrn.6330138

Dina Ebouel, F.J., Bineli Betsi, T., Eiche, E., Norra, S., Eze, P.N., 2026. Decoupling climate and local hydrology in Central Botswana: new insights from carbonate δ13C, δ18O isotopes, and elemental geochemistry. Front. Environ. Sci. Volume 14-2026.

Dina Ebouel, F.J., Kono Ebede, C.G., Bineli Betsi, T., Eze, P.N., 2025a. Distribution and potential of rare earth elements fingerprinting as tracers for carbonate sources in soils developed on contrasting parent materials. Geoderma Regional 43, e01009. https://doi.org/https://doi.org/10.1016/j.geodrs.2025.e01009

Dina Ebouel, F.J., Molwalefhe, L.N., Betsi, T.B., Eze, P.N., 2025b. A Multi-Proxy Pedosedimentary Insight into Calcium Origin, Sediment Provenance, and Depositional Environments in a NW Botswana Landform. Earth Systems and Environment. https://doi.org/10.1007/s41748-025-00724-w

Doebelin, N., Kleeberg, R., 2015. Profex: a graphical user interface for the Rietveld refinement program BGMN. J. Appl. Crystallogr. 48, 1573–1580.

Durand, N., Monger, H.C., Canti, M.G., 2010. 9 - Calcium Carbonate Features, in: Stoops, G., Marcelino, V., Mees, F. (Eds.), Interpretation of Micromorphological Features of Soils and Regoliths. Elsevier, Amsterdam, pp. 149–194. https://doi.org/https://doi.org/10.1016/B978-0-444-53156-8.00009-X

Durand, N., Monger, H.C., Canti, M.G., Verrecchia, E.P., 2018. Calcium Carbonate Features, in: Interpretation of Micromorphological Features of Soils and Regoliths. Elsevier, pp. 205–258. https://doi.org/10.1016/b978-0-444-63522-8.00009-7

Eze, P.N., 2022. Soil Development in the Eastern Hardveld, in: Eckardt, F.D. (Ed.), Landscapes and Landforms of Botswana. Springer International Publishing, Cham, pp. 327–344. https://doi.org/10.1007/978-3-030-86102-5_19

Eze, P.N., Dina Ebouel, F.J., Nkonga, I., Musiol, A., Schleicher, A.M., Günter, C., Norra, S., 2025. Weathering intensity and trace elements (Ni, Sr, Zn, and Cr) distribution in Vertisols developed on basalt in a semiarid environment: agronomic implications. Frontiers in Soil Science 5. https://doi.org/10.3389/fsoil.2025.1530962

Franchi, F., Kelepile, T., Di Capua, A., De Wit, M.C.J., Kemiso, O., Lasarwe, R., Catuneanu, O., 2021. Lithostratigraphy, sedimentary petrography and geochemistry of the Upper Karoo Supergroup in the Central Kalahari Karoo Sub-Basin, Botswana. Journal of African Earth Sciences 173. https://doi.org/10.1016/j.jafrearsci.2020.104025

Garzanti, E., Pastore, G., Stone, A., Vainer, S., Vermeesch, P., Resentini, A., 2022. Provenance of Kalahari Sand: Paleoweathering and recycling in a linked fluvial-aeolian system. Earth. Sci. Rev. https://doi.org/10.1016/j.earscirev.2021.103867

Gile, L.H., 1993. Carbonate Stages in Sandy soils of Leasburg surface, Souther New Mexico. Soil Sci. 156.

Goldich, S.S., 1938. A Study in Rock-Weathering. J. Geol. 46, 17–58. https://doi.org/10.1086/624619

Haque, F., Santos, R.M., Chiang, Y.W., 2021. Urban Farming with Enhanced Rock Weathering As a Prospective Climate Stabilization Wedge. Environ. Sci. Technol. 55, 13575–13578. https://doi.org/10.1021/acs.est.1c04111

IUSS Working Group WRB, 2022. World Reference Base for Soil Resources. International soil classification system for naming soils and creating legends for soil maps, 4th edition. ed. International Union of Soil Sciences, Vienna.

Lal, R., Monger, C., Nave, L., Smith, P., 2021. The role of soil in regulation of climate. Philosophical Transactions of the Royal Society B: Biological Sciences 376. https://doi.org/10.1098/rstb.2021.0084

Millière, L., Gussone, N., Moritz, T., Bindschedler, S., Verrecchia, E.P., 2019. Origin of strontium and calcium in pedogenic needle fibre calcite (NFC). Chem. Geol. 524, 329–344. https://doi.org/10.1016/j.chemgeo.2019.06.022

Moloi, K., Chimidza, S., Lindgren, E.S., Viksna, A., Standzenieks, P., 2002. Black carbon, mass and elemental measurements of airborne particles in the village of Serowe, Botswana. Atmos. Environ. 36, 2447–2457. https://doi.org/https://doi.org/10.1016/S1352-2310(02)00085-7

Monger, H.C., 2014. Soils as Generators and Sinks of Inorganic Carbon in Geologic Time, in: Soil Carbon. Springer International Publishing, pp. 27–36. https://doi.org/10.1007/978-3-319-04084-4_3

Naorem, A., Jayaraman, S., Dalal, R.C., Patra, A., Rao, C.S., Lal, R., 2022. Soil Inorganic Carbon as a Potential Sink in Carbon Storage in Dryland Soils—A Review. Agriculture (Switzerland) 12. https://doi.org/10.3390/agriculture12081256

Ohta, T., Arai, H., 2007. Statistical empirical index of chemical weathering in igneous rocks: A new tool for evaluating the degree of weathering. Chem. Geol. 240, 280–297. https://doi.org/https://doi.org/10.1016/j.chemgeo.2007.02.017

Ridgwell, A., Zeebe, R.E., 2005. The role of the global carbonate cycle in the regulation and evolution of the Earth system. Earth Planet. Sci. Lett. 234, 299–315. https://doi.org/https://doi.org/10.1016/j.epsl.2005.03.006

Ringrose, S., Matheson, W., Vanderpost, C., 1998. Analysis of soil organic carbon and vegetation cover trends along the B otswana Kalahari Transect, Journal of A rid Environments.

Rollinson, H., Pease, V. (Eds.), 2021. Using Major Element Data, in: Using Geochemical Data: To Understand Geological Processes. Cambridge University Press, Cambridge, pp. 49–95. https://doi.org/DOI: 10.1017/9781108777834.006

Rowley, M.C., Grand, S., Adatte, T., Verrecchia, E.P., 2020. A cascading influence of calcium carbonate on the biogeochemistry and pedogenic trajectories of subalpine soils, Switzerland. Geoderma 361. https://doi.org/10.1016/j.geoderma.2019.114065

Sheldon, N.D., Tabor, N.J., 2009. Quantitative paleoenvironmental and paleoclimatic reconstruction using paleosols. Earth. Sci. Rev. 95, 1–52. https://doi.org/https://doi.org/10.1016/j.earscirev.2009.03.004

Smith, A., R., 1984. The Lithostratigraphy of the Karoo Supergroup in Botswana. Geol. Mag. 123, 710–711. https://doi.org/DOI: 10.1017/S0016756800024328

Stadler, S., Osenbrück, K., Suckow, A.O., Himmelsbach, T., Hötzl, H., 2010. Groundwater flow regime, recharge and regional-scale solute transport in the semi-arid Kalahari of Botswana derived from isotope hydrology and hydrochemistry. J. Hydrol. (Amst). 388, 291–303. https://doi.org/https://doi.org/10.1016/j.jhydrol.2010.05.008

Stoops, G., Marcelino, V., Mees, F., 2018. Chapter 30 - Micromorphological Features and Their Relation to Processes and Classification: General Guidelines and Overview, in: Stoops, G., Marcelino, V., Mees, F. (Eds.), Interpretation of Micromorphological Features of Soils and Regoliths (Second Edition). Elsevier, pp. 895–917. https://doi.org/https://doi.org/10.1016/B978-0-444-63522-8.00030-9

Taksavasu, T., 2025. Petrographic Analysis of Mafic and Ultramafic Rocks in Northern Thailand: Implications for CO2 Mineralization and Enhanced Rock Weathering Approach. Geosciences (Basel). 15. https://doi.org/10.3390/geosciences15030089

Ussiri, D.A.N., Lal, R., 2017. The Global Carbon Inventory, in: Ussiri, D.A.N., Lal, R. (Eds.), Carbon Sequestration for Climate Change Mitigation and Adaptation. Springer International Publishing, Cham, pp. 77–102. https://doi.org/10.1007/978-3-319-53845-7_4

Van Der Hoven, S.J., Quade, J., 2002. Tracing spatial and temporal variations in the sources of calcium in pedogenic carbonates in a semiarid environment.

Vienne, A., Poblador, S., Portillo-Estrada, M., Hartmann, J., Ijiehon, S., Wade, P., Vicca, S., 2022. Enhanced Weathering Using Basalt Rock Powder: Carbon Sequestration, Co-benefits and Risks in a Mesocosm Study With Solanum tuberosum. Frontiers in Climate Volume 4-2022.

Wassenburg, J.A., Riechelmann, S., Schröder-Ritzrau, A., Riechelmann, D.F.C., Richter, D.K., Immenhauser, A., Terente, M., Constantin, S., Hachenberg, A., Hansen, M., Scholz, D., 2020. Calcite Mg and Sr partition coefficients in cave environments: Implications for interpreting prior calcite precipitation in speleothems. Geochim. Cosmochim. Acta 269, 581–596. https://doi.org/https://doi.org/10.1016/j.gca.2019.11.011

Weremeichik, J.M., Gabitov, R.I., Sadekov, A., Novak, A., Jimenez, A., Thirumalai, R.V.K.G., Varco, J.J., Dygert, A., 2021. Mg/Ca Ratios in Synthetic Low-Magnesium Calcite: An Experimental Investigation. Minerals 11. https://doi.org/10.3390/min11111158

White, Art F, 1995. Chemical weathering rates of silicate minerals in soils, in: White, Arthur F, Brantley, S.L. (Eds.), . De Gruyter, pp. 407–462. https://doi.org/doi:10.1515/9781501509650-011

Whitney, D.L., Evans, B.W., 2010. Abbreviations for names of rock-forming minerals. American Mineralogist 95, 185–187. https://doi.org/10.2138/am.2010.3371

Zádorová, T., Penížek, V., Mihaljevič, M., Koubová, M., Lisá, L., Ettler, V., Tejnecký, V., Drábek, O., Pavlů, L., Kříbek, B., Vaněk, A., Sracek, O., Rojas, J.R., Hrdlička, T., Vokurková, P., Mapani, B., 2025. Local diversity of soil forming processes in the semi-arid tropics and its environmental

drivers: An example from Otavi Mountains, northern Namibia. Catena (Amst). 249, 108671. https://doi.org/https://doi.org/10.1016/j.catena.2024.108671

Zamanian, K., Pustovoytov, K., Kuzyakov, Y., 2016. Pedogenic carbonates: Forms and formation processes. Earth. Sci. Rev. https://doi.org/10.1016/j.earscirev.2016.03.003

Appendices

Appendix 6.1. Quality control.

Quality Check		Na_2O	MgO	Al_2O_3	SiO_2	P_2O_5	K_2O	CaO	TiO_2	MnO	Fe_2O_3 - tot	*Sr*
		% w	*% w*	*% w*	*% w*	*% w*	*% w*	*% w*	*% w*	*% w*	*% w*	*mg/kg*
AGV-1	09/09/2025 10:49	4.25	1.52	17.1	59.1	0.50	2.90	4.91	1.04	0.097	7.0	662
	Nominal Value	4.25	1.51	17.1	59.4	0.49	2.94	4.89	1.05	0.097	6.8	662
	Accuracy [%]	100.0	100.6	99.8	99.6	102.0	98.9	100.3	99.0	100.4	103.5	100.0
AGV-1	11/09/2025 09:47	4.24	1.54	17.1	59.1	0.50	2.9	4.87	1.0	0.095	7.0	659
	Nominal Value	4.25	1.51	17.1	59.4	0.49	2.94	4.89	1.05	0.097	6.8	662
	Accuracy [%]	99.7	102.1	99.9	99.5	101.4	99.0	99.6	99.5	98.3	103.2	99.6
AGV-1	12/09/2025 14:04	4.27	1.53	17.1	59.2	0.50	2.9	4.90	1.0	0.096	7.0	655
	Nominal Value	4.25	1.51	17.1	59.4	0.49	2.94	4.89	1.05	0.097	6.8	662
	Accuracy [%]	100.4	101.5	99.9	99.7	101.6	99.1	100.2	99.2	99.4	103.4	98.9
GXR-2	09/09/2025 11:05	0.65	1.21	32	38.4	0.12	1.3	1.0	0.41	0.10	2.3	160
	Nominal Value	0.75	1.41	31.1	47.5	0.24	1.65	1.30	0.5	0.130	2.7	160
	Accuracy [%]	86.5	85.6	102.3	80.8	50.4	79.6	77.8	82.4	79.2	87.1	100.1
GXR-2	12/09/2025 14:20	0.65	1.24	32	38.3	0.12	1.3	1.0	0.41	0.10	2.3	160
	Nominal Value	0.75	1.41	31.1	47.5	0.24	1.65	1.30	0.5	0.130	2.7	160
	Accuracy [%]	86.7	87.8	102.9	80.6	50.0	79.4	77.8	82.6	80.0	86.8	99.8
GXR-5	09/09/2025 11:20	0.92	1.78	38	36.5	0.07	0.93	1.0	0.36	0.034	4.5	109
	Nominal Value	1.05	1.97	38.2	41.4	0.07	1.06	1.17	0.37	0.040	4.8	110
	Accuracy [%]	87.9	90.3	100.1	88.2	100.0	88.0	87.5	95.9	85.0	93.3	98.8
GXR-5	12/09/2025 14:35	0.94	1.78	39	36.9	0.071	0.93	1.0	0.36	0.034	4.5	108
	Nominal Value	1.05	1.97	38.2	41.4	0.070	1.06	1.17	0.37	0.040	4.8	110
	Accuracy [%]	89.3	90.3	100.8	89.3	101.4	88.1	87.9	96.5	85.0	93.8	98.4
Soil 7	09/09/2025 11:35	0.36	1.98	9.3	38.8	0.13	1.6	25	0.57	0.092	3.9	332
	Nominal Value	-	1.97	10.0	37.9	0.13	-	-	-	0.080	4.8	330
	Accuracy [%]	-	100.7	92.5	102.3	100.0	-	-	-	115.0	79.7	100.8
Soil 7	12/09/2025 14:50	0.38	2.00	9.3	38.6	0.128	1.5	25	0.57	0.091	3.8	331
	Nominal Value	-	1.97	10.0	37.9	0.130	-	-	-	0.080	4.8	330
	Accuracy [%]	-	101.6	92.3	101.9	98.5	-	-	-	113.8	79.3	100.3

Appendix 6.2. Major oxides in weight percent

Sample	SiO_2	Al_2O_3	Fe_2O_3	MnO	MgO	CaO	Na_2O	K_2O	TiO_2	P_2O_5	LOI
	wt.%										
B	49	12	16	0.20	4.9	9.2	2.2	0.71	4.1	0.39	0.64
AB	46	15	10.7	0.16	5.8	8.5	3.8	0.17	0.91	0.15	7.68
S1	95	2.3	0.35	0.009	0.15	0.11	0.025	1.1	0.079	0.012	1.15
S2	59	21	3.8	0.075	1.2	0.356	4.6	3.68	1.2	0.082	3.32
Nd01	29	3.6	2.5	0.054	4.5	29	0.32	0.32	0.25	0.018	29.3
Nd02	16	2.0	1.0	0.085	4.8	38	0.16	0.14	0.15	0.010	36.24
Nd03	19	2.3	1.1	0.073	7.8	32	0.13	0.13	0.17	0.009	35.35
Nd04	19	2.7	1.4	0.062	2.8	37	0.19	0.14	0.19	0.010	34.35
Ps	38	4.4	3.2	0.031	1.9	25	0.44	0.39	0.41	0.020	24.59
Nd05	11	1.3	0.53	0.009	3.0	43	0.051	0.048	0.095	0.007	38.46
Nd06	14	1.9	0.88	0.12	1.6	43	0.11	0.043	0.13	0.014	36.38
Nd07	14	1.7	0.79	0.17	1.4	43	0.091	0.07	0.12	0.017	36.41
Nd08	8	0.99	0.50	0.072	0.8	48	0.056	0.035	0.091	0.009	37.57
Nd09	11	1.2	0.51	0.039	1.0	46	0.08	0.039	0.086	0.012	36.11
Nd10	10	1.4	0.60	0.034	1.0	48	0.079	0.058	0.097	0.013	34.2
Nd11	9	0.95	0.36	0.039	0.8	48	0.066	0.026	0.069	0.011	34.22
Nd12	14	1.6	0.60	0.12	0.95	45	0.12	0.031	0.11	0.011	34.67
Nd13	14	1.4	0.75	0.046	1.0	44	0.031	0.079	0.11	0.013	36.73
Nd14	11	1.0	0.53	0.026	0.9	46	0.025	0.049	0.084	0.011	37.77
Nd15	14	1.8	0.91	0.051	1.1	43	0.061	0.082	0.13	0.012	36.45
Nd16	13	1.4	0.67	0.023	1.0	45	0.057	0.071	0.11	0.010	36.79
Nd17	11	1.2	0.52	0.038	1.0	47	0.049	0.066	0.095	0.008	37.29
Nd18	12	1.7	0.77	0.012	1.1	45	0.075	0.076	0.14	0.012	37.04

B1=Dolerite; AB1=Amygdaloidal Basalt; S1=Sandstone; S2=Mudstone

CHAPTER SEVEN

Decoupling climate and local hydrology in Central Botswana: New insights from carbonate $\delta^{13}C$, $\delta^{18}O$ isotopes, and elemental geochemistry[6]

Abstract

Pedogenic carbonates provide valuable archives of past environmental conditions through their elemental and isotopic compositions. This study integrates stable carbon ($\delta^{13}C$) and oxygen ($\delta^{18}O$) isotopes, obtained from carbonate features alongside manganese (Mn) and iron (Fe) concentrations in carbonate features and soil horizons across four pedosedimentary sections (SC01–SC04), to reconstruct vegetation dynamics, climatic stability, and local hydrological variability. Elemental concentrations of Mn and Fe are reported in molar percent (mol%). Soil profiles exhibit low Mn content (0.04–0.11%), in contrast to higher Fe concentrations (2.68–7.47%). Carbonate features are systematically depleted in Fe relative to their host matrices (0.42–3.13%), while Mn is selectively enriched in several nodules, reaching up to 0.22% (Nd07, SC02). Stable isotope data reveal tightly clustered values within each section. $\delta^{13}C$ values range from -3.17 to -0.24‰ for nodules, which is consistent with a C3-C4 mixed savannah ecosystem. However, deep-seated pseudomycelia exhibit a distinct $\delta^{13}C$ signature of -6.85‰, interpreted as a biogenic signal from C3 shrub roots in a closed, riparian sub-surface environment rather than a vegetation shift. $\delta^{18}O$ values display a narrow range of -5.52 to -3.39‰ across all sections, indicating limited variability in meteoric water composition and evaporative conditions. High Mn/Fe ratios correlate with

[6] *This chapter is based on a research article co-authored with Thierry Bineli Betsi, Elisabeth Eiche, Stefan Norra, and Peter N. Eze; published in Frontiers in Environmental Science. 14:1821521. https://doi.org/10.3389/fenvs.2026.1821521*

depleted $\delta^{18}O$ values (≤ -5‰), marking periods of increased freshwater input and seasonal waterlogging. Crucially, the decoupling of redox signals in some nodules, characterised by a combined high Mn/Fe ratio with $\delta^{18}O$ enrichment, highlights the occurrence of episodic fluvial pulses and overbank flooding superimposed on a generally semi-arid background. These findings demonstrate that while the regional macro-climate remained stable, local hydrology was highly dynamic, driven by high-frequency fluctuations in river-water influence.

Keywords: Fluvial influence; palaeosols; redox processes; semi-arid environments; soil geochemistry; Southern Africa

7.1. Introduction

Pedogenic carbonate serves as a vital natural pathway for carbon sequestration in arid and semi-arid environments, while also acting as a proxy for past climatic and environmental change (Naorem et al., 2022; Dina Ebouel et al., 2024). These carbonates typically form either through the dissolution and recrystallisation of precursor lithogenic or biogenic minerals such as dolomite or calcite or through the weathering of silicate minerals (Monger et al., 2015). Both processes play a critical role in the global carbon cycle by facilitating carbon dioxide (CO_2) sequestration through fluvial and marine systems, as well as terrestrial carbon storage within the soil profiles of dryland ecosystems (Lal et al., 2021). While these carbonates are recognised as active pathways for CO_2 sequestration that can be enhanced or degraded by current land use (Raheb et al., 2016; Bughio et al., 2017; An et al., 2019; Liu et al., 2022), they are also frequently identified as the result of long-term accumulation over geological timescales, particularly within palaeosols (Monger, 2014). Consequently, they serve as accurate proxies for palaeoenvironmental and palaeoclimatic reconstruction (Fox et al., 2012; Khormali et al., 2020; Valera-Fernández et al., 2020; Breecker et al., 2025).

The established methodological framework for using pedogenic carbonate as a palaeoenvironmental proxy relies on the origin of the carbon trapped within the mineral lattice, which is primarily derived from root respiration and organic matter decomposition (Zamanian et al., 2016). Consequently, analysing the stable carbon isotope ratios ($\delta^{13}C$) within these carbonates makes it possible to infer the dominant vegetation type (C4 vs. C3 plants) prevailing during their formation (Railsback, 2021; Kirkels et al., 2022). However, the $\delta^{13}C$ signal may also be influenced by the dissolved inorganic carbon (DIC) from which carbonates precipitate, including potential contributions from lithogenic carbonate dissolution (Monger et al., 2015; Park et al., 2026). In

addition, kinetic fractionation during rapid precipitation and post-depositional diagenetic processes may lead to deviations from equilibrium conditions, thereby modifying the primary $\delta^{13}C$ signature (Stoll et al., 2023). As a result, while broad ecological interpretations (e.g., C3 vs C4 dominance) remain robust, more detailed quantitative reconstructions should be treated with caution (Breecker et al., 2025).

Palaeoclimatic reconstruction is supported by the relationship established between the meteoric water, from which the oxygen present in pedogenic carbonate was derived and the resulting isotopic signature (Cerling, 1984). Thus, the stable isotopic ratio of oxygen in pedogenic carbonate is mainly controlled by the climatic conditions prevailing during mineral precipitation. This is because the fractionation of oxygen isotopes ($^{18}O/^{16}O$) during carbonate precipitation is temperature-dependent, effectively recording the climatic conditions at the time of their formation (Hoefs, 2015). Although seasonal variations and the multiple dissolution-reprecipitation cycles inherent in the development of pedogenic carbonates are often cited as limitations to palaeoenvironmental and palaeoclimatic reconstructions based on stable isotopes (Breecker et al., 2009; Stevenson et al., 2010; Domínguez-Villar et al., 2022), the approach remains demonstrably effective. These processes, while complex, do not negate the capacity of the carbonates to record significant environmental signals, particularly when interpreted within their specific pedosedimentary context (Yang et al., 2012; Zhang et al., 2021; Mohammednoor et al., 2025).

In pedosedimentary environments where active pedogenesis is interrupted by allochthonous deposits, it is often difficult to determine whether these interruptions signify a sustained transition to a humid climate or whether they simply represent isolated large-scale flooding events. However, as established by Sipos et al. (2025), pedogenic carbonates in hydromorphic or fluctuating environments are dynamic archives rather than static minerals. They exist in complex

"paragenetic" relationships with other redox-sensitive phases. Mn and Fe in pedogenic carbonates often occur as secondary phases (e.g., oxyhydroxides), and therefore reflect redox dynamics within the soil system rather than strictly syn-depositional conditions. Manganese is reduced and mobilised more rapidly than iron under conditions of increasing anoxia (Otero et al., 2009). Consequently, the relative abundance of these elements in the pedogenic carbonate reflects the specific duration and intensity of the wetting event, allowing transient pulses to be distinguished from prolonged waterlogging.

Pedogenic carbonates play a central role in shaping the pedological landscape of Botswana (Eze, 2022; Dina Ebouel et al., 2025b, 2025a). Recently, pedosedimentary sections characterised by significant accumulations of carbonate features have been described along an ephemeral watercourse in the Central District (Dina Ebouel et al. 2026a, under review). The result demonstrated a pedogenic origin of the carbonate features, in theses sections. Furthermore, mineralogical characterisation identified calcite as the predominant phase. The calcium trapped in these pedogenic carbonates comes mainly from the basaltic bedrock (Dina Ebouel et al., 2026b, under review). However, the high-resolution environmental conditions, particularly the specific vegetative cover and the transient redox dynamics that governed carbonate precipitation, remain poorly constrained. This study aims to reconstruct these palaeoenvironmental conditions, including palaeohydrological fluctuations and redox potentials, by combining stable isotope ($\delta^{13}C$ and $\delta^{18}O$) analyses with the Mn/Fe ratio as a novel redox proxy.

7.2. Materials and methods

7.2.1. Study site and sampling strategy

As mentioned above, the study site has already been the subject of other research, particularly with the aim of understanding the formation of the landscape and tracing the origin and processes of

calcium ion mobilisation by carbonates (Dina Ebouel et al. 2026a, 2026b, under review). It is in the Central District of Botswana, between 22.34° and 22.42° south latitude and between 26.67° and 26.76° east longitude.

The general environmental setting highlights a relict landscape composed of gently sloping plains interspersed with isolated ravines subject to active erosion, characteristic of the Eastern Hardveld geomorphological unit of Botswana (Atlhopheng et al., 2022). The geological substrate is mainly dominated by the Late Carboniferous to Early Jurassic Karoo Supergroup formations, covered in places by Cenozoic Kalahari Group sands (Smith, 1984). According to the lithostratigraphic description of Franchi et al. (2021), the Lower Karoo Supergroup (comprising the Ecca and Beaufort groups) is characterised by a basal sequence of conglomerates and breccias that fines upward into coal-rich mudrocks with organic shales, followed by poorly lithified, grey-to-purple claystones (Beaufort Group). Field observations at the study site reveal a complex stratigraphy where three primary lithologies belonging to the Upper Karoo Supergroup are interbedded. These include alternating mudstones and sandstones from the Lebung Group and basaltic deposits from the Stormberg Lava Group. The Kalahari Group consists of loose aeolian sand containing buried palaeosols rich in carbonate nodules (Franchi et al., 2021).

The local climate is hot and semi-arid (corresponding to BSh type, Köppen–Geiger classification), characterised by long dry periods and a short rainy season from November to March. Rainfall data analysed by Kenabatho (2025) over a 60-year period indicate a mean annual precipitation of approximately 431 mm. However, rainfall is marked by strong interannual variability, with frequent droughts and episodic flooding (Nkemelang et al., 2018; Akinyemi, 2021). The winter season (May to September) is dry and sunny. Daytime temperatures remain warm, whereas nights

and early mornings can be cold, with temperatures occasionally reaching 0 °C. Maximum temperatures occur during the summer months and may exceed 45 °C (Batisani and Yarnal, 2010). Vegetation corresponds to a bush savannah ecosystem, dominated by woody species such as *Acacia, Terminalia*, and *Boscia*, with a diverse herbaceous layer of perennial grasses (Ringrose et al., 1998). This vegetation assemblage reflects a mixed C3–C4 system (Mantlana et al., 2008) , in which woody plants are predominantly C3 photosynthetic, whereas the grass layer is largely composed of C4 species (Ellery et al., 1992) . Such a vegetation structure is characteristic of semi-arid regions of Botswana (Ellery et al., 1992; Mantlana et al., 2008).

Four pedosedimentary sections were selected along an ephemeral river locally known as Metsimasweu (Fig. 7.1). These sections were selected for their representativity of the local landscape marked by prominent carbonates features in soil. Full description of the sections is given by Dina Ebouel et al. (2026a, under review). In general, all these sections reflect an alternation between periods of stability, favouring pedogenesis, and periods of instability characterised by fluvial sedimentary deposits resulting from river flooding during wet periods. Thus, the stratigraphy reveals ancient soils (palaeosol) mostly palaeo-Calcisols buried under fluvial sediments, which are themselves covered by poorly developed modern soils, mainly Arenosols or Cambisols. Chemical weathering is generally low, characterised by a low clayeyness and robust chemical weathering index (RW). However, the grain size distribution revealed finer particles towards the downstream sections (SC03 and SC04), reflecting local translocation. The sedimentary layers also show a dominance of angular to sub-angular quartz grains and the presence of opaque fragments, characteristic of accessory minerals in basaltic rocks. This reflects the dominance of local contribution also supported by the presence of basalt and sandstone fragments in soil horizons. The main carbonate features observed are nodules and diffuse powders. Nevertheless,

some horizons at the bottom of the sections, generally in contact with or adjacent to the watercourse, often show accumulations in the form of pseudomycelia.

Section (SC01) stands out as the most significant profile in the study. Nodules are present throughout this section, occurring in both the modern soil (Nd01 in the Bk2 horizon; 6.35 wt.% $CaCO_3$) and the buried palaeosols. In the latter, $CaCO_3$ equivalents increase significantly, ranging from 9.39 wt.% in the AB1b horizon (Nd02) to a peak of 24.61 wt.% in the Bkkb horizons (Nd03, Nd04). Additionally, the base of SC01 is characterised by pseudomycelia (Ps) with a lower carbonate content of 2.18 wt.%. In contrast, carbonate features in the modern soils of SC02, SC03 and SC04 are poorly developed, appearing only in powder form with $CaCO_3$ contents generally below 5 wt.%. Identifiable features are much more prominent in the buried palaeosols of these sections. Specifically, the BCkkb and BCkb horizons across SC02, SC03, and SC04 show a consistent abundance of nodules. The BCkkb horizons consistently exhibit higher concentrations, ranging from 14.24 wt.% in SC02 to 21.09 wt.% in SC04, while the BCkb horizons maintain lower equivalents, fluctuating between 4.00 wt.% and 6.19 wt.%.

These carbonate features result primarily from pedogenic processes, with calcite serving as the dominant mineralogical phase. The transition from powdery forms in modern horizons to well-defined nodules in buried layers suggests varying stages of carbonate development and secondary mineral precipitation over time.

Dina Ebouel et al. (2026b, under review) demonstrated that local basaltic rocks are the dominant source of calcium ions for pedogenic carbonates observed in these sections. This supply involves two distinct pathways: first, the mechanical transport of basaltic fragments which are reworked into sediments and subsequently incorporated into the soil, where their weathering releases calcium ions to the soil solution that are mobilised by capillary rise and evaporation during the dry

season to form pedogenic carbonates. Second, the *in-situ* chemical weathering of the parent material releases calcium ions directly into solution; these ions are then transported by the river and move from the fluvial system into the soil profiles during dry periods, where they are eventually fixed as pedogenic carbonates.

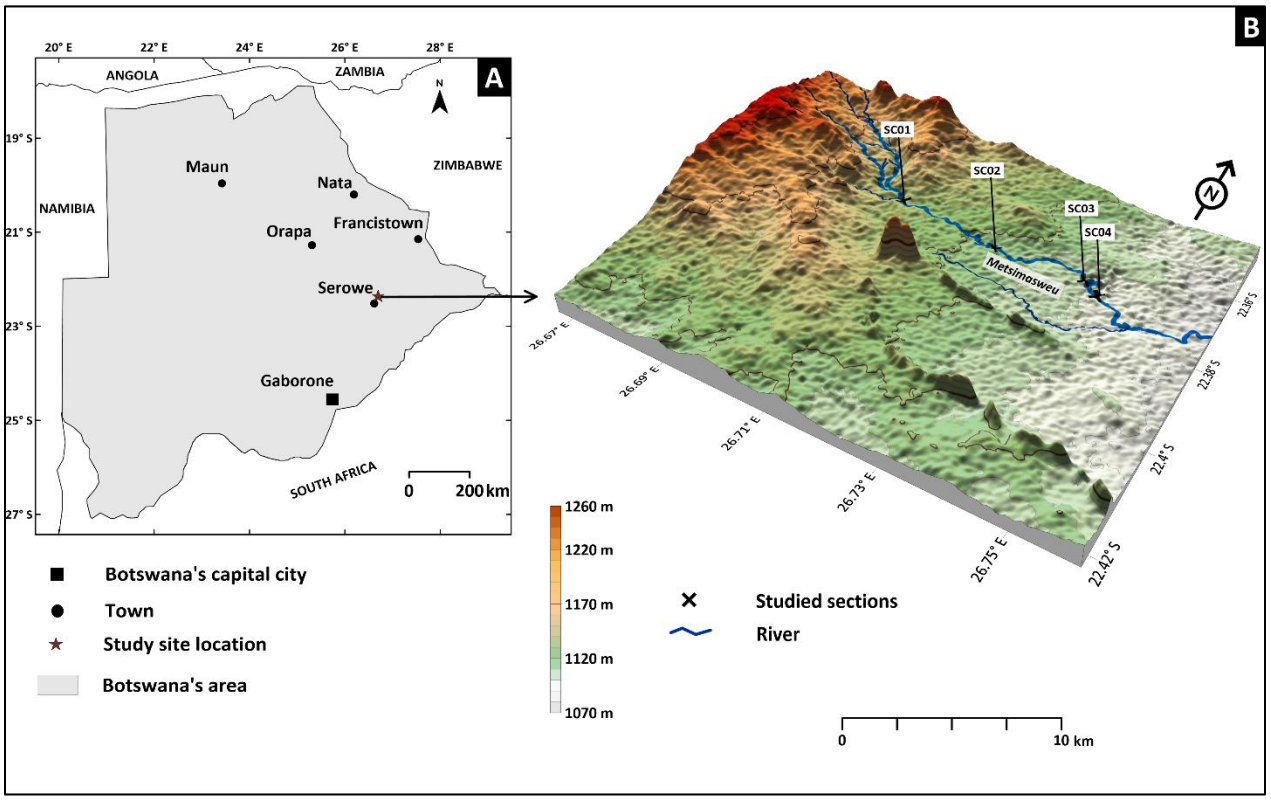


Fig. 7.1. A. localisation of the study area in the map of Botswana; B. 3D topographic model of the study area, showing the river setting and the four selected sections.

Stratigraphy and locations of carbonate features is presented in Fig. 7.2. Carbonate features (nodules and pseudomycelia) were selectively sampled from horizons displaying significant carbonate accumulation for elemental geochemistry, as well as stable carbon and oxygen isotope analyses. In Section 1 (SC01), five features were collected: nodules Nd01 (Bk2), Nd02 (AB1b), and Nd03–Nd04 (Bkkb), alongside pseudomycelia (Ps) from AB3b. Section 2 (SC02) yielded three nodules, comprising Nd05 (BCkkb) and Nd06–Nd07 (BCkb). Sampling in Section 3 (SC03)

included five nodules: Nd08–Nd11 (BCkkb) and Nd12 (BCkb). Finally, six nodules were recovered from Section 4 (SC04), consisting of Nd13–Nd15 (BCkkb) and Nd16–Nd18 (BCkb). Soil samples were also collected in each horizon of the four soil profiles for elemental geochemical analyses.

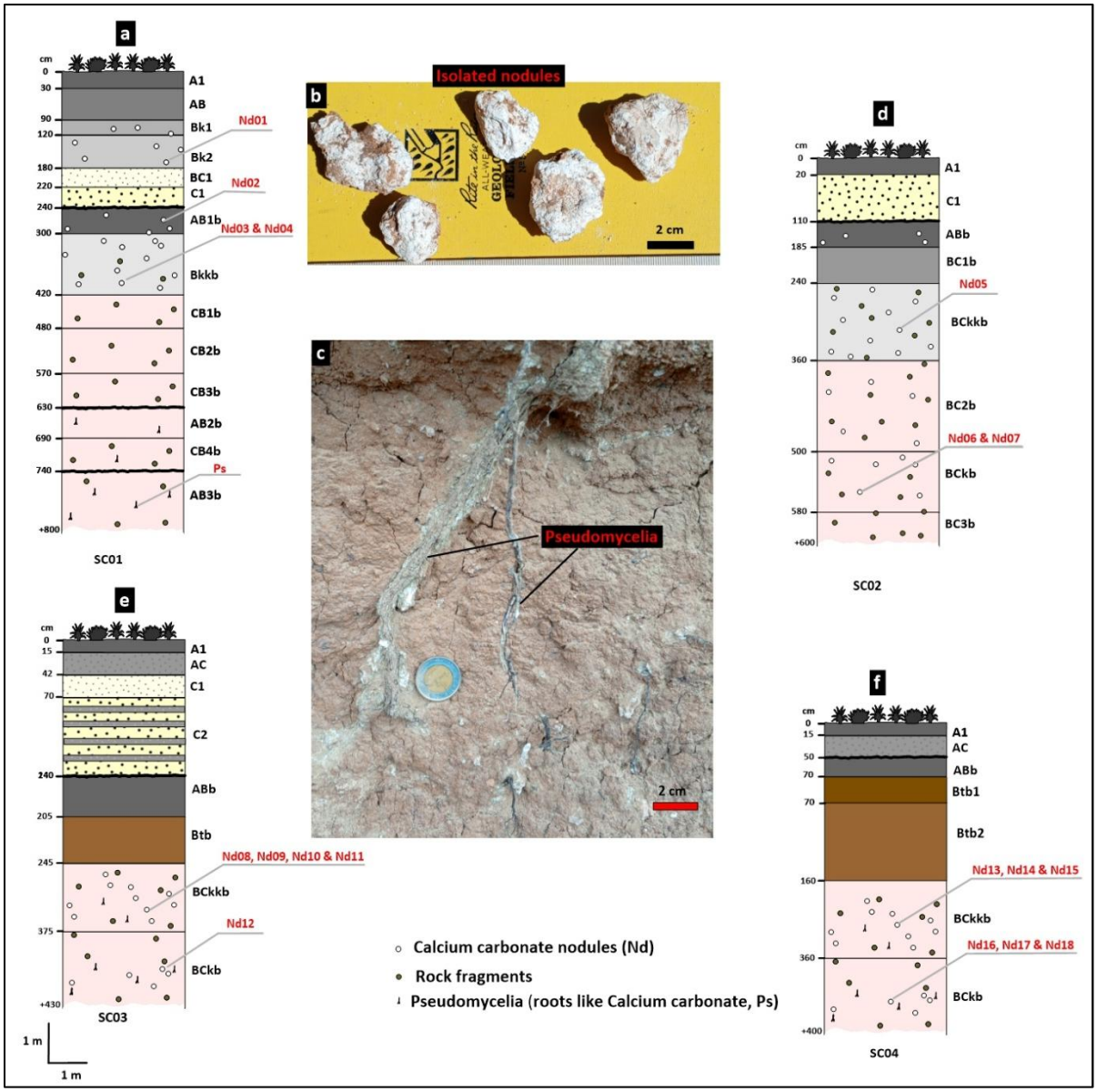


Fig. 7.2. a, d, e, f. Stratigraphy of the four study sections; b. photograph of calcium carbonate nodules isolated from SC04; and c. photograph of pseudomycelia calcium carbonate accumulation in SC01.

7.2.2. Sample preparation

To ensure the analysis targeted the pedogenic carbonate phase specifically, the samples were cleaned of adhering silicate particles and organic matter. Soil and carbonates samples were then ground into a fine homogeneous powder, using an agate mortar.

7.2.3. Iron and manganese elemental analysis

Iron and Mn concentrations, originally reported as oxide weight percentages, were determined for all samples (soil and carbonate) using a Bruker AXS S4 Explorer wavelength dispersive X-ray fluorescence spectrometer (WDX), housed at the Laboratory for the Environmental and Raw Materials Analysis (LERA), Institute of Applied Geosciences, Karlsruhe Institute of Technology (KIT), Germany. Analyses were conducted on fused beads. Prior to element quantification, the loss on ignition (LOI) of the pulverised samples was determined by heating them to 950 °C for 3 hours and recording the weight difference before and after heating. Fused beads were prepared by mixing the ignited sample powder with a 66.5:33.5 ratio of Li-tetraborate and Li-metaborate (Spectroflux 110, Alfa Aesar) before melting it at 1000–1100 °C using a fusion instrument. An Rh X-ray tube (50 keV, 1 kW) was used as the radiation source. Signals were detected using a proportional flow counter (Ar-CH_4 gas) and a scintillation counter. XS-55, LIF2000 and PET were used as analyser crystals. Four certified reference materials, including AGV-1, GXR-2, GXR-5 and Soil 7, were used to verify the accuracy of the produced data. All the uncertainty obtained were below the detection limit.

Mn/Fe ratios in pedogenic carbonates were used as an indirect proxy for redox fluctuations within the soil system, as Sipos et al. (2025) demonstrated that trace Mn and Fe, primarily occurring as secondary oxyhydroxides, are sensitive to hydrological dynamics and redox cycling. To facilitate stoichiometric comparison, bulk geochemical data from soil samples, originally reported as oxide weight percentages (wt.%), were recalculated into elemental molar proportions. For each oxide, the reported weight percentage was divided by its molecular weight to obtain the corresponding oxide molar proportion. This value was then multiplied by the cation stoichiometric coefficient of the oxide (e.g. 2 for Al_2O_3; 1 for CaO) to derive the unnormalised cation molar proportion. Final

elemental molar percentages (mol%) were obtained by normalising these values to the total molar sum of all analysed elements (Rollinson and Pease, 2021). This approach ensures that the geochemical signal represents the actual chemical activity and redox-driven availability of these metals in the soil solution at the time of mineral precipitation (Brimhall and Dietrich, 1987; Chadwick et al., 1990).

7.2.4. Stable isotope analyses

The ratios of stable isotopes of carbon ($^{13}C/^{12}C$) and oxygen ($^{18}O/^{16}O$) in carbonate features were determined at LERA. The samples were analysed for the stable isotope composition of oxygen ($\delta^{18}O$) and carbon ($\delta^{13}C$) by isotope-ratio mass spectrometry (IR-MS) using a Delta V Advantage mass spectrometer (Thermo Fisher Scientific) coupled to an on-line, automated carbonate preparation system (GasBench II; Thermo Fisher Scientific). In this system, the sample vials sealed by rubber septa are flushed with He so that the atmosphere inside the vials is free of CO_2 and O_2, and 103% orthophosphoric acid is added to release CO_2 from the complete dissolution of the ~ 1 mg carbonate samples over 90 minutes at 72°C. Using He as carrier gas, the sample CO_2 then passes a gas-phase chromatograph to separate it from other gases and is injected into the mass spectrometer for analysis (e.g. Clark and Fritz, 1997), in this case in ten pulses of 100 µL each. The results obtained from these ten injections are then averaged to yield the final results.

Calibration was conducted using the NBS19 standard material. Precision is determined by the absolute standard deviation (ASD) of repeated measurements of the Carrara Marble standard material, with an average accuracy of 0.03 ‰ for $\delta^{13}C$ and of 0.09 ‰ for $\delta^{18}O$, respectively (n = 150) All results are reported in the δ notation [‰] relative to the V-PDB standard (Appendix 7.1).

7.3. Results

7.3.1. Manganese and iron concentration in the sections

As detailed in Section 7.2.3, elemental concentrations are reported as molar percentages (mol%). Fig. 7.3 illustrates the vertical variations of Mn and Fe for each study section (numerical values are presented in Appendix 7.2). Throughout the profiles, Mn occurs primarily as a minor or trace element, ranging from 0.04% to 0.11%, whereas Fe constitutes a major component, with concentrations ranging from 2.68% to 7.47%.

In SC01, the distribution of Mn reveals relative enrichment in horizons Bk1, Bk2, AB1b and Bkkb, where values generally exceed 0.09%. Regarding Fe, a clear stratigraphic distinction emerges: the lower horizons (CB1b to AB3b) exhibit notably higher concentrations (5.86–7.47%) than the upper sequence (A1 to Bkkb; 2.74–4.97%).

Sections SC02, SC03 and SC04 display more variable patterns. In SC02, both elements exhibit largely uniform profiles, typically remaining below 0.05% for Mn and 4% for Fe. The BCkb horizon is a notable exception, with higher values of 0.10% Mn and 4.70% Fe. SC03 exhibits a coupled distribution, with peak values for both Mn and Fe occurring in the AC, C2, and ABb horizons, while other horizons remain below 0.05% and 5%, respectively. Similarly, in SC04, both elements follow a twin-peak pattern, with the highest concentrations in the ABb (5.88% for Fe and 0.09% for Mn) and Bt1b (5.23% for Fe and 0.09% for Mn) horizons, while the rest of the profile shows significant depletion.

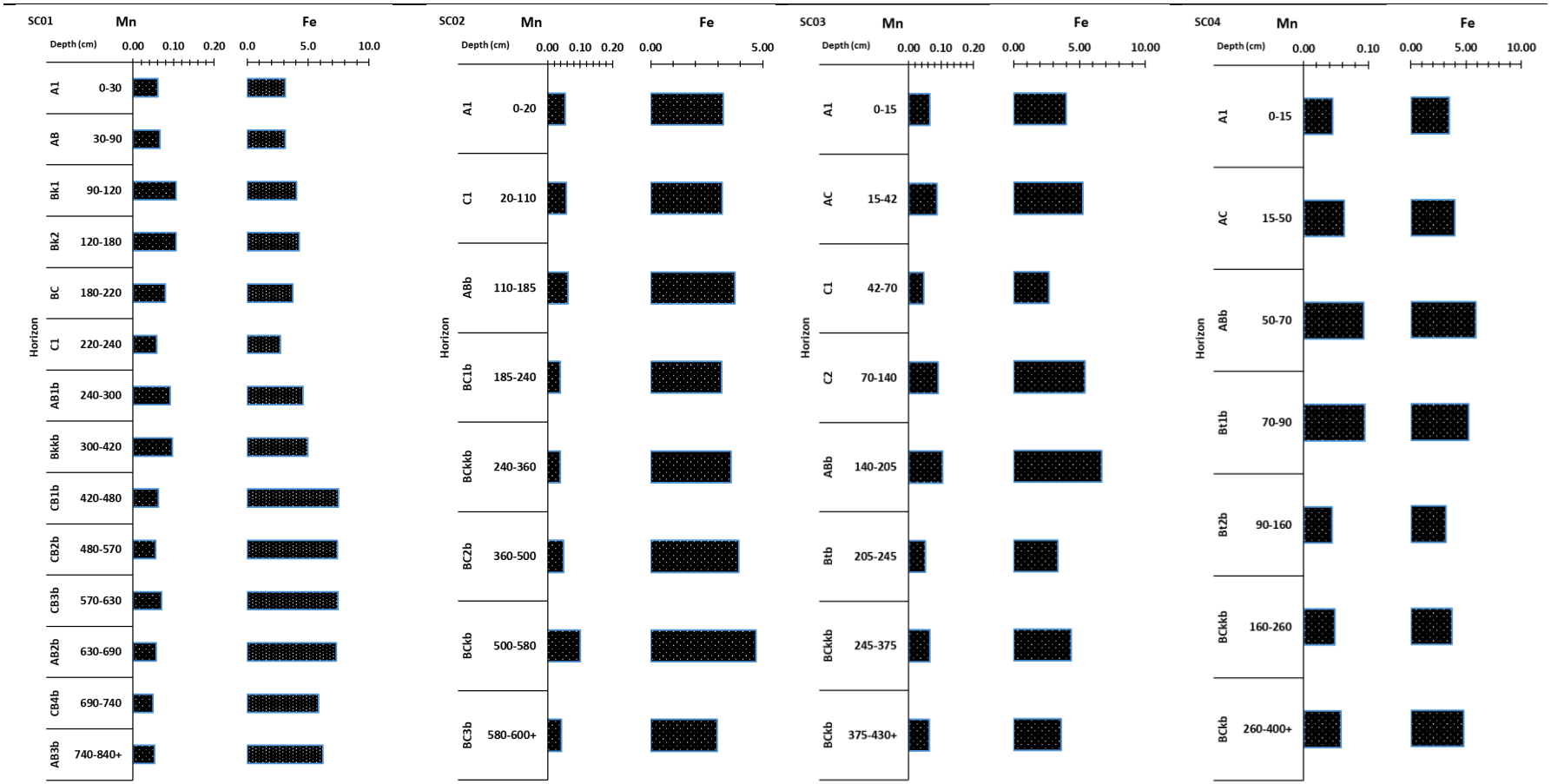


Fig. 7.3. Trend of Mn and Fe in the four study sections (SC01, SC02, SC03 and SC04).

7.3.2. Manganese and iron concentration in carbonate features

Table 7.1 shows the concentrations of Mn and Fe in the carbonate features. The distribution of these elements within the carbonate features contrasts with the patterns observed in the bulk soil profiles. While Fe concentrations are consistently lower than those in the surrounding matrix, Mn concentrations exhibit selective enrichment in several features.

In SC01, most features (Nd01, Nd03, Nd04 and Ps) are depleted in Mn relative to their respective host horizons (Bk2, Bkkb and AB3b). However, Nd02 (0.11%) is an exception, with higher Mn levels than its host, AB1b (0.09%). More pronounced enrichment is observed in SC02, where Nd06 (0.16%) and Nd07 (0.22%) significantly exceed the Mn content of their host BCkb (0.09%), though Nd05 (0.01%) remains depleted compared to BCkb (0.04%).

In SC03, Nd08 (0.10%) and Nd12 (0.15%) are similarly enriched relative to their hosts BCkkb (0.06%) and BCkb (0.06%). Nd09 (0.05%), Nd10 (0.04%) and Nd11 (0.05%) in BCkkb follow a contrasting depletion pattern. In SC04, Nd13 (0.06%) and Nd15 (0.07%) have higher Mn content than their host BCkkb (0.04%), while Nd14 (0.03%), Nd16 (0.03%), Nd17 (0.05%) and Nd18 (0.02%) have lower concentrations than their surrounding matrices (BCkb; 0.06%).

Table 7.1. Manganese and iron contents (mol%) in the selected carbonate features

Section	Horizon	Depth (cm)	Sample	Mn	Fe
				(mol%)	
SC01	Bk2	120-180	Nd01	0.06	2.49
	AB1b	240-300	Nd02	0.11	1.16
	Bkkb	300-360	Nd03	0.09	1.22
		360-420	Nd04	0.08	1.53
	AB3b	740-840+	Ps	0.03	3.13
SC02	BCkkb	240-360	Nd05	0.01	0.62
	BCkb	500-540	Nd06	0.16	1.01
		540-580	Nd07	0.22	0.91
SC03	BCkkb	245-285	Nd08	0.10	0.59
		285-305	Nd09	0.05	0.61
		305-345	Nd10	0.04	0.69
		345-375	Nd11	0.05	0.42
	BCkb	375-400	Nd12	0.15	0.69
SC04	BCkkb	160-190	Nd13	0.06	0.86
		190-220	Nd14	0.03	0.62
		220-260	Nd15	0.07	1.04
	BCkb	260-300	Nd16	0.03	0.78
		300-330	Nd17	0.05	0.61
		330-400+	Nd18	0.02	0.90

The different trends of the ratio Mn/Fe of the selected carbonate features are presented in Fig. 7.4. Overall, features from sections SC01 (0.01—0.09) and SC04 (0.02—0.08) exhibit lower ratios compared to those from SC02 (0.02—0.24) and SC03 (0.06—0.22). Within SC01, the highest ratio is observed in nodule Nd02 (0.09), followed by Nd03 (0.07), whereas the pseudomycelia (Ps) yield the lowest values (0.01). In SC02, the maximum ratio occurs in Nd07 (0.24), with Nd05 (0.02) representing the minimum for that section. A similar trend is observed in SC03, where Nd12 (0.22) and Nd08 (0.16) display the highest ratios, while Nd10 (0.06) shows the most significant depletion. Finally, in SC04, Nd17 (0.08) reaches the highest ratio, contrasting with Nd18 (0.02) at the base of the section, which records the lowest value.

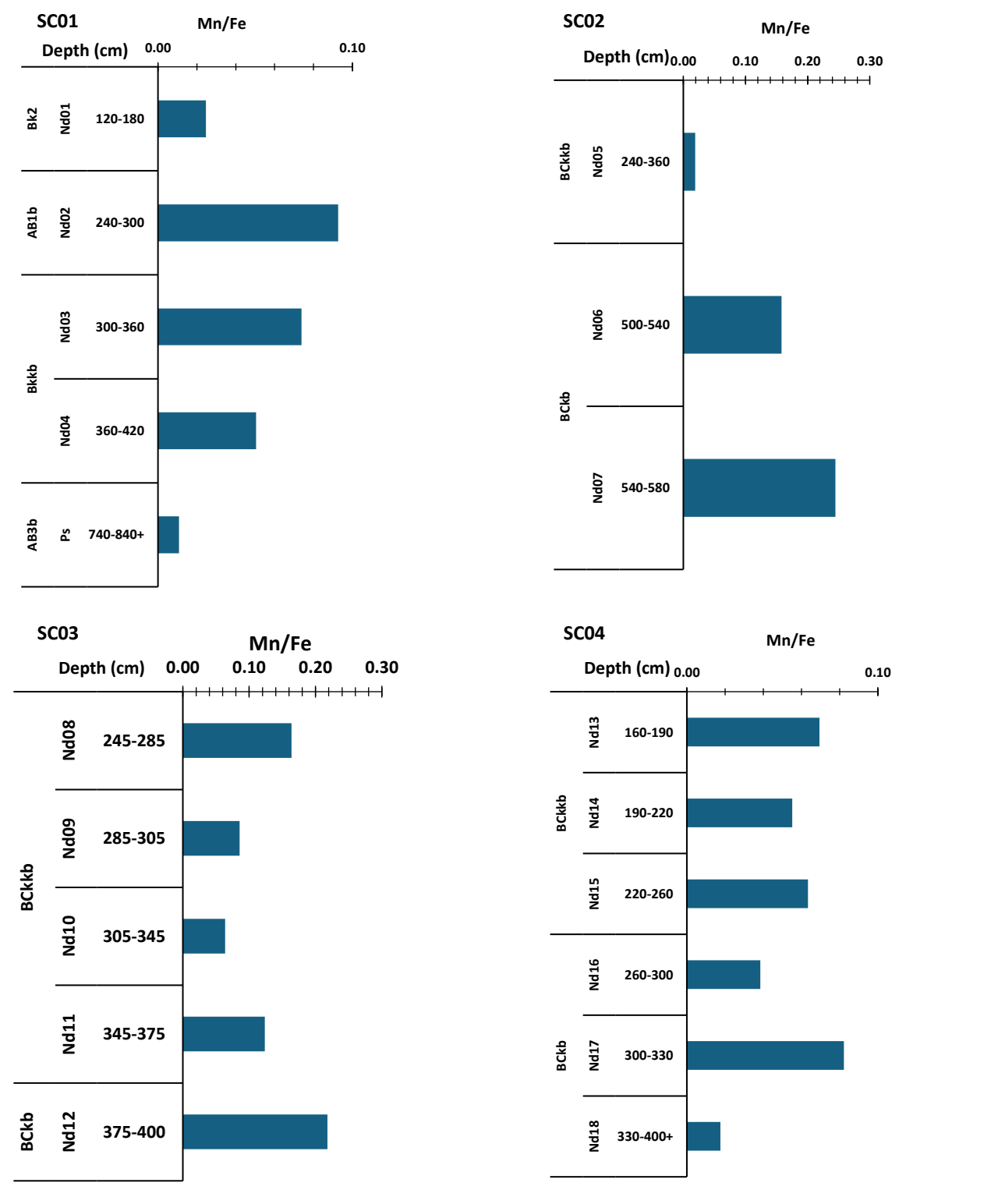


Fig. 7.4. Patterns of Mn/Fe ratio of the selected carbonate features

7.3.3. Stable isotope of carbon and oxygen in carbonate features

Fig. 7.5 shows the $\delta^{13}C$ and $\delta^{18}O$ values of the carbonate features from the four sections (SC01–SC04), plotted against depth (numerical value are presented in Appendix 7.1). Across the four sections, $\delta^{13}C$ and $\delta^{18}O$ values define well-structured datasets characterised by relatively narrow ranges and clear clustering within each section. For both isotopic systems, most measurements fall within restricted intervals, with limited dispersion among samples from the same section. Differences between sections are mainly expressed as shifts in the central value and overall range, rather than as large internal variability. Where present, contrasts between carbonate features are expressed as offsets in isotopic values relative to the dominant clusters.

In SC01, $\delta^{13}C$ values of nodules are tightly grouped between -3.17‰ and -2.19‰. Though within the same range, a slight shift is observed when moving from Nd01 (-3.17‰) in modern soil to Nd02 (-2.63‰) in buried palaeosols. Pseudomycelia at the base of the section is displaying a distinctly lower $\delta^{13}C$ value (-6.85‰), clearly separated from the nodule cluster. The $\delta^{18}O$ values of the nodules in SC01 form a consistent group ranging from -4.49‰ to -3.39‰. Although pseudomycelia have a slightly lower value (-4.94‰), this is not far from the range observed in the nodules.

In SC02, the $\delta^{13}C$ values of the nodules fall within a relatively narrow range between -2.40‰ and -0.24‰. However, there is a slight discrepancy between Nd05 (in BCkkb), exhibiting a $\delta^{13}C$ value of -0.24‰, and the nodules in the horizon below (BCkb), Nd06 and Nd07, with $\delta^{13}C$ values of -2.00 and -2.40‰, respectively. No significant differences were observed in the $\delta^{18}O$ values. They are clustered between -5.17‰ and -4.67‰. In SC03, nodules display compact fields for both stable isotopes. $\delta^{13}C$ values are concentrated between approximately -2.39‰ and -1.08‰. Even though a slight shift toward more negative values is observed with depth. The $\delta^{18}O$ values form a more

tightly clustered group, ranging from -5.52‰ to -5.39‰, indicating minimal dispersion within the section.

In SC04, except for a more negative $\delta^{13}C$ observed in Nd18 (-3.00‰), the other nodules have $\delta^{13}C$ values that form a compact group between -1.22‰ and -1.70‰. The $\delta^{18}O$ is characterised by a cluster of values ranging from -5.01‰ to -4.86‰.

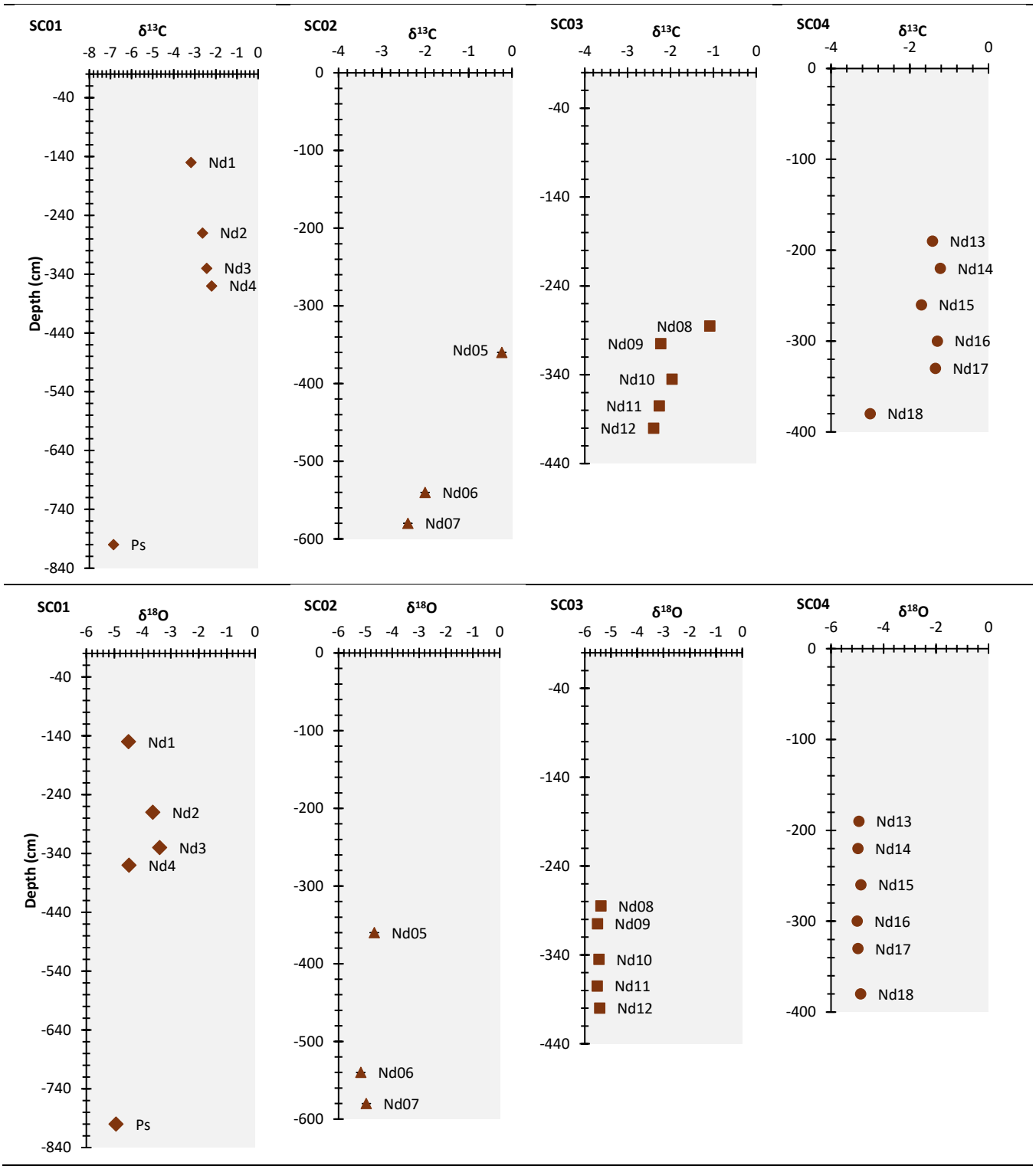


Fig. 7.5. Stable carbon and oxygen isotopes of carbonate features.

7.4. Discussion

7.4.1. Vegetation dynamics and stable carbon isotopes in pedogenic carbonates

The relationship between the carbon source of pedogenic carbonates and soil CO_2 dynamics has been well established by numerous studies, which show that the carbon incorporated into pedogenic carbonate features is predominantly derived from soil CO_2 produced by plant respiration (Cerling 1984; Quade et al. 1989; Ryskov et al. 2008; Ning et al. 2025). The $\delta^{13}C$ composition of this carbonate is therefore linked to the C3/C4 ratio of the vegetation (Cerling and Quade 1993). However, in soil with low respiration rate, the $\delta^{13}C$ value of soil CO_2 is not controlled by vegetation alone. In this type of environment, a substantial fraction of soil CO_2 derives from diffusive exchange with the atmosphere ($\delta^{13}C \approx -8‰$), which shifts the soil CO_2 signal toward less negative values relative to the purely biogenic signal (Quade et al. 1989). This effect is particularly relevant in open-canopy, semi-arid settings such as the one studied here, and is further amplified by the fact that pedogenic carbonate precipitation predominantly occurs during the dry season, when respiration rates are lowest (Breecker et al. 2009; Fischer-Femal and Bowen 2021; Sarangi et al. 2021). As a result, nodule $\delta^{13}C$ values may not directly reflect the true, year-round isotopic composition of the vegetation, but rather a signal biased toward enrichment by this seasonal, low-respiration effect. For this reason, the raw values obtained from the nodules should be regarded as a smoothed, potentially biased indicator, rather than a direct snapshot of past plant composition (Breecker et al. 2009; Huth et al. 2019).

Nodules (Nd), the dominant carbonate feature identified in the upper horizons of section SC01 and throughout sections SC02–SC04, have $\delta^{13}C$ values ranging from -3.17‰ to -0.24‰, corresponding, under the 14–16‰ enrichment factor (Cerling 1984), to a soil CO_2 source of -14 to -17‰. These values are slightly more negative than a pure C4 biomass signal (average -12‰),

which on its own would point to a minor C3 contribution to an otherwise C4-dominated system. Given the bias associated with the dry season and low respiration mentioned above, this signal is likely to be more negative in reality. It is therefore influenced to a greater extent by C3 plants than these raw values would suggest. This is consistent with the modern vegetation at the site, a bush savannah dominated by woody C3 taxa comprising species such as *Acacia*, *Terminalia* and *Boscia* (Ringrose et al. 1998). This explains the apparent contradiction between the herbaceous/C4-like signal suggested by the raw nodule values and the shrub-dominated cover observed in the field.

The similarity between the $\delta^{13}C$ value of Nd01, the nodules observed in modern soil, and the $\delta^{13}C$ values of the numerous nodules in the buried palaeosol in SC01 indicates that the same vegetation structure persisted over a prolonged period of time. This vegetation remained dominated by C3 woody taxa, with a variable and comparatively minor C4 herbaceous component, throughout the different pedosedimentary cycles.

The pseudomycelia (Ps) identified at the base of section SC01 (horizon AB3b), show a markedly more negative $\delta^{13}C$ value (-7‰). Unlike nodules, which represent cumulative, time-averaged features, pseudomycelia reflects an incipient, near-instantaneous stage of carbonate accumulation, here linked to shrub roots reaching this depth in a riparian, hydrologically stable setting (Durand et al., 2010, 2018; Field observations, Fig. 7.2). Because this depth is buffered from atmospheric CO_2 infiltration by the hydric influence of the river, the pseudomycelia likely capture a comparatively unbiased, purely biogenic C3 root-respiration signal (Quade et al., 1989). This is reinforcing the idea that the enriched nodule signal reflects a seasonal/respiration artefact rather than a genuinely distinct, C4-dominated vegetation history. Together, the nodule and pseudomycelia records are consistent with a stable savannah structure combining C3 woody

vegetation with a variable, and possibly more limited, C4 herbaceous component than initially inferred from the raw carbonate values alone.

7.4.2. Climate dynamics and stable oxygen isotopes in pedogenic carbonates

The source of oxygen in pedogenic carbonate is meanly related to soil water and therefore, meteoric water (Zamanian et al., 2016). According to Cerling (1984), the $\delta^{18}O$ in pedogenic carbonates records climate because it faithfully tracks the isotopic composition of precipitation, which is itself controlled by temperature and rainfall regime at the time of carbonate formation. In tropical and subtropical regions, the "amount effect" dictates that high precipitation rates lead to a significant decrease in the ^{18}O content of meteoric water (Dansgaard, 1964; Rozanski et al., 1993). This leads to lower $\delta^{18}O$ values in soil carbonates for a given temperature, while dry climates produce enriched ^{18}O values due to low rainfall and intense evaporation (Quade et al., 1989; Fischer-Femal and Bowen, 2021). This enrichment occurs because evaporation preferentially removes the lighter ^{16}O isotope to the atmosphere, leaving residual soil water and the resulting pedogenic carbonates enriched in ^{18}O (Licht et al., 2022). As suggested by our results, the stable oxygen isotopes ($\delta^{18}O$) of the carbonate features in these pedosedimentary sections are clustered around a very narrow range of values from -5.52‰ to -3.39‰. This apparent isotopic homogeneity under comparable hydrological conditions across multiple pedosedimentary sections suggests a period of significant climatic stability. Specifically, it indicates that the isotopic composition of the meteoric water source and the subsequent evaporative enrichment in the soil profile remained relatively constant throughout the period of carbonate precipitation (Cerling, 1984; Quade et al., 1989). This is further highlighted by the cross-plot of $\delta^{13}C$ and $\delta^{18}O$ (Fig. 7.6), which shows a highly concentrated cluster of data points rather than a clear linear trend or several distinct groups. In stable isotope geochemistry, a cluster reflects the absence of significant changes in vegetation

type (C3-C4 mixed vegetation) or regional water balance (precipitation vs. evaporation). If there had been significant transitions from wet to dry conditions, the samples would likely have been distributed along a "covariation line"; on the contrary, the overlap between modern surface nodules and deeper features reinforces the conclusion that environmental parameters, particularly seasonal aridity and open-canopy savannah structure, remained fundamentally unchanged during the various deposition cycles.

Nevertheless, vertical trends in SC01 highlighted some slight variations in the $\delta^{18}O$ signatures. Nd02 and Nd03 are characterised by relatively high $\delta^{18}O$ values, respectively -3.64‰ and -3.39‰, while Nd01 and Nd04 showed relatively low values, respectively -4.50‰ and -4.48‰. These internal fluctuations likely reflect vertical gradients in soil water evaporation during the time of carbonate precipitation. The enriched (higher) values in Nd02 and Nd03 suggest formation during periods of peak evaporative stress or at shallower depths more exposed to solar radiation. Conversely, the more depleted (lower) values in Nd01 and Nd04 may represent formation during slightly wetter seasons or at depths where soil moisture was better insulated from atmospheric evaporation (Quade et al., 1989; Breecker et al., 2009) The stratigraphic framework established by Dina Ebouel et al. (2026a, under review) strongly supports this "depth effect" interpretation. According to this stratigraphy, the AB1b horizon containing Nd02 constituted the upper part of the buried palaeosol, likely representing an exposed or near-surface landform prior to the deposition of C1 sediments. The enriched $\delta^{18}O$ signal of Nd03, located in the upper part of the Bkkb horizon, follows this same logic of surface-proximal evaporation. In contrast, the more depleted values in Nd01 (Bk1) and Nd04 (lower Bkkb) reflect carbonate precipitation in deeper accumulation horizons, where the isotopic composition of soil water remains more closely aligned

with that of local meteoric water and is less influenced by secondary evaporative enrichment (Cerling and Quade, 1993).

This model of depth-controlled buffering also extends to the pseudomycelia, though their signature is further modified by the specific hydrological dynamics of the riparian zone. Given their proximity to the river channel, these features likely precipitated from groundwater associated with the local watercourse. Their isotopic value represents a balance between the original depleted signature of the river water and subsequent evaporative enrichment at the capillary fringe during periods of water-table recession (Arenas-Abad et al., 2010; Sanz-Montero et al., 2023). This distinguishes the pseudomycelia from the nodules; while the former are controlled by fluctuating groundwater levels near the channel, the latter are primarily influenced by the downward infiltration and evaporation of meteoric waters in the upper soil profile.

While the $\delta^{18}O$ variability observed among soil carbonates in this study (ranging from -5.52‰ to -3.39‰, a spread of approximately 3‰) has been primarily interpreted above in terms of hydrological and climatic controls (precipitation/evaporation balance, seasonal aridity), temperature is also known to exert a direct control on $\delta^{18}O$ values through its effect on the calcite-water oxygen isotope fractionation factor (O'Neil et al. 1969; Kim and O'Neil 1997), independently of any change in the isotopic composition of soil water. Since most pedogenic carbonates form within a temperature range bounded by mean annual and maximum monthly soil temperatures (Breecker et al., 2009), seasonal or interannual temperature variability alone could account for a substantial portion of the observed 3‰ range, even under a constant meteoric water $\delta^{18}O$ composition. Testing this alternative would require comparing measured carbonate $\delta^{18}O$ values with theoretical equilibrium values calculated across a range of plausible formation temperatures, using the $\delta^{18}O$ of local meteoric water as an input. In the absence of local

precipitation-isotope data or a nearby monitoring station for the study area, this calculation could not be performed with confidence in the present study, as it would rely on regional or interpolated water $\delta^{18}O$ estimates (e.g., from the Global Network of Isotopes in Precipitation) introducing an additional and difficult to constrain source of uncertainty. Consequently, while the interpretation proposed above emphasises hydrological/climatic drivers, a temperature-driven contribution to the observed $\delta^{18}O$ variability cannot be excluded, and disentangling the relative roles of temperature and water isotopic composition remains an important avenue for future work, contingent on the acquisition of local meteoric water isotope data.

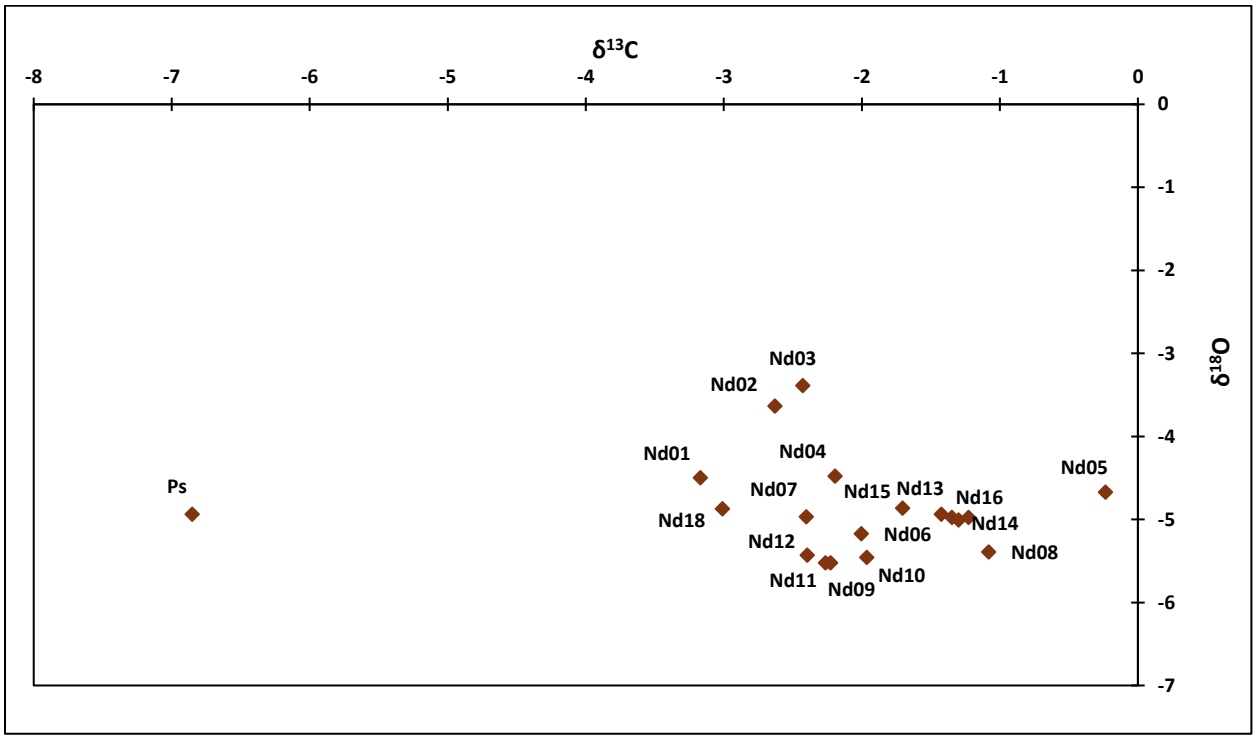


Fig. 7.6. Cross-plot of $\delta^{13}C$ and $\delta^{18}O$ for pedogenic carbonate features.

7.4.3. Hydrological conditions and carbonate precipitation

Despite a stable regional climate, Dina Ebouel et al. (2026a, under review) highlighted localised fluvial changes that interrupted soil development. This dynamic demonstrates the need to analyse variations in local hydrological conditions using Mn/Fe ratios to better understand the specific

environment of carbonate formation. Chemical comparisons between pedogenic carbonate features and their host horizons reveal a systematic depletion of iron in the nodules compared to the pedogenic matrix. Conversely, some features (e.g. Nd02, Nd06, Nd07) show significant Mn enrichment. It is important to note that Mn and Fe in pedogenic carbonates are commonly present as secondary oxyhydroxide phases rather than being structurally incorporated into calcite. As a result, Mn/Fe ratios likely integrate both syn- and post-pedogenic redox processes, reflecting fluid circulation, transient saturation, and redox cycling within the soil system (Sipos et al., 2025). This chemical signature aligns with the stratigraphic position of the AB1b horizon (hosting Nd02) in SC01; the overlying C1 deposit indicates a period of fluvial overbank flooding, which would have induced the temporary saturation and reducing conditions necessary to drive this Mn-Fe partitioning.

The Fig. 7.7 shows a scatter plot of Mn/Fe ratios versus $\delta^{18}O$ values for carbonate samples. Overall, higher Mn/Fe ratios tend to be associated with more depleted $\delta^{18}O$ values ($\leq -5‰$), whereas samples with less negative $\delta^{18}O$ values cluster at lower Mn/Fe ratios. This likely reflects reducing conditions affecting the soil system, possibly associated with periods of increased moisture and redox fluctuations. Such conditions are consistent with more reducing soil or pore-water environments, in which Mn^{4+} is preferentially reduced and mobilised compared to Fe^{3+}. In contrast, samples characterised by low Mn/Fe ratios likely reflect more oxidising and/or better-drained settings, where Fe remains relatively immobile and Mn availability is limited (Islam and Mostafa, 2023; Sipos et al., 2025).

The dispersion of Mn/Fe ratios at similar $\delta^{18}O$ values indicates that, in addition to the isotopic composition of soil water, local redox heterogeneity and hydrological dynamics (such as fluctuating water tables or episodic saturation) played a major role in controlling trace element

signatures. Within this framework, samples Nd02 and Nd03 are distinctive. They combine relatively high Mn/Fe ratios with less negative $\delta^{18}O$ values (around -3.64 to -3.39‰), setting them apart from the main cluster. The $\delta^{18}O$ enrichment suggests precipitation from more evaporated soil waters as mentioned in section 7.4.2, and commonly associated with drier conditions. However, their elevated Mn/Fe ratios imply that carbonate recorded episodes of locally reduced conditions, which promoted Mn mobilisation despite an overall evaporative hydrological context (Sipos et al., 2025). Nd02 and Nd03 therefore record a partial decoupling between hydrological and redox signals and are best interpreted as reflecting short-lived reducing events superimposed on a generally dry background climate. These samples likely capture episodic hydrological pulses (e.g., transient saturation following rainfall or perched water tables) rather than sustained wet conditions, highlighting the importance of micro-environmental variability during pedogenic carbonate formation (Driese and Mora, 1993).

The solubility of Mn^{2+} (by extension the Mn/Fe ratio) is also directly controlled by pH, independently of Eh (Lindsay 2001). Thermodynamically, Mn^{2+} oxidation is favoured above pH $\approx$ 4, and its kinetics are strongly pH-dependent (Morgan 2005), so that increasing soil-solution pH can drive Mn re-precipitation as oxide or carbonate phases even without a shift in redox state. Because Fe^{2+} does not respond identically to pH changes, local pH variability, for instance linked to evaporative concentration, organic matter decomposition, or carbonate buffering during nodule growth, could itself generate part of the observed Mn/Fe variability without requiring a discrete reducing event. This is particularly relevant to samples such as Nd02 and Nd03, where elevated Mn/Fe ratios coincide with $\delta^{18}O$ enrichment consistent with strong evaporative concentration. The concurrent rise in local pH may have promoted Mn retention, offering a complementary explanation to the transient reducing-pulse hypothesis proposed above. Distinguishing between

these mechanisms would ideally rely on immobile trace-element ratios (e.g., Ti/Zr, Zr/Th), commonly used to isolate detrital/lithogenic control from authigenic, redox- or pH-driven mobility (McLennan 2001; Tribovillard et al. 2006). However, Th and Zr concentrations were not determined for the samples in this study, precluding this additional line of evidence. Consequently, while the Mn/Fe ratio remains a useful qualitative indicator of hydrological variability, its interpretation here should be regarded as reflecting the combined influence of redox state, local pH conditions, and lithological heritage, rather than redox alone.

The group formed by samples Nd06, Nd07, Nd08, Nd11 and Nd12 exhibits high Mn/Fe ratios that contrast with the stability of their $\delta^{18}O$ signatures. This geochemical trend probably reflects a change related to lithological heritage rather than climatic changes. The local geology consists of alternating basaltic rocks (Mn/Fe ≈ 0.01-0.02), mudstones (Mn/Fe ≈ 0.02) and sandstones (Mn/Fe ≈ 0.03) (Franchi et al., 2021). Furthermore, Dina et al. (2026a, under review) demonstrated that the weathering of these parent materials, individually or in combination, directly influences the development of these pedosedimentary sections. In addition, the absence of oxygen isotopic deviation confirms that these chemical variations occurred under a constant regional climate regime.

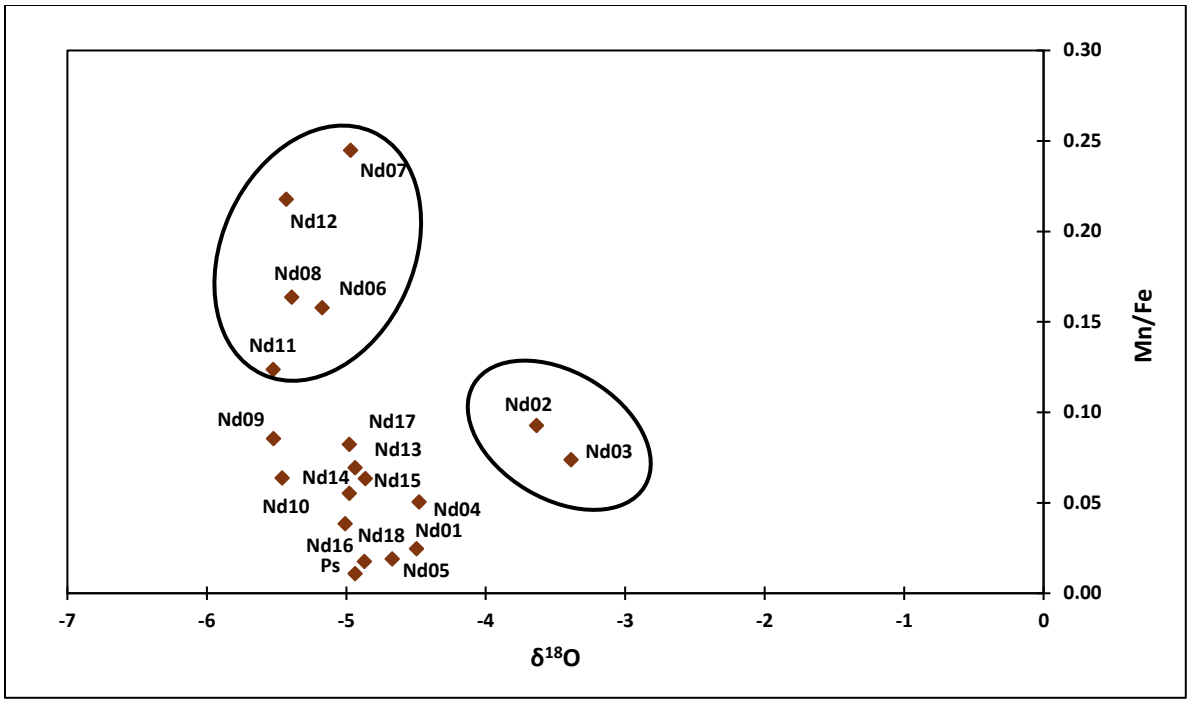


Fig. 7.7. Cross-plot of $\delta^{18}O$ and Mn/Fe of pedogenic carbonate features.

In summary, the combination of stable isotopes ($\delta^{13}C$, $\delta^{18}O$) and elemental ratios (Mn/Fe) allows for a reliable reconstruction of a resilient shrub savannah ecosystem. The main strength of this multifaceted approach lies in its ability to dissociate regional climate from local hydrology. While the close clustering of isotopic data indicates long-term regional climate stability and a stable plant structure dominated by C4 plants, Mn/Fe ratios reveal the 'hidden' complexity of the site's fluvial history. Specifically, the ability to correlate Mn enrichment in nodules with stratigraphic evidence of off-channel flooding (e.g., deposit C1) validates the use of the ratio as a high-resolution indicator of transient redox events that isotopic averages might otherwise overlook. However, certain limitations must be acknowledged. The intrinsic "temporal averaging" nature of larger carbonate nodules means that they likely smooth out decades or even centuries of environmental variability, potentially masking short-term ecological changes. Furthermore, the "seasonal bias" of carbonate precipitation, which favours the dry season, means that $\delta^{13}C$ and $\delta^{18}O$ values may disproportionately reflect arid phase conditions rather than the absolute annual mean. While

pseudomycelia offer a more “instantaneous” hydrological snapshot, their localised formation along modern root paths and near the riverbed complicates their use as a direct analogue for older, deeper pedosedimentary cycles. The bulk concentrations of Mn and Fe measured in the carbonate features do not allow us to determine their specific mineralogical hosts. Our interpretation was based on the model proposed by Sipos et al. (2025), who showed that Fe- and Mn-oxyhydroxides may precipitate within pre-existing carbonate features, particularly in microfractures, cavities, and as coatings on soil-matrix particles, in response to water circulation and fluctuating redox conditions. This model is particularly relevant to the present study area, where carbonate features occur in soils affected by fluctuations in the hydrological regime of the adjacent river system. However, confirming whether the measured Mn and Fe are predominantly associated with discrete Fe/Mn oxyhydroxides and occluded materials, or are incorporated into the calcite crystal lattice, would require petrographic and microchemical investigations, which were beyond the scope of the present study. Therefore, the interpretation of Mn and Fe concentrations should be considered as a plausible hypothesis rather than definitive evidence of the redox conditions prevailing during carbonate formation. Finally, the absence of independent chronological constraints means that a robust temporal framework cannot be established, so interpretations are necessarily process-based rather than time-resolved. Despite these constraints, converging evidence suggests that the study area has maintained a consistent ecological character, punctuated periodically by river pulses, throughout the recorded sections.

7.5. Conclusions

Overall, the combined analysis of stable isotopes ($\delta^{13}C$ and $\delta^{18}O$) and elemental ratios (Mn/Fe) in pedogenic carbonate features enables the reconstruction of long-term environmental stability and short-lived hydrological disturbances within the study area. The $\delta^{13}C$ values of the carbonate

nodules (-3.17‰ to -0.24‰) consistently indicate a resilient, C3-C4 mixed savannah ecosystem. The relatively narrow range of $\delta^{18}O$ values (-5.52‰ to -3.39‰) suggests limited variability in the isotopic composition of soil water; however, this signal should not be interpreted as a direct indicator of regional climatic stability. Instead, it likely reflects a combination of local controls, including evaporation, soil water residence time, and seasonal bias in carbonate precipitation. Minor vertical variations, particularly in SC01, are therefore more plausibly linked to depth-dependent evaporative processes than to climatic shifts. Meanwhile, Mn/Fe ratios provide valuable insights into redox dynamics and hydrological variability within the soil system, although their interpretation must consider the potential contribution of secondary processes and post-depositional redistribution. Although the time-averaging nature of carbonate precipitation and its seasonal bias may smooth out short-term variability, the convergence of isotopic and elemental evidence suggests that there is a stable ecological framework which is periodically interrupted by river-driven hydrological pulses. Applying this multi-proxy approach to further pedosedimentary sections in different geomorphic settings would enable the evaluation of the regional representativeness of these signals and help to distinguish between local and climate-driven influences. Furthermore, improved chronological constraints would refine the timing and significance of hydrological events.

References

Akinyemi FO (2021) Vegetation Trends, Drought Severity and Land Use-Land Cover Change during the Growing Season in Semi-Arid Contexts. Remote Sens (Basel) 13:. https://doi.org/10.3390/rs13050836

An H, Wu X, Zhang Y, Tang Z (2019) Effects of land-use change on soil inorganic carbon: A meta-analysis. Geoderma 353:273–282. https://doi.org/10.1016/j.geoderma.2019.07.008

Arenas-Abad C, Vázquez-Urbez M, Pardo-Tirapu G, Sancho-Marcén C (2010) Chapter 3 Fluvial and Associated Carbonate Deposits. In: Alonso-Zarza AM, Tanner LH (eds) Developments in Sedimentology. Elsevier, pp 133–175

Atlhopheng J, Brown Mthanganyika Mapeo R, Eckardt FD (2022) Introduction to the Landscapes and Landforms of Botswana. In: Eckardt FD (ed) Landscapes and Landforms of Botswana. Springer International Publishing, Cham, pp 1–13

Batisani N, Yarnal B (2010) Rainfall variability and trends in semi-arid Botswana: Implications for climate change adaptation policy. Applied Geography 30:483–489. https://doi.org/10.1016/j.apgeog.2009.10.007

Breecker DO, Michel LA, Rasmussen C, Tabor NJ (2025) A biogeochemical perspective on pedogenesis from soils to paleosols. In: Anbar A, Weis D (eds) Treatise on Geochemistry (Third edition). Elsevier, Oxford, pp 353–409

Breecker DO, Sharp ZD, McFadden LD (2009) Seasonal bias in the formation and stable isotopic composition of pedogenic carbonate in modern soils from central New Mexico, USA. Bulletin of the Geological Society of America 121:630–640. https://doi.org/10.1130/B26413.1

Brimhall GH, Dietrich WE (1987) Constitutive mass balance relations between chemical composition, volume, density, porosity, and strain in metasomatic hydrochemical systems: Results on

weathering and pedogenesis. Geochim Cosmochim Acta 51:567–587. https://doi.org/https://doi.org/10.1016/0016-7037(87)90070-6

Bughio MA, Wang P, Meng F, et al (2017) Neoformation of pedogenic carbonate and conservation of lithogenic carbonate by farming practices and their contribution to carbon sequestration in soil. Zeitschrift fur Pflanzenernahrung und Bodenkunde 180:454–463. https://doi.org/10.1002/jpln.201500650

Cerling TE (1984) The stable isotopic composition of modern soil carbonate and its relationship to climate

Cerling TE, Quade J (1993) Stable Carbon and Oxygen Isotopes in Soil Carbonates. In: Climate Change in Continental Isotopic Records. pp 217–231

Chadwick OA, Brimhall GH, Hendricks DM (1990) From a black to a gray box — a mass balance interpretation of pedogenesis. Geomorphology 3:369–390. https://doi.org/https://doi.org/10.1016/0169-555X(90)90012-F

Clark I, Fritz P (1997) Environmental Isotopes in Hydrogeology, 1st edn. CRC press, Boca Raton

Curtis Monger H, Kraimer RA, Khresat S, et al (2015) Sequestration of inorganic carbon in soil and groundwater. Geology 43:375–378. https://doi.org/10.1130/G36449.1

Dansgaard W (1964) Stable isotopes in precipitation. Tellus 16:436–468. https://doi.org/https://doi.org/10.1111/j.2153-3490.1964.tb00181.x

Dina Ebouel FJ, Betsi TB, Eze PN (2024) Soil inorganic carbon: A review of global research trends, analytical techniques, ecosystem functions and critical knowledge gaps. Catena (Amst) 242:108112. https://doi.org/https://doi.org/10.1016/j.catena.2024.108112

Dina Ebouel FJ, Kono Ebede CG, Bineli Betsi T, Eze PN (2025a) Distribution and potential of rare earth elements fingerprinting as tracers for carbonate sources in soils developed on contrasting

parent materials. Geoderma Regional 43:e01009. https://doi.org/https://doi.org/10.1016/j.geodrs.2025.e01009

Dina Ebouel FJ, Molwalefhe LN, Betsi TB, Eze PN (2025b) A Multi-Proxy Pedosedimentary Insight into Calcium Origin, Sediment Provenance, and Depositional Environments in a NW Botswana Landform. Earth Systems and Environment. https://doi.org/10.1007/s41748-025-00724-w

Domínguez-Villar D, Bensa A, Švob M, Krklec K (2022) Causes and implications of the seasonal dissolution and precipitation of pedogenic carbonates in soils of karst regions – A thermodynamic model approach. Geoderma 423:115962. https://doi.org/10.1016/J.GEODERMA.2022.115962

Driese SG, Mora CI (1993) Physico-chemical environment of pedogenic carbonate formation in Devonian vertic palaeosols, central Appalachians, USA. Sedimentology 40:199–216. https://doi.org/https://doi.org/10.1111/j.1365-3091.1993.tb01761.x

Durand N, Monger HC, Canti MG (2010) 9 - Calcium Carbonate Features. In: Stoops G, Marcelino V, Mees F (eds) Interpretation of Micromorphological Features of Soils and Regoliths. Elsevier, Amsterdam, pp 149–194

Durand N, Monger HC, Canti MG, Verrecchia EP (2018) Calcium Carbonate Features. In: Interpretation of Micromorphological Features of Soils and Regoliths. Elsevier, pp 205–258

Ellery K, Ellery WN, Verhagen BTh (1992) The distribution of C3 and C4 plants in a successional sequence in the Okavango Delta. South African Journal of Botany 58:400–402. https://doi.org/https://doi.org/10.1016/S0254-6299(16)30829-8

Eze PN (2022) Soil Development in the Eastern Hardveld. In: Eckardt FD (ed) Landscapes and Landforms of Botswana. Springer International Publishing, Cham, pp 327–344

Fischer-Femal BJ, Bowen GJ (2021) Coupled carbon and oxygen isotope model for pedogenic carbonates. Geochim Cosmochim Acta 294:126 – 144. https://doi.org/10.1016/j.gca.2020.10.022

Fox DL, Honey JG, Martin RA, Peláez-Campomanes P (2012) Pedogenic carbonate stable isotope record of environmental change during the Neogene in the southern Great Plains, southwest Kansas, USA: Oxygen isotopes and paleoclimate during the evolution of C4-dominated grasslands. Bulletin of the Geological Society of America 124:431–443. https://doi.org/10.1130/B30402.1

Franchi F, Kelepile T, Di Capua A, et al (2021) Lithostratigraphy, sedimentary petrography and geochemistry of the Upper Karoo Supergroup in the Central Kalahari Karoo Sub-Basin, Botswana. Journal of African Earth Sciences 173:. https://doi.org/10.1016/j.jafrearsci.2020.104025

Hoefs J (2015) Isotope Fractionation Processes of Selected Elements. In: Hoefs J (ed) Stable Isotope Geochemistry. Springer International Publishing, Cham, pp 47–190

Huth TE, Cerling TE, Marchetti DW, et al (2019) Seasonal Bias in Soil Carbonate Formation and Its Implications for Interpreting High-Resolution Paleoarchives: Evidence From Southern Utah. J Geophys Res Biogeosci 124:616 – 632. https://doi.org/10.1029/2018JG004496

Islam MdS, Mostafa MG (2023) Occurrence, Source, and Mobilization of Iron, Manganese, and Arsenic Pollution in Shallow Aquifer. Geofluids 2023:6628095. https://doi.org/https://doi.org/10.1155/2023/6628095

Kenabatho PK (2025) Innovative trend analysis of long-term spatial-temporal rainfall patterns over Botswana: Implications for water resources management. J Hydrol Reg Stud 58:102217. https://doi.org/https://doi.org/10.1016/j.ejrh.2025.102217

Khormali F, Shahriari A, Ghafarpour A, et al (2020) Pedogenic carbonates archive modern and past precipitation change – A transect study from soils and loess-paleosol sequences from northern Iran. Quaternary International 552:79–90. https://doi.org/10.1016/j.quaint.2019.12.011

Kim S-T, O'Neil JR (1997) Equilibrium and nonequilibrium oxygen isotope effects in synthetic carbonates. Geochim Cosmochim Acta 61:3461–3475. https://doi.org/https://doi.org/10.1016/S0016-7037(97)00169-5

Kirkels FMSA, De Boer HJ, Concha Hernández P, et al (2022) Carbon isotopic ratios of modern C3 and C4 vegetation on the Indian peninsula and changes along the plant-soil-river continuum - implications for vegetation reconstructions. Biogeosciences 19:4107–4127. https://doi.org/10.5194/bg-19-4107-2022

Lal R, Monger C, Nave L, Smith P (2021) The role of soil in regulation of climate. Philosophical Transactions of the Royal Society B: Biological Sciences 376:. https://doi.org/10.1098/rstb.2021.0084

Licht A, Kelson J, Bergel S, et al (2022) Dynamics of Pedogenic Carbonate Growth in the Tropical Domain of Myanmar. Geochemistry, Geophysics, Geosystems 23:. https://doi.org/10.1029/2021GC009929

Lindsay WL (2001) Chemical Equilibria in Soils. Blackburn Press

Liu J, Wu P, Zhao Z, Gao Y (2022) Afforestation on cropland promotes pedogenic inorganic carbon accumulation in deep soil layers on the Chinese loess plateau. Plant Soil 478:597–612. https://doi.org/10.1007/s11104-022-05494-2

Mantlana KB, Arneth A, Veenendaal EM, et al (2008) Photosynthetic properties of C4 plants growing in an African savanna/wetland mosaic. J Exp Bot 59:3941–3952. https://doi.org/10.1093/jxb/ern237

McLennan SM (2001) Relationships between the trace element composition of sedimentary rocks and upper continental crust. Geochemistry, Geophysics, Geosystems 2:. https://doi.org/https://doi.org/10.1029/2000GC000109

Mohammednoor M, Bibi F, Struck U, et al (2025) Pleistocene pedogenic carbonates from alluvial paleosols in eastern Sudan reveal a semi-arid and seasonal climate, similar to today. Catena (Amst) 248:108583. https://doi.org/https://doi.org/10.1016/j.catena.2024.108583

Monger HC (2014) Soils as Generators and Sinks of Inorganic Carbon in Geologic Time. In: Soil Carbon. Springer International Publishing, pp 27–36

Morgan JJ (2005) Kinetics of reaction between O2 and Mn(II) species in aqueous solutions. Geochim Cosmochim Acta 69:35–48. https://doi.org/https://doi.org/10.1016/j.gca.2004.06.013

Naorem A, Jayaraman S, Dalal RC, et al (2022) Soil Inorganic Carbon as a Potential Sink in Carbon Storage in Dryland Soils—A Review. Agriculture (Switzerland) 12:. https://doi.org/10.3390/agriculture12081256

Ning M, Luo J, Liang Z, et al (2025) Pedogenic carbonates in deep time: Characteristics, geological significance, and co-evolution with plant terrestrialization. Earth Sci Rev 271:105314. https://doi.org/https://doi.org/10.1016/j.earscirev.2025.105314

Nkemelang T, New M, Zaroug M (2018) Temperature and precipitation extremes under current, 1.5 °c and 2.0 °c global warming above pre-industrial levels over Botswana, and implications for climate change vulnerability. Environmental Research Letters 13:. https://doi.org/10.1088/1748-9326/aac2f8

O'Neil JR, Clayton RN, Mayeda TK (1969) Oxygen Isotope Fractionation in Divalent Metal Carbonates. J Chem Phys 51:5547–5558. https://doi.org/10.1063/1.1671982

Otero XL, Ferreira TO, Huerta-Díaz MA, et al (2009) Geochemistry of iron and manganese in soils and sediments of a mangrove system, Island of Pai Matos (Cananeia — SP, Brazil). Geoderma 148:318–335. https://doi.org/https://doi.org/10.1016/j.geoderma.2008.10.016

Park S-W, Baek N, Shin E-S, et al (2026) Substitution of lithogenic with pedogenic soil carbonates in Korean coastal rice paddy under desalinization: Evidences from δ13C. Agric Ecosyst Environ 396:109993. https://doi.org/https://doi.org/10.1016/j.agee.2025.109993

Quade J, Cerling TE, Bowman JR (1989) Systematic variations in the carbon and oxygen isotopic composition of pedogenic carbonate along elevation transects in the southern Great Basin, United States. GSA Bulletin 101:464–475. https://doi.org/10.1130/0016-7606(1989)101<0464:SVITCA>2.3.CO;2

Raheb A, Heidari A, Mahmoodi S (2016) Storage of organic and inorganic carbon in arid-semihumid soils: A case study of the rangelands of northwestern Iran. Soil Sci 181:473–486. https://doi.org/10.1097/SS.0000000000000183

Railsback LB (2021) Pedogenic carbonate nodules from a forested region of humid climate in central Tennessee, USA, and their implications for interpretation of C3-C4 relationships and seasonality of meteoric precipitation from carbon isotope (δ13C) data. Catena (Amst) 200:. https://doi.org/10.1016/j.catena.2021.105169

Ringrose S, Matheson W, Vanderpost C (1998) Analysis of soil organic carbon and vegetation cover trends along the B otswana Kalahari Transect

Rollinson H, Pease V (eds) (2021) Using Major Element Data. In: Using Geochemical Data: To Understand Geological Processes, 2nd edn. Cambridge University Press, Cambridge, pp 49–95

Rozanski K, Araguás-Araguás L, Gonfiantini R (1993) Isotopic Patterns in Modern Global Precipitation. In: Climate Change in Continental Isotopic Records. pp 1–36

Ryskov YG, Velichko AA, Nikolaev VI, et al (2008) Reconstruction of the paleotemperature and precipitation in the Pleistocene according to the isotope composition of humus and carbonates in

loess on the Russian Plain. Eurasian Soil Science 41:937–945. https://doi.org/10.1134/S1064229308090044

Sanz-Montero ME, del Buey P, Cabestrero Ó, Sánchez-Román M (2023) Isotopic Signatures of Microbial Mg-Carbonates Deposited in an Ephemeral Hyperalkaline Lake (Central Spain): Paleoenvironmental Implications. Minerals 13:. https://doi.org/10.3390/min13050617

Sarangi V, Agrawal S, Sanyal P (2021) The disparity in the abundance of C4 plants estimated using the carbon isotopic composition of paleosol components. Palaeogeogr Palaeoclimatol Palaeoecol 561:. https://doi.org/10.1016/j.palaeo.2020.110068

Sipos P, Kovács I, Tóth A, et al (2025) Paragenetic relationship between ferromanganese and calcareous nodules in a hydromorphic toposequence. Geoderma 454:117179. https://doi.org/https://doi.org/10.1016/j.geoderma.2025.117179

Smith A, R (1984) The Lithostratigraphy of the Karoo Supergroup in Botswana. Geol Mag 123:710–711. https://doi.org/DOI: 10.1017/S0016756800024328

Stevenson BA, Kelly EF, McDonald E V., et al (2010) Oxygen isotope ratios in Holocene carbonates across a climatic gradient, eastern Washington State, USA: Evidence for seasonal effects on pedogenic mineral isotopic composition. Holocene 20:575–583. https://doi.org/10.1177/0959683609356588

Stoll HM, Day C, Lechleitner F, et al (2023) Distinguishing the combined vegetation and soil component of δ^13C variation in speleothem records from subsequent degassing and prior calcite precipitation effects. Climate of the Past 19:2423–2444. https://doi.org/10.5194/cp-19-2423-2023

Tribovillard N, Algeo TJ, Lyons T, Riboulleau A (2006) Trace metals as paleoredox and paleoproductivity proxies: An update. Chem Geol 232:12–32. https://doi.org/https://doi.org/10.1016/j.chemgeo.2006.02.012

Valera-Fernández D, Cabadas-Báez H, Solleiro-Rebolledo E, et al (2020) Pedogenic carbonate crusts (calcretes) in karstic landscapes as archives for paleoenvironmental reconstructions – A case study from Yucatan Peninsula, Mexico. Catena (Amst) 194:. https://doi.org/10.1016/j.catena.2020.104635

Yang S, Ding Z, Wang X, et al (2012) Negative δ 18O-δ 13C relationship of pedogenic carbonate from northern China indicates a strong response of C 3/C 4 biomass to the seasonality of Asian monsoon precipitation. Palaeogeogr Palaeoclimatol Palaeoecol 317–318:32–40. https://doi.org/10.1016/j.palaeo.2011.12.007

Zamanian K, Pustovoytov K, Kuzyakov Y (2016) Pedogenic carbonates: Forms and formation processes. Earth. Sci. Rev. 157:1–17

Zhang D, Beverly EJ, Levin NE, et al (2021) Carbon isotopic composition of plant waxes, bulk organics and carbonates from soils of the Serengeti grasslands. Geochim Cosmochim Acta 311:316–331. https://doi.org/10.1016/j.gca.2021.07.005

Appendices

Appendix 7.1 Stable isotope ratios of carbon ($^{13}C/^{12}C$) and oxygen ($^{18}O/^{16}O$) in carbonate features and laboratory quality control.

Section	Layer	Depth (cm)	Sample	$\delta^{13}C$(VPDB)	SD	$\delta^{18}O$(VPDB)	SD	n
SC01	Bk2	120-150	Nd01	-3.17	0.08	-4.50	0.05	10
	AB1b	240-300	Nd02	-2.63	0.06	-3.64	0.06	10
	Bkkb	300-330	Nd03	-2.43	0.06	-3.39	0.07	10
		330-360	Nd04	-2.19	0.06	-4.48	0.03	10
	AB3b	740-840+	Ps	-6.85	0.07	-4.94	0.06	10
	BCkkb	240-360	Nd05	-0.24	0.06	-4.67	0.05	10
	BCkb	500-540	Nd06	-2.00	0.06	-5.17	0.06	10
		540-580	Nd07	-2.40	0.04	-4.97	0.02	10
SC03	BCkkb	245-285	Nd08	-1.08	0.05	-5.39	0.05	10
		285-305	Nd09	-2.23	0.04	-5.52	0.06	10
		305-345	Nd10	-1.96	0.05	-5.46	0.05	10
		345-375	Nd11	-2.26	0.05	-5.52	0.06	10
	BCkb	375-400	Nd12	-2.40	0.04	-5.43	0.04	10
SC04	BCkkb	160-190	Nd13	-1.42	0.04	-4.94	0.05	10
		190-220	Nd14	-1.23	0.05	-4.98	0.06	10
		220-260	Nd15	-1.71	0.04	-4.86	0.05	10
	BCkb	260-300	Nd16	-1.30	0.05	-5.01	0.05	10
		300-330	Nd17	-1.35	0.04	-4.98	0.05	10
		330-400+	Nd18	-3.01	0.04	-4.87	0.05	10

Reference	Commend	$\delta^{13}C$(VPDB)	SD	$\delta^{18}O$(VPDB)	SD	n
Carrara	Marble / House	-2.52	0.06	-0.90	0.05	9
NBS18	Carbonatite / RM	-5.01	0.04	-23.01	0.1	3
	(recommended value)	-5.01	0.04	-23.01	0.1	

Appendix 7.2. Fe, Mn concentration in molar percent and Mn/Fe ratio in the study sections.

Location	Samples	Depth (cm)	Fe	Mn	Mn/Fe
SC01	A1	0-30	3.13	0.06	0.02
	AB	30-90	3.13	0.07	0.02
	Bk1	90-120	4.06	0.11	0.03
	Bk2	120-180	4.27	0.11	0.02
	BC	180-220	3.73	0.08	0.02
	C1	220-240	2.74	0.06	0.02
	AB1b	240-300	4.59	0.09	0.02
	Bkkb	300-420	4.97	0.10	0.02
	CB1b	420-480	7.47	0.06	0.01
	CB2b	480-570	7.41	0.06	0.01
	CB3b	570-630	7.46	0.07	0.01
	AB2b	630-690	7.33	0.06	0.01
	CB4b	690-740	5.86	0.05	0.01
	AB3b	740-840+	6.19	0.05	0.01
SC02	A1	0-20	3.24	0.05	0.02
	C1	20-110	3.19	0.06	0.02
	ABb	110-185	3.76	0.06	0.02
	BC1b	185-240	3.16	0.04	0.01
	BCkkb	240-360	3.58	0.04	0.01
	BC2b	360-500	3.93	0.05	0.01
	BCkb	500-580	4.71	0.10	0.02
	BC3b	580-600+	2.97	0.04	0.01
SC03	A1	0-15	3.98	0.07	0.02
	AC	15-42	5.25	0.09	0.02
	C1	42-70	2.68	0.05	0.02
	C2	70-140	5.40	0.09	0.02
	ABb	140-205	6.67	0.10	0.02
	Btb	205-245	3.35	0.05	0.02
	BCkkb	245-375	4.36	0.06	0.01
	BCkb	375-430+	3.62	0.06	0.02
SC04	A1	0-15	3.45	0.05	0.01
	AC	15-50	3.99	0.06	0.02
	ABb	50-70	5.88	0.09	0.02
	Bt1b	70-90	5.23	0.09	0.02
	Bt2b	90-160	3.20	0.04	0.01
	BCkkb	160-260	3.75	0.05	0.01
	BCkb	260-400+	4.80	0.06	0.01

CHAPTER EIGHT

Rare Earth Element Fractionation: A High-Resolution Indicator of Carbonate Origin and Pedogenic Signatures in Semi-Arid Landscapes[7]

Abstract

Pedogenic carbonates constitute an important pool of soil inorganic carbon in semi-arid environments, yet distinguishing their formation mechanisms and origin remains a challenge, especially in pedosedimentary landscapes where lithogenic carbonates may also occur. This study investigates rare earth element (REE) signatures in pedogenic carbonates and their surrounding soil matrix within a calcic landscape of the eastern Hardveld of Botswana. Four pedosedimentary sections developed along the Metsimasweu River were analysed, including 37 soil samples and 18 pedogenic carbonate (nodules and pseudomycelia) samples. Soil REE concentrations range from 34.28 to 82.37 mg kg^{-1}, whereas carbonates have a much wider variability (29.81–200.55 mg kg^{-1}). Principal component analysis reveals contrasting geochemical controls between soil and carbonate samples. REE enrichment in bulk soils is primarily associated with clay-rich horizons, while carbonate exhibit strong relationships between Ca content and REE fractionation indices. All carbonate samples display pronounced negative cerium anomalies (δCe = 0.09–0.78) and relative heavy rare earth element (HREE) enrichment, consistent with pedogenic carbonate formation. The strongest REE enrichments occur in samples Nd06 and Nd07 (up to 200.55 mg kg^{-1}), likely reflecting the relationship with calcium enrichment in pedogenic. These geochemical signatures indicate that carbonate precipitation most likely occurred under oxidising conditions

[7] *This chapter is based on a research article co-authored with Thierry Bineli Betsi, Elisabeth Eiche, Stefan Norra, and Peter N. Eze; currently under review in Scientific Report*.

during short-lived wetting–drying cycles typical of semi-arid climates. The results demonstrate that analysing individual carbonate features allows the isolation of carbonate-specific REE signatures that may be masked at the bulk-soil matrix. This high-resolution approach provides a robust geochemical tool for identifying pedogenic carbonates and reconstructing their formation processes in complex pedosedimentary environments.

Keywords: Alkaline Soils; Kalahari Basin; LREE/HREE Fractionation; Soil inorganic carbon; Weathering Indices.

8.1. Introduction

Pedogenic carbonates, a specific type of soil inorganic carbon (SIC), play a significant role in carbon sequestration in dry environments (Zamanian et al., 2021). Depending on the degree of development, several morphological forms may occur within the soil profile, including diffuse powder, coatings, pseudomycelia, nodules and petrocalcic horizons (Gile, 1993; Zamanian et al., 2016). The synergy of low precipitation and high evapotranspiration concentrates solutes within the soil. As the soil solution reaches supersaturation, calcium and magnesium react with bicarbonate ions, triggering the precipitation and progressive preservation of carbonates (Stanbery et al., 2023). Although upward mechanisms, namely capillary rise and evaporation, typically drive carbonate formation, seasonal rainfall can induce periodic dissolution, facilitating the downward translocation of carbonates from the topsoil to subsurface horizons (Zamanian et al., 2016). Consequently, it is often challenging to disentangle the relative contributions of these opposing flux mechanisms to the net long-term architecture of the soil profile.

In arid and semi-arid environments, landscapes often evolve from a combination of pedogenic processes and sediment deposition, often incorporating lithogenic carbonate deposits (Dina Ebouel et al. 2025a, b). Unlike pedogenic carbonates, lithogenic carbonates originate primary from

sedimentary processes. It is therefore important to differentiate carbonates of pedogenic origin from those derived from lithogenic processes. A clear understanding of pedogenic formation processes is essential for enhancing soil carbon sequestration and ensuring preservation through sustainable land use (Egli et al., 2021).

Current methodologies used to study SIC formation rely on a combination of laboratory and field techniques, the choice of which to use is often decided by the technical infrastructure and financial resources available (Dina Ebouel et al., 2024). While macromorphological characterisation provides the basic morphological information, its inherent limitations in terms of resolution necessitates a shift to more sophisticated, multi-scalar approaches. Recent studies now increasingly combine traditional physical descriptions with micromorphological observations and isotopic geochemistry to gain a high-resolution understanding of precipitation processes (Dal Sasso et al., 2018; Kelson et al., 2025). Specifically, the analysis of stable carbon ($\delta^{13}C$) and oxygen ($\delta^{18}O$) isotopes in carbonate formations makes it possible to reconstruct the environmental and climatological conditions that prevailed at the time of their formation (Cerling and Quade 1993; Eze and Meadows, 2015; Fischer-Femal and Bowen 2021). In addition, while the application of strontium ($^{87}Sr/^{86}Sr$) isotope ratio serves as a robust proxy for tracing parent rock sources (Dietrich et al., 2017; Millière et al., 2019), the study of the behaviour of major and trace elements in soil carbonates provides further insight into the specific chemical pathways and biophysical-chemical factors involved in the formation process (Dina Ebouel et al., 2025b; Wolff et al., 2017).

According to Laveuf and Cornu (2009), REEs signatures in carbonates can be used to discriminate between lithogenic and pedogenic carbonates, mainly through LREEs/HREEs fractionation patterns. This approach was used for carbonates from the Kalahari Basin in Botswana by Dina Ebouel et al. (2025a).In the study, REEs signatures in soils marked by high carbonate contents

were used to deduce carbonate sources from contrasting parent materials. Nevertheless, the authors highlighted several limitations. The REEs distributions were strongly controlled by lithology and clay-affinity elements, while the relationship between $CaCO_3$ and REEs indices was weak or inconsistent across sites. These indicate that bulk soil REEs signatures may mask the specific geochemical signal of carbonate formation, particularly when multiple sources and processes overlap. Hence a need for empirical improvement.

Applying REEs fingerprinting at a landscape scale, by directly comparing the REEs signatures of distinct carbonate forms (e.g., nodules, pseudomycelia) with those of the surrounding soil matrix, could help overcome these limitations. Such an approach would allow for better isolation of the carbonate-specific signals from soil background noise, thereby improving the interpretation of carbonate genesis and associated pedogenic processes.

This study investigates a pedosedimentary landscape in central Botswana, characterised by widespread carbonate accumulation. Its objectives are to (i) characterise the REEs signatures of the pedogenic carbonates; (ii) compare these signatures with those of their host soil horizons; and (iii) elucidate the mechanisms controlling REEs fractionation and, ultimately, the origin and formation pathways of the carbonates. Findings from studies of this nature have significant implications for the use of pedogenic carbonates as proxies for palaeoenvironmental and palaeoclimate reconstructions.

8.2. Material and methods

8.2.1. Study area

The study area, located at Serowe in the eastern Hardveld of Botswana (22.34°–22.42° S, 26.67°–26.76° E), is characterised by a complex geological architecture of the Karoo Supergroup unconformably overlain by Cenozoic Kalahari sands (Smith, 1984). The local lithostratigraphy is

dominated by the Lebung Group sandstones capped by Stormberg lavas, which serve as the primary geochemical reservoir for the landscape's development (Franchi et al., 2021). Recent investigations at this site have demonstrated that the weathering of these basaltic units from Stormberg lavas drives calcium enrichment in the pedogenic carbonates in the area (Dina Ebouel et al., under review b). Under the prevailing semi-arid BSh climate (mean annual precipitation of 442.4 mm), high evapotranspiration rates and ephemeral hydrological pulses promote intense calcification and pedogenic carbonate accumulation, with eq$CaCO_3$ contents reaching up to 22 wt.% in some horizons (Dina Ebouel et al., under review a). These pedogenic carbonates are mainly in form of diffuse powder, nodules and some pseudomycelia observed in sub-surface horizon adjacent to the river. Furthermore, calcite ($CaCO_3$) is the dominant mineralogical species observed in these carbonates (Dina Ebouel et al., under review b). The hydrochemical environment is typically dominated by Ca–Mg–HCO_3 signatures (Stadler et al., 2010), reflecting limited water-soil interaction during recharge events. While previous stable isotope studies ($\delta^{13}C$, $\delta^{18}O$) have highlighted the influence of local hydrology on carbonate formation (Dina Ebouel et al., under review c).

Table 8.1. Location of the studied sections

Section	Longitude (E)	Latitudes (S)	Altitudes m asl	Depth (m)	Number of horizons	Number of carbonates samples and labels	
P01	26.70315	22.37167	1127	8.4	14	5	Nd01, Nd02, Nd03, Nd 04 and Ps
P02	26.7214	22.37266	1101	6	8	3	Nd05, Nd06 and Nd07
P03	26.73786	22.37144	1090	4.3	8	5	Nd08, Nd09, Nd10, Nd11 and Nd12
P04	26.74099	22.37386	1086	4	7	5	Nd13, Nd14, Nd15, Nd16 and Nd17

*P: profile; Nd: nodule; Ps: pseudomycelia

8.2.2. Sampling strategy

The sampling plan followed a systematic approach in the four pedosedimentary sections (Table 8.1) previously established by Dina Ebouel et al. (under review c). These sections, which occur naturally along a seasonal river locally known as Metsimasweu, were strategically selected to represent the geomorphological and lithological diversity of the Serowe landscape, which includes both basaltic and sedimentary substrates.

In each profile, representative soil samples were taken from identified pedogenic horizons and sedimentary layers, to the maximum accessible depth. To fulfil the specific objectives of this study, samples of carbonate (Fig. 8.1), including nodules (Nd) and pseudomycelia (Ps), were carefully collected *in situ* to ensure minimal contamination. Corresponding host matrix samples were collected in the immediate surrounding of each carbonate sample to allow direct comparison of REEs signatures. A total of 18 carbonate samples and 37 soil samples were collected and stored in ziplock polyethylene bags and transported to the laboratory for further analysis.

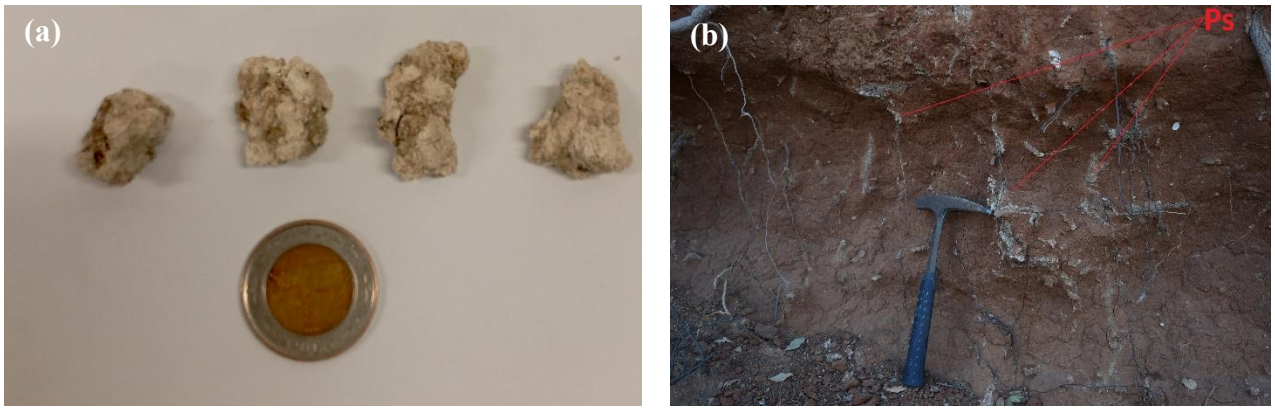


Fig. 8.1. a. isolated pedogenic carbonates nodules; b. pseudomycelia carbonate (Ps) in P01 (the coin and the geologist's hammer are used as a scale).

8.2.3. Analytical methods

8.2.3.1. Physico-chemical properties of soil

Pretreatment prior to physico-chemical analyses involved 2 mm sieving and manual removal of coarse roots. Particle size distribution was determined after a two-step pretreatment process. This involved treating the sample with a 30% hydrogen peroxide solution for 24 hours to remove organic matter, followed by treatment with a 10% hydrochloric acid solution for 24 hours to remove carbonates. The samples were then dispersed using sodium hexametaphosphate, after which the proportion of clay, silt and sand was determined using the Bouyoucos hydrometer method and reported in mass percentage.

Soil pH and electrical conductivity (EC) were determined in a 1/2.5 soil:deionised water ratio solution as recommended in FAO Guidelines for soil description (Food and Agriculture Organization of the United Nations, 2006). The carbonate content equivalent ($eqCaCO_3$) of the soil was determined with an Eijkelkamp calcimeter using the Scheibler method, in accordance with NEN-ISO 10693. The sample react with hydrochloric acid (4 M HCl), generating CO_2 gas. The volume of CO_2 produced is measured volumetrically using a burette system and the carbonate content is expressed as calcium carbonate equivalent ($eqCaCO_3$). Calibration was carried out using calcium carbonate standards (0.2 g and 0.4 g $CaCO_3$), and blank determinations were carried out to ensure accuracy. Results were calculated using the standard formula, incorporating corrections for blank values and moisture content (ISO 11465). Results obtained in g kg^{-1} were converted to weight percentages. The soil organic matter (SOM) content was determined via wet oxidation (Walkley and Black, 1934).

8.2.3.2. Elemental analysis

The carbonate samples were cleaned with a brush to remove the soil and organic matter covering them. Following these steps, the soil (2 mm sieved) and carbonate samples were then pulverised into a fine, homogeneous powder using an agate mortar.

Magnesium (Mg) and Calcium (Ca) concentrations were determined only for the pedogenic carbonates. The analysis was performed on fused beads using an S4 Explorer (Bruker AXS) wavelength dispersive X-ray fluorescence spectroscope (WDX) at the Laboratory for the Environmental and Raw Materials Analysis (LERA), Institute of Applied Geosciences, Karlsruhe Institute of Technology (KIT), Germany. Prior to element quantification, the loss on ignition (LOI) of the pulverised samples was determined by heating them to 950 °C for 3 hours and recording the weight difference before and after heating. Fused beads were prepared by mixing the ignited sample powder with a 66.5:33.5 ratio of Li-tetraborate and Li-metaborate (Spectroflux 110, Alfa Aesar) before melting it at 1000–1100 °C using a fusion instrument. An Rh X-ray tube (50 keV, 1 kW) was used as the radiation source. Signals were detected using a proportional flow counter (Ar-CH_4 gas) and a scintillation counter. XS-55, LIF2000 and PET were used as analyser crystals. Four certified reference materials including AGV-1, GXR-2, GXR-5 and Soil 7, were used for quality control to ascertain the accuracy of the produced data.

Rare Earth Element concentrations were determined using ICP-MS at the Laboratory for Environmental and Raw Materials Analysis (LERA), Institute of Applied Geosciences, Karlsruhe Institute of Technology (KIT), Germany, with a Thermo Scientific iCAP instrument. Prior to analysis, samples were subjected to an open/semi-open full acid digestion using HNO_3(HCl)–HF–$HClO_4$. Measurements were performed in kinetic energy discrimination (KED) mode with helium

as the collision gas to suppress polyatomic oxide interferences, ensuring reliable quantification of Sc, Y, and the full lanthanide series (La–Lu).

External calibration was carried out using multi-element REEs standards spanning 0–100 ppb, yielding excellent linearity for all REEs ($R^2 > 0.999$). Limits of quantification were typically ≤ 0.001 ppb for most REEs. Instrumental stability was monitored throughout the analytical session by repeated analysis of a 5-ppb control standard, which consistently remained within ±5% of the target concentration.

Analytical accuracy was assessed through repeated measurements of SLRS-6 river water reference material, with REEs recoveries generally ranging between ~90% and 97%. Additional validation was provided by the analysis of geological reference materials (BHVO-1, BIR-1, SAG-1, GXR-5, Soil-7), which yielded internally consistent REEs patterns. Oxide interference suppression was verified using a 250 ppb La/Ce solution, which showed negligible signal in heavy REEs mass channels. Procedural blanks (1% HNO_3) confirmed a low analytical background throughout.

8.2.4. Data treatment

To facilitate stoichiometric comparison, the calcium (Ca) and magnesium (Mg) content of the carbonate samples, originally reported as oxide weight percentages (wt.%), were recalculated into elemental molar percentages (mol%) (Rollinson and Pease, 2021). The reported weight percentage of each oxide was divided by its molecular weight to obtain the corresponding oxide molar proportion. This value was then multiplied by the oxide's cation stoichiometric coefficient (e.g. 2 for Al_2O_3; 1 for CaO) to derive the unnormalized cation molar proportion. The final elemental molar percentages (mol%) were obtained by normalising these values to the total molar sum of all analysed elements.

The sum of rare earth elements (∑REEs), from lanthanum (La) to lutetium (Lu), was calculated for each sample. Light rare earth elements (LREEs) were defined as La to Eu, whereas heavy rare earth elements (HREEs) were defined as Gd to Lu. The LREEs/HREEs ratio was then determined by dividing the sum of LREEs by the sum of HREEs.

REEs indices including the cerium (δCe) and europium (δEu) anomalies, along with the $(La/Yb)_N$, $(La/Sm)_N$ and $(Gd/Yb)_N$ fractionation ratios, were calculated using UCC values as a reference (Taylor and McLennan, 1985).

The REEs contents of the soil and carbonates were normalised to the concentrations of the upper continental crust (UCC) (Taylor and McLennan, 1985) to illustrate vertical variation of REEs.

Principal component analysis (PCA) was conducted on two different set of samples using R version 4.5.1. The first PCA examined the relationships between REEs concentrations and indices, and physico-chemical properties in bulk soil samples. The second PCA focused specifically on carbonates to investigate interactions between REEs signatures, Ca and Mg.

To account for the disparity in scales of the variables, ranging from parts per million (ppm) to molar percentage (mol%), a two-step data pre-treatment was applied. First, the concentration data were $\log_{10}$-transformed to normalise the distributions and reduce the influence of extreme values. Secondly, all variables were standardised using Z-score transformation by subtracting the mean of each variable from its individual values and dividing by the standard deviation. This procedure ensured that each variable, regardless of its original unit, contributed equally to the PCA, with a final mean of zero and unit variance of one.

8.3. Results

8.3.1. Physico-chemical properties of the soils

Detailed description of the morphological and physico-chemical properties of the sections available in Dina Ebouel et al. (under review a). Brief overview of the physico-chemical results relevant to this study including particle size distribution, pH(H_2O), EC, SOM, and eq$CaCO_3$ are presented in Appendix 8.1.

Sand is generally the dominant fraction across the soil profiles, with contents mostly above 50%. Clay fraction is typically below 15%. However, some horizons in P03 and P04 are characterised by high contents of clay. In P03, ABtb is characterised by a dominant clay fraction (50%), while clay fraction constitutes 31% of C2 and Bt. In P04, the clay content of ABb and Bt1b are 39% and 33%, respectively. Silt fraction is typically between 10 and 25%, with average value of 17%.

The lowest soil pH values across the four sections (P01–P04) are predominantly observed in the topsoil horizons (A1), ranging from a slightly acidic minimum of 6.40 in P04 to a slightly alkaline maximum of 7.30 in P03. Most of the horizons are characterised by slightly alkaline conditions with an average pH of 7.60. Furthermore, maximums corresponding to moderately alkaline pH were recorded, ranging from 8.00 to 8.40, with the latter occurring in the lowest horizon of P02 (BC3b).

The EC ranges from 0.14 $dS.m^{-1}$ in the A1 horizon of P04 to a maximum of 2.81 $dS.m^{-1}$ in the BCkkb horizon of P02. The BCkkb horizon in P02 is a typical example of this, with the maximum EC values observed.

The SOM content of the soils is typically low, ranging from 0.19 wt.% to 0.62 wt.%. Topsoil horizons mostly have the highest SOM content, reaching a maximum of 0.62 wt.% in P04, while P01 and P03 have the lowest content at 0.41 wt.%.

The equivalent $CaCO_3$ content ranges from 0.02 wt.% to 24.41 wt.%. As expected, the highest values are observed in horizons with calcium carbonate features: Bkkb in P01 (24.41 wt.%), BCkkb in P02, P03 and P04 with concentrations of 14.24%, 16.26% and 21.09% respectively.

8.3.2. Ca and Mg in Carbonates

As shown in Table 8.2, all pedogenic carbonates of this study are characterised by high Ca content, ranging from 35.06 mol% in Ps of P01 to 81.83 mol% in Nd08 from P03. Nevertheless, carbonates P01 have relatively low concentrations ranging from 35.06 to 60.19 mol%. In contrast, the carbonates in P02–P04 are characterised by a Ca content within the same range, between 72.24 and 81.83 mol%.

The Mg concentration in the carbonates is relatively low, ranging from 1.93 to 16.91 mol%. The general pattern of Mg concentrations in pedogenic carbonates highlights relatively high concentrations in P01 and P02, ranging from 3.16 to 16.91 mol%, while carbonates from P03 and P04 have concentrations below 2.54 mol%.

Table 8.2. Ca, Mg, REEs concentration and fractionation indices of REEs in the carbonates

Profile	Samples	Mg	Ca	LREEs	HREEs	∑REEs	LREEs/HREEs	δCe	δEu	$(La/Yb)_N$	$(La/Sm)_N$	$(Gb/Yb)_N$
		Mol.%		mg kg^{-1}								
P01	Nd01	9.00	42.15	24.55	5.55	30.10	4.42	0.72	1.34	0.50	0.69	0.92
	Nd02	10.70	60.19	61.97	15.56	77.52	3.98	0.57	1.14	0.58	0.67	1.16
	Nd03	16.91	49.72	27.15	9.42	36.57	2.88	0.57	1.20	0.33	0.59	0.82
	Nd04	6.04	58.63	22.68	7.12	29.81	3.18	0.78	1.25	0.29	0.62	0.67
	Ps	3.58	35.06	87.53	34.64	122.17	2.53	0.40	1.14	0.35	0.46	1.17
P02	Nd05	6.95	72.47	30.69	9.69	40.38	3.17	0.23	1.26	0.54	0.63	1.16
	Nd06	3.64	70.09	166.65	33.91	200.55	4.91	0.10	1.22	1.35	0.86	1.91
	Nd07	3.16	70.84	157.64	26.92	184.56	5.86	0.11	1.23	1.68	0.87	2.07
P03	Nd08	1.93	81.83	42.37	13.54	55.92	3.13	0.22	1.17	0.62	0.81	1.17
	Nd09	2.24	77.69	61.87	20.01	81.88	3.09	0.18	1.18	0.59	0.75	1.15
	Nd10	2.29	78.33	55.58	18.30	73.88	3.04	0.17	1.19	0.58	0.74	1.14
	Nd11	1.97	80.88	37.73	11.26	48.99	3.35	0.26	1.19	0.57	0.71	1.10
	Nd12	2.15	72.51	142.44	35.89	178.33	3.97	0.18	1.24	0.83	0.76	1.39
P04	Nd13	2.34	72.24	34.84	12.23	47.08	2.85	0.31	1.28	0.42	0.61	0.97
	Nd14	2.14	77.53	25.33	8.37	33.69	3.03	0.24	1.27	0.51	0.68	1.05
	Nd15	2.54	70.96	41.80	13.39	55.19	3.12	0.32	1.29	0.46	0.58	1.07
	Nd16	2.25	74.12	57.66	18.14	75.80	3.18	0.18	1.27	0.56	0.59	1.24
	Nd17	2.31	78.02	80.26	28.79	109.05	2.79	0.09	1.25	0.50	0.64	1.05

8.3.3. REEs in the soil profiles

The concentrations of each REE in the studied sections are presented in Appendix 8.2, while summarised indices are presented in Table 8.3.

The general pattern highlights a profound variation in REEs concentration and indices. ∑REEs vary from a minimum of 34.28 mg kg^{-1} to a maximum of 82.37 mg kg^{-1}. HREEs ranges from 4.39 mg kg^{-1} to 13.34 mg kg^{-1}, while LREEs ranges from 29.75 mg kg^{-1} to 69.03 mg kg^{-1}, and LREEs/HREEs ranging from 4.06 to 7.48. Cerium anomalies vary from 0.71 to 1.17, while δEu are all above 1, ranges from 1.20 to 1.59. $(La/Yb)_N$ and $(La/Sm)_N$ both has values below 1, ranging from 0.39 to 0.84 and from 0.50 to 0.80, respectively. $(Gb/Yb)_N$ on the other hand are mostly characterised by close or above 1, ranging from 0.90 to 1.45.

Variation across each profile shows a more contrasted pattern. P01, P02 and P04 show relatively low REEs abundance as compared to P03. ∑REEs ranges from 37.42 mg $kg^{-1}$to 65.68 mg kg^{-1}, from 37.22 mg kg^{-1} to 69.45 mg kg^{-1} and from 34.28 mg kg^{-1} to 70.05 mg kg^{-1}, respectively in P01, P02 and P04. ∑REEs in P03 on the other hand vary from 42.60 mg kg^{-1} to 82.37 mg kg^{-1}. LREEs follows the same pattern as ∑REEs, while the gaps in HREEs abundance not significantly pronounce between P01, P03 and P04. HREEs ranges from 5.74 mg kg^{-1} to 12.88 mg kg^{-1}, from 6.49 mg kg^{-1} to 13.34 mg kg^{-1} and from 4.53 mg kg^{-1} to 11.39 mg kg^{-1}, respectively in P01, P03 and P04. HREEs in P02 ranges from 4.39 mg kg^{-1} to 9.85 mg kg^{-1}.

Vertical/Depth variations in the LREEs/HREEs across the different profiles, on the other hand, highlight similar variations between the different profiles. LREEs/HREEs range from 4.06 to 5.52 in P01, from 5.36 to 7.48 in P02, from 4.87 to 6.72 in P03, and from 5.15 to 6.57 in P04. Comparable pattern is observed in δCe and δEu variations. δCe ranges from 0.75 to 1.00, from 0.73 to 1.01, from 0.71 to 1.13, and from .076 to 1.17, respectively for P01, P02, P03 and P04. δEu ranges from 1.28 to 1.59 in P01, from 1.27 to 1.42 in P02, from 1.20 to 1.41 in P03, and from 1.25 to 1.44 in P04.

$(La/Yb)_N$, $(La/Sm)_N$ and $(Gb/Yb)_N$ show contrasting variations from one profile to another. $(La/Yb)_N$ in P01 has relatively low values ranging from 0.39 to 0.61, while the values for P02, P03 and P04 range from 0.61 to 0.79, 0.50 to 0.72 and 0.56 to 0.70, respectively. $(La/Sm)_N$ varies from 0.51 to 0.71 in P01, from 0.61 to 0.79 in P02, from 0.65 to 0.77 in P03 and from 0.64 to 0.80 in P04. $(Gb/Yb)_N$ varies from 0.90 to 1.08 in P01, from 0.98 to 1.45 in P02, from 0.91 to 1.13 in P03 and from 0.98 to 1.04 in P04.

Table 8.3. Concentration of REEs and fractionation indices of REEs in the studied soil profiles

Profile	Horizon	LREEs	HREEs	∑REEs	LREEs/HREEs	δCe	δEu	$(La/Yb)_N$	$(La/Sm)_N$	$(Gb/Yb)_N$
		mg kg^{-1}								
P01	A1	31.68	5.74	37.42	5.52	0.78	1.41	0.61	0.71	0.97
	AB	35.53	6.58	42.11	5.40	0.79	1.36	0.59	0.67	0.99
	Bk1	44.51	8.66	53.17	5.14	0.82	1.31	0.57	0.64	1.04
	Bk2	44.78	8.71	53.49	5.14	0.85	1.38	0.55	0.65	1.01
	BC	38.95	7.54	46.50	5.16	0.86	1.45	0.54	0.65	0.99
	C1	33.21	6.13	39.34	5.41	0.81	1.33	0.59	0.69	0.98
	AB1b	38.36	7.01	45.37	5.48	0.87	1.42	0.57	0.68	0.97
	Bkkb	36.91	8.83	45.74	4.18	0.82	1.34	0.42	0.58	0.92
	CB1b	42.56	8.66	51.22	4.91	1.00	1.59	0.46	0.60	0.90
	CB2b	52.05	11.36	63.42	4.58	0.95	1.44	0.44	0.55	0.98
	CB3b	52.33	12.88	65.21	4.06	0.93	1.42	0.39	0.50	1.00
	AB2b	53.78	11.90	65.68	4.52	0.84	1.39	0.48	0.54	1.08
	CB4b	51.58	11.10	62.69	4.65	0.82	1.36	0.50	0.56	1.06
	AB3b	50.48	11.24	61.72	4.49	0.75	1.28	0.50	0.57	1.08
P02	A1	37.01	6.51	43.52	5.68	0.73	1.37	0.69	0.79	0.98
	C1	34.56	6.45	41.00	5.36	0.77	1.35	0.59	0.68	0.99
	ABb	43.90	7.39	51.29	5.94	0.85	1.27	0.66	0.70	1.07
	BC1b	39.39	6.46	45.86	6.09	0.80	1.27	0.72	0.73	1.08
	BCkkb	31.26	5.35	36.62	5.84	0.90	1.29	0.63	0.67	1.04
	BC2b	35.50	5.92	41.42	6.00	0.96	1.35	0.61	0.61	1.08
	BCkb	59.60	9.85	69.45	6.05	0.71	1.33	0.84	0.61	1.45
	BC3b	32.83	4.39	37.22	7.48	1.01	1.42	0.74	0.67	1.07
P03	A1	45.75	8.27	54.02	5.53	0.80	1.40	0.63	0.69	1.06
	AC	55.44	10.61	66.05	5.22	0.82	1.41	0.59	0.66	1.06
	C1	36.11	6.49	42.60	5.57	0.71	1.28	0.69	0.70	1.13
	C2	55.69	11.43	67.11	4.87	0.81	1.37	0.50	0.62	0.95
	ABtb	69.03	13.34	82.37	5.18	0.83	1.28	0.58	0.65	1.07
	Btb	56.70	8.79	65.49	6.45	0.87	1.21	0.72	0.77	1.06
	BCkkb	46.99	7.45	54.45	6.30	0.98	1.23	0.67	0.74	1.04
	BCkb	47.30	7.04	54.35	6.72	1.13	1.20	0.59	0.70	0.91
P04	A1	42.25	6.82	49.07	6.20	0.81	1.39	0.70	0.80	0.98
	AC	40.58	7.86	48.44	5.16	0.76	1.46	0.57	0.65	0.99
	ABb	58.66	11.39	70.05	5.15	0.80	1.39	0.58	0.65	1.06
	Bt1b	48.61	9.30	57.91	5.22	0.83	1.36	0.56	0.65	1.00
	Bt2b	33.35	5.37	38.72	6.21	0.84	1.25	0.69	0.74	1.02
	BCkkb	30.96	5.45	36.41	5.68	0.88	1.28	0.63	0.70	1.04
	BCkb	29.75	4.53	34.28	6.57	1.17	1.44	0.59	0.64	0.98

Normalised REEs profiles relative to UCC are shown in Fig. 8.2. The general trend of the four studied profiles (P01–P04) is similar. They are generally characterised by a positive slope on LREEs side (La-Eu), while the slope is almost flat on the HREE side. However, horizon BCkb of P02 is an exception, with steeper slopes on both the left and right sides.

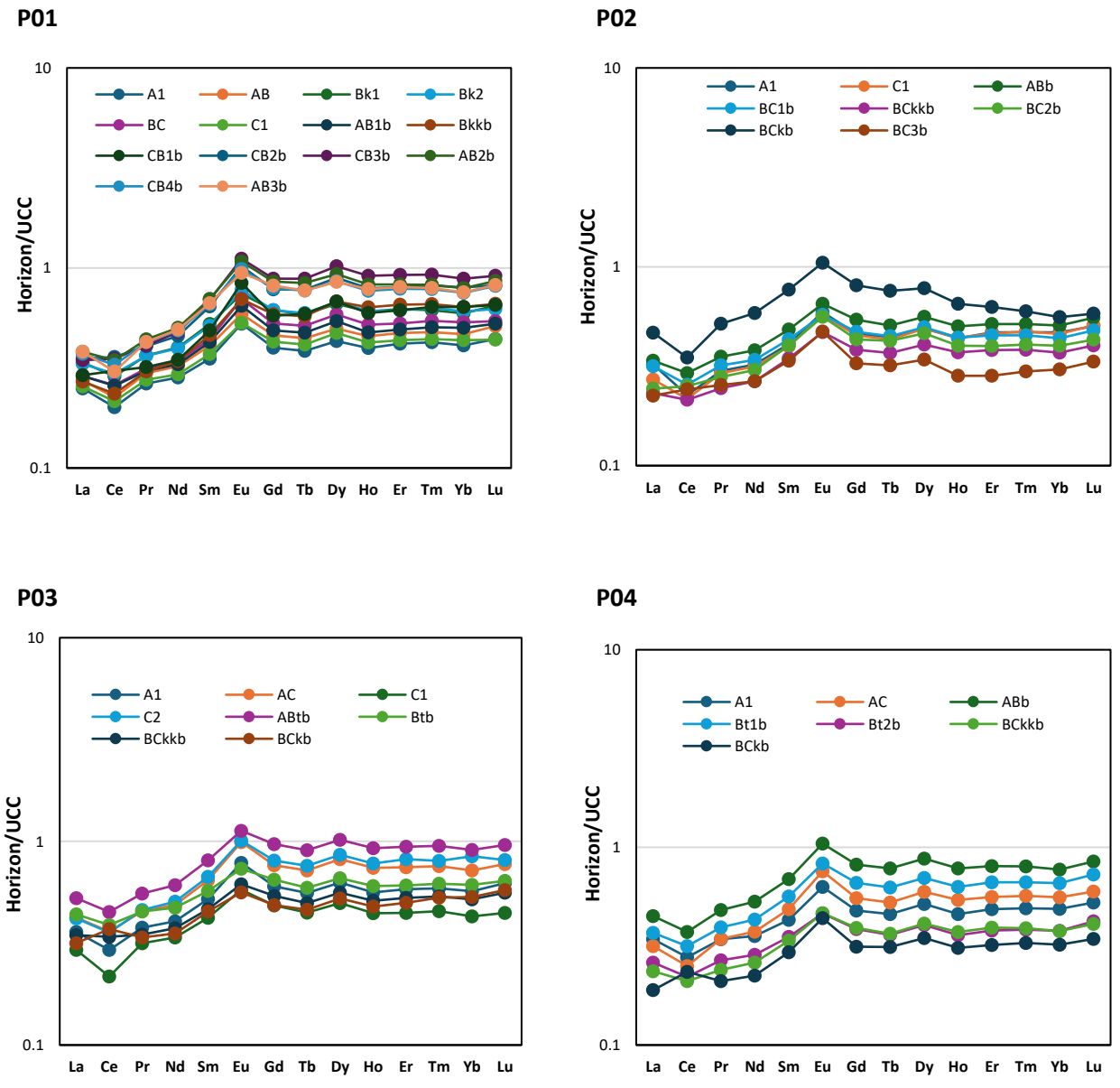


Fig. 8.2. Patterns of REEs in each of the studies soil profiles

8.3.4. REEs in the pedogenic carbonates

The abundance of REEs and their associated indices within the studied carbonates are presented in Table 8.2. These carbonates exhibit a broader range than the surrounding soil matrix. ∑REEs are between a minimum of 29.81 mg kg^{-1}, lower than that observed in the soil matrix and a maximum 200.55 mg kg^{-1}, significantly higher than those in the bulk soil. LREEs range from 22.68 mg kg^{-1} to 166.65 mg kg^{-1}, while HREEs range from 5.55 mg kg^{-1} to 35.89 mg kg^{-1}. LREEs/HREEs is between 2.53 and 5.86.

The δCe in carbonates is characterised by values significantly below 1. They are range from 0.09 to 0.78. Although δEu values are characterised by values above 1, they are within a narrower range than that of the bulk soil matrix, varying between 1.14 and 1.34.

In contrast to $(La/Yb)_N$ values all below 1 observed in the soil matrix, $(La/Yb)_N$ in carbonates range from 0.29 to 1.68, while $(La/Sm)_N$ have values below 1. The values observed are even in a similar range than that in the soil, range from 0.46 to 0.87. $(Gb/Yb)_N$ on the other hand is mostly characterised by values above 1, with a maximum value of 2.07. Furthermore, some carbonates, especially Nd01 (0.92), Nd03 (0.82), Nd04 (0.67) and Nd13 (0.93) are all recorded values below 1.

Patterns of REEs in the carbonates along each profile are presented in Fig. 8.3. P01 samples exhibit a consistent, sub-parallel fractionation trend characterised by a steady increase from LREEs toward HREEs. This positive slope is punctuated by a prominent and sharp negative Cerium anomaly across all profiles, where normalised values drop significantly below the neighbouring La and Pr. Additionally, subtle positive inflections are observed at Eu and Gd before the curves plateau in the HREE region. While the overall morphology of the patterns remains uniform across the dataset, the concentrations vary, with sample Ps displaying the highest enrichment, exceeding the UCC

reference line for most of the series, whereas the Nd01, Nd03, and Nd04 samples remain consistently depleted relative to UCC.

P02 samples show a sharp, overall increase within the LREE group, rising from the initial light elements to a distinct maximum at Eu. This LREE segment is interrupted by a significant and deep negative Cerium anomaly, which marks the absolute minimum across the entire series. Within the HREE group, the profiles exhibit a consistent and gradual negative slope, with normalised values decreasing steadily from Ga through to Lu. Consequently, the transition between these two groups is defined by a peak, with the Nd06 and Nd07 samples remaining largely enriched relative to the UCC, while the Nd05 profile follows a parallel but consistently depleted trend.

P03 and P04 profiles exhibit striking similitudes, both displaying a "plateau-like" morphology characterised by a steep upward gradient in the LREE group followed by a remarkably stable, near-horizontal trend across the HREE group. In both datasets, the LREE segment is defined by a sharp rise that culminates at a distinct Eu peak, though this progression is consistently interrupted by a deep, V-shaped negative Ce anomaly representing the absolute minimum for every sample. The HREE regions for both P03 and P04 show negligible internal fractionation, with the normalised values remaining sub-parallel to the UCC reference line throughout the Dy–Lu range. Furthermore, both profiles share a similar hierarchy of enrichment, featuring a single dominant sample (Nd12 in P03 and Nd17 in P04) that sits largely above the UCC line, while the remaining samples in each set cluster together in a more depleted range.

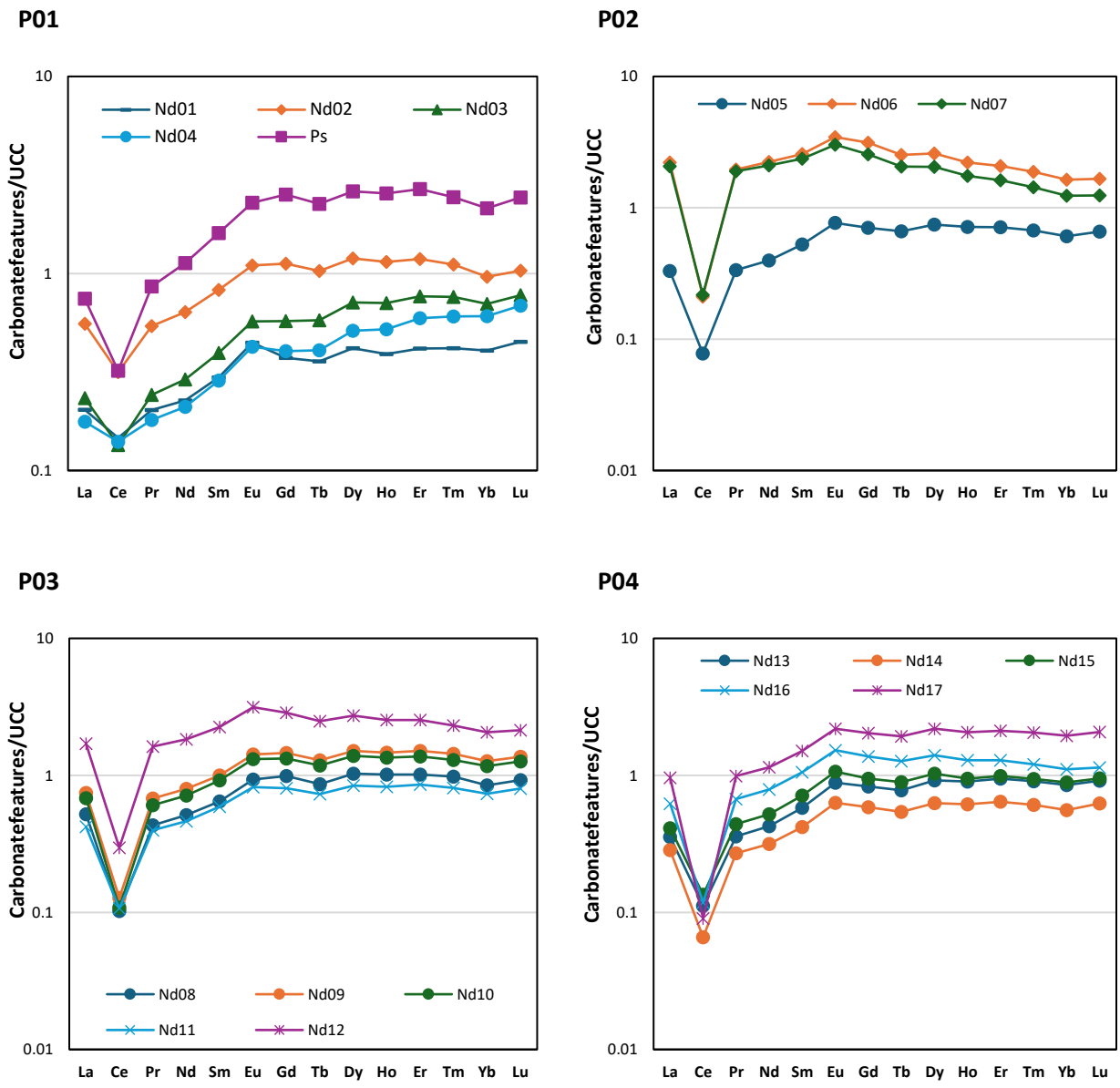


Fig. 8.3. Patterns of REEs in the pedogenic carbonates.

8.3.5. Principal component analysis

The results of the PCA examined the relationships between REEs concentrations and indices, and physico-chemical properties in bulk soil are summarised in Table 8.4 and Fig. 8.4 (a - c). As presented in Table 8.4, PCA reveals that approximately 68% of the total variance in the dataset is explained by the first three dimensions. The first dimension (29.43%) is primarily driven by REEs abundance and fractionation parameters, specifically HREEs, ∑REEs and LREEs/HREEs. The

second dimension (23.84%) identifies the soil's physico-chemical environment as a major factor, with SOM, clay content, pH, and eq$CaCO_3$ acting as the dominant variables. Finally, the third dimension (14.64%) highlights characteristics, such as the $(Gd/Yb)_N$ and δEu. Together, these results indicate that while the absolute concentration of REEs is the primary differentiator (Dim. 1), the soil's' matrix properties (Dim. 2) and the specific internal fractionation patterns (Dim. 3) provide separate, significant layers of geochemical information.

Table 8.4. Contribution of each variable to the first three dimensions of PCA of soil profiles.

	Dim.1	Dim.2	Dim.3
δCe	0.49	5.60	4.61
δEu	1.53	0.00	17.32
LREEs	13.88	1.41	7.75
HREEs	19.32	0.38	1.36
∑REEs	15.36	1.16	6.22
LREEs/HREEs	12.56	0.19	3.71
$(La/Yb)_N$	9.29	1.90	17.24
$(La/Sm)_N$	10.39	7.35	1.20
$(Gb/Yb)_N$	0.01	0.23	32.06
pH(H2O)	0.90	13.66	0.90
EC	1.53	10.24	3.49
OM	0.00	20.47	0.58
EqCaCO3	0.50	13.25	1.79
Clay	2.74	16.59	0.22
Silt	4.40	0.79	1.55
Sand	7.08	6.77	0.00
Eigenvalue	4.58	3.71	2.28
% of variation	29.43	23.84	14.64
% of accumulated variation	29.43	53.28	67.91

Correlation matrix (Fig. 8.4a) and the individual boxplot (Fig. 8.4b) form by the two first dimensions represent 53.28% of the total variance. The variable factor map reveals three distinct clusters of geochemical drivers. The first cluster, aligned heavily with the positive axis of Dim1 (29.4%), consists of ∑REEs, HREEs, and LREEs, indicating that this dimension primarily reflects

the total concentration flux of these elements. Opposing this on the negative Dim1 axis are the fractionation ratios LREEs/HREEs, $(La/Yb)_N$, and $(La/Sm)_N$, demonstrating that as total REE abundance increases, the relative dominance of light elements tends to decrease. The second major grouping is found along the positive Dim2 (23.8%) axis, where pH(H_2O), eq$CaCO_3$, and EC cluster together alongside the δCe. Finally, the negative Dim2 axis is dominated by SOM and Clay, which are inversely related to the carbonate indicators. Moreover, abundance of REEs (∑REEs, HREEs, and LREEs) forms an acute angle with the clay vector, although this angle is notably greater than 60°. This geometric alignment reveals a positive correlation. In contrast, the abundance of REEs forms an oblique angle with the eq$CaCO_3$ group (including pH and EC). This near-orthogonal to obtuse relationship suggests that the total concentration of REEs is poorly correlated to the carbonate content in these soil sections.

The biplot highlights a disparate distribution of individuals, which are scattered across the entire surface of the diagram. Nevertheless, certain significant relationships between the samples and variables can be observed. Horizons with identified carbonate features (Bkkb, BCkkb, BCkb) are mostly aggregated with the eq$CaCO_3$ group. Furthermore, horizons with a high clay content (C2, ABb and Bt1b in P03; AC and AB1tb in P04) are projected around the REEs abundance group.

Principal component analysis results on carbonates are presented in Table 8.5 and Fig. 8.4 (b and d). As reveals by the Table 8.5, the three first dimensions carry 87.51% of the total variation, which is quite significant. Dimension 1 is the primary driver of variance (53.54%), dominated by REE concentrations (∑REEs, LREEs) and heavy-end fractionation indices like $(Gd/Yb)_N$. Dimension 2 (18.18%) shows a distinct shift toward Mg (28.99%) and Ca (18.47%), alongside the LREEs/HREEs and δCe. Dimension 3 (15.80%) is uniquely characterised by the highest contribution from δEu at 23.65% and a significant contribution from Ca and HREEs.

Table 8.5. Contribution of each variable to the first three dimensions of PCA of carbonates.

	Dim.1	Dim.2	Dim.3
δCe	9.69	15.72	0.78
δEu	1.16	0.40	23.65
LREEs	14.41	0.25	6.45
HREEs	11.19	1.64	15.65
∑REEs	14.01	0.03	8.11
LREEs/HREEs	6.63	23.63	6.57
$(La/Yb)_N$	13.30	6.41	3.73
$(La/Sm)_N$	8.46	1.58	14.29
$(Gb/Yb)_N$	14.90	2.88	0.22
Mg	3.57	28.99	1.75
Ca	2.67	18.47	18.80
Eigenvalue	5.56	1.89	1.64
% of variation	53.54	18.18	15.80
% of accumulated variation	53.54	71.72	87.51

The correlation circle (Fig. 8.4b) reveals three distinct geochemical groupings based on their orientation within the factor space. The first group, clustered tightly on the positive side of Dim1, consists of total REE abundance (∑REEs, LREEs) and fractionation indices $(Gb/Yb)_N$ and $(La/Yb)_N$, indicating these variables are highly positively correlated and drive over half of the total variance. In contrast, δCe and Mg are positioned on the negative side of Dim1 and the positive side of Dim2, suggesting an inverse relationship with the main REEs group. A third notable grouping appears in the lower-right quadrant, where Ca and HREEs are positively correlated with each other but negatively correlated with the Mg-rich group. δEu remains relatively central, reflecting a lower contribution to the first two dimensions compared to other variables.

The biplot (Fig. 8.4d) reveals some key relationship between variables and samples. Nd07, Nd06, and Nd12 are characterised by high positive coordinates on Dim1, aligning with the cluster containing ∑REEs, LREEs, and fractionation indices such as $(Gd/Yb)_N$. In contrast, a distinct group of individuals located in the upper-left quadrant, including Nd01, Nd03, and Nd04, shows an association with δCe and Mg. The lower half of the plot features a high density of samples

(Nd08 to Nd11 and Nd13 to Nd17) that align with the negative loading of Ca and HREEs on Dim2. Samples like Nd05 and Ps are positioned near the origin, indicating a minimal contribution.

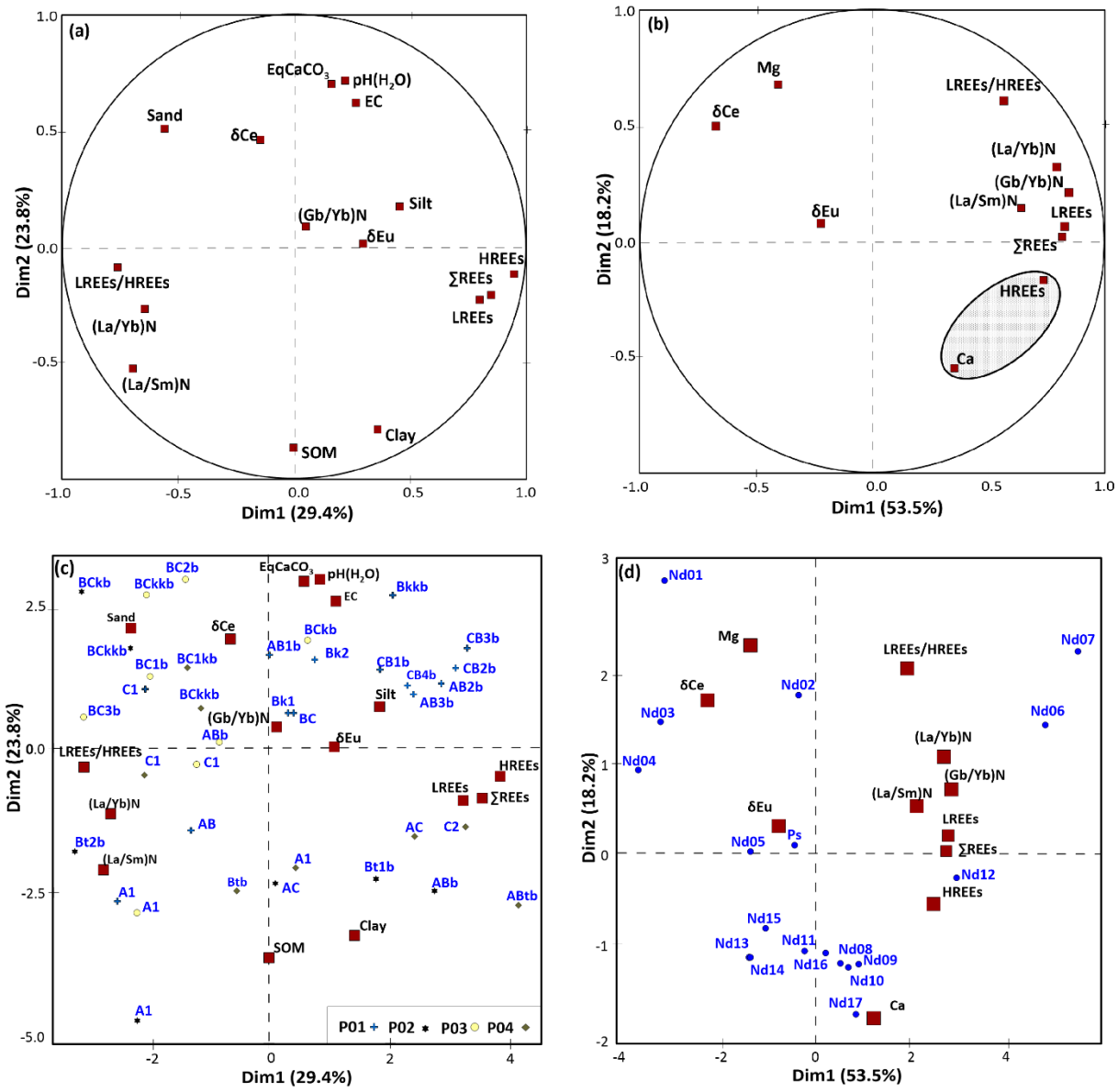


Fig. 8.4. **a.** and **c.** correlation circle and biplot showing relationship between physico-chemical properties, REEs abundance and REEs indices in the soil; **b.** and **d.** correlation circle and biplot showing relationships between Ca, Mg, REEs concentrations and REEs indices in pedogenic carbonates.

8.4. Discussion

8.4.1. REE signatures of pedogenic carbonates and their controls

The results of this study clearly highlight significant differences in REE concentrations and indices between pedogenic carbonates and the bulk soil matrix. For instance, the maximum ∑REE in the soil matrix reaches 82.37 mg kg^{-1}, whereas carbonate samples e.g., Nd07 shows a concentration of 200.55 mg kg^{-1}. PCA further reveals contrasting geochemical behaviours between the soil matrix and carbonates.

In the bulk soil, the correlation circle (Fig. 8.4a) shows opposite trends between total REE abundance and fractionation indices. The group associated with $eqCaCO_3$ contributes only weakly to total REE concentrations, whereas clay content strongly influences REE enrichment. The biplot (Fig. 8.4c) confirms the dominant contribution of clay-rich horizons (ABtb and C2 in P03; ABb and Bt1b in P04) to total REE concentrations. This observation may appear surprising, as previous work had demonstrated that calcification represents the dominant pedogenic process in the studied landscape, whereas chemical weathering and clay formation remain limited (Dina Ebouel et al., under review a). However, this pattern is consistent with the broader understanding that clay formation and soil organic matter complexation exert stronger controls on REE enrichment in soils than carbonate accumulation (Dina Ebouel et al., 2025a).

In contrast, PCA of pedogenic carbonates shows that total REE abundance varies in the same direction as fractionation indices (Fig. 8.4b). Calcium exerts a strong influence on REE abundance in carbonates, particularly for HREEs, whereas Mg and δCe display opposite trends. These results indicate a successful isolation of a carbonate-specific REE signal associated with pedogenic carbonate formation processes. As reported in previous studies (Hum et al., 2026; Valera-Fernández et al., 2020) , pedogenic carbonates are typically characterised by HREE enrichment, a

pattern that is also evident in the UCC-normalised REE distributions of the carbonate analysed in this study (Fig. 8.3).

While the strong influence of Ca on REE abundance is consistent with previous work suggesting that pedogenic carbonate formation involves incorporation of REEs within the crystal lattice (Laveuf and Cornu, 2009), an important caveat merits explicit consideration. Given the trace-element nature of REEs, minor occluded secondary phases (clay or Fe–Mn oxyhydroxides) could, even at low abundance, disproportionately contribute to the bulk REE signal observed in the carbonate features. To evaluate this possibility, a correlation matrix was computed among Ca, Mg concentrations and REE indices in the carbonate features (Appendix 8.3). This reveals only a weak relationship between Ca content and total REE abundance ($r = 0.1$), which is inconsistent with a simple dilution model in which REE enrichment would scale inversely with carbonate purity as occluded, REE-enriched impurities decrease with increasing Ca content. Furthermore, in contrast to the LREE-enriched pattern that characterises the clay-dominated bulk soils (Figure 8.4a), the pedogenic carbonates display a consistent HREE-enriched pattern, which argues against a dominant contribution of detrital clay occlusions to the carbonate REE abundance. Together, these indirect lines of evidence favour crystalline incorporation as the principal control on the REE signatures reported here. Nonetheless, these geochemical arguments alone cannot formally exclude a contribution from occluded Fe–Mn oxyhydroxides, as invoked in the previous chapter. This could impart a comparable HREE-enriched, Ce-depleted signature. Further petrographic characterisation, such as scanning electron microscopy, will be required to conclusively resolve the site of REE incorporation within these carbonates.

Comparison among the studied soil profiles also reveals marked differences in total REE abundances. P01, P02 and P04 exhibit relatively low REE concentrations compared with P03, most

likely reflecting lithological variability. The landscape is underlain by an alternation of sandstone, mudstone and basaltic rocks belonging to the Karoo Supergroup (Dina Ebouel et al., under review a; Smith 1984). Numerous studies have demonstrated that the absolute abundance of REEs in soils is primarily controlled by the parent material, which determines the initial REE signature inherited by the soil matrix (Alfaro et al., 2018; Sababa et al., 2021; Temga et al., 2021). This lithological influence also extends to REE concentrations in pedogenic carbonates. The PCA biplot (Fig. 8.4d) indicates that Nd12 from P03 exerts strong influence on the overall REE trend.

In addition to lithological control, seasonal watercourses likely play a key role in shaping the observed REE distribution. These systems promote the reworking of local rock fragments during episodic depositional events and facilitate the mobilisation and enrichment of elements from soil solutions (Dina Ebouel et al. 2025b; Dina Ebouel et al., under review b). Such hydrological processes likely explain the particularly high REE concentrations observed in carbonate samples Nd06 and Nd07. Moreover, the consistency of δEu between the bulk soil and the carbonates supports a common lithogenic origin, as Eu anomalies are typically controlled by the primary mineralogical composition of the parent material (Sousa et al., 2022).

8.4.2. REEs in pedogenic carbonate as indicator of redox and environmental conditions

The integration of REE signatures with stable isotope data ($\delta^{13}C$, $\delta^{18}O$) and Mn/Fe ratios provides a refined understanding of the mechanisms controlling pedogenic carbonate precipitation along this landscape. Previous work by Dina Ebouel et al. (under review c) showed that the stable isotope composition reflects a relatively stable regional environmental framework, with $\delta^{13}C$ values consistent with a persistent C3-C4 mixed savannah ecosystem and $\delta^{18}O$ values suggesting limited hydroclimatic variability. In contrast, Mn/Fe ratios reveal strong local heterogeneity associated with transient redox conditions linked to episodic soil saturation and fluvial pulses. Within this

context, the cerium anomaly (δCe) identified in the present REE dataset provides a particularly sensitive indicator of the immediate geochemical conditions prevailing during carbonate precipitation.

The negative Ce anomaly observed in the pedogenic carbonates likely reflects oxidising conditions in the soil environment prior to carbonate formation (Dietrich et al., 2021). Cerium is unique among the rare earth elements because it can be oxidised from Ce^{3+} to the less soluble Ce^{4+}, which readily precipitates or becomes preferentially scavenged by Fe–Mn oxyhydroxides (Davranche et al., 2005; Li et al., 2023). As a result, soil pore waters become relatively depleted in Ce compared with neighbouring REEs. Carbonates precipitating from these solutions therefore incorporate proportionally less Ce, producing a negative Ce anomaly.

Unlike Mn/Fe ratios, which display strong local heterogeneity across samples a pronounced negative Ce anomaly is consistently observed in all analysed carbonates (P01–P04), reaching extreme depletion in samples such as Nd06 (δCe = 0.10). This contrast is consistent with the fundamentally different redox behaviour of Ce relative to Fe and Mn. Once oxidised to the less soluble Ce^{4+}, Ce is removed from the soil solution, whether through direct precipitation as cerianite (CeO_2) or through scavenging onto Fe–Mn oxyhydroxides. This depletion typically persists in the regolith even as the remaining trivalent REEs continue to be mobilised (Braun et al., 1990). Because REEs are incorporated into the calcite lattice via substitution for Ca^{2+}, with partition coefficients that are comparatively high and broadly uniform across the REE series (Webb and Kamber, 2000; Zhong and Mucci, 1995). The pronounced Ce depletion recorded in the carbonates is unlikely to result from differential incorporation kinetics during crystal growth. Rather, it more plausibly reflects the cumulative oxidative history of the parent soil solution, imprinted prior to precipitation, rather than requiring carbonate formation itself to be short-lived or episodic.

However, this interpretation remains provisional: as noted in Section 8.4.1, the internal microtextural distribution of Fe–Mn oxyhydroxides within the nodules, and hence the specific pathway through which Ce depletion is imprinted and preserved, has not yet been directly confirmed petrographically, and represents a priority for future work.

Expanding beyond the stable isotope signals discussed in Dina Ebouel et al. (under review c), which primarily reflect evaporation and the isotopic composition of recharge waters, the REE data provide a complementary, process-based perspective on carbonate genesis. Rather than reflecting the composition of the bulk soil matrix, from which it is expected to differ even under equilibrium conditions owing to preferential REE fractionation during solid–solution exchange (e.g., clay-controlled LREE retention, oxidative Ce scavenging; Section 8.4.1), the carbonate REE signature instead records the composition of the pore-water solution at the time of precipitation. The pronounced and consistent Ce depletion, together with the marked LREE/HREE fractionation revealed by UCC-normalised patterns (Fig. 8.3), indicates that this pore-water solution was itself highly evolved, having already undergone substantial, largely irreversible REE fractionation prior to, rather than during, carbonate precipitation.

Consequently, the observed REE fractionation cannot be explained simply as a by-product of progressive evaporative concentration, since evaporation alone would not selectively deplete Ce or fractionate LREE from HREE. Rather, these patterns are best explained by the redox-driven, largely irreversible evolution of the soil pore-water solution described above (Section 8.4.2), which imprints a distinctive geochemical signature on the carbonate irrespective of whether precipitation itself occurred rapidly, following discrete rainfall events, or more gradually, over the course of seasonal wetting–drying cycles. Both scenarios are broadly consistent with the semi-arid climate of the region, characterised by fluctuating redox conditions associated with wetting–drying cycles.

However, it is impossible to distinguish between them using the resolution provided by the current ERE dataset. This would require independent textural or petrographic evidence (e.g. growth bands, microstratigraphy), which we consider to be a priority for future work.

8.4.3. Pedogenic vs. lithogenic origin: A high-resolution approach

As opined by Laveuf and Cornu (2009), pedogenic carbonates can be distinguished from lithogenic carbonates based on their REE fractionation patterns, particularly the LREE/HREE ratio and the cerium anomaly. Pedogenic carbonates are typically characterised by a negative cerium anomaly and a relative enrichment in HREEs compared with LREEs. This geochemical signature has been documented in several previous studies and is considered diagnostic of pedogenic carbonate formation (Dietrich et al., 2021; Hum et al., 2026; Valera-Fernández et al., 2020).

In this study, all the carbonates have negative cerium anomalies together with HREE enrichment. These fractionation patterns therefore support a pedogenic origin for the carbonates rather than a lithogenic or sedimentary source. This result further demonstrates that a small-scale approach focusing on individual carbonates forms allows the origin of carbonates to be reconstructed using REE signatures as a geochemical fingerprint. At the scale of the soil profile, however, this signal may be partially obscured by other pedogenic processes, which tend to homogenise the REE composition of the bulk soil (Dina Ebouel et al., 2025a).

Despite this common pedogenic signature, it remains difficult to establish a clear distinction between the carbonate forms based solely on their stage of development or morphology. As illustrated by the biplot in Fig. 8.4d, the main variations in REE signatures among the carbonates are instead related to the relative abundance of Ca and Mg, which likely reflects differences in lithology. Carbonates from profile P01, including both nodules and pseudomycelia, are characterised by relatively high Mg contents and comparatively low REE concentrations. In

contrast, carbonate forms from the other profiles exhibit a relative enrichment in Ca together with higher REE abundances, suggesting that lithological controls exert a stronger influence on REE distribution than the morphological type of the carbonates.

Overall, there is a finding that pedogenic carbonates possess REE signatures distinct from those of the surrounding soil matrix. Whereas REE enrichment in the bulk soil is mainly controlled by clay-rich horizons, carbonates exhibit coupled variations between REE abundance and fractionation indices, together with a characteristic HREE enrichment. Variations in absolute REE concentrations among profiles primarily reflect lithological differences within the Karoo Supergroup, with additional influence from local hydrological reworking. The systematic negative Ce anomalies recorded in the carbonate samples indicate oxidising conditions during carbonate formation and emphasise the sensitivity of REE signatures to short-lived geochemical conditions. Collectively, these patterns confirm the pedogenic origin of the carbonates and demonstrate that REE distributions preserved within individual carbonate structures provide a robust geochemical fingerprint of their formation processes.

8.5. Conclusions

This study demonstrates that rare earth element signatures provide a useful geochemical framework for disentangling the processes controlling carbonate accumulation in semi-arid soils. The contrasting behaviour observed between the bulk soil matrix and discrete carbonate forms highlights that REE distributions recorded at the scale of individual pedogenic structures capture geochemical signals that may be obscured in bulk soil analyses. The systematic cerium depletion and HREE enrichment identified in the carbonates indicate precipitation from oxidised soil solutions that evolved during episodic wetting–drying cycles. At the landscape scale, variations in absolute REE concentrations further reflect the influence of parent lithology and local hydrological

redistribution along the seasonal drainage system. These results emphasise the importance of combining micro-scale carbonate sampling with REE geochemistry to better constrain carbonate formation pathways in pedosedimentary environments. Such an approach contributes to improving the identification of pedogenic carbonates and offers new perspectives for interpreting soil inorganic carbon dynamics in semi-arid landscapes.

References

Alfaro, M.R., Nascimento, C.W.A. do, Biondi, C.M., Silva, Ygor Jacques Agra Bezerra da, Silva, Yuri Jacques Agra Bezerra da, Accioly, A.M. de A., Montero, A., Ugarte, O.M., Estevez, J., 2018. Rare-earth-element geochemistry in soils developed in different geological settings of Cuba. Catena (Amst). 162, 317–324. https://doi.org/10.1016/J.CATENA.2017.10.031

Braun, J.-J., Pagel, M., Muller, J.-P., Bilong, P., Michard, A., Guillet, B., 1990. Cerium anomalies in lateritic profiles. Geochim. Cosmochim. Acta 54, 781–795. https://doi.org/https://doi.org/10.1016/0016-7037(90)90373-S

Cerling, T.E., Quade, J., 1993. Stable Carbon and Oxygen Isotopes in Soil Carbonates, in: Climate Change in Continental Isotopic Records, Geophysical Monograph Series. pp. 217–231. https://doi.org/https://doi.org/10.1029/GM078p0217

Dal Sasso, G., Zerboni, A., Maritan, L., Angelini, I., Compostella, C., Usai, D., Artioli, G., 2018. Radiocarbon dating reveals the timing of formation and development of pedogenic calcium carbonate concretions in Central Sudan during the Holocene. Geochim. Cosmochim. Acta 238, 16–35. https://doi.org/10.1016/j.gca.2018.06.037

Davranche, M., Pourret, O., Gruau, G., Dia, A., Le Coz-Bouhnik, M., 2005. Adsorption of REE(III)-humate complexes onto MnO2: Experimental evidence for cerium anomaly and lanthanide tetrad effect suppression. Geochim. Cosmochim. Acta 69, 4825–4835. https://doi.org/https://doi.org/10.1016/j.gca.2005.06.005

Dietrich, F., Diaz, N., Deschamps, P., Ngounou Ngatcha, B., Sebag, D., Verrecchia, E.P., 2017. Origin of calcium in pedogenic carbonate nodules from silicate watersheds in the Far North Region of Cameroon: Respective contribution of in situ weathering source and dust input. Chem. Geol. 460, 54–69. https://doi.org/10.1016/j.chemgeo.2017.04.015

Dietrich, F., Diaz, N., Deschamps, P., Sebag, D., Verrecchia, E., 2021. Calcium transfer and mass balance associated with soil carbonate in a semi-arid silicate watershed (North Cameroon): An overlooked geochemical cascade? Depositional Record 2021. https://doi.org/10.1002/dep2.134ï

Dina Ebouel, F.J., Betsi, T.B., Eze, P.N., 2024. Soil inorganic carbon: A review of global research trends, analytical techniques, ecosystem functions and critical knowledge gaps. Catena (Amst). 242, 108112. https://doi.org/https://doi.org/10.1016/j.catena.2024.108112

Dina Ebouel, F.J., Kono Ebede, C.G., Bineli Betsi, T., Eze, P.N., 2025a. Distribution and potential of rare earth elements fingerprinting as tracers for carbonate sources in soils developed on contrasting parent materials. Geoderma Regional 43, e01009. https://doi.org/https://doi.org/10.1016/j.geodrs.2025.e01009

Dina Ebouel, F.J., Molwalefhe, L.N., Betsi, T.B., Eze, P.N., 2025b. A Multi-Proxy Pedosedimentary Insight into Calcium Origin, Sediment Provenance, and Depositional Environments in a NW Botswana Landform. Earth Systems and Environment. https://doi.org/10.1007/s41748-025-00724-w

Egli, M., Bösiger, M., Lamorski, K., Sławiński, C., Plötze, M., Wiesenberg, G.L.B., Tikhomirov, D., Musso, A., Hsu, S.-Y., Raimondi, S., 2021. Pedogenesis and carbon sequestration in transformed agricultural soils of Sicily. Geoderma 402, 115355. https://doi.org/https://doi.org/10.1016/j.geoderma.2021.115355

Fischer-Femal, B.J., Bowen, G.J., 2021. Coupled carbon and oxygen isotope model for pedogenic carbonates. Geochim. Cosmochim. Acta 294, 126 – 144. https://doi.org/10.1016/j.gca.2020.10.022

Food and Agriculture Organization of the United Nations, 2006. Guidelines for soil description. Food and Agriculture Organization of the United Nations.

Fox, D.L., Honey, J.G., Martin, R.A., Peláez-Campomanes, P., 2012. Pedogenic carbonate stable isotope record of environmental change during the Neogene in the southern Great Plains, southwest Kansas, USA: Oxygen isotopes and paleoclimate during the evolution of C4-dominated grasslands. Bulletin of the Geological Society of America 124, 431–443. https://doi.org/10.1130/B30402.1

Franchi, F., Kelepile, T., Di Capua, A., De Wit, M.C.J., Kemiso, O., Lasarwe, R., Catuneanu, O., 2021. Lithostratigraphy, sedimentary petrography and geochemistry of the Upper Karoo Supergroup in the Central Kalahari Karoo Sub-Basin, Botswana. Journal of African Earth Sciences 173. https://doi.org/10.1016/j.jafrearsci.2020.104025

Gile, L.H., 1993. Carbonate Stages in Sandy soils of Leasburg surface, Souther New Mexico. Soil Sci. 156.

Hum, H.Z., Chu, M.-F., Huang, W.-S., Zehetner, F., Hseu, Z.-Y., 2026. Fractionation of rare earth elements in carbonate nodules of alluvial soils along a chronosequence. Catena (Amst). 264, 109704. https://doi.org/https://doi.org/10.1016/j.catena.2025.109704

Kelson, J.R., Huth, T.E., Andrews, K., Bartleson, M.N., Cerling, T.E., Jin, L., Salinas, M.P., Levin, N.E., 2025. Pedogenic carbonate as a transient soil component in a humid, temperate forest (Michigan, USA). Quat. Res. 124, 105–120. https://doi.org/DOI: 10.1017/qua.2024.41

Laveuf, C., Cornu, S., 2009. A review on the potentiality of Rare Earth Elements to trace pedogenetic processes. Geoderma 154, 1–12. https://doi.org/10.1016/J.GEODERMA.2009.10.002

Li, W., Nakada, R., Takahashi, Y., Gaschnig, R.M., Hu, Y., Shakouri, M., Rudnick, R.L., Liu, X.-M., 2023. Cerium geochemical composition of the upper continental crust through time: Implications for tracing past surface redox conditions. Geochim. Cosmochim. Acta 359, 20–29. https://doi.org/https://doi.org/10.1016/j.gca.2023.08.024

Millière, L., Gussone, N., Moritz, T., Bindschedler, S., Verrecchia, E.P., 2019. Origin of strontium and calcium in pedogenic needle fibre calcite (NFC). Chem. Geol. 524, 329–344. https://doi.org/10.1016/j.chemgeo.2019.06.022

Rollinson, H., Pease, V. (Eds.), 2021. Using Major Element Data, in: Using Geochemical Data: To Understand Geological Processes. Cambridge University Press, Cambridge, pp. 49–95. https://doi.org/DOI: 10.1017/9781108777834.006

Sababa, E., Essomba Owona, L.G., Temga, J.P., Ndjigui, P.-D., 2021. Petrology of weathering materials developed on granites in Biou area, North-Cameroon: implication for rare-earth elements (REE) exploration in semi-arid regions. Heliyon 7. https://doi.org/10.1016/j.heliyon.2021.e08581

Smith, A., R., 1984. The Lithostratigraphy of the Karoo Supergroup in Botswana. Geol. Mag. 123, 710–711. https://doi.org/DOI: 10.1017/S0016756800024328

Sousa, T.A., Venancio, I.M., Marques, E.D., Figueiredo, T.S., Nascimento, R.A., Smoak, J.M., Albuquerque, A.L.S., Valeriano, C.M., Silva-Filho, E.V., 2022. REE Anomalies Changes in Bottom Sediments Applied in the Western Equatorial Atlantic Since the Last Interglacial. Front. Mar. Sci. Volume 9-2022. https://doi.org/10.3389/fmars.2022.846976

Stadler, S., Osenbrück, K., Suckow, A.O., Himmelsbach, T., Hötzl, H., 2010. Groundwater flow regime, recharge and regional-scale solute transport in the semi-arid Kalahari of Botswana derived from isotope hydrology and hydrochemistry. J. Hydrol. (Amst). 388, 291–303. https://doi.org/https://doi.org/10.1016/j.jhydrol.2010.05.008

Stanbery, C., Ghahremani, Z., Huber, D.P., Will, R., Benner, S.G., Glenn, N., Hanif, T., Spaete, L., Terhaar, D., Lohse, K.A., Seyfried, M., Freutel, W., Pierce, J.L., 2023. Controls on the presence and storage of soil inorganic carbon in a semi-arid watershed. Catena (Amst). 225, 106980. https://doi.org/https://doi.org/10.1016/j.catena.2023.106980

Taylor, S.R., McLennan, S.M., 1985. The Continental Crust: Its Composition and Evolution. Geol. Mag. 122, 673–674. https://doi.org/DOI: 10.1017/S0016756800032167

Temga, J.P., Sababa, E., Mamdem, L.E., Bijeck, M.L.N., Azinwi, P.T., Tehna, N., Zo'o Zame, P., Onana, V.L., Nguetnkam, J.P., Bitom, L.D., Ndjigui, P.D., 2021. Rare earth elements in tropical soils, Cameroon soils (Central Africa). Geoderma Regional 25, e00369. https://doi.org/10.1016/J.GEODRS.2021.E00369

Valera-Fernández, D., Cabadas-Báez, H., Solleiro-Rebolledo, E., Landa-Arreguín, F.J., Sedov, S., 2020. Pedogenic carbonate crusts (calcretes) in karstic landscapes as archives for paleoenvironmental reconstructions – A case study from Yucatan Peninsula, Mexico. Catena (Amst). 194. https://doi.org/10.1016/j.catena.2020.104635

Walkley, A., Black, I.A., 1934. An examination of the degtjareff method for determining soil organic matter, and a proposed modification of the chromic acid titration method. Soil Sci. 37.

Webb, G.E., Kamber, B.S., 2000. Rare earth elements in Holocene reefal microbialites: a new shallow seawater proxy. Geochim. Cosmochim. Acta 64, 1557–1565. https://doi.org/https://doi.org/10.1016/S0016-7037(99)00400-7

Wolff, K., Tiddy, C., Giles, D., Hill, S.M., Gordon, G., 2017. Distinguishing pedogenic carbonates from weathered marine carbonates on the Yorke Peninsula, South Australia: Implications for mineral exploration. J. Geochem. Explor. 181, 81–98. https://doi.org/10.1016/j.gexplo.2017.06.019

Zamanian, K., Pustovoytov, K., Kuzyakov, Y., 2016. Pedogenic carbonates: Forms and formation processes. Earth. Sci. Rev. https://doi.org/10.1016/j.earscirev.2016.03.003

Zamanian, K., Zhou, J., Kuzyakov, Y., 2021. Soil carbonates: The unaccounted, irrecoverable carbon source. Geoderma 384, 114817. https://doi.org/https://doi.org/10.1016/j.geoderma.2020.114817

Zhong, S., Mucci, A., 1995. Partitioning of rare earth elements (REEs) between calcite and seawater solutions at 25°C and 1 atm, and high dissolved REE concentrations. Geochim. Cosmochim. Acta 59, 443–453. https://doi.org/https://doi.org/10.1016/0016-7037(94)00381-U

Appendices

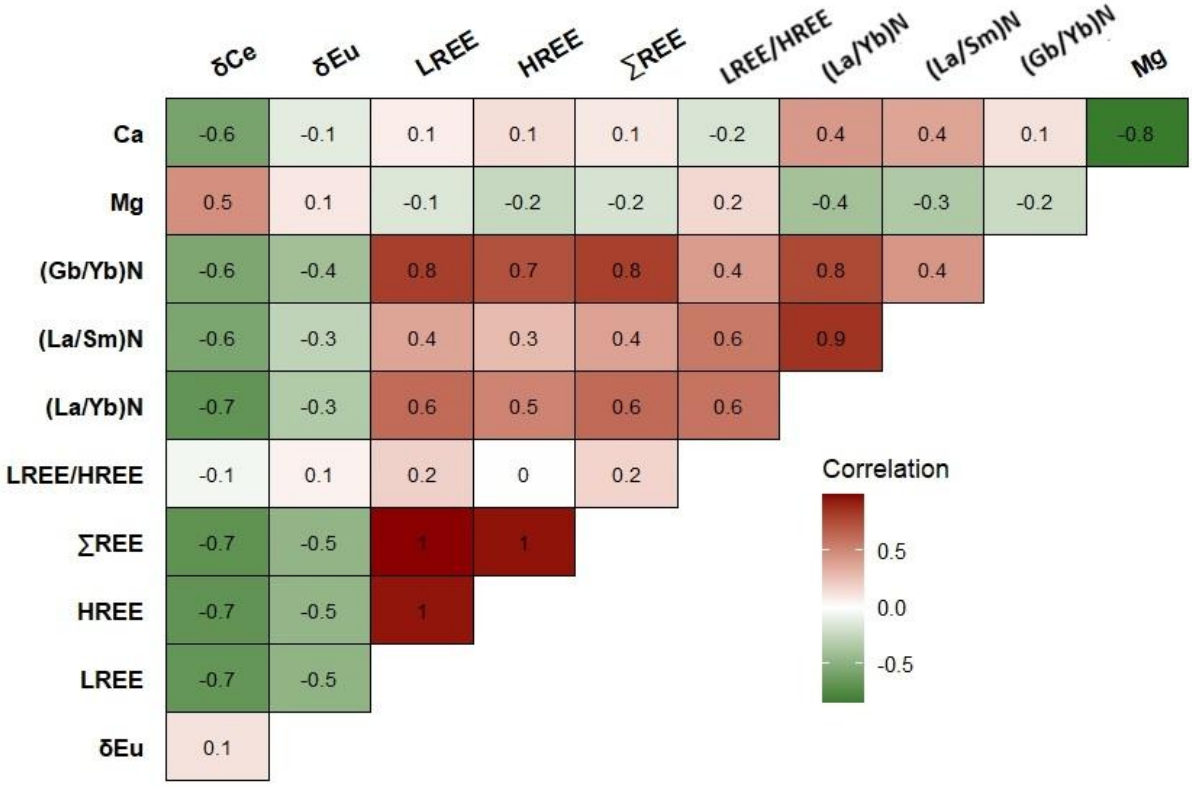
Appendix 8.1. Physico-chemical properties of the studied soil profiles.

Profile	Horizon	pH(H2O)	EC (dS/m)	SOM (wt.%)	EqCaCO$_3$ (wt.%)	Clay	Silt	Sand
P01	A1	6.80	0.21	0.41	0.07	18	8	74
	AB	7.55	0.22	0.31	0.10	19	10	71
	Bk1	7.80	0.56	0.34	2.62	5	16	79
	Bk2	7.95	0.56	0.24	6.35	5	21	74
	BC	8.10	0.40	0.28	3.56	16	18	66
	C1	8.30	0.28	0.21	1.62	10	6	84
	AB1b	7.90	1.44	0.24	9.39	9	24	67
	Bkkb	8.10	0.94	0.21	24.61	7	36	58
	CB1b	8.00	0.87	0.28	0.92	9	27	64
	CB2b	7.73	1.17	0.25	0.98	8	25	67
	CB3b	7.80	0.81	0.24	0.57	6	13	81
	AB2b	7.65	1.41	0.19	0.73	14	12	74
	CB4b	7.70	1.00	0.19	1.05	12	13	75
	AB3b	7.73	1.67	0.24	2.18	14	13	73
P02	A1	6.90	0.35	0.52	0.22	12	14	74
	C1	7.35	0.21	0.27	1.52	9	20	71
	ABb	7.55	1.55	0.38	1.18	6	18	76
	BC1b	7.60	1.95	0.21	1.56	4	15	81
	BCkkb	7.83	2.81	0.26	14.24	4	19	78
	BC2b	7.85	2.50	0.19	1.96	4	15	81
	BCkb	7.95	2.40	0.21	5.94	3	16	81
	BC3b	8.40	0.34	0.28	0.29	14	20	66
P03	A1	7.30	0.31	0.41	0.58	21	22	57
	AC	7.60	0.26	0.34	2.44	25	28	47
	C1	7.60	0.24	0.25	1.11	11	8	81
	C2	7.77	0.38	0.34	1.70	31	25	43
	ABtb	7.83	0.35	0.43	2.91	50	23	27
	Btb	7.70	0.28	0.33	0.28	31	10	59
	BCkkb	7.83	0.25	0.24	16.25	9	19	73
	BCkb	7.80	0.22	0.21	4.00	5	19	76
P04	A1	6.40	0.14	0.62	0.02	15	16	69
	AC	6.80	0.25	0.34	0.07	17	18	65
	ABb	7.40	0.37	0.43	1.73	39	18	43
	Bt1b	7.30	0.78	0.48	0.50	33	22	45
	Bt2b	7.35	0.41	0.36	0.29	22	6	72
	BCkkb	7.53	0.42	0.24	21.09	4	22	74
	BCkb	7.73	0.34	0.23	6.19	3	15	82

Appendix 8.2. REEs concentration in the studied soil profiles.

Profile	Sample	La	Ce	Pr	Nd	Sm	Eu	Gd	Tb	Dy	Ho	Er	Tm	Yb	Lu
		mg kg^{-1}													
P01	A1	7.50	12.89	1.88	7.37	1.58	0.46	1.52	0.25	1.51	0.32	0.96	0.14	0.90	0.14
	AB	8.23	14.44	2.11	8.39	1.84	0.52	1.75	0.28	1.74	0.36	1.09	0.16	1.03	0.16
	Bk1	10.12	18.38	2.59	10.40	2.36	0.65	2.33	0.38	2.31	0.48	1.43	0.20	1.31	0.21
	Bk2	9.95	18.94	2.58	10.31	2.31	0.68	2.33	0.38	2.35	0.49	1.41	0.21	1.33	0.20
	BC	8.65	16.61	2.23	8.87	1.98	0.62	2.00	0.33	2.05	0.42	1.21	0.18	1.18	0.17
	C1	7.67	13.80	1.96	7.64	1.67	0.47	1.63	0.26	1.66	0.34	1.00	0.15	0.96	0.14
	AB1b	8.65	16.47	2.17	8.58	1.92	0.57	1.85	0.30	1.90	0.38	1.13	0.17	1.11	0.17
	Bkkb	8.10	15.06	2.16	8.90	2.08	0.61	2.23	0.37	2.38	0.51	1.51	0.22	1.40	0.21
	CB1b	8.74	19.59	2.27	9.02	2.20	0.74	2.19	0.38	2.38	0.48	1.41	0.21	1.40	0.21
	CB2b	10.56	22.93	2.88	11.90	2.89	0.90	2.97	0.50	3.12	0.63	1.85	0.27	1.76	0.26
	CB3b	10.38	22.54	2.91	12.41	3.12	0.98	3.36	0.57	3.56	0.73	2.12	0.31	1.94	0.29
	AB2b	11.42	22.11	3.12	13.03	3.15	0.95	3.24	0.54	3.26	0.66	1.90	0.27	1.74	0.28
	CB4b	11.16	20.96	3.01	12.61	2.97	0.87	3.01	0.49	3.01	0.62	1.81	0.26	1.65	0.26
	AB3b	11.42	19.42	3.03	12.79	2.99	0.83	3.10	0.49	2.98	0.63	1.85	0.26	1.66	0.26
P02	A1	9.68	14.47	2.12	8.38	1.84	0.52	1.75	0.28	1.72	0.35	1.08	0.15	1.03	0.16
	C1	8.14	13.86	2.07	8.19	1.79	0.50	1.72	0.28	1.71	0.35	1.06	0.16	1.01	0.16
	ABb	10.09	18.68	2.50	9.88	2.17	0.57	2.06	0.32	1.96	0.40	1.18	0.17	1.12	0.18
	BC1b	9.49	16.34	2.27	8.85	1.94	0.50	1.79	0.29	1.74	0.35	1.04	0.15	0.96	0.15
	BCkkb	6.94	13.70	1.74	6.91	1.56	0.41	1.46	0.24	1.42	0.30	0.88	0.13	0.81	0.13
	BC2b	7.31	16.04	1.98	7.87	1.81	0.49	1.64	0.27	1.62	0.32	0.92	0.13	0.88	0.14
	BCkb	14.00	22.35	3.67	15.21	3.45	0.92	3.07	0.48	2.73	0.52	1.44	0.20	1.23	0.19
	BC3b	6.75	15.45	1.81	6.90	1.52	0.41	1.24	0.20	1.19	0.23	0.65	0.10	0.67	0.11
P03	A1	10.77	18.74	2.68	10.52	2.34	0.69	2.29	0.36	2.20	0.45	1.34	0.19	1.25	0.20
	AC	12.67	23.09	3.22	12.69	2.90	0.87	2.90	0.46	2.86	0.59	1.72	0.25	1.58	0.25
	C1	8.80	13.89	2.24	8.78	1.90	0.51	1.84	0.29	1.74	0.36	1.02	0.15	0.94	0.14
	C2	12.56	22.83	3.27	13.13	3.01	0.89	3.05	0.49	3.00	0.62	1.88	0.27	1.86	0.26
	ABtb	15.80	28.83	3.93	15.84	3.64	0.99	3.68	0.58	3.56	0.74	2.16	0.31	1.99	0.31
	Btb	13.14	24.86	3.21	12.27	2.57	0.65	2.47	0.38	2.31	0.48	1.40	0.20	1.35	0.20
	BCkkb	10.39	21.76	2.48	9.73	2.09	0.54	2.05	0.32	1.96	0.41	1.21	0.18	1.14	0.18
	BCkb	9.50	23.70	2.39	9.18	2.04	0.49	1.85	0.30	1.83	0.38	1.15	0.18	1.17	0.18
P04	A1	10.28	17.79	2.44	9.25	1.93	0.55	1.82	0.29	1.81	0.37	1.12	0.16	1.07	0.17
	AC	9.48	16.06	2.45	9.73	2.20	0.67	2.10	0.34	2.09	0.43	1.29	0.19	1.23	0.19
	ABb	13.48	23.89	3.43	13.83	3.11	0.92	3.11	0.50	3.08	0.63	1.85	0.26	1.70	0.27
	Bt1b	11.08	20.25	2.80	11.21	2.54	0.73	2.51	0.40	2.45	0.51	1.53	0.22	1.45	0.23
	Bt2b	7.84	14.17	1.90	7.44	1.59	0.41	1.47	0.23	1.42	0.29	0.87	0.13	0.83	0.14
	BCkkb	7.07	13.46	1.70	6.79	1.52	0.41	1.49	0.23	1.44	0.30	0.90	0.13	0.83	0.13
	BCkb	5.69	15.02	1.50	5.83	1.33	0.39	1.20	0.20	1.22	0.25	0.74	0.11	0.71	0.11

Appendix 8.3. Correlation matrix between REE indices, Mg and Ca within carbonate features.



CHAPTER NINE

Conclusions

9.1. Recapitulation of the problem statement and objectives

This thesis was driven by the need to tackle the "missing" parts of the global carbon budget, particularly the often-ignored role of SIC in carbon sequestration. While global efforts have mainly concentrated on SOC, the significant potential of drylands, which cover nearly 70% of the African continent, is still largely absent from carbon accounting and climate policy. The main goal of this research was to characterise and quantify SIC in Botswana's landscapes, identify the main sources of calcium using high-resolution geochemical tracers, and reconstruct the past environmental conditions preserved in these carbonate records.

9.2. Synthesis of key findings

The research conducted across the diverse landscapes of Botswana produces several key insights into the formation processes, the sources of calcium ions, and environmental significance of SIC. Calcification is the predominant pedogenic process, with pedogenic carbonate accumulations reaching concentrations of up to 22%, consistent with the substantial contribution of SIC to soil carbon storage in semi-arid environments (Raheb et al., 2016).

The study also highlights contrasting geochemical pathways governing calcium mobilisation in SIC across Botswana's landscapes. In north-western Botswana (the Chobe enclave), calcium originates primarily from the weathering of distal felsic rocks or from local lithogenic carbonate accumulation, which is favoured by fluvial-lacustrine systems. Conversely, the fluvial landscapes of central Botswana primary exhibit local lithogenic control, with calcium mainly supplied by the

in-situ weathering of basaltic rocks (Stormberg lavas). This process provides a direct and efficient pathway for the capture of atmospheric CO_2 through the formation of pedogenic carbonates.

This study establishes a transferable framework for predicting calcium mobilisation and SIC formation across dryland systems. These results highlight that carbon sequestration processes in drylands are highly context-dependent, and that effective carbon management strategies must account for fundamental differences between geological contexts.

The ability to differentiate between the origins of carbonates using REEs depends strongly on the resolution of the analytical approach. Regional-scale analyses based on bulk soil samples were insufficient to clearly differentiate lithogenic carbonates dominated from pedogenic carbonates dominated area. By contrast, high-precision analyses at the fluvial landscape scale, combined with the isolation of carbonate features (nodules and pseudomycelia), effectively eliminate environmental noise and reveal diagnostic fractionation patterns. These include HREE enrichment and negative cerium anomalies in pedogenic carbonates.

Stable isotopic signatures ($\delta^{13}C$ and $\delta^{18}O$) preserved in pedogenic carbonates can be used to reconstruct past vegetation dynamics and hydroclimatic conditions. Moreover, Mn/Fe ratio and negative Ce anomalies of pedogenic carbonate highlighted act as a geochemical snapshot of brief saturation followed by rapid desiccation. These demonstrate that pedogenic carbonates constitute a robust long-term archive, particularly in regions where other terrestrial palaeoenvironmental proxies are limited or absent.

9.3. Significance and contributions

This thesis makes three key contributions with direct implications on land management and sustainable development in dryland environment. From a methodological perspective, the study demonstrates the value of integrating REEs with morphological and isotopic analyses to trace the

origin of carbonates. This synergy provides a robust tool for refining carbon accounting frameworks in the soils of these regions. From a theoretical point of view, this work challenges the systematic overlooked of SIC. By revealing high prevalence of pedogenic carbonates in the semi-arid area of Botswana, the thesis highlights the imperative to integrate this natural pathway of carbon sequestration into climate change mitigation strategies. At the regional scale, the study establishes the first comprehensive geochemical baseline analysis of SIC in Botswana, identifying contrasting sequestration mechanisms between basaltic and sedimentary systems. This scientific distinction justifies spatially tailored land management: to be effective, carbon conservation and storage policies must be adapted to local geological contexts. Collectively, these findings provide a scientific basis for the systematic integration of SIC into sustainable land-use planning and climate governance frameworks in drylands.

9.4. Limitations of the study

Despite the high resolution of the geochemical data, some limitations remain. While spatial contrasts between the Kalahari Basin and the Eastern Hardveld are considered, a fully comprehensive account of variability across all of Botswana's microclimates is not provided. These microclimates are characterised by a complex geological background and subtle variations in rainfall from south to north (Batisani & Yarnal, 2010). The study does not clearly establish the carbon sequestration budget through pedogenic carbonate, nor does it account for all potential contributors. This contrasts with certain analyses that consider all calcium input (Dietrich et al., 2017). Moreover, the impacts of land use are not considered either. Furthermore, the lack of absolute geochronological dating of the carbonate restricts the precise temporal correlation between the identified palaeoenvironmental changes and global climatic events.

9.5. Perspectives and recommendations

Future research should aim to integrate real-time monitoring of CO_2 fluxes with static SIC inventories to better understand the rate of modern carbon capture. These findings highlight the need for the Botswana government to consider the SIC in land management and the development of the National Carbon Market Framework. They also emphasise the importance for the African Union to formally incorporate SIC into its strategic vision for sustainable development. Furthermore, the high-resolution REE tracing method developed here should be applied to other basaltic landscapes worldwide to improve the global model for enhanced rock weathering (ERW). In conclusion, this thesis demonstrates that SIC is an active and quantifiable component of the Earth's climate regulation system. By transforming the "missing sink" of the African drylands into a documented and quantifiable resource, this work provides a foundation for more equitable global carbon strategies and a deeper understanding of Africa's environmental systems.

References

Batisani, N., & Yarnal, B. (2010). Rainfall variability and trends in semi-arid Botswana: Implications for climate change adaptation policy. *Applied Geography*, *30*(4), 483–489. https://doi.org/10.1016/j.apgeog.2009.10.007

Dietrich, F., Diaz, N., Deschamps, P., Ngounou Ngatcha, B., Sebag, D., & Verrecchia, E. P. (2017). Origin of calcium in pedogenic carbonate nodules from silicate watersheds in the Far North Region of Cameroon: Respective contribution of in situ weathering source and dust input. *Chemical Geology*, *460*, 54–69. https://doi.org/10.1016/j.chemgeo.2017.04.015

Raheb, A., Heidari, A., & Mahmoodi, S. (2016). Storage of organic and inorganic carbon in arid-semihumid soils: A case study of the rangelands of northwestern Iran. *Soil Science*, *181*(11–12), 473–486. https://doi.org/10.1097/SS.0000000000000183